MARCH 15, 1990

Analytical CHEMISTRY

Diode Lasers

AND PRACTICAL TRACE ANALYSIS

363 A

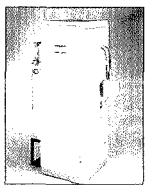

CIRCLE NUMBER 40

Questor II High-Speed Process Analyzer

Over 98.5% uptime monitoring hundreds of process streams in production plants, pilot plants and process research facilities worldwide. Fast and accurate, it replaces multiple instruments to boost efficiency and provide rapid payback. Easy communications with control and host computers, enclosures for classed environments, ready-to-use statistical packages, menu-driven software and applications support from EXTREL process engineers.
Call EXTREL Corp. at (412) 963-7530.

Laser Probe FT/MS®

New surface probe instrument combines the power of EXTREL's 2001 FT/MS® system with laser ablation and sample viewing for solving tough materials characterization problems. A versatile, easy-to-use industrial problem solver for analysis of advanced polymer, biopolymers, catalysts, ceramics, superconductors and fibers. Features high-resolution, accurate mass measurement, simultaneous measurement of all ions and MS/MS. Call EXTREL FTMS at (608) 273-8262.

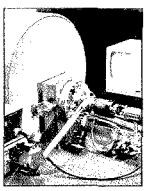

CIRCLE NUMBER 41

CIRCLE NUMBER 42

Glow Discharge Mass Spectrometer (GD/MS)

The EXT-1000 Glow Discharge Quadrupole Mass Spectrometer performs complete major and trace elemental analyses of metals and alloys. Simple one-step sample preparation, sub ppm detection limits and minimal matrix effects. Easy to calibrate and remains stable over long periods of time. For more information, contact EXTREL Corp. at (412) 963-7530.

ELQ 400-3 Triple Quadrupole MS

Perform more high-level analyses with this flexible triple quad. Provides the widest array of inletting and ionization techniques in the industry: LC, GC, SFC or probes ... EI, CI or FAB for ThermaBeam® particle beam MS. Plus, switch inletting techniques in minutes without venting. Full range of pumping options, mass ranges up to 4000 u and new 2000 data software for automatic data batching. Call EXTREL at (412) 963-7530.

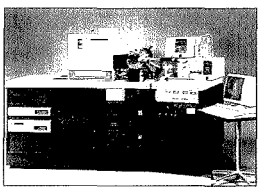

CIRCLE NUMBER 43

Components for FT/MS® and ICR

Build award-winning FT/MS® systems with the finest FT/MS® components available: data systems, electronic modules, trapped-ion cells, vacuum components and superconducting magnets. A patented dual ion source / analyzer provides excellent sensitivity for many ionization methods. Non-magnetic cells are manufactured through proprietary processes that minimize magnetic susceptibility and engineered for easy maintenance and cleaning. EXTREL FTMS components save time, money and frustration when building an FT/MS System. Call EXTREL FTMS at (608) 273-8262.

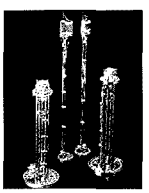

CIRCLE NUMBER 44

Superconducting Magnets for Instruments

EXTREL FTMS superconducting magnets are designed for versatility and ease of use. Large, horizontal bores provide convenient access and positioning in powerful, highly homogenous central fields. Low field drift provides high magnetic stability for long periods. Proprietary engineering means low maintenance, low coolant consumption, reliable operation and rapid installation. Available with bores up to 8 inches (20 cm) and in multiple field strengths with a variety of accessories. Call EXTREL FTMS at (608) 273-8262.

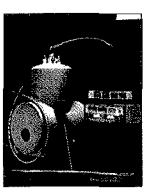

CIRCLE NUMBER 45

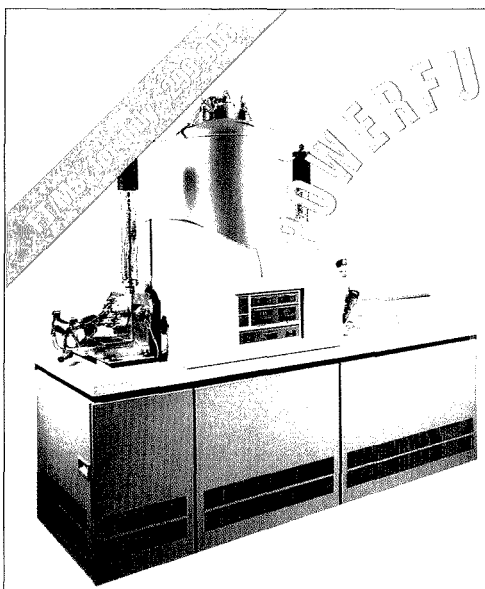

2001 Fourier Transform Mass Spectrometer

EXTREL's new 2001 FT/MS® system makes high-performance analytical mass spectrometry *affordable.* This problem solver gives you unprecedented analytical power: ultra-high resolution better than 1,000,000 at m/z 131... accurate mass-measurements better than 2 ppm ... mass ranges upwards of 16,000 u ... and pico to attomole detection limits. Plus, our patented dual ion source/analyzer design allows you to trap and then manipulate ions in both space and time.

Our revolutionary SWIFT™ method provides unmatched experimental versatility. And our software — the most powerful in the industry — is menu-driven, making it easy to use.

Power. Versatility. Ease of use. At an affordable price. Once again, EXTREL pushes technology further — giving you more in a mass spectrometer. For more information on the 2001 FT/MS® system call EXTREL FTMS today.

EXTREL FTMS • 6416 SCHROEDER ROAD • MADISON, WI 53711 • (608) 273-8262 • FAX (608) 273-8719

CIRCLE NUMBER 46

Why buy an AA that analyzes tough samples two elements at a time?

Samples/hour analyzed for 2 elements by our dual channel furnace AA.

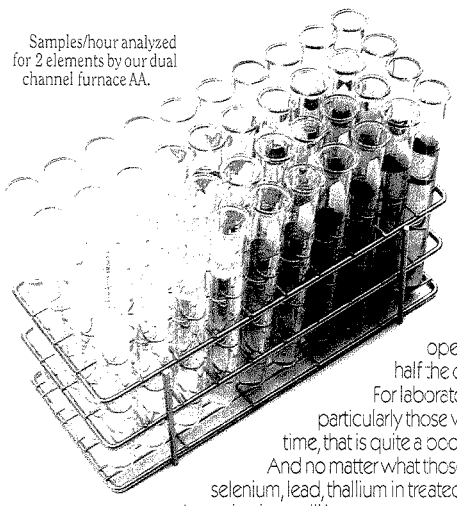

The Smith-Hieftje 22 was built for environmental and other laboratories for whom productivity, unit cost of analysis and accuracy of results are key concerns.

This dual channel Flame/Furnace AA spectrophotometer with Prep Station and Sample Changer costs approximately the same as a comparable single channel instrument, and yet, in the hands of a single operator, it can do twice as many determinations per day, at half the cost per determination.

For laboratories with a fixed or growing sample load, particularly those who are concerned about turn around time, that is quite a boon.

And no matter what those laboratories are measuring – arsenic, selenium, lead, thallium in treated water, seawater or sludge – the determinations will be accurate every single time.

That's because the Smith-Hieftje 22 employs the Smith-Hieftje background correction system – vastly superior to deuterium and recommended by the EPA* – and is equipped with the Delayed Atomization Cuvette (DAC) and aerosol sampling device, innovations which virtually eliminate vapor and solid phase matrix interferences.

Method development, run initiation, and the display and printing of results are all menu-driven, and, therefore, can be quickly learned even by a novice operator, and sophisticated software allows for overnight unattended operation.

And the Smith-Hieftje 22 comes complete with a full program of service and support including installation, documentation, user training, warranty and field service.

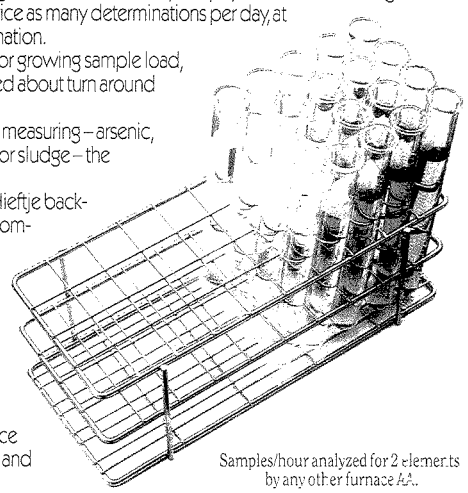

Samples/hour analyzed for 2 elements by any other furnace AA.

For an appointment to see our new Smith-Hieftje 22 AA Spectrophotometer in operation, call (508) 520-1880. Or write Thermo Jarrell Ash Corporation, 8 E Forge Parkway, Franklin, MA 02038-9101.

*EPA Test Methods for Evaluating Solid Waste, Vol 1A, two-17, Sept 1986

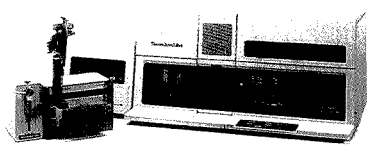

Smith-Hieftje 22 Flame/Furnace AA Spectrophotometer With Prep Station & Sample Changer

Correction Method	Arsenic True Value	Arsenic Determined Value
Smith-Hieftje	32.4 ppb	32.1 ppb
Deuterium	32.4 ppb	56.0 ppb

The EPA recommends Smith-Hieftje background correction over deuterium, largely on the basis of performance evaluation results such as shown here.

Thermo Jarrell Ash Corporation

A Division of Thermo Instrument Systems, Inc.

CIRCLE 135 ON READER SERVICE CARD

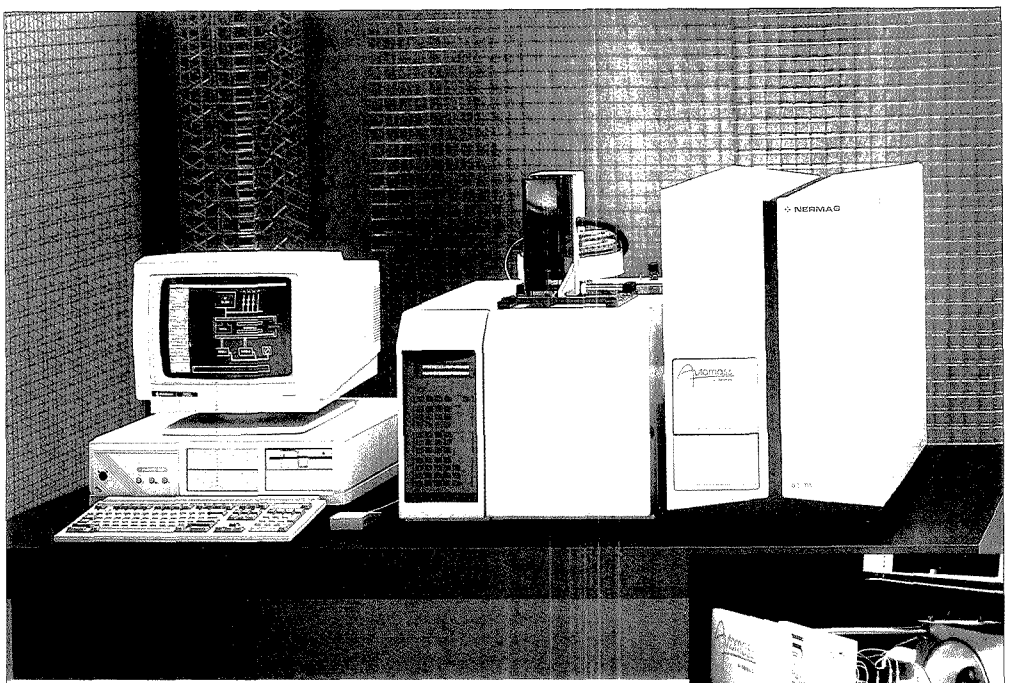

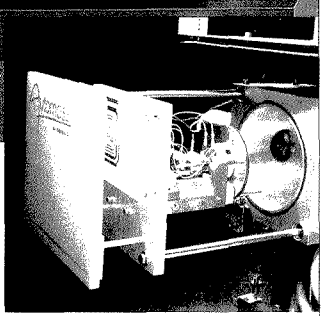

Automass

The Power of Original Thinking

When Nermag set out to develop the premier Automated Benchtop GC/MS Workstation, we were aware there was a need - *your need*, for more analytical power. Power that is simple to use, yet flexible enough to tackle the toughest problems. A true research-grade mass spectrometer was required, not a compromised mass analyzer camouflaged by glitzy game-show software.

Introducing Automass, the benchtop mass spectrometer that only Nermag could build, and the only one of its kind in the world today. The basis of Automass is a state of the art quadrupole with plug-in prefilters and an optimized Ionization Source for EI, CI, and negative ions. Our original Off Axis Ion - Photon Conversion Detector and patented Resolver electronics are enhanced by a differentially pumped vacuum system for real CI spectra.

Automass is controlled by our exclusive LUCY™ software. LUCY does window after window of instrument configuration setting, auto or manual tuning, calibration, mass spectra, chromatographic trace, and data reduction; while simultaneously examining the complete library and quantifying results. You'll Love LUCY.

Automass can flawlessly perform routine analysis all day virtually unattended, or help you tackle the most difficult analytical problem.

Automass advances Mass Spectrometry into the 90's.

Powerfully.

DELSI NERMAG INSTRUMENTS

France: Delsi-Nermag Instruments, 98terBlvd. Heloise, Argenteuil 9500. Tel: (1) 39.47.66.22, Fax : (1) 39.47.85.66
USA: Delsi Inc., 15701 West Hardy Rd. Houston, TX 77060. Tel: (713) 847-0811, Fax (713) 591-2132
Netherlands: Delsi Instruments BV, Gebouw aetsvelt, van Houten Ind Pk 11, 1381 Weesp, Tel: (0)2940-19611
U.K.: Delsi Instruments Ltd, 38 Thrapston Rc., Brampton, Huntington, Cambs PE 18 8TE, Tel: 0480 431 609
West Germany: Delsi Instruments Gmbh, Oizbachstr 1 D4020 Metimann, Tel. 02104/25086-87-88
Belgium: Intersmatt, 103, Av. des Volontaires, 1160 Bruxelles, Tel: 2 733.16.32

CIRCLE 30 ON READER SERVICE CARD

MARCH 15, 1990
VOLUME 62
NUMBER 6

The Audit Bureau
ANCHAM
62(6) 347A-400A/545-656 (1990)
ISSN 0003-2700

ANALYTICAL CHEMISTRY (ISSN 0003-2700) is published semimonthly by the American Chemical Society at 1155 16th St., N.W., Washington, DC 20036. Editorial offices are located at the same ACS address (202-872-4570; FAX 202-872-4574; TDD 202-872-8733). Second-class postage paid at Washington, DC, and additional mailing offices. Postmaster: Send address changes to ANALYTICAL CHEMISTRY Member & Subscriber Services, P.O. Box 3337, Columbus, OH 43210.

Claims for missing numbers will not be allowed if loss was due to failure of notice of change of address to be received in the time specified; if claim is dated (a) North America: more than 90 days beyond issue date, (b) all other foreign: more than one year beyond issue date, or if the reason given is "missing from files."

Advertising Management: Centcom, Ltd., 500 Post Rd. East, Westport, CT 06880 (203-226-7131)

1990 subscription rates include air delivery outside the U.S., Canada, and Mexico

	1 yr	2 yr
Members		
Domestic	$ 29	$ 49
Canada and Mexico	64	119
Europe	96	183
All Other Countries	118	227
Nonmembers		
Domestic	59	100
Canada and Mexico	94	170
Europe	186	336
All Other Countries	208	380

Three-year and other rates contact: Member & Subscriber Services, ACS, P.O. Box 3337, Columbus, OH 43210 (614-447-3776 or 800-333-9511).

Subscription orders by phone may be charged to VISA, MasterCard, Barclay card, Access, or American Express. Call toll free 800-ACS-5558 in the continental United States; in the Washington, DC, metropolitan area and outside the continental United States, call 202-872-8065. Mail orders for new and renewal subscriptions should be sent with payment to the Business Management Division, ACS, P.O. Box 28597, Central Station, Washington, DC 20005.

Subscription service inquiries and changes of address (Include both old and new addresses with ZIP code and *recent mailing label*) should be directed to the ACS Columbus address noted above. Please allow six weeks for changes to become effective.

ACS membership information: Lorraine Bowlin (202-872-4567)

Single issues, current year, $8.00 except review issue, $14.00, and LabGuide, $49.00; **back issues and volumes and microform editions** available by single volume or back issue collection. For information or to order, call the number listed for subscription orders by phone; or write the Microform & Back Issues Office at the Washington address.

Nonmembers rates in Japan: Rates above do not apply to nonmember subscribers in Japan, who must enter subscription orders with Maruzen Company Ltd., 3-10 Nihonbashi 2-chome, Chuo-ku, Tokyo 103, Japan. Tel: (03) 272-7211.

Analytical® CHEMISTRY

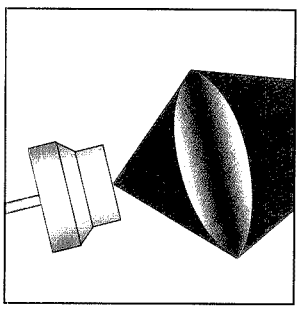

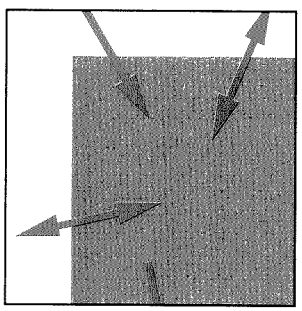

INSTRUMENTATION **363 A**

On the cover. **Diode lasers and practical trace analysis.** Diode lasers are smaller than conventional lasers, have a lifetime of $\sim 10^5$ h, and have a high conversion efficiency from electricity to light. Totaro Imasaka and Nobuhiko Ishibashi of Kyushu University (Japan) describe state-of-the-art implementation of diode lasers, optical fibers, and electrooptical components in analytical instrumentation

A/C INTERFACE **389 A**

Local area networks in the laboratory. Deciding what information is required, who needs it, and where it should go is the first step in successfully implementing a laboratory LAN. In the second of a two-part series, Steven A. Warner of ANDRULIS Research Corporation describes the necessary planning process and examples of commercially available solutions

BRIEFS **354 A**

NEWS **361 A**

Call for nominations for **1991 Division of Analytical Chemistry Awards.** ▸ International garbage

MEETINGS **373 A**

11th International Symposium on Capillary Chromatography. ▸ Third Symposium on Computer-Enhanced Analytical Spectroscopy. ▸ Conferences. ▸ Short courses and workshops. ▸ Call for papers

BOOKS **378 A**

Textbooks. College textbooks in analytical chemistry are reviewed by Paul Bohn, Petr Zuman, Galen W. Ewing, Steven D. Brown, and Stephen N. Chesler

FOCUS **383 A**

PACIFICHEM '89. More than 7400 scientists attended the Second International Chemical Congress of Pacific Basin Societies, held December 17–22 in Honolulu. Speakers emphasized the need for policy decisions to be based on sound scientific knowledge

NEW PRODUCTS & MANUFACTURERS' LITERATURE **386 A**

AUTHOR INDEX **545**

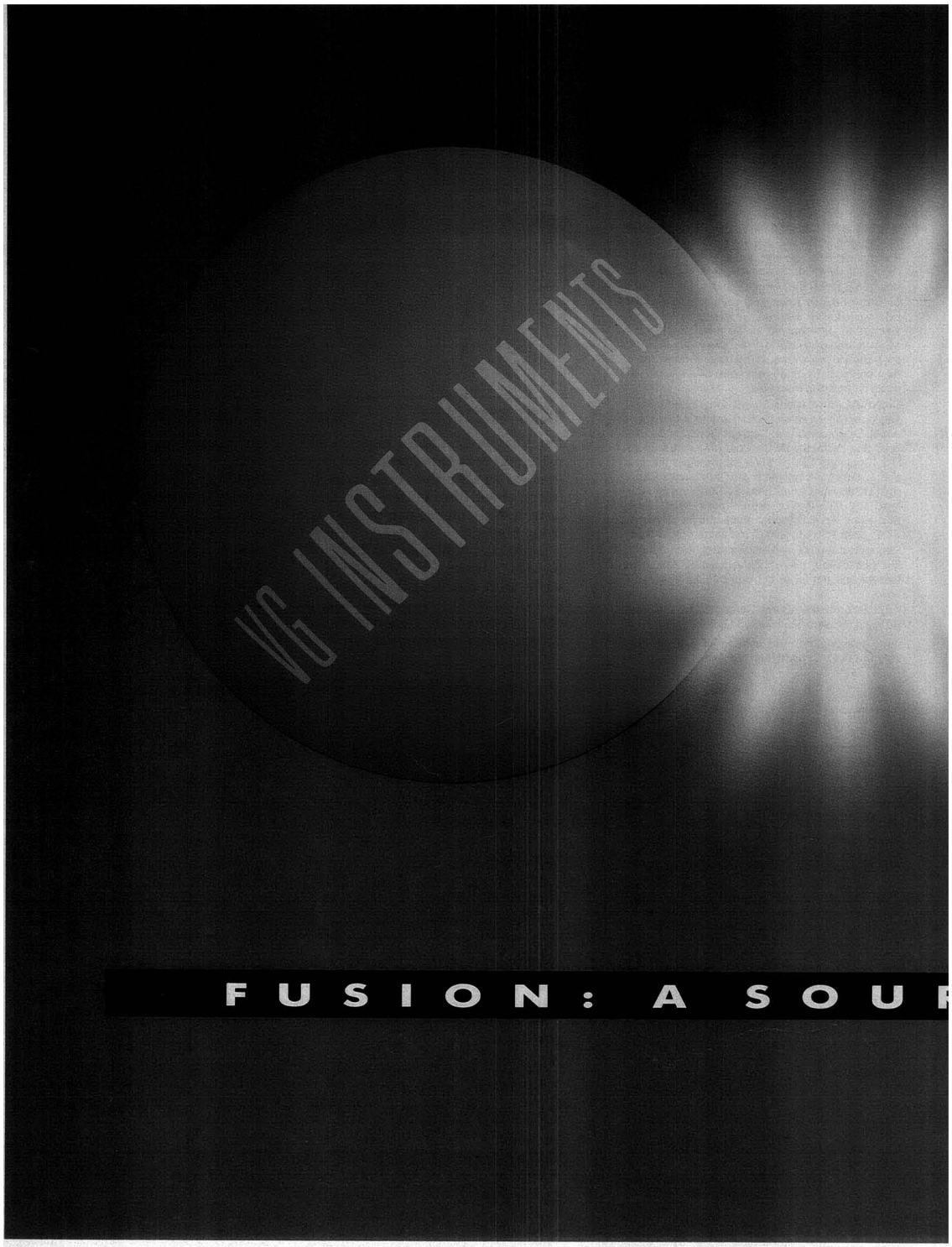

A R L CARLO ERBA INSTRUMENTS HAAKE

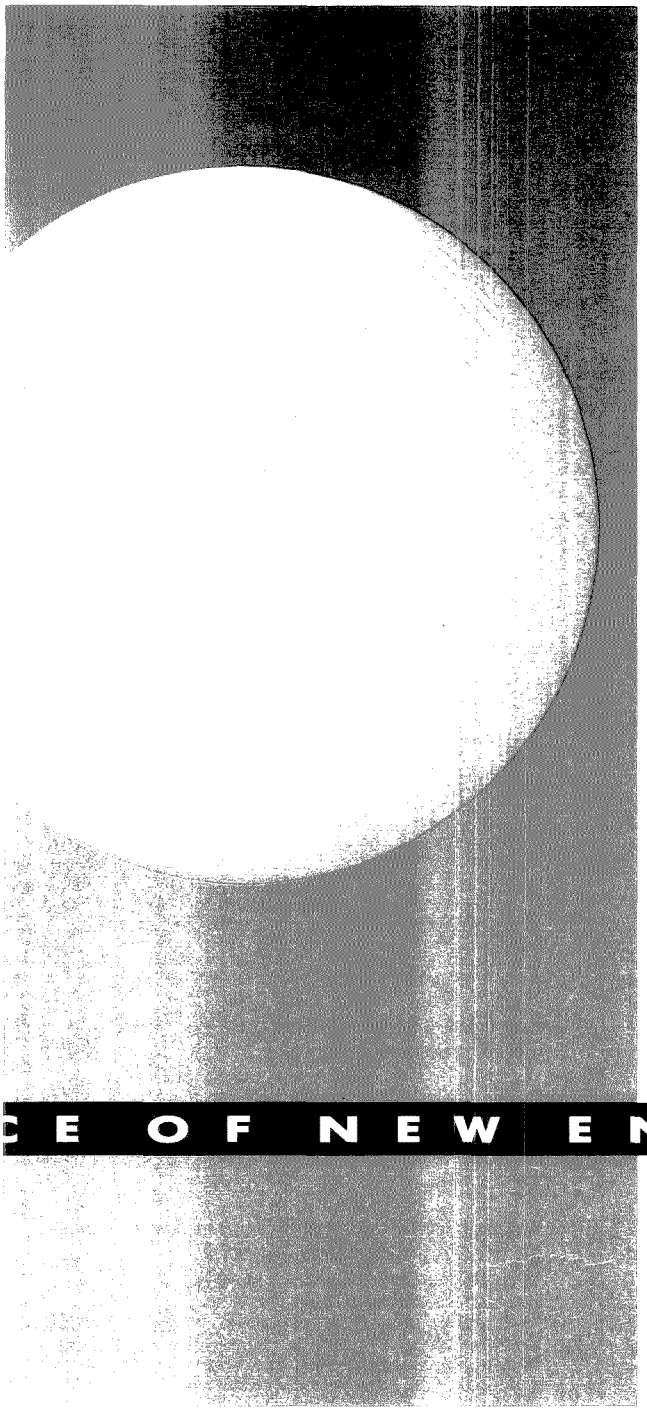

There is a new, vibrant source of energy in the world of analytical instrumentation. The VG Group has just joined forces with a company that has a proven record in fostering the talents and services of innovative, specialised companies. That company is Fisons and with this important acquisition Fisons Instruments is now among the very largest analytical instrumentation enterprises in the world.

VG is the most recent instrument company to join this highly successful parent. Among its companies Fisons Instruments already counts other well-known market leaders like ARL, Carlo Erba Instruments and Haake.

What did companies with marked success in their own right stand to gain from this fusion?

Simply, more energy for their business and their customers. A new dynamic environment that promotes the fusion of ideas from many technologies, producing rapid advancements in hyphenated techniques. A huge pool of expertise and resources to promote creativity and turn concepts into realities. And the power of one of the largest customer support networks in the scientific world behind them.

The VG Group is known worldwide as the leading innovator in mass and X-ray spectrometry, surface analysis and ultra-high vacuum technology. Fisons is internationally respected as the company that really helps its customers to benefit from the latest advances in analytical instrumentation.

Together they become your indispensable partners in scientific endeavour.

Whatever your own field of work, let us tell you more about the choices now open to you through the new Fisons Instruments. Contact us for a copy of our brochure.

E OF NEW ENERGY

FISONS Instruments

Fisons Instruments, 24911 Avenue Stanford, Valencia, CA 91355, USA
Telephone: (800) 551-8741 Interstate
(800) 631-6841 California

KEVEX VG INSTRUMENTS

CIRCLE 50 ON READER SERVICE CARD

BRIEFS

Articles

Analytical Strategies Using Interdigitated Filar Microelectrodes 546

The transient current response of twin interdigitated filar electrodes is measured and compared with the analytic solutions and digital simulations of the electrochemical boundary value problem.

M. S. Harrington and L. B. Anderson*, Department of Chemistry, The Ohio State University, 120 West 18th Avenue, Columbus, OH 43210

Determination of Trace-Element Deposition Parameters from Electrolytic Preconcentration Transients 550

A method for the estimation of the mass transfer coefficient and the specific rate of deposit dissolution from experimental preconcentration transients is described.

Roman E. Sioda, Institute of Industrial Chemistry, Warsaw 01-793, Poland and **Thomas Z. Fahidy***, Department of Chemical Engineering, University of Waterloo, Waterloo, Ontario, Canada N2L 3G1

Determination of Barium in Seawater Using Vanadium/Silicon Modifier and Direct Injection Graphite Furnace Atomic Absorption Spectrometry 553

A V_2O_5/Si modifier is used to determine Ba in seawater. Sensitivity is 0.8 absorbance s/ng (M_o = 5.6 pg/0.0044 absorbance s). The detection limit is 2.5 pg Ba in a 25-μL sample. Precision is 1–2% and accuracy is 2–3%.

James K. B. Bishop, Lamont-Doherty Geological Observatory of Columbia University, Palisades, NY 10964

Single Optical Fiber, Position-Sensitive Detector-Based Multiwavelength Absorbance Spectrophotometer 558

The spectrophotometer provides a 1.1×10^{-4} AU detection limit when used as a microbore LC detector. Molar absorptivity ratios of eluting peaks are simultaneously provided.

Curtiss N. Renn and Robert E. Synovec*, Center for Process Analytical Chemistry, Department of Chemistry, BG-10, University of Washington, Seattle, WA 98195

Optimization of γ-Ray Spectrometric and Other Measurements Yielding Biased Results by Means of Information Theory 565

Information quantities can be used for the optimization of analytical procedures yielding results with various levels of precision and bias. Advantages of this approach are demonstrated with a γ-counting experiment.

Ivan Obrusník* and Karel Eckschlager, Nuclear Physics Institute, Czechoslovak Academy of Sciences, 250 68 Řež, Czechoslovakia, and Institute of Inorganic Chemistry, Czechoslovak Academy of Sciences, 250 68 Řež, Czechoslovakia

General Least-Squares Smoothing and Differentiation by the Convolution (Savitzky–Golay) Method 570

The convolution approach to least-squares smoothing and differentiation (Savitzky–Golay technique) is extended to cover all points in the spectrum for all orders, filter lengths, and derivatives.

Peter A. Gorry, Department of Chemistry, University of Manchester, Manchester, England M13 9PL

Pulsed and Transient Modes of Atomization by Cathodic Sputtering in a Glow Discharge for Atomic Absorption Spectrometry 574

The pulsed and transient modes of atomization for a cathodic sputtering atomizer are described and shown to be more sensitive than the conventional steady-state mode of atomization.

Chuni L. Chakrabarti*, Kurt L. Headrick, J. Craig Hutton, Zhang Bicheng, Peter C. Bertels, and Margaret H. Back, Department of Chemistry, Carleton University, Ottawa, Ontario K1S 5B6, Canada, and Department of Chemistry, University of Ottawa, Ottawa, Ontario K1N 9B4, Canada

Long Path Atomic/Ionic Absorption Spectrometry in an Inductively Coupled Plasma 586

The ability to perform long path atomic and ionic absorption in an ICP with detection limits comparable to those of commercial AA spectrometry is demonstrated.

Michael A. Mignardi, Benjamin W. Smith, and James D. Winefordner*, Department of Chemistry, University of Florida, Gainesville, FL 32611

Mass Spectrometric System for the Measurement of Aroma/Flavor Permeation Rates across Polymer Films 592

An MS system with a flow-through hollow fiber interface is developed to measure permeability, diffusivity, and solubility of gaseous aroma/flavor constituents at the ppm level in polymeric films.

J. C. Tou*, D. C. Rulf, and P. T. DeLassus, The Analytical Sciences Laboratories, The Dow Chemical Company, Midland, MI 48667

* Corresponding author

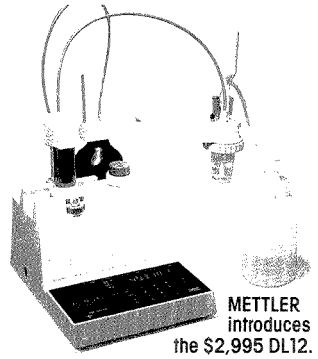

METTLER introduces the $2,995 DL12.

The DL12 Autotitrator. Because no two people see things exactly the same.

You might see two profiles. Someone else, a crystal goblet.

Which illustrates the fact that subjective judgments are hardly the stuff of consistent analysis. Unfortunately for many smaller labs, objective pH determination has just been too costly.

Enter the DL12—a low-cost autotitrator that brings you METTLER accuracy at an unheard-of price. And exit the subjective determination of pH end points.

With a crystal-clear display, the DL12 brings any lab or quality control department expanded pH measurement capabilities. Offers static measurements to ±.002 units. And records results in user-selected increments.

But accuracy is only half the picture. The METTLER DL12 is also faster and more cost effective than manual burettes. So it's perfect for anyone involved in repetitive titrations for both in-process and end-product quality control.

Just call 1-800-METTLER, and we'll have you seeing eye-to-eye in no time.

CIRCLE 92 ON READER SERVICE CARD

Mettler Instrument Corporation
Box 71
Hightstown, NJ 08520
1-800-METTLER
(NJ 1-609-448-3000)

METTLER

We understand.
Precisely.

In Vivo Microdialysis and Thermospray Tandem Mass Spectrometry of the Dopamine Uptake Blocker 1-[2-[Bis(4-fluorophenyl)methoxy]ethyl]-4-(3-phenylpropyl)-piperazine (GBR-12909) 597

In vivo concentrations of the dopamine uptake blocker GBR-12909 are determined by microdialysis in conjunction with thermospray ionization and tandem MS.

Stanley D. Menacherry and Joseph B. Justice, Jr.*, Department of Chemistry, Emory University, Atlanta, GA 30322

Adduct Ion Formation in the Methane-Enhanced Negative Chemical Ionization Mass Spectrometry of 2-(Alkylthio)- and 2-Alkoxy-*s*-triazines 602

Using quadrupole MS, HRMS, and CAD MS/MS, it is shown that adduct ions observed at significant abundance in the NCI MS of 2-(alkylthio)- and 2-alkoxy-*s*-triazine compounds originate from reactions between the methane enhancement gas and the *s*-triazine.

M. J. Incorvia Mattina and Lee Q. Huang*, Department of Analytical Chemistry, The Connecticut Agricultural Experiment Station, P.O. Box 1106, New Haven, CT 06504 and **Roger N. Hayes**, Midwest Center for Mass Spectrometry, University of Nebraska, Lincoln, NE 68588

Microchannel Plate for Surface-Induced Dissociation in Mass Spectrometry 609

A method for surface-induced dissociation applied to MS uses an inline microchannel electron multiplier plate as the collision target to obtain efficient molecular ion fragmentation at relatively high translational energy.

William Aberth, University of California, Department of Pharmaceutical Chemistry, Mass Spectrometry Facility, San Francisco, CA 94143-0446

Suspension Postcolumn Reaction Detection Method for Liquid Chromatography 612

A detection method for LC uses the addition of a colloidal suspension postcolumn to the eluant stream. The solid-phase suspension reagent produces detectable peaks but has a low background signal.

Douglas T. Gjerde*, Sarasep, Inc., 1600 Wyatt Drive, Suite 10, Santa Clara, CA 95054 and **James V. Benson**, Benson Polymeric, Inc., 4255 Garlan Lane, Reno, NV 89509

Nile Red as a Solvatochromic Dye for Measuring Solvent Strength in Normal Liquids and Mixtures of Normal Liquids with Supercritical and Near Critical Fluids 615

The solvent strength of normal liquids and modified supercritical fluids is measured using Nile Red as a solvatochromic probe. The impact of observed nonlinearities in solvent strength versus composition on chromatographic retention is discussed.

Jerry F. Deye and T. A. Berger*, Hewlett-Packard, P.O. Box 900, Route 41 and Starr Road, Avondale, PA 19311-0900 and **Albert G. Anderson**, Central Research and Development Department, E. I. du Pont de Nemours and Co., Wilmington, DE 19880-0328

Extraction of Tervalent Lanthanides as Hydroxide Complexes with Tri-*n*-octylphosphine Oxide 622

A selective extraction system for tervalent lanthanides is based on the extraction of their hydroxides using tri-*n*-octylphosphine oxide in chloroform.

Ted Cecconie and Henry Freiser*, Strategic Metals Recovery Research Facility, Department of Chemistry, University of Arizona, Tucson, AZ 85721

Reshaping of Staircase Voltammograms by Discrete Spherical Convolution 625

A method for transforming a reversible staircase voltammogram, obtained at a spherical electrode, into a neopolarographic wave is presented.

Sten O. Engblom* and Keith B. Oldham, Department of Chemistry, Trent University, Peterborough, Ontario K9J 7B8, Canada

Continuous Generation System for Low-Concentration Gaseous Nitrous Acid 630

Nitrous acid vapor at ppb levels is generated by the reaction of sodium nitrite solution with sulfuric acid. Variations in nitrous acid output are achieved by adjusting sodium nitrite concentration.

Masafumi Taira and Yukio Kanda*, National Laboratory for High Energy Physics, Oho, Tsukuba, Ibaraki-ken, 305 Japan

Enhanced Signal-to-Noise Ratios in the Nuclear Magnetic Resonance Analysis of Solids, Using Large-Sample Magic-Angle Spinners 633

The development of large-volume, magic-angle spinning devices for solid-state NMR has increased S/N ratios. As a result, natural abundance ^{15}N NMR analysis is possible for synthetic polymers and proteins and the time-vs.-S/N characteristics for many types of ^{29}Si NMR analyses are improved.

Ming Zhang and Gary E. Maciel*, Department of Chemistry, Colorado State University, Fort Collins, CO 80523

Jet-Enhanced Sputtering Cell as an Ion Source for Mass Spectrometry 639

A jet-enhanced sputtering cell is interfaced to the mass spectrometer of an ICP/MS, replacing the ICP; and the effects of pressure, current, anode voltage, sampling distance, and sampling flange orifice diameter are studied to improve analytical performance.

Hyo J. Kim and Edward H. Piepmeier*, Department of Chemistry, Oregon State University, Corvallis, OR 97331 and **Gary L. Beck, Gary G. Brumbaugh, and O. Thomas Farmer, III**, Analytical Laboratory, Teledyne Wah Chang Albany, Albany, OR 97321

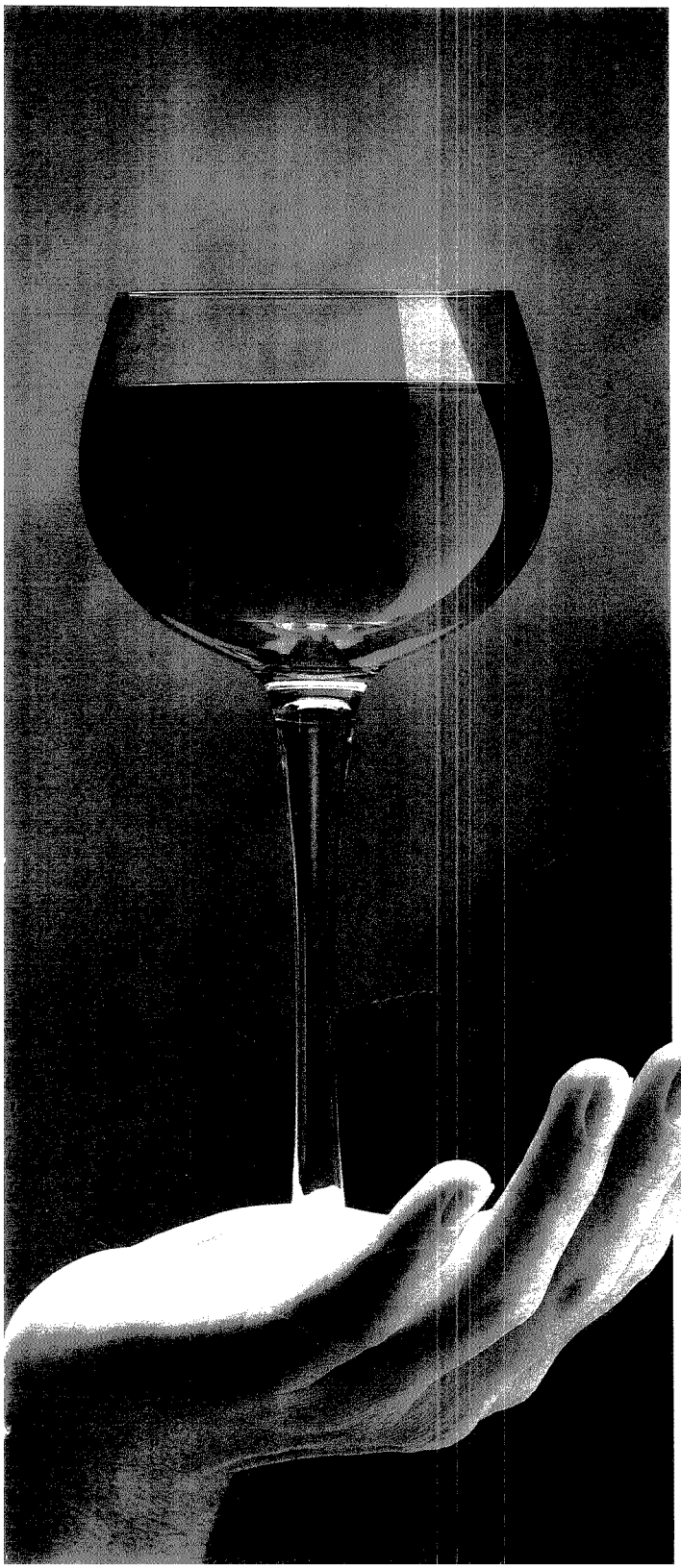

DABS brings stability to reversed phase amino acid analysis.

Stability. It's more than holding something steady for just a moment. It's *keeping* it that way. For a long, long time.

With DABS you won't measure derivative stability in minutes. Or even hours. DABS remains stable for weeks.

So you can do repeated runs from the same sample. Or go back days later and analyze a sample again using the same derivative, the same method — without changes.

And DABS only takes minutes to set up with our exclusive Dabsylation Kit.

Add the advantages of visible detection, and DABS is obviously the wise choice for high speed, high sensitivity amino acid analysis.

System Gold

And because you'll be using the world's easiest, most advanced HPLC — System Gold,™ the Personal™ Chromatograph — you'll have guaranteed methods and reference chromatograms available on disk.

To add stability to your reversed phase amino acid analyses, contact your local Beckman representative. Offices in major cities worldwide.

Call 800/742-2345 in the US. Or write Beckman Instruments, Inc., Altex Division, 2350 Camino Ramon, P.O. Box 5101, San Ramon, CA 94583.

BECKMAN

Australia, Sydney. **Austria**, Vienna. **Canada**, Toronto. **Denmark**, Birkerød. **France**, Gagny. **Germany**, Munich. **Hong Kong**, Aberdeen. **Italy**, Milano. **Japan**, Tokyo. **Mexico**, Mexico City. **Netherlands**, Mijdrecht. **Norway**, Oslo. **Puerto Rico**, Carolina. **Singapore**. **South Africa**, Johannesburg. **Spain**, Madrid. **Sweden**, Bromma. **Switzerland**, Nyon. **Taiwan**, Taipei. **United Kingdom**, High Wycombe. **United States**, San Ramon. AX88-1025

Circle 15 to send Representative and Literature.
Circle 16 for Literature only.

BRIEFS

Bicontinuous Microemulsions as Media for Electrochemical Studies 644

Electroactive species dissolved in oil or water microphases of a conductive, bicontinuous microemulsion of didodecyldimethylammonium bromide/dodecane/water undergo voltammetry as if they are in a homogenous medium. PAHs are reduced by an ECE-type pathway with nearly reversible cyclic voltammograms at high scan rates.

Maurice O. Iwunze, Artur Sucheta, and James F. Rusling*, Department of Chemistry (U-60), University of Connecticut, Storrs, CT 06269-3060

Correspondence

Ion-Exchange Electrokinetic Chromatography with Polymer Ions for the Separation of Isomeric Ions Having Identical Electrophoretic Mobilities 650

Shigeru Terabe* and Tsuguhide Isemura, Department of Industrial Chemistry, Faculty of Engineering, Kyoto University, Sakyo-ku, Kyoto 606, Japan

Technical Notes

Preparative Method for Fabricating a Microelectrode Ensemble: Electrochemical Response of Microporous Aluminum Anodic Oxide Film Modified Gold Electrode 652

Kohei Uosaki*, Kentaro Okazaki, and Hideaki Kita, Department of Chemistry, Faculty of Science, Hokkaido University, Sapporo 060, Japan and **Hideaki Takahashi,** Analytical Chemistry Laboratory, Faculty of Engineering, Hokkaido University, Sapporo 060, Japan

Correction. Manual Headspace Method To Analyze for the Volatile Aromatics of Gasoline in Groundwater and Soil Samples 656

Valerie D. Roe, Michael J. Lacy, and James D. Stuart*, Department of Chemistry, U-60, 215 Glenbrook Road, University of Connecticut, Storrs, CT 06269-3060 and **Gary A. Robbins,** Department of Geology and Geophysics, U-45, 345 Mansfield Road, University of Connecticut, Storrs, CT 06269-3045

Backed by Matheson's more than 60 years of experience.

Questionable quality of standard gases or calibration mixtures is intolerable. Purity and consistency are the by-words of the analytical chemist.

Matheson's experience and reputation as a supplier of the highest quality laboratory gases and mixtures eliminate uncertainty. Each Matheson UHP, Zero Gas, and Matheson Purity Gas is guaranteed to be exactly what the label says. Nothing more. Nothing less. Matheson Primary Standards are of the highest accuracy. Our complex calibration standards required in gas chromatography are the benchmark of the industry. And. our gas handling equipment will never jeopardize the integrity of our gases.

So whether your work is in the field of pharmaceuticals, petroleum, lasers, or aerospace. . . insist on quality. Insist on Matheson.

APPLICATIONS

Atomic Absorption Spectroscopy

Calibration Standards

Primary Standards
Certified Standards

Gas Chromatography Detectors

DID	Discharge Ionization Detector
ECD	Electron Capture Detector
FID	Flame Ionization Detector
FPD	Flame Photometric Detector
GADE	Gas Density Detector
HECD	Hall Electroconductivity Detector
HID	Helium Ionization Detector
NPD	Nitrogen Phosphorus Detector
PID	Photoionization Detector
TCD	Thermal Conductivity Detector
TID	Thermionic Ionization Detector

Supercritical Fluid Chromatography

Medical / Biological

Blood Gas Analysis
Pulmonary Function
Surgical Lasers
Biological Atmospheres

Flame Photometry

Nuclear Counters

Emissions Testing

E.P.A. Protocol

Burner Calibration (BTU Verification)

Leak Detection

Matheson®
Gas Products
World Leader in Specialty Gases & Equipment
30 Seaview Dr., Secaucus, NJ 07096-1587
FAX: (201) 867-4572

CIRCLE 90 ON READER SERVICE CARD

Me? Enroll in the ACS Employment Service?

I'm head of a major research department!

Even for the successful chemist or scientist in an allied field, sometimes the best way to get ahead is to make a change.

The ACS Employment Service offers the opportunity to investigate the possibilities discreetly—and at very low cost.

Our Employment Service is free to all ACS members. If you request confidentiality from current employers or other designated organizations there is a nominal charge.

For more information write, use coupon, or CALL TOLL FREE 800-227-5558

Employment Services Office,
American Chemical Society
1155 Sixteenth Street, NW,
Washington, DC 20036

Yes. I am a member of ACS and I would like to learn how the ACS Employment Service can help me advance my career.

Name (please print) _____

Membership # _____

Address _____

_____

City _____

State _____ ZIP _____

Nominations Sought for 1991 ACS Division of Analytical Chemistry Awards

Nominations are being solicited for the 1991 Division of Analytical Chemistry Awards in Chemical Instrumentation, Excellence in Teaching, Spectrochemical Analysis, and Electrochemistry. All four awards will be presented at the 1991 fall ACS national meeting in New York City.

The **Award in Chemical Instrumentation,** sponsored by Dow Chemical Co., is given to an individual who has advanced the field of chemical instrumentation and has achieved one or more of the following:

- conceptualized and developed unique instrumentation that has made a significant impact on the field
- demonstrated innovative use of instrumentation in chemical measurement
- stimulated the use of instrumentation in chemical measurement by other researchers
- published research papers or books that have had an influence on the use of chemical measurement

The **Award for Excellence in Teaching,** cosponsored by the Division and Du Pont, recognizes a scientist who has enhanced the personal and professional development of students studying analytical chemistry in one or more of the following ways:

- published an influential textbook for an analytical chemistry course
- designed and implemented a successful new approach for teaching analytical chemistry
- encouraged through teaching or research mentorships a significant number of students to become analytical chemists
- developed and published innovative experiments
- designed improved equipment for teaching labs
- published widely quoted articles on teaching analytical chemistry

The **Awards in Spectrochemical Analysis** (sponsored by Perkin-Elmer Corp.) and **Electrochemistry** (sponsored by EG&G Princeton Applied Research) are presented to individuals who have advanced the fields of spectrochemical analysis and optical spectrometry or the field of electrochemical analysis, respectively.

Candidates for these awards must have achieved one or more of the following:

- conceptualized and developed unique instrumentation that has a significant impact on the field
- developed novel and important instrumentation or methods
- elucidated fundamental events or processes involved in or important to the field
- published research papers or books that influence the development of the field

Each award consists of a $4000 honorarium, a plaque, and a travel allowance to the 1991 fall ACS national meeting. Nominees must be members of the Division, and all nominees for the Excellence in Teaching Award must have been full-time faculty members of U.S. or Canadian colleges or universities for at least five years at the time the award is presented.

Nominating documents should include a letter of recommendation, one or more seconding letters, and a brief biographical sketch emphasizing the candidate's accomplishments. Nomination materials should not exceed 12 pages of text and must be sent in one package by Sept. 1 to Gary Christian, Department of Chemistry, University of Washington, Seattle, WA 98195.

Garbage Report

In a survey of 11 industrialized nations, Americans have the dubious honor of producing the most garbage. According to a technical brief prepared for the American Society of Mechanical Engineers (ASME), U.S. households average 3.6 lb of trash daily. Canadians, just behind Americans in the survey, generate 3.4 lb each day.

Most of this North American trash ends up in landfills. Eighty percent of U.S. waste is buried, 10% is incinerated, and 10% is recycled. In Canada, 90% of the waste is put in landfills and just 12 waste incinerators burn a small percentage of the remainder. (The United States has 172 such facilities.)

In Switzerland and Japan, 80% and 70% of the garbage, respectively, is incinerated. Furthermore, the Swiss recycle most of their remaining waste, including batteries and fluorescent bulbs that are returned to retailers or special collection sites. Battery collection sites are also maintained in Amsterdam, and West German manufacturers are required to accept "button" batteries for recycling.

For more information, request a copy of the report, "Overview of International Solid Waste Management Methods," from ASME State Government Relations, 1825 K Street, N.W., Suite 218, Washington, DC 20006.

For Your Information

The National Institute of Standards and Technology (NIST) has prepared a **standard reference material for measuring 11 polycyclic aromatic hydrocarbons (PAHs) in marine sediment.** The material, collected from the Chesapeake Bay near Baltimore's harbor, also contains noncertified concentrations of other PAHs, polychlorinated biphenyls, and chlorinated pesticides. For more information, contact the Office of Standard Reference Materials, NIST, Room 204, Building 202, Gaithersburg, Md 20899 (301-975-6776).

NIST has also released a **PC version of a reference database that provides calculations of electron and positron stopping powers and ranges for various materials.** The database also provides continuous-slowing-down approximation ranges and the radiation yields for electrons or positrons with kinetic energies from 1 keV to 10 GeV. For more information, contact the Office of Standard Reference Data Programs, NIST, A323 Physics Building, Gaithersburg, Md 20899 (301-975-2208).

NOW YOU CAN SEARCH RSC JOURNALS ONLINE

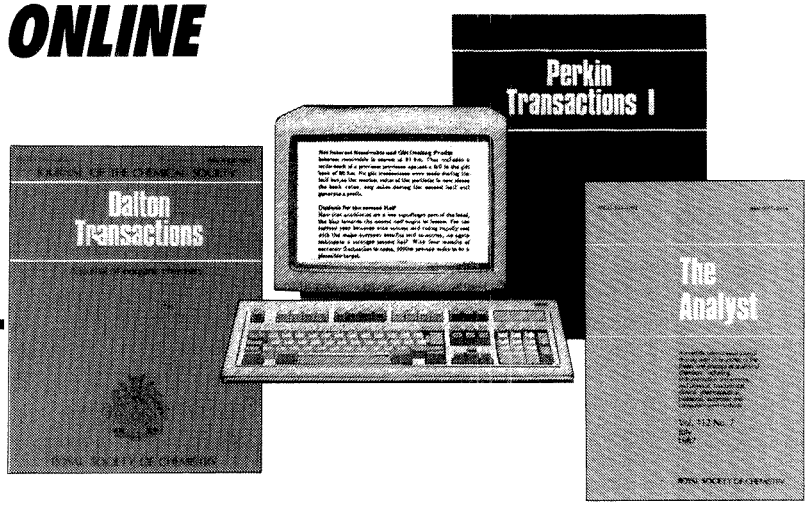

The main primary journals published by the Royal Society of Chemistry (RSC) are now searchable online via **CHEMICAL JOURNALS ONLINE (CJO)** – a family of new online files produced by the American Chemical Society and available through STN International.

The RSC journals file **(CJRSC)** includes Chemical Communications. Dalton Transactions. Faraday Transactions (I* & II). Perkin Transactions (I & II). The Analyst. Journal of Chemical Research.* Journal of Analytical Atomic Spectrometry. Faraday Discussions.
*Available from 1988

CJRSC may be searched alone or in conjunction with other components of the **CJO** database which includes ACS journals and polymer journals published by Wiley.

The unique Crossover facility from STN enables you to perform the same search on CJRSC and CAS ONLINE thereby combining the breadth of coverage of Chemical Abstracts with the depth of coverage of RSC journals.

Online access to the RSC journals provides you with a convenient, rapid and economical means of keeping up with the latest significant research in the chemical sciences.

For more information, call (614) 421-3600, or return the form below to: STN International, c/o Chemical Abstracts Service, 2540 Olentangy River Road, P.O. Box 02228, Columbus, OH 43210.

Please send me more information on CJRSC and the Chemical Journals Online data base.

Name .....

Address .....

.....

.....

CHEMICAL JOURNALS ONLINE

Diode Lasers AND PRACTICAL TRACE ANALYSIS

Totaro Imasaka and Nobuhiko Ishibashi
Faculty of Engineering
Kyushu University
Hakozaki, Fukuoka 812
Japan

The laser has many advantages as a light source because of its beam-focusing capability and large photon flux. It has been used in atomic and molecular spectrometries, and provides ultrahigh sensitivity. Its monochromaticity allows the recording of high-resolution spectra, providing valuable information for the assignment of chemical species. Moreover, ultrashort laser pulses are essential in the temporal discrimination of a component, which further improves selectivity.

Although commercial Raman spectrometers have employed lasers for more than 25 years, the use of lasers in other commercial spectrometers has not been widespread, most likely because of the cost and difficulties in operation and maintenance. The laser is less reliable than a conventional source, and requires additional maintenance (e.g., replacing the plasma tube).

In practical applications, a continuous wave (CW) laser with low output power seems to be advantageous. One possibility is an air-cooled argon ion laser (10 mW). This laser is reliable and requires no water for cooling and it costs half as much as the medium-size Ar ion laser (1 W). A He–Cd laser, which is small and generates a UV beam, might also be useful. However, the plasma tube must be replaced every 4000 h, at a cost of more than half the price of the initial equipment.

Another approach might be to use a small N_2-laser-pumped dye laser, which contains a gas reservoir and is turnkey operated. Unfortunately, the output power is unstable and pulse-to-pulse variation is typically 10–50%. Moreover, rf interference noise sometimes induces a serious problem in signal measurements. A more reliable and stable laser with a lower cost is necessary in practical laser spectrometry.

The diode laser

Recently, a near-IR diode laser has been developed for use in telecommunications and data processing. Worldwide, more than 10^6 laser diodes are produced every month for use in compact disk players, bar code scanners, and laser printers. The devices are manufactured by mass production technology, and the price for one chip has been reduced to about $10.

Performance characteristics of the commercial diode laser are summarized in Table I. The output power of the diode laser corresponds to that of the air-cooled Ar ion laser. It is tunable and has a narrow linewidth, similar to a dye laser commonly used in spectrometry.

A diode laser has other advantages over conventional lasers. It is smaller and has a long life ($\sim 10^5$ h). Furthermore, it has a high conversion efficiency from electricity to light and can be directly driven, even by an integrated circuit. A photodiode is usually installed in the same package for power monitoring, and the output power can be feedback-controlled by an electronic circuit, providing a stability of $\sim 10^{-5}$.

Unfortunately, a diode laser has an inevitable disadvantage: The wavelength is restricted to the near-IR region. This results from an energy gap of the semiconductor used. Many manufacturers are working to develop a diode laser oscillating at shorter wavelengths, but the current practical limit for a commercial diode laser is 670 nm.

Optical fibers

We predict that in the twenty-first century all communications will be transmitted by photons through optical fibers, instead of by electrons through copper wire. In industrial operations, local area networks using optical fibers and diode lasers will connect computers, control centers, factory monitoring instruments, and business areas. Although all analytical instruments are now designed to use electricity, we believe that in the next century all analytical data will probably be transmitted and received by optical fibers and be further processed by an optical integrated circuit and visually displayed. Thus the coupling of analytical instruments with a diode laser–optical fiber system appears likely in the future. The simplest example might be two optical fibers facing each other; this arrangement allows sensitive absorption detection because of the photothermal effect induced (*1*).

0003-2700/90/0362-363A/$02.50/0

Table I. Typical performance of a commercial diode laser

Parameter	Performance	Special features
Output power	3–40 mW	Continuous wave
	10 W	Pulsed
Wavelength	670–850 nm	Fundamental
	420 nm	SHG, 0.4 mW
Linewidth	1 nm	Conventional
	10 MHz	Stabilized
Tunable range	20 nm	Temperature controlled
Pulse width	0.1–100 ns	No mode locking
Stability	0.006 %	Controlled
Efficiency	10–20 %	Continuous wave

Other electrooptical components

A variety of optical components have been developed for data communication and processing. For example, a package containing a laser diode and a photodiode, which might be useful for construction of a compact spectrometer, is already commercially available. A fast detector developed for data communication is advantageous in time-resolved fluorometry. An avalanche photodiode has an ultrafast response time, and the transit time spread is reported to be 20 ps (*2*). A small package containing an optical fiber, an avalanche diode, a Peltier electric cooler, and a discriminator is commercially available; this may be useful as a single-photon counting device in trace analysis.

In this article, we will describe state-of-the-art implementation of diode lasers, optical fibers, and electrooptical components.

Molecular absorption spectrometry

In 1982 we became aware of the commercial availability of a diode laser that had an output power of 20 mW and seemed to be sufficient for analytical spectrometry. We tried to use the laser in a photoacoustic spectrometry application; phosphorus was measured after color development by a molybdenum blue method (*3*). The configuration of the experimental apparatus is shown in Figure 1. The 780-nm diode laser is used as an exciting source, and the sound induced by light absorption is detected by a piezoelectric transducer installed in the cell. Unfortunately, this first spectrometric application of the diode laser was neither sensitive nor compact.

Since then, a diode laser has been applied to various absorption spectrometries. Conventional absorption spectrometry of molecules such as NH_3 (*4*), H_2O (*4*), or CH_4 (*5*) in the gas phase has been reported. This work is based on measurements of overtone vibration of the molecule, so that the sensitivity is limited to 2.3 mTorr · m for NH_3. Detection of the pollutant NO_2, which has an electronic absorption band in the near-IR region, is possible at pressures down to 1.8 μTorr for a 5-cm pathlength by heterodyne spectrometry (*6*).

Absorption spectrometry of condensed-phase samples is also reported elsewhere (*7*). The sensitivity is further enhanced by thermal lens spectrometry (*8*) and intracavity absorption spectrometry (*9*). Several complexes of heavy metals and organic chelates have absorption bands in the near-IR region. Phosphorus and iron are determined with 10–20× better sensitivity than with conventional absorption spectrometry.

Near-IR spectrometry has an inevitable disadvantage in the application to trace analysis. Background light absorption in this spectral region is not negligible in most cases, because of overtone vibrational bands of the solvent that are appreciable for organic solvents containing hydrogen atoms (e.g., CH_3Cl or CH_3OH). A solvent such as CCl_4 or CS_2 provides lower background, but solubility is poor with such nonpolar solvents. Thus further improvement of sensitivity is difficult in near-IR absorption spectrometry.

Molecular fluorescence spectrometry

A diode laser provides better sensitivity when it is applied to fluorescence spectrometry. Excitation of the solvent to high vibrational levels, which prevents more sensitive detection in absorption spectrometry, gives no background fluorescence signal. Thus ultratrace analysis is possible in fluorescence spectrometry. Furthermore, because most chemical species are nonfluorescent in the near-IR region, no impurity fluorescence interferes with detection of the fluorescent sample molecule.

In preliminary work, we could detect some polymethine dyes that fluoresce in the near-IR region down to a concentration of 5×10^{-12} M (*10*). When an optical fiber and a capillary cell were used for light transmission and sample detection, the mass detection limit could be reduced to 12 fg (*11*).

More recently, Winefordner and coworkers detected 46,000 molecules of a near-IR dye [5,5′-dichloro-11-(diphenylamino)-3,3′-diethyl-10,12-ethylenethiatricarbocyanine perchlorate] in a volume of 56 nL (*12*). These results imply that near-IR fluorescence spectrometry using a diode laser will be useful for ultratrace analysis.

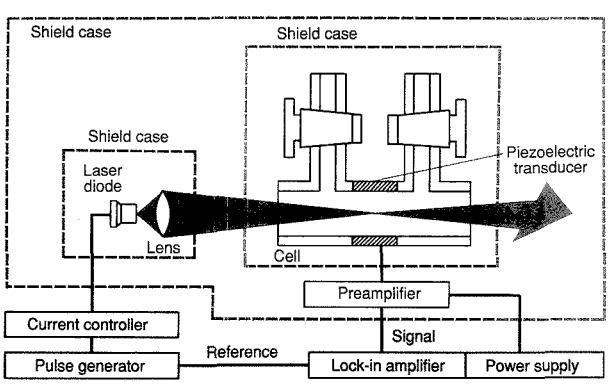

Figure 1. Photoacoustic spectrometer using a diode laser.
(Adapted from Reference 3.)

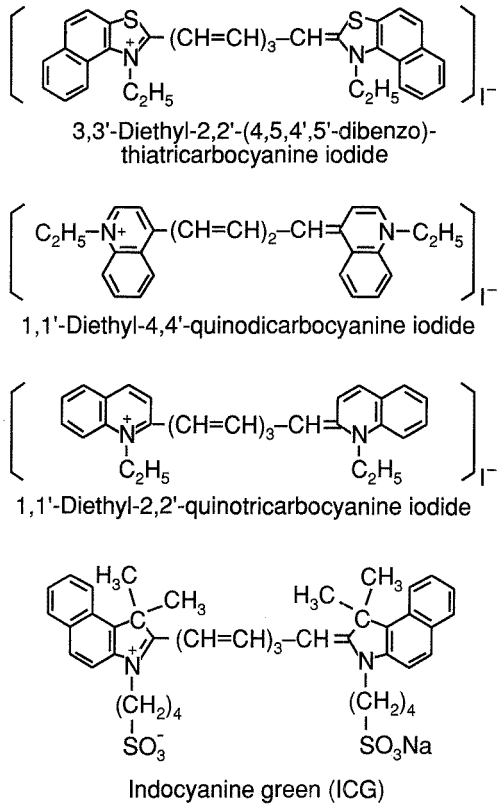

Figure 2. Chemical structures of polymethine dyes that are fluorescent in the near-IR spectral region.

We have also demonstrated time-resolved fluorometry at a time resolution of 480 ps, which is useful in the evaluation of solvent polarity (*13*). This work involved the use of picosecond light pulses generated by a diode laser (136 ps, 1.3 W).

A potential problem in near-IR fluorometry is the lack of fluorescent organic dyes in this spectral region. To our knowledge, only one group of molecules, polymethine dyes, are fluorescent in this region. Though chromatographic determination of polymethine dyes has been demonstrated using diode laser fluorometry (*14*), practical application to a real sample is quite limited. However, it might be possible to use polymethine dyes as probe molecules. This situation is perhaps analogous to the fact that because few substances are naturally radioactive, radioimmunoassay is extremely useful in trace analysis because of the low background signal.

A variety of molecular species are commercially available for polymethine dyes. The number of compounds synthesized and commercially available exceeds 3000. Developed for use as photosensitive dyes, they have been used more recently as laser dyes. The molecular structures of some polymethine dyes are shown in Figure 2. Unfortunately, they have no reactive sites in the molecule, although perhaps the ethyl side chains in the quinocarbocyanines could be modified, and the phenyl rings offer opportunities for introducing reactive substituents. The top three dyes are less soluble than the fourth in aqueous solution and form nonfluorescent dimers. The exception in this group is indocyanine green [2-[7-[1,3-dihydro-1,1-dimethyl-3-(4-sulfobutyl)-2*H*-benz[*e*]indol-2-ylidene]-1,3,5-heptatrienyl]-1,1-dimethyl-3-(4-sulfobutyl)-1*H*-benz[*e*]indolium hydroxide inner salt sodium salt]; it has negatively charged sulfonic groups and is soluble in water.

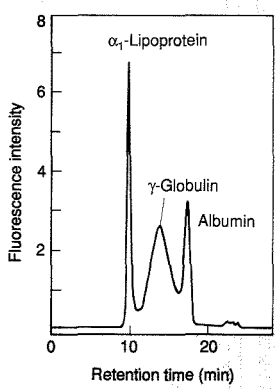

Figure 3. Liquid chromatogram of protein in human serum obtained using a diode laser fluorometric detector.
(Adapted from Reference 15.)

The chemical properties of indocyanine green have recently been investigated. Because it has been found to be adsorbed on the surface of protein and to increase the fluorescence intensity, this molecule can be used for labeling protein. Figure 3 shows the chromatogram recorded by labeling protein in human serum with indocyanine green and by separating the complex with a gel filtration column. The detection limit reported is 1.3 pmol for albumin (*15*).

Recently, the fluorescence intensity of indocyanine green has been found to be quenched by an OH radical, probably because of the formation of a nonfluorescent dimerlike compound. Thus an enzyme reaction producing H_2O_2 can be monitored by using a catalyst of Fe(II), which converts H_2O_2 to OH. By the following reaction, xanthine is determined in the presence of xanthine oxidase (*16*).

$$\text{xanthine} + O_2 + H_2O \xrightarrow{\text{xanthine oxidase}} \text{uric acid} + H_2O_2$$

More recently, peroxidase generating OH from H_2O_2 has been measured in the similar reaction scheme, which is further extended to enzyme immunoassay of insulin (*17*).

Visible semiconductor laser fluorometry

Near-IR laser fluorometry has high sensitivity because of the large photon

Next Month We'll Introduce The Fastest Lab Balance Ever.

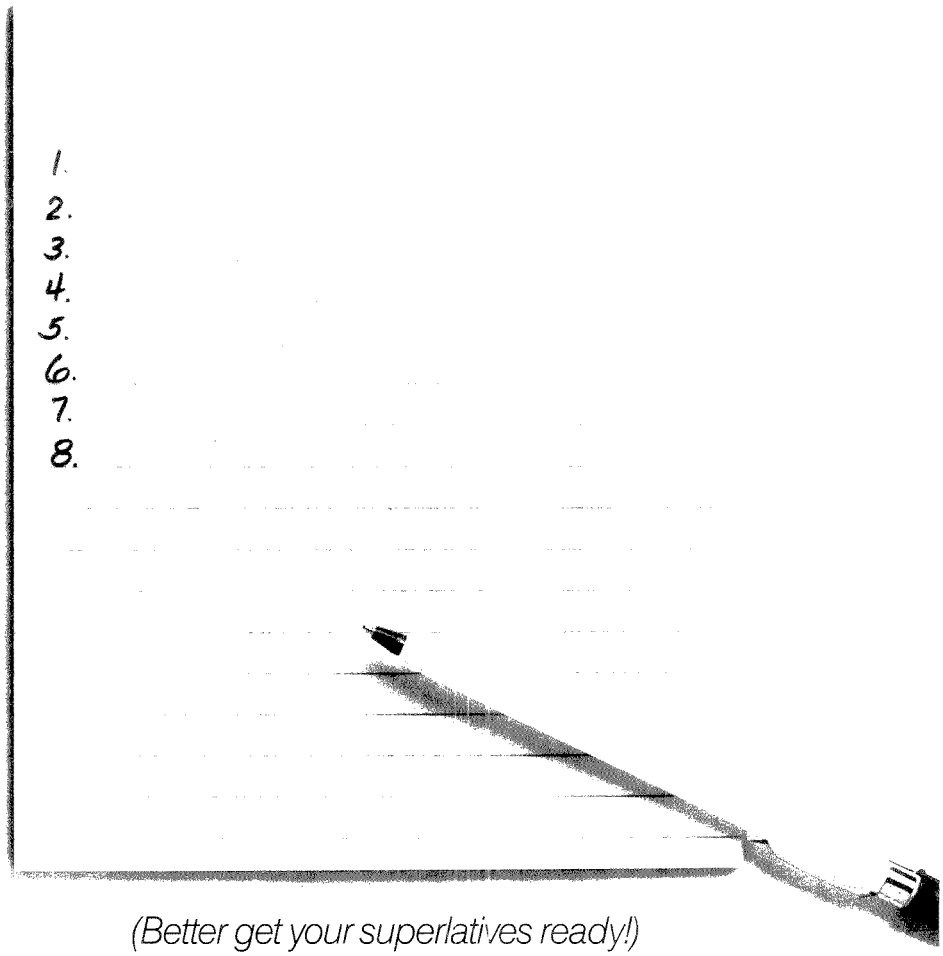

(Better get your superlatives ready!)

The fastest, brightest, most versatile lab balances ever have the power of the new MC 1 technology from Sartorius. Those are our words; we can't wait to hear yours. We'll tell the full MC 1 story right here, next month.

Can't wait? Call 800-544-3409 for a "No-Wait" demo of MC 1 technology or a "No-Wait" info package.

We take the wait out of weighing.

sartorius

CIRCLE 125 ON READER SERVICE CARD

flux and low background signal. However, this approach suffers from a lack of suitable dyes for color development and for labeling a molecule. This situation was unchanged even when a 750-nm diode laser appeared. A recently developed diode laser oscillating at 670 nm is quite versatile, however, and extends the application field because of the availability of many dyes in this spectral region.

Figure 4 shows chemical structures of dyes that fluoresce in the deep-red region. Rhodamine, oxazine, and thiazine dyes are useful as chromophores for labeling biological molecules. By using a bifunctional reagent of water-soluble carbodiimide, albumin is labeled with a fluorescent tag by a covalent bond (*18*). The detection limit of albumin obtained by labeling it with oxazine 750 is reported to be 0.13 pmol and is determined by the limited labeling efficiency.

Another dye, methylene blue, is widely used, for example, in measurements of oxidation and reduction potential, in determinations of enzymes and metabolites, and also in staining DNA by intercalation to the double helix. Therefore, visible diode laser fluorometry may have wide application in biological assay in the future.

In indirect chromatography detection, the fluorescence intensity of the reagent in a carrier is measured to observe the displacement by the eluted compounds. The approach using a visible diode laser for universal detection of organic compounds has been studied elsewhere (*19*).

Atomic absorption spectrometry

The wavelength of the diode laser is determined by the cavity length, which is controlled by changing the diode current and the temperature. In atomic spectrometry the wavelength should be tuned to a resonance line within an error of 0.001 nm, so that the temperature of the laser diode is controlled within 0.01 °C. Because of mode hopping, the diode laser may skip over certain wavelength regions, so it should be carefully selected to operate at a specified wavelength. This characteristic of the commercial diode laser is reported in detail elsewhere (*20*).

A resonance line of Rb is located at 780.2 nm and an intercombination line of Ba at 791.1 nm. A diode laser, instead of a hollow cathode lamp, has been used in atomic absorption spectrometry (*21*). The detection limit of Rb is reported to be 500 pg/mL. This approach not only decreases the dimension and the power consumption but also allows background subtraction by tuning the laser wavelength on and off the resonance line. This is useful when a strong molecular absorption band is superimposed. Another possible advantage of diode laser spectrometry is high sensitivity resulting from a multiple pass effect; the laser beam is well collimated and the pathlength can be extended by reflecting the beam using a cavity filled with sample.

Atomic fluorescence spectrometry

Atomic fluorescence spectrometry is essentially more sensitive than atomic absorption spectrometry because the signal intensity increases linearly as the intensity of the light source increases. The application of the diode laser to atomic fluorescence spectrometry has already been studied (*22*). A detection limit of 2.1 ppb has been reported for Rb and was achieved by using a 200-mW diode laser.

A potential problem in atomic spectrometry is the narrow tunable range of the diode laser. The resonance lines used in conventional atomic absorption spectrometry are widespread in the visible and UV regions, although some of them are in principle covered by the fundamental and frequency-doubled beams generated by the state-of-the-art diode laser. An alternative method is the use of other spectral lines, although sensitivity will be substantially decreased.

Other spectrometries

In a refractive index (RI) detector, a light source with stable output power and good beam-pointing stability is required. The diode laser has excellent performance in these respects. In RI gradient detection, a detection limit of 4×10^{-9} RI units, corresponding to a mass detection limit of 540 pg (1.1 fmol) for polystyrene, has been reported (*23*). This technique has been applied to detectors for chromatography (*23*) and for electrophoresis (*24*). A diode laser has also been used to measure optical rotation and as an LC detector (*25*). In Raman spectrometry a near-IR diode laser is advantageously used to discriminate Raman emission from fluorescence. The low output power of the diode laser is partly compensated for by combining it with a sensitive charge-coupled device for measurements of the spectrum (*26*). The advantage of the diode laser has been demonstrated using a fluorescent sample in surface-enhanced Raman spectrometry (*27*).

Frequency-doubled diode laser

The wavelength of the commercial diode laser is limited to 670 nm. However, the wavelength of the laser can be extended to much shorter wavelengths by second harmonic generation (SHG) or frequency mixing (FMX). Efficient SHG is achieved by passing the laser beam through a nonlinear crystal, such as potassium dihydrogen phosphate (KDP) or the more efficient potassium niobate ($KNbO_3$).

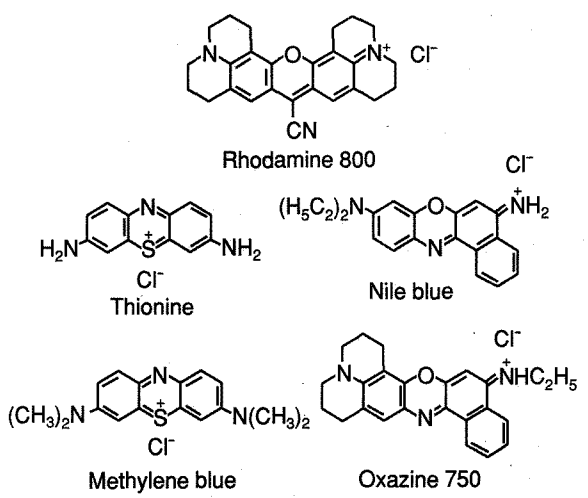

Figure 4. Chemical structures of organic dyes that are fluorescent in the deep-red spectral region.
(Adapted from Reference 18.)

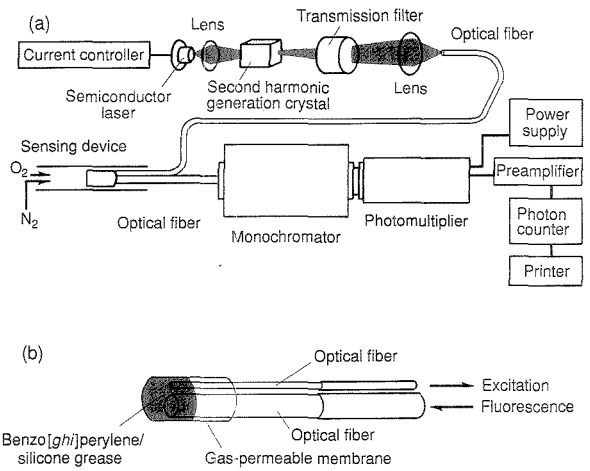

Figure 5. Optical fiber sensor sensitive to oxygen using second harmonic emission of the diode laser. (a) Total system and (b) sensing device.
(Adapted with permission from Reference 28.)

Figure 5 shows a block diagram of an optical fiber sensor sensitive to oxygen. A frequency-doubled beam is focused onto the distal end of an optical fiber, and fluorescence is measured by passing it through a different optical fiber. The conversion efficiency of SHG is 2.5×10^{-6} but it is sufficient as a light source in the optical fiber sensor system (*28*). The concentration of oxygen is determined at 0–15% levels.

A diode laser is made of a nonlinear crystal, so that SHG occurs even in the laser diode itself. The output power obtained is at picowatt levels, but it is still sufficient for use in atomic absorption (*29*) and molecular fluorescence (*30*) spectrometries.

Visible fluorometry using a frequency-doubled diode laser has wide application because visible fluorometry is already established and in use. However, some of the advantages of near-IR fluorometry (e.g., low background signal) are lost with this approach.

Future developments

The technology of the diode laser is progressing rapidly. The output power doubles every year, and the cost is cut in half. A high-power, diode-laser-pumped Nd:YAG laser is a hot topic in laser technology because of its high conversion efficiency (10%) from electricity to a coherent light beam. A frequency-doubled Nd:YAG laser producing 80 mW is already commercially available. Such a laser may be quite useful in future analytical work.

On average, the wavelength of the diode laser has been shortened 10 nm every year. This rapid rate of change can be attributed to applications of the laser diode to such commercially successful products as the bar code scanner and the laser printer. We believe that a more powerful laser oscillating at shorter wavelengths will soon appear. Its availability will further extend analytical applications.

For recording data to an optical disk, a laser that oscillates at much shorter wavelengths is advantageous because the focused beam diameter can be reduced to the order of the laser wavelength. Thus electronic engineers are concentrating their attention on frequency doubling of the diode laser. Their research has shown that the conversion efficiency of SHG is improved to 14% (24 mW/167 mW) (*31*). If this diode laser is available as an excitation source for chromatography or electrophoresis detectors, it will become a powerful tool in trace analysis.

At present, no commercial diode laser spectrometer is available. We expect that a commercial instrument will appear in the next few years and will find practical analytical usefulness. Its appearance will also help stimulate the development of chemical reagents and analytical procedures for near-IR or deep-red spectrometry.

Combining a diode laser with advanced electrooptical components will provide the best instrument performance. For example, the dimension and the weight of the diode laser spectrometer are now limited by the detector, that is, a photomultiplier and its power supply. Replacement with a sensitive photodiode is essential for its practical use. A one-chip integrated circuit consisting of a diode laser, a transmitter, a receiver, a detector, and a data processor, which can be directly coupled with an optical fiber system, might be the ultimate approach for practical spectroscopic analysis.

References

(1) Imasaka, T.; Nakanishi, K.; Ishibashi, N. *Anal. Chem.* **1987,** *59,* 1554.
(2) Cova, S.; Lacaita, A.; Ghioni, M.; Ripamonti, G.; Louis, T. A. *Rev. Sci. Instrum.* **1989,** *60,* 1104.
(3) Kawabata, Y.; Kamikubo, T.; Imasaka, T.; Ishibashi, N. *Anal. Chem.* **1983,** *55,* 1419.
(4) Ohtsu, M.; Kotani, H.; Tagawa, H. *Japan. J. Appl. Phys.* **1983,** *22,* 1553.
(5) Chan, K.; Ito, H.; Inaba, H. *Appl. Opt.* **1983,** *22,* 3802.
(6) Lenth, W.; Gehrtz, M. *Appl. Phys. Lett.* **1985,** *47,* 1263.
(7) Imasaka, T.; Kamikubo, T.; Kawabata, Y.; Ishibashi, N. *Anal. Chim. Acta* **1983,** *153,* 261.
(8) Nakanishi, K.; Imasaka, T.; Ishibashi, N. *Anal. Chem.* **1985,** *57,* 1219.
(9) Unger, E.; Patonay, G. *Anal. Chem.* **1989,** *61,* 1425.
(10) Imasaka, T.; Yoshitake, A.; Ishibashi, N. *Anal. Chem.* **1984,** *56,* 1077.
(11) Kawabata, Y.; Imasaka, T.; Ishibashi, N. *Talanta* **1986,** *33,* 281.
(12) Johnson, P. A.; Barber, T. E.; Smith, B. W.; Winefordner, J. D. *Anal. Chem.* **1989,** *61,* 861.
(13) Imasaka, T.; Yoshitake, A.; Hirata, K.; Kawabata, Y.; Ishibashi, N. *Anal. Chem.* **1985,** *57,* 947.
(14) Sauda, K.; Imasaka, T.; Ishibashi, N. *Anal. Chim. Acta* **1986,** *187,* 353.
(15) Sauda, K.; Imasaka, T.; Ishibashi, N. *Anal. Chem.* **1986,** *58,* 2649.
(16) Imasaka, T.; Okazaki, T.; Ishibashi, N. *Anal. Chim. Acta* **1988,** *208,* 325.
(17) Imasaka, T.; Nakagawa, H.; Okazaki, T.; Ishibashi, N., unpublished results.
(18) Imasaka, T.; Tsukamoto, A.; Ishibashi, N. *Anal. Chem.* **1989,** *61,* 2285.
(19) Folestad, S.; Ahlberg, H. International Symposium on Column Liquid Chromatography, Stockholm, June 26–30, 1989.
(20) Lawrenz, J.; Niemax, K. *Spectrochim. Acta* **1989,** *44B,* 155.
(21) Hergenröder, R.; Niemax, K. *Spectrochim. Acta* **1988,** *43B,* 1443.
(22) Johnson, P. A.; Vera, J. A.; Smith, B. W.; Winefordner, J. D. *Spectrosc. Lett.* **1988,** *21,* 607.
(23) Hancock, D. O.; Synovec, R. E. *Anal. Chem.* **1988,** *60,* 1915.
(24) Chen, C. Y.; Demana, T.; Huang, S. D.; Morris, M. D. *Anal. Chem.* **1989,** *61,* 1590.
(25) Lloyd, D. K.; Goodall, D. M.; Scrivener, H. *Anal. Chem.* **1989,** *61,* 1238.
(26) Williamson, J. M.; Bowling, R. J.; McCreery, R. L. *Appl. Spectrosc.* **1989,** *43,* 372.
(27) Angel, S. M.; Myrick, M. L. *Anal. Chem.* **1989,** *61,* 1648.
(28) Okazaki, T.; Imasaka, T.; Ishibashi, N. *Anal. Chim. Acta* **1988,** *209,* 327.
(29) Sakurai, K.; Yamada, N. *Opt. Lett.* **1989,** *14,* 233.
(30) Imasaka, T.; Hiraiwa, T.; Ishibashi, N. *Mikrochim. Acta* **1989,** *2,* 225.
(31) Goldberg, L.; Chun, M. K. *Appl. Phys. Lett.* **1989,** *55,* 218.

Nobuhiko Ishibashi (left) is professor of applied analytical chemistry at Kyushu University, where he has been a member of the faculty since 1954. He is chairman of the Japanese Association of Flow Injection Analysis and past vice-president of the Japan Society for Analytical Chemistry and the Electrochemical Society of Japan. His research interests include laser fluorometry, supersonic molecular beam fluorometry, optical fiber sensors, ion-selective electrodes, ion-exchange membranes, and flow analysis.

Totaro Imasaka (right) received his Ph.D. from Kyushu University, where he has been a member of the Faculty of Engineering since 1980. His research interests include investigations of supersonic jet spectrometry and semiconductor laser spectrometry. More recently, he has concentrated on developing a widely tunable laser system based on two-color stimulated Raman emission.

MEETINGS

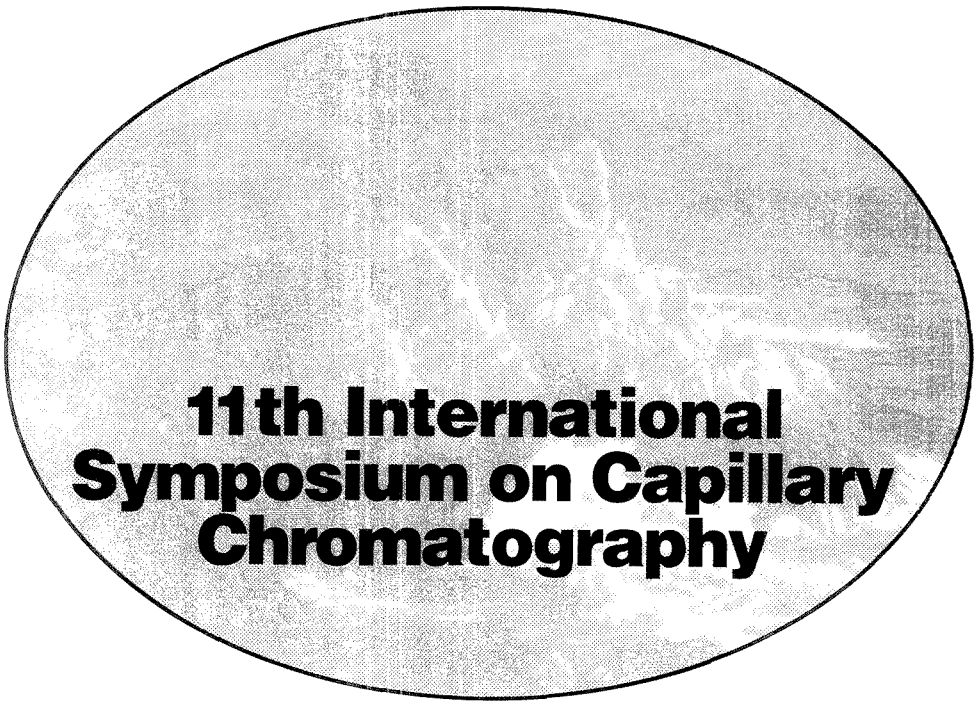

The 11th International Symposium on Capillary Chromatography will be held in Monterey, CA, May 14–17. The symposium will focus on microseparation techniques, including capillary GC, GC/MS, GC/FT-IR, GC/AES, microcolumn HPLC, SFC, and capillary zone electrophoresis. Applications to be covered include the analysis of environmental compounds; pharmaceuticals; petrochemicals; biochemicals; proteins and peptides; and foods, flavors, fragrances, and beverages.

The program will consist of review papers by leading scientists in the field, contributed oral and poster presentations, discussion groups, workshop-type seminars, and an exhibition of modern chromatographic instrumentation. Posters will be accepted until May 1 for inclusion in the program; prospective authors should send 300-word abstracts to Pat Sandra, Laboratory of Organic Chemistry, University of Gent, Gent, Belgium (FAX 91 228 321). A number of scholarships are available for young scientists interested in attending the symposium.

For additional information about the meeting, including details on registration, housing, and transportation, contact the International Symposium on Capillary Chromatography, Service Partners, Ltd., 19490 Glen Una Dr., Saratoga, CA 95070 (408-395-4333). The preliminary program for the symposium follows.

MONDAY MORNING

8:30 **Opening Address.**
8:45 **M.J.E. Golay Award Presentation.**
8:50 **Award Address.**

Advances in Capillary Chromatography—I

L. S. Ettre, *Chairman*

9:15 **Capillary Chromatography—State of the Art.** C. Cramers, Eindhoven U of Technology, The Netherlands
9:40 **New Novel Selective Stationary Phases for Open-Tubular GC and SFC.** M. Lee, Brigham Young U
10:05 **CGC Enantiomer Separation by Complexation and Inclusion.** V. Schurig, U of Tübinger, F.R.G.
11:00 **Posters.**

MONDAY AFTERNOON

Advances in Capillary Chromatography—II

R. Kaiser, *Chairman*

1:45 **Advances in Microcolumn Technology and the Analysis of Single Cells.** R. Kennedy, U of North Carolina, Chapel Hill
2:10 **Polymer-Coated Support Surfaces in Capillary and Micro Packed Columns.** G. Schomburg, Max Planck Institute, F.R.G.
2:35 **Advances in Optical Detection Methods in Microcolumn Separations.** E. Yeung, Iowa State U
3:00 **Reversed-Phase LC/Capillary GC with a NP Detector Using a Loop-Type Interface Combined with a Sandwich-Type Phase Separator.** P. van Zoonen and G. van der Hoff, NI of Public Health and Environmental Protection, The Netherlands
3:45 **Posters.**
4:45 **Discussion Sessions: CC in Environmental Analysis; Sample Introduction in CC.**

TUESDAY MORNING

Applications of Capillary Chromatography

W. Jennings, *Chairman*

8:30 **Ultrasensitive Determinations of Amino Sugars by Capillary Electrophoresis–Laser-Induced Fluorescence Detection.** J. Liu, O. Shirota, and M. Novotny, Indiana U
8:55 **Investigations into the Use of Capillary GC with Atomic Emission Detection: Influence of the Molecular Structure on the Element Response.** J. Th. Jelink and A. Venema, AKZO, The Netherlands
9:20 **Stereochemical Analysis of Constituents of Essential Oils and Flavor Compounds by Enantioselective Capillary GC.** W. Konig, R. Krebber, P. Evers, and G. Bruhn, U of Hamburg, F.R.G.

9:45 **Microcolumn Chromatography for the Analysis of Detergents and Lubricants.** P. Sandra, U of Gent, Belgium
10:40 **Posters.**

TUESDAY AFTERNOON

Sampling in Capillary Chromatography

J. Rijks, *Chairman*

1:45 **Advances in Sampling Techniques for Capillary GC.** J. Roeraade, Royal Institute of Technology, Sweden
2:10 **Thermal Modulation for Sample Introduction into Ultrasmall-Diameter Capillary Columns in GC.** J. Phillips, Southern Illinois U
2:35 **Simultaneous Cryogenic Focusing as a Side Product during SFE in CGC.** B. Wright, Battelle Pacific Northwest Laboratories
3:00 **Quantitative SFE Coupled to CGC.** J. Levy, A. C. Roselli, D. S. Boyer, and K. Cross, Suprex
3:45 **Posters.**
4:45 **Discussion Sessions: Multidimensional and Coupled Techniques; SFE.**

WEDNESDAY MORNING

Coupled and Hyphenated Techniques

H. McNair, *Chairman*

8:30 **Analytical SFE Coupled to Microcolumn Chromatography.** J. King, Agricultural Research Service
8:55 **Chromatographic Separations through On-Line Coupled Techniques: HPLC/HRGC. Selected Applications.** F. Andreolini and F. Munari, Carlo Erba Instruments, Italy
9:20 **Characterization of Water Contaminants through On-Line HPLC/Capillary GC with Photodiode Array and Element-Selective Detection.** C. Kellogg and S. Schachterle, Varian Instrument Division
9:45 **Investigation of GC with Atomic Emission Detection for the Determination of Empirical Formulas.** P. L. Wylie and J. J. Sullivan, Hewlett-Packard
10:30 **Posters.**
11:30 **Panel Discussion: Future of GC Column Development.** W. Jennings, Chairman

THURSDAY MORNING

Supercritical Fluid Chromatography

K. Markides, *Chairman*

8:30 **Packed and Open-Tubular Microcolumns in SFC.** K. Payne, Brigham Young U
8:55 **Possibilities and Limitations of Coiling-Induced Secondary Flow in Capillary SFC.** J.G.M. Janssen, J. A. Rijks, and C. A. Cramers, Eindhoven U of Technology, The Netherlands
9:20 **Recent Developments in SFC/MS.** S. Olesik, Ohio State U
9:45 **SFC Analysis of Lube-Oil Additives on Packed Capillary Columns.** S. Ashraf, R. Moulder, M. W. Raynor, K. D. Bartle, and A. A. Clifford, U of Leeds, U.K.
10:40 **Posters.**
11:30 **Panel Discussion: HPCE vs. Micro LC—Future for Bioseparation?** M. Novotny, Chairman

THURSDAY AFTERNOON

Micro LC, Electrokinetic Capillary Chromatography, and Capillary Zone Electrophoresis

F. Everaerts, *Chairman*

1:45 **Micro LC. Present State of the Art.** K. Jinno, Toyohashi U of Technology, Japan
2:10 **Micellar Electrokinetic Capillary Chromatography.** M. Sepaniak, U of Tennessee
2:35 **Electrooptic Detection Techniques in Capillary Electrophoresis.** M. Morris, U of Michigan
3:00 **New Approach for Generating Linear and Shaped Gradients of Nanoliter Volumes Compatible with Electrophoresis in Capillaries.** V. Berry, Salem State College, and E. Rowher, U of Pretoria, South Africa
3:45 **Posters.**
4:45 **Closing Address.** S. Cram

MEETINGS

Third Symposium on Computer-Enhanced Analytical Spectroscopy

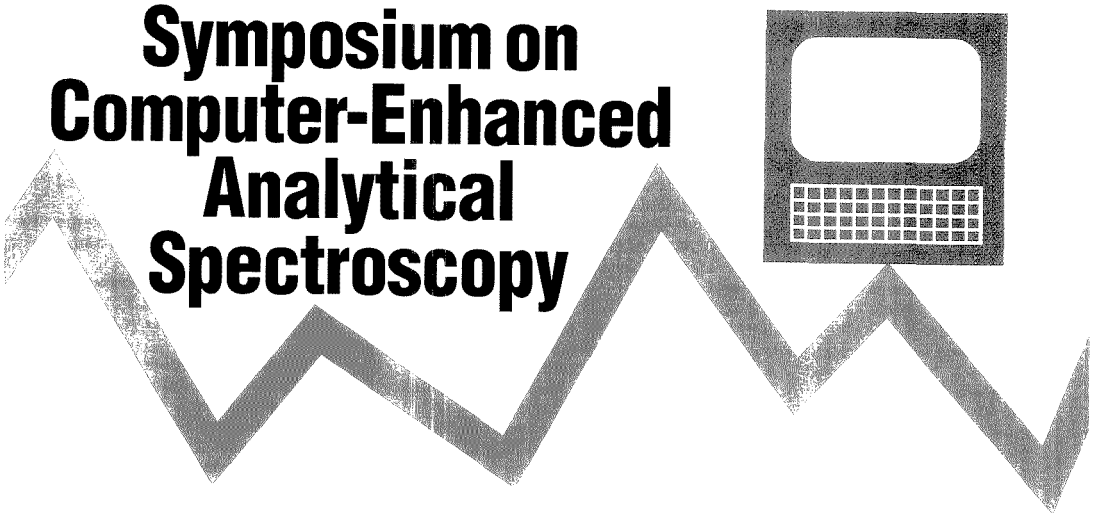

The Snowbird resort near Salt Lake City, UT, will be the site of the Third Symposium on Computer-Enhanced Analytical Spectroscopy, June 6–8, 1990. The symposium format will be similar to that of the Gordon Research Conferences; sessions will be held in the mornings and evenings, leaving the afternoons free for recreational activities and informal discussions.

Topics will include theory and practice of multivariate analysis relevant to analytical spectroscopy (e.g., IR, MS, NMR, UV–vis, near-IR), optimization and exploratory data analysis, spectral interpretation and library searching, visualization of higher dimensional data and nonlinear mapping, cluster and classification analysis of multivariate data, numerical extraction of multicomponent spectra, integration of spectral data from different spectroscopic sources, optimization and process control involving spectroscopic methods, numerical modeling of spectral information, automated spectral interpretation and expert systems, multicomponent analysis, spectral enhancement and deconvolution, and factor and discriminant analysis. Authors wishing to contribute poster presentations should submit titles to Peter Jurs at the address given below.

The registration and meals fee for the symposium is approximately $220 and includes all meals, coffee breaks, a Western-style barbecue, a tram excursion, and a copy of the symposium proceedings. Participants should deal directly with Snowbird (800-453-3000) to arrange for their accommodations, estimated to cost about $60 per night.

The National Science Foundation has provided a grant to support the participation of untenured assistant professors and faculty from undergraduate institutions. For additional information about the grant and for further details about the symposium, contact Peter Jurs, Dept. of Chemistry, 152 Davey Laboratory, The Pennsylvania State University, University Park, PA 16802 (phone 814-865-3739 or FAX 814-865-3314). Following is a tentative list of speakers and titles.

Mass Spectrometry

Computer-Assisted Mass Spectral Interpretation: MS/MS/MS Analysis. C. Enke, Michigan State U
Analysis of Data from Pyrolysis MS of Fossil Fuels. H. Meuzelaar, U of Utah
Computer Analysis of Pyrolysis Mass Spectral Data. P. Harrington, Ohio U

IR and Near-IR Spectroscopy

Computer-Assisted Methods in IR Spectroscopy. D. Haaland, Sandia National Laboratory
Computer-Assisted Interpretation of IR Spectra. S. Tomellini, U of New Hampshire
Computer-Assisted Methods in Near-IR Spectroscopy. H. Mark, Bran + Luebbe/Technicon
Computer-Assisted Methods in Near-IR Spectroscopy. T. Naes, Norwegian Food Research Institute

NMR Spectroscopy and Structure Elucidation

Computer-Assisted Structure Elucidation Utilizing NMR Spectra. M. Munk, Arizona State U
Multidimensional Spectral Data and Structure Elucidation. W. Bremser, Rheinische Olefinwerke, GMBH

Chemometric Methods and Signal Processing

Hadamard Methods in Signal Processing. W. Fateley, Kansas State U
Interactive Self-Modeling Multivariate Analysis. W. Windig, Eastman Kodak

Atomic Spectroscopy

Computer Applications in Multichannel Atomic Emission Spectroscopy. R. B. Bilhorn, Eastman Kodak

Ion Mobility Spectrometry

Advanced Signal Processing and Data Analysis Techniques Applied to Ion Mobility Spectrometry. D. M. Davis, CRDEC, U S. Army

Conferences

■ **International Symposium on Near-Infrared Spectroscopy.** April 24–26. Kolding, Denmark. *Contact: Lone Vejgaard, Bioteknisk Institut, Holbergsvej 10, 6000 Kolding, Denmark*

■ **International Conference and Exhibition on Fiber Optics and Opto-Electronics (Fiber Optics '90).** April 24–26. London, U.K. *Contact: Sira Ltd., South Hill, Chislehurst, Kent BR7 5EH, U.K.*

■ **4th International Symposium on Nondestructive Characterization of Materials.** June 11–14. Annapolis, MD. *Contact: Center for Nondestructive Evaluation, Maryland Hall 102, Johns Hopkins University, Baltimore, MD 21218 (301-338-6115)*

■ **45th Symposium on Molecular Spectroscopy.** June 11–15. Columbus, OH. *Contact: K. Narahari Rao, Dept. of Physics, Ohio State University, 174 West 18th Ave., Columbus, OH 43210*

■ **International Meeting on Infrared Technology and Applications.** June 25–29. London, U.K. *Contact: Sira Ltd., South Hill, Chislehurst, Kent BR7 5EH, U.K.*

■ **Annual Conference of the Canadian Society of Forensic Science.** Oct. 1–5. Ottawa, Ontario, Canada. *Contact: Canadian Society of Forensic Science, 2660 Southvale Crescent, Suite 215, Ottawa, Ontario, Canada K1B 4W5 (613-731-2096)*

Short Courses and Workshops

For information on the following courses, contact the Center for Professional Advancement, P.O. Box H, East Brunswick, NJ 08816 (201-238-1600)

■ **Modern Instrumental Methods of Analysis.** March 26–30. East Brunswick, NJ

■ **Practical Atomic Spectroscopy.** March 28–30. Somerset, NJ

■ **Near-Infrared Spectroscopy.** April 2–4. Somerset, NJ

■ **Practical Mass Spectrometry.** April 18–20. Somerset, NJ

■ **Quality Assurance for the Analytical Laboratory.** April 30–May 3. East Brunswick, NJ

■ **Laboratory Information Management Systems.** May 7–10. East Brunswick, NJ

For information on the following courses, contact Toula Hionis, Pharmacia LKB Biotechnology, 800 Centennial Ave., Piscataway, NJ 08854 (201-457-8470)

■ **Process Chromatography Techniques—Theory and Practice.** April 3–5. Piscataway, NJ

■ **Validation Issues in Chromatography.** April 6 and May 25. Piscataway, NJ

■ **Downstream Processing of Recombinant DNA Proteins.** April 24–27. Piscataway, NJ

■ **Pilot-Scale (from Milligrams to Grams) Protein Purification.** May 15–18. Piscataway, NJ

■ **Production-Scale (from Grams to Kilograms) Protein Purification.** May 21–24. Piscataway, NJ

■ **Workshop on Modern Thin-Layer Chromatography.** April 23–24. Wrightsville Beach, NC. *Contact: Camag Scientific, P.O. Box 563, Wrightsville Beach, NC 28480 (800-334-3909)*

■ **Short Courses in Applied Optics.**

May 14–18. Las Cruces, NM. *Contact: Leon Radziemski, Arts and Sciences Research Center, NMSU, P.O. Box 30001, Dept. RC, Las Cruces, NM 88003 (505-646-2611)*

■ **2nd Hands-On Workshop on Field-Flow Fractionation.** June 11. Salt Lake City, UT. *Contact: Julie Westwood, FFFRC, Dept. of Chemistry, University of Utah, Salt Lake City, UT 84112 (801-581-5419)*

Call for Papers

■ **Meeting of the American and International Electrophoresis Societies.** Washington, DC. June 30–July 3. Symposium topics will include risk assessment, capillary electrophoresis, detection and imaging methods, applications of high-resolution 2D electrophoresis to clinical medicine, and electrophoresis and the genome. Authors wishing to contribute poster or oral presentations should request information from the American Electrophoresis Society, 27 Music Square East, Suite 134, Nashville, TN 37203 (615-327-7064). Deadline for submission of abstracts is April 1.

■ **2nd International Conference on Trace Metals in the Aquatic Environment.** Sydney, Australia. July 8–14. The program will consist of oral, poster, and video presentations on the following topics: extent of trace metal contamination of the aquatic environment, effects of trace metals on biota, trace metal chemistry and speciation, chemical and biological monitoring, rehabilitation, comparative studies, and regional studies in Australasia and Southeast Asia. Information on the preparation of abstracts (deadline for submission is March 31) is available from K. R. Brown, University of Technology, Sydney, P.O. Box 123, Broadway NSW 2007, Australia.

■ **Pacific Conference on Chemistry and Spectroscopy.** San Francisco, CA. Oct. 31–Nov. 2. Session topics include atomic spectroscopy; clinical applications; computers in chemistry; drug abuse testing; electrochemistry; forensic chemistry; GC/MS; ICP/MS; GC; LC; SFC; IR; MS; laser spectroscopy; molecular spectroscopy; NMR; process chemistry; polymer chemistry; Raman spectroscopy; robotics; sample introduction techniques; surface analysis; artificial intelligence; and environmental, pharmaceutical, nuclear, and petroleum chemistry. Prospective authors should submit 150–200-word abstracts on standard ACS abstract forms to the following program chairs: Richard Gaver (American Chemical Society), Chemistry Dept., San Jose State University, San Jose, CA 95192 (408-924-4974); Joseph Snyder (Society for Applied Spectroscopy), ICI Americas, 1200 South 47th St., Richmond, CA 94804 (415-231-1125); or Kenneth Straub (Bay Area Mass Spectrometry), Syntex Research, R6-002, 3401 Hillview Ave., Palo Alto, CA 94304 (415-855-5067). Abstracts must be received by May 1.

These events are newly listed in the JOURNAL. See back issues for other events of interest.

Textbooks

Polarography and Other Voltammetric Methods. Tom Riley and Arthur Watson. xii + 283 pp. John Wiley & Sons, 605 Third Ave., New York, NY 10158. 1987. $29

Reviewed by Petr Zuman, Department of Chemistry, Clarkson University, Potsdam, NY 13699

Polarography—electrolysis with a dropping mercury electrode, involving recording of current–voltage curves obtained at practically potentiostatic conditions—is often taught by using the simplest experiments in undergraduate laboratories. Nevertheless, few research groups in the United States actively and systematically make use of polarographic methods. This is rather unfortunate, as polarographic methods offer important information that is useful in understanding electrode processes—particularly the number of electrons transferred in individual steps, the nature of the species undergoing electrolysis, and the chemical reactions occurring before the electron transfer.

Such information about the mechanism of the electrode process, which can form a solid basis for investigation by more sophisticated voltammetric and other electrochemical techniques, is in turn important for development of electroanalytical methods using polarography, voltammetry with solid electrodes, stripping methods, or development of sensors (e.g., for chromatographic or flow injection methods). On the other hand, polarographic—particularly differential pulse and square-wave—methods are used in analytical practice by people with little or no background in electrochemistry. Such users need a manual to help them to use polarography and its variants in simple analytical situations in which the needed sensitivity can be achieved and analyses can be made without prior separation.

The existing introductory texts are either outdated (e.g., *Polarographic Techniques* by L. Meites and *Practical Polarography* by J. Heyrovsky and P. Zuman) or they deal with the introduction in more detail and more theoretically than the user needs (e.g., the monograph *Modern Polarographic Methods in Analytical Chemistry* by A. M. Bond). *Polarography and Other Voltammetric Methods* tries to fill this gap. It is a part of a series of texts, initiated by the Committee of Heads of Polytechnic Chemistry Departments in the United Kingdom, called Open Learning Texts. These books are aimed at self-study for those who cannot take conventional courses. Other volumes of this series dealing with related subjects are *Principles of Electroanalytical Methods* and *Potentiometry and Ion-Selective Electrodes*. The text is divided into relatively short segments, each accompanied by self-assessment questions (answers are at the back of the book).

The individual chapters deal with dc polarography, electrode processes, pulse polarographic techniques, and stripping voltammetry and analytical applications of these techniques. The chapter on classical dc polarography discusses the principles of circuits and cells used, the construction of the dropping mercury electrode, the slope of polarographic current–voltage curves, the nature of solvent and the role of supporting electrodes, and construction of the calibration curve and the method of standard addition. The importance of three electrolyte systems for studies of aqueous solutions is overestimated. Descriptions of tests for reversibility (logarithmic analysis, difference of $E_{3/4}$ and $E_{1/4}$) are insufficient. Identity of the $E_{1/2}$ for reduction of the oxidized form with $E_{1/2}$ for oxidation of the reduced form must be verified. The lower limit of concentration is usually 5×10^{-6} M rather than 1×10^{-4} M (for dc polarography); concentrations higher than 1×10^{-3} M (rather than 1×10^{-2} M) should be avoided.

The concepts of charging, maximum, diffusion, migration, kinetic, catalytic, and adsorption currents are introduced. The concept of diffusion currents with a kinetic contribution is misleading: The transport is governed either by the rate of diffusion or the rate of a chemical reaction, or these two rates are comparable. In the case of reducible acids, the limiting current becomes controlled solely by the rate of protonation of the conjugate base, when the limiting current of the reduction of the acid is smaller than about 15% of the total limiting current. Examples of successful analytical applications of kinetic waves (e.g., of aliphatic aldehydes) are well documented. The decrease of the limiting current of reducible acids (e.g., diphenylarsinic acid, p. 136) does not occur in the pH range comparable with pK_a, but usually at pH values several pH units higher, where the *rate* of protonation of the base decreases with increasing pH.

The section dealing with the voltammetry at solid electrodes is brief but to the point. Their use for the studies of process (mostly oxidations) at positive potentials is indicated, as well as their more limited reproducibility and potential range for reductions. Normal and differential pulse polarography as well as stripping voltammetry are discussed. Relative merits of polarography and other analytical methods are objectively compared.

Some references are given in text by name of author and year, but they are missing from the bibliography.

On the whole, this paperback text is a useful addition to electroanalytical literature and will be useful as an introductory text for self-learners.

Chemical Instrumentation: A Systematic Approach. Howard A. Strobel and William Heineman. 1210 pp. John Wiley & Sons, 605 Third Ave., New York, NY 10158. 1989. $50

Reviewed by Paul Bohn, School of Chemical Sciences, 1209 West California St., University of Illinois at Urbana–Champaign, Urbana IL 61801

The third edition of Strobel's text, *Chemical Instrumentation: A Systematic Approach*, co-authored with William Heineman, lives up to its title. It is without question the most thorough and encyclopedic text in the field of chemical instrumentation of which this reviewer is aware.

The text is subdivided into thematic sections of several chapters each which,

after a short introductory chapter, include "Basic Electronics," "Basic Optics," "Basic Quantification," "Optical Spectroscopic Methods," "Energetic Particle and X-ray Methods," "Chromatographic Methods," and "Electroanalytical Methods."

By having all underlying fundamental material on optics and electronics in the beginning, followed by chapters devoted to specific experiments, the book can be used in many ways. It is appropriate first and foremost for a thorough treatment of analytical principles, with selected examples, at the graduate level. With proper selection of material and rearrangement of time sequence of presentation, it is also appropriate for a junior–senior-level course in chemical instrumentation. In fact, with carefully chosen segments, it would be appropriate for students first being exposed to principles of chemical analysis.

The authors have taken pains to be systematic. Each of the chapters (with the exception of the first) is succeeded by a series of problems and selected solutions. These problems tend to test strict comprehension of the material presented rather than ability to extend the material to new chemical situations and measurements. References at the ends of chapters are reasonably thorough and up to date. From the student's perspective (especially the analytical graduate student), this will be a reference to keep.

My main criticisms have more to do with the genre of chemical instrumentation textbooks than they do with this specific textbook, since the following comments also apply to the other major instrumental analysis textbooks. These involve what is considered the target of an analytical investigation. Although in the introductory chapter this is explicitly described as the solution to a problem, all too often this is decoded to mean the determination of a concentration. In point of fact the questions of what (no discussion of magnetic resonance techniques) and where (minimal coverage of microscopies and microprobe techniques) are largely ignored. It seems that the question of structure, especially as it pertains to molecules in real samples, is left for someone else to answer. An excellent example of this is found in the chapter on light scattering. Although modern laser light scattering finds widespread use in characterizing problems as divergent as atmospheric chemistry and the shape and molecular weight of polymers in solution, the treatment sticks to a discussion of turbidimetry, as is found in other textbooks on chemical instrumentation.

The other major problem with this textbook concerns the balance between description and explanation. For example, Fourier transforms are one of the most important concepts in modern chemical instrumentation. In the four or five pages devoted to the topic they are described but are certainly not explained in sufficient detail to impart a working knowledge of them. Another example comes from the discussion of absorption spectrometry, in which no mention is made of the importance of calorimetric methods and their ability to circumvent the problems associated with light scattering in conventional transmission-based methods. Perhaps it is asking too much for a text to be both encyclopedic and to contain strong coherent discussions of important physical concepts. However, this reviewer would opt for a better balance.

Visible and Ultraviolet Spectroscopy. Ronald C. Denney and Roy Sinclair. xvii + 197 pp. John Wiley & Sons, 605 Third Ave., New York, NY 10158. 1988. $22

Reviewed by Galen W. Ewing, 3009 Raybun St., Las Vegas, NM 87701

The general introduction to the series to which this book belongs states that the material is intended for use by "distance learners," which I take to mean for home study. The level of the work would seem to be about right for this audience, but I would expect many readers to be frustrated by some inconsistencies and omissions.

In the first place I can see no excuse for not having an index in a technical book. This text would also profit by the inclusion of a glossary defining not only the technical terms used but also common synonyms that do not appear in the text. For instance, such words as spectrophotometer, liter, and molarity are not mentioned anywhere.

The format of the book is disconcerting at times. Many figures are printed against a gray background, and in some cases detail of the drawing is lost (e.g., the figure on p. 43). It took me some time to discover what is meant by "SAQ," an abbreviation for Self-Assessment Questions. Examples in text are designated by the symbol ▯, with no explanation.

There are a few errors, but the most confusing one is a formula containing the number 120^{-3}, where 10^{-3} was intended (p. 28). The calculation on p. 120 is fine except for the omission of a multiplier of 2 in the last term of Equation 1, but even with this correction it is difficult to justify the number of significant figures in the answer. Another confusing point was the computation on pages 133–36, where insufficient data are given to permit the desired solution. In another spot, the authors arbitrarily change from "$dm^3\ mol^{-1}\ cm^{-1}$" to "$m^2\ mol^{-1}$" as units for molar absorptivity; both are correct, but the change lacks adequate explanation. The treatment (p. 128) of the Morton and Stubbs method of evaluating spectra is inadequate, especially in view of the accompanying Figure 3.3c, where the line styles do not conform to the legend. Most of the few other errors are merely typographical and can be overlooked.

It is easy to pick flaws in this book and not so easy to see its good points. The examples and problems (SAQs) are well chosen. I like the idea of including, in facsimile, an official method description of a typical analysis (pp. 100–102). The treatment of different methods of plotting spectral data is well done. The discussion of instrument types is good, but there is no description of how a diffraction grating works; Figure 1.3b (p. 39) gives a fine opportunity for this, and one wonders why it was omitted.

All in all, however, there are other books that I would recommend over this one for a student or technician just entering the field.

Algorithms for Chemists. Jure Zupan. xv + 290 pp. John Wiley & Sons, 605 Third Ave., New York, NY 10158. 1989. $88

Reviewed by Steven D. Brown, Department of Chemistry, University of Delaware, Newark, DE 19716

The recent increase in interest in chemometrics has prompted a number of books offering introductions to the subject. Most of them offer a good deal of statistical preliminaries, then cover the field rather broadly with a few partially worked examples and perhaps some figures.

Algorithms for Chemists is also an introduction to computer-aided data analysis, but Zupan takes a different approach. The book's three sections on data representation, handling, and transformations cover most routine procedures required in data analysis, from generation of normally distributed random numbers to two-dimensional Fourier and Hadamard transforms useful in image processing. The usual statistical preliminaries are absent, but cellular automata, expert systems, and neural networks—subjects not covered

in other popular chemometrics books—are covered here, albeit briefly.

The most important difference between this and other books on chemometrics lies in the author's approach. Zupan uses the development of computer algorithms from mathematical detail as the main point in each section; thus, the student is helped over one of the main stumbling blocks to learning to use the computer to analyze data: the difficult task of translating equations on the page into a workable computer code.

Each of the 31 algorithms is broken into sections, and many of the more complex ones make use of algorithms previously developed—an approach that encourages good, "top-down" programming style. The algorithms are written in a mix of Pascal, Basic, Fortran, and Knuth's pseudocode to ensure that any reader with basic programming skills can understand them. He also explains the rationale behind the algorithm, indicating where use of the code is appropriate.

The author's humor and enthusiasm for the subject help make difficult material interesting. No exercises are provided, but the interested student can get more help from the lists of recent references provided at the end of each chapter.

The lack of coverage of statistical background material makes this book unsuitable for use as the single text in a typical introductory course in data analysis, but its strengths make it attractive for use in data analysis courses presuming some statistics or for use with another, more statistical text. This book is more a tutorial on the methodology and the philosophy of computer-aided data analysis than it is a compendium of research in the area, a fact that makes it both accessible to students of computer-aided data analysis and useful to students who have completed the course.

Gas Chromatography. J. E. Willet. 253 pp. John Wiley & Sons, 605 Third Ave., New York, NY 10158. 1987. $25

Reviewed by Stephen N. Chesler, Center for Analytical Chemistry, National Institute of Standards and Technology, Gaithersburg, MD 20899

This book is intended for persons who have taken at least one year of college-level chemistry and wish to gain some knowledge of gas chromatography (GC) using self-study techniques. The book is constructed differently from the conventional college textbook because the author cannot depend on accompanying lectures to explain details of the subject matter presented in the text. Each section discusses a major area of GC, and the initial chapters provide a foundation for understanding material in the later chapters.

At significant points in the text, the student is asked to perform exercises that are designed to reinforce understanding of the material and also indicate whether the student has assimilated the major concepts presented. At the end of each chapter the student encounters a series of thought-provoking questions. The answers to these questions are given in an appendix at the end of the book that includes relevant discussions about the questions. The answer section is a useful study tool in itself.

The text stresses the pragmatic aspect of GC and presents little formal theory. There are chapters on instrumentation, columns, optimization, high-temperature applications, and qualitative and quantitative analysis. The style of the author's prose is informal and easy to read. This book, however, appears to be technically out of date in some areas. For instance, there is little discussion of macrobore or bonded-phase thick film capillaries. Instead, the author emphasizes SCOT and PLOT columns, which most chromatographers consider obsolete. But on the whole, this book is quite well suited to its purpose and I would recommend it to serious-minded students wanting to gain an acquaintanceship of GC.

Books Received

Modern NMR Spectroscopy: A Workbook of Chemical Problems. Jeremy K. M. Sanders, Edwin C. Constable, Brian K. Hunter. 118 pp. Oxford University Press, 200 Madison Ave., New York, NY 10016. 1989. $20

The five chapters in this paperback are entitled "Errors I Have Made," "Interpretation of Spectra," "Symmetry and Exchange," "Structure Determination Using NMR Alone," and "Structure and Mechanism." The book is intended as a companion text for *Modern NMR Spectroscopy—A Guide for Chemists*, but it can be used with other texts as well. It is easy to read and contains several figures. Hints, answers, and an index are included.

Analytical Methods for Geochemical Exploration. J. C. Van Loon and R. R. Barefoot. x + 344 pp. Academic Press, 1250 Sixth Ave., San Diego, CA 92101-4311. 1989. $50

The 10 chapters cover sample preparation, reagents, field methods, soils, lithogeochemical and biogeochemical analyses, platinum group metals, gold, and ICP/MS. This book is not a traditional text but does discuss methods such as AAS, X-ray fluorescence, neutron activation spectroscopy, and electrochemical methods. Most of the references are from the 1970s through 1985; a few are from 1986 and 1987. An index is included.

Principles and Applications of Electrochemistry. D. R. Crow. ix + 230 pp. Chapman & Hall, 29 West 35th St., New York, NY 10001. 1989. $28

The nine chapters cover equilibria, electrolytic conduction, potentials, interfacial phenomena, and electrode processes. Each chapter includes problems and suggested readings. Answers to the problems and an index are included.

Introduction to Nonlinear Laser Spectroscopy. Marc D. Levenson and Satoru S. Kano. xvi + 299 pp. Academic Press, 1250 Sixth Ave., San Diego, CA 92101-4311. 1988. $40

The seven chapters are entitled "Introduction," "Theory," "Saturation Spectroscopy," "Coherent Raman Spectroscopy," "Multiphoton Absorption," "Optical Coherent Transients," and "Nonlinear Sources for Linear and Nonlinear Spectroscopy." Most of the references are from the 1970s, and a few are as recent as 1987. Problems, answers, a glossary, and an index are included.

Principles and Practice of Chromatography. B. Ravindranath. 502 pp. John Wiley & Sons, 605 Third Ave., New York, NY 10158. 1989. $80

The nine chapters cover basic principles, GC (general features, separations, and detectors), LC (instrumentation and planar chromatography), and many applications. Most of the references are from the 1970s; some are as recent as 1987. A list of abbreviations, a chemical index, and a general index are included.

Chaos and Integrability in Nonlinear Dynamics: An Introduction. Michael Tabor. xiii + 364 pp. John Wiley & Sons, 605 Third Ave., New York, NY 10158. 1989. $55

The eight chapters are entitled "Dynamics of Differential Equations," "Hamiltonian Dynamics," "Classical Perturbation Theory," "Chaos in Hamiltonian Systems and Area-Preserving Maps," "Dynamics of Dissipative Systems," "Chaos and Integrability in Semiclassical Mechanics," "Nonlinear Evolution Equations and Solitons," and "Analytic Structure of Dynamical Systems." Most of the references are from the 1970s; a few are as recent as 1987. An index is included.

Modern Spectroscopy. J. Michael Hollas. xx + 388 pp. John Wiley & Sons, 605 Third Ave., New York, NY 10158. 1987. $25

The nine chapters are entitled "Some Important Results in Quantum Mechanics," "Electromagnetic Radiation and its Interaction with Atoms and Molecules," "General Features of Experimental Methods," "Molecular Symmetry," "Rotational Spectroscopy," "Vibrational Spectroscopy," "Electronic Spectroscopy," "Photoelectron and Related Spectroscopies," and "Lasers and Laser Spectroscopy." Each chapter includes questions and a bibliography. Units, constants, conversion factors, character tables, and an index are also included.

Fundamentals of Molecular Spectroscopy. Walter S. Struve. xii + 379 pp. John Wiley & Sons, 605 Third Ave., New York, NY 10158. 1989. $50

The 11 chapters cover radiation–matter interactions, electronic structure, diatomics, polyatomic vibrations, lineshapes, lasers, photon processes, and nonlinear optics. Appendices include constants, conversion factors, Beer's law, and angular momenta. Most chapters contain problems but not answers. Of the 100 references, most are from the 1960s and 1970s; a dozen or so are from the 1980s. Author and subject indices are included.

Molecular Spectroscopy. Jack D. Graybeal. xix + 732 pp. McGraw-Hill, 1221 Avenue of the Americas, New York, NY 10020. 1988. $50

The 18 chapters cover wave mechanical methods, matrix methods, electric and magnetic properties of matter, diatomic molecules, magnetic and electron spin resonance quadrupole interactions, diatomic vibrotors, and polyatomic molecules. Each chapter contains problems, but the answers are not given. Most of the references are from the 1960s and 1970s; a few are from the 1980s. Many references are historical. Twenty-four appendices cover everything from classical harmonic motion to the Tanabe–Sugano diagrams. An index is included.

Labeled compounds from Merck Sharp & Dohme/Isotopes

MSD Isotopes – research products that work, bringing results to researchers in biology, chemistry, physics, medicine and related fields.

Did you know that we now offer thousands of compounds labeled with deuterium, carbon-13, nitrogen-15 and other stable isotopes too? And did you know that even if you require a compound which is not available from us immediately 'off-the shelf', we have the world's best facilities to custom synthesize it for you?

Just call or write to us for more information on what we have in stock and can make for you.

MSD

MSD ISOTOPES

DIVISION OF MERCK FROSST CANADA INC., Montreal, Canada

For technical information call 1-800-361-0460.

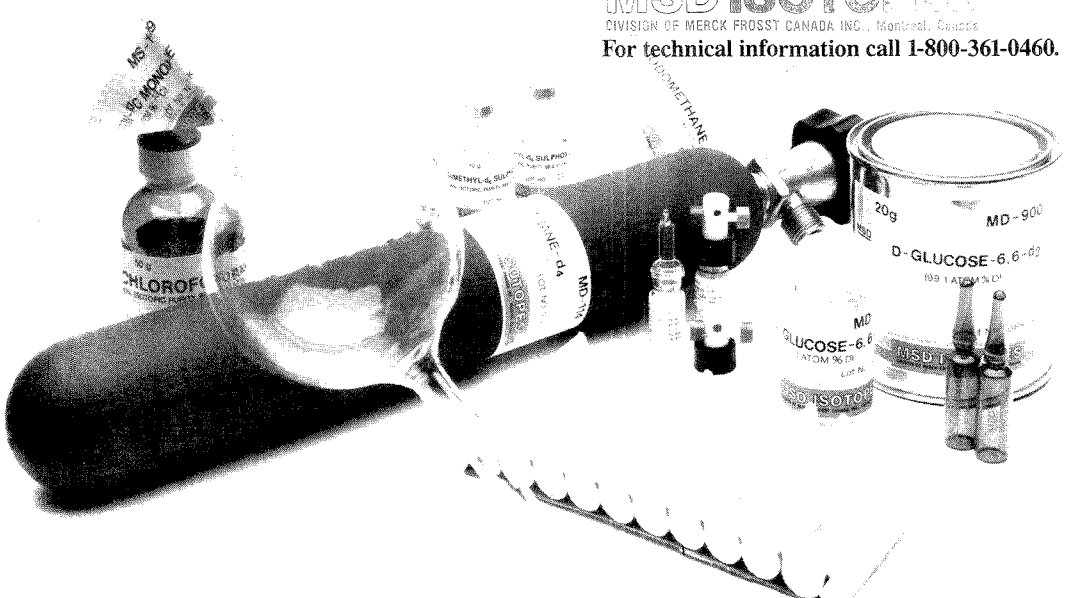

WEST COAST
P.O. Box 2951
Terminal Annex
Los Angeles, CA 90051
Los Angeles Area: (213) 723-9521
Outside State of CA: (800) 423-4977
State of CA: (800) 372-6454

EAST COAST & CENTRAL
4545 Olentha Avenue
St. Louis, MO 63116
Outside state of MO: (800) 325-9034
State of Missouri: (314) 353-7000

CANADA
P.O. Box 899
Pointe Claire/Dorval, Quebec
Canada H9R 4P7
Telephone: (514) 697-2823

CIRCLE 88 ON READER SERVICE CARD

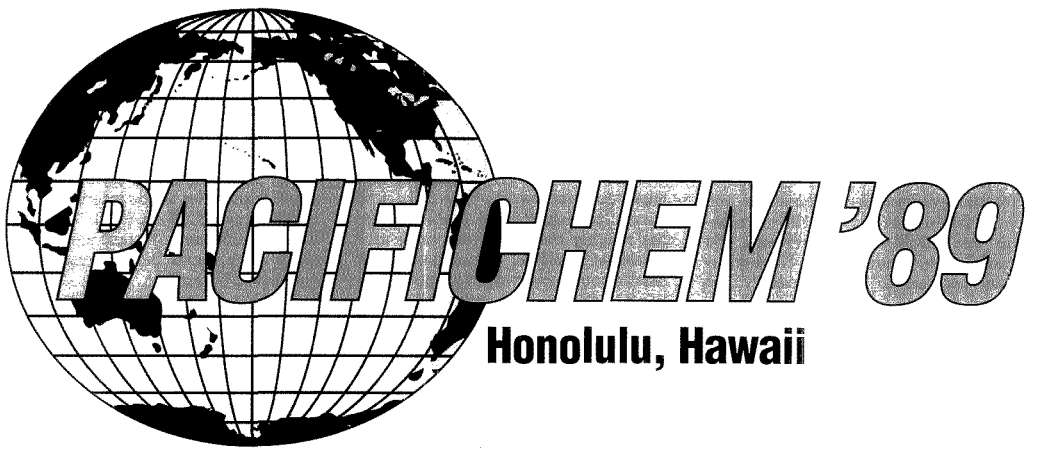

A ceremonial Hawaiian chant opened the Second International Chemical Congress of Pacific Basin Societies (PACIFICHEM '89) in Honolulu on Sunday, December 17. During the week approximately 7400 registrants and exhibitors could choose from the more than 4500 presentations to learn about recent advances in agrochemistry, applied chemistry, bioscience and technology, information transfer, and macromolecular chemistry as well as the more traditional areas of chemistry (analytical, organic, inorganic, and physical). Major emphasis was placed on the science relating to the environment, health, food, and technology in general.

Sponsored by the Chemical Society of Japan (CSJ), the Chemical Institute of Canada (CIC), and the American Chemical Society (ACS), the Congress was hosted by CSJ. The Federation of Asian Chemical Societies, the Federación Latinoamericana de Asociaciones Químicas, and 21 chemical societies headquartered in Pacific Basin countries were official participants. Chair of the congress organizing committee was Professor Michinori Oki of the Okayama University of Science.

The opening day symposium on the public's current perception of chemistry reflected the increasing realization that we are surrounded by chemophobia—by unreasonable, irrational fear of what chemists do. Because many major policy decisions are based on an understanding of chemistry, we need to look for better ways to educate the public. Roald Hoffmann, Nobel laureate at Cornell University, touching on the interaction of chemistry, education, and democracy, reminded us that "our society, of course, is not a single one, but many distinct ones, the product of culture and history. Yet there is a dream, an ideal that in our time the societies that we inhabit all aspire to, and that is democracy. And democracy requires intelligent, sincere action on the part of all of its citizens, not only chemists. Those actions often impact

FOCUS

on chemistry. If our collective decisions are to be rational they must be educated ones. Ordinary people must know some chemistry to make informed democratic judgments. They need not know as much as chemists do, but they need to know a little." Chemists should continue to educate themselves on subjects relating to the use of chemicals and should remain empathetic to the concerns expressed by the public (i.e., Alar on apples), commented Hoffmann.

James Guillet, a professor of chemistry at the University of Toronto who has spent more than 20 years working on plastics-related questions, used the "plastics problem" to demonstrate the importance of ordinary people knowing some chemistry. Although we all sense this imperative, he says we haven't even done a good job training our own practitioners or our students to think in scientific terms about these problems. Education must change at all levels, he emphasized.

Guillet comments that huge sums of money are being spent to solve problems that aren't even problems—much more than is being spent on basic research, at least in Canada. The lack of information both in the environmental movement and in the general public about the role of chemistry and the nature of the evidence (i.e., risk assessment and how you carry out toxicology testing, which are both very complex ideas that are being oversimplified) often results in not only wasting money but, in fact, making the environment poorer. For instance, the idea that replacing plastics with paper helps the environment is completely wrong, says Guillet. Paper requires large areas of land to produce the trees. In the United States one acre of land will produce approximately 500 lbs of paper a year on a renewable basis. "If you look at packages," comments Guillet, "you find that paper packages are from three to five times as heavy as the plastic packages. If you convert from plastic to paper you would be throwing away three to five times as much garbage." Guillet emphasized that if you look at the environmental cost of producing paper, we would need to convert a very large amount of land that is either in national parks or forest or used for farming to the growing of trees (120 million acres would be required if we

were to replace all plastic with paper). This would require an area larger than five times the size of Tennessee. "It seems that when we are adopting a policy to stop people from cutting down trees in China and Brazil, we shouldn't adopt a policy at home that would make us cut down two to three times as many trees as we are already cutting down," he comments.

If you look at energy costs, it turns out that the energy required to produce paper is about twice what is required for the production of plastic. If you work that out in terms of the extra paper you would have to produce, you would have to build about 50 new nuclear reactors to get the energy you would need to fuel the paper plants. There is little water pollution from plastics production, whereas paper plants are one of the major contributors to water pollution throughout North America. "So," comments Guillet, "the public seems to think that by going to a natural product you actually save energy resources and reduce pollution, whereas in fact it is just the opposite."

A second issue, he says, is the need to carry out an energy balance calculation, comparing the energy required to make various packaging materials. When you compare the cost of a glass milk bottle, which is returnable, with that of a plastic polyethylene package, the milk bottle would have to go through more than 100 cycles of use before you would have a system equivalent in energy costs to the plastic one. The energy cost of making the plastic is 1/100 the cost of making the glass bottle, and that does not include the energy associated with going back and forth to the dairy or heating the water to clean the bottle. He pointed out that not all recycling systems save energy or resources. In many cases we are wasting energy resources by not using a disposable system.

What do we consider a nonrenewable resource to be? It turns out, Guillet says, that a nonrenewable resource is considered to be something like an oil well where we put a pipe down and take the oil up, burn it, and get carbon dioxide, water, and energy. But we also know that if we supply energy, such as solar energy, we can take carbon dioxide and water and make oil and pump it back down the oil well. All things that we consider major nonrenewable resources are really renewable, provided that we have enough energy. If you have enough energy, you can make hydrocarbons and you don't have to worry about using them up. We don't consume anything. Every atom of C, H, O, Fe, and Al is still around on the planet in some form. We simply have converted it from a high-energy, low-entropy form into a low-energy, high-entropy form. To reverse that process, we have to apply energy on the right-hand side of the equation and force it back the other way. If you look at what we consider to be renewable resources (e.g., water power, biomass, and trees), we find that those sources are renewed by sunlight.

"What should we do with all the plastic? If the plastic is found in garbage, the best way to recycle it is to burn it, because every pound of plastic has roughly the same heat value as a pound of gasoline. If you burn that plastic you recover much of the energy you had tied up in the barrel of oil you borrowed in the first place to make the plastic device. Certainly no other country that I am aware of, except the U.S. and Canada, is thinking of replacing plastic packaging with paper," says Guillet. Much of what lies ahead involves the making of intelligent decisions by individuals who are not necessarily chemists but who have been given accurate and relevant information.

"We, as chemists, must continue to probe the universe and attempt to understand all aspects of our environment. One such area is coal research. The use of microprobe techniques is providing a wealth of information in the area of coal chemistry," says P. C. Lyons of the U.S. Geological Survey, organizer (C. A. Palmer and R. R. Martin, co-organizers) of a symposium on new frontiers in coal-quality research. Several important advances are highlighted here.

Geoffrey Taylor of the Australian National University is examining what were thought to be homogeneous macerals (the basic petrographic units of coal) by transmission electron microscopy (TEM). The submicron world of macerals, not visible to previous workers using light microscopy, is really heterogeneous and contains bacterial products and fungal remains as well as lipid material. TEM, for the first time, shows the detailed nature of macerals and provides an explanation for the differences in reflectance and fluorescence noted in macerals that are homogeneous by light microscopy. A new subdiscipline within coal petrology has been opened up by this work. "This is fascinating!" comments Lyons.

Ronald R. Martin of the University of Western Ontario uses secondary ion mass spectrometry (SIMS) to study the spatial distribution of trace elements in macerals. This microprobe technique reveals whether the trace element is organically complexed (spatial distribution in the maceral would be expected to be uniform) or is in mineral matter (spatial distribution would be expected to be fairly irregular).

Lyons says that he, David Hercules, and John Morelli (a former graduate student) at the University of Pittsburgh have come up with a semiquantitative approach to the study of the occurrence of trace elements in macerals. This laser-microprobe MS technique (LAMMS) compares the relative concentration of trace elements in macerals by normalizing the elemental m/z signal intensities to the intensity of an organic peak (C_7H, m/z 85). "You can look at differences in macerals in the same sample and between samples," comments Lyons.

Another interesting technique was described by C.F.K. Diessel of the University of Newcastle in Australia. He finds that fluorescence intensities from surface samples show significant differences from samples from the same horizon collected up to 150 m below the surface, most probably because of surface weathering and oxidation. "All of these methods," says Lyons, "attempt to give us a better understanding of coal at the molecular level and make us realize that there are a huge number of variables involved in coal chemistry."

The ocean also provides fertile ground for research, both in the isolation of natural products from marine organisms and in the study of marine geochemistry. Paul Scheuer, a natural products chemist at the University of Hawaii, uses a research submarine supported by the National Oceanic & Atmospheric Administration (NOAA) to collect coral and sponge specimens from the Pacific Ocean. He dives to depths of about 350 m, collecting gorgonians and other corals. From a shallow water coral he has isolated prostaglandins with unprecedented structures and very different biological activities (i.e., anti-tumor activity) when compared with the mammalian prostaglandins. A shallow water sponge metabolite is the toxic polyether, okadaic acid, which in itself isn't very interesting but which is related to important fish and seafood toxins, ciguatoxin and the diarrhetic shellfish toxins. Okadaic acid is chemically and structurally related to the Gulf Coast red tide toxin, the brevetoxins. "More recently okadaic acid has become a molecular probe and is being used widely as a phosphatase inhibitor in biochemical research," says Scheuer.

One of the most recent important discoveries is the isolation of manoalide, a terpenoid that has been shown to have anti-inflammatory activity. Isolated from the sponge *Luffariella* sp., this has opened up a totally new vista

of potential anti-inflammatory agents. Its mechanism of action is different from all other known agents in that it acts by inhibiting phospholipases. "This is really exciting!" said Scheuer.

Much of the fundamental research in marine geochemistry relates to global warming and the CO_2 balance. In the symposium on marine geochemistry, John Martin at Moss Landing Marine Laboratories described the first accurate measurement of dissolved iron in seawater. Scientists have been trying for decades to obtain reliable numbers; however, the contamination and measurement problems have been enormous. Most ships are made of iron, and rust is everywhere. Martin—whose laboratory was recently destroyed by the earthquake in California and will have to be bulldozed—was able to collect samples from the ocean and manipulate them, avoiding contamination, and measure iron in nanomolar amounts using extraction preconcentration and atomic absorption spectrophotometry.

What Martin discovered was that in many parts of the ocean iron appears to be the limiting nutrient. There are places where there is plenty of surface phosphate, nitrate, and sunlight; however, plants do not thrive. Martin hypothesizes that they do not thrive because they are missing trace amounts of iron. A stoichiometric amount of iron appears to be required for nitrogen metabolism. He postulates that atmospheric dust events provide the necessary iron. For example, dust blows off the Asian continent and is deposited over broad areas of the North Pacific Ocean. However, in areas with excess phosphate and nitrate present, there does not appear to be the necessary iron to stimulate plant growth and turn the ocean green, a process that should be visible from a satellite. Martin was able to demonstrate this phenomenon in shipboard experiments in the following way. He takes a seawater sample under ultraclean conditions and adds a few nanomoles of unchelated iron. Rapid growth occurs in a few days with added iron, whereas little growth occurs without iron.

The interest in this comes from the greenhouse effect and the global CO_2 balance. We know that in the last Ice Age the world had ~30% less CO_2 in its atmosphere. Martin hypothesizes that in Ice Age conditions the planet was drier and dustier and that more dust blew off the continents and fertilized the ocean by adding trace amounts of iron. This allowed the plants to thrive, and productivity increased. More CO_2 and fixed carbon were pulled down into the deep ocean, which lowered the atmospheric CO_2 levels.

Mitsuo Uematsu at Hokkaido Tokai University, studying the mineral aerosol deposition over the North Pacific Ocean, has collected weekly samples since 1981 at 14 stations. He has been able to show the likelihood of the Martin hypothesis by demonstrating that aerosol iron input rates are very low in the equatorial Pacific, a region with unused major plant nutrients. "This is a tour de force for trace metal chemistry," comments Peter Brewer of Woods Hole Oceanographic Institution, one of the symposium organizers.

Some of the fundamental problems relating to waste disposal, the rates at which processes such as adsorption and respiration occur, can be studied by using classic techniques of ocean chemistry. Yoshiyuki Nozaki at the University of Tokyo and co-workers make use of the uranium–thorium series of nuclides to study the transport of matter from the atmosphere to deep-sea environments in the Japan trench. Uranium, which is present naturally in seawater, decays to form thorium isotopes. "Measuring this decay provides a marvelous diagnostic signal for oceanic processes, and these workers have done this with great elegance," comments Brewer. The hydrolytic materials containing thorium adsorb onto particles, and a strong disequilibrium is established between the parent uranium and the daughter thorium. Looking at this disequilibrium, you can measure the rate of removal of thorium by adsorption and estimate the rate at which reactive pollutants are being scavenged from the oceans. From a knowledge of surface science and adsorption processes, you can obtain the rates at which oceanic processes occur. You start with large samples, concentrate them, and measure small amounts of radioactivity.

One of the biggest controversies in oceanography is the amount of dissolved organic carbon (DOC) and dissolved organic nitrogen (DON) in seawater. The theory about how the ocean operates is as follows. If we look at the biogeochemical cycles, plants grow in the upper layer, which is rich in phosphate, nitrate, and silicate. They are eaten and the debris falls to the bottom and creates the ocean sediments. Particles are regenerated and go back to phosphate, nitrate, and CO_2, and the cycle repeats itself. For years, little mention was made of an active cycle of DOC or DON, which was felt to contribute a stable, inert background signal. A Japanese scientist, Yoshimi Suzuki, carried out new high-temperature catalytic measurements showing that DOCs and DONs were not generating what was considered to be background signals, but were abundant, highly reactive, and provided the dominant signal. "This has a tremendous impact on the carbon budget of the world, because if we believe the new data then the amount of DOCs is a reservoir that exceeds the amount of CO_2 in the atmosphere by a factor of 2. Large issues are at stake," says Brewer. "Is this really a major cycle or do we leave it out of our calculations?" The technical problem is one of precise conversion to CO_2 of trace organics of unknown composition in a salt-rich medium.

Brewer himself studies the carbon balance of the North Atlantic. Using coulometric analysis, he looks at the atmospheric CO_2 imprint on the ocean. By working with the data, he can modify the signal and strip off changes from $CaCO_3$ dissolution and respiration of organic matter. What this reveals is the amount of contamination of the upper ocean that has taken place by industrial CO_2. We can compute, using models, what the balance would have been a century ago before we contaminated the ocean. "What we observe today," comments Brewer, "is an ocean in which the upper layers are enriched in CO_2 by as much as 40 μmol/kg, but deep waters that show no signs of enrichment. So we all are biased in the way we observe the ocean; we must recognize the invasion of a massive pollution signal, which in reality is yet a small perturbation on a very large background. Using gas extraction, followed by coulometry, our goal is to obtain a precision of one part in 2000 when measuring about 2000 micromoles of CO_2/kg of seawater at the surface. Warming thus far has not significantly affected the ocean, but as greenhouse gases build up, we can at present only badly diagnose what the interaction between a chemically and physically changing ocean and atmosphere will be."

The hidden agenda of the symposia was to bring together the U.S., Canadian, and Japanese counterparts to discuss how to proceed with the global-observing program to study geochemical cycles of the ocean in the face of global climate change. Scientists in the three countries hope to start up a program, the Joint Global Ocean Flux Study, using satellites to study ocean color. It involves the debate over the fundamental measurements, predictions of what will happen if we get a CO_2-rich ocean, and the effect of large-scale perturbations on the climate. The groundwork was laid in Hawaii for a major experiment next year in the equatorial Pacific, and plans for an international meeting in Tokyo in April 1990 were formalized. *Sharon Boots*

NEW PRODUCTS

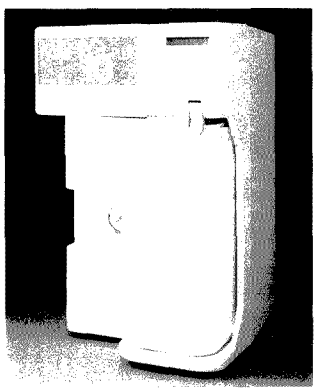

Milli-RO reverse osmosis systems for water purification reduce base levels of organic and inorganic contaminants and improve the performance of downstream systems. Millipore 401

Spectrophotometer. Otsuka DLS-700 laser light-scattering spectrophotometer operates in a dynamic light-scattering mode for particle size determinations and in a static light-scattering mode for molecular weight measurements. Particles ranging in size from 3 nm to 3 μm can be analyzed. Polymer Laboratories 404

Electrochemistry. Model 3001 amperometric biosensor detector is a microprocessor-controlled instrument for constant potential control of amperometric electrodes. Features include concentration and rate modes, digital display, three filter selections, and an internal test cell. Universal Sensors 405

Density/RI/color. DRC-400 automated system for density, refractive index, and color determination uses sealed vessels and includes computerized data archiving for product information and customer logging. The system is particularly suited for use in the flavor and fragrance industry. Questron 406

Detector. Soma S-3702 variable-wavelength UV–vis detector for HPLC features automatic baseline correction, nine sensitivity settings, a cassette-type flow cell design, LED display, and microprocessor-controlled electronics for unattended operation. JM Science 407

Alkalinity. FPA 312 automatic on-line alkalinity analyzer measures concentrations of dissolved carbonate, bicarbonate, and hydroxide ions using acid–base titration with a pH electrode for end-point detection. The unit features a flow-through reaction cell and contains only one moving part in the sampling system. Tytronics 408

Microbalance. Model 200-1 surface acoustic wave (SAW) mass microbalance, which features a mass sensitivity of 1.8×10^{11} Hz cm^2/g and mass resolution of 5×10^{-13} g, includes a power supply and six-digit LCD readout of the beat frequency. Two separate 200-MHz SAW crystals are mounted on a common thermal base for temperature stability. Femtometrics 409

Flash unit. Palflash 500 is a pulsed flash unit designed for flash photolysis, fluorescence spectroscopy, aerosol, droplet, and general spray behavior studies. The instrument produces flashes with discharge energies from 12 to 24 J and exposure duration times from 250 to 750 ns. Photonics Analysis 410

Calorimeter. Model 4252 isothermal flow calorimeter consists of a measuring unit; a constant-temperature bath; dual programmable high-precision pumps; and a data acquisition, graphics, and analysis software package. Hart Scientific 411

Autosampler. Model 738 autosampler can inject volumes ranging from 1 μL to 1 mL from up to 96 different samples. Features include programmable injection volumes, precolumn derivatization, and software for on-the-fly programming and priority sample interruption. Alcott Chromatography 412

Oxygen. Model 311 oxygen analyzer offers measuring ranges of 0–10, 0–100, 0–1000, and 0–10,000 ppm O_2 and a special span range for air calibration. The electrochemical sensor features an absolute zero and output that is linear with respect to oxygen concentration. Teledyne Analytical Instruments 413

Software

IR. Heyden Spectrafile IR Plus provides spectral manipulation, quantitative analysis, searching, archiving, plotting, and computer control of commercial IR and FT-IR spectrometers. The software can be operated via mouse or keyboard-accessed menus. CECON Group 415

Document processing. BBN/Slate 1.1, designed for collaborative document development, runs on all Sun workstations under the SunOS version of UNIX. Features include voice annotation within documents, multilingual text editing and printing, and integrated teleconferencing for collaborative review and editing. BBN Software Products 416

Manufacturers' Literature

Instrumentation. Application notes and tutorial articles discuss scanners, multiplexers, and matrix switching techniques. Included is information on noise, error analysis, cabling, and grounding. Keithley Instruments 418

LIMS. Technical bulletin describes EasyLIMS software for IBM personal computers. Sample registration, worksheet generation, test data entry and calculations, report generation, and archiving are discussed. 16 pp. Beckman 419

IR. *Scan Time*, No. 17, features articles on the application of FT-IR to the study of proteins in solution and contaminant analysis by FT-IR microscopy. 6 pp. Spectra-Tech 420

Peptides. Application brief discusses a four-step liquid chromatographic pro-

For more information on listed items, circle the appropriate numbers on one of our Readers' Service Cards

cedure for the purification of neurotensin. Waters Chromatography Division of Millipore 421

Newsletter. *Biotext*, Vol. II, No. 3, includes information on nonporous resin columns for analysis of growth hormone, effective use of narrow-bore HPLC columns, and purification of monoclonal antibodies. 12 pp. Supelco 422

Electrochemistry. Application note AC-3 describes electrochemical impedance measurements. Information is provided on instrumentation, software, and single and multisine techniques. EG&G Princeton Applied Research 423

Catalogs

Environmental analysis. Catalog features products for hazardous waste testing, including high-capacity rotary extractors; filtration units; and equipment for liquid release testing, purge-and-trap sampling methods, and groundwater monitoring. Associated Design and Manufacturing 425

Environmental analysis. Catalog includes solution standards for EPA and CLP methods. Also featured are isomers of PCBs, dioxins, furans, PAHs, and pesticides. AccuStandard 427

Gases. Catalog lists handling equipment and delivery systems for specialty gases and cryogenic liquids. Equipment specifications and construction materials are discussed. Airgas 428

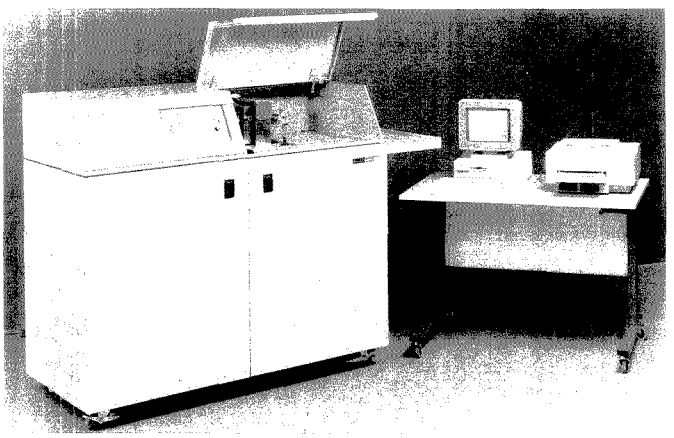

ELAN 5000 ICP mass spectrometer features single-button control of the vacuum system and ICP. The instrument is controlled by an industry standard 386-based computer with a multitasking operating system. Perkin-Elmer **402**

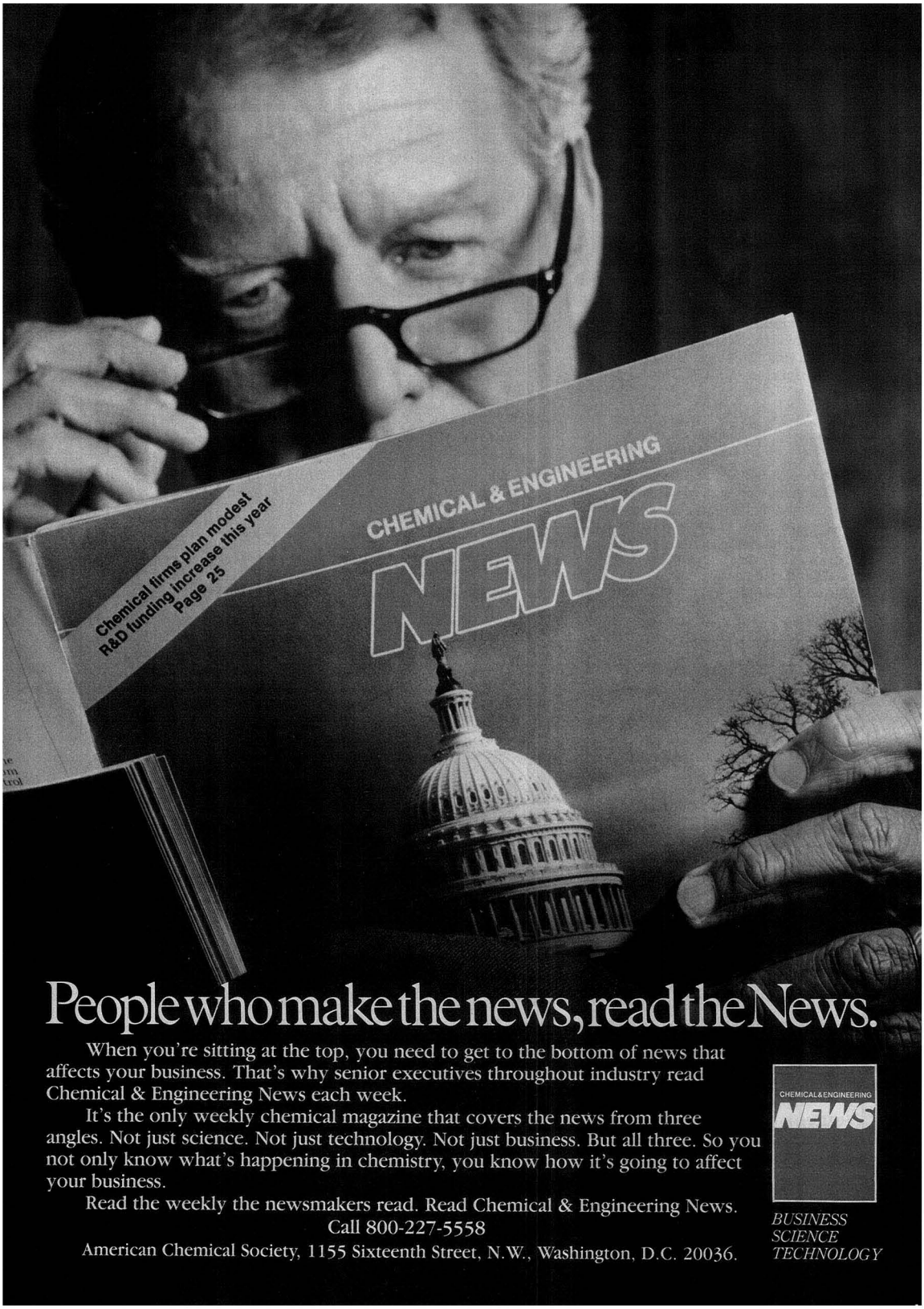

People who make the news, read the News.

When you're sitting at the top, you need to get to the bottom of news that affects your business. That's why senior executives throughout industry read Chemical & Engineering News each week.

It's the only weekly chemical magazine that covers the news from three angles. Not just science. Not just technology. Not just business. But all three. So you not only know what's happening in chemistry, you know how it's going to affect your business.

Read the weekly the newsmakers read. Read Chemical & Engineering News.

Call 800-227-5558

American Chemical Society, 1155 Sixteenth Street, N.W., Washington, D.C. 20036.

CHEMICAL&ENGINEERING
NEWS

BUSINESS
SCIENCE
TECHNOLOGY

Local Area Networks in the Laboratory

PART II

Steven A. Warner
ANDRULIS Research Corporation
4600 East-West Highway, Suite 900
Bethesda, MD 20814

A local area network (LAN) combines cable, hardware, and software to achieve *physical* connectivity between instruments and computers. *Logical* connectivity, however, is the basis for integrating laboratory information into an organization's overall information architecture. Developing this logical integration (e.g., what information is required, who needs it, and where it should go) enables the LAN to be used to its best advantage.

Before selecting any tool one must consider the job for which it will be used. LANs belong to the collection of tools termed *management information systems*, or MIS. Looking at the "big picture" and overall goals of an organization within the context of MIS is termed *information systems planning*, or ISP. Effective ISP ensures that a LAN, or any other new MIS tool, can easily be interfaced with current and future systems when introduced into an organization.

In the first part of this two-part series, published in the January 15, 1990, issue, the basics of LAN technology were presented, including the International Standards Organization Open Systems Interconnect (ISO-OSI) model for network protocols and standards. This article will present applicable ISP concepts followed by examples of various vendor approaches to implementing laboratory LANs.

Information systems planning—planning to succeed

A laboratory usually exists within the confines of a larger organization such as a corporation, a federal agency, or a university. The laboratory generates information and should be part of the total information architecture of the organization. How a laboratory LAN is planned, installed, and used is the key to successfully providing new capabilities within both the laboratory and the organization.

Organizations use and manage information to achieve their strategic goals. Information management typically defines standards for communications, security, data structure, user interfaces, hardware, and software. ISP is a component of information management that defines the requirements that new systems must meet, how new systems must interface with existing systems, what types of data will be processed, where the data will be processed, who will have access to the data, and so forth. Implementation of MIS components involves making choices within this framework, such as what type of computer environment is desired and whether processing will be centralized or distributed.

Components of MIS. MIS ideally is an enterprise-wide solution that meets all of the information needs of an organization. There are three components of MIS. *Data processing systems* (DP) assist an organization in the planning, execution, and control of its mission. Common examples include laboratory information management systems (LIMS) and computer-integrated manufacturing systems (CIMS). *Decision support systems* (DSS) assist management with semistructured tasks. They support managerial judgment and improve the effectiveness of decision making. A common example is the mathematical models used to conduct simulations. *Office automation* (OA) assists an organization with its office/administrative processes. OA typically includes word processing, electronic mail, and scheduling.

Together DP, DSS, and OA make up the overall MIS architecture for an organization. Effective MIS is the proper utilization of these components when and where they are needed. LANs (and also wide-area networks, or WANs) provide the communication links for this information architecture (enterprise-wide network) and would permit, for example, a laboratory in a chemical manufacturing facility to provide quality control data to a DSS component for management analysis of supplier quality, provide administrative data to an OA component for status reports, and print shipping labels with certificates of analysis directly within a packaging facility. The actual development of this architecture, however, requires careful consideration of technical and management factors.

Technical factors. An organization rarely begins information management in an automation-free environment. Most organizations have obtained their existing automated systems in a piecemeal manner over time, leading to a proliferation of dissimilar computer systems within any given organization.

A LAN that is based on the ISO-OSI model supplies the connectivity, security, format conversion, and interapplication communications that enable compliant, although dissimilar, systems to interoperate. Unfortunately, however, because the ISO-OSI model was only recently formalized, most automated systems in operation do not comply with it. Only a few vendors offer new systems that exhibit varying degrees of compliance with the model,

A/C INTERFACE

0003-2700/90/0362-389A/$02.50/0

and matching vendor claims of OSI compliance to reality can be a challenge for the systems designer—even within a single vendor's product line.

So, there's no free lunch. How can we achieve interoperability today? The answer is to use the standards available now and plan to move toward fully ISO-OSI compliant systems in the future. Today's standards typically equate to the lower four layers of the ISO-OSI model. Much of the decision as to which standards to select will be based on your organization's information management guidelines. Your laboratory LAN could be a TCP/IP Ethernet or an IBM Token Ring Network, depending on your organization's networking strategy.

Interoperability between systems at the upper three layers of the model is less easily achieved. Three common approaches exist to achieve interoperability at these higher layers. One approach is to use software that is available for whatever different hardware platforms are within your organization. For example, the Oracle database management system is available for many different vendors' computer systems. One component of the Oracle system is SQLNet, which enables access to Oracle applications across a variety of LANs. Direct communication between Oracle applications is supported with SQLNet, which provides some functional capabilities corresponding to the presentation and session layers of the ISO-OSI model.

A second approach to achieving interoperability at the higher layers of the model is to use common electronic file formats. These file formats may be peculiar to a particular application, or, more likely, can be read from or written to by the application. Examples of common file formats include ASCII, dBASE, JCAMP-DX, and DIF.

A third approach is to process all of an organization's data on a single centralized computer system. Depending on the size of the organization, this could range from a single microcomputer to a large mainframe computer system, with support of a broad range of DP, DSS, and OA functions. Centralized processing eliminates many problems associated with achieving interoperability, as a result of the single vendor environment, but it creates a new set of problems, including a single point of failure for all of an organization's MIS activities, unsatisfactory technical solutions resulting from the limited choices that may be available from a single vendor, and poor system response because of the potentially high number of activities being performed on the single system. These problems could lead to a system that does not meet the organization's technical requirements, or whose performance makes its use unbearable. The latter point emphasizes the human element of MIS and leads directly into the management factors that must be considered during ISP.

Management factors. The status of modern technology is such that projects rarely are in jeopardy as a result of unsolvable technical problems. Rather, the common reasons for project failure include failure to obtain executive and management commitment to the proposed system, failure to determine *all* the requirements that the system must satisfy (the partial solution syndrome), failure to consider that implementing a network involves more than just the purchase of hardware and software, failure to plan the implementation of the proposed system, failure to design the proposed system from *all* the users' viewpoints, and failure to test a prototype of the proposed system. Once you are aware of what not to do, you are in a better position to achieve success.

Achieving the successful solution. Whether you are planning a bench-top LAN with only a few connections or an organization-wide LAN with thousands, there is a sequence of steps that should be followed to ensure success. The only differences between a large and small project are the degree of detail, amount of time, regulatory requirements, and cost involved with each of these steps. Note that the range of elapsed time for all the steps can be from a few days to several years. The following discussion is based on an intermediate-size project.

Development of an initial statement of the problem is the first step in achieving success. You must understand the problem to identify the functional requirements that will resolve the problem. Why do you need a LAN? What are the advantages of using a LAN? Benefits that are most attractive to an organization usually involve either eventual reduction in operating costs or increased efficiency in communications (see box).

If a LAN is identified as the optimum solution, the supporting information should be used to obtain management's commitment to its implementation. The minimum level of management that should be approached is the level that has oversight for all the organizational components that will be affected by the LAN.

Once management has given permission to proceed, a more formal definition of the requirements and benefits associated with a LAN is initiated. This definition is usually accomplished through interviews with the potential users of the LAN and assessment of appropriate policy/regulatory documentation. Documentation review can be extensive for federal organizations, organizations that must comply with federal regulations, or organizations that perform contract work for the federal government.

The data collection and analysis associated with a formal definition of requirements can be formidable for a large project. For example, at ANDRULIS our approach to this data collection and analysis makes use of automated tools. Data from interviews are collected on automated questionnaires on portable microcomputers. The questionnaires are developed using either Symantec Q&A or Asksam software, depending on the types of questions being asked. Data are analyzed using either the capabilities in this software or a variety of statistical and computer-assisted software engineering tools.

Common requirements and justifications for installing a LAN

Requirement	Justification
Need to connect data acquisition inputs directly into a LIMS	Eliminates rekeying of data, staff time used for data entry, and keypunch errors
Need to share an expensive printer/plotter with multiple data acquisition devices	Eliminates the need to buy multiple printer/plotters or to relocate a single printer/plotter as needed Enables relocation away from the lab bench
Need to access other automated systems from within the laboratory	Allows direct access of data from other automated systems and eliminates the need for physical transfer of data on diskette

Analysis of data centers around identification of work activities; their priority, frequency, and amount; and the problems and deficiencies associated with the activities. From this analysis we then are able to formulate the general functional requirements for a new system, with associated benefits. Management review and concurrence with the general functional requirements should occur at this point.

Development of a technical solution to meet the requirements can begin upon completion of requirements definition. The requirements should lead to the definition of the solution, not the reverse. You should determine the generic (vendor-independent) solution before selecting a vendor or vendors to implement it. This does not mean that you should avoid talking to vendors. Vendors are in the business of developing solutions and are a valuable source of guidance and information. One should talk with *multiple* vendors, however, during technical solution development. Vendor demonstration facilities (e.g., Hewlett-Packard's in Paramus, NJ) can be a valuable source of ideas.

Technical solution development thus blends into the next step—the market survey, including detailed vendor analysis. Fit vendor products to the solution, not the reverse! Multiple approaches to providing the solution probably will occur. Frequently, more than one vendor will be required to provide a single solution. A multivendor solution can sometimes provide greater capability at a reduced purchase cost than a single-vendor solution, but with the probable loss of a single source for training and maintenance. Which is better, single vendor or multivendor? It depends on your organization's particular requirements.

Especially important are demonstrations of vendors' abilities to implement your technical solution. Never design a system based on brochures, advertisements, or verbal claims. Avoid pie-in-the-sky claims.

At this point, you have management commitment to the need for a LAN; a clear statement, with management concurrence, of the general functional requirements for the LAN and the qualitative benefits that it will provide; one or more generic technical solutions to satisfy the requirements; and one or more vendors that can provide the technical solution(s).

From here, we move into planning for implementation. The next step is to package the above data in a form that management can use to make an informed decision on how to proceed. This process consists of planning for acquisition, prototyping, installation, testing, maintenance, training, and support.

The implementation plan defines when required activities will occur. It is also the basis for estimating labor costs when this is required. The plan establishes a time frame for meeting project goals and ensures that these goals are kept in sight. It also can be the basis for installing the LAN in phases, if there are financial or organizational reasons for not doing a complete installation at one time.

Once the implementation plan has been approved, actual implementation can begin. Hardware and software can be ordered or put out for bid, and services can be scheduled. A prototype that thoroughly exercises the system in an *operational* environment should be developed—thus any unforeseen problems can be encountered and dealt with on a smaller scale. Upon completion of these steps, final installation, testing, and acceptance can be executed. User training on the LAN and the new MIS capabilities provided can now occur. Finally, cut-over to the new system can be scheduled. A LAN that satisfies the general functional requirements is now an operational solution for its trained users. Success has been achieved. But, don't forget that proper maintenance and user support are required for it to remain successful.

In summary, implementing a LAN is more than just a hardware and software purchase (Figure 1). It is the result of a structured process that begins with the definition of requirements and ends with the testing of the installed product to ensure that it meets these requirements.

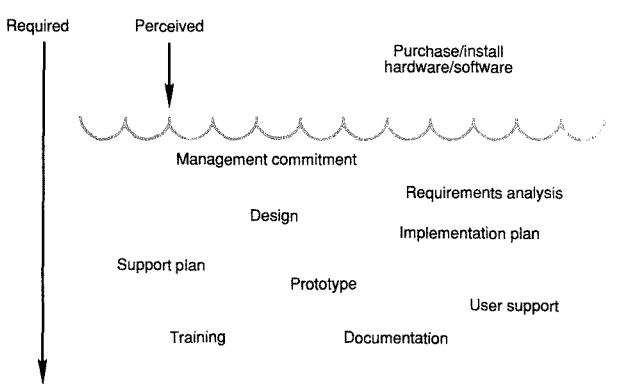

Figure 1. Difference between perceived and required activities for a successful LAN installation.

Vendor solutions

This section presents the LAN offerings, as well as additional relevant laboratory automation components, of three major vendors. Inclusion constitutes recognition as a major vendor only and is not to be construed as an endorsement. Conversely, exclusion is not an indication of unsatisfactory capabilities or a minor market share.

Hewlett-Packard. Hewlett-Packard's laboratory systems concept is The Unified Laboratory, which uses a TCP/IP-based IEEE 802.3 LAN. This is an industry standard LAN approach, although not formally compliant with the ISO-OSI model above the data link layer. Upper layer protocols are provided primarily through HP's ARPA Services, which is HP's implementation of the usual upper layer protocols associated with TCP/IP (e.g., FTP). HP's proprietary Network Services is also available for migration of HP 1000 minicomputer systems. In addition, the HP LAN Manager (developed with Microsoft Corp.) is available for microcomputers and HP Unix-based computers.

Data acquisition and analysis (Figure 2) are performed via either LAS software executing on an HP 1000 minicomputer or Unix, MS-DOS, or proprietary (Pascal) operating system-based microcomputers (ChemStations, which also provide for control of the instruments). These computers are then connected either serially or through a LAN to a LIMS. HP's LIMS consist of either LABSAM software executing on an HP 1000 minicomputer or LAB/UX soft-

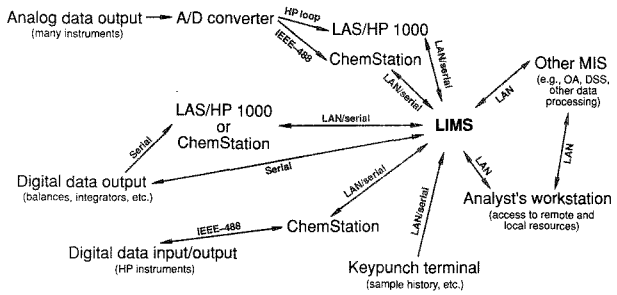

Figure 2. Data flow from instruments to LIMS within The Unified Laboratory.
The LIMS can be either LABSAM (HP 1000) or LAB/UX (HP 9000/800).

ware executing on an HP 9000/800 Unix-based minicomputer. Data can be further analyzed on the LIMS and then routed either back to the site of data acquisition or elsewhere. An additional focus is placed on the analyst's workstation (terminal or microcomputer) as a single point of access to these and other organizational resources, referred to as The Office of the Chemist concept.

Data exchange between computer systems is mediated via upper layer protocol programs. Exchange between HP systems is by file transfer using either the Network Services DSCOPY program or the ARPA Services FTP program. Exchange between an HP system and another vendor's system (e.g., a Digital VAX minicomputer) uses either FTP or a Network Services program, if the latter is available for the other system. HP's Unix-based products use the X-Windows environment (a user-friendly user interface), which permits data exchange on-the-fly between systems that support it. Either LAN Manager or ARPA Services mediates this exchange between Unix-based computers on the same LAN. Most of HP's MS-DOS-based products use the Microsoft Windows environment (another user-friendly user interface), which can mediate data exchange between applications on the same computer, and either LAN Manager or ARPA Services for data exchange between computers.

Data is exchanged between HP systems as binary format raw data, ASCII format raw data, ASCII format reports, or a variety of graphic formats (e.g., HP-GL). Import of data from other vendors' data acquisition/analysis systems can be accomplished via ASCII report data. Export of data to other systems (e.g., a DSS) can be accomplished through ASCII reports, which can be formatted so they can then be imported into database management system applications, word processors, statistical software, and so on. This capability, combined with an industry standard networking approach, permits, for example, HP LIMS reports to be routed to SAS or RS/1 analysis software or an Oracle database on a Digital VAX minicomputer.

An example of The Unified Laboratory is found within the U.S. Navy as shown in Figure 3. Terminal and microcomputer (PC) connections to the HP 1000 systems are via serial asynchronous multiplexers, instead of the LAN, because of internal considerations.

Digital. DEC's laboratory systems architecture is called Computer Integrated Research. It is based on four standards programs: the Integrated Laboratory Automation (ILA) Standards, Real Time Calling Standard (RTCS), Applications for Science (AFS), and Integrated Visualization Environment (IVE). Although there are aspects involving data communications in all of these programs, the primary areas of interest for this article are within ILA and, to a lesser extent, IVE. These programs apply to Digital and third-party vendor products.

ILA defines levels of compliance or noncompliance with standards defined by Digital that deal with communications, data management, and data integration. International and industry standards are used where they exist; otherwise "gaps" are filled with proposed standards. Communications compliance is based on degrees of support for DECNet, Digital's family of communications hardware and software. Data management compliance is based on the ability to exchange database data with or directly use Digital data structures. Data integration compliance is based on either a published vendor-supplied data interchange capability or direct use of Digital's Compound Document Architecture (CDA), which supports text, graphics, and images. IVE primarily defines standards for imaging and graphics, but also overlaps with ILA. In addition to DECNet, TCP/IP is supported.

DECNet is based on Digital Network Architecture (DNA), which was originally a proprietary network approach. DNA specifies protocols for both LANs and WANs. Phase V of DNA, which will be fully compliant with the ISO-OSI model, is scheduled for mid-1990 availability. In addition to this compliance, the proprietary DNA session control layer may replace the OSI session, presentation, and application layers. DECNet specifies 802.3 for media access control, but can also support Ethernet. Exchange with TCP/IP environments is also supported.

Data acquisition and analysis are performed by the VAXlab family of systems (based on Digital VAX minicomputers) or by third-party products that meet ILA standards, such as Lab-

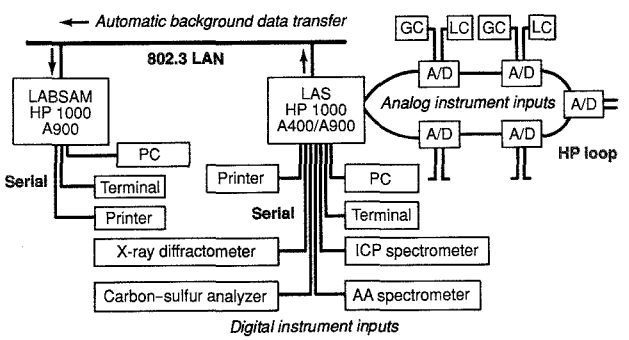

Figure 3. The Unified Laboratory at work: Navy laboratories.

tech Notebook. These systems are then connected through a LAN to a third-party LIMS or data analysis software, such as BBN's RS/1 series of data analysis products. Thus, laboratory automation based on Computer Integrated Research will exist in a multivendor environment, based on Digital computer and communications systems with additional third-party components. (An example of a third-party approach is described in the following section.)

Perkin-Elmer Nelson Systems. PE Nelson laboratory systems architecture is based on both Digital's Computer Integrated Research and integration of unrelated third-party vendors' products. The actual PE Nelson product line uses MS-DOS-based microcomputers, Digital VAX computer hardware, the VMS operating system, and DECNet.

Data acquisition and analysis (Figure 4) can be performed using a variety of microcomputer (80286- or 80386-based) or minicomputer platforms. Turbochrom II software executing on a microcomputer under Microsoft Windows is the high-end microcomputer system. ACCESS*CHROM software executing on a Digital VAX platform minicomputer is the premier minicomputer system. Of special interest is the PE Nelson 941 A/D converter, which contains an internal buffer that permits continuous data acquisition even if computer services are interrupted.

The microcomputers can pass data across a LAN to a LIMS. The minicomputer can pass data across a LAN to a LIMS or directly to the LIMS if it is executing on the same computer. PE Nelson's premier LIMS is ACCESS*LIMS, which is based on the Oracle database management system. In addition, integration with the Digital VAXlab family of products and third-party LIMS, such as Beckman's CALS, can be achieved with customer-developed software interfaces.

DECNet is the preferred LAN environment. Extensive use of Digital's Personal Computing Systems Architecture (PCSA), which is based on DECNet, provides a high degree of interoperability between the microcomputer and VAX environments at selected installations. Data exchange is mediated entirely through DECNet.

Integration with other network operating environments, such as Novell, and other network access schemes, such as IBM Token Ring, has also been achieved. Exchanged data are in ASCII format. This integration has been achieved through appropriate use of communications gateways, for example. Data exchange in these instances is mediated by third-party approaches, such as Datability RAF.

Examples of PE Nelson configurations are found at several pharmaceutical research facilities. Both Turbochrom II and ACCESS*LIMS are used. A typical configuration is shown in Figure 5 on p. 396 A. Background data transfer between the microcomputers ("clients") and VAX host ("server") is mediated by PCSA.

The missing link—The logical connection between LIMS and DSS

LANs cannot be considered an issue separate from laboratory automation and its place within an organization's MIS. Vendors supply excellent off-the-shelf solutions for laboratory automation—LIMS, data acquisition hardware/software, and LANs. Although each vendor's offering is unique, there is a large degree of overlap at the laboratory level. The ability to satisfy organization-specific functional requirements is almost always within the limits of the vendor system's customization capability. *Physical connectivity* of a laboratory's data processing with other parent organization (or cus-

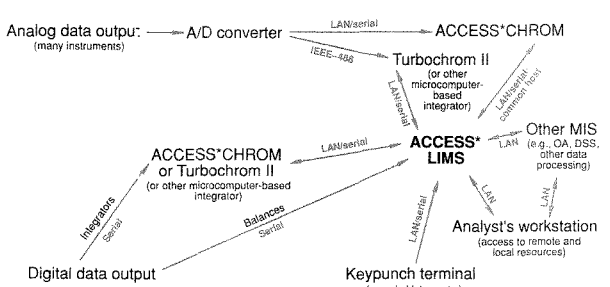

Figure 4. Data flow from instruments to LIMS within a laboratory based on PE Nelson laboratory automation products.

For Over Six Decades...

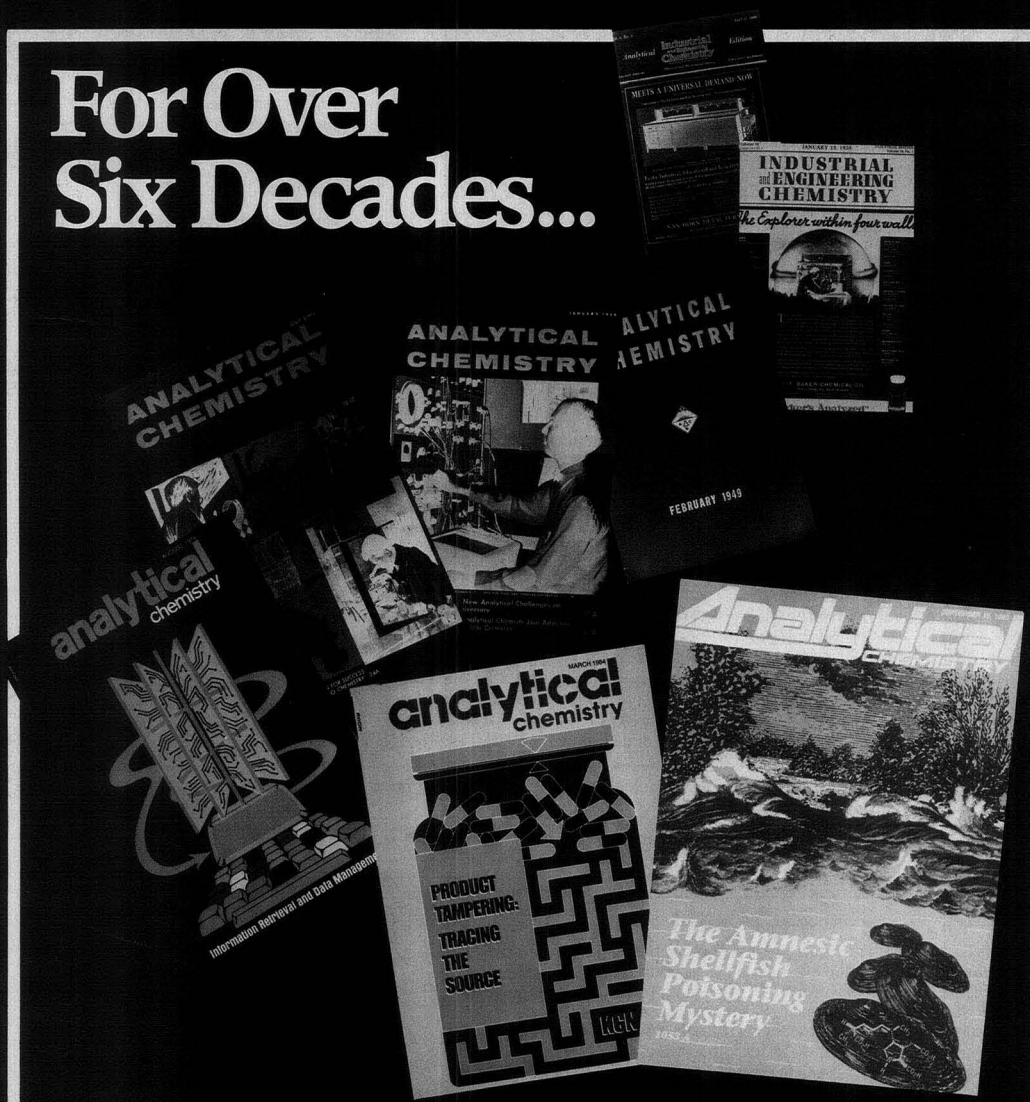

The Leader in the Field.

ANALYTICAL CHEMISTRY, the world's foremost publication in the vital field of measurement science, comes to you semi-monthly packed with *more* research articles, special features and application papers.

Keeping pace with the changes has continued to make *ANALYTICAL CHEMISTRY* the pinnacle of publications in the field . . . for over 6 decades.

For your personal subscription:

CALL TOLL FREE (800) 227-5558 (U.S. only)
Outside U.S. (202) 872-4363

Telex: 440159 UI
89 2582 ACSPUBS

American Chemical Society
1155 16th St., NW
Washington, DC 20036

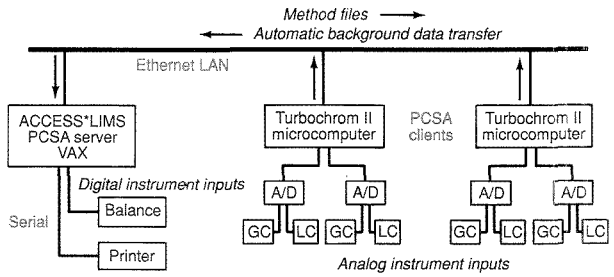

Figure 5. PE Nelson laboratory automation within the pharmaceutical industry.

tomer) MIS components is also relatively simple within the scope of current technology.

Logical connectivity with other MIS components (e.g., DSS) is not as simple to achieve as physical connectivity. A problem arises in the logical integration of laboratory-generated information into the corporate information pool. This integration simply is not available off-the-shelf, because its achievement is based on an understanding of what an organization's business is, how the organization does business, and so on, followed by the imposition of this understanding onto an information architecture. Failure to do this will result in the "logical disconnect" of the laboratory's information output from the remainder of the organization. Until this problem is recognized and resolved, management has little to gain by the installation of LIMS or a laboratory LAN. Laboratory information, like other types of information, must provide management with an advantage if it is to compete successfully for the organization's budget dollar.

Recommended reading

On building corporate networks:
Maxson, M. A. *LAN Technol.* **1990**, *6*, 49.
On the JCAMP-DX file format:
McDonald, R. S.; Wilks, P. A., Jr. *Appl. Spectrosc.* **1988**, *42*, 151.
On MIS:
McLeod, R. *Management Information Systems*, 3rd ed.; Science Research Associates, Inc.: Chicago, IL, 1986.
On LIMS:
Megargle, R. *Anal. Chem.* **1989**, *61*, 612 A.
LAN Technology and *LAN Magazine* are two periodicals that an aspiring LAN designer or installer should read on a regular basis.

This article is derived from lessons learned, both directly and indirectly, from approximately 30 projects during the past 10 years. It has been my pleasure to have shared the past four years of this experience with Jim Sywilok. I would like to thank him both for the teamwork involved in these experiences and for his technical input into and review of this article.

Numerous individuals from each vendor provided input for this article. I thank especially Lisa Buurma, Gray Gilfilan, Dan Holmes, Bev Lesko, Steve Maykowski, and Susan Strong of Hewlett-Packard; Ron Olson of Digital; and Jim Feuker and Jim Zito of PE Nelson for their efforts.

INDEX TO ADVERTISERS IN THIS ISSUE

CIRCLE INQUIRY NO.	ADVERTISERS	PAGE NO.
15, 16	*Beckman Instruments, Inc. AC&R Advertising, Inc.	357A
22	Corporation Scientifique Claisse, Inc.	380A
30	Deisl/Nermag Instruments	350A
35	Eastman Kodak Company	365A–366A
32, 33	*EG&G Princeton Applied Research Market Force	370A
40–46	Extrel Blattner/Brunner, Inc.	IFC
50	Fisons Instruments Kempsters, The Advertising Agency	352A–353A
60	*Hewlett-Packard Company Brooks Communications	OBC
80	Lee Scientific	371A
90	*Matheson Gas Products Kenyon Hoag Associates	359A
88	*Merck Sharp & Dohme Isotopes BGH Advertising Associates, Inc.	382A
92	*Mettler Instrument Corporation Gilbert, Whitney & Johns, Inc.	355A
125	*Sartorius Instruments Techmarketing	368A
132	*Tekmar Company Kenyon Hoag Associates	358A
135	*Thermo Jarrell Ash Corporation Noon, Inc.	349A

Directory section, see page 396A.

** See ad in ACS Laboratory Guide.*

Advertising Management for the American Chemical Society Publications

CENTCOM, LTD

President
James A. Byrne

Executive Vice President
Benjamin W. Jones

Clay S. Holden, *Vice President*
Robert L. Voepel, *Vice President*
Joseph P. Stenza, *Production Director*

500 Post Road East
P.O. Box 231
Westport, Connecticut 06880
(Area Code 203) 226-7131
Telex No.643310
FAX: 203-454-9939

ADVERTISING SALES MANAGER
Bruce E. Poorman

ADVERTISING PRODUCTION MANAGER
Jane F. Gatenby

SALES REPRESENTATIVES

Philadelphia, PA . . . CENTCOM, LTD., GSB Building, Suite 405, 1 Belmont Avenue, Bala Cynwyd, Pa. 19004. Telephone: 215-667-9666, FAX: 215-667-9353.

New York, NY . . . John F. Raftery, CENTCOM, LTD., 60 East 42nd St., New York, N.Y. 10165. Telephone: 212-972-9660

Westport, CT . . . Edward M. Black, CENTCOM, LTD., 500 Post Road East, P.O. Box 231, Westport, Ct. 06880. Telephone: 203-226-7131, Telex 643310, FAX: 203-454-9939

Cleveland, OH . . . Bruce E. Poorman, John C. Guyot, CENTCOM, LTD., 325 Front St., Suite 2, Berea, Ohio 44017. Telephone: 216-234-1333, FAX: 216-234-3425

Chicago, IL . . . Michael J. Pak, CENTCOM, LTD., 540 Frontage Rd., Northfield, Ill. 60093. Telephone: 708-441-6383, FAX: 708-441-6382

Houston, TX . . . Michael J. Pak, CENTCOM, LTD. Telephone: 708-441-6383

San Francisco, CA . . . Paul M. Butts, CENTCOM, LTD., Suite 1070, 2672 Bayshore Frontage Road, Mountain View, CA 94043. Telephone: 415-969-4604

Los Angeles, CA . . . Clay S. Holden, CENTCOM, LTD., Newton Pacific Center, 3142 Pacific Coast Highway, Suite 200, Torrance, CA 90505. Telephone: 213-325-1903

Boston, MA . . . Edward M. Black, CENTCOM, LTD. Telephone: 203-226-7131

Atlanta, GA . . . John C. Guyot, CENTCOM, LTD. Telephone: 212-972-9660

Denver, CO . . . Paul M. Butts, CENTCOM, LTD. Telephone: 415-969-4604

United Kingdom

Reading, England . . . Malcolm Thiele, Technomedia Ltd., Wood Cottage, Shurlock Row, Reading RG10 OQE, Berkshire, England. Telephone: 073-434-3302, Telex #848800, FAX: 073-434-3848

Lancashire, England . . . Technomedia Ltd., c/o Meconomics Ltd., Meconomics House, 31 Old Street, Ashton Under Lyne, Lancashire, England. Telephone: 061-308-3025

Continental Europe . . . Andre Jamar, International Communications, Inc., Rue Mallar 1, 4800 Verviers, Belgium. Telephone: (087) 22-53-85, FAX: (087) 23-03-29

Tokyo, Japan . . . Sumio Oka, International Media Representatives Ltd., 2-29 Toranomon, 1-Chome Minato-ku Tokyo 105 Japan. Telephone: 502-0656, Telex #22633, FAX: 591-2530

Analytical CHEMISTRY

EDITOR: **GEORGE H. MORRISON**

ASSOCIATE EDITORS: **Catherine C. Fenselau, Georges Guiochon, Walter C. Herlihy, Robert A. Osteryoung, Edward S. Yeung**

Editorial Headquarters

1155 Sixteenth St., N.W.
Washington, DC 20036
Phone: 202-872-4570
Telefax: 202-872-4574

Managing Editor: Sharon G. Boots

Assistant Managing Editor: Mary Warner

Associate Editor: Louise Voress

Assistant Editors: Grace K. Lee, Alan R. Newman

Editorial Assistant: Felicia Wach

Contributing Editor: Marcia Vogel

Director, Operational Support: C. Michael Phillippe

Head, Production Department: Leroy L. Corcoran

Art Director: Alan Kahan

Designers: Amy Meyer Phifer, Robert Sargent

Production Editor: Elizabeth E. Wood

Circulation: Claud Robinson

Editorial Assistant, LabGuide: Joanne Mullican

Journals Dept., Columbus, Ohio

Associate Head: Marianne Brogan

Journals Editing Manager: Joseph E. Yurvati

Senior Associate Editor: Rodney L. Temos

Published by the
AMERICAN CHEMICAL SOCIETY
1155 16th Street, N.W.
Washington, DC 20036

Publications Division

Director: Robert H. Marks

Journals: Charles R. Bertsch

Special Publications: Randall E. Wedin

Manuscript requirements are published in the January 1, 1990 issue, page 89. Manuscripts for publication (4 copies) should be submitted to ANALYTICAL CHEMISTRY at the ACS Washington address.

AUTHOR INDEX

Aberth, W., 609
Anderson, A. G., 615
Anderson, L. B., 546

Back, M. H., 574
Beck, G. L., 639
Benson, J. V., 612
Berger, T. A., 615
Bertels, P. C., 574
Bicheng, Z., 574
Bishop, J. K. B., 553
Brumbaugh, G. G., 639

Cecconie, T., 622
Chakrabarti, C. L., 574

DeLassus, P. T., 592
Deye, J. F., 615

Eckschlager, K., 565
Engblom, S. O., 625

Fahidy, T. Z., 550
Farmer, O. T., III, 639
Freiser, H., 622

Gjerde, D. T., 612
Gorry, P. A., 570

Harrington, M. S., 546
Hayes, R. N., 602
Headrick, K. L., 574
Huang, L. Q., 602
Hutton, J. C., 574

Isemura, T., 650
Iwunze, M. O., 644

Justice, J. B., Jr., 597

Kanda, Y., 630
Kim, H. J., 639
Kita, H., 652

Lacy, M. J., 656

Maciel, G. E., 633
Mattina, M. J. I., 602
Menacherry, S. D., 597
Mignardi, M. A., 586

Obrusník, I., 565
Okazaki, K., 652
Oldham, K. B., 625

Piepmeier, E. H., 639

Renn, C. N., 558
Robbins, G. A., 656
Roe, V. D., 656
Rulf, D. C., 592
Rusling, J. F., 644

Sioda, R. E., 550
Smith, B. W., 586
Stuart, J. D., 656
Sucheta, A., 644
Synovec, R. E., 558

Taira, M., 630
Takahashi, H., 652
Terabe, S., 650
Tou, J. C., 592

Uosaki, K., 652

Winefordner, J. D., 586

Zhang, M., 633

Analytical Strategies Using Interdigitated Filar Microelectrodes

M. S. Harrington and L. B. Anderson*

Department of Chemistry, The Ohio State University, 120 West 18th Avenue, Columbus, Ohio 43210

Two innovations are described that allow us to better understand the analytical value of multiple, intercommunicating microelectrodes. We describe an approximate solution for the transient currents at twin interdigitated electrodes. Then, by computing the algebraic sum and difference between the generator and collector currents, we show how new and valuable analytical information may be obtained. Inspection of the analytic solution for the difference current shows that this current approaches steady state 4 times faster than either generator or collector currents alone. This is verified experimentally, and the electrodes behave as though the distance between them were halved.

Several recent reports have discussed the advantages of using interdigitated microband array electrodes as analytical sensors (*1–8*). We have called such sensors *filar* electrodes because they produce large currents, high sensitivity, and a rapid rise to steady state as a direct consequence of their threadlike geometry. Figure 1 shows two electrically independent arrays of filar electrodes, interdigitated alternately, with a gap between adjacent filaments equal to the filament width. While electrodes such as these exhibit microelectrode behavior (*9*), their macroscopic areas provide large current signals that do not require a preamplifier for measurement with conventional electrochemical apparatus (*6, 10*).

One way to achieve true steady-state currents at filar electrodes is to confine the diffusional process to a thin solution layer adjacent to the interdigitated array (*6*). In Figure 1, where the array substrate ($W = 100$ μm) is made one wall of a thin-layer cell ($l_z \approx 100$ μm), steady state is achieved in about 10 s, an analysis time comparable to the drop time of a polarographic experiment. Reduction of the interelectrode spacing, W, to smaller values reduces this time monotonically, but even at W values of 2–5 μm, this time is reported to be about 0.1 s (*11, 12*).

For general electroanalytical purposes, twin filar electrodes with the smallest interelectrode separation may not be the best choice. Fabrication problems increase as W becomes smaller, for example. When W is greater than ≈10 μm, standard thick-film technology may be employed and rigorous application of clean room methods may be avoided (*6, 13, 14*). This simplification assures that electrode design and fabrication can remain a component of the analytical laboratory process. Second, steady-state current magnitudes decrease in approximate proportion to the interelectrode spacing (*6, 11*), and analytical measurement is more practical if the current signal is of nanoampere magnitude or greater.

This paper describes a theoretical and experimental investigation of generation/collection cyclic voltammetry at interdigitated filar electrodes. We discuss the effects of electrode and cell dimensions and methods of data manipulation with the intent of optimizing the analytical utility of these electrodes.

EXPERIMENTAL SECTION

Apparatus. Twin electrode experiments were performed with a multiple electrode potentiostat, which was designed in our laboratory for experiments that required monitoring currents at up to 11 independent working electrodes (*15*). The cyclic triangular excitation waveform for the generator electrode was provided by a waveform generator (Krohn-Hite Corp., Avon, MA). Data acquisition was performed either digitally with a LabMaster DMA interface board (Scientific Solutions, Solon, OH) operating from a PC-Designs GV-286 microcomputer (PC-Designs, Broken Arrow, OK) or directly by two XY recorders (Moseley Model 2D-2M and 7001 AM, Hewlett-Packard, Pasadena, CA). Thin-layer experiments were performed in a Bioanalytical Systems thin-layer flow cell (Bioanalytical Systems, West Lafayette, IN) modified to contain a 1 in. square Superstrate (Materials Research Corp., Pearl River, NY) as described previously (*15*). Open solution experiments were performed with a dip-type probe assembly as described by Clough (*14*). Gold interdigitated filar microelectrodes were fabricated photolithographically by using a method described previously (*6, 14, 15*). The twin filar electrode used in this study was characterized by a center-line distance (W in Figure 1) of 100 μm. The reference electrode employed was a saturated calomel electrode.

Reagents. Hydroxymethylferrocene (HMF) and bis(hydroxymethyl)ferrocene (BHMF) (Strem, Newburyport, MA) were used as received. All solutions were prepared with doubly distilled deionized water which had been purified by a Nanopure II filtration system (SYBRON Barnstead, Boston, MA). The supporting electrolyte solution consisted of 0.1 M monobasic potassium phosphate buffer adjusted to pH 7.00 with concentrated ammonium hydroxide.

Procedure. All solutions were deaerated with nitrogen for 10 min prior to use. The electrode was cleaned prior to each experiment by sonication in stripper no. 400 (Photofabrication Chemical and Equipment Co., Frazer, PA) for 5 min followed by rinsing with reagent-grade methanol. Experiments were performed at an ambient temperature of 25 °C. With the analyte present in the reduced form only, the potential of the collector electrode was selected to reduce the analyte at a diffusion-limited rate in addition to providing a minimum background current. The potential of the generator electrode was then scanned to a switching potential where the analyte was oxidized at the diffusion-limited rate. The currents flowing at both electrodes were monitored as a function of the generator electrode potential. Sum and difference currents were calculated by computer for data that were acquired digitally. Data obtained on the XY recorders required manual computation of the sum and difference currents.

RESULTS AND DISCUSSION

Generation/Collection Cyclic Voltammetry. Several research groups have reported the use of interdigitated microband array electrodes in cyclic voltammetric experiments in an effort to improve the signal to background (S/B) response (*3, 11, 16, 17*). By selection of a fixed potential for the collector electrode where there is a minimum background current, improved S/B behavior is observed by monitoring the collector electrode current as a cyclic triangular waveform is applied to the generator electrode. Species produced at the generator electrode diffuse across the interelectrode gap and are subsequently detected at the collector electrode as a substantial current on top of a very small background electrolysis current.

Figure 2 illustrates generation/collection cyclic voltammetric experiments (G/C-CV) at a twin filar electrode ($W = 100$ μm) at three different scan rates. At scan rates on the order of several hundred millivolts per second, very little of the electrogenerated product has time to diffuse the necessary 50–100 μm to the collector electrode in one cycle (Figure 2A). Conventional peak-shaped voltammograms are observed at the generator electrode due to the fact that diffusion layers of adjacent filaments do not overlap, and mass transport is

0003-2700/90/0362-0546$02.50/0

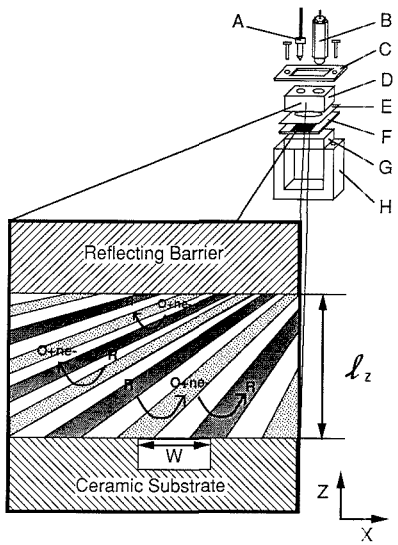

Figure 1. Foreground: Cross-sectional interior view of thin-layer filar electrode geometry: W, center-line distance between adjacent twin electrode filaments; l_z, depth of the thin layer. Background: Modified BAS thin-layer electrochemical cell: A, sample inlet; B, reference electrode; C, stainless steel retaining plate, D, reflecting barrier cell cap; E, Teflon gasket; F, ceramic substrate/electrode; G, Teflon support; H, stainless steel cell body.

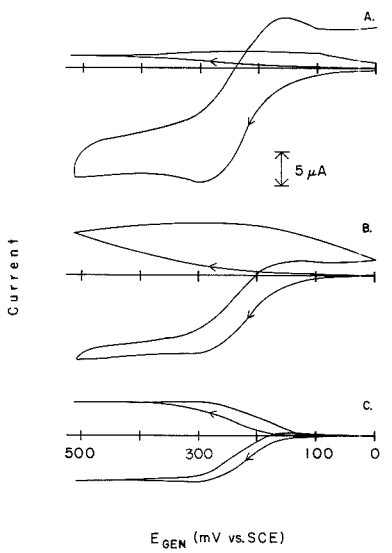

Figure 2. Generation/collection cyclic voltammograms of 0.675 mM BHMF in pH 7.0 phosphate buffer: scan rates (mV/s), (A) 348, (B) 116, (C) 5.8; thickness of Teflon gasket (l_z), 380 μm; E_{COL} = 0 V vs SCE. Upper traces are collector electrode voltammograms and lower traces are generator electrode voltammograms.

approximately cylindrical (*18*). At scan rates on the order of several tens of millivolts per second (Figure 2C), species produced at the generator electrode have adequate time to diffuse to adjacent collector electrodes where they are detected and recycled. The shapes of both generator and collector electrode voltammograms are sigmoidal, indicating nearly steady-state diffusion conditions. At intermediate scan rates (Figure 2B), voltammograms at the generator electrode show evidence of diffusional feedback from the collector electrode but do not reach steady-state, and both currents show substantial hysteresis. When twin electrodes with spacings larger or smaller than 100 μm are used (*11*), the response to varying scan rates is similar, though there will be quantitative differences in the rates resulting in the three classes of response shown in Figure 2.

Table I. Collection Efficiencies at the Switching Potential for Generation/Collection Cyclic Voltammetry[a]

	l_z/W			
scan rate, mV/s	0.51	1.27	3.80	open[b]
5.8	86.2	86.0	73.9	
11.6	86.5	77.6	65.8	67.0
23.2	82.0	67.7	56.2	59.7
58.0	66.1	43.8	51.1	52.0
116.0	39.9	32.9	48.5	42.0
232.0	22.6	22.1	23.4	31.4
348.0	14.7	16.8	20.0	

[a] For electrolysis of 0.675 mM BHMF in pH 7.0 phosphate buffer; E_{COL} = 0 V vs SCE; switching potential at 510 mV vs SCE. [b] The scan rates for the open solution geometry were 12.0, 24.1, 48.2, 120.5, and 241.0 mV/s.

When the G/C-CV experiment is performed in a thin-layer cell, steady state is achieved more rapidly, and the collection efficiency (defined as $i_{COL}/i_{GEN} \times 100$) is increased. The cap of the cell in Figure 1 is a reflecting barrier that confines the product of the generator electrode reaction to the immediate vicinity of the electrodes, enhancing collection of the product. In addition, it creates a finite diffusion condition that limits the flux of reactant normal to the generator electrode surface.

If a reflecting barrier is placed at a distance, $l_z = W$ from the electrode plane, collection efficiencies of 70–90% are observed, and steady-state currents are achieved in a time comparable to W^2/D. This is illustrated in Table I. At slow scan rates and small values of l_z, collection efficiencies approach 90%, while at rapid scan rates, there is little difference among the collection efficiencies for the four geometries, all of which are below 20%. At rapid scan rates, there is insufficient time for the diffusion layers to reach either the adjacent electrode or the reflecting barrier before the scan is reversed.

Unfortunately, it is not possible to create thin layers smaller than ≈25 μm, therefore the thin-layer enhancements described above cannot be extended to the 2–4-μm W values reported by Wrighton and others (*11*, *19*). Nevertheless, what cannot be achieved by mechanical means can be approached by data manipulation. In the following section, we describe the achievement of a factor of 4 enhancement in the time required to reach steady-state through difference voltammetry. This technique is apparently applicable to all W values for open solution as well as thin-layer methods.

Difference and Summation Currents. A general method for solving boundary value problems describing diffusion in a quiescent solution at twin filar electrodes is lacking in the literature. In general, analytic solutions in two dimensions cannot be obtained by standard LaPlace transform methods, but Aoki and co-workers have shown, for the special case of these interdigitated coplanar electrodes, that the two-dimensional diffusion problem may be reduced to an equivalent one-dimensional representation (*19*). With the Schwarz–Christoffel transformation, Aoki maps a semiinfinite rectangle (the filar electrode pair) onto a line, which has no direct physical meaning. A second coordinate transformation maps this line onto a plane consisting of a rectangular enclosure

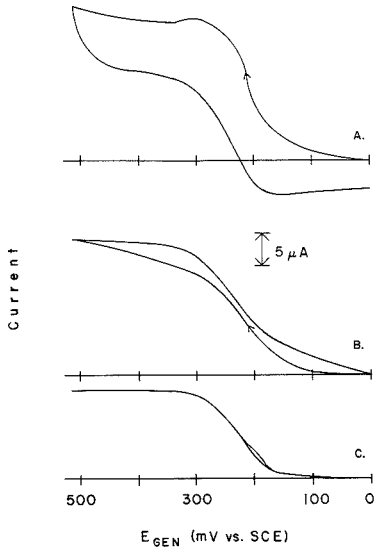

Figure 3. Difference voltammograms for the data presented in Figure 2.

wherein the twin electrodes face one another across an intervening solution layer. The two transformations exactly map the coplanar twin interdigitated electrode geometry onto the geometry of a cofacial twin electrode. Analytic solutions to a variety of electrochemical boundary value problems at cofacial twin electrodes have been reported (*20*, *21*), and these solutions may now be used to approximate the electrochemical behavior of interdigitated filar electrodes.

As an example of the utility of this insight, consider the exact solution for the transient current in chronoamperometry at twin cofacial electrodes, which has been solved in closed form (*22*) (see Appendix). Equations A1 through A3 show that the algebraic difference between the collector and generator currents at cofacial twin electrodes converges to a steady-state value 4 times faster than either current alone. If one assumes the validity of Aoki's transformations, the 4-fold increase in the rate of convergence to steady-state will also be observed for twin filar electrodes. We have verified this conclusion by digital simulation of the two-dimensional diffusion problem (*11*, *22*). Experimentally, nearly hysteresis-free voltammograms are *in fact* observed for larger values of W and at higher scan rates if the "difference voltammogram" is computed for a G/C-CV experiment.

In Figure 3, difference voltammograms are computed from the data in Figure 2, for electrolysis of BHMF at twin filar electrodes for three different scan rates. In the difference voltammograms, hysteresis is much less than was observed in either the collector or the generator voltammogram alone (Figure 2). Of course, hysteresis diminishes for all three types of voltammogram as the scan rate is decreased. At scan rates on the order of 10 mV/s, the difference voltammograms have collapsed to a single sigmoidal line, virtually free of hysteresis (Figure 3C). Nernst analysis of this voltammogram (plotting the generator electrode potential as a function of $\ln ((i_{lim} - i)/i)$), yields a straight line (r = 0.998) with a slope of 0.0259 V (T = 26.2 °C). The intercept of the line, 260 mV versus SCE, is identical with $E_{1/2}$ for BHMF determined from cyclic voltammetry at a single macroscopic gold disk electrode under identical conditions. To obtain comparably small hysteresis in a steady-state voltammogram at a single disk electrode of

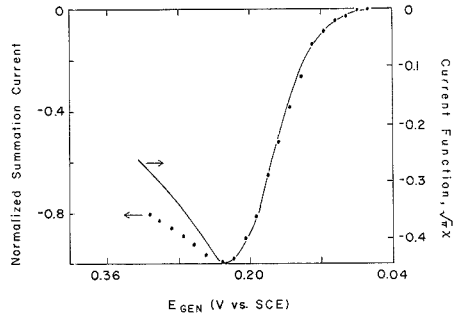

Figure 4. Summation voltammogram of 1.80 mM HMF in pH 7.0 phosphate buffer, obtained in open solution at a scan rate of 7 mV/s. Solid line is the theoretical response expected for one-dimensional diffusion to a planar macroscopic electrode.

a diameter equal to the width of one band of our filar electrode (50 μm), the required scan rate would be 25 nV/s, an experiment that would last 11 h (*23*)!

These observations seem to justify the statement that two electrodes are (in some manner) better than one. These data also appear to be a specific and useful example of a far more general property of twin, intercommunicating electrodes. Because currents observed at independently potentiostatted electrodes contain different information, these currents or linear combinations of these currents, might be used to separate two analytical signals from one another, or signals from background and noise currents.

For example, the collector and generator currents in Figure 2B contain different proportions of information from molecules transported by diffusion in the orthogonal x and z directions. The generator current, particularly at short times, is enriched in information about molecules which arrive from the bulk solution, along the z axis. The collector current is almost entirely the result of electrolysis of molecules diffusing along the x axis from the generator electrode. Taking the algebraic *difference* of the two currents tends to reinforce the x axis components of both and tends to cancel a portion of the z axis flux, causing the difference to behave as though the mean distance between filaments had been halved.

The algebraic *sum* of the collector and generator currents in Figure 2, on the other hand, produces a signal with quite different analytical properties. This "summation voltammogram" resembles an ordinary peak-shaped cyclic voltammogram (Figure 4). This characteristic shape reflects a diffusion process dominated by normal or z-axis diffusion. At slow scan rates, the radial diffusion component (along the x axis) experienced by the collector electrode will nominally be equal in magnitude yet opposite in sign to the radial diffusion at the generator electrode. Upon summation, these two components effectively cancel to provide a voltammogram due primarily to the normal diffusion occurring at the generator electrode. The degree of cancellation of these radial components is a function of the time, the scan rate, and the cell geometry. In fact, for a potental step experiment, the sum of the generator and collector electrode currents exhibits Cottrellian behavior (Figure 5), and a plot of the sum current versus $t^{-1/2}$ yields a straight line (r = 0.996) with a slope of 6.66 $\mu A/s^{-1/2}$. This value is consistent with the calculated value for the slope from the Cottrell equation of 6.82 $\mu A/s^{-1/2}$, where the sum of the projected geometric areas of the electrodes was used for the area term.

The signal-to-noise ratios in the four current transients of Figure 5 are not identical. The relative standard deviations of the currents at steady state are 1.4%, 2.2%, 1.8%, and 4.5% for the collector, generator, difference, and summation current,

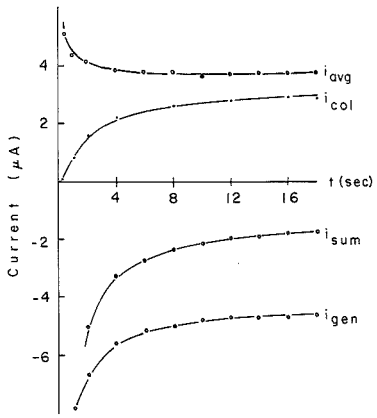

Figure 5. Twin electrode potential-step experiment for 0.496 mM BHMF in pH 7.0 phosphate buffer: thickness of Teflon gasket (l_z), 380 μm; E_{COL} = 100 mV, E_{GEN} = 400 mV vs SCE. The uncertainty in the experimental data is indicated by the size of the data points. $i_{avg} = i_{dif}/2$.

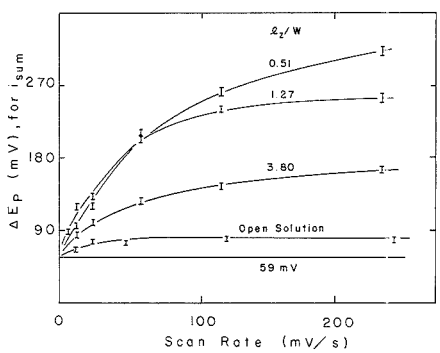

Figure 6. Effect of radial mass transport on peak separation in summation voltammograms. Thin solution layers (small l_z/W) produce large peak separations, particularly at rapid scan rates.

respectively. In addition, the rates at which each of the currents approach steady-state are consistent with the rates predicted by eqs A1 through A3. The times required to reach steady state to within 5% were 4, 12, and 12 s for the difference, collector, and generator currents, respectively.

Heinze has used digital simulation methods to examine the effects of radial diffusion at microelectrodes and its influence on the peak potential separation in cyclic voltammetric experiments for Nernstian redox couples (*24*). Large deviations from the expected ΔE_p value of $59/n$ mV (at 25 °C) are observed for cases that experience substantial radial diffusion. Figure 6 is a plot of ΔE_p of the summation voltammogram as a function of scan rate for four different cell geometries at a W = 100 μm twin filar electrode. At low scan rates, ΔE_p for all cases approaches the theoretical "linear diffusion only" value of $59/n$ mV, indicating the establishment of virtually identical radial steady-state diffusion profiles at both electrodes, for which the radial current components cancel upon summation. The open solution geometry illustrates that the ΔE_p value is virtually scan rate independent and nearly equal to the theoretical value of $59/n$ mV.

The semiinfinite linear diffusion condition provided by the open solution geometry enables identical radial diffusion profiles to be established at both electrodes. In addition, at very rapid scan rates, the collector electrode current is negligible, so the summation voltammogram results only from the generator electrode current, which experiences predominantly normal diffusion. At slow scan rates of about 10 mV/s, the shape of the summation voltammogram can be described as one-dimensional (normal) diffusion. In Figure 4, experimental data for the forward scan of the summation voltammogram of BHMF is compared to the theoretical current function for one-dimensional diffusion (*25*).

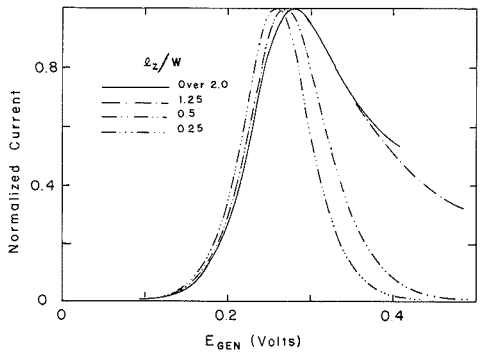

Figure 7. Summation voltammograms calculated for varying ratios of thin layer depth, l_z, to center line distance, W. Scan rate was $1.28D/W^2$ V/s.

At sufficiently slow scan rates, the summation voltammogram yields a macroelectrode response indicative of the cell geometry. We have also examined the summation voltammogram behavior as a function of the dimensionless geometric factor, l_z/W, using digital simulation techniques. Figure 7 shows the dimensionless current for the forward scan normalized to the peak current for several different values of l_z/W (*26*). For very thin solution layers, the sum current yields a response indicative of restricted one-dimensional diffusion to a macroscopic electrode where the half-wave potential of the redox couple occurs at the current peak. As the thickness of the solution layer becomes larger, the forward scan response approaches a limit predicted for semiinfinite one-dimensional diffusion where the half-wave potential is now the potential where the current equals 85% of the current peak (*25*).

The methods and results described here have several consequences to analytical electrochemistry. Partially redundant information, communicated between potential-independent electrodes, has been used effectively to accelerate, by a factor of 4, the rate at which the current approaches steady state. Currents observed at such information-rich multielectrode arrays are being used to study multiplex electrochemistry (*15, 26*), background correction (*27*), and self-correction of correlated noise (*28*).

APPENDIX

One-dimensional cofacial twin electrode solutions

$$I_{GEN} = \frac{+nFADC^*}{l}[1 + 2\sum_{k=1}^{\infty} \exp(-k^2\pi^2 Dt/l^2)] = \frac{+nFADC^*}{(\pi Dt)^{1/2}}[1 + 2\sum_{k=1}^{\infty} \exp(-k^2 l^2/(Dt))] \quad \text{(A1)}$$

$$I_{COL} = \frac{-nFADC^*}{l}[1 + 2\sum_{(k=1}^{\infty} (-1)^k \exp(-k^2\pi^2 Dt/l^2)] = \frac{-2nFADC^*}{(\pi Dt)^{1/2}}[\sum_{k=0}^{\infty} \exp(-(2k+1)^2 l^2/(4Dt))] \quad \text{(A2)}$$

$$I_{DIF} = I_{COL} - I_{GEN} = \frac{-2nFADC^*}{l}[1 + 2\sum_{k=1}^{\infty} \exp(-4k^2\pi^2Dt/l^2)] \quad (A3)$$

$$I_{SUM} = I_{COL} + I_{GEN} = \frac{nFADC^*}{(\pi Dt)^{1/2}}[1 + 2\sum_{k=1}^{\infty} (-1)^k \exp(-k^2l^2/(4Dt))] \quad (A4)$$

LITERATURE CITED

(1) Anderson, J. L.; Ou, T. Y.; Moldoveanu, S. *J. Electroanal. Chem.* **1985**, *196*, 213–226
(2) Bond, A. M.; Henderson, T. L. E.; Thormann, W. *J. Phys. Chem.* **1986**, *90*, 2911–2917.
(3) Chidsey, C. E.; Feldman, B. J.; Lundgren, C.; Murray, R. W. *Anal. Chem.* **1986**, *58*, 601–607.
(4) Feldman, B. J.; Murray, R. W. *Anal. Chem.* **1986**, *58*, 2844–2847.
(5) Fosdick, L. E.; Anderson, J. L. *Anal. Chem.* **1986**, *58*, 2481–2485.
(6) Sanderson, D. G.; Anderson, L. B. *Anal. Chem.* **1985**, *57*, 2388–2393.
(7) Sanderson, D. G.; Anderson, L. B.; Gross, E. *Biochim. Biophys. Acta* **1986**, *852*, 269–278.
(8) Seddon, B. J.; Girault, H. H.; Eddowes, M. J. *J. Electroanal. Chem.* **1989**, *266*, 227–238.
(9) Howell, J. O. *BAS Current Separations* **1987**, *8*, 2–16.
(10) Huang, H. J.; He, P.; Faulkner, L. R. *Anal. Chem.* **1986**, *58*, 2889–2891.
(11) Bard, A. J.; Crayston, J. A.; Kittleson, G. P.; Shea, T. V.; Wrighton, M. S. *Anal. Chem.* **1986**, *58*, 2321–2331.
(12) Aoki, K.; Tanaka, M. *J. Electroanal. Chem.* **1989** *266*, 11–20.
(13) Clough, A. E. Ph.D. Dissertation, The Ohio State University, 1989.
(14) Heiger, D. N. M.S. Thesis, The Ohio State University, 1987.
(15) Harrington, M. S.; Anderson, L. B.; Roberts, J. A.; Karweik, D. H. *Rev. Sci. Instrum.* **1989**, *60*, 3323–3328.
(16) Bartlet, J. E.; Deakin, M. R.; Amatore, C.; Wightman, R. M. *Anal. Chem.* **1988**, *60*, 2167–2171.
(17) Deakin, M. R.; Wightman, R. M.; Amatore, C. A. *J. Electroanal. Chem.* **1986**, *215*, 49–61.
(18) Szabo, A.; Cope, D. K.; Tallman, D. E.; Kovach, P. M.; Wightman, R. M. *J. Electroanal. Chem.* **1987**, *217*, 417–423.
(19) Aoki, K.; Morita, M.; Niwa, O.; Takei, H. *J. Electroanal. Chem.* **1988**, *256*, 269–282.
(20) Anderson, L. B.; Reilley, C. N. *J. Electroanal. Chem.* **1966**, *12*, 477–494.
(21) Hubbard, A. T.; Anson, F. C. In *Electroanalytical Chemistry*; Bard, A. J., Ed.; Marcel Dekker: New York, 1970; Vol. 4, pp 129–214.
(22) Anderson, L. B., unpublished results, The Ohio State University, 1989.
(23) Zoski, C. G.; Bond, A. M.; Colyer, C. L.; Myland, J. C.; Oldham, K. B. *J. Electroanal. Chem.* **1989**, *263*, 1–21.
(24) Heinze, J. *Ber. Bunsen-Ges. Phys. Chem.* **1981**, *85*, 1096–1103.
(25) Nicholson, R. S.; Shain, I. *Anal. Chem.* **1964**, *36*, 706–723.
(26) Harrington, M. S.; Anderson, L. B. *Book of Abstracts*; 196th ACS National Meeting of the American Chemical Society, Los Angeles, September 1988; American Chemical Society: Washington, DC, 1988; ANYL 192.
(27) Clough, A. E.; Anderson, L. B. *Book of Abstracts*; 196th ACS National Meeting of the American Chemical Society, Los Angeles, September 1988; American Chemical Society: Washington, DC, 1988; ANYL 193.
(28) Harrington, M. S.; Anderson, L. B. *Book of Abstracts*; 198th ACS National Meeting of the American Chemical Society, Miami Beach, September 1989; American Chemical Society: Washington, DC, 1989; ANYL 1.

RECEIVED for review October 24, 1989. Accepted December 28, 1989.

Determination of Trace-Element Deposition Parameters from Electrolytic Preconcentration Transients

Roman E. Sioda

Institute of Industrial Chemistry, Warsaw 01-793, Poland

Thomas Z. Fahidy*

Department of Chemical Engineering, University of Waterloo, Waterloo, Ontario, Canada N2L 3G1

A rapid approximate and a rigorous computation scheme for the estimation of the mass transfer coefficient and the specific rate of deposit dissolution are presented. The approach employs experimentally determined preconcentration transient data. The approximate calculation can be readily carried out via an electronic slide rule, while the rigorous method requires a programmable calculator or a microcomputer. The approach is illustrated numerically by experimental copper and lead deposition transients observed by previous researchers in the initial concentration range of 25 nmol/dm^3 to 2.5 μmol/dm^3 for copper and 14 nmol/dm^3 to 1.4 μmol/dm^3 for lead. The computed k_1 and k_2 values decrease with decreasing initial concentrations, suggesting the possibility of a fractal-kinetic process mechanism. Equilibrium concentrations estimated from these results are in reasonable-to-good agreement with values obtained by earlier experimenters.

INTRODUCTION

Preconcentration is a standard analytical method (*1*) for the analysis of trace components (analytes) present initially in a sample of a concentration level below a detection or quantification limit of a chosen instrumental method of analysis. The typical electrodes used in electrolytic preconcentration are the hanging mercury drop electrode, reticulated vitreous carbon, gold, platinum, and tungsten. When the electrodeposition stage (5–60 min) is terminated, analysis is carried out by standard instrumental methods, e.g. spectroscopy, radiometry, electroanalysis, etc. In the latter case, the same cell is often used. Electrolytic preconcentration is not recommended for long times due to complications, such as nonstationary diffusion, restructuring of the electrode surface and of the deposit, and chemical reactions involving the deposit. Among the many possible applications of the technique, the determination of trace amounts of Cd, Cu, Pb, Hg, and Zn in biological substances and fluids (plants, tissues, fish, blood, and food) merits particular mention.

Previous attempts to obtain the governing parameters (*2–4*) met with limited success, since earlier determinations of rate coefficients and equilibrium concentrations were not sufficiently precise and could not be obtained from a single determination. Only the recent experimental data of Ciszewski and co-workers (*5*) permit the evaluation of pertinent kinetic and equilibrium parameters at a reasonable accuracy, since the limits of the new determination methods are 2 to 4 orders of magnitude lower than those obtained in previous attempts

0003-2700/90/0362-0550$02.50/0

cited above. Recent experimental data obtained (*6*) on the deposition of lead on gold using the novel quartz microbalance technique (*7, 8*) in the initial concentration range of 3–30 nmol/L confirm a mathematical model of equilibrium concentrations (*2, 3, 9, 10*), which serves as a starting point for the current work.

The equilibrium conditions and concentration limits for a typical preconcentration process consist of an electrodeposition step

$$M^{n+} + ne^- = M^0 \quad (1)$$

for cationic species M, followed by the chemical dissolution

$$M^0 + X = M^{n+} + Y \quad (2)$$

Since the dissolution restores partially the initial substrate M^{n+} in solution, the process resembles closely the Nicholson–Shain (*11, 12*) catalytic reaction mechanism. The purpose of the current paper is to present a method whereby the kinetic and mass transport parameters of the process may be determined from the same transient data (such as obtained in the experimental work of Ciszewski et al. (*5*)) employed in the evaluation of equilibrium and preconcentration limit conditions, thus extending the scope of the mathematical model.

RESULTS AND DISCUSSION

1. Analysis of the Transient. The transient equation (eq 3, ref 1) is rewritten as

$$dR/dt = \alpha[(1 - R) - \beta(1 - \exp\{-yc_0R\})] \quad (3)$$

where $\alpha = sk_1$, $\beta = k_2/k_1c_0$, and $R = (c_0 - c)/c_0$. As shown previously, s is the specific area (cm^{-1}) of the electrolytic cell, k_1, is the mass transfer coefficient (cm/s) of the deposition process, k_2 is the specific rate (mol/(cm^2·s)) of deposit dissolution, c_0 is the initial trace concentration (mol/cm^3) in the electrolyte, and y is the ratio of the molar monolayer area constant p (cm^2/mol) and the specific area s. In the case of copper and lead (*5*) the magnitude of the yc_0 product varies between unity and slightly above one hundred indicating that if c_0 is relatively high (order of 10^{-9}–10^{-10} mol/cm^3), the exponential term in eq 3 might be neglected at some risk. Under such circumstances the recovery (or conversion) is quickly obtained by straightforward integration as

$$R = (1 - \beta)[1 - \exp(-\alpha t)] \quad (4)$$

It is to be noted that eq 3 cannot be integrated a priori to obtain an analytical form and, consequently, the parameters α and β cannot be determined by a nonlinear regression applied to the (nonexistent) analytical form. In a rigorous approach, eq 3 is considered fully and it is noted that by setting the recovery derivative to zero, the important algebraic relationship, allowing the determination of β

$$1 - R_\infty = \beta[1 - \exp(-yc_0R_\infty)] \quad (5)$$

$$\lim_{t \to \infty} R = R_\infty$$

is first obtained. The solution of eq 3 may conveniently be expressed as a quadrature for the explicit denomination of α

$$\alpha = \frac{\phi(R,\beta)}{t_R} = \frac{\displaystyle\int_0^R \frac{d\lambda}{(1 - \lambda) - \beta[1 - \exp(-yc_0\lambda)]}}{t_R} \quad (6)$$

where t_R is the time required to reach a certain recovery R. For a specified value of β, the integral may be evaluated by standard methods of numerical integration (*13*).

Table I. Summary of the Deposition Process Parameters Estimated from Transient Data by Ciszewski et al. (*5*)

species	initial concn, mol/dm^3	k_1, cm/s: approx method	k_1, cm/s: rigorous method	$10^{11}k_2$, mol/(cm^2·s): approx method	$10^{11}k_2$, mol/(cm^2·s): rigorous method
copper	2.5×10^{-6}	0.1296	0.1107	1.296	1.107
	2.5×10^{-7}	0.0797	0.0794	0.658	0.655
	2.5×10^{-8}	0.0628	0.0163	0.0974	0.0763
lead	1.4×10^{-6}	0.2072	0.2103	0.839	0.852
	1.5×10^{-7}	0.0942	0.1173	0.632	0.788
	1.4×10^{-8}	0.0768	0.0166	0.0819	0.0875

2. Determination of the Deposition Parameters. In a primitive approach experimental $R(t)$ data could be fitted by a regression carrying arbitrary parameters without a mechanistic (i.e. physicochemical) basis; in principle, several competing regressions could be devised whose statistical properties might be similar enough to render them statistically indistinguishable. Consequently, the extraction of rate parameters from the fit would be indeterminate. Further, the numerical work associated with this approach would not be less or simpler than in the approach, described in the sequel, which carries a fundamental mechanistic structure with it. The simplified version of the proposed approach yields a quick estimate of the rate parameters, whose refined values may be obtained by the rigorous version. The higher c_0 the better the quick estimate.

(A) Simplified Method. It follows from eq 4 that as $t \to \infty$, $R \to R_\infty = 1 - \beta$. Moreover, if eq 4 is an acceptable approximation to experimental (R,t) data, the value of R at $t_\alpha = 1/\alpha$ is

$$R_\alpha = (1 - \beta)(1 - 1/\epsilon);\ \epsilon = 2.71828 \quad (7)$$

Consequently, if R_α is known experimentally, α can be computed from eq 7. The straightforward computation procedure consists of the following steps: (A.1) obtain experimentally R_∞, then compute $\beta = 1 - R_\infty$ and $R_\alpha = 0.632R_\infty$; (A.2) obtain from the transient curve t_α corresponding to R_α and compute $\alpha = 1/t_\alpha$; (A.3) since $\alpha \equiv sk_1$ and $\beta \equiv k_2/k_1c_0$, the deposition parameters are calculated as $k_1 = \alpha/s$ and $k_2 = k_1c_0\beta$.

(B) Rigorous Method. (B.1) From eq 5 calculate β

$$\beta = \frac{1 - R_\infty}{1 - \exp(-yc_0R_\infty)} \quad (8)$$

(B.2) using the value of β hereby computed, obtain several numerical estimates for selected R values of the integral

$$\phi(R,\beta) = \int_0^R \frac{d\lambda}{(1 - \lambda) - \beta[1 - \exp(-yc_0\lambda)]} \quad (9)$$

in eq 6, using experimental (R,t_R) data, and compute in each case a value of α; (B.3) obtain a mean value of α by averaging the individual α values obtained in step B.2; (B.4) obtain mean estimates of k_1 and k_2 according to step A.3.

3. Discussion of the Numerical Illustration. Table I contains the results of the determination of deposition process parameters using the concentration transient data of Ciszewski et al. (*5*) in the case of copper and lead. The procedure is illustrated numerically in the Appendix. At relatively high concentrations the approximate and rigorous methods yield reasonably close estimates of k_1 and k_2, but as c_0 decreases, the discrepancy becomes large. The decrease of k_1 and k_2 with decreasing c_0 might be explainable in terms of fractal reaction kinetics theory (*14*) which postulates concentration-dependent rate constants: it is quite plausible, in effect, that deposition from trace concentrations is a fractallike process. Comparison of the values of the equilibrium concentration obtained in the current work with values computed by Ciszewski et al. (*5*)

Table II. Comparison of Computed Equilibrium Concentrations

species and initial concn, mol/cm³	eq no. in ref 5	$10^{11}C_{eq}$, mol/cm³ approx method	$10^{11}C_{eq}$, mol/cm³ rigorous method	Ciszewski et al. (5) comp.	Ciszewski et al. (5) exptl
copper (2.5×10^{-11})	2	1.640	4.95	2.02	1.8 ± 0.2
	5	0.796	1.55	2.00	
lead (1.4×10^{-11})	2	1.07	5.28	1.13	1.1 ± 0.5
	5	0.530	1.105	1.11	

Table III

R	$\phi(R,\beta)$ (eq 9)	t_R, s	α^a (eq 6), s⁻¹
0.14	0.185 10	300	6.170×10^{-4}
0.24	0.376 34	600	6.272×10^{-4}
0.42	0.902 68	1200	7.522×10^{-4}
0.58	1.914 37	2400	7.976×10^{-4}
0.59	2.031 21	3600	5.642×10^{-4}
0.65	3.402 14	7200	4.725×10^{-4}

[a] The mean value of α is 6.384×10^{-4} s⁻¹. Hence, the parameter estimates are $k_1 = (6.384 \times 10^{-4})/(8.04 \times 10^{-3}) = 0.0794$ cm/s and $k_2 = (0.0794)(2.5 \times 10^{10})(0.33) = 6.55 \times 10^{-12}$ mol/(cm²·s).

shows a certain discrepancy when the simple relationship (eq 2, ref 5)

$$c_{eq} = \frac{y(c_e)_1 c_0}{y(c_e)_1 c_0 + 1}; \quad (c_e)_1 = k_2/k_1 \qquad (10)$$

is employed. However, the discrepancy becomes minimal when the relationship (eq 5, ref 5)

$$c_{eq} = (c_e)_1[1 - \exp(-yc_0 + yc_{eq})] \qquad (11)$$

is used for estimating c_{eq} combined with the rigorous method of estimating k_1 and k_2 (hence $(c_e)_1$), as shown in Table II. The closeness of these (c_{eq}) values indicates the validity of parameter determination based on experimental deposition transients and the soundness of the analysis. In view of the common availability of microcomputers equipped with fast and rugged integration software, the handling of eq 9 is essentially a routine operation (in this work a standard Romberg quadrature method was used for rapidity and accuracy), but the approximate method can be retained for a quick preliminary order-of-magnitude estimation as a guide for the more involved computation scheme.

The principal value of knowing c_{eq}, k_1, and k_2 is in optimizing an electrolytic preconcentration process, e.g. to decrease as much as possible the limit of detection and to increase its sensitivity. The proposed method has this goal for its target.

APPENDIX: NUMERICAL ILLUSTRATION

The numerical calculations are illustrated in the case of copper deposition from an electrolyte with an initial cupric ion concentration of 2.5×10^{-7} mol/dm³ (Figure 1, curve b, ref 5).

Approximate Procedure. From the steady-state portion of the curve $R_\infty = 0.67$ and $\beta = 1 - 0.67 = 0.33$. Hence, $R_\alpha = (0.632)(0.67) = 0.4234$. The corresponding time instant is 26 min; hence $\alpha = 1/(26)(60) = 6.410 \times 10^{-4}$ s⁻¹. Since $s = 8.04 \times 10^{-3}$ cm⁻¹ and $p = 3.4 \times 10^8$ cm²/mol in the case of copper, it follows that $k_1 = (6.410 \times 10^{-4})/(8.04 \times 10^{-3}) = 0.0797$ cm/s. Consequently, $k_2 = (0.0797)(2.5 \times 10^{-10})(0.33) = 6.58 \times 10^{-12}$ mol/(cm²·s).

Rigorous Procedure. Since $yc_0 = (3.4 \times 10^8)(2.5 \times 10^{-10})/(8.04 \times 10^{-3}) = 10.572$ and $R_\infty = 0.67$, it follows from eq 8 that $\beta = 0.33/0.99916 \simeq 0.33$. This is essentially the same value as obtained by the approximate procedure since yc_0 is relatively large. Continuing with eq 9 and considering the experimental points denoted by circles in ref 5; Figure 1b, the values given in Table III are obtained via numerical integration.

LITERATURE CITED

(1) Neiman, N. M.; Zolotov Yu. A. *Preconcentration of Trace Elements*; Nauka: Moscow, 1988 (in Russian).
(2) Sioda, R. E. *Talanta* **1984**, *31*, 135–137.
(3) Sioda, R. E. *Talanta* **1985**, *32*, 1083–1087.
(4) Sioda, R. E. *Monatsch. Chem.* **1985**, *116*, 49–52.
(5) Ciszewski, A.; Fish, J. R.; Malinski, T.; Sioda, R. E. *Anal. Chem.* **1989**, *61*, 356–860.
(6) Schmidt, H.-J. Diploma Thesis, Technical University of Darmstadt, FRG. 1989.
(7) Melroy, O.; Kanazawa, K.; Gordon, J. G., II; Buttry, D. *Langmuir* **1986**, *2*, 697–700.
(8) Deakin, M. R.; Melroy, O. *J. Electroanal. Chem.* **1988**, *239*, 321–331.
(9) Sioda, R. E. *Anal. Chem.* **1988**, *60*, 1177–1179.
(10) Sioda, R. E. *Anal. Lett.* **1983**, *16* (A10), 739–746.
(11) Nicholson, R. S.; Shain, I. *Anal. Chem.* **1964**, *36*, 706–723.
(12) Bard, A. J.; Faulkner, L. R. *Electrochemical Methods*; Wiley: New York, 1980; Chapter 11.
(13) Hornbeck, R. W. *Numerical Methods*; QPI Series: New York, 1975; Chapter 8.
(14) Kopelman, R. *Science* **1988**, *241*, 1620–1626.

RECEIVED for review June 26, 1989. Accepted December 7, 1989. The numerical work was carried out on equipment obtained under a University of Waterloo/Digital Equipment Corporation research agreement.

Determination of Barium in Seawater Using Vanadium/Silicon Modifier and Direct Injection Graphite Furnace Atomic Absorption Spectrometry

James K. B. Bishop

Lamont-Doherty Geological Observatory of Columbia University, Palisades, New York 10964

Barium is determined in seawater by direct injection Zeeman modulated graphite furnace atomic absorption spectrometry. The V_2O_5/Si modifier added to undiluted seawater samples promotes injection, sample drying, graphite tube life, and the elimination of most seawater components in a slow char at 1150–1200 °C. Atomization is at 2600 °C. Detection is at 553.6 nm, and calibration is by peak area. Sensitivity is 0.8 absorbance s/ng (M_0 = 5.6 pg/0.0044 absorbance s) at an internal argon flow of 60 mL/min. Detection limit is 2.5 pg (1 standard deviation) Ba in a 25-μL sample. Precision is 1–2% and accuracy is 2–3% for natural seawater (5.6–28 μg L^{-1}). The method works well in organic-rich seawater matrices and sediment porewaters.

INTRODUCTION

Barium is of oceanographic interest since it is a nonconservative stable trace element. In spite of the relatively short 11 000 year oceanic residence time for Ba (*1*), ocean biology largely determines its distributions in the ocean interior. Dissolved concentrations in the major oceans—mapped as part of the GEOSECS program—range between 40 and 200 nmol kg^{-1} (5.6–28 μg L^{-1}) and profiles show lowest concentrations near the surface and enrichment at depth (*2*) in a fashion similar (but not identical) to the distribution of the nutrient element Si. Its determination to a precision of better than 1% by isotope dilution mass spectrometry (IDMS) has earned barium the distinction of being the "best measured" nutrient-like trace metal in seawater (*3*).

Seawater is a high ionic strength (0.7 M) salt (35 g L^{-1}) solution dominated by cations Na^+, Mg^{2+}, Ca^{2+}, and K^+ and anions Cl^-, SO_4^{2-}, and HCO_3^-. Precise determination of any trace substance in seawater is a demanding analytical problem (*3*). IDMS methods for Ba determination require extensive sample manipulation (addition of isotope spike, purification by ion exchange, evaporation, etc.) and are limited to the determination of six samples per day. Roe and Froelich (*4*) investigated direct injection graphite furnace atomic absorption spectrometer (GFAAS) methods hoping to overcome the labor and sample throughput limitations of IDMS. Their method for simple aqueous solutions and seawater gave a precision of 13% (1 standard deviation), a sensitivity at internal flow rate of 100 mL/min of 0.16 absorbance s/ng (characteristic mass, M_0 = 28 pg/0.0044 absorbance s) Ba, and detection limit of 30 pg of Ba in a 50-μL sample; standard curves were concave upward; severe degradation of sensitivity occurred after 25 determinations; the method of standard additions had to be used for seawater and only two samples could be determined per graphite tube. Sample throughput was not significantly better than IDMS.

A more recent approach to the problem (*5*) involved ion-exchange separation of Ba from seawater followed by GFAAS. Precision of better than 5% and an 8-fold improvement in graphite tube life was reported due to the elimination of the seawater matrix (M_0 not available). However, the 10–25% contributions of Ba from the ion-exchange resin blank, 100-mL sample size, and extensive sample manipulation prior to analysis remained problems.

Many factors explain the poor performance of the direct injection GFAAS method for seawater (reviewed by Roe and Froelich, ref 4): (1) barium carbide formation within the heated graphite tube during atomization; (2) furnace emission at the analytical wavelength; (3) smoke from NaCl at atomization; (4) Ba ionization; and (5) chloride vapor phase interferences. Roe and Froelich demonstrated that items 3–5 could be overcome with appropriate modifiers or were unimportant, but carbide formation, short tube life, and furance emission appeared to remain unsolved. The method below appears to overcome these remaining problems allowing barium to be now routinely determined in seawater by direct injection GFAAS to a precision of better than 2% with a better than 4-fold improvement in sensitivity. This technique has the potential to replace IDMS methods which achieve comparable precision yet by comparison are slow and cumbersome.

EXPERIMENTAL SECTION

Apparatus. We used a Perkin-Elmer Zeeman 5000 atomic absorption spectrometer equipped with a HGA-500 graphite furnace, AS-40 autosampler, and RS-232C communications interface. Argon is used as purge gas. We tried Ringsdorff (batch numbers begin with Roman numerals) and Schunk and Ebe (batch numbers begin with arabic numerals) pyrolytically coated graphite tubes from Perkin-Elmer (both supplied under the same part number 0290-1821). Furnace cooling was maintained with a Neslab CFT-75 refrigerated recirculator. Peak response (peak area, peak height, and associated error statistics) was computed by MS-DOS (or MAC) computer after aquisition of high-speed (60 Hz) raw digital data directly from the PE-5000. The software is available through the author. Instrumental settings were 553.6 nm, slit 0.4 nm, read 15 s, and lamp current 50 mA (energy 58–60), peak area, Zeeman background correction was used.

Standards and Reagents. The primary standard was prepared by micropipet addition of 0.5 mL of 1001 mg L^{-1} Ba aqueous standard solution (Ba in 2% HCl; SPEX Industries, AQBA1-100) added to approximately 135 mL of distilled deionized water within a preweighed polypropylene (PP) bottle (4 oz, Nalgene). Pipet accuracy (determined gravimetrically) was better than 0.2% and error in estimating total solution volume (determined gravimetrically) was <0.1%. Running standards were prepared by micropipet additions of between 0.05 and 1.0 mL of the 27.01 ± 0.05 μmol L^{-1} primary standard to 135-mL volumes of 400-m deep Sargasso Sea water (salinity = 36.48 g kg^{-1}; density 1.025 g mL^{-1}; Ba = 43 nmol L^{-1}) acidified by the addition of 1 mL of Vycor-distilled 6 N HCl. These standards increased the reference seawater concentration by 9.8, 24.8, 49.5, 73.6, 98.4, 144.7, and 200.4 nmol L^{-1} (1.3–28 μg L^{-1}). Standards so prepared are stable for months provided the polypropylene bottles are properly capped.

Matrix modifiers are 1000 mg L^{-1} vanadium (V_2O_5 in 5% HCl) and 1000 mg L^{-1} silicon (sodium silicate in distilled water) standard solutions (Fisher Scientific Co.).

Procedure. The 135-mL seawater samples from the South Atlantic ocean were acidified upon collection by addition of 1.0 mL of Vycor-distilled 6 N HCl and stored in acid-leached 4-oz

0003-2700/90/0362-0553$02.50/0

Table I. Enhancement of GFAAS Signal by Vanadium[a]

added V, ng	enhancement peak area	enhancement peak height	run date yy/mm/dd
0	1.00	1.00	870724
50	1.35	1.16	870724
100	1.52	1.22	870724
250	1.82	1.38	870724
250	1.87	1.40	870730
500	1.97	1.55	870724
1000	2.39	1.67	870724
1000	2.30	1.71	870730
5000	2.91	1.89	870730

HGA 500 Program

step	1	2	3	4	5	6	7
temp	100	120	1500	1500	2550	2650	20
ramp	1	15	15	1	0	1	1
hold	1	20	15	4	10	3	10
read					−5		
int flow					80		

[a] Injections of 0.89 ng of Ba in 35 μL of 0.12 N HCl.

Table II. Effect of Pyrolysis Temperature on GFAAS Peak Area[a]

pyrolysis temp, °C	no vanadium added	1000 ng of V, added	enhancement
1100	0.1218	n.d.	n.d.
1200	0.1230	0.2624	2.13
1300	0.1174	0.2617	2.23
1400	0.1171	0.2606	2.23
1500	0.1061	0.2582	2.43
1600	0.0843	0.2501	2.97
1700	0.0602	0.2323	3.86
1800	0.0371	0.1933	5.21
1900	n.d.	0.1397	n.d.

HGA 500 Program

step	1	2	3	4	5	6	7
temp	100	120	×	×	2550	2650	20
ramp	1	15	15	1	0	1	1
hold	1	20	15	4	10	3	10
read					−5		
int flow					80		

[a] Injections of 0.89 ng of Ba in 35 μL of 0.12 N HCl.

Table III. Effect of Internal Flow Rate on GFAAS Signal[a]

Ar flow rate, mL min^{-1}	peak area, abs s	precision (σ)	n
10	0.4267	0.0033	5
20	0.4017	0.0030	2
40	0.3390	0.0013	2
80	0.2395	0.0014	3
160	0.1440	0.0004	2

HGA 500 Program

step	1	2	3	4	5	6	7
temp	100	120	1200	1200	2550	2800	20
ramp	1	15	15	1	0	1	1
hold	1	20	15	4	10	7	10
read					−5		
int flow					×		

[a] Injections of 0.89 ng of Ba in 35 μL of 0.12 N HCl, 1000 ng of added V.

polypropylene bottles. Nine hundred microliters of running standards and samples were pipetted directly into 1.5-mL polyethylene autosampler cups already containing 250- and 100-μL volumes of vanadium and silicon modifiers. Duplicate injections of 25-μL volumes of mixed solution into the furnace were sufficient for precise seawater analysis. Typical sample runs consisted of a randomly ordered series of five standards and then a repeating series of low standard, high standard, and five samples. The low and high standards were chosen to bracket the expected range of sample concentration and used to compensate for drift in sensitivity. Termination of the series occurred when sensitivity decreased by 10–20%. Graphite tubes survive 70–100 determinations prior to significant (5%) loss of sensitivity.

The furnace program for seawater is as follows: (1) 200 °C, 1-s ramp, 1-s hold; (2) 160 °C, 1-s ramp, 29-s hold; (3) 1150 °C, 1-s ramp, 14-s hold; (4) 1200 °C, 15-s ramp, 50-s hold; (5) 2600 °C, at max power (0-s ramp), 10-s hold, read −5 s, internal flow 60 mL min^{-1}; (6) 2800 °C, 0-s ramp, 5-s hold; and (7) 20 °C, 4-s ramp, 11-s hold. Furnace temperatures above 1000 °C were verified by optical pyrometer to be accurate within 50 °C.

RESULTS AND DISCUSSION

The method above evolved from one developed for the determination of Ba in 0.12 N HCl leach solutions of oceanic particulate matter samples (*6*). Briefly, it was noticed that simple standards and samples (without modifiers), although made identical in HCl concentration, gave peak height/area ratios = 1.5 and 0.8, respectively. Standard additions experiments revealed a 50% greater response for Ba added to samples compared to that predicted by the simple standards. Given this analytical bias, a search was undertaken for a chemical modifier which would make the sample and standard solutions yield identical peak shape. We tried $NH_4H_2PO_4$, HNO_3, Eu, Mo, Nd, Ti, V, and Yb. Many of the elements in the list were chosen because they have atomization temperatures near that of Ba (2600 °C) and could be removed from the furnace in a high-temperature clean out step. Some were reported to exhibit memory effects in GFAAS. Europium, an element chemically very similar to Ba, enhanced sensitivity 2-fold but also enhanced memory effects as well. Neodymium, also enhanced sensitivity 2-fold, but did not improve reproducibility. Ytterbium, Mo, and $NH_4H_2PO_4$ had no effect. Ti enhanced sensitivity but had a significant Ba blank. Vanadium showed up to a 3-fold enhancement of sensitivity, precision better than 1% (Tables I–III), and a negligible Ba blank.

We quickly learned that traditional approaches to GFAAS method development did not work for Ba in seawater. In particular, Perkin-Elmer recommends drying slightly warmer than solution boiling temperature (110–120 °C). This worked well for simple solutions (Tables I–III) but the seawater method has a step 1 temperature of 200 °C and decreases to 160 °C in step 2. With seawater, sensitivity may be irreversibly lost at drying temperatures 130 °C and lower. Traditional guidance for metal determinations discourages the use of HCl as an acid matrix due to the known volatility of metal chlorides. Use of the recommended HNO_3 acid matrix modifier for seawater (*4*) does severely shorten tube life. The method described below is the synthesis of 20–30 experimental runs with seawater conducted during 1988. It has been independently tested in several laboratories and is in routine use in this laboratory.

Lamp Current. Technical consultations with Perkin-Elmer during our early work with barium (*6*) suggested that the effect of high levels of furnace continuum emission at the analytical wavelength of barium could be overcome by increasing hollow cathode lamp current to 50 mA (2 times the maximum recommended level). This high lamp current does decrease sensitivity by 21% due to emission line broadening but this is more than compensated for by the 3-fold drop in noise during atomization (raw 60 Hz data, σ = 0.0028 vs 0.0091 A). The 50 mA current does not appear to cause self-absorption in Zeeman mode nor does it appear to seriously affect lamp life.

Graphite Tubes. Ringsdorff (R), Schunk and Ebe (S&E), and heavy duty Schunk and Ebe tubes used in this study weigh typically 1.15, 1.2, and 1.45 g, respectively. Although they are resistively identical, their mass influences the rate

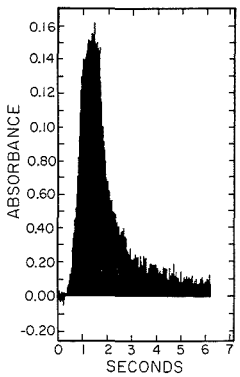

Figure 1. Ba peak from injection of 25 μL of mixed (900:250:100) 141.4 nmol of Ba L^{-1} in seawater, 1000 mg L^{-1} V, 1000 mg L^{-1} Si solutions.

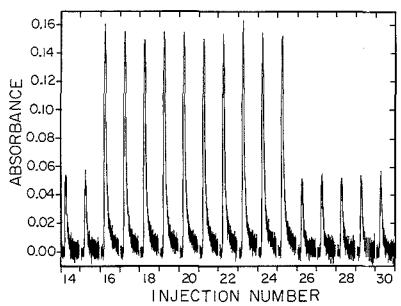

Figure 2. Replicate peaks for a series of determinations of 43 and 141.4 nmol L^{-1} seawater. Mean and standard deviation of 10 replicates shown is 0.2347 ± 0.0022 absorbance s. Unsmoothed 60 Hz data are plotted. Each division corresponds to 10 s.

of heating achieved under maximum power heating. The heavy duty S&E tubes gave broad peaks (height/area ratio <0.5). Furthermore, the greater wall thickness and required 100 °C increased atomization temperature for the heavy duty S&E tube also result in greater continuum emission. Both these considerations suggest that the heavy tubes are not appropriate for this application. The lighter tubes give height/area ratios of between 0.7 and 0.8 and sample absorbance should approach base-line values after 6–8 s of atomization (Figure 1). Software diagnostics show that a factor of 2 increase in base-line noise between the last seconds of the pyrolysis and atomization steps is typical for the lighter tubes (e.g. Figure 2). The Schunk and Ebe tubes (Batch 8/00116 137) routinely lasted 100 determinations prior to significant loss of sensitivity. Ringsdorf tubes (Batch X/57/222) lasted 70 determinations. It is impossible to tell presently if differences in tube life are due to differences in tube batches or due to different fabrication methods (SEM analysis shows insides of tubes to be different) used by the two manufacturers.

Matrix Modification. The combined modifiers allow in excess of 100 determinations (S&E tubes) to be made from a single graphite tube before significant loss of sensitivity occurs. This is a >4-fold improvement of tube life over that reported by Roe and Froelich (*4*). The main effect of the silicon modifier is to extend tube life by 30% and to increase sensitivity by 10–20% compared to using the vanadium modifier alone. All other effects described in the sections below are due to the action of the vanadium pentaoxide

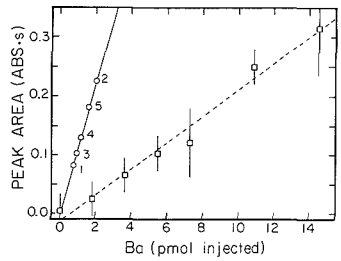

Figure 3. Sensitivity and reproducibility of this method (O, error bars smaller than symbols) compared with Roe and Froelich (□, ref 4).

modifier. Scanning electron microscope/energy dispersive X-ray fluorescence (SEM/EDXRF) analysis of several graphite tubes removed from the furnace after interruption of the furnace cycle at different steps aided in understanding the action of the modifier. Welder's goggles were worn during visual examination of the furnace during the higher temperature (>1200 °C) stages of the program cycle.

Injection. The direct mixture of sample and modifiers in the autosampler cups was preferred over having the autosampler perform modifier addition because time between determinations was minimized and sample injection reliability improved considerably for solutions with high surface tension (such as complex marine porewaters or organic-rich seawater culture media).

Furnace Program. *Drying (Steps 1 and 2).* Solutions (25 μL) dry within 5–10 s; drying requires 25–30 s without V_2O_5. The drying reaction causes the sample to wet a large area of the graphite tube. SEM/EDXRF analysis shows that sea salt components (Na, Cl, Mg, S, Ca, and K) form an amorphous microcrystalline coating on the tube. Particulate contamination of the furnace (from the vicinity of the injection port) must be avoided or else rapid boiling will occur. It is not necessary to filter open ocean seawater due to its low particulate matter content. **Warning**: drying temperatures lower than 140 °C can cause a sudden and unexplained loss of all sensitivity with seawater solutions. Sensitivity is enhanced significantly (compared with simple standards dried at 100–120 °C; Table II) as drying temperature is increased.

Pyrolysis (Steps 3 and 4). Sample on wall of tube becomes shiny (NaCl melts at 800 °C), a yellow spectral emission within the argon flow (out of injection hole) is observed. Smoke may be also observed during these steps. SEM/EDXRF shows only Ca and Mg sea salt components remaining as CaO [mp 2616 °C] and MgO [mp 2850 °C]); V and Si are still present. Final pyrolysis temperature can be as high as 1500 °C (up to 1700 °C for 5 s) without loss of sensitivity. This suggests a probable oxide form for Ba.

Atomization (Step 5). Minimal smoke is observed. Little effect upon sensitivity was found above 2600 °C. Absorbance should be close to base line by 6–8 s after atomization (Figure 1). Noise increases significantly above 2650 °C and sensitivity decreases below 2500 °C. Internal Ar flow rates lower than 60 mL min^{-1} result in significant condensation of materials at ends of the tube and contact cylinders.

Clean Out [step 6]. Temperature should be >2750 °C or else V and MgO are not removed from the furnace and/or condense at the points of tube contact with the contact cylinders. SEM/EDXRF also shows no residue of modifier or sea salt in the area of sample deposition after burn out.

Cool Down [step 7]. Cool down helps system recover from the 15-s high temperature steps 5 and 6.

Analytical Figures of Merit. Figure 3 shows the comparison between sensitivity and precision for Ba in HCl acidified seawater using the procedure above (this method,

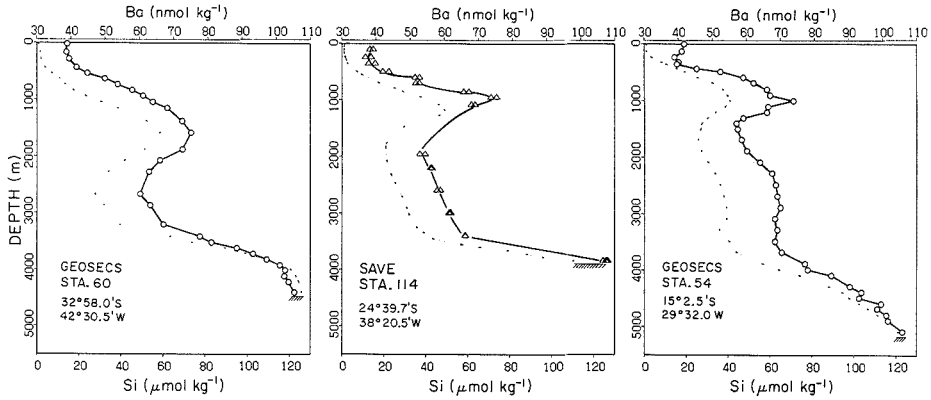

Figure 4. Left and Right: profiles of dissolved Si (small symbols, dashed lines) and dissolved Ba determined by IDMS (*2*) for GEOSECS sations 54 and 60 in the South Atlantic Ocean. Center: SAVE Station 114. Si data from preliminary data report. Ba data for each depth was determined by the GFAAS method. Standard deviation of replicate determinations of samples from each depth averaged 0.8 nmol kg^{-1} (range 0.1–1.3 nmol kg^{-1}).

solid line) and data for Ba in 0.4% HNO_3 previously reported by Roe and Froelich (ref 4, dashed line). Roe and Froelich used the method of additions for seawater. Order of analysis (this method) of standards indicates that memory effects are negligible. Error bars represent 2 times standard deviation limits for duplicate (this method) and quadruple (Roe and Froelich) determinations of the standards. Least-squares fits to the two standard curves (± indicates 95% confidence limits = 2 standard deviations in parentheses) gave the following results: this method, peak area = (0.1086 ± 0.0048)Ba − (0.0015 ± 0.0069), σ_y = 0.0024; Roe and Froelich method, peak area = (0.0223 ± 0.0027)Ba − (0.0130 ± 0.0209), σ_y = 0.0173. We report a 5-fold improvement in sensitivity (0.79 abs s/ng vs 0.16 abs s/ng; M_0 = 5.6 pg vs 28 pg). Only a small fraction of the difference in sensitivity is explained by the different internal flow rates used (Table III).

L'vov (*7*) reports Ba sensitivity in simple solutions (M_0 = 2.5 pg for peak height and 4.3 pg for peak area) under stop flow conditions using Ta foil graphite tube liners and a Ta platform. Manning and Slavin (*8*) used the L'vov method and obtained M_0 values of 2.2 pg (precision 13%) and 2.8 pg (precision 4%) for peak area in two different experiments. These M_0 values are substantially better than the value of 6.0 based on their earlier work with pyrolytically coated graphite tubes. The Ta lining causes the partial pressure of carbon to be lowered significantly during atomization, thus the improved sensitivity is due to reduced barium carbide formation (*7*).

In order to compare our results with those above, we must extrapolate our sensitivity (M_0 = 5.6 at 60 mL/min and 50 mA lamp current) to 0 mL/min (stop flow conditions) and normal 25 mA lamp operating current. Using data from Table III we estimate that sensitivity will increase by a factor of 1.6 at stopped flow. Similarly, our data show that decreasing lamp current to 25 mA increases sensitivity by a factor of 1.27. Thus our M_0 would be reduced by a factor of 1.55 × 1.27 = 1.96 to yield a value of 2.9 pg. Therefore, in terms of sensitivity, the V_2O_5/Si method appears to perform as well as the Ta-foil method and it is concluded that the gaseous environment within the furnace at the time of atomization is not favorable to the formation of barium carbide. The L'vov Ta-foil method awaits improvement in precision and tube life (typically 50 firings) and has yet to be evaluated for seawater.

Precision of single determinations is estimated by 4 sets of 10 replicate injections (a portion shown in Figure 2), alternating between surface seawater (43 nmol L^{-1}) and Ba-enriched seawater (142 nmol L^{-1}; typical deep Pacific Ocean concentration) as 0.0702 ± 0.0043 (low), 0.2347 ± 0.0022 (high), 0.0744 ± 0.0018 (low), and 0.2397 ± 0.0038 (high) absorbance s. If single determinations were eliminated from the first and last sets, then means and standard deviations would change to 0.0714 ± 0.0015 and 0.2407 ± 0.0022 absorbance s, respectively. Thus precision is estimated to be 0.0020 absorbance s or 2.5 pg injected. This value is representative of detection limits since the Ba blank due to combined modifier and acid is less than 2.5 pg. This is over 10 times better than precision and detection limits of Roe and Froelich (*4*). The 0.0020 absorbance s precision is only 2 times worse than the statistical estimate (0.0010 absorbance s, using measured base-line noise during the last second of atomization) for determination of peak area. Also from these data, drift in sensitivity is less than 0.2% per determination and can be compensated for.

Day to day precision and accuracy over a full run were estimated by determining barium in samples of seawater collected during the 1988 South Atlantic Ventillation Experiment (SAVE) and comparing them with published GEOSECS values for the same ocean region (*2*) (Figure 4). The SAVE station 114 profile was determined on two separate days with the exception of the bottom most point, which was determined on three separate days. This station was located midway between GEOSECS stations 54 and 60 (for which IDMS Ba data are available) but slightly closer to the continental margin. Standard deviation of multiple sample determinations (two injections/sample) averaged 0.8 nmol kg^{-1} (range 0.1–1.3 nmol kg^{-1}) and translates to an average precision of 2 pg injected, consistent with the findings above. The data showed excellent agreement with the GEOSECS data, especially for mid-water column values.

An accuracy check and a further test of precision were achieved by determining barium in archived samples from GEOSECS station 60 (Ba determined by IDMS; 2) provided by Dr. Chan. Since the samples were spiked with ^{135}Ba in a way that roughly doubled their Ba concentration, direct comparison of profile data is not meaningful; however, since the quantity of ^{135}Ba spike added is known to better than 0.2%, and since evaporative losses (typically 2–3%) from the sample between 1972 (collection) and 1988 (L-DGO analysis) could be precisely calculated, a valid comparison could be made. The results of a single 20-sample run show that

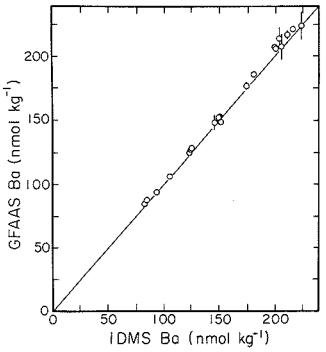

Figure 5. Comparative determinations of Ba by IDMS (*2*) and GFAAS methods in 20 GEOSECS station 60 samples in a single run. The samples have been enriched in ^{135}Ba so as to double their Ba concentration as a necessary step for IDMS analysis. Error bars represent 2 standard deviations of replicate injections. Samples with large deviation would normally be rerun. Line shown has a slope of 1.

agreement of the two methods is better than 3% (Figure 5). Error bars plotted indicate 2 standard deviations of duplicate determinations. All sample data are shown. Samples with poor replication would normally be rerun. Linear regression analysis (±95% confidence intervals) gave the following: GFAAS Ba = 1.027 (±0.021)·IDMS Ba −1.3 (±3.5) nmol kg^{-1}. The departure of the line from a 1:1 fit, although only slightly outside the 95% confidence interval, deserves further investigation. These data and those from Figure 3 indicate linearity of the standard curve to concentrations at least as high as 225 nmol kg^{-1} (4 pmol of Ba injected − peak area = 0.44 absorbance s). The 10% variation of salinity of the samples had no discernible effect on Ba determination.

CONCLUSIONS

The novel use of vanadium pentaoxide and silicon modifiers has demonstrated that the barium carbide formation reaction within the graphite furnace is no longer a problem. Operation of the hollow cathode lamp at 2 times higher than recommended current contributed to a 2–3-fold reduction in noise by reducing the relative effect of continuum furnace emission on peak detection. These two changes overcame the last obstacles to development of a sucessful GFAAS method for barium determination in seawater. The GFAAS method described above also has been used with success in this laboratory for barium determination in marine sediment porewaters, organic-rich seawater plankton culture media, and simpler aqueous solutions.

While IDMS presently achieves slightly better precision, the GFAAS method has the following advantages: (1) complete determination of Ba in 30–50 seawater samples/day may be easily accomplished by GFAAS (this is 5–10 times faster than IDMS); (2) direct injection GFAAS requires no labor-intensive sample preparation unlike IDMS; (3) GFAAS analysis requires less than 1 mL of seawater per run (this compares with 130 mL required for each IDMS analysis); (4) the potential for high sample throughput and small sample requirement makes Ba perhaps the first trace element that could be determined routinely from oceanographic hydrocasts (a single instrument and analyst could easily process 7000 samples/year); (5) GFAAS instrumentation is relatively inexpensive and is available at most universities and oceanographic institutions.

The vanadium pentaoxide modifier may improve the precision and sensitivity of GFAAS analysis of other carbide and non-carbide forming elements in complex matrices. Experience in this laboratory has already shown the vanadium modifier to improve significantly the determination of Fe in marine porewaters.

ACKNOWLEDGMENT

The author wishes to thank the following persons who contributed to the development of the barium method: W. Slavin and G. Carnrick (Perkin-Elmer); M. Fleisher, R. Anderson, R. Mortlock, and P. Froelich (Lamont-Doherty Geological Observatory); and L.-A. Yang (Tufts University). L. H. Chan (Louisiana State University) is thanked for providing GEOSECS samples and IDMS data. R. Key (Princeton) is thanked for collecting 1600 Ba samples from the South Atlantic during 1988 and 1989. W. Slavin is thanked for his contributions to the final version of the paper.

Registry No. Ba, 7440-39-3; V_2O_5, 1314-62-1; sodium silicate, 1344-09-8; water, 7732-18-5.

LITERATURE CITED

(1) Edmond, J. M.; Measures, C.; McDuff, R. E.; Chan, L. H.; Collier, R.; Grant, B.; Gordon, L. I.; Corliss, J. B. *Earth Planet. Sci. Lett.* **1979**, *46*, 1–19.
(2) Chan, L. H.; Drummond, D.; Edmond, J. M.; Grant, B. *Deep-Sea Res.* **1977**, *24*, 613–649.
(3) Bruland, K. W. *Chemical Oceanography*; Academic Press: London, 1985; Vol. 8, pp 157–220.
(4) Roe, K. K.; Froelich, P. N. *Anal. Chem.* **1984**, *56*, 2724–2726.
(5) Dehairs, F.; De Bondt, M.; Baeyens, W.; Van Den Winkel, P.; Hoenig, M. *Anal. Chim. Acta* **1987**, *196*, 33–40.
(6) Bishop, J. K. B. *Nature* **1988**, *332*, 341–343.
(7) L'vov, B. V. J. *Anal. At. Spectrom.* **1988**, *3*, 9–12.
(8) Manning, D. C.; Slavin, W. Study 262, Perkin-Elmer Corporation: Norwalk, CT, 1988.

RECEIVED for review October 6, 1989. Accepted December 6, 1989. Funding was provided by National Science Foundation Grants OCE-8802773 and OCE-8902478. Contribution number 4580 from Lamont-Doherty Geological Observatory.

Single Optical Fiber, Position-Sensitive Detector-Based Multiwavelength Absorbance Spectrophotometer

Curtiss N. Renn and Robert E. Synovec*

Center for Process Analytical Chemistry, Department of Chemistry, BG-10, University of Washington, Seattle, Washington 98195

A relatively simple, yet stable and versatile, multiwavelength absorbance spectrophotometer is described. A broad-band mercury–xenon source was coupled into a single UV–vis transmitting optical fiber, through a detection cell, and dispersed by a monochromator onto the face of a continuous position-sensitive detector (PSD). Two wavelength regions illuminated opposite ends of the PSD while the remainder of the dispersed light was masked. Photocurrent contributions by the two wavelength regions were readily balanced to achieve a stable electronic null condition. The resulting optical configuration provided absorbance measurements simultaneously at two wavelengths, while also correcting for light source intensity fluctuations and refractive index aberrations. The absorbance detector was applied in microbore liquid chromatography with a 6 mm path length *z*-configuration flow cell (1.2 μL volume). A 1.1×10^{-4} au ($3 \times$ root mean square noise level, 60-s intervals) was routinely achieved, which constitutes over a factor of 10 reduction in noise due to light source fluctuations. Aldehyde derivatives with 2,4-dinitrophenylhyrazine were chromatographically analyzed as a test system. The mass detection limit of injected formaldehyde was 4 pg. Since two wavelength regions are simultaneously measured, molar absorptivity ratios of the aldehyde derivatives were obtained and compared to absorbance spectra obtained from a commercial instrument. Results suggest that molar absorptivity measurements can be obtained more simply than with the typical photodiode array based instruments. The new detection system should be advantageous in remote-sensing applications, including flow injection analysis, high-temperature liquid chromatography, biological monitoring, and environmental monitoring.

INTRODUCTION

Absorbance spectrophotometry is widely used in chemical analysis. Photodiode array (PDA) based instruments offer multiwavelength detection (*1*), where an analyte absorbance spectrum may be measured and used for identification. In tandem with liquid chromatography (LC), absobance spectrophotometry is a powerful tool. In LC, the ratio of the absorbance at two wavelengths may be measured and applied to analyte identification (*2*). Wavelength selection is a common task in developing a chemical analysis based upon PDA absorbance spectrophotometry (*3*, *4*). Optimization is important in either single wavelength absorbance (*3*) or dual-wavelength absorbance ratio (*4*) measurements. One drawback to PDA-based absorbance spectrophotometry is instrument cost, due to the inherent complexity.

Remote absorbance measurements are also of interest, where fiber optics are utilized (*5–13*). Remote absorbance sensing is important in process analysis (*5*, *7*, *9*, *12*, *13*), in bioanalytical monitoring (*6*), and in field-portable or applied instruments (*11*). In each case, the fiber optic arrangement provides a means to successfully analyze an otherwise difficult sample environment. Optical fibers have also been useful in thermal lens spectrometry (*14–16*), as an optic providing well-defined beam properties. Optical fiber technology has also been incorporated into LC and flow injection analysis (FIA) absorbance detection methods (*10*, *14*, *17–20*). Although open optics are also popular, fiber optics solve detection problems associated with miniaturization. Specifically, the path length in capillary separation methods is generally limited to the inside diameter of the capillary when open optics are used (*21*, *22*). Fiber optics may be employed to maximize optical path length, while maintaining a flow cell volume commensurate with preserving chromatographic information (*10*, *18*). Fiber optic based absorbance spectrophotometers do have the tendency to suffer from stray light (*6*, *10*) and refractive index (RI) (*23*, *24*) effects. Furthermore, ultraviolet (UV) and X-ray radiation is known to damage or solarize fiber optics (*25–27*). Solarization must be evaluated for a given fiber optic based absorbance spectrophotometer. Since qualitative results are generally reported (*5*), more thorough investigation is warranted.

Recently, we reported the concept of using a position-sensitive detector (PSD) for dual-beam absorbance detection, where the sample and reference beams originated from the same light source (*28*, *29*). A continuous PSD was used, with a uniform resistance per unit length, thus providing a completely analog absorbance measurement—analogous, but inherently more stable than the dual-photodiode approach. In contrast, PDA-based absorbance detection begins with discrete information that must be subsequently processed to provide an absorbance measurement. It was clear from our previous work that a multiwavelength or, in the simplest sense, dual-wavelength absorbance measurement could be made with the continuous PSD. Thus, we have replaced the PDA in a gating monochromator arrangement with a PSD, and with proper spatial masking of unwanted spectral regions, a simple, reliable and low-cost absorbance spectrophotometer capable of low absorbance detection levels is obtained. Furthermore, the analog nature of the device makes it easy to tune, while the data is straightforward to interpret and spectrally informative, by providing the absorbance ratio at two wavelengths. Coupling the dual-wavelength PSD-based absorbance spectrometer to a single fiber optic, with a suitable light source and sample cell fiber optic, provides a complete system for remote, small-volume measurements. This system has been developed and evaluated as an LC detector employing a *z*-configuration flow cell, although important ramifications for FIA were also examined. Specifically, RI effects that often plague absorbance measurements of unretained analytes, as in FIA, were minimized by the unique instrument reported here. The RI effects are due to concentration gradients in the *z*-configuration flow cell (*30*, *31*) and reflection/transmission dependencies on major matrix constituents (*23*, *24*) and numerical aperture changes with RI (*16*). Indeed, the RI effect due to concentration gradients in the *z*-configuration flow cell can be quite large under the proper hydrodynamic conditions (*32–34*). Solarization of the optical fiber in the UV range was investigated. Stray light was also considered (*35*).

0003-2700/90/0362-0558$02.50/0

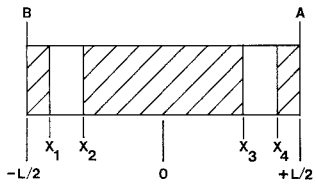

Figure 1. Continuous position-sensitive detector (PSD) providing photocurrent measurements at electrodes A and B. The PSD length is L along the x axis, and centered $x = 0$ such that $-L/2 \leq x \leq L/2$.

In order to properly evaluate the single fiber optic, multiwavelength PSD-based absorbance spectrophotometer, well-characterized 2,4-dinitrophenylhydrazones of selected aldehydes were analyzed. 2,4-Dinitrophenylhydrazine (DNPH) derivatives of aldehydes and ketones are straightforward to separate by LC and are known to absorb strongly in the 300–420 nm range (*36*), offering selective and sensitive analysis of environmentally significant chemical species (*37*). We also report a substantial improvement in injected mass detectability of DNPH derivatives over previous reports (*36*, *37*), that is of importance for sample limited environmental studies. The DNPH derivative absorbance spectra differ slightly from one species to the next. The capabilities of the detection system reported here will be high-lighted in the LC analysis of DNPH derivatives. Simultaneous absorbance measurements at two well-separated wavelengths will be made and the results discussed in comparison to the conventional PDA-based absorbance ratio measurement. The absorbance limits of the fiber optic, PSD-base multiwavelength spectrophotometer will be reported and compared to other fiber optic absorbance systems.

THEORY

Absorbance measurements for the continuous PSD must be defined for a spectrally dispersed light source. In previous work (*28*, *29*), a single wavelength was used and split to form sample and reference beams, respectively, in a conventional dual-beam arrangement. In our present work, referring to Figure 1, the PSD has been defined in terms of electrodes A and B, and position indices x_i, along the photoactive surface with uniform resistance per unit length, for the PSD of total length, L. For mathematical convenience, the x axis is centered on the PSD so $-L/2 \leq x \leq L/2$. It is helpful to first consider a single incident wavelength with regard to the PSD configuration of Figure 1.

For a single wavelength incident at position x, the measured photocurrents I_A and I_B are given by

$$I_A = I_{0,\lambda}\left(\frac{\frac{L}{2} + x}{L}\right) \tag{1}$$

and

$$I_B = I_{0,\lambda}\left(\frac{L - \left(\frac{L}{2} + x\right)}{L}\right) \tag{2}$$

where $I_{0,\lambda}$ is the total photocurrent produced.

PSD outputs labeled as the diff, sum, and ratio are as follows, from eqs 1 and 2

$$\text{diff} = I_A - I_B = I_{0,\lambda}\left(\frac{2x}{L}\right) \tag{3}$$

$$\text{sum} = I_A + I_B = I_{0,\lambda} \tag{4}$$

$$\text{ratio} = \frac{I_A - I_B}{I_A + I_B} = \frac{2x}{L} \tag{5}$$

For light spectrally dispersed along the PSD x axis, one must consider the photocurrent produced per unit length of the PSD, $I_{0,\lambda}(x)/L$, given by

$$\frac{I_{0,\lambda}(x)}{L} = K_\lambda(x)\frac{I_\lambda^\circ(x)}{L} \tag{6}$$

where $I_\lambda^\circ(x)/L$ is the photon flux intensity per unit length and $K_\lambda(x)$ is a conversion factor from photons to photocurrent. In this way one can define the total photocurrent produced by the PSD, $I_0(T)$, assuming no spatial masking of unwanted wavelength regions, by integrating eq 6

$$I_0(T) = \int_{-L/2}^{L/2}\frac{I_{0,\lambda}(x)}{L}\,dx \tag{7}$$

which is the maximum obtainable sum signal over a given spectral region. For simplicity, it is helpful to assume $I_{0,\lambda}(x)/L$ is a constant, implying a uniformly produced photocurrent, but produced by a spectrally dispersed light source. This assumption, although not rigorously valid, is reasonable and allows one to readily derive the important PSD absorbance equations. Referring back to Figure 1, let interval x_1 to x_2 define an average wavelength $\lambda(1,2)$ with a photocurrent per unit length of $I_{0,\lambda}(1,2)$, and interval x_3 to x_4 define an average wavelength $\lambda(3,4)$ with $I_{0,\lambda}(3,4)$. The x_i indices are defined such that $-L/2 \leq x_1 < x_2 \leq 0$ and $0 \leq x_3 < x_4 \leq L/2$, for practical operation. The diff and sum signals are given by

$$\text{diff} = \frac{1}{L}\int_{x_1}^{x_2} I_{0,\lambda}(1,2)\left(\frac{2x}{L}\right)dx + \frac{1}{L}\int_{x_3}^{x_4} I_{0,\lambda}(3,4)\left(\frac{2x}{L}\right)dx \tag{8}$$

and

$$\text{sum} = \frac{1}{L}\int_{x_1}^{x_2} I_{0,\lambda}(1,2)\,dx + \frac{1}{L}\int_{x_3}^{x_4} I_{0,\lambda}(3,4)\,dx \tag{9}$$

After integrating and simplifying eqs 8 and 9, the ratio signal becomes

$$\text{ratio} = \frac{1}{L}\left[\frac{I_{0,\lambda}(1,2)\,(x_2^2 - x_1^2) + I_{0,\lambda}(3,4)\,(x_4^2 - x_3^2)}{I_{0,\lambda}(1,2)\,(x_2 - x_1) + I_{0,\lambda}(3,4)\,(x_4 - x_3)}\right] \tag{10}$$

Since $I_{0,\lambda}(x)/L$ is assumed constant, an electronic null is obtained when $\Delta x = x_2 - x_1 = x_4 - x_3$ in eq 10. Working at the electronic null, eq 10 becomes

$$\text{ratio} = \frac{1}{L}\left[\frac{I_{0,\lambda}(1,2)\,(x_2 + x_1) + I_{0,\lambda}(3,4)\,(x_4 + x_3)}{I_{0,\lambda}(1,2) + I_{0,\lambda}(3,4)}\right] = 0 \tag{11}$$

Equation 11 simplifies at an electronic null to

$$\text{ratio} = \frac{X}{L}\left[\frac{I_{0,\lambda}(3,4) - I_{0,\lambda}(1,2)}{I_{0,\lambda}(3,4) + I_{0,\lambda}(1,2)}\right] = 0 \tag{12}$$

with

$$X = \frac{x_4 + x_3}{2} - \frac{x_2 + x_1}{2} \tag{13}$$

where as a point of reference, X is equivalent to the distance separating two equivalent photocurrent sources, equidistant from the PSD center, consistent with previous work (*28*, *29*).

Now it is possible to consider an absorbance at either $\lambda(1,2)$, labeled as $A(1,2)$, or $\lambda(3,4)$, labeled as $A(3,4)$, or both wavelength regions simultaneously. Analogous to previous work (*28*, *29*), the ratio signal of eq 12 becomes

$$\text{ratio} = \frac{X}{L}\left(\frac{10^{-A(3,4)} - 10^{-A(1,2)}}{10^{-A(3,4)} + 10^{-A(1,2)}}\right) \quad (14)$$

where transformation through eq 6 and Beer's law absorbance was made for a path length b and an analyte of molar absorptivity ϵ, concentration C, where A equals ϵbC. For small absorbances eq 14 reduces to

$$\text{ratio} = \frac{\text{diff}}{\text{sum}} = \frac{2.303}{2}\left(\frac{X}{L}\right)[A(1,2) - A(3,4)] \quad (15)$$

which is a very simple and useful approach to measure absorbance differences between two wavelength regions.

It is also interesting to consider the diff and sum contributions separately, instead of proceeding straight to the ratio signal (eq 15). In a typical sample modulation experiment one measures an analytical signal relative to a background signal, for instance, the height or area of a liquid chromatographic peak. For the diff signal, starting from eq 8, one obtains

$$\text{diff} = 2.303\left(\frac{X}{L}\right)\left(\frac{\Delta x}{L}\right)I_0(T)[A(1,2) - A(3,4)] \quad (16)$$

where $I_0(T)$ was defined in eq 7 and Δx was defined in the development of eq 11. The diff signal provides the same absorbance information as the ratio signal in eq 15. In practice, the diff signal is operated at a high signal-to-noise ratio when the base line is initially at the electronic null. The electronic null condition allows the diff signal to reject correlated noise, as will be experimentally supported.

Likewise, one may measure the absorbances at $\lambda(1,2)$ and $\lambda(3,4)$ via the sum signal, *after* base-line subtraction or correction, labeled as sum_{corr}, where starting from eq 9 one obtains

$$\text{sum}_{\text{corr}} = -2.303\left(\frac{\Delta x}{L}\right)I_0(T)[A(1,2) + A(3,4)] \quad (17)$$

where the negative sign indicates a decrease in measured intensity from the base line, as is the case. In eqs 16 and 17, $\Delta x/L$ indicates the fractional portion of $I_0(T)$ used in the measurement. Note that dividing diff by sum_{corr}, instead of by sum, does not result in the usual ratio signal as defined by eq 5 and derived leading to eq 15. There is a significant difference between dividing by the true sum (eq 9), as in eqs 10–14, and dividing by base line corrected sum (eq 17). Essentially, for small absorbances, sum_{corr} in eq 17 is not significant relative to the total sum given by eq 9. After base-line correction, sum_{corr} is significant. One may define a new ratio measurement, $\text{ratio}_{\text{corr}}$, by dividing diff (eq 16) by the base line corrected sum (eq 17)

$$\text{ratio}_{\text{corr}} = \frac{\text{diff}}{\text{sum}_{\text{corr}}} = \frac{X}{L}\left[\frac{A(3,4) - A(1,2)}{A(3,4) + A(1,2)}\right] \quad (18)$$

For a given absorbing species at concentration, C, eq 18 reduces to

$$\text{ratio}_{\text{corr}} = \frac{X}{L}\left[\frac{\epsilon(3,4) - \epsilon(1,2)}{\epsilon(3,4) + \epsilon(1,2)}\right] \quad (19)$$

where ϵ is the molar absorptivity at a particular wavelength or, more specifically, the average ϵ over a Δx region on the PSD. In practice, X/L may be calibrated, and the quantity $\epsilon(1,2)/\epsilon(3,4)$ may be measured for unknown analytes, and is given by

$$\frac{\epsilon(1,2)}{\epsilon(3,4)} = \frac{1 - \text{ratio}_{\text{corr}}\left(\frac{L}{X}\right)}{1 + \text{ratio}_{\text{corr}}\left(\frac{L}{X}\right)} \quad (20)$$

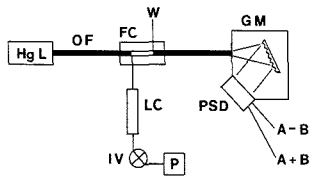

Figure 2. Experimental schematic for the single optical fiber, multiwavelength PSD-based absorbance detector with microbore liquid chromatography: Hg L, mercury–xenon lamp; OF, optical fiber (bold line); FC, flow cell; P, pump; IV, injection valve; LC, microbore liquid chromatography column; W, waste; GM, grating monochromator; PSD, position sensitive detector; A–B, diff signal; A+B, sum signal.

The quantity $\epsilon(1,2)/\epsilon(3,4)$ is useful in analyte purity and spectral shift measurements. Generally, more elaborate and expensive PDA-based instruments were required to make the measurement. The PSD-based device described here is simpler and much less expensive, while providing the same $\epsilon(1,2)/\epsilon(3,4)$ measurement. Furthermore, the simultaneous detection of diff (eq 16) and sum_{corr} (eq 17) allows one to effectively double the monitoring capability of an absorbance monitor with easy to interpret analytical signals, vide infra. As will be shown experimentally, the diff measurement is more stable than the sum measurement.

Presently, we have considered only a single absorbing analyte species that has not been complicated by the presence of an absorbing eluent or coeluting analytes. These circumstances will be treated rigorously in subsequent work since correlated concentrations of an absorbing analyte and another absorbing species, such as an eluent, will lead to special conditions not described by the development here. In most practical circumstances, the wavelength regions of interest can be tuned in with ease, and the PSD signals derived here are most appropriate. With regard to the theory, eqs 15–20 will be tested and evaluated by using absorbing analytes with well-defined spectral properties and known concentrations.

EXPERIMENTAL SECTION

The experimental schematic for the single optical fiber multiwavelength PSD-based absorbance detector, as used for microbore HPLC is shown in Figure 2. A medium pressure, 150-W mercury–xenon lamp from a fluorescence spectrometer (Perkin-Elmer, Model 203, Norwalk, CT) was used as a continuous wavelength UV–vis spectral source. A UV–vis transmissive optical fiber (Figerguide Industries, Superguide-MG UV-Vis Fiber, Stirling, NJ) was used to guide the continuous wavelength spectrum from the mercury–xenon lamp to the HPLC flow cell and subsequently to the monochromator (American Holographic, Chemspec 100S or 100M, Littleton, MA). The optical fiber, as specified from the manufacturer, consisted of a fused silica core with a doped silica cladding construction and with a 400/480 μm core/clad diameter, 630 μm buffer diameter, and a 950 μm Tefzel jacket diameter, with a numerical aperture (NA) of 0.12. The Tefzel coating along with the fused silica construction provided the mechanical and temperature stability necessary for the fiber to operate in close proximity to the elevated temperature of the mercury–xenon lamp. The optical fiber, 1 m length, was used to collect the mercury–xenon lamp spectrum without focusing optics and, therefore, placed 1 mm from the mercury–xenon lamp envelope to maximize the collection efficiency. Long-term use (over 200 h) of the optical fiber resulted in solarization damage that made it transmit poorly below about 300 nm.

The z-configuration flow cell (510 μm i.d. × 6 mm path length) was made in-house of copper–beryllium alloy and designed to connect to standard $^1/_{16}$ in. LC fittings as well as for the optical fiber connections. Both the flow cell entrance and exit optical fibers were held in place by insertion of the optical fiber into a short length of 0.0625 in. o.d. × 0.038 in. (965 μm) i.d. PEEK HPLC tubing (Upchurch Scientific, Inc., Oak Harbor, WA) with stainless steel ferrules subsequently locked onto the HPLC tubing

to provide a high-pressure seal around the optical fibers in the flow cell. The fiber optic buffer and Tefzel coating were removed for short lengths within the bore of the flow cell. The calculated volume of the flow cell was 1.2 μL, which was adequate for microbore chromatography, i.e., no additional chromatographic band broadening due to the flow cell design. Light that was transmitted across the flow cell was then collected by a second optical fiber of the same dimensions as the entrance optical fiber and guided to the monochromator. One of two monochromators was used, either the 100M or 100S, as previously mentioned. Both the monochromators were specified with a focal number (fn) of 2.2 or a numerical aperture (NA) of 0.23. The monochromator then dispersed the continuous wavelength spectrum on to the PSD (Hamamatsu, S1545, Hamamatsu City, Japan), which was at the exit focal plane. The protective glass window on the PSD was carefully removed to allow use in the UV range. The wavelength region of interest is then simply changed by adjusting the monochromator. The Model 100S monochromator provided a reciprocal linear dispersion of 25 nm/mm, while the Model 100M had a reciprocal linear dispersion of 6.1 nm/mm. The photoactive surface of the PSD was 1 mm × 12 mm, which resulted in a total wavelength range of 300 nm across the photoactive surface of the PSD with the Model 100S monochromator, and a 75 nm range with the Model 100M monochromator. An optical mask was placed across the surface of the PSD to allow two wavelength regions of interest to impinge on the photoactive surface at opposite ends of the PSD. With the Model 100S monochromator, the wavelength regions were about 40 nm wide, centered 260 nm apart, while the 100M monochromator utilized 10 nm regions centered about 65 nm apart. The optical mask was then carefully positioned to provide an electronic null, i.e., maximum source stabilization for the diff signal.

In practice, the mask is slightly different than the mask shown in Figure 1. The difference is that on one end of the PSD the mask is open, while on the other end of the mask there is a fixed aperture. Thus, the difference between $\lambda(1,2)$ and $\lambda(3,4)$ is a constant. In tuning the device to the desired wavelength region, one would first tune the monochromator so the desired center wavelength is at the open end of the PSD. Then, a second-order adjustment of the mask will achieve an electronic null. Finally, the device would require calibration with the desired analyte standard. Thus, wavelength selection is not sacrificed and spectral information is readily obtained. The only constraint in the current design is that the wavelength difference is held constant for a particular monochromator/mask combination. Use of the mask is critical to reduce stray light also.

The PSD was configured with a current to voltage conversion of 10^8 V/A at each output A and B. A typical photocurrent contribution, in the absence of an absorbance in the flow cell, was 7.0 V from outputs A and B, or 70 nA from each electrode. After the currents at electrode A and B were converted to voltages, the sum and diff of the voltages were calculated from an analog circuit and collected simultaneously on a computer (IBM-XT, Armonk, NY) by a laboratory interface (Metra Byte, DASH-16, Taunton, MA) which facilitated the analog to digital (A/D) conversion for storage and subsequent analysis. The data were collected with the aid of direct memory access (DMA) at a rate of 1000 points/s, averaged, and stored on the fly, to a rate of 1 point/s. This was done to minimize the PSD output noise, while providing adequate chromatographic frequency response; i.e., no additional chromatographic band broadening was introduced due to the time constant imposed by the averaging process. The ratio was calculated on the computer by dividing the diff signal by the sum signal. Whereas, the corrected ratio ($\text{ratio}_{\text{corr}}$) was calculated as in eq 18. Base-line adjusting the diff and sum signal about a numerical value of zero and then integrating the chromatographic peaks to provide peak areas facilitated the $\text{ratio}_{\text{corr}}$ calculation. In practice, the diff signal should already be centered about zero if an electronic null is achieved. The ratio L/X was determined to be 1.14 in the molar absorptivity calculation experiments.

The experimental apparatus used to substantiate the reduction of correlated noise via the diff signal included a light emitting diode (LED), function generator (Wavetek, Model 190, San Diego, CA), and the PSD mounted to a high precision translational stage (Newport, 460-X, Fountain Valley, CA). The function generator was used to drive the LED to provide an ac light source with a constant dc offset. A pin-hole aperture, made in-house, was placed between the LED and PSD to provide a well-defined beam size incident on the PSD. The PSD was then moved incremental distances orthogonal to the LED beam, with the sum and diff signals recorded at each position.

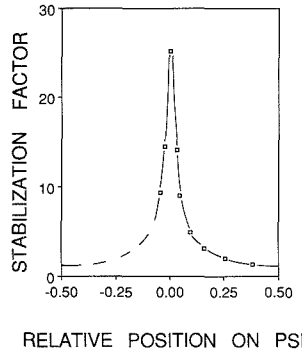

Figure 3. Stabilization factor defined as sum/diff of a 50-Hz ac component as a function of the relative position of a single LED beam on the PSD. The relative position range of ±0.5 spans the full length L of the PSD. The PSD center is defined as 0.0 on the x axis.

This experiment is strictly an evaluation of the PSD performance with regard to the diff and sum outputs. The results are shown in Figure 3 where the "stabilization factor" is effectively the ac amplitude of the sum divided by the ac amplitude of the diff as a function of position on the PSD. Indeed, the optimum reduction of correlated "noise" occurs at the PSD center, with a stabilization factor of about 26 for the data shown at an ac frequency of 50 Hz. For the experimental points shown in Figure 3, the ac amplitude and dc offset on the sum was constant to within about 1%. The ramification of Figure 3 for dual-beam work is that an electronic null condition should stabilize the diff signal by an order of magnitude relative to the sum signal even when balanced within ±5% of the PSD center.

A microbore separation of 2,4-dintrophenylhydrazone (DNPH) (Aldrich Chemical Co., Milwaukee, WI) derivatives of aldehydes was included in this study to demonstrate the utility of the multiwavelength PSD-based absorbance detector with flowing liquid systems. The HPLC system consisted of a syringe pump (ISCO, LC-250, Lincoln, NE) coupled to a 0.5-μL injection valve (Rheodyne, 7125, Cotati, CA) and on to a 1 mm × 250 mm, 5 μm, C18 column (Alltech, Abosbosphere HS, Deerfield, IL) which was connected to the UV–vis flow cell previously described. The eluent used for the reversed-phase separation of the aldehyde–DNPH derivatives consisted of 80% methanol (EM Science, Omnisolv, Cherry Hill, NJ) and 20% water (EM Science, Omnisolv, Cherry Hill, NJ) at a volumetric flow rate of 50 μL/min and a typical column pressure drop of 1580 psi.

The aldehyde–DNPH derivatives were prepared from reagent grade DNPH by the addition of 10 mL of a saturated DNPH/acetonitrile (ACN) (EM Science, Omnisolv, Gibbstown, NJ) solution with 10 mL of a 1% solution of the appropriate reagent grade aldehyde (Aldrich) in ACN in the presence of 50 mL of a 20% concentrated HCl/80% deionized water solution. Formaldehyde, propanal, and benzaldehyde were used as analytes. Note that propanal contained an impurity at about the 5% level, which was chromatographically resolved and did not detract from the objective of the work. The aldehyde–DNPH derivatives precipitated out of the aqueous solution and were filtered and washed with in-house deionized water. The precipitate was then dissolved in ACN and recrystallized by slow evaporation of the solvent. The purified crystals were then filtered and dried at room temperature to remove residual solvent. The standards were then prepared from weighed amounts of the dried, recrystallized aldehyde–DNPH products and dissolved in ACN.

RESULTS AND DISCUSSION

In order to evaluate the absorbance detector and the equations describing the anticipated detector response, DNPH

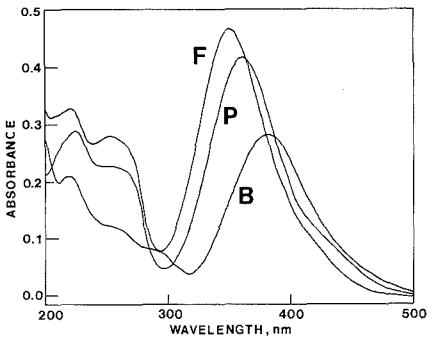

Figure 4. Absorbance spectra for DNPH derivatives of aldehydes using a commercially available instrument with a 1 cm path length cell: F, formaldehyde–DNPH (2.55×10^{-5} M); P, propanal–DNPH (2.18×10^{-5} M); B, benzaldehyde–DNPH (9.5×10^{-6} M).

Table I. Spectral Data and Microbore Liquid Chromatography Detection Limits for the DNPH Aldehyde Derivatives Applied in the Detector Evaluation

aldehyde	DNPH derivative molar mass, g/mol (aldehyde only)	wavelength, absorbance maximum,[a] nm	log ϵ_{max}[b]	detection limit, aldehyde only, pg[c]
formaldehyde	210 (30)	350	4.26	4
propanal	238 (58)	361	4.28	28
benzaldehyde	286 (106)	380	4.46	90

[a] On 300–450 nm wavelength range. [b] Molar absorptivitiy, ϵ_{max} (L mol^{-1} cm^{-1}) at absorbance maximum on 300–450 nm wavelength range. [c] Detection limit (3 × rms base line noise) of injected aldehyde (only) mass for microbore liquid chromatography separation and absorbance detection optimized for formaldehyde (see Figure 6).

derivatives of formaldehyde, propanal, and benzaldehyde were prepared and characterized. The absorbance spectra of the DNPH derivatives of these aldehydes are shown in Figure 4. The absorbance of the DNPH derivatives is quite favorable in the approximately 300–450 nm range. Results for the spectral characterization are summarized in Table I, as well as chromatographic detection limits that will be discussed shortly. Absorbance maxima and molar absorptivities at the absorbance maxima reported in Table I are consistent with previous work with this chemical system (*36*). The microbore LC separation of the DNPH derivatives was followed by absorbance detection, where both the sum and diff signals were simultaneously monitored by using the detection system with the Model 100S monochromator. The resulting chromatogram for the sum_{corr} signal (eq 17) is shown in Figure 5, where $\lambda(1,2)$ was centered at 350 nm and $\lambda(3,4)$ was centered at 610 nm under initial electronic null conditions for the diff signal. The wavelength regions chosen coincide with optimized absorbance for DNPH–formaldehyde around 350 nm, and no appreciable absorbance at 610 nm, which is used strictly as a reference beam to balance the PSD diff signal at the electronic null prior to absorbance. The sum signal was collected on a computer and processed according to eq 17 to yield the absorbance signal. In contrast, the diff signal after converting to absorbance units by eq 16 is shown in Figure 6. It is apparent from Figures 5 and 6 that single fiber optic, dual-wavelength detection by the PSD diff signal is effective in reducing noise due to light source fluctuations.

By use of eqs 16 and 17, the absorbance detection limits can be predicted, and compared to the experimental data for

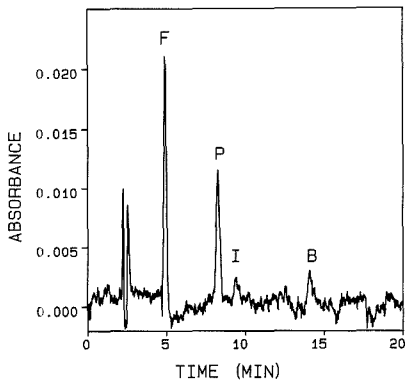

Figure 5. Sum_{corr} signal at $\lambda(1,2) = 350$ nm and $\lambda(3,4) = 610$ nm (converted to absorbance units by eq 17) following the microbore reversed-phase LC separation of an aldehyde–DNPH mixture (1 mm × 250 mm C18 column, 50 μL/min 80% CH_3OH to 20% H_2O by volume, 0.5 μL injected). Injected masses of the DNPH derivatives are as follows: F, formaldehyde–DNPH (13.4 ng); P, propanal–DNPH (13.0 ng); B, benzaldehyde–DNPH (5.0 ng). An injection disturbance occurs before formaldehyde at about 2.5 min, and an impurity in propanal is labeled as I.

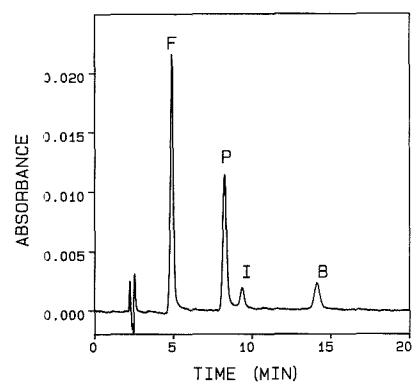

Figure 6. Diff signal (converted to absorbance units by eq 16) simultaneously measured with sum_{corr} signal shown in Figure 5.

the formaldehyde–DNPH derivative. This exercise was performed similarly in a previous report (*29*). By use of eq 17, the absorbance detection limit for the sum_{corr} output was predicted to be 1.2×10^{-3} au (3 × root mean square noise), which is the stability level of the mercury–xenon lamp. The detection limit for the diff signal was predicted to be 1.1×10^{-4} au (3 × rms noise) using eq 16, or over a factor of 10 better than the light source fluctuation level and is consistent with the data shown in Figure 3. The experimentally obtained absorbance detection limit was calculated from 2.5 μM injected formaldehyde–DNPH standard. The resulting chromatographic peak was diluted by a factor of 25 at a signal-to-noise ratio of 7.8 (using 3 × rms noise level). With ϵ equal to 18200 L mol^{-1} cm^{-1} and b equal to 0.6 cm, the experimentally obtained absorbance detection limit is 1.4×10^{-4} au. This absorbance detection limit agrees well with the predicted value using eq 16. If eq 15 is applied to calculate the ratio from the diff and sum signals, the noise on the resulting chromatogram is indistinguishable from the diff chromatogram in Figure 6. In practice, the primary reason to convert the diff signal to a ratio signal is not to reduce the noise but to normalize the

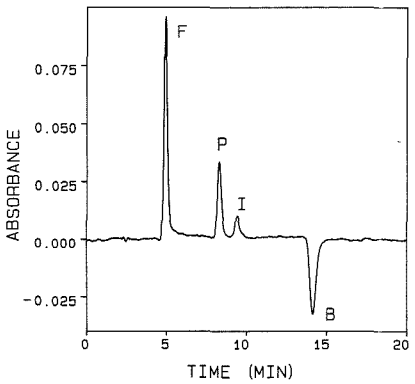

Figure 7. Diff signal at λ(1,2) = 345 nm and λ(3,4) = 410 nm (converted to absorbance units by eq 16) using the same chromatographic conditions as in Figure 5. Injected masses of the DNPH derivatives are as follows: F, 53.6 ng; P, 518 ng; B, 40.0 ng.

data to an absolute absorbance scale. Clearly, detection via the PSD diff signal offers light source stabilization even though two distinct wavelength regions are employed to balance the signal at the PSD. Our detection limit is also at least an order of magnitide better than other optical fiber based absorbance detectors for microbore LC (*10*, *18*, *20*).

Linearity and calibration of the diff signal were evaluated, and results for the formaldehyde–DNPH derivative follow the log–log equation

$$\log_{10}(\text{absorbance}) = 0.87 \log_{10}(\text{pg of formaldehyde}) - 4.43 \quad (21)$$

for 3 orders of magnitude injected formaldehyde–DNPH derivative. Although aldehyde DNPH derivatives are analyzed, it is conventional to express the detection limits in terms of the mass of the aldehyde only. The detection limit was 1.1 × 10^{-4} au (3 × rms noise for 60-s intervals) or $\log_{10}$ (absorbance) equal to −3.94, thus for formaldehyde (only) the detection limit was 4 pg injected. The other aldehydes behaved similarly with detection limits at a 350-nm excitation wavelength reported in Table I. Note that the system was optimized for formaldehyde, with a mass detection limit of about 200 times better than previous reports with conventional LC (*36*). The detector was not linear, unless a log–log plot is used, as is evident from eq 21, but the response was readily calibrated. The slope of eq 21 would need to be 1.00 to be exactly linear; thus, 0.87 is acceptable. The consequence of a nonlinear detector is to require calibration, as is the case with most detectors.

Another interesting feature of the diff signal is the possibility of obtaining spectral information directly from a single chromatogram. For this exercise the Model 100M monochromator was employed. By choosing λ(1,2) centered at 345 nm and λ(3,4) centered at 410 nm, it is possible to obtain both "positive" and "negative" absorbance signals, as defined by eq 16. From Figure 4, for the two center wavelengths chosen, one would predict a positive absorbance signal for the formaldehyde and propanal DNPH derivatives, but a negative absorbance signal for the benzaldehyde DNPH derivative. This prediction is supported by the chromatogram obtained for the conditions stated in Figure 7. Not shown for brevity is the sum_{corr} signal for the separation in Figure 7, which included all positive peaks when converted to absorbance data. The diff signal chromatogram in Figure 7 effectively contains twice the spectral information as typically obtained in absorbance detection, and in such a way as to clearly point out

Table II. Evaluation of Molar Absorptivity Ratios Obtained by the Detection System

aldehyde[a] (derivative)	ε(385)/ ε(450)[b]	(s)	predicted[c] λ(3,4), nm
formaldehyde	6.6	0.5	442
propanal	4.5	0.4	450
benzaldehyde	2.8	0.2	434

[a] Analyte as DNPH derivative. [b] Molar absorptivity ratio for λ(1,2) nominally centered at 385 nm and λ(3,4) nominally centered at 450 nm obtained with the standard deviation, *s*, for seven trials. Amounts injected spanned the following ranges: formaldehyde (26.8–107.2 ng), propanal (25.9–103.6 ng), benzaldehyde (10.0–80.0 ng). [c] Predicted λ(3,4), in nm, assuming λ(1,2) was centered at 385 nm and solving for λ(3,4) using the spectra in Figure 4.

to the analyst the spectral dependence of a given eluting analyte, and points toward the possibility of obtaining molar absorptivity ratios of eluting analytes without elaborate PDA instrumentation.

The molar absorptivity ratio was previously defined in eq 20 in terms of the experimentally obtainable $\text{ratio}_{\text{corr}}$ signal. Recall that $\text{ratio}_{\text{corr}}$ was obtained by dividing the diff signal (eq 16) by the sum_{corr} (eq 17). The Model 100M monochromator on the detector was adjusted so λ(1,2) was centered at 385 nm and λ(3,4) was centered at 450 nm for the generation of $\text{ratio}_{\text{corr}}$. In practice, one must first calibrate the detector in order to obtain the value of X/L. This calibration is straightforward and requires the measurement of the diff signal and sum_{corr} signal of an analyte that absorbs at only one of the two wavelength regions, either λ(1,2) or λ(3,4). A value of X/L = 1.14 was experimentally determined. Then, in order to achieve significance in the molar absorptivity ratio calculation, a given analyte must absorb appreciably at both wavelength regions chosen. The peak areas for the diff and sum_{corr} chromatograms were measured and the molar absorptivity calculated for each aldehyde derivative. The concentration dependence of the molar absorptivity determination was examined, since a given spectral feature cast upon a detected wavelength region will result in a finite shift in the "center" of the beam, resulting in a nonlinearity with absorbance (as observed in calibration). It is instructive to compare the experimentally obtained molar absorptivity ratios to values that may be predicted from the spectra in Figure 4. In this evaluation procedure the spectral absorbance nominally centered at λ(1,2) equal to 385 nm was divided by the molar absorptivity ratio ε(385)/ε(450) obtained by the new absorbance detection system. The resulting value is the absorbance required at λ(3,4), thus defining by inspection to the spectra (Figure 4) the wavelength centered on that interval. The results of this study are given in Table II. The predicted center wavelength on the λ(3,4) interval was consistently less than or equal to 450 nm, the wavelength experimentally set on the monochromator for one side of the PSD. The difference from 450 nm is reasonable, considering the accuracy and precision levels of the monochromator indicating that the experimentally obtained molar absorptivity ratios are accurate for analyte identification. Furthermore, the precision of the experimentally obtained molar absorptivity ratios was found to be independent of the concentration (over the range tested).

The unique approach to absorbance detection offers improvements for FIA (*19*) in process monitoring and other remote-sensing applications. A severe problem in absorbance measurements for FIA is the RI aberration that cannot be avoided entirely because the analyte is not retained beyond the solvent or matrix disturbance. The detection approach described here offers a good first-order correction for the RI aberration that is born from incomplete mixing in the *z*-configuration flow cell (*31–34*) or temperature gradients (*30*).

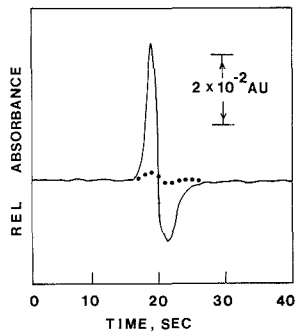

Figure 8. Sum (solid line) and diff (dotted line) signals obtained by the injection of 0.5 μL of acetone into acetonitrile as the carrier solvent at 100 μL/min through a short length of tubing prior to the flow cell. Although no absorbance occurs, the magnitude of the RI effect in terms of absorbance units is plotted.

The same RI aberration can be accurately modeled as a dynamic lens (*38*). This improvement was demonstrated by injecting an aliquot of acetone into acetonitrile as the carrier solvent through a 122 cm length of 0.007 in. i.d. Teflon tubing without the LC column. A typical derivative response was obtained for both the sum and diff signals, as shown in Figure 8, although no sample absorbance occurs at the wavelengths chosen, λ(1,2) nominally at 365 nm and λ(3,4) nominally at 430 nm. With the sum signal, any RI effect is not corrected to any extent, but rather, added together. In contrast, the diff signal offers a good first-order correction for a RI-induced intensity transmission gain or loss. In the limit that λ(1,2) approaches λ(3,4), the diff signal correction for RI effects is complete; unfortunately no absorbance signal could be detected. Yet, it is clear from Figure 8 that for a useful difference between λ(1,2) and λ(3,4), that the diff signal provides about a factor of 15 improvement in RI aberration attenuation relative to the sum signal. The attenuation of the RI aberration is comparable to the improvement in stability obtained in the modulated LED experiment reported in Figure 3. The ramification of Figure 8 is that a more accurate and well-behaved absorbance measurement can be achieved in remote sensing, as in FIA. The results of Figure 8 also suggest why the absorbance signal obtained by the diff output is quite stable with time, specifically, a single fiber and analog detector is used, allowing light source, fiber, and flow cell phenomena induced light intensity fluctuations to be routinely corrected down to the 1.1×10^{-4} au level (3 × rms).

ACKNOWLEDGMENT

We gratefully acknowledge the technical assistance of Ed Ristau (flow cell construction) and Roy Olund (PSD electronics).

LITERATURE CITED

(1) Jones, D. G. *Anal. Chem.* **1985**, *57*, 1057A–1073A.
(2) Drouen, A. C. J. H.; Billiet, H. A. H.; DeGalan, L. *Anal. Chem.* **1984**, *56*, 971–978.
(3) Warren, F. V., Jr.; Bidlingmeyer, B. A.; Delaney, M. F. *Anal. Chem.* **1987**, *59*, 1890–1896.
(4) Warren, F. V., Jr.; Bidlingmeyer, B. A.; Delaney, M. F. *Anal. Chem.* **1987**, *59*, 1897–1907.
(5) Saturday, K. A. *Anal. Chem.* **1983**, *55*, 2459–2460.
(6) Eastham, J. F.; Sepaniak, M. J. *Anal. Chem.* **1984**, *56*, 2246–2249.
(7) Freeman, J. E.; Childers, A. G.; Steele, A. W.; Hieftje, G. M. *Anal. Chim. Acta* **1985**, *177*, 121–128.
(8) Swan, J. M.; Sacks, R. D. *Appl. Spectrosc.* **1985**, *39*, 704–710.
(9) Fuh, M.-R. S.; Burgess, L. W. *Anal. Chem.* **1987**, *59*, 1780–1783.
(10) Skogerboe, K. J.; Yeung, E. S. *Anal. Chem.* **1987**, *59*, 1812–1815.
(11) Kraus, P. R.; Wade, A. P.; Crouch, S. R.; Holland, J. F.; Miller, B. M. *Anal. Chem.* **1988**, *60*, 1387–1390.
(12) Josefson, M.; Johansson, E.; Torstensson, A. *Anal. Chem.* **1988**, *60*, 2666–2671.
(13) DeGrandpre, M. G.; Burgess, L. W. *Anal. Chem.* **1988**, *60*, 2582–2586.
(14) Buffett, C. E.; Morris, M. D. *Anal. Chem.* **1982**, *54*, 1824–1825.
(15) Nakanishi, K.; Imasaka, T.; Ishibashi, N. *Anal. Chem.* **1987**, *59*, 1550–1554.
(16) Imasaka, T.; Nakanishi, K.; Ishibashi, N. *Anal. Chem.* **1987**, *59*, 1554–1557.
(17) Fujiwara, K.; Fuwa, K. *Anal. Chem.* **1985**, *57*, 1012–1016.
(18) Janeček, M.; Kahle, V.; Krajči, M. *J. Chromatogr.* **1988**, *438*, 409–413.
(19) Ružička, J.; Hansen, E. H. Flow Injection Analysis. In *Chemical Analysis*, Vol. 62, 2nd ed.; Wiley-Interscience: New York, 1988; Vol. 62, pp 289–290.
(20) Janeček, M.; Foret, F.; Šlais, K.; Boček, P. *Chromatographia* **1988**, *25*, 815–816.
(21) Walbroehl, Y.; Jorgenson, J. W. *J. Chromatogr.* **1984**, *315*, 135–143.
(22) Fields, S. M.; Markides, K. E.; Lee, M. L. *Anal. Chem.* **1988**, *60*, 802–806.
(23) Brown, R. D. H.; Hardy, D.; Thomas, B.; Thomas, E. *J. Phys. E: Sci. Instrum.* **1986**, *19*, 298–301.
(24) Lanquesse, M. *J. Phys. E.: Sci. Instrum.* **1988**, *21*, 63–67.
(25) Marrone, M. J. *Appl. Phys. Lett.* **1981**, *38*, 115–117.
(26) Pressy, H. M. *Appl. Opt.* **1981**, *20*, 701–706.
(27) Taylor, R. S.; Leopold, K. E.; Mihailov, S.; Brimacombe, R. K. *Opt. Commun.* **1987**, *63*, 26–31.
(28) Renn, C. N.; Synovec, R. E. *Anal. Chem.* **1988**, *60*, 1188–1193.
(29) Renn, C. N.; Synovec, R. E. *Appl. Spectrosc.* **1989**, *43*, 1393–1398.
(30) Stewart, J. E. *Anal. Chem.* **1981**, *53*, 1125–1128.
(31) Peck, K.; Morris, M. D. *J. Chromatogr.* **1988**, *448*, 193–201.
(32) Hancock, D. O.; Synovec, R. E. *Anal. Chem.* **1988**, *60*, 1915–1920.
(33) Hancock, D. O.; Synovec, R. E. *Anal. Chem.* **1988**, *60*, 2812–2818.
(34) Hancock, D. O.; Synovec, R. E. *J. Chromatogr.* **1989**, *464*, 83–91.
(35) Sharp, M. R. *Anal. Chem.* **1984**, *56*, 339A–356A.
(36) Funç, K.; Grosjean, D. *Anal. Chem.* **1981**, *53*, 168–171.
(37) Tejada, S. B. *Int. J. Environ. Anal. Chem.* **1986**, *26*, 167–185.
(38) Evans, C. E.; Shabushnig, J. G.; McGuffin, V. L. *J. Chromatogr.* **1988**, *459*, 119–138.

RECEIVED for review September, 5, 1989. Accepted December 7, 1989. C.N.R. thanks Battelle Pacific Northwest Laboratories for a Research Fellowship.

Optimization of γ-Ray Spectrometric and Other Measurements Yielding Biased Results by Means of Information Theory

Ivan Obrusník*[1] and Karel Eckschlager[2]

Nuclear Physics Institute, Czechoslovak Academy of Sciences, 250 68 Řež, Czechoslovakia, and Institute of Inorganic Chemistry, Czechoslovak Academy of Sciences, 250 68 Řež, Czechoslovakia

Analytical methods and procedures yielding biased results can be effectively optimized with information quantities like information gain and profitability of the results. This possibility has been studied on a simple γ-counting experiment. We have supposed that the differences in the height of the samples counted are the main source of a measurement bias. Both the bias and precision of such simple measurements can be calculated in a theoretical way by the program GEO developed for this purpose. The program also calculates the values of information quantities like gain and profitability of the results to find the optimum conditions for various experimental arrangements such as constant counting time or counting error. The dependence of the information gain and profitability on the measurement parameters, especially the bias and precision, shows a critical influence of the measurement bias on the information content of the results. Many conclusions derived for this simple case can be adopted for analytical measurements in general.

INTRODUCTION

The use of information theory in analytical chemistry can yield rather useful and interesting results. Both principles and applications of information theory to analytical problems have been described in several review articles and monographs (*1–4*). As a rule, analytical information serves as a basis for making decisions in ecology, hygiene, medicine, economy, etc. As the importance of such decisions has rapidly increased, the demands on the quality of analytical results and their information content have also increased.

The amount of information obtained from an analysis (*information gain*) is conditioned especially by metrological properties (precision, accuracy, detection limit, etc.) of the analytical system, in which information arises and is decoded. Another information property—*information profitability*—brings time or the economic point of view and also relevance of results into our decision making. The information quantities (gain, profitability) enable us to compare relative suitability and effectiveness of various analytical methods and procedures for different applications. In addition, rather effective optimization can be performed by employing an information quantity as a response function.

Up to now information theory has been applied to the evaluation and optimization of various analytical methods including *neutron activation analysis* (*NAA*) (*5*). The optimization of a NAA procedure has been based on a calculation of information gain and profitability for a multielement NAA with respect to irradiation, decay and counting times, precision, relevance, and also economic aspects of the results. This new approach to the optimization of the NAA method involves both the properties of the analytical method itself and the requirements of a potential user of analytical results.

[1] Nuclear Physics Institute.
[2] Institute of Inorganic Chemistry.

In this work, we have tried to include within the optimization procedure an influence of the bias of the results. It can be shown that information theory can give better tools for the optimization of the analytical procedures yielding biased results than can mathematical statistics.

The possibilities of such optimization have been demonstrated on a rather simple example—γ-ray spectrometric measurements for NAA.

THEORY

The above-mentioned optimization of NAA (*5*) has been based on the use of the information gain calculated from the following equation:

$$I(q,p) = \ln \frac{x_2 - x_1}{\sigma(2\pi e)^{1/2}} \tag{1}$$

where $I(q,p)$ is the information gain. We assume that the value of the concentration x is known before the measurement is made (a priori) to be only within the broad interval $\langle x_1, x_2 \rangle$ with the same probability at any x (rectangular distribution) and that after the measurement (a posteriori), the value has been determined with a standard deviation σ (normal distribution). Equation 1 is derived for the case of a quantitative analysis provided that the method used yields *unbiased results*. This equation is valid under the reasonable approximation that the mean concentration $\bar{x}$ is not closer than 3σ to either limit of the concentration interval $\langle x_1, x_2 \rangle$.

However, information theory can also treat procedures yielding *biased results* (results with a systematic error) (*6, 7*). In this case, eq 2 should be used instead of (1):

$$I(q,p) = \ln \frac{x_2 - x_1}{\sigma(2\pi e)^{1/2}} - \frac{1}{2}\left(\frac{\delta}{\sigma}\right)^2 \tag{2}$$

where δ denotes the bias (*1*).

Equation 2 can be used for the optimization of analytical methods or particular steps of analytical procedures. It is always necessary to have an estimate of the possible bias δ for this purpose. However, obtaining such an estimate might be a rather difficult task in judging complex analytical procedures.

Analytical methods involving the measurement of radioactivity allow the estimation of the measurement precision in a theoretical way (*8*). The precision of a simple counting experiment is assumed to be governed by the Poisson distribution, which can be approximated by the normal one for a higher number of counts. Then, the variance (σ^2) is taken equal to the number of counts observed.

We have chosen a rather simple model—a γ-ray counting of radionuclides that is routinely used as a measurement step in NAA procedures. We can estimate the values of σ and δ both experimentally and theoretically and study the influence of these parameters on the information quantities of analytical results. Some conclusions found for this simple case can also be applied to other analytical methods that cannot be treated on a theoretical basis.

Most activation analysis detection systems consist of a single γ-ray detector (e.g. Ge) and associated electronics with a

0003-2700/90/0362-0565$02.50/0

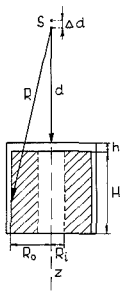

Figure 1. Configuration of a point source and coaxial Ge detector: S, source; d, source to detector Al cap distance; Δd, uncertainty in the sample height; z, central axis of the detector; R, chord length; R_o and R_i, detector and core radius, respectively; H, length of the detector; h, distance from Al cap to the surface of the detector.

sample positioning device of some sort. With such a system, a variety of sample radioactivity levels can be counted rather easily. What often is not realized is that even relatively small differences between sample and standard location, or from sample to sample, often can produce a significant bias in the resulting activities (counting rates) (*9–12*). Becker (*9*) separated the systematic errors associated with γ-ray counting into eight subgroups. One of them, the bias caused by a different sample–detector configuration and especially by variations in the sample height, has been studied in this work.

In our simple model let us suppose that a point source S is counted with a coaxial Ge detector in the distance d (from the detector Al cap) (see Figure 1). We do not suppose any shift of the source from the detector central axis z as well as any coincidence summing or loss effect in closer source to detector configurations. Then we can calculate the bias δ from the difference of the total detector efficiencies ϵ between the distance d and $d + \Delta d$:

$$\delta\ (\%) = \frac{|\epsilon_{d+\Delta d} - \epsilon_d|}{\epsilon_d} \times 100 \qquad (3)$$

The total detector efficiencies have been calculated from the known parameters of our Ge detector by means of equations proposed by Ozmutlu et al. (*13*) through the mean chord length $\bar{R}$. The bias δ depends on both a possible source shift Δd and the source to detector distance d. The calculations of efficiencies, δ, and σ (from counting statistics) for several modes of γ-counting (constant counting time or σ, etc.) are included in the first part of the program GEO (in Basic Plus 2; copies can be obtained from the authors). Then, the program calculates the information gain $I(q,p)$ according to eq 2. In all calculations we have supposed that the expected concentration x lies within the interval ⟨0, 100 ppm⟩ and the activity (peak area) corresponds to the mean concentration $\bar{x}$ of 10 ppm.

The value of σ should be expressed absolutely (in parts per million) in the first member of the right-hand side of eq 2. The values of σ and δ in the second member on this side of (2) can be expressed (both) either absolutely or relatively. The program GEO can also compute the information profitability from known costs of the measurement, e.g. the price per unit of counting time.

EXPERIMENTAL SECTION

Counting Equipment. All measurements were performed by a Nuclear Data computer-based γ-ray spectrometer ND 683. The system consisted of a Ge coaxial detector PGT (20% relative efficiency, 1.8-keV full width at half maximum (fwhm) and peak-to-Compton ratio 50:1 for 1332-keV photons of ^{60}Co) connected through Ortec linear electronics to a Nuclear Data ADC ND 570 (100-MHz clock), loss-free counting module ND 599, and a multichannel analyzer ND 66. The spectra were evaluated by a standard ND spectroscopy software package designed for PDP 11 DEC computers running under the RSX 11M operating system.

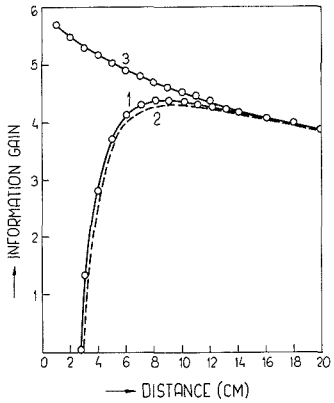

Figure 2. Information gain $I(q,p)$ calculated for experimental and theoretical values of δ and σ: curves 1 and 2, $I(q,p)$ based on δ and σ measured and calculated, respectively; curve 3, $I(q,p)$ for unbiased measurements ($\delta = 0$); counting time $t_c = 55$ s; σ (5 cm) = 1.59%; $\Delta d = 1$ mm.

Sample positioning and simulation of a 1-mm shift in the source to detector distance (Δd) were performed with a precise sample holder made from Perspex. The source to detector position could be changed in steps of 0.5 cm (in the range 0–4 cm from the detector cap) or of 1 cm (above 4-cm distance). The accuracy of the source position is estimated to be within 0.1 mm.

Radioactive Sources. ^{137}Cs precise calibration source EG3 (441 kBq) (UVVVR Prague) was used in all experiments.

RESULTS AND DISCUSSION

Figure 2 compares the values of information gain calculated by the program GEO from theoretical values of σ and δ with those calculated from the experimentally found σ and δ. The following measurement has been performed to estimate δ experimentally. The source of ^{137}Cs was counted twice in each source to detector distance d chosen (with and without the shift $\Delta d = 1$ mm). The counting times t_c for the evaluation of δ were chosen long enough to ensure good counting statistics necessary for a precise determination of δ in each distance d. Then we have chosen a reasonably long counting time (t_c = 55 s), and the source has been measured five times in each distance d to obtain average values of the precision σ.

It can be seen from Figure 2 that the $I(q,p)$ values based on the theoretical and experimental values of δ and σ are in very good agreement. The addition of the distance between the detector Al cap and the detector surface ($h = 4$ mm) and the detector dead layer 1 mm to the distance d improved the agreement between $I(q,p)$ curves.

The dependence of $I(q,p)$ on the source to detector distance d has a typical shape with a flat maximum ($d = 9$ cm). Curve 3 depicts the information gain of unbiased measurements ($\delta = 0$). We can see from the figure that it is always worthwhile to count sources in the optimum distance d. Counting in closer source–detector configurations can cause a rather high decrease of $I(q,p)$. Moreover, $I(q,p)$ can reach zero or negative values. Counting of the source in longer distances ($d > 9$–10 cm) also yields a lower value of the information gain. However, the $I(q,p)$ decreases to a much smaller extent than in close source–detector configurations.

Figure 3 shows the dependences of $I(q,p)$ on σ (δ = constant) or on δ (σ = constant) for various levels of constant parameters

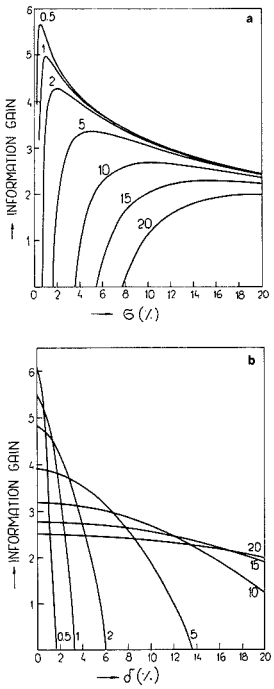

Figure 3. Dependence of $I(q,p)$ on σ and δ according to eq 2: (a) dependence of $I(q,p)$ on σ (δ = constant), δ = 0.5, 1, 2, 5, 10, 15, 20% relative; (b) dependence of $I(q,p)$ on δ (σ = constant), σ = 0.5, 1, 2, 5, 10, 15, 20% relative.

δ and σ, respectively. The $I(q,p)$ curves in Figure 3a (δ = constant) exhibit maxima for $\sigma = \delta$. These maxima can also be found by the calculation of partial derivatives of $I(q,p)$ in eq 2 providing that δ is kept constant. The maxima are rather steep and high for low levels of the parameter δ. This kind of dependence of $I(q,p)$ on σ can occur in practical applications of NAA, e.g. in the case when standards have been prepared with a systematic error and each sample in the set has been analyzed with a different precision.

The $I(q,p)$ curves in Figure 3b (σ = constant) exhibit maxima corresponding to $\delta = 0$ (unbiased results). The position of these maxima can also be derived from eq 2. The information gain decreases with increasing δ rather rapidly for highly precise results (low σ). From the curves in Figure 3 the optimum conditions of a measurement ensuring high information gain of the results can be chosen provided that we can estimate σ and δ.

In our simple counting experiment both δ and σ depend on the distance d and on the counting mode chosen. We can keep either counting time t_c or statistical error σ constant. The plots of the dependence of δ on the source to detector distance d for various values of the source height difference Δd are shown in Figure 4. The bias δ can reach rather high levels and then drops down very rapidly with d for the measurements with high values of the source height difference Δd. These plots are very useful for applied γ-ray spectrometry. They also show a rather steep increase of the bias level for the measurements performed in close source–detector configurations.

Figure 5 shows the dependence of $I(q,p)$, σ, and δ calculated by the program GEO on the distance d for two counting modes. In the first mode (dashed lines) the counting time t_c is kept

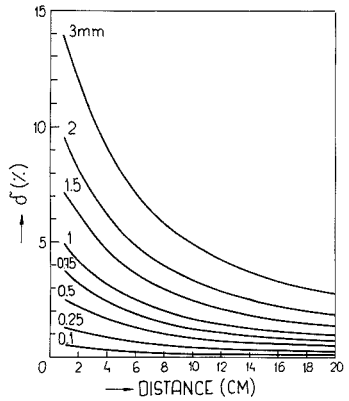

Figure 4. Dependence of the measurement bias δ on the source to detector distance d. Possible source height difference Δd was 0.1–3 mm.

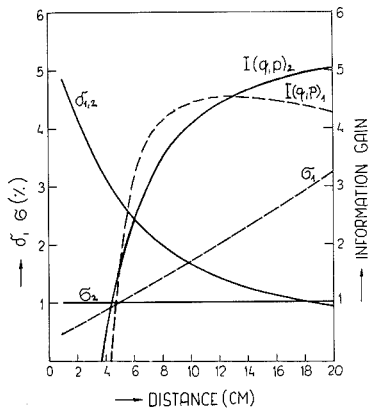

Figure 5. Dependence of $I(q,p)$, δ, and σ on the distance d: dashed lines (with subscript 1), counting time t_c = constant, σ (5 cm) = 1%, Δd = 1 mm; solid lines (with subscript 2), σ = constant = 1%, Δd = 1 mm.

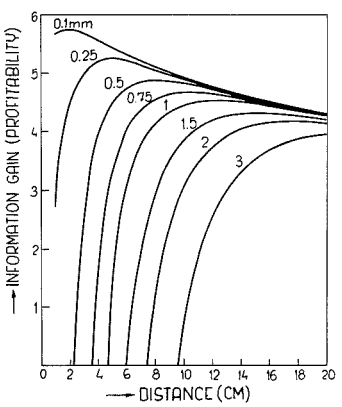

Figure 6. Dependence of $I(q,p)$ or IP on the distance d: counting time t_c = constant, σ (5 cm) = 1%, Δd in the range 0.1–3 mm.

constant by changing the source to detector distance d and σ. The $I(q,p)$ curve exhibits a maximum for the distance d

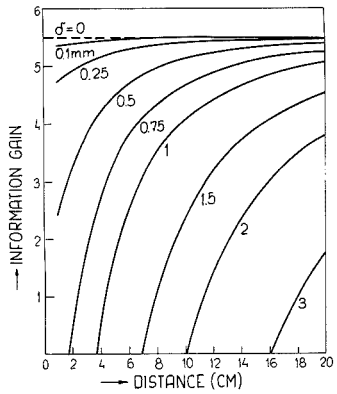

Figure 7. Dependence of $I(q,p)$ on the distance d: statistical error σ = constant = 1%; Δd in the range 0.1–3 mm.

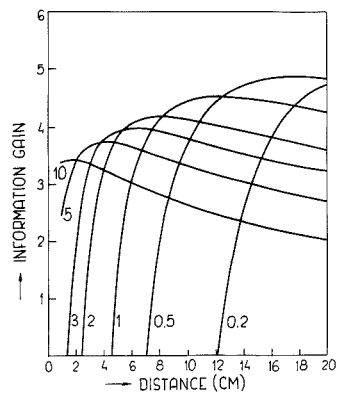

Figure 8. Dependence of $I(q,p)$ on the distance d: Counting time t_c = constant, Δd = constant = 1 mm, σ (5 cm) in the range 0.2–10% relative.

= 12 cm. In the second mode σ is kept constant (σ = 1% relative) by changing both t_c and d (solid lines). The information gain will reach the maximum for $\delta \rightarrow 0$ ($d \rightarrow \infty$).

Figure 6 shows more plots of the dependence of $I(q,p)$ on d for several levels of Δd (δ) provided that t_c is kept constant and σ in the 5-cm distance is 1%. The information gain exhibits a shift of the maximum toward the longer distances d. Simultaneously, the absolute value of $I(q,p)$ decreases. Figure 7 contains similar plots for experiments with a constant value of the statistical error σ instead of t_c. Then, t_c increases with d and the $I(q,p)$ curves exhibit no maximum. The lower the difference in the sample height Δd, the higher $I(q,p)$ can be achieved. $I(q,p)$ can reach maximally the value of the limiting curve (straight line) corresponding to $\delta = 0$.

Another kind of dependence of $I(q,p)$ on the distance is depicted in Figure 8, when both the counting time t_c and Δd have been kept constant. The $I(q,p)$ plots have been constructed for several levels of σ (5 cm) chosen. The maxima of $I(q,p)$ curves shift toward higher distances d for more precise results (lower σ). The absolute values of $I(q,p)$ also increase with improving precision of the results.

Up to now we have discussed the optimization of counting experiments from the point of view of the amount of information obtained. However, in everyday practice we should also take into account the cost of an analysis (measurement).

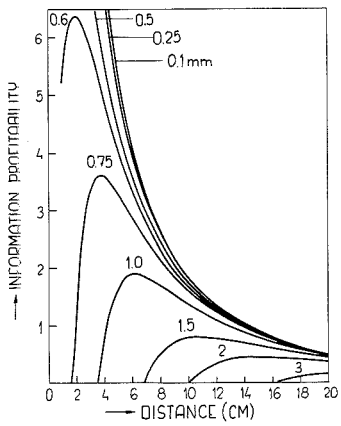

Figure 9. Dependence of the information profitability IP on the distance d: counting error σ = constant = 1%, Δd in the range 0.1–3 mm.

For this purpose, another information quantity—*information profitability* (*IP*)—can be used. This quantity brings time or an economic view together with the information gain into our decision making (*14*). IP can be expressed for simple cases by the following relation:

$$\mathrm{IP} = I(q,p)/\tau \qquad (4)$$

where τ denotes the cost of an analysis.

In our model counting experiment we can suppose that the cost of the measurement is proportional to the counting time used. Therefore, we can investigate the dependence of the information profitability IP on the source to detector distance similarly as in the case of the information gain.

For instance, Figure 9 shows the dependence of IP on the distance d for the counting mode with the statistical error σ = constant. Several curves in this figure correspond to different values of the sample height difference Δd.

The maxima on the IP curves are rather steep and high for the measurements performed with low sample height differences. Moreover, these maxima are shifted toward shorter source to detector distances than those obtained for the measurements with higher Δd levels. The similar dependence of the information gain $I(q,p)$ for that type of counting (see Figure 7) does not exhibit any maximum. That means the use of the information profitability can often be more advantageous for the optimization of analytical procedures than the use of the information gain alone, as the time and cost factors can have rather strong effects.

Figure 9 shows very clearly that the measurements performed with more precise source configurations (lower Δd values) are much more profitable (effective) than those with unprecise configurations (higher Δd values). In general, it is always worthwhile to prepare the sources (samples) for γ-ray counting with greater care to diminish the bias by possible differences in the height of samples. The decrease of the bias is more advantageous for obtaining the high level of the information gain, and especially the profitability, than the improvement of the measurement precision.

The dependence of the information profitability in the second model of counting—with constant counting time t_c—has the same shape as that of the information gain (see Figure 6) because the cost of the measurement is also constant for various values of Δd. In comparison with Figure 9, the maxima are not so steep and the information profitability decreases rather slowly with increasing source to detector distance d.

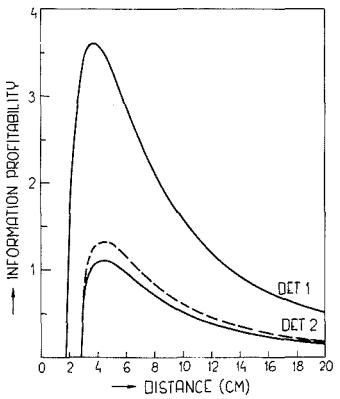

Figure 10. Dependence of the information profitability IP on the distance d: σ = constant = 1%; DET 1, 20%, DET 2, 7% relative efficiency; Δd = 0.75 mm; dashed line, price of spectrometers taken into account.

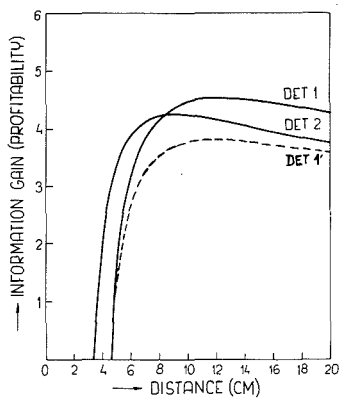

Figure 11. Dependence of the information profitability IP (and also gain) on the distance d: counting time t_c = constant; DET 1, 20%, DET 2, 7% relative efficiency; σ (5 cm) = 1% (DET 1) and 1.64% (DET 2, which was normalized to DET 1 by means of the ratio of efficiencies); Δd = 1 mm; dashed line, price of spectrometers taken into account.

Information quantities and especially the information profitability can be useful for judging which of the detectors used is better—the larger (and more expensive) or the smaller (and less expensive) one. To illustrate this kind of use of information properties, we have chosen two Ge coaxial detectors having 20% and 7% relative efficiency. Other parameters of the detectors like fwhm (resolution) and a peak-to-Compton ratio are supposed to be equal for both detectors for simplicity.

For the evaluation of the cost of the measurement with these detectors we have made the following estimation of the prices of counting equipment: the larger detector (DET 1) $14 160; the smaller detector (DET 2), $9000. Other parts, the same for both detectors, linear electronics and a computer-based multichannel analyzer, cost approximately $20 000. That means that the spectrometer with the larger Ge detector is approximately 1.18 times more expensive than that with the smaller one.

The dependencies of IP on the source to detector distance d for counting with the constant counting error σ are shown in Figure 10. We can see that the use of the larger detector is more effective under the counting conditions chosen even if we take into account the lower price of detector 2 (dashed line).

The counting in the second mode (t_c = constant) shows different features (Figure 11). The information gain (and also IP) for the measurement with the larger detector are slightly higher, especially in longer source to detector distances. However, when the different costs of the above-mentioned two counting systems with different detectors are taken into account, the information profitability becomes lower for the larger detector system (dashed curve). It means that the price difference of both spectrometers plays a more important role in this measurement mode than in the previous one (σ = constant). In any case, the use of the information profitability can often yield interesting results in practical optimization of various analytical procedures.

CONCLUSIONS

This work has shown that both the information gain and profitability of analytical results are strongly influenced by the levels of precision and bias (see eq 2). Usually the bias has a more critical effect on the value of $I(q,p)$ than does the precision. The lower the bias level, the higher information gain can be expected. However, when biased results occur, it is always advisable *to keep the precision σ close to the bias level δ* (see Figures 3a, 5, 6, and 8).

In the case of simple γ counting, often used as the last step in the NAA procedure, it is often possible to estimate the mean level of the systematic error δ from the theory. In this work, we have supposed for simplicity that the only source of bias is the maximum possible difference in the sample height Δd. However, the real (true) bias δ_a, occurring in actual measurements, is not known. We can always suppose that $0 \leq \delta_a \leq \delta$, and then the true information gain $I(q,p)_a$ corresponding to δ_a should lie within the interval

$$\ln \frac{x_2 - x_1}{\sigma(2\pi e)^{1/2}} - \frac{1}{2}\left(\frac{\delta}{\sigma}\right)^2 \leq I(q,p)_a \leq \ln \frac{x_2 - x_1}{\sigma(2\pi e)^{1/2}} \quad (5)$$

The lower limit of this interval can have a zero or even negative value (see Figure 2, 3, 5–8, where the negative values obtained for closer source–detector configurations have not been plotted).

Unlike the "classic" information theory, which fails to define negative information gain of analytical results, the inclusion of a pragmatic point of view has enabled us to interpret $I(q,p) \leq 0$ as the case when incorrect results misinform us instead of bringing relevant information (7). The results with $I(q,p) \leq 0$ can be encountered in the analysis giving highly precise (low σ) and, simultaneously, highly biased results. Such results can be obtained, for example, in precise γ-ray spectrometric measurements performed in close source–detector geometries and with a high level of sample height difference Δd! Highly accurate measurements such as the certification of reference materials (RMs) by INAA should be done with precisely prepared samples and in sufficiently long distances from the detector. Fleming (15) measured such samples in the distance d = 40 cm.

The use of the information profitability instead of the information gain is usually more effective for an optimization of real analytical procedures, as time, cost, and other factors are also taken into account. The program GEO, proposed in this work, can be very useful for the optimization of γ-ray spectrometric measurements under various experimental conditions.

The relations shown in this work can be used after minor changes for the expression of $I(q,p)$ and IP of the results obtained by other analytical methods. However, in this case we cannot influence the value of σ so easily by the measurement arrangement as in NAA and γ-ray spectrometry.

Moreover, we cannot derive the bias level δ from theory. In such cases we can estimate σ and especially δ empirically by the analysis of reference materials with certified concentrations of an analyte x_c. Then

$$\delta\ (\%) = \frac{|\bar{x}_e - x_c|}{x_c} \times 100 \qquad (6)$$

where $\bar{x}_e$ is an average result of the analysis of an RM (see details in ref 7).

We can expect that information theory can be successfully used in the optimization and comparison of various analytical methods and procedures, in the evaluation of the results obtained in collaborative tests for the certification of new RMs, and in many other applications.

LITERATURE CITED

(1) Eckschlager, K.; Štěpánek, V. *Anal. Chem.* **1982**, *54*, 1115A–1127A.
(2) Eckschlager, K.; Štěpánek, V. *Information Theory as Applied to Chemical Analysis*; Wiley: New York, 1979.
(3) Eckschlager, K.; Štěpánek, V. *Analytical Measurement and Information*; Research Studies Press: Letchworth, Great Britain, 1985.
(4) Eckschlager, K.; Štěpánek, V. *Chemom. Intell. Lab. Syst.* **1987**, *1*, 273–284.
(5) Obrusník, I.; Eckschlager, K. *J. Radioanal. Nucl. Chem., Articles* **1987**, *112*, 233–242.
(6) Eckschlager, K.; Štěpánek, V. *Collect. Czech. Chem. Commun.* **1985**, *50*, 1359–1367.
(7) Eckschlager, K.; Fusek, J. *Collect. Czech. Chem. Commun.* **1988**, *53*, 3021–3028.
(8) Lindstrom, R. M. *Nuclear Analytical Methods in Standards Certification*; IAEA-TECDOC-435; IAEA: Vienna, 1987.
(9) Becker, D. Analytical Design in Activation Analysis: The Role of Accuracy and Precision. In *Accuracy in Trace Analysis: Sampling, Sample Handling, and Analysis*; NBS Special Publication 422; NBS: Washington, DC, 1976; pp 1143–1155.
(10) De Bruin, M. Gamma-Ray Spectroscopy in Neutron Activation Analysis. In *Quality Assurance in Biomedical Neutron Activation Analysis*; IAEA-TECDOC-323; IAEA: Vienna, 1984; pp 163–177.
(11) Greenberg, R. R. *J. Radioanal. Nucl. Chem., Articles* **1987**, *113*, 233–247.
(12) Heft, R. E. *Control of Sample Configuration as an Aid to Accuracy in INAA*; NBS Special Publication 422; NBS: Gaithersburg, MD, 1976; pp 1275–1281.
(13) Ozmutlu, C.; Ortaovali, A. Z. *Nucl. Instrum. Methods* **1976**, *133*, 149–155.
(14) Eckschlager, K. *Anal. Chem.* **1977**, *49*, 1265–1267.
(15) Fleming, R. F.; Lindstrom, R. M. *J. Radioanal. Nucl. Chem., Articles* **1987**, *113*, 35–42.

RECEIVED for review August 7, 1989. Accepted November 27, 1989.

General Least-Squares Smoothing and Differentiation by the Convolution (Savitzky–Golay) Method

Peter A. Gorry

Department of Chemistry, University of Manchester, Manchester, England M13 9PL

Smoothing and differentiation of large data sets by piecewise least-squares polynomial fitting are now widely used techniques. The calculation speed is very greatly enhanced if a convolution formalism is used to perform the calculations. Previously tables of convolution weights for the center-point least-squares evaluation of $2m + 1$ points have been presented. A major drawback of the technique is that the end points of the data sets are lost ($2m$ points for a $2m + 1$ point filter). Convolution weights have also been presented in the special case of initial-point values. In this paper a simple general procedure for calculating the convolution weights at all positions, for all polynomial orders, all filter lengths, and any derivative is presented. The method, based on the recursive properties of Gram polynomials, enables the convolution technique to be extended to cover all points in the spectrum.

INTRODUCTION

In 1964 Savitzky and Golay (*1*) provided a simplified method for calculating smoothing and differentiation of data by a least-squares technique. Since then the Savitzky–Golay approach has been widely used because it produces a significant improvement in computational speed—replacing the traditional lengthy least-squares calculation by a simple, but equivalent, convolution. In this approach the least-squares value of a given point is calculated as a weighted combination of itself and m points on either side of it. This corresponds to performing a moving ($2m + 1$ point) least-squares fit across the data. The purpose of the original work was to provide a methodology for calculating the required weights and to provide tables of commonly used values. The original tables of convolution weights contained several errors however and were subsequently corrected by Steinier et al. (*2*) who recast the calculation in a matrix form.

The Savitzky–Golay approach suffers from one major drawback: it truncates the data by m points at each end. This occurs because the convolution requires m points to the left and right of a point in order to calculate the required least-squares value. The problem of data truncation is compounded if repeated smoothing/differentiation is applied since each application removes a further $2m$ points. For large spectra with zero values at the ends this is not important, and indeed zero values can easily be reinserted. However for more limited data sets without base-line values at both ends, the Savitzky–Golay algorithm is not applicable.

In principle the above limitation is easy to overcome. The first $2m + 1$ point least-squares fit can simply be used to evaluate least-squares values for the first m points as well as the $m + 1$. Similarly the last $2m + 1$ point fit can be used to calculate the last m least-squares values. Indeed if a normal least-squares calculation has been performed, yielding the least-squares coefficients, evaluating the fit of any of the m values, rather than the middle, is a simple task. This approach has been adopted by Khan (*3*) in a matrix formulation of the full least-squares method. Unfortunately we now lose the main advantage of the convolution method—its greatly enhanced speed.

Extending the convolution approach to accommodate "end points" requires calculating a different set of weights for each position. The special case of initial-point smoothing and slope evaluation has been considered by Leach, Carter, and Harris (*4*) where the Savitzky–Golay approach was modified to provide quadratic convolution weights for smoothing and the

0003-2700/90/0362-0570$02.50/0

first derivative for the initial point. The tables were presented as real numbers and were later calculated to higher accuracy by Baedecker (5).

It would be very desirable to have a means of extending the convolution approach to performing least-squares calculations for any general position. We present here a simple method of calculating the least-squares convolution weights required for a general order polynomial fit, and all its derivatives, at all positions.

METHOD

(a) The General Problem. First we must define the problem more fully. We assume a spectrum containing p evenly spaced data points, $[y_i]$, which we wish to smooth, or differentiate (to order s), with a $2m + 1$ point filter and polynomial of order n. Since this requires repetitively fitting a polynomial of order n to $2m + 1$ consecutive points, we convert each group of points to a temporary coordinate system (1, 2) in which the ordinate values range from $i = -m$ to $i = +m$, i.e. the midpoint is $i = 0$. The least-squares polynomial then has the form

$$f_n(i) = \sum_{k=0}^{n} b_k i^k \tag{1}$$

Application of the least-squares criterion

$$\frac{\partial}{\partial b_k}\left[\sum_{i=-m}^{m} (f_n(i) - y_i)^2\right] = 0 \tag{2}$$

leads to $n + 1$ simultaneous equations in the unknown coefficients b_k. The Savitzky–Golay approach evaluates eq 1 at $i = 0$ and hence only requires an expression for b_0. Equally, differentiation of eq 1 reveals that the sth derivative (evaluated at $i = 0$) requires an expression for b_s only. This allows eq 1 to be reduced to an expression of the form (1, 2)

$$f_n^{\,s}(0) = \sum_{i=-m}^{m} h_i^s y_i \tag{3}$$

where the n and s denote the polynomial and derivative order, h_i^s is the convolution weight of the ith point, and y_i its value.

In the Savitzky–Golay algorithm a $2m + 1$ point smooth/differentiation requires one set (of $2m + 1$) weights to calculate the midpoint values. If we wish to calculate least-squares values at *any* of the $2m + 1$ positions, then we require $2m + 1$ *sets* of weights. Thus if we are to calculate the convolution weights required for all possible cases of orders, derivatives, and positions, it becomes impractical to produce general numerical tables of the weights and an alternative strategy must be pursued. The calculation techniques of Savitzky and Golay (1), Steinier et al. (2), and Harris et al. (4), based on the direct solution of the simultaneous equations, are complex and unsuited for such a generalization. Instead we turn to an entirely different approach to the problem.

(b) Gram Polynomials. It is well-known that the least-squares approximation to a function can equally well be cast in terms of a weighted expansion of discrete orthogonal polynomials, rather than a simple powers series (6, 7). Particularly suitable for this application are the Gram polynomials, and we have, analogous to eq 1

$$f_n(t) = \sum_{k=0}^{n} b_k P_k^{\,m}(t) \tag{4}$$

where $P_k^{\,m}(t)$ is the Gram polynomial of order k, over $2m + 1$ points, evaluated at point t. The Gram polynomials (6) are defined by

$$P_k^{\,m}(t) = \sum_{j=0}^{k} \frac{(-1)^{j+k}(j + k)^{(2j)}(m + t)^{(j)}}{(j!)^2(2m)^{(j)}} \tag{5}$$

where $(a)^{(b)}$ is a generalized factorial function: $(a)(a - 1) \ldots (a - b + 1)$, and $(a)^{(0)} = 1$. Substitution of eq 5 into eq 4 and application of the least-squares criterion eq 2 yields an expression of the form

$$f_n(t) = \sum_{i=-m}^{m}\sum_{k=0}^{n} \frac{(2k + 1)(2m)^{(k)}}{(2m + k + 1)^{(k+1)}} P_k^{\,m}(i)P_k^{\,m}(t)y_i \tag{6}$$

We can generalize eq 6 for the sth derivative very simply and thus produce an expression in exactly the form required for a convolution calculation

$$f_n^{\,s}(t) = \sum_{i=-m}^{m}\sum_{k=0}^{n} \frac{(2k + 1)(2m)^{(k)}}{(2m + k + 1)^{(k+1)}} P_k^{\,m}(i)P_k^{\,m,s}(t)y_i \tag{7}$$

where

$$P_k^{\,m,s}(t) = \left(\frac{\mathrm{d}^s}{\mathrm{d}x^s} P_k^{\,m}(x)\right)_{x=t}$$

Comparison of eq 3 and eq 7 provides the required expression for the convolution weight for data point i ($-m \le i \le m$), with polynomial order n, and sth derivative, evaluated at position t

$$h_i^{t,s} = \sum_{k=0}^{n} \frac{(2k + 1)(2m)^{(k)}}{(2m + k + 1)^{(k+1)}} P_k^{\,m}(i)P_k^{\,m,s}(t) \tag{8}$$

The tables of Savitzky and Golay are obtained from eq 8 by setting $t = 0$. Indeed this approach had been used previously by Ernst (8) to derive analytic expressions for the weights in the special case of smoothing ($s = 0$, $t = 0$) and small n ($n = 2$ and 4), corresponding to Tables I and II of Savitzky and Golay. The tables of Harris (4) and Baedecker (5) correspond to $t = -m$ and $s = 0$, $s = 1$.

In the case of differentials ($s > 0$) where the original data points are separated by Δx, rather than unity, we must modify eq 7 to take this into account (1)

$$f_n^{\,s}(t) = \frac{\sum_{i=-m}^{m} h_i^{t,s} y_i}{\Delta x^s} \tag{9}$$

The division by Δx^s is easily carried out after the convolution calculation.

Although eq 8 is a powerful way of expressing the weight values, the ordinary definition of the Gram polynomials, eq 5, is not very practical for calculation purposes, especially in the case of the derivatives. We thus need an alternative approach for actual calculation. Fortunately it is possible to derive a recursive relationship between the Gram polynomials

$$P_k^{\,m}(i) = \frac{2(2k - 1)}{k(2m - k + 1)} iP_{k-1}^{\,m}(i) - \frac{(k - 1)(2m + k)}{k(2m - k + 1)} P_{k-2}^{\,m}(i) \tag{10}$$

with $P_0^{\,m}(i) = 1$ and $P_{-1}^{\,m}(i) = 0$.

This provides an easy method of calculating the Gram polynomial values, but more importantly, it also provides a straightforward method of evaluating the general sth derivative, simply by differentiating eq 10

$$P_k^{\,m,s}(i) = \frac{2(2k - 1)}{k(2m - k + 1)}[iP_{k-1}^{\,m}(i) + sP_{k-1}^{\,m,s-1}(i)] - \frac{(k - 1)(2m + k)}{k(2m - k + 1)} P_{k-2}^{\,m,s}(i) \tag{11}$$

with $P_0^{\,m,s}(i) = 0$ and $P_{-1}^{\,m,s}(i) = 0$.

In fact eq 11 alone can be used to generate both the Gram polynomials ($s = 0$) and their derivatives ($s > 0$) providing account is taken of the different starting values in these two cases. Thus eq 8 and eq 11 together provide a simple and

Table I. Convolution Weights for Quadratic Smoothing and Differentiation

	5 pt, quadratic, smooth					7 pt, quadratic, smooth						
i	−2	−1	0	1	2	−3	−2	−1	0	1	2	3
−3						32	5	1	−2	−2	−1	5
−2	31	9	−3	−5	3	15	4	3	3	1	0	−3
−1	9	13	12	6	−5	3	3	4	6	3	1	−6
0	−3	12	17	12	−3	−4	2	4	7	4	2	−4
1	−5	6	12	13	9	−6	1	3	6	4	3	3
2	3	−5	−3	9	31	−3	0	1	3	3	4	15
3						5	−1	−2	−2	1	5	32
norm	35	35	35	35	35	42	14	14	21	14	14	42

	5 pt, quadratic, 1st deriv					7 pt, quadratic, 1st deriv						
i	−2	−1	0	1	2	−3	−2	−1	0	1	2	3
−3						−13	−29	−19	−3	1	11	7
−2	−54	−34	−2	6	26	−2	−6	−6	−2	−6	−6	−2
−1	13	3	−1	−17	−27	5	9	3	−1	−9	−15	−7
0	40	20	0	−20	−40	8	16	8	0	−8	−16	−8
1	27	17	1	−3	−13	7	15	9	1	−3	−9	−5
2	−26	−6	2	34	54	2	6	6	2	6	6	2
3						−7	−11	−1	3	19	29	13
norm	70	70	10	70	70	28	84	84	28	84	84	28

practical method for calculating the required weights.

(c) Implementation. We are now in a position to calculate the convolution weights by using the recursive definition of the Gram polynomials and their derivatives eq 11. A function to calculate the general convolution weight eq 8, as a real number, can be achieved in just a few lines of PASCAL code as shown in Figure 1. PASCAL was chosen since recursion is a standard feature of the language. However many modern implementations of more traditional languages (e.g. FORTRAN, BASIC) also now provide this facility and conversion is straightforward. The code in Figure 1 has been made to resemble the expressions in eq 8 and eq 11 as closely as possible with no attempt to optimize speed. If only low-order smoothing is required it is easy to avoid recursion simply by providing explicit expressions for the Gram polynomials (e.g. $P_0^m(i) = 1$, $P_1^m(i) = i/m$, $P_2^m(i) = (3i^2 - m(m+1))/(m(2m-1))$ etc.).

```
function GramPoly(i,m,k,s : integer) : real;
{ Calculates the Gram Polynomial (s=0), or its s'th    }
{ derivative evaluated at i, order k, over 2m+1 points }
begin
  if k>0 then
    GramPoly := (4*k-2)/(k*(2*m-k+1))*(i *GramPoly(i,m,k-1,s) +
    s*GramPoly(i,m,k-1,s-1)) - ((k-1)*(2*m+k))/(k*(2*m-k+1))*GramPoly(i,m,k-2,s)
  else
    if (k=0) and (s=0) then GramPoly:=1 else GramPoly:=0;
end;

function GenFact(a,b: integer) : real;
{ Calculates the generalised factorial (a)(a-1)...(a-b+1) }
  var
    j : integer;
    gf : real;
begin
  gf:=1; for j:=(a-b+1) to a do gf:=gf * j;  GenFact:=gf;
end;

function Weight(i,t,m,n,s : integer) : real;
{ Calculates the weight of the i'th data point for the t'th Least-Square  }
{ point of the s'th derviative, over 2m+1 points, order n .               }
  var
    k : integer;
    sum : real;
begin
  sum:=0;
  for k:=0 to n do sum := sum + (2*k+1)*(GenFact(2*m,k)/GenFact(2*m+k+1,k+1))
                *GramPoly(i,m,k,0)*GramPoly(t,m,k,s);
  Weight:=sum;
end;
```

Figure 1. Pascal code to perform the calculation of a general weight value $h_t^{i,s}$. Function *Weight* corresponds to eq 8, function *GramPoly* to eq 11, and function *GenFact* to the generalized factorial defined after eq 5.

A program to produce integer weights over a common normalizing factor requires the code to be modified to accumulate the numerator and denominator separately and to provide for common factor cancellations. Both versions of the program are available from the author.

Tables I and II give examples of the complete tables required for smoothing and calculating the first derivative for some small values of m and n. The column heading is the position at which the least-squares value is to be evaluated (t) and the row heading is the data point index (i). The center column ($t = 0$) values are the weights provided in the original work of Savitzky and Golay and Steinier et al. So, for instance, if we wish to calculate the least-squares fit to the first point ($t = -2$) in a five-point quadratic smooth, we have from Table I

$$\bar{Y}_{-2} = \frac{31y_{-2} + 9y_{-1} - 3y_0 - 5y_1 + 3y_2}{35} \qquad (12)$$

Equation 12 is an example of the weights provided by Harris

Table II. Convolution Weights for Cubic Smoothing and Differentiation

	5 pt, cubic, smooth					7 pt, cubic, smooth						
i	−2	−1	0	1	2	−3	−2	−1	0	1	2	3
−3						39	8	−4	−2	1	4	−2
−2	69	2	−3	2	−1	8	19	16	3	−4	−7	4
−1	4	27	12	−8	4	−4	16	19	6	2	−4	1
0	−6	12	17	12	−6	−4	6	12	7	12	6	−4
1	4	−8	12	27	4	1	−4	2	6	19	16	−4
2	−1	2	−3	2	69	4	−7	−4	3	16	19	8
3						−2	4	1	−2	−4	8	39
norm	70	35	35	35	70	42	42	42	21	42	42	42

	5 pt, cubic, 1st deriv					7 pt, cubic, 1st deriv						
i	−2	−1	0	1	2	−3	−2	−1	0	1	2	3
−3						−257	−122	−29	22	31	−2	−77
−2	−125	−19	1	5	−29	122	17	−46	−67	−46	17	122
−1	136	−1	−8	−13	88	185	62	−19	−58	−55	−10	77
0	48	12	0	−12	−48	72	48	24	0	−24	−48	−72
1	−88	13	8	1	−136	−77	10	55	58	19	−62	−185
2	29	−5	−1	19	125	−122	−17	46	67	46	−17	−122
3						77	2	−31	−22	29	122	257
norm	84	42	12	42	84	252	252	252	252	252	252	252

Table III. Convolution Weights for Quadratic Initial-Point Smoothing: Polynomial Order = 2, Derivative = 0

	h (2m + 1)								
i	21	19	17	15	13	11	9	7	5
−10	631								
−9	513	257							
−8	405	204	409						
−7	307	156	315	158					
−6	219	113	231	117	47				
−5	141	75	157	81	33	83			
−4	73	42	93	50	21	54	109		
−3	15	14	39	24	11	30	63	32	
−2	−33	−9	−5	3	3	11	27	15	31
−1	−71	−27	−39	−13	−3	−3	1	3	9
0	−99	−40	−63	−24	−7	−12	−15	−4	−3
1	−117	−48	−77	−30	−9	−16	−21	−6	−5
2	−125	−51	−81	−31	−9	−15	−17	−3	3
3	−123	−49	−75	−27	−7	−9	−3	5	
4	−111	−42	−59	−18	−3	2	21		
5	−89	−30	−33	−4	3	18			
6	−57	−13	3	15	11				
7	−15	9	49	39					
8	37	36	105						
9	99	68							
10	171								
norm	1771	665	969	340	91	143	165	42	35

Table IV. Convolution Weights for Quadratic Initial-Point First Derivative: Polynomial Order = 2, Derivative = 1

	h (2m + 1)								
i	21	19	17	15	13	11	9	7	5
−10	−23 370								
−9	−17 233	−5661							
−8	−11 696	−4012	−792						
−7	−6759	−2543	−533	−7917					
−6	−2422	−1254	−306	−4966	−330				
−5	1315	−145	−111	−2435	−187	−945			
−4	4452	784	52	−324	−68	−456	−1428		
−3	6989	1533	183	1367	27	−67	−511	−13	
−2	8926	2102	282	2638	98	222	166	−2	−54
−1	10 263	2491	349	3489	145	411	603	5	13
0	11 000	2700	384	3920	168	500	800	8	40
1	11 137	2729	387	3931	167	489	757	7	27
2	10 674	2578	358	3522	142	378	474	2	−26
3	9611	2247	297	2693	93	167	−49	−7	
4	7948	1736	204	1444	20	−144	−812		
5	5685	1045	79	−225	−77	−555			
6	2822	174	−78	−2314	−198				
7	−641	−877	−267	−4823					
8	−4704	−2108	−488						
9	−9367	−3519							
10	−14 630								
norm	336 490	67830	7752	61880	2002	4290	4620	28	70

(*4*) and Baedecker (*5*)—but in integer format—so that they can be evaluated to the full accuracy of the computer. Since these initial-point values are so important for initial slope evaluations (*4*, *5*, *9*) we present their integer values in Tables III and IV.

Such tables can be used to write programs to perform the smoothing/differentiation for particular cases. However, the ease of calculation of weights from eq 8 and eq 11 means that they can be generated "in situ" to provide a completely general smoothing/differentiation routine for all m, n, and s. Such a routine first calculates a weight table, $\mathbf{h}[t,i]$, for all positions t ($-m \le t \le m$) and all filter points i ($-m \le i \le m$) for a given m, n, and s (see Table I for examples). The table is then used to evaluate the least-squares smooth/differentiation for every point in the spectrum. The first m points and the last m points are calculated by using the appropriate columns in $\mathbf{h}$ ($t = -m$ to -1, and $t = 1$ to m, respectively). The rest of the spectrum uses the center point weighting $\mathbf{h}[0,i]$. The advantage of constructing a weight table is that it only needs calculating once providing the m, n, and s values are not changed.

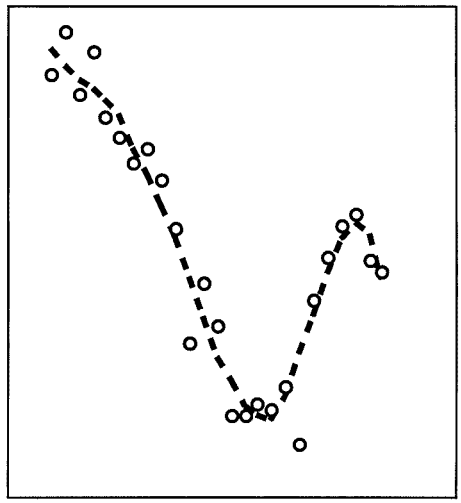

Figure 2. Least-squares smoothing using convolution weights for all points in the spectrum. The circles are the original data points. The dashed line joins the values from an 11 point cubic smooth. The correct smoothing of the end point values is clearly shown.

Figure 2 shows an example of smoothing (11 point cubic) using the algorithm described above. The data were chosen to provide an example of where the end-point information is particularly important. Whereas the traditional Savitzky–Golay smooth would have truncated the results by five points at each end, the current method correctly smooths the end points.

CONCLUSIONS

The convolution approach to least-squares smoothing and differentiation has been extended to remove the data truncation problem of the original Savitzky and Golay algorithm. A formalism based on the recursive properties of Gram polynomials provides a simple and direct means of calculating the convolution weights for all cases and thus enables a short but completely general routine to be written.

LITERATURE CITED

(1) Savitzky, A.; Golay, M. J. E. *Anal. Chem.* **1964**, *36*, 1627–1639.
(2) Steinier, J.; Termonia, Y.; Deltour, J. *Anal. Chem.* **1972**, *44*, 1906–1909.
(3) Khan, A. *Anal. Chem.* **1987**, *59*, 654–657.
(4) Leach, R. A.; Carter, C. A.; Harris, J. M. *Anal. Chem.* **1984**, *56*, 2304–2307.
(5) Baedecker, P. A. *Anal. Chem.* **1985**, *57*, 1477–1479.
(6) Ralston, A. *A first Course in Numerical Analysis*; McGraw-Hill Book Co.: New York, 1965; pp 235–254.
(7) Hamming, R. W. *Numerical Methods for Scientists and Engineers*; McGraw-Hill: New York, 1962; Chapter 24.
(8) Ernst, R. R. *Adv. Magn. Reson.* **1966**, *2*, 1.
(9) Khan, A. *Anal. Chem.* **1988**, *60*, 369–371.

RECEIVED for review September 22, 1989. Accepted November 28, 1989.

Pulsed and Transient Modes of Atomization by Cathodic Sputtering in a Glow Discharge for Atomic Absorption Spectrometry

Chuni L. Chakrabarti,*[1] Kurt L. Headrick,[1] J. Craig Hutton,[1] Zhang Bicheng,[1] Peter C. Bertels,[1] and Margaret H. Back[2]

Department of Chemistry, Carleton University, Ottawa, Ontario K1S 5B6, Canada, and Department of Chemistry, University of Ottawa, Ottawa, Ontario K1N 9B4, Canada

Analytical applications of cathodic sputtering in a glow discharge have almost wholly involved the production of a steady-state atomic vapor from a bulk solid. Kinetic limitations result in relatively poor sensitivity and limit of detection for the steady-state mode of atomization. A method that overcomes these limitations, using the rapid production of analyte atoms to produce a greater transient concentration of atoms in the analysis volume than is possible for the steady-state mode of atomization, is described in this paper. Two new modes of atomization are presented. The transient mode of atomization uses a high-power discharge for the rapid production of analyte atoms, whereas the pulsed mode of atomization uses a discharge of much shorter duration and higher power to achieve even faster atomization than is possible with the transient mode of atomization. An important factor leading to faster production of analyte atoms is the difference in bonding between the solution residues and the solid, bulk samples as the source of atoms. The faster kinetics of atom formation for the pulsed and the transient mode of atomization result in better (sometimes, much better) sensitivity for these modes of atomization compared to the steady-state mode of atomization. Since both the pulsed and the transient mode of atomization are based on faster production of analyte atoms and differ in that in the former a short (milliseconds) duration discharge is used, whereas in the latter a long (seconds) duration discharge is used, they are treated together as a new analytical technique. The new analytical technique and the conventional steady-state vapor technique have been evaluated by using a commercially available cathodic sputtering atomizer, Atomsource. These techniques have been characterized by kinetic modeling, and the superiority of the new analytical technique in sensitivity over the conventional technique based on the steady-state atomic vapor is shown. The sensitivity of the new analytical technique is, in some cases, similar to or greater than that of graphite furnace atomic absorption spectrometry. Factors affecting the sensitivity and areas for future improvement are discussed. The performance of the new analytical technique is also discussed in terms of the linear dynamic range of analytical calibration curves, interferences, and recoveries. Interferences seem to depend on whether the matrix is conducting or not. The use of peak-area absorbance, rather than peak-height absorbance, has been found to eliminate interferences when the matrix is conducting. A way to eliminate interferences for nonconducting matrices is suggested.

INTRODUCTION

Cathodic sputtering in a glow discharge (CSGD) is an electrical means of atomization in which atoms of the cathode are ejected from the cathode into the vapor phase as a result of bombardment by and subsequent momentum transfer from accelerated discharge-gas ions to the target cathode material. The atoms thus sputtered have been analyzed by atomic absorption (*1–16*), atomic emission (*17–29*), atomic fluorescence (*30–34*), and mass spectrometry (*35–38*). Westwood (*39*) has discussed the operating parameter dependencies for glow discharge sources employed in the film deposition process. Fang and Marcus (*40*) have recently done parametric evaluation of sputtering in a planar, diode glow discharge. Stocker (*41*) has studied the atomization properties of a planar glow discharge. Chapman (*42*) has discussed sputtering and plasma etching processes in glow discharges. Hannaford and Walsh (*43*) recently reviewed the work done in their laboratories on sputtered atoms in absorption and fluorescence spectroscopy.

L'vov (*44*) has pointed out the limitations inherent in thermal atomizers which arise from the temperature dependence of vapour pressure—limitations that can only be overcome by the use of nonthermal atomization, such as by CSGD. That CSGD is a promising means of atomization was recognized as early as 1959 by Russell and Walsh (*4*). So far, however, its application has been limited mostly to the direct, emission-spectrometric analysis of solid, conducting samples to generate a steady-state atomic vapor. The sensitivity of the steady-state technique is relatively poor because of the inherent limitation in the analytical sensitivity of all techniques based on a steady-state population, and because in the solid, bulk samples the analyte is more strongly bound in the three-dimensional lattice of the cathode atoms than for a solution residue on the cathode surface. An increase in the sensitivity can be obtained by basing the analytical determination on the pulsed atomization or the transient atomization of solution residues of samples. In this paper these three modes of atomization, the pulsed, the transient, and the steady-state mode of atomization, have been characterized for the Atomsource cathodic sputtering atomizer for atomic absorption spectrometry. The results of our studies on interferences and recoveries by the transient mode of atomization using the Atomsource are also presented.

THEORY

Cathodic Sputtering. The atomsource produces a Grimm-type glow discharge (*21*). In our previous work (*3*) using the Atomsource and a pyrolytic graphite cathode we have reported that for the transient atomization of Co (taken as an aqueous solution of the nitrate), the peak-height absorbance shows a linear relationship to both power and discharge current. Fang and Marcus (*40*), using preliminary factor analysis of their experimental results, found that for oxygen-free hard copper the weight loss was directly proportional to the applied power. Both the above studies (*3, 40*) suggest that power is the key to increasing the analytical sensitivity of CSGD. We have therefore used the highest power which the power supplies are capable of giving, that provide a stable discharge, using the pulsed and the transient mode of atomization. As the results of this study will show,

* Author to whom correspondence should be addressed.
[1] Carleton University.
[2] University of Ottawa.

0003-2700/90/0362-0574$02.50/0

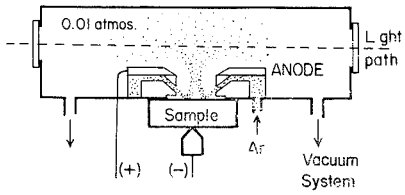

Figure 1. Schematic diagram of the Atomsource. Reprinted with permission from ref 3. Copyright 1989 Royal Society of Chemistry.

application of even greater power than we have been able to apply is likely to increase the analytical sensitivity still further.

Kinetic Modeling. For simplicity, we shall confine the kinetic analysis to the introduction of atoms into and the removal of atoms from the analysis volume. If the atoms are sputtered direct from the surface of the cathode without the formation of any condensed-phase or gas-phase intermediates, and the convection/diffusion of the atoms out of the analysis volume is a first-order process, then we can represent atom introduction and atom loss by the following consecutive, first-order reactions:

$$A \xrightarrow{k_1} B \xrightarrow{k_2} C \qquad (1)$$

where A represents the analyte atoms entering the analysis volume, B the analyte atomic species within the analysis volume, C the analyte atomic vapor that has been lost from the analysis volume by diffusion/convection, and k_1 and k_2 are first-order rate constants for the introduction of atoms into and their subsequent loss from the analysis volume, respectively. It should be noted at this point that the geometry of the atomizer has a spatial separation between the location of atom formation (the cathode surface) and the analysis volume (defined by the geometry of the beam of radiation from the hollow-cathode lamp), as can be seen in Figure 1. We therefore cannot directly measure the rate of analyte atom formation at the cathode surface, which may be different from the rate of introduction of the analyte atoms into the analysis volume which we do measure.

When there is no analyte atom initially present in the analysis volume, this mechanism gives the following equation for the time-dependent concentration of analyte atoms within the analysis volume, $[B]_t$:

$$[B]_t = [A]_0 \frac{k_1}{k_1 - k_2} [(e^{-k_2 t}) - (e^{-k_1 t})] \qquad (2)$$

The form of this equation requires that the concentration of B, which is initially zero, increases to a maximum and then decays at a rate that is controlled by the smaller of the two rate constants. Absorbance due to analyte atoms within the analysis volume, B, is used as a measure of the concentration, [B], recognizing that the absorbance is proportional to the analyte atom density and that the latter is proportional to [B].

When one of the rate constants is smaller than the other, the tail of the absorbance profile decays exponentially at a rate controlled by the smaller of the two rate constants as follows:

$$[B]_t' = C[A]_0 (e^{-k_a t}) \qquad (3)$$

where $[B]_t'$ is the concentration of B at later times, C is a constant dependent upon which of the two rate constants is smaller, and k_a is the smaller of the two rate constants. Therefore a plot of ln $[B]_t'$ vs t has a slope of $-k_a$ and an intercept of $C[A]_0$. The value of the intercept, and therefore also of the peak-height absorbance, depends on C, the value of which depends on which of the rate constants is larger than the other. From eq 2, if $k_1 \gg k_2$, then $C = 1$, whereas if $k_2 > k_1$, then $C = k_1/k_2$, which is less than 1 since $k_2 > k_1$. The maximum sensitivity can therefore be expected when $k_1 \gg k_2$, i.e., when atomization is rapid, as in the case of the pulsed and the transient mode of atomization, as opposed to the slow atomization which occurs when a solid, bulk sample is sputtered to give a steady-state atom population.

To get the larger of the two rate constants, we first take the difference between eq 2 and 3

$$[B]_t' - [B]_t = \Delta B = C[A]_0(e^{-k_b t}) \qquad (4)$$

where ΔB is the difference between the measured absorbance due to B and the extrapolation of eq 2, C is as previously defined, and k_b is the larger of the two rate constants. It can be seen that a plot of ln ΔB vs t has a slope of $-k_b$ and an intercept of $C[A]_0$. These two kinetic plots are used to determine the magnitude of the two rate constants.

The above method (to be called the "kinetic plot" method) requires fairly lengthy data treatment and is used only to check that the plots generated are indeed linear. In practice, we determine k_a from the half-life of the signal decay (i.e. $k_a = \ln 2/t_{1/2}$). We then use this value for k_a and the time required for the signal to reach its maximum value, t_{max}, to determine k_b by using the following equation:

$$t_{max} = (\ln k_b - \ln k_a)/(k_b - k_a) \qquad (5)$$

The values obtained in this manner can be easily checked against those obtained by using the "kinetic plot" method, and this was done frequently.

It is impossible to say from the shape of the absorbance profile which of the two rate constants, k_1 or k_2, is larger. Other information is required to make this determination possible. The following two experiments can make this determination: (1) the rate for atom loss, k_2, can be identified by cutting off the discharge power (and thus stopping the formation of analyte atoms) while there is still a measurable analyte atomic vapor in the analysis volume; (2) the rate of atom formation should increase with an increase in the applied power at a given pressure, while the rate of atom loss should stay the same, thus allowing k_1, the rate constant for atom formation, to be identified. If the discharge power is cut off during the falling portion of a transient signal, the resulting decay of the signal will indicate the loss of the analyte atoms from the analysis volume. If there is no change in the slope of the plot for the decay corresponding to eq 3 when the voltage is switched off, then k_2 corresponds to k_a, the smaller of the two rate constants. On the other hand, if the slope of the plot becomes more negative when the voltage is switched off and the new slope is equal to $-k_b$ (eq 4), then k_2 is the larger of the two rate constants.

The validity of the above model can be tested by determining the rate constants from an experimental absorbance profile and then using these values to calculate a theoretical absorbance profile using eq 2. Agreement of the experimental absorbance profile with the theoretical profile will indicate the validity of the model.

EXPERIMENTAL SECTION

Apparatus. The experiments were performed with an Atomsource cathodic sputtering atomizer for atomic absorption spectrometry, manufactured by Analyte Corp., Grants Pass, OR. Software versions 3.14 and 3.15 were used for all experiments. The atomsource sputtering cell is shown schematically in Figure 1. The Atomsource consists of a sputtering cell with a power supply, gas regulation equipment, operator interface, and supporting software, and is designed to replace the flame or graphite furnace of an existing atomic absorption spectrophotometer (it is also available with an atomic absorption spectrophotometer designed for rapid, sequential multielement analysis by atomic absorption spectrometry (*45*)). The Atomsource was used with two different spectrophotometers and power supplies to suit the needs of the particular experiment being performed. A summary

Table I. Apparatus Used for Different Experiments

experiment	spectrophotometer	power supply
determination of characteristic mass, analytical calibration curves, and % recovery using the transient mode of atomization	Perkin-Elmer Z 5000	Atomsource
transient mode of atomization	Varian-Techtron AA-5	Atomsource
pulsed mode of atomization	Varian-Techtron AA-5	MDX
steady-state mode of atomization	Perkin-Elmer Z 5000 or Varian-Techtron AA-5	MDX

of the four different experimental arrangements is given in Table I; the details of the different equipment are given below. The experiments on the analytical performance comprised studies on analytical calibration curves and matrix interferences and were done using the transient mode of atomization.

For experiments not requiring a fast detection system or where background correction was desired (the analytical determinations and the steady-state measurements) the Atomsource was mounted in the usual place of the burner assembly in a Perkin-Elmer atomic absorption spectrophotometer, Model Zeeman 5000, equipped with a deuterium-arc background corrector, and was operated as a part of the spectrophotometer. The time constant of the above spectrophotometer is ~17 ms (60 Hz). The experimental absorbance profiles were recorded with a Perkin-Elmer professional computer, Model 7500, and hard copies of the plots were obtained with a Printer, Model Prism 132 (Integral Data Systems, Milford, NH). The discharge voltage was recorded with a Nicolet Model 2090-III, two-channel digital oscilloscope. For experiments where a fast detection system was required or where background correction was not required (the pulsed and transient mode of atomization experiments), the Atomsource was used in conjunction with a fast detection system (*46*). This fast detection system consisted of a Varian-Techtron atomic absorption spectrophotometer, Model AA-5, with a laboratory-built power supply for the hollow-cathode lamp modulated at 843 Hz and a synchronous detection system with a laboratory-built lock-in amplifier having a time constant variable from 2 to 104 ms. A time constant of 2 ms was used unless otherwise specified. The absorbance and the discharge voltage were recorded simultaneously with the Nicolet digital oscilloscope. Hard copies were obtained with a plotter, Model 7470A (Hewlett-Packard, Palo Alto, CA).

The Atomsource power supply was used for analytical determinations and for the transient atomization experiments. The Atomsource power supply is capable of either direct current or voltage regulation. The atomsource was used in the current regulation mode. The power supply has a maximum output of 300 mA at 1500 V, giving a maximum output of 450 W. The microprocessor controlling the power supply allows for discharges of 1 s and multiples thereof. For the other experiments, a different power supply was used to achieve fine control of the discharge duration and to investigate the use of higher powers than the Atomsource power supply is capable of. Fine control of the discharge duration was required for the steady-state experiments and also for the verification of the rate constants for the pulsed mode of atomization, whereas for the pulsed mode of atomization experiments discharges of high power and short duration were required. For these experiments the Atomsource power supply was disconnected from the atomizer. The power supply used for these experiments was a 1-kW High Z DC Magnetron, Model MDX-1K, manufactured by Advanced Energy Industries, Inc., Fort Collins, CO. The MDX power supply has a rated output of 1 A at 1000 V for a maximum power output of 1000 W. This power supply was used in conjunction with a function generator, Model No. 164, manufactured by WAVETEK, San Diego, CA. This combination allows for single or multiple positive-going square-wave pulses of variable duration (frequency) and amplitude. Typical discharge durations with this power supply were of the order of 50 ms. The power supply permits current, voltage, or power regulation. Power regulation was generally used for these studies as it was found to give more reproducible results than current or voltage regulation.

For the steady-state atomization experiments the Atomsource was used with the Perkin-Elmer spectrophotometer for Mo and the Varian-Techtron spectrophotometer was used with a time constant of 16 ms for all other elements. A Mettler microbalance, Model M5 (Mettler, Zurich, Switzerland), was used for the measurements of mass.

The following hollow-cathode lamps were used: Ag, Au, Cd, Fe, Mg, Mn, Mo, Ni, and Pb, manufactured by Westinghouse, Al, Co, Cr, and Cu by Varian, Ag, Cd, Mo, and V by Perkin-Elmer, Au and Cd by Cathodeon, Mn by EEL, and Mo by Analyte Corporation.

Test Solutions and Reagents. Chemically pure metals or their salts were used to prepare standard solutions. Stock solutions containing 1000 μg/mL were prepared as follows. For Al, the metal was dissolved in 50% (v/v) HCl (Ultrex) with heating and the solution was diluted with ultrapure water. For Au, the stock solution was supplied by Harleco (Philadelphia, PA)—the solution was prepared by dissolving the metal in aqua regia. For Mo and V, the stock solution of each metal was prepared separately by dissolving MoO_3 or V_2O_3 in ammonium hydroxide (ACS reagent grade) and diluting the solution with ultrapure water. For Cd, CdO was dissolved in 50% (v/v) nitric acid (Ultrex) with heating and the solution diluted with ultrapure water. For Mg, MgO was dissolved in 10% (v/v) nitric acid (Ultrex) and the solution diluted with ultrapure water. For Pb, $Pb(NO_3)_2$ was dissolved in 2% (v/v) nitric acid (Ultrex) and the solution diluted with ultrapure water. For Cr, $K_2Cr_2O_7$ was dissolved in 1% (v/v) nitric acid (Ultrex). For Co and Ni, each metal was separately dissolved in concentrated nitric acid (Ultrex) with heating and the solution diluted with ultrapure water. For Ag, Cu, Fe, and Mn, each metal was separately dissolved in 50% (v/v) nitric acid (Ultrex) with heating and the solution diluted with ultrapure water. All stock solutions were made to contain 1% (v/v) of the acids or the ammonium hydroxide used to dissolve the metals or their salts except for Al, which contained 2% (v/v) HCl. The Ultrex brand acids were manufactured by Baker Chemical Co. Ultrapure water of resistivity 18.3 MΩ cm was obtained direct from a Milli-Q2 Water Purification System (Millipore Corp.). All test solutions were prepared by serial dilution of the above stock solutions immediately prior to determination.

Gas. Argon gas (99.997% pure) was used as the discharge gas. A molecular sieve trap (Chromatographic Specialities Model No. MT120-4) was used to remove water vapor from the discharge gas.

Procedure. Cathodes of copper (99% pure), steel, anisotropic pyrolytic graphite, or tantalum (99.99% pure), as described below, were used. Excluding tantalum (which was supplied by the manufacturer as a polished sheet of metal), the cathodes were polished (working surface only) to 400 grit with an electric polishing machine, then cleaned with ethanol, and air-dried. The clean, dry cathode was then clamped to the atomizer. The following procedure was used for all the experiments except for the steady-state atomization experiments, where the analyte was present in the bulk, solid steel (cathode). This was in contrast with the other experiments where the analyte was present as a discrete (solution) residue on the surface of the cathode. The procedure for the steady-state atomization experiments is given later. Prior to every atomization cycle, the cathodes were sputter-cleaned to ensure a reproducible atomization surface and to prepare a circular depression (cavity) into which the sample solution was deposited. The depth of the cavity was found to have no effect on the results; however, the cavity must be of sufficient depth to contain the sample solution. For copper and tantalum, about 5–10 s sputtering at the optimum operating conditions (Tables III and IV) for the particular experiment was found to be sufficient. For graphite, the cathode was sputtered for 240 s at 12 Torr argon gas pressure and a current of 100 mA.

The cathode was then detached from the atomizer and laid flat with the prepared surface facing up. A 1-μL volume of the test

Table II. Hollow-Cathode Lamps and Monochromator Settings

element	wavelength, nm	hollow-cathode lamp manufacturer	hollow-cathode lamp current, mA	spectral bandpass, nm
Al	309.3	Varian	4	0.2
Ag	328.1	Westinghouse	5	0.08
Au	242.8	Westinghouse	6	1.0
Cd	228.8	Cathodeon	6	0.1
Co	240.7	Varian	11	0.08
Cr	357.9	Varian	2	1.0
Cu	324.8	Varian	4	0.3
Fe	248.3	Westinghouse	6	0.5
Mg	285.2	Westinghouse	1	1.0
Mn	279.5	Westinghouse	3	1.0
Mo	313.3	Westinghouse	3	1.0
Ni	232.0	Westinghouse	11	0.1
Pb	283.3	Westinghouse	3	0.5
V	318.5	Perkin-Elmer	4	0.8

solution was then deposited in the center of the cavity with a Hamilton microsyringe, fitted with a Chaney adaptor, Model 7105 NCH, part no. H88004 (Chromatographic Specialties). The test solution was then air-dried outside the atomizer and the cathode was reclamped to the atomizer. When the Atomsource power supply was used, the following gas flushing sequence was used as a part of the run mode. The atomizer pressure was maintained at 10 Torr of argon for 10 s; the atomizer was evacuated to 0.3 Torr, then repressurized to the preselected operating pressure. When the atomizer reached the operating pressure, the electric discharge was automatically initiated. The Nicolet oscilloscope (and the Perkin-Elmer spectrophotometer, if used) was triggered manually just prior to the initiation of the discharge. When the MDX power supply was used, the atomizer standby flush pressure mode was used to flush the atomizer at the desired operating pressure. Once the operating pressure was reached, the discharge could be initiated whenever desired. The oscilloscope (and spectrophotometer, if necessary) were triggered as before. For low concentrations of the aqueous standard solutions used for most of the experiments, a discharge of 25 ms duration was found to be sufficient to ensure complete atomization of the sample. Longer sputtering times were occasionally needed, particularly for the interference studies and when determining the peak-area absorbance for high analyte concentrations. In all cases, blanks were run to ensure that there was no sample carryover from run to run and to determine blanks and background absorbance.

The procedure for the steady-state atomization experiments was as follows. The cathode for all elements was the National Bureau of Standards, Standard Reference Material 1264a, High Carbon Steel. A preliminary test was done on the cathode to determine the minimum pulse duration required to reach the first point on the steady-state peak-height absorbance plateau. The cathode was sputtered for a period of time sufficiently long to establish the steady-state peak-height absorbance. The pulse duration was then reduced until a transient signal (i.e., a peak-shaped signal) was obtained. Another sample of the same cathode was used for the remaining parts of the steady-state atomization experiments. The clean, dry cathode was weighed on the microbalance and then clamped to the atomizer. By use of the predetermined pulse duration, the cathode was then subjected to 10–15 pulses to cleave the surface. The cathode was then subjected to a further 16 single pulses and the absorbance and the discharge voltage were recorded. The discharge was then continuously pulsed and the total number of pulses was determined. Several hundered pulses were accumulated in order to obtain a reasonable weight loss. The cathode was then reweighed. The mass of analyte sputtered in one pulse was then calculated, from which the characteristic mass for the steady-state atomization was calculated after subtraction of a blank consisting simply of the noise from the hollow-cathode lamp (since that was the only blank). For Co and Mo, a total of four determinations were made consisting of 16 absorbance values for each determination. For each of the other elements, a total of 64 atomization cycles were completed and absorbance measurements made but only one mass determination was made for the cumulative loss of mass over the 64 atomization cycles. The number of pulses used for the determination of the weight loss was made large in order to reduce the relative error in the measurement of mass.

Table III. Discharge Parameters for the Transient Mode of Atomization[a]

element	instrumental setting pressure, Torr	instrumental setting current, mA	measured voltage, V	calculated power, W
Al	8	260	1300	338
Ag	8	230	1000	230
Au	8	220	750	165
Cd	10	260	1270	330
Co	8	250	1290	323
Cr	12	260	940	244
Cu	10	250	1180	295
Fe	8	150	613	92
Mg	8	280	560	157
Mn	12	250	723	157
Mo	8	250	640	181
Ni	8	260	1240	322
Pb	8	250	1100	275
V	8	250	1144	286

[a] Copper was used as the cathode for all elements except for Cu, for which tantalum was used.

Table IV. Discharge Parameters for the Pulsed Mode of Atomization[a]

element	instrumental setting pressure, Torr	instrumental setting power, W	measured current, mA	measured voltage, V
Al	8	229	250	920
Ag	8	400	287	1400
Au	8	410	284	1410
Cd	10	250	305	820
Co	8	200	227	880
Cr	8	301	251	1200
Cu	10	149	198	750
Fe	8	200	240	830
Mg	8	299	262	1140
Mn	10	300	310	970
Mo	8	203	285	810
Ni	10	200	227	880
Pb	10	249	312	800
V	8	250	250	1000

[a] Copper was used as the cathode for all elements except for Cu, for which tantalum was used.

Experimental Conditions. The hollow-cathode lamp and monochromator settings normally used for all the experiments are given in Table II. The discharge parameters used for the analytical studies and the transient atomization experiments are given in Table III. The discharge parameters used for the pulsed and the steady-state mode of atomization are given in Tables IV and V, respectively. The discharge parameters for each element were optimized individually for each mode of atomization.

RESULTS AND DISCUSSION

The experimental conditions shown in Tables II–V were the conditions found to give the maximum analytical sensitivity and were used to determine the characteristic masses and limits of detection. The characteristic masses and the limits of detection are given in Table VI for the transient mode of atomization. The characteristic masses for graphite furnace atomic absorption spectrometry (GFAAS) are those reported by L'vov et al. (*47*). Of the 14 elements in the table, six have sensitivities within an order of magnitude of GFAAS, whereas four elements have sensitivities better than GFAAS. The pulsed and the transient mode of atomization is a new technique, which is still in its infancy, and we feel that there is still a lot of room for improvement in these values, as will be discussed later. It should be noted that we have thus far

Table V. Discharge Parameters for the Steady-State Mode of Atomization[a]

element	concn in SRM, %	instrumental setting		measured		time sputtered, ms
		pressure, Torr	current, mA	power, W	voltage, V	
Co	0.15	8	152	97	710	50
Cu	0.25	15	151	70	460	50
Mn	0.25	8	99	53	540	100
Mo	0.49	8	152	97	710	50
Ni	0.14	10	169	95	560	50
V	0.10	15	200	95	480	100

[a] The cathode used for all elements was the National Bureau of Standards, Standard Reference Material 1264a, High-Carbon Steel.

Table VI. Characteristic Mass and Limits of Detection for the Transient Mode of Atomization

element	detection limit,[a] pg	characteristic mass	
		transient atomization, pg	GFAAS, pg
Al	7.0	2.9	11.8
Ag	140	26	1.2
Au	550	47	7.3
Cd	27	4.9	0.39
Co	3000	130	5.4
Cr	0.5	0.25	1.8
Cu	43	8.0	3.0
Fe	210	30	2.8
Mg	0.5	0.11	0.30
Mn	68	25	1.7
Mo	0.34	0.041	5.4
Ni	1500	210	0.5
Pb	1600	210	7.7
V	185	68	69

[a] Mass giving a signal = 3σ/slope of the analytical calibration curve (σ = 1 standard deviation).

confined our attention to elements that are commonly determined by GFAAS. As Ohls (*12*) has demonstrated, it is possible to determine by CSGD elements such as Zr which are not suitable for determination in a graphite furnace because of the formation of refractory carbides.

The values presented in Table VI are at least an order of magnitude more sensitive than our previously published values (*3*) for the characteristic mass for the transient mode of atomization. There are a number of reasons for the increase in sensitivity. These reasons are discussed in detail below, and include the time constant of the detection system, the hollow-cathode lamp current, the design of the hollow-cathode lamp, the method of modulation, and the discharge power. The differences in sensitivity are also partly due to the different optics of the two spectrophotometers used. However, these differences have not been quantified and will therefore not be discussed further.

One reason for the above-mentioned improvement in the characteristic mass is that our previous values were obtained by using the Perkin-Elmer spectrophotometer, the time constant of which is ~17 ms, which is too large to define accurately the peak of the rapidly changing transients (*1*). The values in Table VI were all obtained by using the fast detection system described in the Experimental Section. A time constant of 2 ms was used. However, even a time constant of 2 ms is too large for some elements which have faster signals. For some elements, the absorbance peak near the limit of detection has a duration of only about 5 ms. There is therefore a need for a detection system whose time constant is even smaller than the 2 ms presently available. We are now working on a new detection system that will have a time constant down to 0.1 ms. The effect of the time constant of the detection system on the characteristic mass can be seen from the characteristic mass of the transient mode of atomization for Mo in Table VII. The hollow-cathode lamp used was the "new" lamp (Westinghouse); the meaning of the "new" lamp is given later.

Table VII. Effect of Time Constant on the Characteristic Mass of Mo

time constant, ms	characteristic mass, pg
2	0.11
8	0.50

Table VIII. Effect of Hollow-Cathode Lamp Current on the Characteristic Mass of Mo

hollow-cathode lamp current, mA	characteristic mass, pg
3	4.8
10	11

Hollow-Cathode Lamps. Piepmeier (*48*) has recently reported on the influence of the spectral profile of the source lamp on the analytical results for low pressure, cathodic sputtering cells for atomic absorption spectrometry. One of the assumptions of the Walsh method for atomic absorption spectrometry is that the emission line from the hollow-cathode lamp is much narrower than the absorption line. One would expect that this condition would be fulfilled for a flame or a graphite furnace, since the atomizer is at atmospheric pressure and at a high temperature, whereas the hollow-cathode lamp is at a low pressure and a lower temperature, and therefore the absorption line is much more broadened by Lorentz and Doppler broadening than is the emission line from the hollow-cathode lamp. For a cathodic sputtering atomizer, however, this is not the case. The atomizer pressure is only slightly greater than that of the hollow-cathode lamp, whereas the temperature of the atomizer is less than that of the hollow-cathode lamp because of the fact that the cathode is water cooled and that very short sputtering times were generally used, thereby preventing any temperature change for the cathode. The absorption and emission line widths are therefore probably not much different. We have found that the highest sensitivity is obtained when the lowest possible lamp current is used, in agreement with the findings of Bernhard (*11*). A low current for the hollow-cathode lamp means a lower lamp temperature and, therefore, a narrower emission line. Of course, using a low current for the hollow-cathode lamp means a decrease in the intensity of radiation and a resulting increase in the signal noise. The conditions that we have employed are those that have been found to give the highest sensitivity (lowest characteristic mass) but not necessarily the lowest limit of detection. The effect of the lamp current on the characteristic mass is shown for Mo in Table VIII; the hollow-cathode lamp used was the Perkin-Elmer lamp. For use with the 0.1-ms time-constant detection system, we are building a power supply for the electronically modulated hollow-cathode lamp, with improved current resolution at low lamp currents. It is important to use electronic, rather than mechanical modulation of the radiation from the

Table IX. Effect of Hollow-Cathode Lamp on Characteristic Mass

element	hollow-cathode lamp	characteristic mass, pg
Mo	Westinghouse, old	0.041
Mo	Westinghouse, new	0.11
Mo	Perkin-Elmer	4.8
Mo	Analyte	17
Mn	Westinghouse	25
Mn	EEL	33
Cd[a]	Westinghouse	150
Cd[a]	Perkin-Elmer	1500
Cd	Westinghouse	6.4
Cd	Cathodeon	7.3

[a] Perkin-Elmer Zeeman 5000 atomic absorption spectrophotometer. Graphite cathode.

hollow-cathode lamp (as is the case with the Perkin-Elmer spectrophotometer), since for electronic modulation the average power dissipated in the cathode is less than that when the current is dc and the radiation is mechanically modulated. The former results in a lower temperature for the hollow-cathode lamp, a narrower width for the emission line, and, therefore, a lower characteristic mass than if the radiation from the hollow-cathode lamp were mechanically modulated. Another advantage of electronic modulation is, of course, an increase in the useful life of the hollow-cathode lamp.

The age and the type of hollow-cathode lamp used were found to have a large effect on the characteristic mass. This is shown in Table IX for Cd, Mn, and Mo. In our earlier work (*1*, *3*) we generally used Perkin-Elmer lamps. When an old Westinghouse Mo lamp was used, the sensitivity was enhanced by 2 orders of magnitude over that given by the Perkin-Elmer lamp. Both of the hollow-cathode lamps were tested and were found to be in good, working condition. The Westinghouse lamp was purchased in 1973 and even though it was still usable, it was near the end of its useful life, as was soon discovered. This hollow-cathode lamp will be referred to as the "old" Westinghouse Mo lamp, as opposed to the "new" Westinghouse lamp, which we purchased in late 1988 to replace it. As can be seen from Table IX, the new Westinghouse lamp was not as sensitive as the old Westinghouse lamp, but it was still much better in sensitivity than the Perkin-Elmer lamp. We also tried a hollow-cathode lamp marketed by Analyte Corp., the manufacturer of the Atomsource. As can be seen, it was the least sensitive of the Mo lamps tested. These results are confirmed by the results obtained for Cd (Table IX). As can be seen from Table IX, hollow-cathode lamps by Westinghouse and Cathodeon gave similar sensitivities, whereas the Westinghouse lamp was found to be an order of magnitude more sensitive than the Perkin-Elmer lamp. Although we have not yet made a direct comparison, we suspect that Varian lamps also give good sensitivity, as evidenced by the high sensitivity of Al and Cr. The only other hollow-cathode lamps that we have compared directly are Mn lamps by EEL and by Westinghouse, which had similar sensitivities. Obviously, there is a need for a detailed study of the sensitivity given by various, commercial hollow-cathode lamps for use in atomic absorption spectrometry when using cathodic sputtering atomization. It should be kept in mind that these hollow-cathode lamps (and the rest of the apparatus for that matter) were not used as advised by the manufacturers. The Perkin-Elmer Mo lamp, for example, had a continuous current rating of 30–40 mA; the lamp current that we used was 3 mA. The maximum lamp currents recommended by the manufacturer are shown in Table X, along with the currents at which the hollow-cathode lamps were actually used.

Table X. Hollow-Cathode Lamp Currents

		hollow-cathode lamp	
element	manufacturer	recommended max current, mA	current used, mA
Al	Varian	20	4
Ag	Perkin-Elmer	25	13
Ag	Westinghouse	20	5
Au	Cathodeon	10	12
Au	Westinghouse	20	6
Cd	Cathodeon	6	6
Cd	Perkin-Elmer	8	6
Cd	Westinghouse	12	6
Co	Varian	25	11
Cr	Varian	?	2
Cu	Varian	15	4
Fe	Westinghouse	20	6
Mg	Westinghouse	20	1
Mn	EEL	20	3
Mn	Westinghouse	25	3
Mo	Analyte	30	3
Mo	Perkin-Elmer	40	3
Mo	Westinghouse	30	3
Ni	Westinghouse	20	11
Pb	Westinghouse	8	3
V	Perkin-Elmer	40	4

We feel that the above observations can be explained by taking into account the work of Wagenaar et al. (*49*), who studied the emission line profiles and intensities of various hollow-cathode lamps as a function of lamp current. They found that the 423-nm Ca line from a Perkin-Elmer lamp was strongly self-reversed at 15-mA lamp current, whereas the same line from a Varian lamp showed no self-reversal up to 25-mA lamp current. They found that the intensity of the line of the Perkin-Elmer lamp at 15-mA lamp current was equal to the intensity of the line of the Varian lamp at 25-mA lamp current and that self-reversal for both hollow-cathode lamps began at the same intensity, although the current densities were different. Thus, for a given lamp current, Perkin-Elmer lamps produce broader, more intense lines than Varian lamps because of diffrences in filler gas or cathode material (*49*), as well as in geometry and size. For atomic absorption spectrometry using flame or graphite furnace atomization, the width of the emission line usually does not have a large effect on the sensitivity. This is not the case for cathodic sputtering atomizers for atomic absorption spectrometry. Our results indicate that any loss in sensitivity due to the decrease in the intensity of the emission line with decreasing lamp current is more than offset by the increase in sensitivity due to the better overlap between the emission and the absorption line as the emission line becomes narrower. At present, manufacturers of hollow-cathode lamps for atomic absorption spectrometry make their hollow-cathode lamps as intense as possible, as evidenced by a number of hollow-cathode lamps that bear labels stating "high spectral output" on the hollow-cathode lamp. Our results indicate that for the cathodic sputtering atomizers the greatest sensitivity is obtained with hollow-cathode lamps that have the narrowest emission line and that the intensity of the hollow-cathode lamp is of secondary importance. This explains why the old Westinghouse lamp was more sensitive than the new Westinghouse lamp—the new Westinghouse lamp has a "high spectral output" sticker, whereas the old Westinghouse lamp does not. Probably, at a given lamp current the emission line from the new Westinghouse lamp is broader than the emission line from the old Westinghouse lamp.

Pulsed Mode and Transient Mode of Operation. It was realized early on that the sensitivity of the transient mode of atomization was limited by the power available from the

Table XI. Limits of Detection and Characteristic Masses for the Pulsed Mode of Atomization

element	limit of detection,[a] pg	characteristic mass, pg
Al	7.0	2.6
Ag	280	46
Au	260	48
Cd	5.6	2.0
Co	260	38
Cr	0.23	0.17
Cu	31	7.5
Fe	140	53
Mg	6.5	1.1
Mn	71	27
Mo	0.32	0.08
Ni	410	100
Pb	560	1900
V	140	840

[a] Mass giving a signal = 3σ/slope of the analytical calibration curve (σ = 1 standard deviation).

Table XII. Effect of Pulse Duration on Mo Peak-Height absorbance

pulse duration, ms	peak-height absorbance
500	0.579
50	0.555
25	0.568
10 + 500	0.208 + 0.363 = 0.571

Atomsource power supply (*3*). It was decided that a higher effective power (and a higher sensitivity) could be obtained by concentrating a great deal of power into short pulses rather than using a dc discharge. The pulsed mode of operation uses constant power and a strike voltage (about 300 V) of microsecond duration superimposed on single or multiple, positive-going square-wave pulses of millisecond duration and of higher amplitude (compared to the transient mode of atomization). The transient mode of atomization uses constant current and positive-going square-wave pulses of seconds duration and lower amplitude (compared to the pulsed mode of operation). The pulsed mode of operation offers the capability of high power (which is required for a fast rate of atomization and, therefore, for maximizing the sensitivity), whereas the transient mode of atomization uses limited current at maximum voltage. We also wanted to compare the sensitivity of the pulsed and the transient mode of atomization with the sensitivity of the steady-state mode of atomization by variation of the pulse duration, as explained in the Theory. It should be emphasized that the difference between the pulsed and the transient mode of atomization is the much shorter duration of the discharge and the higher power capability of the pulsed power supply used for the pulsed mode of atomization compared with the Atomsource power supply used for the transient mode of atomization. The pulsed mode of atomization is similar to the transient mode of atomization and can be expected to give similar results for similar experimental conditions; it is, however, easier to achieve high-power discharges (and therefore, higher sensitivity) for the pulsed mode of atomization than for the transient mode of atomization.

The characteristic mass obtained for the pulsed mode of atomization is shown in Table XI. Typically, a single pulse of 50–500-ms duration was used. Pulses under 25-ms duration were found to result in incomplete atomization of the sample, as shown in Table XII. After the 10-ms pulse a second pulse of 500-ms duration was applied in order to check for the completeness of atomization. When the peak-height absorbances for a 10-ms pulse and a subsequent 500-ms pulse were added, the combined absorbance was found to be the same as for a pulse of 25 ms or greater duration. The characteristic mass for the pulsed mode of atomization is smaller than or equal to that of the transient mode of atomization for 9 of the 14 elements listed in Table XI. Of the other five elements, four are within a factor of about 2 of the characteristic mass obtained for the transient mode of atomization. The characteristic masses obtained for the pulsed mode of atomization are higher than expected. This is probably because of the low voltage rating of the MDX power supply. As can be seen from Tables III and IV, the discharge parameters for the pulsed mode of atomization are not very different from those used for the transient mode of atomization. The MDX power supply is rated at only 1000 V, and although it was possible to draw up to 1400 V, the performance degraded above ~900 V. Above this voltage, the rise time of the power supply output increased and multiple bursts of variable power were often seen, usually producing a number of small absorbance peaks (as many as seven were observed) instead of just one large peak. The behavior of the power supply is illustrated in Figure 2. Figure 2a is for 10 ng of Mo taken as an aqueous solution of ammonium molybdate atomized with a single pulse of 50-ms duration; the discharge voltage was 720 V. Figure 2b is for 10 ng of Mn taken as an aqueous solution of the nitrate, atomized with a single pulse of 500-ms duration; the discharge voltage was 920 V. Figure 2c is for 10 ng of Mn taken as an aqueous solution of the nitrate, atomized with a single pulse of 500-ms duration; the discharge voltage was 1180 V.

Table XIII. Variation in Argon Gas Flow Rate with Argon Gas Pressure in the Atomsource

pressure, Torr	measured flow rate, L/min	pressure, Torr	measured flow rate, L/min
10	0.9	40	4.1
15	1.9	50	>4.4
20	2.6	60	>4.4
30	3.5		

Figure 3 presents the dynamic resistance of the Atomsource as a function of pressure. Figure 3 was obtained with the Atomsource power supply in the current regulation mode using a copper cathode with no sample. From this figure one finds that if one is limited to 900 V and wants to increase the power, the pressure must be increased. The problem is that an increase in pressure also means an increase in the flow rate of the argon gas (Table XIII), with a consequent decrease in the residence time of the analyte atoms in the analysis volume, since the Atomsource is not capable of independent control of the pressure and the flow rate of the discharge gas (flow rates of the discharge gas were measured with a Matheson Model 603 flow meter on the atomizer gas inlet). A power of 1000 W could be obtained if the pressure was high enough, but use of higher pressures was found to decrease the sensitivity, presumably because an increase in the gas pressure meant an increased flow rate of the gas (Table XIII), resulting in an increased convectional loss, which more than compensated for any increase in the sputtering rate due to higher power. We have constructed another atomizer that allows independent control of the pressure and the flow rate of the discharge gas (*50*). This allows us to use higher pressures and powers while still maintaining an optimum flow rate of the discharge gas.

The MDX power supply was also used to determine the characteristic mass of the steady-state mode of atomization. This was done in order to compare directly the sensitivity of the steady-state mode of atomization with that of the pulsed and the transient mode of atomization. This is normally not done since the sensitivity of the steady-state mode of atom-

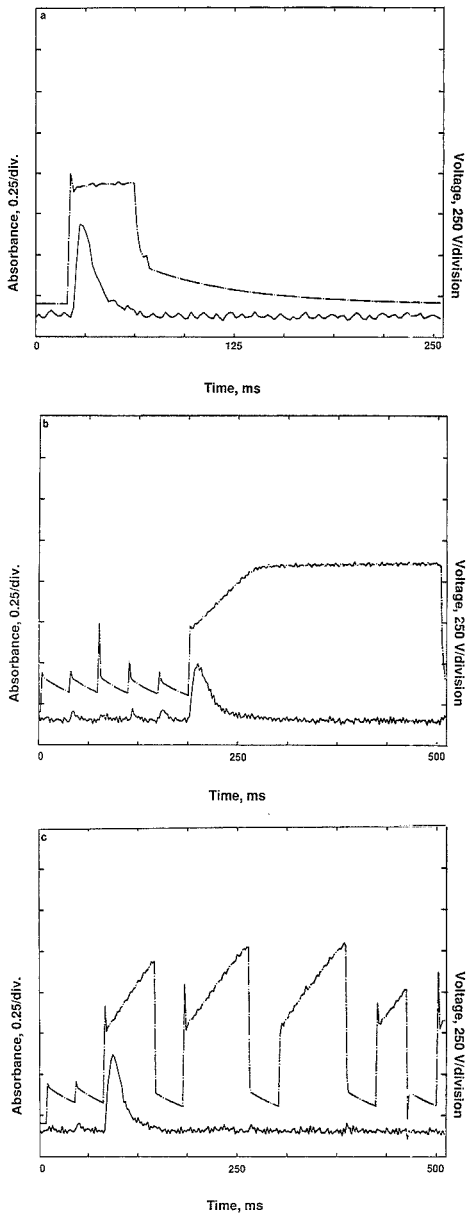

Figure 2. Absorbance profiles and discharge voltages by the pulsed mode of atomization: (a) 10 ng of Mo taken as ammonium molybdate in an aqueous solution. Solid line is absorbance. Experimental conditions: argon pressure, 8 Torr; power, 155 W; discharge current, 205 mA; *V*, 720 V; for other details see Table I. (b) 10 ng of Mn taken as the nitrate in an aqueous solution. Solid line is absorbance. Experimental conditions: argon pressure, 10 Torr, power, 298 W, discharge current, 324 mA, *V*, 920 V; for other details see Table I. (c) 10 ng of Mn taken as the nitrate in an aqueous solution. Solid line is absorbance. Experimental conditions: argon pressure, 8 Torr; power, 298 W; discharge current, 252 mA; V, 1180 V; for other details see Table I.

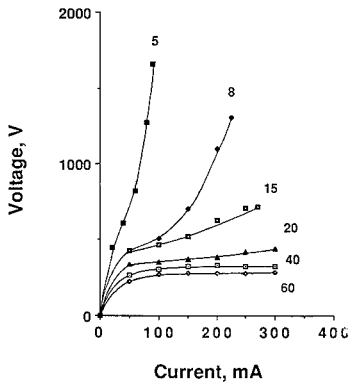

Figure 3. Dynamic resistance as a function of argon pressure for the Atomsource. Pressures are in Torr.

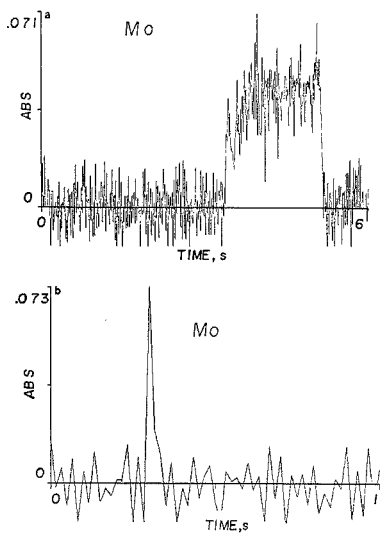

Figure 4. Absorbance profiles of Mo in steel by the steady-state mode of atomization: (a) 1.7-s pulse; (b) 50-ms pulse. Hollow-cathode lamp current was 10 mA. For other details see Tables I and V.

ization is expressed in terms of the concentration required to give 1% absorption, whereas for the pulsed and the transient mode of atomization the sensitivity is expressed in terms of the absolute mass required to give 1% absorption. In order to make the comparison valid we therefore created a pseudo transient signal for the steady-state mode of atomization by varying the steady-state pulse duration. This is illustrated in Figure 4 for 0.49% Mo in the National Bureau of Standards, Standard Reference Material 1264a, High Carbon Steel. Figure 4a is for a pulse of 1.7-s duration, whereas Figure 4b is for a pulse of 50-ms duration. Parts a and b of Figure 4 were obtained by using the Perkin-Elmer spectrophotometer and the "new" Westinghouse hollow-cathode lamp operated at 10-mA current; all other experimental conditions were as listed in Table V. With a lamp current of 3 mA, the results were similar except that the peak-height absorbance was approximately 0.22. Similar results were obtained for the other elements by using the Varian-Techtron spectrophotometer. From Figure 4, it can be seen that it is possible to turn a steady-state signal into a transient signal of the same peak-

Table XIV. Average Mass of Steel Sputtered for the Steady-State Mode of Atomization

instrumental setting of		measured		mass
pressure, Torr	current, mA	power, W	voltage, V	sputtered, μg/s
8	99	53	540	3.4
8	152	97	710	11
10	169	95	560	12
15	151	70	460	3.5
15	200	95	480	9.0

Table XV. Characteristic Mass of the Steady-State vs the Transient and the Pulsed Mode of Atomization

	characteristic mass			characteristic mass ratio	
element	steady state, pg	transient, pg	pulsed, pg	transient/ steady state	pulsed/ steady state
Co	60	130	38	0.46	1.6
Cu	27	8.0	7.5	3.4	3.6
Mn	230	25	27	9.3	8.6
Mo	52	0.11	0.08	473	650
Ni	72	210	100	0.36	0.72
V	990	68	140	15	7.1

height simply by varying the pulse duration, thereby allowing the absolute mass required to give 1% absorption (the characteristic mass) to be determined so that the sensitivity of the steady-state mode of atomization can be compared directly with the pulsed and the transient mode of atomization.

The average mass of steel sputtered per second at the various experimental conditions is shown in Table XIV. The sensitivity of the steady-state mode of atomization expressed as the characteristic mass is presented in Table XV. When this characteristic mass is compared with that of the pulsed and the transient mode of atomization, in most cases the characteristic mass of the pulsed and the transient mode of atomization is lower (in some cases, much lower) than that of the steady-state mode of atomization, the exceptions being Co and Ni. Both of these elements also show a significant improvement in sensitivity for the pulsed mode of atomization over the transient mode of atomization, which is important to note. The sensitivity of the steady-state mode of atomization is not likely to improve since the maximum sensitivity for the steady-state mode of atomization is obtained for relatively low-power discharges; there is therefore no possibility for improving the sensitivity of the steady-state mode of atomization by changing the experimental conditions. This is in contrast with the pulsed and the transient mode of atomization, the sensitivity of which is at present limited by the usable power available from the present power supplies. The sensitivity of the pulsed and the transient mode of atomization, but not the steady-state mode of atomization, can be also expected to increase with the use of a faster detection system because a faster detection system will allow one to follow the rapidly rising peak-height absorbance without any distortion caused by the relatively long time constant of the slower detection system. There is therefore a lot of room for improvement in the sensitivity of the transient mode and especially of the pulsed mode of atomization that is not possible for the steady-state mode of atomization. When the above factors are taken into account in light of the present sensitivity, it may reasonably be expected that the pulsed mode of atomization can be made at least as sensitive as GFAAS for most elements.

Kinetic Modeling. In our earlier work (*1*), it was concluded that the entry of atoms into and the loss of atoms from the analysis volume of the Atomsource could be described by eq 1 and the kinetic equations derived from it in the Theory. At that time it was stated that it was not known which of the rate constants corresponded to k_1, the rate constant for atom entry into the analysis volume, and which corresponded to k_2, the rate constant for atom loss from the analysis volume. Parts a and b of Figure 5 present absorbance pulses for 50 ng of Ag and Au, respectively, obtained with the Perkin-Elmer spectrophotometer for a discharge current of 150 mA at an argon pressure of 6 Torr. The two absorbance profiles have similar rise times but dissimilar fall times. Since they were both atomized at the same pressure (and therefore, the same argon gas flow rate), they should have similar values for k_2, but not necessarily for k_1. That this should be so can be seen from the results of Gough et al. (*15*), who found that the analyte atoms are efficiently entrained within the flow of the argon discharge gas. If this is so, the mechanism of atom loss would be by diffusion/convection of the analyte atoms out of the analysis volume, which should be roughly similar for all elements at a given pressure and flow rate if they are entrained in the argon discharge gas. This seems to indicate that for the low-sensitivity (low-power) experimental conditions deliberately used to obtain these absorbance peaks, atomization of the sample is the rate-limiting step. Since the smaller of the two rate constants corresponds to the rate-limiting step, k_2 must be greater than k_1 for Figure 5.

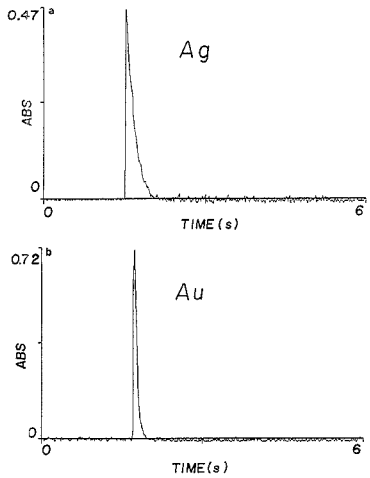

Figure 5. Absorbance profiles by the transient mode of atomization: (a) 50 ng of Ag taken as the nitrate in an aqueous solution. Experimental conditions: argon pressure, 6 Torr; discharge current, 150 mA; Perkin-Elmer hollow-cathode lamp, hollow-cathode lamp current, 13 mA; spectral band-pass, 0.7 nm; Ag wavelength, 328.1 nm. (b) 50 ng of Au taken as the chloride in an aqueous solution. Experimental conditions: argon pressure, 6 Torr; discharge current, 150 mA; Cathodeon hollow-cathode lamp, hollow-cathode lamp current, 12 mA; spectral band-pass, 0.7 nm; Au wavelength, 242.8 nm.

Table IV shows the high-sensitivity (high-power) experimental conditions used for the pulsed mode of atomization, as explained in the Theory. The rate constants for the pulsed mode of atomization are presented in Table XVI. Figure 6 illustrates how the rate constants are determined and the subsequent curve-fitting to the experimental data is done by using eq 1 and the parameters given in Table XVI for 10 ng of Ni. Preliminary assignments of the determined rate constants as k_1 or k_2 were made for each element as explained in the Theory. The absorbance profiles obtained with the high-sensitivity (high-power) experimental conditions for the pulsed mode of atomization gave profiles that had dissimilar

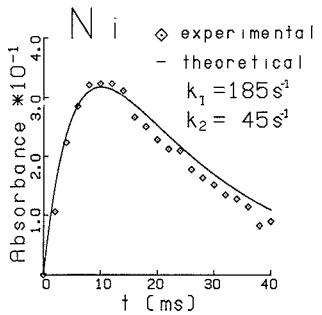

Figure 6. Rate constant determination for 10 ng of Ni taken as the nitrate in an aqueous solution. For other details see Tables I and IV.

Table XVI. Rate Constants for the Pulsed Mode of Atomization

element	mass, ng	A_0[a]	k_1, s^{-1}	k_2, s^{-1}	k_1/k_2
Al	1	0.61	740	105	7.0
Ag	1	0.25	100	52	1.9
Au	10	0.60	90	26	3.5
Cd	0.1	0.59	170	110	1.5
Co	10	0.92	160	58	2.8
Cr	0.01	0.47	750	310	2.4
Cu	1	0.35	140	90	1.6
Fe	10	0.94	115	87	1.3
Mg	0.1	0.37	500	140	3.6
Mn	1	0.18	160	80	2.0
Mo	10	1.15	200	110	1.8
Ni	10	0.50	185	45	4.1
Pb	10	0.23	160	120	1.3
V	10	0.31	190	40	4.8

[a] A_0 is defined by eq 2.

rise times and similar fall times, which would indicate that now $k_1 > k_2$. An estimate of the theoretical residence time of the analyte atoms within the ATOMSOURCE at an argon pressure of about 8 Torr gave a value of about 12 ms, which corresponds to $k_2 = 80$ s^{-1}. The effect of diffusion was neglected in this calculation, so these numbers are very approximate. Nevertheless, when the rate constants in Table XVI are averaged, we find that they have average values of $k_1 = (150 \pm 40)$ s^{-1} and $k_2 = (80 \pm 40)$ s^{-1}. Although not conclusive, these results do lend support to the rate constant assignments. The rate constants for Al, Cr, and Mg are not very reliable. The reason for this is that their absorbance profiles had a rise time of only 2 ms, which was the time constant for the detection system, so there were no data points on the rising portion of their absorbance profiles, making it impossible to obtain reliable values for their rate constants.

As explained in the Theory, there are two experiments which would allow the unambiguous assignment of the rate constants. The first experiment was performed for Al, Au, Mn, and Mo. Figure 7 shows the results for Mn; the results for the other elements are similar. Figure 7a shows the experimental absorbance and discharge voltage of a low-power discharge and 10 ng of Mn as an aqueous solution of the nitrate. Figure 7b shows the absorbance of Mn (on a logarithmic scale) as function of time, where the arrow indicates the point at which the voltage was terminated. Using the data up to this point the curve was analyzed in the usual way to obtain values of k_a and k_b. The slope of line A represents $-k_a$ (eq 3) and the slope of line B represents $-k_b$ (eq 4). At the point where the voltage is cut off, the only process occurring is the loss of analyte atoms, as explained earlier, which is the process represented by k_2. Figure 7b shows that the slope of

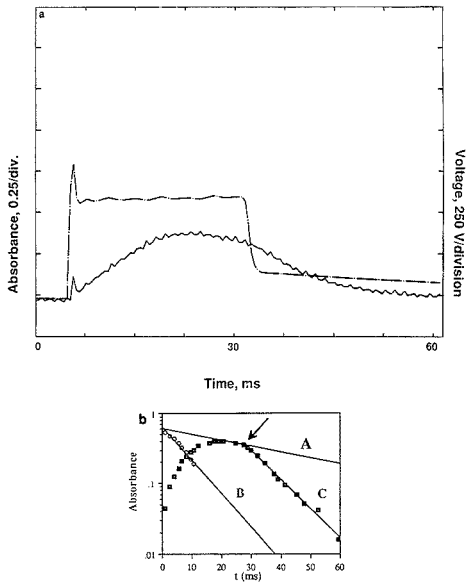

Figure 7. Low-power atomization of 10 ng of Mn taken as the nitrate in an aqueous solution. (a) Experimental absorbance and discharge voltage. Solid line is absorbance. Experimental conditions: argon pressure, 10 Torr; power, 120 W; discharge current, 195 mA; V, 620 V; for other details see Table I. (b) Absorbance (plotted on a logarithmic scale) vs time for Figure 7a. The arrow shows the time at which the voltage was switched off. (A) line corresponding to B_1' (eq 4); (B) line corresponding to ΔB (eq 5); (C) line with slope = $-k_2$.

the plot after the voltage is cut off is equal to the slope of line B, or $-k_b$. Therefore, in this experiment using low power (Figure 7), k_2 is the larger of the two rate constants. The value of $k_2 = 95$ s^{-1} obtained from these figures is in agreement with the theoretical estimate of $k_2 = 80$ s^{-1}, whereas the value of k_1 was found to be 19 s^{-1}.

The second experimental approach was used with only Mn using the high-sensitivity (high-power) experimental conditions given in Table IV. The rate constants were $k_1 = 160$ s^{-1} and $k_2 = 80$ s^{-1}. The value of k_1 has now increased for the more vigorous (high-power) discharge, whereas the value of k_2 has remained constant, as expected from the Theory. These experiments have shown that for the low-power experimental conditions, $k_1 < k_2$, whereas for the high-power experimental conditions used for the pulsed mode of atomization, $k_1 > k_2$. Since the maximum sensitivity is obtained when $k_1 \gg k_2$, it can be seen from Table XVI that there is still room for improvement in the sensitivity of the pulsed mode of atomization.

Analytical Calibration Curves. Thus far the characteristic mass has been evaluated by using peak height and not peak-area absorbance. This is because it has been found that, for the Atomsource equipment (with the limitations imposed by its power supply and gas regulation), the characteristic mass for peak-height absorbance (the mass of analyte required to give a peak-height absorbance of 0.0044) is lower (more sensitive) than the characteristic mass for peak-area absorbance (the mass of analyte required to give an peak-area absorbance of 0.0044 absorbance s). The characteristic mass for peak-area absorbance was determined for Au and Mo and is compared with the characteristic mass for peak-height absorbance in Table XVII. The absorbance profiles obtained with the Atomsource by the pulsed and the transient mode of atom-

Table XVII. Peak Height vs Peak Area Characteristic Mass

element	hollow-cathode lamp type	hollow-cathode lamp current, mA	characteristic mass peak height, pg	characteristic mass peak area, pg	characteristic mass ratio peak height/peak area
Au	Westinghouse	6	47	1420	30
Mo	Perkin-Elmer	10	11	1470	134
Mo	Perkin-Elmer	3	4.8	550	115
Mo	Westinghouse (old)	3	0.041	1.1	27

ization are of very short duration and therefore have a very small peak-area absorbance, whereas the peak-height absorbance can be considerable. This is because the Atomsource, as mentioned previously, does not allow independent control of the pressure and the flow rate of the argon discharge gas. Preliminary results (*50*) have been obtained for Fe for the pulsed mode of atomization with a laboratory-built atomizer (to be henceforth called the new atomizer) of similar geometry (to the Atomsource) but which allows independent control of the pressure and the flow rate of the argon discharge gas. These preliminary results have shown an increase in the peak-height absorbance by a factor of 2, whereas the peak-area absorbance increased by an order of magnitude. Another reason for the high peak-area characteristic masses in Table XVII is that the units of absorbance seconds (this definition is taken from GFAAS) for the characteristic mass do not accurately reflect the true sensitivity of the much faster peaks generated by the pulsed and the transient mode of atomization for cathodic sputtering. In GFAAS, absorbance peaks have similar peak-height and peak-area absorbances and so a peak area of 0.0044 absorbance s would normally be below the detection limit. For the pulsed and the transient mode of atomization, peak-area absorbances of 0.00044 are still above the detection limit, so a peak-area characteristic mass of 0.00044 absorbance s may be more appropriate than 0.0044 absorbance s for peaks generated by the pulsed and the transient mode of atomization for cathodic sputtering. If this alternative definition is used for the peak-area characteristic mass, the peak-area characteristic masses in Table XVII would be 1 order of magnitude smaller. With the new atomizer, the peak-area characteristic mass should be similar to the peak-height characteristic mass.

Analytical calibration curves for aqueous solutions of Cd, Cr, Cu, Fe, Mg, and Mn have been determined for both peak-height and peak-area absorbance using copper and graphite cathodes. Peak-area absorbance has been found to give linear analytical calibration curves, usually extending over a range of mass up to 10^3 ng, whereas peak-height absorbance was found to give linear analytical calibration curves of greater sensitivity (defined as 0.0044 absorbance or absorbance s divided by the slope of the analytical calibration curve), but over a smaller range of analyte mass. An example is Mg atomized from a copper cathode, the analytical calibration curves for which are shown in Figure 8. The characteristic mass of Mg from Figure 8 is 26 pg for peak-height absorbance and 700 pg for peak-area absorbance, whereas the linear dynamic ranges for the analytical calibration curves are up to 5 and 1000 ng, respectively.

Matrix Interferences. It is generally desirable to use peak-area absorbance for the analysis of real samples since peak-area absorbance is not subject to variations as a result of change in the kinetics of sample atomization/entry into the analysis volume, whereas the peak-height absorbance is. The independence of peak-area absorbance on the kinetics of atomization is shown by the preliminary results of our matrix interference studies made by using the transient mode of atomization. Interelement (matrix) interferences were studied on a one-to-one basis (i.e., one analyte and one matrix species), using a fixed mass of analyte element and an increasing mass

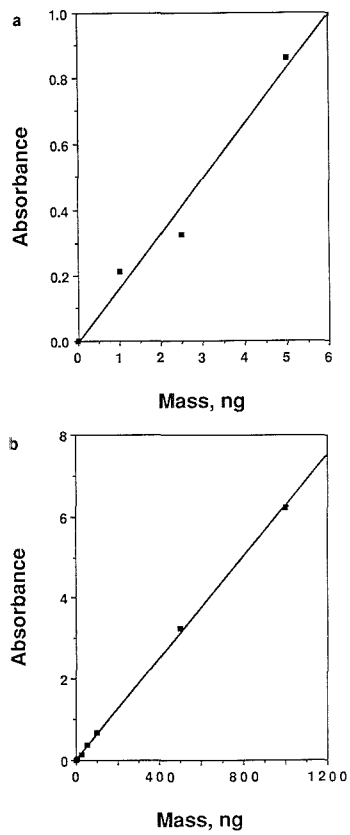

Figure 8. Analytical calibration curves for Mg taken as the nitrate in an aqueous solution: Hollow-cathode lamp current, 2 mA; for other details see Tables I and III. (a) peak-height absorbance; (b) peak-area absorbance.

of the matrix species. Satisfactory recoveries (100 ± 10%) were obtained for a matrix to analyte ratio of up to 100 to 1 for Fe in a matrix of $Ni(NO_3)_2$ atomized from a copper cathode for peak-area absorbance, but not for peak-height absorbance. This also confirms our experimental observations that under the vigorous discharge conditions usual in the transient mode of atomization, peak-height absorbances are more subject to erratic conditions of discharge then are peak-area absorbances. The interferences of alkali and alkali-earth chlorides with various elements were also examined. Severe interferences were found for both peak height and peak-area absorbance. An example of this interference is shown in Figure 9. Figure 9a is the absorbance profile for 50 ng of Au atomized from a copper cathode. Figure 9b is an absorbance profile for 50 ng of Au in the presence of a 400-fold mass excess of NaCl

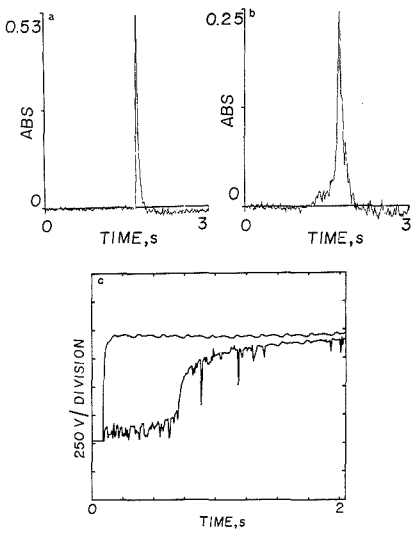

Figure 9. Interference of NaCl with Au taken as the chloride in an aqueous solution: (a) 50 ng of Au; (b) 50 ng of Au + 10 μg of NaCl. Experimental conditions: argon pressure, 6 Torr; discharge current, 150 mA; Cathodeon hollow-cathode lamp, hollow-cathode lamp current, 12 mA; spectral band-pass, 0.7 nm; Au wavelength, 242.8 nm. (c) discharge voltage for parts a and b. The time scale of part c is not the same as that of a and b.

atomized from a copper cathode. Figure 9c gives the discharge voltages for parts a and b of Figure 9. Since parts a and b of Figure 9 were obtained by using the Perkin-Elmer spectrophotometer, it was not possible to obtain the simultaneous absorbance and voltage traces that were obtained by using the Varian-Techtron spectrophotometer and, therefore, the time scale of parts a and b of Figure 9 does not match that of Figure 9c and the exact time that the discharge was initiated must be inferred for parts a and b of Figure 9. It seems that the interference being observed in this case is a result of the formation of a relatively nonconducting surface layer by NaCl. This type of interference had not been observed in the other studies of matrix interference presumably because the dried solution residue was still conductive.

rf Discharge. Cathodic sputtering occurs when atoms of the discharge gas are ionized and subsequently accelerated in the cathode fall as a result of the very steep potential gradient in the cathode fall where the entire applied potential drops. For an insulating surface, such as provided by NaCl matrix, the surface quickly acquires a positive charge, repelling subsequent discharge gas ions and thus slowing any further sputtering. For conducting matrices, the use of peak-area absorbance rather than peak-height absorbance eliminated the effect of this interference. For real samples, particularly those that are nonconductors, however, a more comprehensive solution is needed. Nonconducting powders have been analyzed by CSGD by being diluted with a conducting matrix and pressed into a pellet (*15–19*). Nonconducting substances have also been analyzed directly by CSGD by using an rf (radio-frequency) discharge (*12*, *21–23*, *38*), in which a very high frequency (typically 13.56 MHz) ac power supply is used to prevent the build-up of a surface charge on the cathode, thus allowing even insulators to be sputtered. In addition to not requiring dilution of the sample with and possible contamination from a conducting matrix, rf sputtering has the advantage that it can be used for the analysis of solution residues by the pulsed mode of atomization. Indeed, rf sputtering can be considered a high-frequency variant of the pulsed mode of atomization. The use of an rf power supply will also increase the efficiency of the discharge. With increasing frequency of the rf discharge it is possible to drive more current through the discharge with a given voltage. Also, the addition of a bias current will increase the discharge current significantly. Increasing the frequency from 13.56 to 40.68 MHz will make the sputtering even more vigorous. It is our opinion that the use of pulsed atomization or rf sputtering would be essential for the analysis of real samples, to eliminate any possible interferences due to differences in the sample conductivity. We are at present examining the application of the pulsed mode of atomization and rf sputtering to the elimination of matrix interferences in the analysis of solution residues by CSGD.

CONCLUSIONS

As predicted by the Theory (kinetic modeling), greater (sometimes, much greater) sensitivities are given by the pulsed and the transient mode of atomization compared with the steady-state mode of atomization, and this advantage in sensitivities is bound to increase in favor of the pulsed and the transient mode of atomization with better instrumentation, whereas for the steady-state mode of atomization, with its kinetic limitations, no such increase in sensitivities is possible.

ACKNOWLEDGMENT

The authors are grateful to Analyte Corporation for the supply of an Atomsource at half price. The authors also acknowledge the donation of optical components by T. M. Rettberg of Varian Techtron Pty. and the donation of an Atomsource by Varian Canada, Ltd.

LITERATURE CITED

(1) Chakrabarti, Chuni L.; Headrick, Kurt L.; Hutton, J. Craig; Marchand, Bruno; Back, Margaret. H. *Spectrochim. Acta* **1989**, *44B*, 385–394.
(2) Chakrabarti, Chuni L.; Headrick, Kurt L.; Hutton, J. Craig; Back, Margaret H. *Colloq. Spectrosc. Int., 26th* **1989**, Invited Paper no. 4, 10–20.
(3) Chakrabarti, Chuni L.; Headrick, Kurt L.; Bertels, Peter C.; Back, Margaret H. *J. Anal. At. Spectrom.* **1988**, *3*, 713–723.
(4) Russel, Barbara J.; Walsh, Alan *Spectrochim. Acta* **1959**, *15*, 883–885.
(5) Stirling, A. J.; Westwood, W. D. *J. Appl. Phys.* **1970**, *41*, 742–748.
(6) Walsh, Alan *Appl. Spectrosc.* **1973**, *27*, 335–341.
(7) Gough, David S. *Anal. Chem.* **1976**, *48*, 1926–1931.
(8) McDonald, D. C. *Anal. Chem.* **1977**, *49*, 1336–1339.
(9) Bruhn, C. G.; Harrison, Willard W. *Anal. Chem.* **1978**, *50*, 16–21.
(10) McCamey, D. A.; Niemczyk, T. M. *Appl. Spectrosc.* **1980**, *34*, 692–695.
(11) Bernhard, Alan E. *Spectroscopy* **1987**, *2*, 24–27.
(12) Ohls, Kunt *Fresenius' Z. Anal. Chem.* **1987**, *327*, 111–118.
(13) Stephens, Roger *J. Anal. At. Spectrom.* **1988**, *3*, 1137–1139.
(14) Kim, Hyo J.; Piepmeier, Edward H. *Anal. Chem.* **1988**, *60*, 2040–2046.
(15) Gough, David S.; Hannaford, Peter; Lowe, R. Martin *Anal. Chem.* **1989**, *61*, 1652–1655.
(16) Winchester, Michael R.; Marcus, R. Kenneth *Appl. Spectrosc.* **1988**, *42*, 941–944.
(17) El Alfy, S.; Laqua, Kurt; Massmann, H. *Fresenius' Z. Anal. Chem.* **1973**, *263*, 1–14.
(18) Buzási-Györfi, A.; Caroli, Sergio; Alimonte, Alessandro; Senofonte, Oreste *Acta Chim. Hung.* **1983**, *113*, 295–302.
(19) Caroli, Sergio; Alimonte, Alessandro; Zimmer, Karoly. *Spectrochim. Acta* **1983**, *38B*, 625–631.
(20) Mai, H.; Scholze, H. *Spectrochim. Acta* **1987**, *42B*, 1187–1204.
(21) Grimm, W. *Spectrochim. Acta* **1968**, *23B*, 443–454.
(22) Slevin, P. J.; Harrison, Willard W. *Appl. Spectrosc. Rev.* **1975**, *10*, 201–255.
(23) Broekaert, José A. C. *J. Anal. At. Spectrom.* **1987**, *2*, 537–542.
(24) Caroli, Sergio *J. Anal. At. Spectrom.* **1987**, *2*, 661–680.
(25) Caroli, Sergio; Senofonte, Oreste; Violonte, Nicola; Falasca, Oriano; Marconi, Achille; Barbieri, Mauro *J. Anal. At. Spectrom.* **1986**, *1*, 231–235.
(26) Wagatsuma, Kazuaki; Hirokawa, Kichinosuke *Anal. Chem.* **1988**, *60*, 702–705.
(27) Caroli, Sergio; Petrucci, F.; Alimonte, Alessandro; Zaray, Gy. *Spectrosc. Lett.* **1985**, *18*, 609.
(28) Ko, J. B. *Spectrochim. Acta* **1984**, *39B*, 1405–1423.
(29) Walters, P. E.; Human, H. G. C. *Spectrochim. Acta* **1981**, *36B*, 585–589.
(30) Gough, David S.; Hannaford, Peter; Walsh, Alan *Spectrochim. Acta* **1973**, *28B*, 197–210.
(31) Bubert, H. *Spectrochim. Acta* **1984**, *39B*, 1377–1387.

(32) Patel, B. M.; Winefordner, James D. *Spectrochim. Acta* **1986**, *41B*, 469-474.
(33) Gough, David S.; Meldrum, J. R. *Anal. Chem.* **1980**, *52*, 642-646.
(34) Smith, B. W.; Omenetto, Nicolo; Winefordner, James D. *Spectrochim. Acta* **1986**, *39B*, 1389-1393.
(35) Harrison, Willard W.; Hess, Kenneth R.; Marcus, R. Kenneth; King, Fred L. *Anal. Chem.* **1986**, *58*, 341A-356A.
(36) Hess, Kenneth R.; Harrison, Willard W. *Anal. Chem.* **1986**, *58*, 1696-1702.
(37) Harrison, Willard W.; Bentz, B. L. *Prog. Anal. Spectrosc.* **1988**, *11*, 53-110.
(38) Duckworth, Douglas C.; Marcus, R. Kenneth *Anal. Chem.* **1989**, *61*, 1879-1886.
(39) Westwood, W. D. *Prog. Surf. Sci.* **1976**, *7*, 71-111.
(40) Fang, D.; Marcus, R. Kenneth *Spectrochim. Acta* **1988**, *43B*, 1451-1460.
(41) Stocker, B. J. *Br. J. Appl. Phys.* **1961**, *12*, 465-468.
(42) Chapman, Brian *Glow Discharge Processes*; John Wiley & Sons: New York, 1980.
(43) Hannaford, Peter; Walsh, Alan *Spectrochim. Acta* **1988**, *43B*, 1053-1068.
(44) L'vov, Boris V. *Atomic Absorption Spectrochemical Analysis*; Adam Hilger: London, 1970.
(45) Bernhard, Alan E.; Khan, H. L. 35th Canadian Spectroscopy Conference, **1988**, Paper No. 67.
(46) Chang, Shye-Bin; Chakrabarti, Chuni L. *Prog. Anal. Atom. Spectrosc.* **1985**, *8*, 83-191.
(47) L'vov, Boris V.; Nikolaev, V. G.; Norman, E. A.; Polzik, L. K.; Mojica, M. *Spectrochim. Acta* **1986**, *41B*, 1403-1053.
(48) Piepmeier, Edward H. *Spectrochim. Acta* **1989**, *44B*, 609-616.
(49) Wagenaar, H. C.; Novotný, I.; de Galan, Leo *Spectrochim. Acta* **1974**, *29B*, 301-317.
(50) Unpublished work, Carleton University, 1989.

RECEIVED for review July 11, 1989. Accepted December 5, 1989. The authors are grateful to the Natural Sciences and Engineering Research Council of Canada (NSERC) for financial support of this research project. J. C. Hutton is also grateful to NSERC for the award of a postgraduate scholarship. Part of this paper was presented as an invited keynote paper at the XXVI Colloquium Spectroscopicum Internationale, July 2-9, 1989, Sofia, Bulgaria.

Long Path Atomic/Ionic Absorption Spectrometry in an Inductively Coupled Plasma

Michael A. Mignardi, Benjamin W. Smith, and James D. Winefordner*

Department of Chemistry, University of Florida, Gainesville, Florida 32611

A novel approach was taken to increase the atomic/ionic absorption path length in an inductively coupled plasma (ICP) by using a water-cooled quartz "T-shaped" bonnet. Atomic and ionic absorption spectrometry was performed utilizing a continuum source and line sources. Absorption spectra of synthetic multielement solutions were collected with a photodiode array. Sample introduction into the ICP was accomplished with an ultrasonic nebulizer. To prevent the bonnet from cracking, low radio frequency powers were utilized (i.e., 400-600 W). Plasma diagnostics were performed to study the plasma temperature and electron number density within the "T-shaped" bonnet. Analytical figures of merit were found to be better than those obtained from previous work attempted with inductively coupled plasma atomic absorption spectroscopy and approaching that of flame atomic absorption spectroscopy.

INTRODUCTION

Since the beginning of flame atomic absorption spectrometry (AAS), several workers have tried to enhance the analytical sensitivity by increasing the absorption path length of the atomic absorption reservoir (*1*). Fuwa and Vallee performed a study of the Beer-Lambert law for absorption of molecules in solution as a model for the investigation of atomic absorption (*2*). In their work, a long path absorption cell (90-250 cm) was made of Vycor for flame AAS. The combustion flame burner was positioned such that the tail flame was directed into one end of the absorption cell. Source radiation from a hollow cathode lamp (HCL) passed through the absorption cell and then through focusing optics onto a spectrograph. Compared to conventional flame AAS, they were able to increase the sensitivity for some elements by about 2 orders of magnitude (*2, 3*). Other work using this long path absorption cell showed that the diameter and reflection from the inner walls of the absorption tube affect the absorbance (*4*). The smaller the diameter (up to 1 cm), the higher will be the concentration of absorbing atoms and hence the higher the absorbance (*2, 4*). Earlier stages of the work by Fuwa and Vallee involved placing the tube in a "T-shaped" fashion over the flame burner and thus deflecting the flame in two directions (rather than in one direction as previously done) (*2*); however, this system failed to yield satisfactory results with AAS. Rubeska also used Fuwa long absorption cells in a T-shaped fashion over a flame. In this setup, the absorption cell was electrically heated so as to increase the mean lifetime of free atoms (*1*). With the long path absorption cell, good sensitivities were obtained and the formation of oxides for some elements was reduced since the tube shielded the flame gases from the oxidizing atmosphere.

Most work in AAS has utilized flames and electrothermal atomizers as the atom reservoirs. The choice of an atom reservoir and its atomization efficiency is obviously one of the most important considerations in AAS. Compared to flames and electrothermal atomizers, argon inductively coupled plasmas (ICPs) are excellent vaporization, atomization, excitation, and ionization sources for atomic spectroscopy. Several attractive properties of the ICP are (i) high plasma temperatures and number density of free electrons, (ii) longer residence times of free atoms in an inert chemical environment, and (iii) reduced formation of chemical compounds (e.g., refractory compounds) (*5-8*). There are, however, several disadvantages (*9, 10*): (i) large dilution of gaseous analyte atoms; (ii) small absorption path length; (iii) ionization losses (i.e., a smaller atom ground state population); (iv) a broad continuum spectral background; and (v) higher cost and difficulty of operation compared to flames and electrothermal atomizers. Because of these disadvantages, analytical work in ICP-AAS has been limited.

In 1966, Wendt and Fassel attempted to overcome the small absorption path length in ICPs by utilizing a multipass system for ICP-AAS (*7*). In their setup, a collimated beam from an

* To whom correspondence should be sent.

0003-2700/90/0362-0586$02.50/0

HCL made three passes through an ICP with mirrors placed around the plasma and then into a spectrometer. They achieved detection limits and sensitivities comparable to the best reported flame-AAS values at that time. Veillon and Margoshes uses a modified Wendt and Fassel ICP torch (without the most central concentric tube) in a single-pass system with a modulated source and phase sensitive amplifier (8). They did not observe some of the chemical interferences commonly observed in flames. Biancifiori and Bordonali, using a single-pass ICP-AAS system, also noticed a decrease in chemical interferences compared to flame-AAS (*11*, *12*); their ICP configuration consisted of an absorption chamber inserted into a single torch tube having a length much longer than usual. Veillon and Margoshes concluded that except for a few refractory elements, the ICP did not appear to be a suitable replacement for the chemical flame in AAS. Like Fuwa and Vallee, Greenfield conducted work involving a physical increase in the absorption path length, but, in an ICP (*13*). Greenfield was able to extend the outer sheath of the ICP torch to 60 cm and later found he was able to bend the extended plasma "tail flame" at right angles. Ultimately, the outer sheath of the ICP took on the shape of a "T". When one end of the T was closed with an optical flat, the plasma tail-flame was forced to turn away from the optical flat. A modulated HCL was collimated and sent through the optical flat and into a spectrometer near the open end of the T. Temperatures within the T ranged from 3000 to 8000 K. The high-temperature plasma in the T should minimize chemical interferences due to the formation of stable refractory compounds of the element under investigation. Because of the extended probe region above the ICP load coil, the potential for spectral emission interferences was greatly reduced. Also, a lower background radiation was observed by the tail-flame, thus indicating an advantage over combustion flames in AAS.

A decade later, Abdallah et al. (*14*) and Mermet and Trassy performed work on increasing the absorption path length in a ICP (*10*). Here, the absorption path length was increased by having the light beam pass through the plasma channel along the symmetry axis. The plasma torch was turned on its side and a beam of radiation, focused with a lens at the base of the torch, was sent down the torch axially. The outer sleeve of the torch was extended to further enhance the lifetime of neutral atoms in the plasma. They achieved detection limits and sensitivities competitive with flame-AAS and approaching those of electrothermal atomizers. Other work by Magyar and Aeschbach involved removing the atomization cell from a commercial AA instrument and replacing it with an ICP (*6*). The enhanced atomic emission signal from the ICP made it necessary to use higher intensity HCLs than for flame-AAS. Their results indicated the possible use of ICP-AAS for the determination of metals in complex compounds, which do not efficiently dissociate in combustion flames. Downey and Nogar performed intracavity dye laser absorption spectrometry (IDLAS) by placing an ICP within the cavity of a pulsed, flashlamp-pumped dye laser for AAS. They achieved an enhancement factor of approximately 170 relative to single-pass absorption in an ICP (*9*). Limits of detection (LODs) in the parts-per-million range were obtained for sodium and barium. These workers were able to take advantage of the ICP as an ion source. The tunability of the dye laser allowed investigation of barium ion, Ba(II), absorption at 614.1 nm. Umemoto and Kubato performed ionic absorption spectrometry of scandium in an ICP. In their setup, collimated radiation from a continuum source made two passes through the ICP and into a high-resolution spectrometer. They performed diagnostic studies of the effect of plasma height and radio frequency (rf) power on ionic absorbance. The detection limits they achieved were comparable

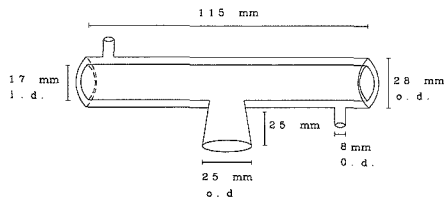

Figure 1. Detailed drawing of T-shaped bonnet.

to ICP-AES (*15*). Several workers have also performed some successful fundamental studies on ICP argon chemistry and plasma diagnostics using atomic and ionic absorption spectrometry (*16–23*). In these studies, continuum sources, HCLs, microwave induced plasmas, and ICPs were used as radiation sources.

Recently, Blades and Ng have independently performed atomic absorption studies using long absorption path lengths. Liang and Blades achieved excellent sensitivities utilizing an atmospheric pressure capacitively coupled plasma and a T-shaped device (*24*). Ng et al. achieved sensitivities comparable to the work performed by Aeschbach utilizing long path absorption within the Beenakker cavity of a microwave-induced plasma (*25*).

In this work, further investigation has been performed utilizing an ICP for AAS studies. An attempt to increase the absorption path length of the ICP was made with the design of a cooled-quartz T-shaped bonnet for the ICP. Unlike Greenfield's T-shaped torch, this bonnet was detachable from the torch, positioned closer to the load coil, and water cooled. A detailed description of the T-shaped bonnet is given. An evaluation of this T-shaped bonnet was performed by atomic and ionic absorption spectrometry in an ICP for pure and multielement synthetic solutions with a continuum source and several line sources (HCLs). Analytical figures of merit and plasma diagnostics (plasma temperature and electron number densities) are given as well.

EXPERIMENTAL SECTION

Design and Construction of the T-Shaped Bonnet. A detailed drawing of the T-shaped bonnet is shown in Figure 1. The bonnet was constructed within our glass shop of Spectrosil quartz tubing (Thermal American Fused Quartz, Monteville, NJ). Tubing for the T portion consisted of two concentric tubes. The tubing used for the outside portion of the T was 25 mm i.d. and 28 mm o.d., and the tubing used for the inside portion of the T was 17 mm i.d. and 19 mm o.d. These two tubes were fused together at their ends so as to create a water jacket between them. The length of the T was 115 mm. The tubing for the stem of the T was 22 mm i.d. and 25 mm o.d. and was 25 mm long. Intake and return of chilled water to the T-shaped bonnet was via 6 mm i.d. and 8 mm o.d. tubing. Chilled water to the bonnet was kept at ≤5 °C (Neslab Instruments, Inc., Portsmouth, NH). The flow rate of water to the bonnet was 7–11 L h^{-1}. The T-shaped bonnet was mounted in two nylon clamps attached to an X,Y,Z-translation axis mount such that the T-shaped bonnet could be carefully positioned on top of the ICP. Figure 2 is a diagram of the bonnet within the nylon clamps. The ICP torch was also mounted on an X,Y,Z-translation axis mount such that the torch could be properly positioned within the T-shaped bonnet. Translation of both the ICP torch and bonnet allowed easy manipulation of the setup and the ability to optically probe different regions within the T.

Plasma Operation. Before plasma ignition, chilled water was allowed to flow through the T-shaped bonnet and ICP load coil for approximately 5 min to ensure that the bonnet was properly cooled. Ignition of the plasma with the torch inside the T-shaped bonnet was difficult; therefore, before plasma ignition, the ICP torch had to be lowered such that the bottom of the bonnet stem was at least 20 to 25 mm above the top of the outer sheath of the torch. Once the plasma was ignited in this lowered position, the

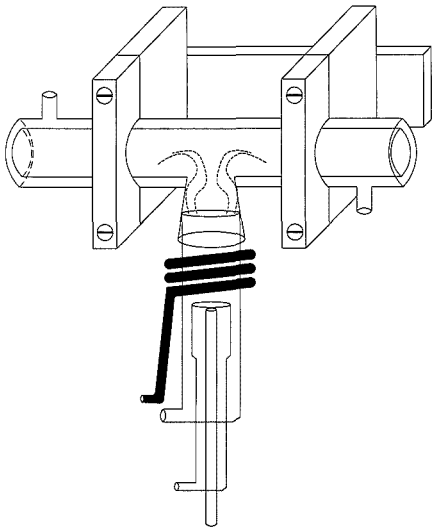

Figure 2. Diagram of ICP torch and bonnet.

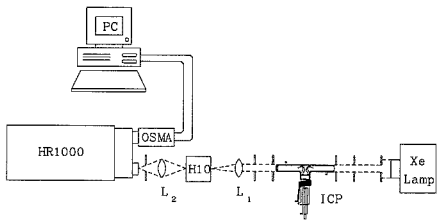

Figure 3. Schematic diagram of CS-ICP-AAS experimental setup.

torch was then slowly raised into the T-shaped bonnet until the center of the longitudinal T portion of the bonnet was approximately 27 mm above the torch load coil. Figure 2 also shows the ICP torch positioned within the T-shaped bonnet during operation. Once in position, the torch was operated as usual. The torch was operated at low powers (i.e., 400–600 W) so as not to overheat and possibly crack the T-shaped bonnet. At these low ICP powers, this experimental setup could be run continuously (the maximum continuous operation at one time was 8 h).

After extended use of this experimental system, and especially after aspiration of high salt concentration into the plasma, an oxide formation was observed within the inner wall of the T-shaped bonnet. Despite this residue formation, there were no analyte memory effects observed within the system. After periodic use, the T-shaped bonnet was removed and immersed in a 10% HNO_3 solution to clean the inner walls of the bonnet. No vitrification of the quartz tubing was observed. Since the T-shaped bonnet is made of quartz, the bonnet acted like a light-pipe; i.e., the plasma continuum emission was reflected from the ends of the bonnet. Most of this plume emission was spatially discriminated against by using appropriate apertures.

Instrumentation. Figures 3 and 4 are schematic diagrams of the optical arrangements used in this work for the continuum and line sources, respectively. The optical probing of atomic and ionic species within the center of the T-shaped bonnet was 27 mm above the ICP load coil. The instrumentation and experimental operating conditions for the continuum source studies were previously described (26). Table I is a list of the instrumentation and operation parameters for the HCL-ICP-AAS studies. All optics used in both setups (see Figures 3 and 4) were of fused silica.

For the HCL-ICP-AAS studies, a 1:1 image of the HCL emission was focused onto a chopper wheel with lens 1, L_1 (5 cm focal length and diameter). A 1:1 image from the chopper wheel to the center

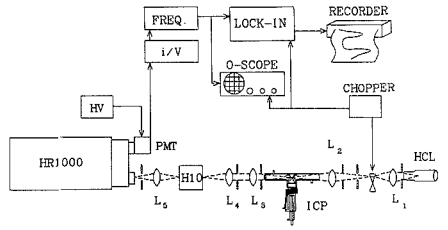

Figure 4. Schematic diagram of HCL-ICP-AAS experimental setup.

Table I. Instrumentation and Operating Parameters for HCL-ICP-AAS

instrumentation	manufacturer and operating parameters
I. ICP	
rf power supply	Plasma-Therm, Inc., Kresson, NJ, Model HPF 2000D
rf frequency	27.12 MHz
forward rf power	400–600 W
reflected rf power	0–20 W
Ar coolant flow rate	14 L min^{-1}
Ar auxiliary flow rate	1.5 L min^{-1}
Ar carrier flow rate	0.9 L min^{-1}
observation height[a]	27 mm
II. ultrasonic nebulizer	
rf power supply	Plasma-Therm, Inc.
rf frequency	1.35 MHz
forward power	37 W
reflected power	3 W
III. HCL	Fisher Scientific, Springfield, NJ
power supply	Heath Co., Benton Harbor, MI, Model EU-703-62
lamp current	3–8 mA
IV. monochromators	Instruments SA, Inc., Metuchen, NJ
predisperser	Jobin-Yvon H10
grating	1200 grooves mm^{-1}
slits	2 mm
linear dispersion	8 nm mm^{-1}
high resolution	Jobin-Yvon HR1000
grating	2400 grooves mm^{-1}
linear dispersion	0.5 nm mm^{-1}
slits	1–2 mm
V. optical chopper	Photon Technology International, Inc., Princeton, NJ, Model OC 4000
modulation frequency	200 Hz
VI. readout	
current amplifier	Keithley Instruments, Inc., Cleveland, OH, Model 427
	1 ms rise time, 10^4 V A^{-1}
nanovolt amplifier	Keithley, Model 103A
	100–300 Hz bandwidth, 100 gain
lock-in amplifier	Princeton Applied Research Corp., Princeton, NJ, Model 186A, 3 s time constant, 1 kHz low-pass filter
strip chart recorder	Fisher Scientific, Recordall, Model 5000

[a] Measured above the load coil.

of the T-shaped bonnet (27 mm above the axial center of the ICP load coil) was made using L_2 (13 cm focal length and 2 cm diameter). The focused radiation at the center of the bonnet was collimated with L_3 (23 cm focal length and 2.5 cm diameter). L_4 (5 cm focal length and diameter) focused the collimated radiation onto the 2-mm entrance slit of the predisperser monochromator. The predisperser minimized any higher orders of emission radiation from the ICP. A 1:1 image from the exit slit of the predisperser was formed at the entrance slit of the HR1000 spectrometer using L_5 (5 cm focal length and diameter). Diaphragms were used throughout the optical path to reduce any stray radiation from the HCL and optical emission from the ICP. The photomultiplier tube (PMT) output from the current-to-voltage amplifier and nanovolt amplifier was acquired by the

lock-in amplifier. The lock-in amplifier was triggered by an external trigger output from the chopper power supply. The optimal slit width (HR1000 monochromator) and PMT high voltage were independently determined for each element studied for an optimal signal-to-noise ratio. Absorption data were collected with a chart recorder.

Sample Preparation. Stock solutions (1000–10000 mg L^{-1} in 2% HNO_3) were obtained from Inorganic Ventures, Inc. (Brock, NJ), for the elements studied. Several synthetic mixtures were made with two to three elements. Working standards were made by serial dilutions of the stock solutions. Distilled, demineralized water (Barnstead Sybron Corp. Boston, MA) was used throughout this work.

Procedure. As discussed previously (*26*), continuum source-ICP-AAS (CS-ICP-AAS) was obtained with the HR1000 set at the fifth order and the predisperser (J-Y H10) set at the first order of the absorption line. Since one complete scan of the photodiode array required 33 ms, 300 data acquisition spectra were averaged for each spectrum for a total acquisition time of 10 s. The transmittance signal of each element was determined as I_a. Although the diaphragms reduced the solid angle of collected ICP emission from the T-shaped bonnet as much as possible from reaching the detector (see Figure 3), any atomic or ionic emission (with the source radiation blocked) that did reach the detector (I_e) was subtracted from I_a. Thus, the transmittance signal for each element was calculated as $I = I_a - I_e$. For each absorption spectrum obtained, a blank spectrum (water aspirated into the ICP) of the incident radiation (I_0) was obtained. The absorption spectrum for each element was determined by $A = \log I_0/I$. All calculations were performed with the supplied OSMA software.

For work involving HCL-ICP-AAS with the T-shaped bonnet, all data were manually manipulated from the chart recorder readings. The light chopper and lock-in amplifier minimized any dc component of emission signals from the ICP. Unlike work with the continuum source, both the J-Y H10 and HR1000 monochromators were operated in first order of the atomic absorption line studied. Blank noise readings were obtained by measuring the peak-to-peak noise on the chart recorder. An instrumental bandwidth of 1 Hz was used. The optimal observation region above the ICP load coil was 27 mm. For both the continuum and line source, the probe beam was directed through the center of the T. This probe beam position seemed the most sensitive for the absorption studies.

Plasma Temperature and Electron Density. Spectroscopic measurements are one of the best means for obtaining spatially and temporally resolved values of temperature and species number densities without perturbing the mechanisms of the plasma or influencing the temperature (*27, 28*). An accurate knowledge of the plasma temperature can lead to a better understanding of analyte vaporization, dissociation, atomization, and ionization processes (*29*). A spectroscopic emission method was performed where neutral iron was selected as the thermometric species. A factor in the line selection process for iron was based on (i) maximal spread in excitation levels, (ii) freedom from plasma spectral interferences, (iii) availability of accurate transition probabilities, and (iv) wavelength proximity, which eliminates the need for calibrating detector instrumentation response with respect to wavelength (*29*). The wavelengths, excitation energies, statistical weights, and transition probabilities were taken from a reference by Fuhr, Martin, and Wiese (*30*).

Determination of relative electron (number) density was based on the measurement of the Stark broadening of an atomic hydrogen line. The H_β (486.1 nm) line was chosen because it is generally free from plasma spectral interferences, has a sufficient intensity for measurement, and has a small half-width (0.1–0.5 nm) and extensive Stark data are available for this line (*31–33*). Both Doppler broadening and instrumental broadening are usually negligible compared to Stark broadening (*32*). For the results presented in this work, the Doppler half widths were deconvoluted from the total line half widths to obtain the Stark half widths. The Doppler half width had less than a 10% effect on the total line half width.

RESULTS AND DISCUSSION

Absorption Spectra. Unlike conventional line sources, the broad band emission from continuum sources allows one to optically probe both atomic and ionic absorption transitions. The ICP allows efficient atomization and ionization of many elements. The HR1000 high-resolution monochromator was operated in the fifth or fourth order to nearly fully resolve atomic and ionic absorption lines. The use of a photodiode array allowed real time, simultaneous multiwavelength measurements. Figure 5 is an atomic absorption spectrum obtained for 0.5 μg mL^{-1} magnesium. The simultaneous observation of more than one element is shown in Figures 6 and 7. The many absorption lines of nickel in Figure 6 demonstrates the great information gathering power of this technique. In Figures 6 and 7, a spectral window was chosen for the prominent nickel and silver absorption line, respectively. Although cobalt and copper have stronger absorption lines elsewhere, they can still be detected within these chosen spectral windows at the microgram per milliliter level. Figure 8 shows not only a multielement scan for magnesium and manganese but an atomic (Mn) and ionic (Mg) absorption scan as well. The ability to investigate ionic absorption lines of easily ionized elements is an attractive alternative to investigating only atomic absorption lines.

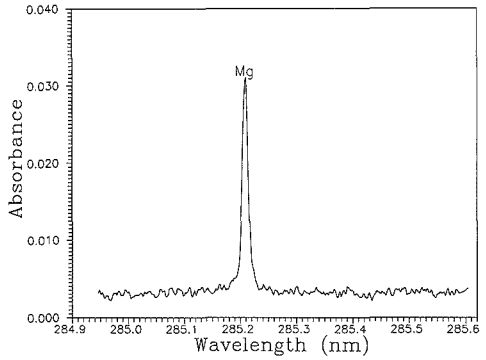

Figure 5. Atomic absorption spectrum of magnesium (0.5 μg mL^{-1}).

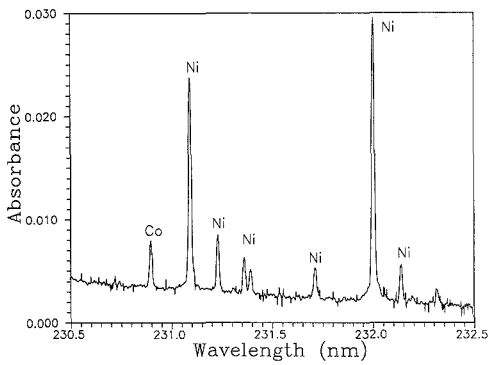

Figure 6. Atomic absorption spectrum of a multielement mixture of nickel and cobalt (100 μg mL^{-1}).

Background Correction and Noise. All spectra shown in Figures 5–8 with the CS-ICP-AAS studies are not background corrected. With the supplied software, the measured absorbance peak height was easily subtracted from a base line that was not positioned at 0.0 absorbance units. For the HCL-ICP-AAS studies, background correction was obtained by subtracting the transmission peak from the blank transmission base-line signal; base-line drift was negligible.

For either study, ICP emission noise was not a significant source of noise. The use of diaphragms significantly mini-

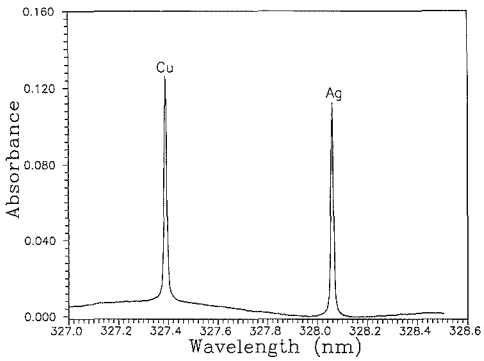

Figure 7. Atomic absorption spectrum of a multielement mixture of copper and silver (100 μg mL^{-1}).

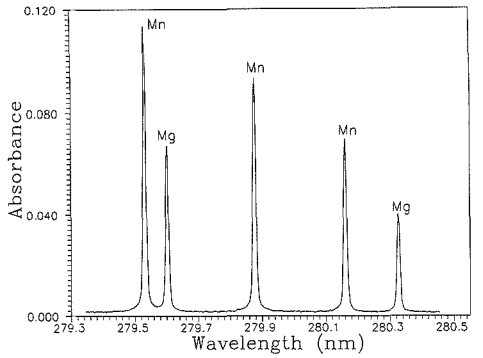

Figure 8. Atomic absorption spectrum showing atomic and ionic absorption of manganese and magnesium (10 μg mL^{-1}), respectively.

Table II. Comparison of Detection Limits for CS-AAS Results

			limits of detection, μg mL^{-1}		
element	λ_{AAS}, nm	sensitivity, μg mL^{-1}	this work "T-shaped" bonnet	previous work CS-ICP-AAS[a]	CS-flame-AAS[b]
Ag(I)	328.1	4	0.2	5	0.007
Ca(I)	422.7	0.2	0.04	3	0.003
Cd(I)	228.8	2	0.5	3	0.03
Co(I)	240.7	2	0.5	10	0.07
Cr(I)	357.9	3	0.6	10	0.02
Cu(I)	324.7	2	0.4	4	0.01
Fe(I)	248.3	2	0.4	8	0.07
Li(I)	670.8	0.07	0.03		0.003
Mg(I)	285.2	0.07	0.01	0.7	0.001
Mn(I)	279.5	0.8	0.2	4	0.01
Na(I)	589.0	0.4	0.06	3	0.003
Ni(I)	232.0	0.3	0.6	10	0.07
Sr(I)	460.7	0.7	0.2	6	0.02
Zn(I)	213.9	10	3	20	0.07
Ba(II)	455.4	10	7	10	c
Ca(II)	393.7	20	4	5	c
Mg(II)	279.5	0.4	0.07	2	c
Mn(II)	257.6	7	4	10	c
Sr(II)	407.8	9	5	6	c

[a] Taken from ref 26 (a single-pass system). [b] Taken from ref 34 (a single-pass system). [c] Not done.

mized any ICP emission from reaching the detector for the CS-ICP-AAS studies. In general, the probed absorption region within the T-shaped bonnet is a relatively dark region; that is, emission from this region is greatly reduced. Along with the lock-in amplifier, additional rejection of noise was provided by the nanovolt amplifier with its frequency band-pass of 100–300 kHz for the HCL-ICP-AAS studies. Source shot noise from the HCLs was the prominent source of noise. However, with the continuum source, source shot noise was prominent at wavelengths greater than 250 nm, while detector (diode-to-diode) noise became prominent below wavelengths of 250 nm because of the relatively poor emission intensity of the continuum source below 250 nm.

Analytical Figures of Merit. For the CS-ICP-AAS studies, detection limits and sensitivities (the characteristic concentration which would yield a 1% absorption signal) are reported in Table II. As a comparison, detection limits by other work involving single-pass CS-AAS are also given in Table II. The detection limits for this work compared to work performed previously in an ICP (with a conventional torch) (*26*) are at least an order of magnitude better. A likely reason for this improvement involves the increase in absorption path length provided by the T-shaped bonnet. The increase in the atomic absorption signal using the bonnet was almost directly proportional to the increase in absorption path length compared to a conventional torch. Detection limits, however, for the best reported CS-flame-AAS results by O'Haver (*34*), were at least an order of magnitude better than the results obtained in this work with the continuum source. Ionization losses for atomic absorption are more significant in an ICP than in a flame leading to poorer atomic absorption detection limits. Although ionization losses are very significant for atomic absorption using a conventional torch, these losses are not as significant when using the T-shaped bonnet. Obviously, the operation at lower rf powers (compared to a conventional torch) with the bonnet has a direct negative effect on the ionic absorption observed (as seen from the data reported in Table II). The use of O'Haver's modulated continuum source and lock-in detection may improve the sensitivity of this experimental system (*34*).

The detection limits and sensitivities for the HCL-ICP-AAS studies are reported in Table III. The best reported detection limits of line source AAS are also given (*35*). The best absorption signal obtained for the refractory element vanadium

Table III. Operational Parameters and Analytical Figures of Merit

				HCL-ICP-AAS		HCL-flame-AAS lit. value
element	λ_{AAS}	HR1000 slits, mm	ICP power, W	sensitivity, μg mL^{-1}	LOD, μg mL^{-1}	LOD[a]
Ba(I)	553.5	1.5	400	8	1	0.01
Ca(I)	422.7	1.0	400	0.1	0.03	0.002
Cd(I)	228.8	2.0	400	0.1	0.1	0.001
Mg(I)	285.2	1.0	400	0.05	0.008	0.0003
Mn(I)	279.5	2.0	400	0.7	0.1	0.002
V(I)	318.5	1.5	600	7	4	0.03

[a] Taken from ref 35.

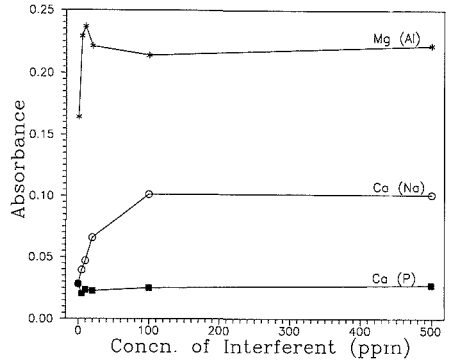

Figure 9. Interferent effects on magnesium and calcium (1 μg mL^{-1}).

was at a higher plasma rf power (i.e., 600 W) compared to the other studied elements. The detection limit obtained for magnesium is competitive compared to commercial AA systems. Overall, detection limits obtained in this work were at least 1 to 2 orders of magnitude poorer than commercial flame-AA values. Again, ionization losses and different limiting noises may explain these differences in detection limits.

Chemical Interferences. We expected that chemical interferences in our plasma system would be markedly reduced compared to flame-AAS. The most serious interferences for magnesium occurs in the presence of other elements that can form stable oxides. Aluminum is known to interfere with magnesium by forming mixed oxides and thus suppressing its absorption signal (*36–38*). Figure 9 shows the effect of adding varying concentrations of aluminum on a 1 μg mL^{-1} solution of magnesium. Instead of a depressed effect, aluminum slightly enhanced the magnesium absorption signal. Further speculation of the enhancement has been deferred until a better understanding of this plasma is made. Figure 9 also shows the effect of interferences on calcium. Calcium in the presence of phosphate produces a stable Ca–P compound removing large numbers of calcium atoms; thus, a severely depressed flame atomic absorption signal results (*39*). With our system, the addition of phosphorus to a 1 μg mL^{-1} solution of calcium had little effect on the absorption signal. Sodium has also been known to be an interferent by enhancing atomic absorption signals due to sodium's ease of ionization and thus shifting the ionization equilibrium in hot flames and ICPs (*40*). A marginal enhancement was observed as sodium slightly enhanced the calcium atomic absorption signal.

Plasma Diagnostics. As described by Kalnicky and Kniseley, the temperature was calculated with the aid of the slope method for several iron (Fe I) emission lines listed by Kalnicky and Fassel (*41*). The temperature determined from this method was 4000 K. The electron density was determined by the calculated half-width of the H_β line as a function of the electron density (*31*). Based on a H_β half-width of 0.07 nm, the electron density corresponds to 2×10^{14} cm^{-3}. The measured electron density has also been used to calculate the electron temperature, $T_{e,LTE}$ (K), assuming local thermodynamic equilibrium. $T_{e,LTE}$ values have been evaluated for the corresponding electron densities by Caughlin and Blades (*42*): The LTE temperature based on the measured electron density corresponds to 6800 K. The difference in this temperature from the emission temperature mentioned above supports nonthermodynamic equilibrium of the plasma.

CONCLUSION

There was very little atomic emission observed within the center of the T of the bonnet. The greatest advantage of this T-shaped bonnet is the ability to optically probe atoms within a fairly dark region. Compared to flames, this is attractive since the background emission is very low. Also compared to flames, chemical interferences were reduced with this plasma setup. LODs for many of the ionic absorption lines (and refractory element atomic absorption lines) would probably improve if the plasma rf power could be increased. However, increasing the rf power currently jeopardizes the structure of our T-shaped bonnet. Low rf operating power allowed prudent operation of the system and prevented the potential of cracking the bonnet.

These preliminary results with the T-shaped bonnet seem promising. The ability to increase the atomic absorption path length and to make use of an excellent atomization cell, such as the ICP for absorption, is very attractive. This increase in absorption path length should increase the atomic/ionic residence times within the path of the optical beam. The bonnet can be used continuously on top of conventional ICP torches making it attractive for commercial use. The ability to probe both atomic and ionic species should improve the multielemental capabilities of this technique. Obviously, a common problem with CS-AAS, is the need for a high-resolution monochromator. An echelle spectrometer with a charge-coupled device would offer good spectral resolution and coverage for multielemental analyses. The use of an ICP with the described T-shaped bonnet in AAS should overcome the "atomizer-related shortcomings" as discussed by Hieftje (*43*). The system described here should provide AAS with a simple to use, easily automated, multielement technique.

Future work will employ the use of an HCL and possibly other line sources as radiation sources with this setup. With the relatively low plasma temperatures determined in this study, the plasma within the middle of the T portion of the bonnet appears to be a very hot inert gas. A smaller inner diameter T-shaped bonnet will be constructed to try and restrict the atoms and ions to a more confined and restricted region: A miniaturized ICP torch may be useful for this application. Mini-ICP torches have been reported to provide the same analytical capabilities and atomization and excitation characteristics as conventional torches, however, at much lower rf powers (*44*, *45*). We may also attempt to simulate the work performed by Fuwa and Vallee but with a conventional ICP torch and its plasma plume directed into one end of a long path absorption tube.

ACKNOWLEDGMENT

Thanks go to Rudi Strohschein and Dick Moshier for their expeditious efforts in constructing several T-shaped bonnets. Support for this work was also funded by a fellowship from British Petroleum of American for M.M. Thanks especially go to Nicolo Omenetto for his stimulating discussions and help concerning the work involved with this system.

LITERATURE CITED

(1) Rubeska, I.; Moldan, B. *Appl. Opt.* **1968**, *7*, 1341.
(2) Fuwa, K.; Vallee, B. L. *Anal. Chem.* **1963**, *35*, 942.
(3) Ando, A.; Fuwa, K.; Vallee, B. L. *Anal. Chem.* **1970**, *42*, 818.
(4) Agazzi, E. J. *Anal. Chem.* **1965**, *37*, 364.
(5) Fassel, V. A. *Science* **1978**, *202*, 183.
(6) Magyar, B.; Aeschbach, F. *Spectrochim. Acta* **1980**, *35B*, 839.
(7) Wendt, R. H.; Fassel, V. A. *Anal. Chem.* **1966**, *38*, 337.
(8) Veillon, C.; Margoshes, M. *Spectrochim. Acta* **1968**, *23B*, 503.
(9) Downey, S. W.; Nogar, N. S. *Appl. Spectrosc.* **1984**, *38*, 876.
(10) Mermet, J. M.; Trassy, C. *Appl. Spectrosc.* **1977**, *31*, 237.
(11) Bordonali, C.; Biancifiori, M. A. *Met. It.* **1967**, *No. 8*, 631.
(12) Biancifiori, M. A.; Bordonali, C. *Com. Naz. Energ. Nucl.* **1967**, *67*, 15.
(13) Greenfield, S.; Smith, P. B.; Breeze, A. E.; Chilton, N. M. D. *Anal. Chim. Acta* **1968**, *41*, 385.
(14) Abdallah, M. H.; Diemiaszonek, R.; Jarosz, J.; Mermet, J. M.; Robin, J.; Trassy, M. *Anal. Chim. Acta* **1976**, *84*, 271.
(15) Umemoto, M.; Kubota, M. *Spectrochim. Acta* **1987**, *42B*, 1053.
(16) Hart, L. P.; Smith, B. W.; Omenetto, N. *Spectrochim. Acta* **1986**, *41B*, 1367.
(17) Uchida, H.; Tanabe, K.; Nojiri, Y.; Haraguchi, H.; Fuwa, K. *Spectrochim. Acta* **1980**, *35B*, 881.
(18) Blades, M. W.; Hieftje, G. M. *Spectrochim. Acta* **1982**, *37B*, 191.

(19) Kornblum, G. R.; De Galan, L. *Spectrochim. Acta* **1977**, *32B*, 71.
(20) Gillson, G.; Horlick, G. *Spectrochim. Acta* **1986**, *41B*, 431.
(21) Uchida, H.; Tanabe, K.; Nojiri, Y.; Haraguchi, H.; Fuwa, K. *Spectrochim. Acta* **1981**, *36B*, 711.
(22) Rybarczyk, J. P.; Jester, C. P.; Yates, D. A.; Koirtyohann, S. R. *Anal. Chem.* **1982**, *54*, 2162.
(23) Nojiri, Y.; Tanabe, K.; Uchida, H.; Haraguchi, H.; Fuwa, K.; Winefordner, J. D. *Spectrochim. Acta* **1983**, *38B*, 61.
(24) Liang, D. C.; Blades, M. W. *Anal. Chem.* **1988**, *60*, 27.
(25) Ng, K. C.; Jensen, R. S.; Brechmann, M. J.; Santos, W. C. *Anal. Chem.* **1988**, *60*, 2818.
(26) Mignardi, M. A.; Jones, B. T.; Smith, B. W.; Winefordner, J. D. *Anal. Chim. Acta*, submitted 1989.
(27) Browner, R. F.; Winefordner, J. D. *Anal. Chem.* **1972**, *44*, 247.
(28) Robinson, D.; Lenn, P. D. *Appl. Opt.* **1967**, *6*, 983.
(29) Kalnicky, D. J.; Kniseley, R. N.; Fassel, V. A. *Spectrochim. Acta* **1975**, *30B*, 511.
(30) Fuhr, J. P.; Martin, G. A.; Wiese, W. L. *J. Phys. Chem. Ref. Data* **1988**, *17*(4).
(31) Wiese, W. L. In *Plasma Diagnostics Techniques*; Huddlestone, R. H., Leonard, S. L., Eds.; Academic Press: New York, 1965; Chapter 6.
(32) Kalnicky, D. J.; Fassel, V. A.; Kniseley, R. N. *Appl. Spectrosc.* **1977**, *31*, 137.
(33) Kirsch, B.; Hanamura, S.; Winefordner, J. D. *Spectrochim. Acta* **1984**, *39B*, 955.
(34) O'Haver, T. C. *Analyst* **1984**, *109*, 211.
(35) Thermo Jarrell Ash Technical Report, 1/88, 5k, Thermo Jarrell Ash: Franklin, MA.
(36) Elwell, W. T.; Gidley, J. A. F. *Atomic Absorption Spectrophotometry*; The Macmillan Company: New York, 1962; Chapter 8.
(37) Menzies, A. C. *Anal. Chem.* **1960**, *32*, 898.
(38) Halls, D. J.; Townshend, A. *Anal. Chim. Acta* **1966**, *36*, 278.
(39) Schrenk, W. G. *Analytical Atomic Spectroscopy*; Plenum Press: New York, 1975; Chapter 2.
(40) Ingle, J. D., Jr.; Crouch, S. P. *Spectrochemical Analysis*; Prentice-Hall: Englewood Cliffs, NJ, 1988; Chapter 7.
(41) Kalnicky, D. J.; Kniseley, R. N. *Spectrochim. Acta* **1975**, *30B*, 511.
(42) Caughlin, B. L.; Blades, M. W. *Spectrochim. Acta* **1984**, *39B*, 1583.
(43) Hieftje, G. M. *J. Anal. Atom. Spectrosc.* **1989**, *4*, 117.
(44) Savage, R. N.; Hieftje, G. M. *Anal. Chem.* **1979**, *51*, 408.
(45) Rezaaiyaan, Y. R.; Hieftje, G. M.; Anderson, H.; Kaiser, H.; Meddings, B. *Appl. Spectrosc.* **1982**, *36*, 627.

RECEIVED for review August 28, 1989. Accepted December 18, 1989. Research supported by NIH-5-R01-GM38434-02.

Mass Spectrometric System for the Measurement of Aroma/Flavor Permeation Rates across Polymer Films

J. C. Tou,* D. C. Rulf, and P. T. DeLassus

The Analytical Sciences Laboratories, The Dow Chemical Company, Midland, Michigan 48667

A mass spectrometric system consisting of a mass spectrometer, a flow-through hollow fiber interface, and a permeation device is developed for the measurement of aroma/flavor permeation rates across polymeric films. The system exhibits parts per billion sensitivity to gaseous organic molecules and, therefore, is capable of determining permeability, diffusivity, and solubility of aroma/flavor constituents in polymeric films with both the feed side and the permeating side at an ambient pressure and the feed concentration down to parts per million level. The response time was found to be less than 1 min when the interface was maintained at 75 °C. The experiments can be performed at a temperature range from subambient to 100 °C. A humidifier system can be connected to the permeation device for an experiment where the humidity effect on the permeation rates is of interest. For films whose diffusivity cannot be determined from the fast rising transient portion of the permeation curve, a desolvation technique is developed from which solubility and therefore diffusivity can be evaluated. Also presented and discussed are the results from two types of the commercial films exhibiting drastically different permeability.

INTRODUCTION

Polymeric materials have become increasingly important in the food packaging industry because of their lighter weight, lower cost, and easier processing than the conventional materials such as glass, steel, and aluminum (*1*). The barrier properties of the polymeric materials against the food aroma/flavor constituents at different conditions are critical to the suitability of such applications. Generally speaking, there are two major channels available for the losses of the aroma/flavor components to the packaging materials. One is the transmission loss due to the permeation of the aroma/flavor molecules across the polymeric films to the environment, and the other is the sorption loss due to the solubility of the aroma/flavor molecules in the polymer. The permeation rate or permeability at normalized conditions depends on both solubility and diffusivity of the molecules in the polymeric films. Both of the losses have an impact on the shelf life of the packaged food. Since useful packaging materials must exhibit very low solubility and diffusivity, the measuring techniques must have high sensitivity. Several techniques have been developed and reported in the literature. Bredeweg and Caldecourt (*2*) reported an electron impact mass spectrometric technique with high sensitivity and specificity for the permeation rate measurements. It requires, however, that the permeating side of a membrane be exposed to high vacuum for mass spectrometric analysis. This requirement may alter the permeation characteristics of a membrane due to possible physical changes resulting from the vacuum seal and support. Zobel (*3*) developed an apparatus based on flame ionization techniques, which is capable of measuring the permeation rates down to about 3×10^{-12} kg·m^{-2}·s^{-1}. Because of the nature of flame ionization, the technique is incapable of measuring the permeation rates of individual components in mixtures. Caldecourt and Tou (*4*) developed two additional techniques based on atmospheric pressure ionization mass spectrometry and photoionization with comparable sensitivity as the flame ionization technique described above. However, the photoionization technique suffers from an additional drawback. The window in the photoionization detector tends to be coated by the photodecomposition products from the permeating molecules resulting in a sensitivity decrease. The atmospheric pressure ionization mass spectrometric technique suffers from its inherently narrow dynamic range and competitive ion–molecular reactions (*5*). Judgement and further validation complicate the operation if the feed is a mixture. Therefore, need still exists for a general and reliable technique for the evaluation of the aroma/flavor permeation across a polymeric

0003-2700/90/0362-0592$02.50/0

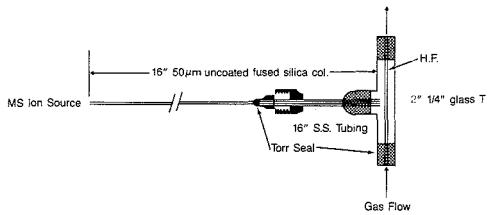

Figure 1. Flow-through hollow fiber interfaces.

film with both sides at ambient pressure.

Westover, Tou, and Mark (*6*) reported a novel mass spectrometric sampling device utilizing silicone polymer hollow fibers as an interface between an analyte and a mass spectrometer and demonstrated that the interface was capable of monitoring volatile organics in an air stream at the parts-per-million (ppm) level. The hollow fiber probe was designed in a flow-over configuration, in which the inside of the hollow fibers was connected to the mass spectrometer ion source and the outside of the hollow fibers was exposed to the analyte. The technique is not sensitive enough to be used for aroma/flavor permeation studies, however. More recently, a mass spectrometer probe was developed (*7*) by flowing the analyte through a semipermeable hollow fiber which can conveniently be placed inside the ion source. This minimizes the sample transport line. This technique has been demonstrated to be useful for reaction monitoring and environmental analysis of volatile organics in aqueous and organic solutions. The probe with this type of physical configuration is called the flow-through hollow fiber probe in this report.

It is discovered in this work that by using the flow-through hollow fiber probe, parts-per-billion sensitivity can be reached for monitoring volatile organics in air or nitrogen. This sensitivity increase allows us to use conventional electron impact mass spectrometry for the aroma/flavor permeation measurements. The electron impact mass spectrometer is known for its wider dynamic range, broader range of application to a variety of chemicals, and more commercial availability than the atmospheric pressure ionization mass spectrometer. This technique has been utilized in the study of the transport and the humidity effect of apple aromas in polymeric films (*8*). In this report, we will describe the design of the permeation measurement system consisting of a mass spectrometer, the interface, and the membrane permeation device and also the permeation data obtained for two commercial packaging films. A patent for the device has been applied for (*9*).

EXPERIMENTAL SECTION

The configuration of the flavor/aroma permeation mass spectrometric system consists of three parts—a mass spectrometer, a flow-through hollow fiber interface, and a permeation device.

The mass spectrometer is a Hewlett-Packard 5970B mass selective detector equipped with a 5997C monochromatic workstation, a 5946A 55Mb disk drive, 2225A Think Jet Printer, and a 7475A six-pen plotter. The hollow fibers used in the experiment are 0.020 in. i.d. × 0.037 in. o.d. Dow Corning Silastic medical grade tubing.

The flow-through hollow fiber interface is shown in Figure 1. An approximately 2.5-in. hollow fiber is sealed with Torr-Seal (Varian Associates, Vacuum Division, Palo Alto, CA) in a 2-in. × $^1/_4$-in. glass or stainless steel tee. After the Torr Seal adhesive is cured, the excess length of the hollow fiber is trimmed off. Both ends of the hollow fiber are kept open for the gas flow. A short piece of $^1/_{16}$-in. stainless steel tubing is sealed into the side arm of the tee and then a 16-in. 50-μm uncoated fused silica column is inserted into the $^1/_{16}$-in. tubing all the way to the inside of the tee. The connection point between the fused silica column and the tubing is sealed again with the Torr-Seal adhesive. The constructed interface is connected to the mass spectrometer and

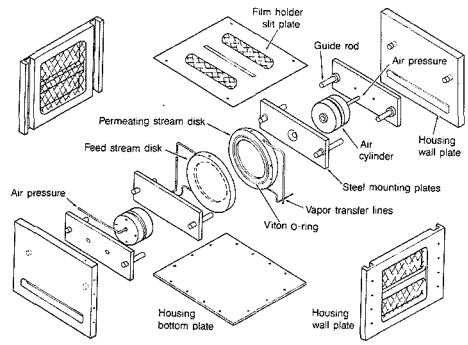

Figure 2. Permeation cell holder and the clamping mechanism.

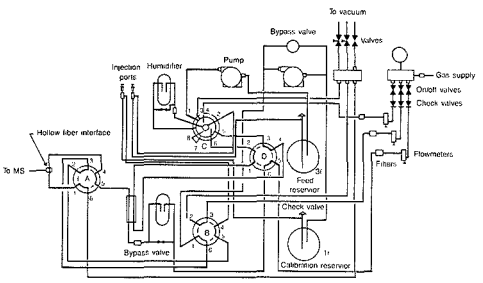

Figure 3. Flow diagram of the permeation device.

to the gas flow with Swaglok fittings using Vespel ferrules. The hollow fiber interface is housed in a thermostated enclosure located between the mass spectrometer entrance point and the side wall of the permeation device oven, as described later.

The permeation device contains the permeation cell, cell housing, cell clamping mechanism, and vapor control, all within a single thermostated enclosure. This enclosure, a Combustion Engineering (Lewisburg, WV) air-bath oven, is mounted on a fabricated aluminum framework, which also holds temperature control and flow control hardware.

As shown in Figure 2, the permeation cell consists of two stainless steel disks, each $3^7/_8$ in. in diameter by $^3/_8$ in. thick. Each disk has a machined cavity in one of its faces. Orifices in the top and bottom of each cavity allow vapor passage into and out of the cell. When the disks are clamped together, the cavities form the permeation chamber. A polymer sample film, when clamped between the disks, separates the permeation chamber into a feed stream side and a permeating stream side. The feed stream side, connected to the vapor feed reservoir, as shown in Figure 3, is 6.67 cm in diameter and 0.236 cm deep. It has a face area of 34.9 cm^2 and a volume of 8.24 cm^3. The permeating stream side, connected to the mass spectrometer membrane interface, is 6.98 cm in diameter and 0.236 cm deep. Its face area and volume are 38.32 and 9.04 cm^3, respectively. The difference in dimensions between the feed stream and permeating stream cavities is due to the presence, on the face of the feed stream disk, of a relatively wide, machined, O-ring seating surface. This surface allows some lateral misalignment to occur, without affecting the seal, when the two disks are clamped together. The permeating stream disk contains a size 151 Viton O-ring, set into a machined groove, which has an inside diameter of 7.62 cm. This O-ring seals the polymer sample film against the machined sealing surface on the feed stream disk.

The two disks are mounted on steel plates, which slide on $^1/_4$-in. guide rods, with a fabricated steel housing. The disks join and separate, along the plane of the guide rods, by the action of two cylinders, which are also within the housing. The air cylinders, acting against the steel housing, clamp the disks together with a force of between 100 and 200 lb, each, in normal operation. The

length of travel of the pistons is about $^1/_2$ in. The clamping time is less than 1 s. The disks and clamping mechanism are completely contained within the steel housing, with access to the permeation cell being only via a $^1/_8$ in. wide split in the top plate of the housing. The polymeric film under study is inserted into the permeation cell through this slit. The cell and clamp design ensure safety and convenience for the operator.

In order to ensure that the polymeric film is aligned parallel to the cell faces and is clamped to the sealing surface without wrinkles or creases, it is mounted on a special holder before being inserted into the cell. This holder consists of die-cut paper card stock, with an adhesive layer on one side. Whether clamped between two pieces of card stock or sealed against only one, the film is held rigidly in position and can be easily inserted into the permeation cell. The adhesive on the card stock makes the film and holder into a permanent assembly. It can be removed and reinserted into the permeation cell, in exactly the same alignment, as often as necessary. It can be handled repeatedly without touching the film.

As shown in Figure 3, the vapor control system consists of 2- and 1-L vapor reservoirs, three 6-port (A, B, D) and one 10-port (C) flow switching valves, two pumps, two injection ports, two humidity control devices, several flow meters, filters, by-pass valves, and check valves. Valves A, B, and D are Valco 2C6PHC valves (Valco Instrument Co., Houston, TX) and valve C is a Valco M2CST4PHC valve. All but the humidity control devices and the flow meters are contained within the oven.

These flow-switching valves allow the vapor flow system to be configured in many ways. Valve A controls the carrier gas, permeant vapor, and the calibration mixture to the mass spectrometer membrane interface and valve B connects the carrier gas inlet and exhaust headers to the calibration mixture system and valve A to the calibration mixture system. The recirculation of the sample vapor mixture and the connections of the external humidity control device to the sample vapor system and the carrier gas inlet and exhaust headers to the sample control system are controlled by valve C. Valve D allows the permeation chamber and the membrane mass spectrometer interface to be purged with carrier gas and also the connection of valve C to the feed stream side of the permeation cell and of the carrier gas to the permeating stream side of the permeation cell.

The air-bath oven is heated by passing a stream of air through a tubular resistance heater and discharging it into the oven. This air, delivered at a rate of about 100 ft^3/h also serves to purge the oven interior. A temperature controller drives the resistance heater, in response to a thermocouple attached to the permeation cell housing within the oven. A flow switch, in the heater circuit, protects the heater if the air flow is cut off. The dual set-point temperature controller can also activate a solenoid valve, so the CO_2 can be passed into the oven. This makes it possible to cool the permeation cell below ambient temperature, if desired.

The concentrations of the calibration gas and the feed gas are prepared by injecting appropriate amounts of the permeant compound(s) under study into the 1-L reservoir and the 3-L feed reservoir, respectively, via the injection ports as shown in Figure 3. The homogeneities of the calibration gas and the feed gas are accomplished by circulating with two gas pumps (Model MB-21, Metal bellows Corp. Sharon, MA). The pumping speed of the pumps is approximately 1.2 L/min, which is too high a flow for the membrane interface. As shown in Figure 3 a bypass valve is installed in parallel with the pump connected to the calibration reservoir. During calibration, the valve is opened and the flow rate to the hollow-fiber interface was controlled by the size of the tubings and is measured to be approximately 23 cm^3/min. However, the flow rate should be measured during each experiment. The carrier gas flow rate during a permeation experiment should be adjusted to approximately the same as the above flow rate to avoid any flow-rate dependence of the hollow fiber interface sensitivity.

Two commercial films are used to characterize the mass spectrometric system. One is a polyethylene film, and the other a plasticized vinylidene chloride copolymer based film. These represent two different categories of materials, one with high permeability and the other with low permeability. The cleanness of the film surface was visually examined. Fingerprint contamination was avoided. No solvent was used for cleaning.

RESULTS AND DISCUSSION

In a typical experiment, a film is exposed to aroma/flavor constituents in the parts per million concentration range. The working concentration of the aroma/flavor constituents on the permeating stream side of the film is typically in the parts per billion concentration range. The sensitivity of the flow-through interface was found to be in the parts per billion range for *d*-limonene and is about 2 orders of magnitude higher than the flow-over hollow fiber interface reported previously.

The response time of the flow-through hollow fiber interface is found to be dependent on the temperature. As the temperature increases, the response time decreases. At 75 °C, the response time is observed to be approximately 1 min. This is attributed to the improved diffusivity at higher temperatures. For most permeation measurements, this response time is adequate. It is also noticed that the response of the ion signals decreases when the temperature increases. For an example, the response at 75 °C is only about 43% of that at 34 °C. This is attributed to the lower solubility of the gas in the interface membrane at higher temperatures.

In a typical permeation experiment, three steps are involved. They are (a) the instrument sensitivity calibration, (b) the permeation rate measurement, and (c) the desolvation experiment. Two typical permeation experimental results from a polyethylene film and a plasticized vinylidene chloride copolymer based film are shown in Figures 4 and 5, respectively. It is evident from the figures that the polyethylene film exhibits much faster rates of permeation and desolvation (curves b and c, respectively) than the plasticized vinylidene chloride copolymer based film. These rates are evaluated quantitatively as below.

The permeability, P (kg m/(m^2 s Pa)), at the steady state is calculated from the permeation and calibration curves, as

$$P = (1.34 \times 10^{-14}) \frac{C_{p,av} f M X}{T_r C_f} \text{ kg m/(m}^2 \text{ s Pa)}$$

where $C_{p,av}$ is the average concentration of the permeant at the steady state calculated from the concentration of the calibrant based on the characteristic ions monitored for the compound, f is the flow rate of the permeating stream carrier gas measured at room temperature, T_r is temperature in K, M is the molecular weight of the compound in grams per mole, X is the thickness in mils of the film, and C_f is the feed concentration in parts per million by volume.

Several odorous organic species are selected for the study. They are *d*-limonene, an important component in citrus fruits, benzaldehyde, a common component in nuts, especially almond, methyl acetate, solvent used in printing inks and some adhesives, and toluene, a common solvent used in the plastic industry. The latter compounds may either enter the packaged food from the environment or get packaged in a plastic container.

Calculations are based on several characteristic ions from each compound such as the ions at m/z 68, 107, 121, and 136 from *d*-limonene, the ions at m/z 106 and 78 from benzaldehyde, the ions at m/z 91 and 92 from toluene, and the ion at m/z 74 from methyl acetate. In the case of a mixture feed, the minor interferences among the compounds are neglected in the calculation. The relative standard deviation among each set of the determinations is estimated to be less than 10%.

The permeabilities of the above organic species were measured for several samples taken from the above films at several feed-concentrations of a pure component or a mixture. It is found that the data are scattered widely. Therefore, it is impossible to make any correlation of the entire data set. However, when the data from the same film sample exposed to similar feed concentration are extracted from the above set,

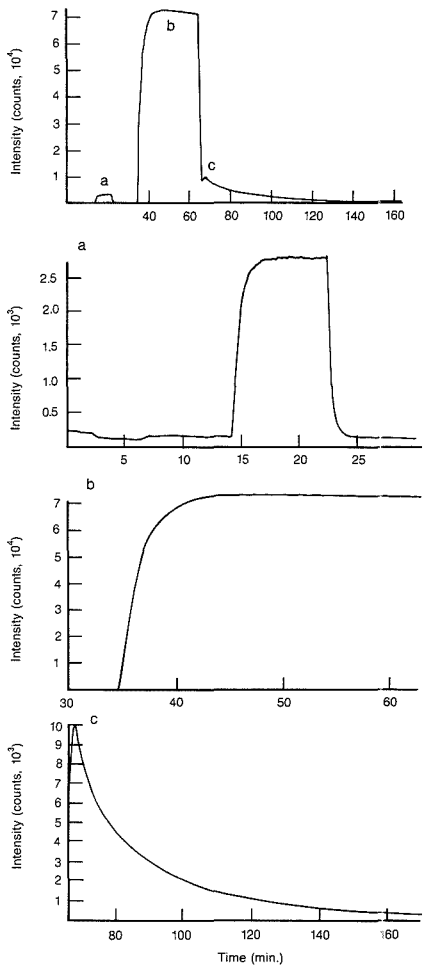

Figure 4. Experimental sequence and curves of a polyethylene film at 40 °C when exposed to 106 ppm *d*-limonene (*m*/*z* 136) in air: (a) the calibration curve (1.75 ppm); (b) the permeation rate curve; (c) the desolvation curve.

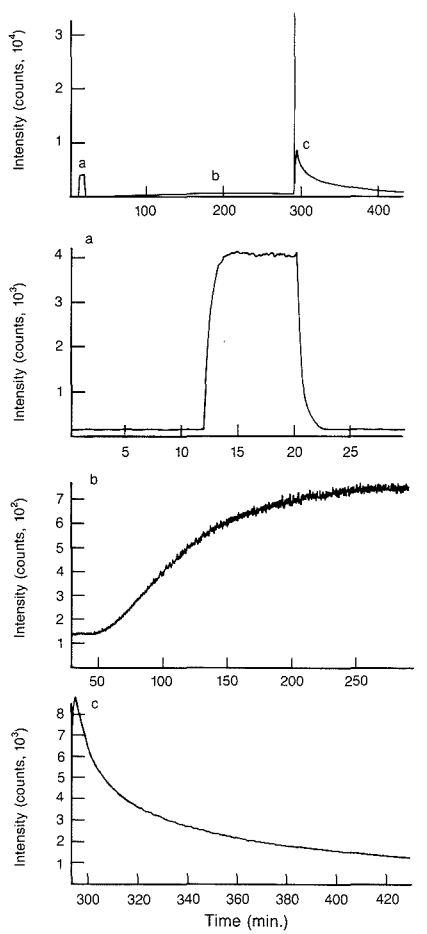

Figure 5. Experimental sequence and curves of a plasticized vinylidene chloride copolymer based film at 56 °C when exposed to a mixture of *d*-limonene (114 ppm), benzaldehyde (182 ppm), toluene (173 ppm), and methyl acetate (231 ppm) in air. The curves are for *d*-limonene (*m*/*z* 136). Key: (a) the calibration curve (1.92 ppm); (b) the permeation rate curve; (c) the desolvation curve.

an expected Arrhenius plot is obtained, as shown in Figure 6 for the polyethylene film and the plasticized vinylidene chloride copolymer based film. The activation energies of permeability for the above two films are calculated to be 6.1 and 20 kcal/mol. However, it can also be seen from Figure 6 that the experimental data point at 77 °C for the plasticized vinylidene chloride copolymer based film is about half what the Arrhenius curve would predict. Differential scanning calorimetric (DSC) study indicates that the plasticized vinylidene chloride copolymer based film exhibits two endothermic peaks at 67.0 and 168.5 °C with about 40% crystallinity. When the film has been held at 77 °C for several days, the lower endothermic peak is found to be shifted to 100 °C with the higher endothermic peak essentially unchanged. The crystallinity is also found to increase to 52%. Also, the plasticizer could be partially evaporated, either or both of these may lead to the observed deviation. In the case of the polyethylene based film, no thermal activity is detected in the DSC curve in this temperature range, and therefore, the Arrhenius relationship is valid for the entire temperature range studied. It is also found that the permeability increases as the concentration of the feed increases.

On the basis of on the above analysis, the observed scattering of the data is due to several factors such as nonuniformity or nonrepresentative sampling of the films, thermal stability of the material in the experimental temperature range, and the concentration dependence of permeability, but not due to the uncertainty of the analytical technique.

As described previously, permeability is a quantity measured at the steady state. The transient portion of a permeation curve provides information about diffusivity, which can be evaluated according to the two published methods $D = L^2/7.2t_{1/2}$ (*10*) and $D = 0.18L^2(dJ/dt)/J$ (*11*), respectively, where D is diffusivity in m^2/s, L the thickness in m, $t_{1/2}$ the time to reach half of the steady-state value, dJ/dt the permeation rate slope in the transient region, and J the steady-state permeation rate. Solubility coefficient, S (kg/(m^3 Pa)), can therefore be evaluated from $S = P/D$. However, for the materials exhibiting very high diffusivity as in the case

Table I. Permeabilities (P), Diffusivities (D), and Solubilities (S) of the Two Commercial Polymeric Films

film material	temp, °C	feed concn, ppm	P^a	D^b		S^c	
				A[f]	B[g]	A[f]	B[g]
polyethylene	55	110 (*d*-limonene)	390		350		11
		180 (benzaldehyde)	360		510		7.1
		170 (toluene)	160		550		2.9
		220 (methyl acetate)	170		400		4.2
plasticized vinylidene chloride copolymer	56	110 (*d*-limonene)	2.7	8.0[d]	5.0	3.4[d]	5.4
				5.6[e]		5.9[e]	
		190 (benzaldehyde)	13.0	15[d]	7.8	9.0[d]	17
				11[e]		12[e]	
		170 (toluene)	1.5	13[d]	9.2	1.1[d]	1.6
				11[e]		1.4[e]	
		230 (methyl acetate)	5.1	12[d]	8.4	4.5[d]	6.1
				9.5[e]		5.4[e]	

[a] $P = 10^{-16}$ kg m/(m² s Pa). [b] $D = 10^{-15}$ m²/s. [c] $S = 10^{-2}$ kg/(m Pa). [d] $D = L^2/7.2t_{1/2}$ (*10*). [e] $D = 0.18L^2(dJ/dt)/J$ steady state (*11*). [f] Calculated from the permeation experiment. [g] Calculated from the desolvation experiment.

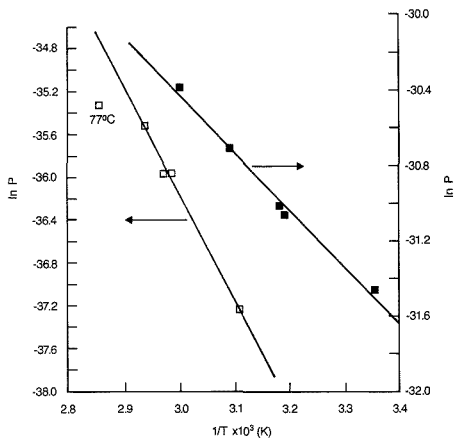

Figure 6. Arrhenius plot of permeability, P, of *d*-limonene through a polyethylene film (■) and a plasticized vinylidene chloride copolymer based film (□) with the feed concentration ranges of 101–103 and 109–127 ppm, respectively.

of the polyethylene film, as shown in Figure 4, the instrumental response time becomes too slow to follow the permeation rate change during the transient portion of the permeation rate curve. A new method was developed for this study by measuring the actual amount of the permeating molecules in a film after the steady state has been reached. The prerequisite for this measurement is to ensure the absence of the residual organic molecules present in the lines of the system before the measurement becomes meaningful. The conditions for this ensurance were studied. At first a glass plate was placed in the film holder. The clearance of the residue organic molecules is studied by flushing the system with 23 cm³/min carrier gas flow or with vacuum and then carrier gas flow. It is found that it takes approximately 5 min to reach the base line via the evacuation route as compared to longer than 20 min via the carrier gas flow routes. The desolvation curves can be fitted with a three-term exponential function

$$I = \sum_{i=1}^{3} a_i e^{-b_i t}$$

where I is the mass spectrometric response of an ion at time t minutes and a_i and b_i are the fitting parameters. The missing data during the first 5 min clearance period are obtained by the extrapolation of the fitted curve. The total amount of the permeating molecules, W, desolvated from the film, can therefore be evaluated by the following equation:

$$W = c\int_0^\infty \sum_{i=1}^{3} a_i e^{-b_i t}\,dt = c\sum_{i=1}^{3} a_i/b_i$$

where c is a proportional constant determined from the instrumental sensitivity calibration. The curve fitting is accomplished by VAX RS-1.

Shown in Table I are the solubilities and the diffusivities determined from the desolvation experiments along with those determined from the transient portions of the permeation rate curves for comparison. In the case of the polyethylene film, the diffusivities are back-calculated from the equation $D = P/S$, where the solubilities S are obtained from the desolvation experiments. As shown in the data of the plasticized vinylidene chloride copolymer based film, the two methods agree reasonable well. It is evident that the two films exhibit comparable magnitude of solubility but drastic difference in diffusivity and therefore permeability. Practically speaking, the sorption losses of the organic molecules to the two film materials at steady state are comparable; however, the time to achieve steady-state sorption will be much longer for the plasticized vinylidene chloride copolymer based film. On the other hand, the transmission losses due to diffusion through the two films are 50–70 times faster in the case of the polyethylene film than in the case of the plasticized vinylidene chloride copolymer based film. These data lead to a conclusion that the plasticized vinylidene chloride copolymer based film is a much better barrier film than the polyethylene based film.

CONCLUSION

The mass spectrometric system presented in this report exhibits parts per billion sensitivity and is therefore capable of determining permeability, diffusivity, and solubility of aroma/flavor constituents in polymeric films with both the feed side and the permeating side at ambient pressure and the feed concentration down to parts-per-million level. The response time is dependent on the temperature of the interface. At 75 °C, it is found to be less than 1 min.

A desolvation technique has been developed from which solubility and therefore diffusivity can be evaluated. This technique is especially useful in the determinations of solubility and diffusivity for films exhibiting fast rising transient permeation rates, where the conventional techniques (*10*, *11*) fail. The data obtained by this technique are in reasonable agreement with those by the conventional methods. It is indicated in the permeability data that the two commercial films studied are not homogeneous. In the case of *d*-limonene,

the activation energies of permeability were determined to be 6.1 and 20 kcal/mol for the polyethylene based film and the plasticized vinylidene chloride copolymer based film, respectively. The solubilities of the films for the four components studied are comparable in magnitude. However, the diffusivities of the polypropylene film are about 50–70 times greater than those of the plasticized vinylidene chloride copolymer based film. These quantities are very important in the determination of the sorption losses of the aroma/flavor constituents to the films and the transmission losses through the films to the environment. Therefore, the plasticized vinylidene chloride copolymer based film is a much better barrier film than the polyethylene film.

ACKNOWLEDGMENT

The authors thank M. Babinec, B. Karp, and P. Savickas for their assistance during the course of the development and A. Pasztor for his DSC work.

LITERATURE CITED

(1) High Barrier Packaging and Flavor and Aroma Packaging—Today and Tomorrow. In *TAPPI Proceedings of the Polymers*; Laminations and coating Conference, Chicago, IL, September 9–11, 1985; Technical Association of the Pulp and Paper Industry: New York, 1985; Book 2, pp 337–339 and 411–450.
(2) Bredeweg, R. L.; Caldecourt, V. J. *Collected Abstracts*; The Fourteenth Annual Conference on Mass Spectrometer and Allied Topics, Dallas, TX, May 22–27, 1966; American Society for Mass Spectrometry: East Lansing, MI, 1966; paper 29.
(3) Zobel, M. G. R. *Polym. Test.* **1982**, *3*, 133–142.
(4) Caldecourt, V. J.; Tou, J. C. *J. Membr. Sci.* **1986**, *29*, 1–9.
(5) Kallos, G. J.; Caldecourt, V. J.; Tou, J. C. *Anal. Chem.* **1982**, *54*, 1313–1316.
(6) Westover, L. B.; Tou, J. C.; Mark, J. H. *Anal. Chem.* **1974**, *46*, 456–571.
(7) (a) Brodbelt, J. B.; Cooks, R. G. *Anal. Chem.* **1985**, *57*, 1153–1155. (b) Cooks, R. G.; Bier, M. E.; Brodbelt, J. S.; Tou, J. C.; Westover, L. B. U.S. patent 4,791,292.
(8) DeLassus, P. T.; Tou, J. C.; Babinec, M. A.; Rulf, D. C.; Karp, B. K.; Howell, B. A. *Food and Packaging Interactions*: ASC Symposium No. 365; Hotchkiss, Joseph H., Ed.; American Chemical Society: Washington, DC, 1988; Chapter 2, pp 11–27.
(9) Tou, J. C.; Rulf, D. C., Dow Docket No. C-36060.
(10) Ziegel, K. D.; Presdorff, H. K.; Blair, D. E. *J. Polym. Sci., Part A-2* **1969**, *7*, 809–819.
(11) Pasternak, R. A.; Schimscheimer, J. F.; Heller, J. *J. Polym. Sci., Part A-2* **1970**, *8*, 467–479.

RECEIVED for review August 14, 1989. Accepted December 5, 1989.

In Vivo Microdialysis and Thermospray Tandem Mass Spectrometry of the Dopamine Uptake Blocker 1-[2-[Bis(4-fluorophenyl)methoxy]ethyl]-4-(3-phenylpropyl)-piperazine (GBR-12909)

Stanley D. Menacherry and Joseph B. Justice, Jr.*

Department of Chemistry, Emory University, Atlanta, Georgia 30322

Microdialysis in conjunction with thermospray tandem mass spectrometry was employed in following the time course of the experimental drug GBR-12909 in vivo. GBR-12909 is 1-[2-[bis(4-fluorophenyl)methoxy]ethyl]-4-3(phenylpropyl)-piperazine. An important feature of microdialysis exploited in the method is the elimination of sample cleanup procedures. The detection limit was determined to be 100 pg and the relative standard deviation of estimates for standard solution in the range of 50 nmol/L to 1 μmol/L concentrations was found to be 17%. Important factors in obtaining high sensitivity and reproducibility were carrier phase composition and operation in the flow injection mode. The maximum concentration of GBR-12909 in the brain for a dose of 100 mg/kg i.p. was determined to be 250 nmol/L with the maximal concentration occurring approximately 2 h postinjection. This represents a 40-fold lower concentration of GBR-12909 in the brain as compared to cocaine concentration obtained at a dose of 30 mg/kg, which was estimated earlier under similar experimental conditions. This observation could explain the discrepency between relative in vivo and in vitro potencies of the two drugs.

In recent years microdialysis has emerged as an important technique for sampling the extracellular fluid of discrete biocompartments in vivo (*1–4*). Extracellular levels of the neurotransmitter dopamine in the brains of awake laboratory rats have been monitored by using this technique (*5*). The advantage of this sampling method is that it delivers a consistent and "clean" sample, i.e. free of tissue debris and biopolymers, from a complex biomatrix. Further, the sampling is continuous, with minimal postinsertion tissue damage, and therefore suited for following the time course of drugs, metabolites, and endogenous biochemicals in vivo. Important parameters and characteristics of this sampling method are discussed by Wages et al. (*6*). The method has been described in detail elsewhere (*7*) but in brief consists of perfusing an isotonic medium through a probe inserted in the tissue to be sampled. The probe is a cylindrical semipermeable membrane connected by inlet and outlet lines made of fused silica capillaries. Small molecules, below the molecular weight cutoff of the semipermeable membrane, diffuse into the perfusion medium and are pumped out to the detection system or collected in microvials for off-line analysis. The dialysis probe arrangement for off-line analysis is schematically depicted in Figure 1. A major requirement of this sampling method is a highly sensitive and selective detection scheme due to the low sample volumes obtained, typically in the order of a few microliters. The most widely used method is liquid chromatography with electrochemical detection. This method has been successfully employed in monitoring catecholamine neurotransmitters in the rat brain. However, most molecules of biological interest are not electroactive and the incorporation of other detection schemes with sufficient sensitivity and universality would promote the scope of the microdialysis sampling technique. This paper investigates the utility of microdialysis in conjunction with thermospray ionization

* Author to whom correspondence should be addressed.

0003-2700/90/0362-0597$02.50/0

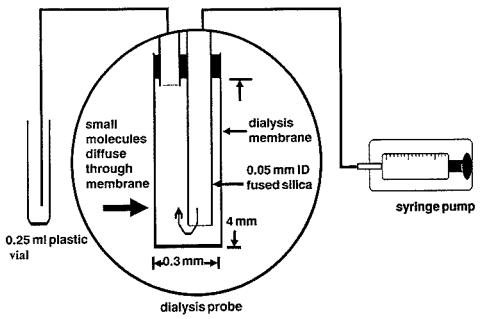

Figure 1. Schematic diagram of an off-line microdialysis setup. Inset shows the dimensions of probes used in the experiment. Perfusion flow rate was at 0.6 μL/min with sample collection at 20-min intervals.

(TSP) and tandem mass spectrometric (MS/MS) detection of the neuroactive drug GBR-12909 in the rat brain.

GBR-12909 is 1-[2-[bis(4-fluorophenyl)methoxy]ethyl]-4-(3-phenylpropyl)piperazine having a molecular formula $C_{28}H_{32}F_2N_2O$ corresponding to a molecular weight of 450 (Figure 2A). This compound has a number of important pharmacological properties described by Van der Zee et al. (*8*). Pharmacologically the drug is similar to cocaine in that it inhibits the reuptake of the neurotransmitter dopamine (*9*) though the behavioral effects of the two drugs show some dissimilarity (*10*). The reinforcing properties of cocaine are thought to be mediated by the release and reuptake inhibition of dopamine (DA) in the nucleus accumbens (*11*, *12*); therefore GBR-12909 could find use as a model in addiction studies. The drug is also being investigated for anti-Parkinsonian activity and as an antidepressant, so a sensitive analytical method would be timely.

GBR-12909 poses a number of analytical constraints on conventional approaches to in vivo determination of the drug. Aqueous solutions of the compound degrade rapidly, necessitating fast analysis and daily dilution of frozen stock standard solutions. The tertiary amine groups in the molecule make it highly polar, so it chromatographs poorly in GC. Further, the compound is thermolabile and relatively involatile; hence it is not easily amenable to high temperatures required in GC analysis. Poor UV absorption and fluorescence limits sensitive HPLC method development.

The availability of commercial LC/MS interfaces have permitted mass spectrometric detection and quantitation of highly polar and thermolabile compounds. The TSP interface has been described by Vestal and Fergusson (*13*). Since the perfusate obtained in a microdialysis experiment is "clean", i.e. contains only low molecular weight compounds, it can be analyzed in a flow injection mode (FI). A tandem mass spectrometer provides the specificity required for flow injection analysis. Analytical separations are performed along the mass axis. Ions characteristic of the analyte are selected by the first mass analyzer and fragmented by collision with an inert gas. This yields specific reaction products (daughter ions) that are monitored by the second analyzer. A triple quadrupole was employed for setting up the tandem mass spectrometric experiment. The application of the triple quadrupole in trace analysis has been reviewed by Johnson and Yost (*14*).

EXPERIMENTAL SECTION

Drugs. GBR-12909 and GBR-13007 were supplied by NOVO industri A/S, DK-2880 Bagsvaerd, Denmark, as the dihydrochloride salts. GBR-13007, an analogue of GBR-12909, was used as the internal standard in the experiments. GBR-13007 is 1-[2-[bis(4-fluorophenylmethoxy]ethyl]-4-(4-phenylbutyl)piperazine

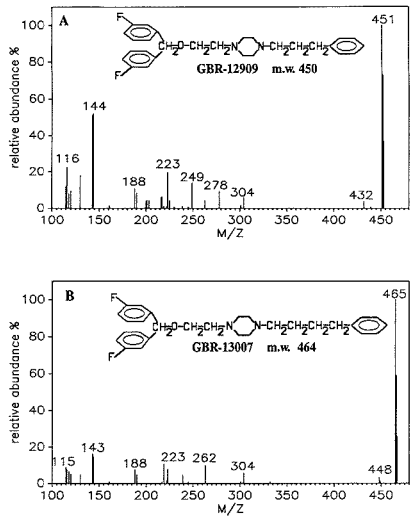

Figure 2. (A) Molecular structure and thermospray mass spectrum of GBR-12909. (B) Structure and mass spectrum of GBR-13007.

with a molecular formula $C_{29}H_{34}F_2N_2O$ and molecular weight 464 (Figure 2B).

Microdialysis. Microdialysis probes (4 mm in length), constructed according to the method of Justice and Church (*15*) were used. The dialyzing medium was artificial cerebrospinal fluid [CSF] (130 mmol/L NaCl, 2.65 mmol/L KCl, 1.4 mmol/L $CaCl_2$, 2.0 mmol/L $MgCl_2$, and 300 μmol/L ascorbic acid in distilled water adjusted to a pH of 7 with 0.01 N NaOH, filtered, and purged with helium). Dialysis rate was set at 0.6 μL/min using a Harvard microliter syringe pump. Samples were collected in 0.25-mL plastic vials. Four male Sprague-Dawley rats weighing 350–420 g were anaesthetized with chloral hydrate and the microdialysis probe stereotaxically implanted in the nucleus accumbens (AP, +3.0 from bregma; ML, +1.7; 8.1 mm below dura, atlas of Pellegrino (*16*)). Two hours after probe implantation the rats were given intraperitoneal (i.p.) injections of 100 mg/kg GBR-12909 dissolved in 1.5 mL of emulsifying solution (15% ethanol, 15% propylene glycol, 70% water). Samples were collected at 20-min intervals for 3 h. The recovery of analyte by individual dialysis probes under these conditions was determined by postcalibration. Postcalibration consisted of withdrawing the probe from the brain and immersing it sequentially in beakers containing standard solutions of 100, 400, and 1000 nmol/L concentrations. Samples were collected after allowing the probe to equilibrate for 20 min in each solution. The ratio of the signal strength of the perfusate versus the standard solution was used to estimate the recovery of individual probes at each concentration. The average of recoveries for the three concentrations was taken as the overall recovery of each probe. Recoveries between concentrations were not significantly different whereas recovery between probes ranged from 5 to 15%. Standard solutions in the range of 100–1000 nmol/L were prepared in artificial CSF to generate calibration curves and measure the variance in repeat measurements using thermospray with tandem mass spectrometric detection.

Instruments. A Finningan-Mat TSQ-70 triple quadrupole mass spectrometer equipped with a TSP interface was used in the experiments. The first and third quadrupoles (Q1 and Q3) can function as mass analyzers or total ion transmission devices whereas the second quadrupole (Q2) is operated as an ion transmission device. Q2 was pressurized with argon as collision gas to yield daughter ion spectra. A Waters 600 dual pump HPLC system equipped with a U6K injector was used to pump the carrier phase at a flow rate of 1.8 mL/min and deliver the sample in the flow injection mode.

The internal standard was introduced at the time of injection by drawing up 10 μL of sample into a syringe followed by 10 μL

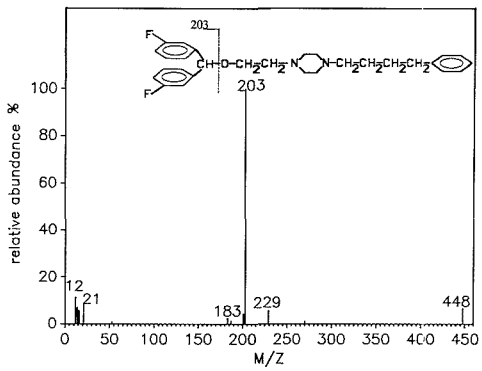

Figure 3. Daughter ion spectrum obtained from the CID of the protonated molecular ion of GBR-13007 (m/z 465). Daughter ion spectrum of the protonated molecular ion of GBR-12909 is similar and not shown.

of the internal standard solution. The carrier phase consisted of 95% methanol and 5% water containing with 0.01% of a detergent (sodium hexylsulfonic acid) and 0.01% of triethylamine for deactivation of adsorptive surfaces. The carrier phase was continuously purged with helium.

TSP vaporizer temperature was 85 °C with a block temperature of 270 °C. Samples were ionized by discharge ionization (DI) at 1500 V. Repeller potential was 80 V. Collision induced dissociation (CID) was obtained by using argon as the collision gas at a pressure of 1.2 mTorr. Collision energy was −20 eV. The electron multiplier was set at 1800 V with a gain of 10^{-6} A/V.

Full scan TSP/DI spectra of GBR-12909 and the internal standard were obtained by using Q3 as the mass analyzer and Q1 and Q2 as transmission devices. The range m/z 1–100 was not scanned due to intense solvent ions in this region. Full scan daughter spectra were acquired by CID of parent ions selected by Q1 and scanning Q3 in the range 10–450 amu. For quantitation the instrument was set in the parent scan mode with Q3 transmitting the common daughter ion and Q1 switching between the parents at 451 and 465 amu. The dwell time on each parent was 0.10 s with a settling time of 0.025 s giving a total cycle time of 0.25 s. Data were acquired for 120 cycles after sample injection corresponding to a run time of 30 s. Full scan spectra were obtained at unit resolution. However, for quantitation the parent ions were slightly under resolved to improve the signal.

RESULTS AND DISCUSSION

Figure 2 shows the TSP mass spectra obtained for GBR-12909 and GBR-13007. Notice the lack of extensive fragmentation which is a desirable property for separations along the mass axis. The base peak is the $[M + H]^+$ ion (protonated molecular ion) in both cases, m/z 451 for GBR-12909 and m/z 465 for GBR-13007.

The $[M + H]^+$ ions were selected as parents to yield CID fragments. Figure 3 shows the collision spectrum obtained for GBR-13007 under the experimental conditions given above. GBR-12909 (not shown) had a similar CID spectrum. The common daughter ion at m/z 203 from both the compounds probably arises from a cleavage at the ether linkage as shown.

Excellent sensitivity was achieved by using flow injection and optimizing experimental conditions. A detection limit of 100 pg with $S/N = 5$ could be obtained routinely. For microdialysis this approximately corresponds to 10 μL of a 20 nmol/L solution. For solutions of lower concentration, 20 μL was injected. Elimination of chromatography is crucial in achieving this sensitivity.

A scheme using flow injection (FI) has four important advantages as compared to a chromatographic separation. [a] Sensitivity is enhanced due to extremely sharp peaks (2 s wide

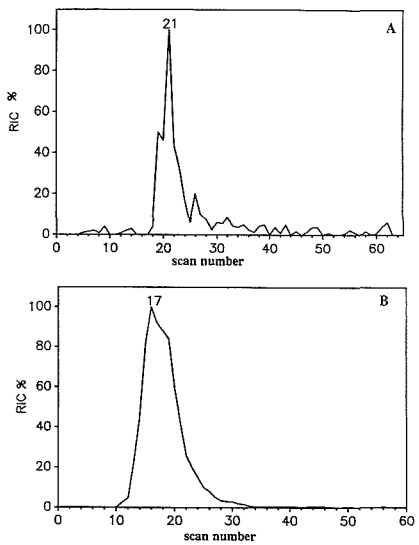

Figure 4. (A) Peak shape obtained when 500 pg of GBR-12909 was injected into a carrier phase of 40% water in methanol. Trace is signal from select ion monitoring of the parent ion of GBR-12909 at m/z 451. (B) Peak shape obtained for 500 pg of GBR-12909 injected in a carrier phase of 5% water in methanol. Smoother peak shape is observed with a significant improvement in sensitivity.

at half height). [b] Analysis is rapid (30 s per sample). Large sample throughput is possible; 30–60 injections/h was achieved in our experiments. [c] Internal standards are often required to adjust for variations in ionization. Isotopomers of the analyte are the best choice; however, they are not always available and analogues may have to be used. With a flow injection scheme the analogue would elute at the same time as the analyte permitting good correction factors. Coelution of analogues would be harder to obtain in a good chromatographic separation. [d] It was found that a carrier phase that had a high aqueous concentration gave poor response, with large fluctuations in ionization efficiency whereas a carrier phase containing 90–95% methanol resulted in smooth peak shapes with less peak tailing and carry over. By elimination of chromatography the carrier solvent can be optimized for efficient ionization without consideration of chromatographic factors. Figure 4 compares the peak shapes obtained with water/methanol mixtures at 40:60 and 5:95 ratios. It can be seen that the higher percent of organic phase is a better transport medium. Further, the exclusion of involatile buffers and high salt content in the carrier phase reduced clogging of the TSP jet.

Repeat injections of standard solutions over a period of 3 h in the range of 50 nmol/L to 1 μmol/L were used to estimate the variability of the method. The average relative standard deviation in this range was found to be 17% by using the analogue as an internal standard. The precision of the assay could be improved by using an isotopomer of GBR-12909. A significant departure from the norm in electrometer gain settings was necessary for obtaining linear calibration curves in this determination. Generally an electrometer gain of 10^{-7} A/V is used for electron impact and chemical ionization in gas chromatography/mass spectrometry (GC/MS). However, at this setting calibration curves for GBR-12909 in the TSP/DI mode were approximately log linear. Linear calibration curves could only be obtained at a gain 10^{-6} A/V, for concentrations ranging from 50 nmol/L to 2 μmol/L.

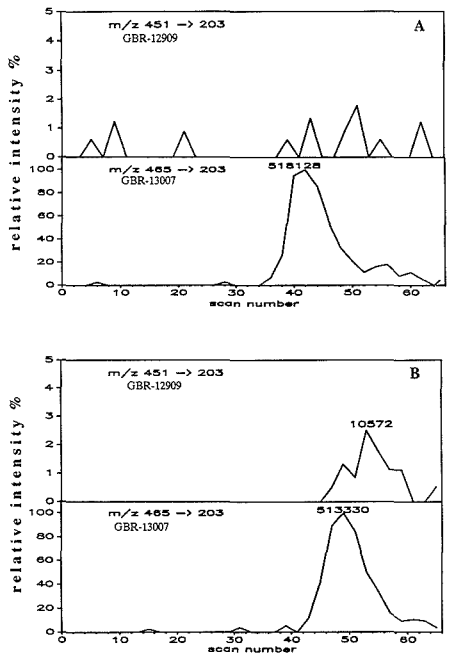

Figure 5. (A) Background noise from perfusate collected before the injection of the drug GBR-12909. The trace in the upper channel is the signal for GBR-12909 and the lower channel is the signal for the internal standard GBR-13007 at a concentration of 200 nmol/L. The numbers above the peaks are integrated areas in arbitrary units. (B) Perfusate obtained from the rat 1 h after an intraperitoneal injection of 100 mg/kg GBR-12909.

The MS/MS technique is highly selective and specific for the compounds of interest. Figure 5A shows the trace of the GBR-12909 signal from perfusate obtained before an animal was injected with the drug. The complex mixture sampled from the rat brain contributes very little by way of interference and only random noise spikes which are below the quantitation threshold of 0.1% of the area of the internal standard are observed. The concentration of the internal standard was 200 nmol/L. Figure 5B shows perfusate obtained from the same rat 1 h after injection of the drug. The signal for GBR-12909 is clearly differentiated from the background noise and quantifiable. An important contributing factor to this selectivity is the fact that TSP/DI predominantly produces the protonated molecular ion. Thus interferences from fragment ions in the first mass analyzer are minimized. Further thermal degradations from matrix constituents do not contribute significantly to the interference due to the low temperatures employed as compared to GC/MS. Specificity is aided by the fact that parent ion chosen has a relatively high molecular weight with a daughter ion fragment that incorporates a significant portion of the parent ion.

Deactivation of the surfaces the analyte comes in contact with is an important precaution for obtaining reproducible results when working with adsorbable analytes such as polar drugs. While this feature has received attention in LC work, it has not been sufficiently addressed in flow injection assay using thermospray ionization. This effect is pronounced at the nanogram and subnanogram level of analysis. The addition of an ion pairing agent/detergent (sodium hexylsulfonic acid) and a highly polar amine (triethylamine) significantly improves the reliability of estimates when working with low

Table I. Changes in the Measured Area of GBR-13007 (Mean ± Standard Deviation for Five Determinations) at a Concentration of 150 nmol/L in the Presence of Different Concentrations of GBR-12909

concn of GBR-12909, nmol/L	mean area[a] of GBR-13007 ± std dev
0	653 ± 191[b]
50	1689 ± 184
100	1916 ± 273

[a] The area count is in arbitrary units. [b] Significance was determined by Tukey-A post hoc comparisons at a p value of 0.01.

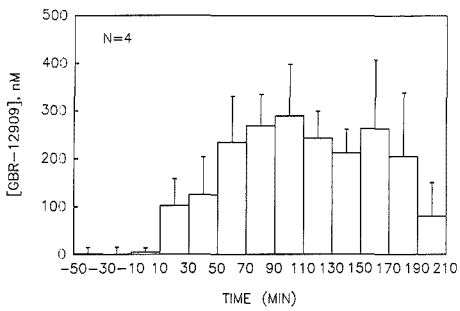

Figure 6. Concentration profile of GBR-12909 in the brain obtained from studies on four rats for a dose of 100 mg/kg i.p. The vertical bars represent the standard error of the mean.

levels of basic drugs. While triethylamine competes for the active sites in general, evidence for the existence of additional sites that adsorb the analogues can be inferred from the observation that the measured area for a given concentration of analyte changes in the presence of varying concentrations of the analogue. Table I shows the changes in measured area of GBR-13007 at a concentration of 150 nmol/L in the presence of GBR-12909 at three different concentrations, 0, 50, and 100 nmol/L. Notice the 2-fold increase in signal between the first two levels whereas the difference between the next two levels is not statistically significant. This suggests that the analogues compete for a limited number of selective active sites. Given this situation the internal standard additionally functions as means for enhancing the sensitivity of the determination. Our findings are supported by a recent report by Wang et al. (*17*) working with continuous flow liquid secondary ion mass spectrometry. They recommend saturation of active sites by injection of a bolus of analyte prior to analysis or the inclusion of an analogue or isotopomer in the carrier phase to deactive the injection valve and tubing surfaces.

The sensitivity obtained in this configuration was sufficient for studying the time course of GBR-12909 at high dose levels (100 mg/kg). Figure 6 shows the data obtained from studies on four animals. Interferences in the preinjection perfusate contribute a small signal equivalent to a 20 nmol/L solution.

It appears from the tests done so far that the transport of the drug from the site of an intraperitoneal injection to the brain is rather slow (1–2 h to reach peak concentration). Behaviorally, the longevity of drug action has been reported by Heikkila and Manzino (*18*) who found that rats exhibited intense ipsilateral rotation even after 6 h of administering 5 and 10 mg/kg doses of GBR-12909 analogues. A half-life of 80 min for GBR-12935 after intravenous administration was found by Andersen et al. (*19*) in binding curve studies.

For an intraperitoneal dose of 100 mg/kg, GBR-12909 exhibited a broad maximum between 1 and 3 h with an average

concentration of 250 nmol/L during this period. This estimate represents a lower limit due to the fact microdialysis probes had to be calibrated in vitro to obtain in vivo recovery factors. The actual concentration may be higher by as much as a factor of 2. However, these results can be compared to results obtained by Nicolaysen (*20*) for cocaine injections under similar dialysis conditions. The maximum concentration of cocaine occurred within 30 min of an intraperitoneal injection with a rapid decline to base line (2–3 h). The maximum concentration of cocaine in the brain for a dose of 30 mg/kg i.p. dose was found to be 10 μmol/L. The peak concentration of cocaine for one-third the dose, i.e. 30 mg/kg versus 100 mg/kg for GBR-12909, is thus about 40 times higher than the peak concentration of GBR-12909; 10 μmol/L versus 250 nmol/L. This significant difference in concentration profile could partially account for the highly attenuated potency of GBR-12909 in vivo relative to its potency in vitro.

This finding highlights some important characteristics of the microdialysis sampling technique. In vitro potency of a drug is estimated by the direct application of solutions of the drug to tissue slices whereas in vivo potency additionally depends on the transport of the drug from the site of an injection to the target areas in the brain. Transport involves the chemistry of the secondary properties of the drug such as solubility in body fluids at physiological pH, bound and free states, rate of metabolism, disposition ratios in various biocompartments, binding with other receptors, and the ability to cross the blood/brain barrier. Since microdialysis samples the extracellular fluid, the net effect of these factors on the availability of the drug at the target site is observed. While GBR-12909 has a higher potency than cocaine in tissue slice studies, microdialysis reveals that it is much less efficiently transported to target areas in the brain and therefore less efficacious in vivo.

CONCLUSIONS

Microdialysis was found to be an elegant technique for sampling the extracellular fluid of the rat brain in vivo and delivering a sample suitabe for flow injection analysis without further cleanup procedures. This technique is amenable for sampling a range of biocompartments in vivo not accessible to common quantitative techniques. Microdialysis in conjunction with FI/TSP/MS/MS was found to be a rapid, sensitive, and selective method for following the time course of GBR-12909 in vivo. With this method the concentration of GBR-12909 in the extracellular fluid was found to be much lower than that of cocaine for an equivalent dose administered intraperitoneally. This method can easily be extended to pharmacokinetic studies of other basic drugs and their metabolites.

ACKNOWLEDGMENT

We wish to thank James Holler of CDC for valuable guidance in this project.

LITERATURE CITED

(1) Ungerstedt, U. In *Measurement of Neurotransmitter Release in Vivo*; Marsden, C. A., Ed.; Wiley: New York, 1984; pp 81–105.
(2) Ungerstedt, U. *Curr. Sep.* **1986**, *7*, 43–46.
(3) Westerink, B. H. C.; Damsma, G.; Rollema, H.; DeVries, J. B.; Horn, A. S. *Life Sci.* **187**, *47*, 1763–1775.
(4) Hamberger, A.; Jacobson, I.; Sandberg, M. In *Measurement Techniques in Biotechnology*; Steinburg, M., Nygren, H., Eds.; Gothenburg: 1984; pp 1–8.
(5) Church, W. H.; Justice, J. B., Jr.; Neill, D. B. *Brain Res.* **1987**, *412*, 397–399.
(6) Wages, S. A.; Church, W. H.; Justice, J. B., Jr. *Anal. Chem.* **1986**, *58*, 1649–1656.
(7) Church, W. H.; Justice, J. B., Jr. In *Advances in Chromatography*; Giddings, J. C., Grushka, E., Brown, P. R., Eds.; Marcel Dekker: New York, 1989; Vol. 28, pp 165–194.
(8) Van der Zee, P.; Koger, H. S.; Gootjes, J.; Hespe, N. *Eur. J. Med. Chem.* **1980**, *15*, 363.
(9) Van der Zee, P.; Hespe, W. *Neuropharmacology* **1985**, *24* (12), 1171–1174.
(10) Nielsen, E. B.; Koger, H. S. In *Transduction Mechanisms of Drug Stimuli*; Colpaert, F. C., Balstter, R. R., Eds.; Springer Verlag: New York, 1988; pp 57–74.
(11) Roberts, D. C. S.; Koob, G. F.; Klonoff, P.; Fibiger, H. C. *Pharmacol., Biochem. Behav.* **1980**, *12* (5), 781–787.
(12) Roberts, D. C. S.; Corcoran, M. E.; Fibiger, H. C. *Pharmacol., Biochem. Behav.* **1977**, *6* (6), 615–620.
(13) Vestal, L. M.; Fergusson, G. J. *Anal. Chem.* **1985**, *57*, 2373–2378.
(14) Johnson, J. V.; Yost, R. A. *Anal. Chem.* **1985**, *57*, 758A–768A.
(15) Church, W. H.; Justice, J. B., Jr. *Anal. Chem.* **1987**, *59*, 712–716.
(16) Pellegrino, L.; Pellegrino, A.; Cushman, A. *A Stereotaxic Atlas of the Rat Brain*; Century-Crofts: New York, 1967.
(17) Wang, T. L.; Shih, M.; Markey, S. P.; Duncan, M. W. *Anal. Chem.* **1989**, *61*, 1013–1016.
(18) Heikkila, R. E.; Manzino, L. *Eur. J. Pharmacol.* **1984**, *103*, 241–248.
(19) Andersen, P. H.; Jansen, A. J.; Nielsen, E. B. *Eur. J. Pharmacol.* **1987**, *144*, 1–6.
(20) Nicolaysen, L.; Pan, H.; Justice, J. B., Jr. *Brain Res.* **1988**, *456*, 317–323.

RECEIVED for review August 21, 1989. Accepted December 12, 1989. Support for this project was provided by NSF Grant BNS 8812768.

Adduct Ion Formation in the Methane-Enhanced Negative Chemical Ionization Mass Spectrometry of 2-(Alkylthio)- and 2-Alkoxy-*s*-triazines

M. J. Incorvia Mattina and Lee Q. Huang*

Department of Analytical Chemistry, The Connecticut Agricultural Experiment Station, P.O. Box 1106, New Haven, Connecticut 06504

Roger N. Hayes

Midwest Center for Mass Spectrometry, University of Nebraska, Lincoln, Nebraska 68588

Adduct ions corresponding to $[M + 11]^-$, $[M + 13]^-$, and $[M + 25]^-$ are observed at significant abundance in the high-pressure, methane-enhanced, negative chemical ionization (NCI) mass spectra of seven 2-(alkylthio)-*s*-triazines. Under the same experimental conditions an adduct ion at $[M + 12]^{+\cdot}$ is noted in the mass spectra of six 2-alkoxy-*s*-triazines. These adduct ions are interferences in the mass spectral analysis of these compounds. Detailed studies using methane-d_4, $^{18}O_2/CH_4$, and Ar as alternate NCI enhancement gases reveal that the species responsible for adduct ion formation originate from the methane gas. This was confirmed by high-resolution accurate mass measurements of the adduct ions. Collisionally activated decomposition tandem mass spectrometry experiments were performed in an attempt to elucidate the structure of the adducts. The variation of the adduct ion abundance as a function of sample pressure, emission current, repeller voltage, and ion source temperature is also reported and possible mechanisms for the formation of the adduct ions are examined.

INTRODUCTION

The conditions prevailing in the high-pressure chemical ionization source of a conventional mass spectrometer are such that, in addition to unimolecular reactions (e.g., ionization of the analyte molecule and fragmentation of the parent ion), bimolecular, collisional reactions may occur with some facility (*1*), producing ions that complicate the mass spectral analysis. Numerous examples of such collisional reactions have been reported for compounds whose spectra are acquired under electron capture negative chemical ionization (NCI) conditions (*2–11*). Examples from the positive chemical ionization (PCI) mode are also known (*12*). The reactions may be divided into two broad classes: class 1 reactions occur exclusively in the gas phase, while reactions belonging to class 2 appear to be mediated by the ion source walls.

Class 1 reactions include the gas-phase addition of a radical species, derived from the enhancement gas, to the analyte molecule to form a neutral adduct (*2*). The adduct may then be ionized by electron capture for detection in the negative ion mode or it may be protonated for detection in the positive ion mode. The PCI and NCI mass spectra of known radical traps such as 7,7,8,8-tetracyanoquinodimethane (TCNQ), tetracyanoethylene (TCNE), and tetracyanopyrazine (TCP) (*3–6*), as well as some PAH compounds (*7, 8*), contain ions attributed to radical/molecule reactions. It has been shown that such gas-phase radical/molecule reactions in the high pressure source occur at rates competitive with ionization (*9*).

A second type of class 1 reaction is an ion/molecule reaction in which both adduct formation and ionization occur in a single step. A well-known example is the reaction of $C_2H_5^+$ from a hydrocarbon enhancement gas with analyte molecules to form the commonly detected $[M + C_2H_5]^+$ adduct in PCI (*1*). Alternatively, both the fragment ion and the neutral molecule may be derived from the sample under analysis, giving rise to either anion adducts (*10, 11*) or cation adducts (*12*). Such gas-phase reactions are presumed to be independent of the moderating enhancement gas. Gas-phase ion/molecule reactions have also been reported for which the ionic component, such as $O^{+\cdot}$, is derived from enhancement gas impurities (*13, 14*).

In contrast to class 1 reactions that occur solely in the gas phase, class 2 reactions are mediated by the source walls. Proposed wall-mediated reactions include the oxidation of PAH compounds by residual oxygen adsorbed on the ion source walls (*15*). The oxidized product is then desorbed from the source walls and ionized in the gas phase to produce unusual ions in the mass spectrum, some of which are observed at m/z greater than the parent ion. In another example of a wall-mediated reaction carboxylic acids have been shown to react with adsorbed chlorine to form an adduct, which is subsequently desorbed and ionized in the gas phase (*16*).

Because of their widespread use as herbicides, considerable interest exists in developing sensitive and specific analytical methods for *s*-triazine compounds by mass spectrometry using electron impact (EI) ionization (*17, 18*), PCI (*19*), and NCI (*20, 21*). In our initial investigation of the utility of NCI for analysis of these compounds, several types of adduct ions at significant abundance were observed (*20*). In contrast to most gas-phase adducts reported previously for other classes of compounds, an *s*-triazine adduct may be observed at an abundance exceeding that of the parent ion and may appear at an m/z value corresponding to the parent ion of a different *s*-triazine. It is, therefore, apparent that such adducts are serious potential interferences in the accurate interpretation of the NCI mass spectra of *s*-triazines and merit a thorough investigation as to their origin and structure.

The studies reported here include the use of argon, methane-d_4, and $^{18}O_2/CH_4$ as alternate CI enhancement gases and identify the hydrocarbon enhancement gas as the source of the reactive species that lead to adduct formation. Collisionally activated decomposition (CAD) tandem mass spectrometry (MS/MS) is used in an attempt to elucidate the structures of the adduct ions. The data suggest that the alkylthio or alkoxy moiety in the 2-position of the *s*-triazine is an active site for reaction with the species derived from the enhancement gas. The abundance of the adduct ion as a function of the source temperature, the repeller voltage, the

* Author to whom correspondence should be addressed.

0003-2700/90/0362-0602$02.50/0

Table I. Relative Abundances of Adduct Ions Observed in the Methane-Enhanced Negative Chemical Ionization Mass Spectra of 2-(Alkylthio)-*s*-triazines

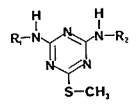

name	mol wt	R_1	R_2	relative abundance,[a] % $[M + 11]^-$	$[M + 13]^-$	$[M + 25]^-$	$[M - 1]^-$
ametryne	227	Et	*i*-Pr		100	69	28
desmetryne	213	Me	*i*-Pr		100	80	30
metoprotryne	271	*i*-Pr	$(CH_2)_2OCH_3$		100	46	55
prometryne	241	*i*-Pr	*i*-Pr		100	63	33
simetryne	213	Et	Et		100	78	34
terbutryne	241	Et	*t*-Bu		100	74	42
dipropetryne[b]	255	*i*-Pr	*i*-Pr	44			100

[a] Spectra were acquired via GC introduction of sample and DIP introduction of methane gas at ion source temperature of 300 °C. [b] Dipropetryne is a 2-(SCH_2CH_3)-*s*-triazine.

emission current, and the sample concentration is examined in an attempt to elucidate the pathway for adduct ion formation.

EXPERIMENTAL SECTION

Reagents. The *s*-triazines at 98% to 99% purity were obtained from the EPA Pesticides and Industrial Chemicals Repository (Research Triangle, NC) or from the manufacturer, Ciba-Geigy, Agricultural Division (Greensboro, NC) and were used without further purification. All solvents were Fisher Optima grade. A separate methanol solution was prepared for each *s*-triazine at 100 to 200 mg/L concentration. Ultrahigh purity methane gas (Linde Specialty Gases) was filtered through an OMI-1 indicating purifier (Supelco, Bellefonte, PA) and an Oxiclear disposable gas purifier (Labclear, Oakland, CA). Argon (ultrahigh purity) was also supplied by Linde. Methane-d_4 at 99.8% enrichment was obtained from Cambridge Isotopes (Woburn, MA) and $^{18}O_2$ at 98% enrichment from MSD Isotopes (Kirkland, Quebec, Canada). These stable isotope gases were supplied in glass flasks fitted with glass break seals.

Instrumentation. Experiments were performed on a Hewlett-Packard 5890 gas chromatograph (GC) coupled via a capillary direct interface to an HP 5988A quadrupole mass spectrometer (MS) modified for negative ion detection. The methanol solution of the *s*-triazine was injected in splitless mode into the glass-lined GC inlet held at 250 °C. The temperature program for the SPB-608 column (Supelco) was 90 °C for 1 min, ramped at 10 °C/min to 250 °C and held for 2 min. The GC/MS interface was held at 250 °C. Helium, filtered through an OMI-1 indicating purifier, was used as the carrier gas. The MS tuning protocol has been reported previously (*20*). Unless otherwise indicated, methane, methane-d_4, and argon were introduced into the source through the heated GC/MS interface by means of a Porter Instrument Co. (Hatfield, PA) Model DFC-1400 flow controller. Source pressure was monitored with a Hastings Raydist (Hampton, VA) DV-24 vacuum gauge tube located at the GC/MS interface. For experiments in which $^{18}O_2$ was doped into methane, both the oxygen-18 and the methane were introduced into the source via a modified calibration probe (HP part number 05985-20585). In these experiments source pressures were measured with a Hastings Raydist vacuum gauge tube fitted to the end of the calibration probe. This probe is inserted into the source through the direct insertion probe (DIP) inlet port which on the HP 5988A is oriented on the source housing directly opposite the GC inlet port. The methane line was connected to the calibration probe after flow control via the DFC-1400 flow controller. The glass neck of the oxygen flask was attached to the calibration probe with appropriate size Teflon ferrules and swage fittings. Oxygen flow was controlled with a Circleseal shut-off valve (HP part number 0101-0297) and a Nupro metering valve (HP part number 0101-0287). There are two major differences between this design for enhancement gas introduction and the usual enhancement gas introduction through the GC/MS interface. First, the gas line is not heated and second, as noted above, the gas is introduced into the source directly opposite the inlet port for the introduction of the GC effluent into the source. These differences required that enhancement gas source pressure values for the optimization of the ionization of DFTPP be reestablished by using the previously described method (*20*). By use of this instrumental configuration for the introduction of the enhancement gas into the MS source, a substantial decrease in the MS sensitivity for samples introduced via the GC was observed. In doping oxygen-18 into methane our procedure was to set the methane pressure to approximately 90% of its optimum value. Oxygen-18 was then leaked into the methane stream until the pressure in the source achieved the full optimum pressure value.

High-resolution accurate mass measurements and CAD MS/MS spectra were acquired on a Kratos MS50 triple analyzer mass spectrometer of EBE configuration (*22*). Ions were formed in a Kratos Mark IV chemical ionization source: source temperature, 150 °C; electron energy, 280 eV; emission current, 500 μA; accelerating voltage, 8 kV. The indicated methane pressure was 1×10^{-5} Torr, corresponding to an estimated source pressure of 10^{-1} Torr. For the CAD measurements, helium was used in the collision cell at pressures that achieved a 50% attenuation of the parent ion beam.

RESULTS AND DISCUSSION

Adduct ions observed for the seven 2-(alkylthio)-*s*-triazines included in the present study are summarized in Table I. Under the experimental conditions given in the table the base peak is the $[M + 13]^-$ ion and the $[M + 25]^-$ ion is observed at greater than 40% relative abundance for six 2-(methylthio)-*s*-triazines. In the NCI mass spectrum of dipropetryne, a 2-(ethylthio)-*s*-triazine, the $[M + 11]^-$ ion is the only adduct observed at significant abundance.

The adduct ions observed for six 2-alkoxy-*s*-triazines included in the present study are given in Table II. For all six of the compounds an adduct ion is observed in the methane-enhanced NCI mass spectrum at an m/z value corresponding to $[M + 12]^{\bullet-}$.

Elemental Composition of the Adduct Ions. Since a substantial amount of the ion current in the NCI mass spectra of 2-(alkylthio)-*s*-triazines (*20*) is carried by the $[M - 1]^-$ rather than the $M^{\bullet-}$ ion, we hypothesized that the observed $[M + 13]^-$ adducts are due to $[M + 14 - H]^-$ rather than to an esoteric combination of elemental additions and losses, resulting in a net gain of 13 amu over the parent molecule. We, therefore, focused our attention on $[M + 14]$ as the species formed, which undergoes subsequent loss of hydrogen and ionization. In this empirical description of the adduct, no mechanism for adduct formation, loss of hydrogen, or ionization is implied.

Previous reports in the literature have attributed $[M + 14]^{\bullet-}$

Table II. Relative Abundances of Adduct Ions Observed in the Methane-Enhanced Negative Chemical Ionization Mass Spectra of 2-Alkoxy-*s*-triazines

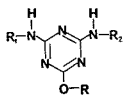

name	mol wt	R_1	R_2	R	relative abundance,[a] % $[M + 12]^{\cdot-}$	$[M - 1]^-$
atratone	211	*i*-Pr	Et	Me	5	100
prometone	225	*i*-Pr	*i*-Pr	Me	10	100
secbumetone	225	*s*-Bu	Et	Me	8	100
simetone	197	Et	Et	Me	7	100
terbutone	225	Et	*t*-Bu	Me	6	100
"dipropetone"[b]	239	*i*-Pr	*i*-Pr	Et	12	100

[a] The spectra were acquired via GC introduction of the compound at an ion source temperature of 250 °C. [b] "Dipropetone" is not a commercially available compound; thus, it is named in quotation marks.

adducts either to a wall-mediated oxidation reaction producing $[M + O - 2H]^{\cdot-}$ ions (*15*) or to a gas-phase radical/molecule reaction producing $[M + CH_2]^{\cdot-}$ (*7–9*). In order to determine whether oxidation is responsible for adduct formation in the 2-(alkylthio)-*s*-triazines, oxygen-18 was doped into the methane stream. Figure 1a is the NCI mass spectrum acquired using $^{18}O_2/CH_4$ as the enhancement gas of desmetryne introduced through the GC into the source held at 300 °C. When this spectrum is compared with that shown in Figure 1b, which was acquired under the same conditions except that 100% CH_4 was used as the enhancement gas, no mass shift of the adduct ions is noted. Thus, under our experimental conditions oxygen incorporation is not involved in the formation of these adduct ions for the 2-(alkylthio)-*s*-triazines.

Subsequently, we focused our attention on the second plausible explanation for the production of the [M + 14] adduct, namely, that of a radical/molecule reaction in which the radical is derived from the hydrocarbon enhancement gas. An attempt to elucidate this role by using methane-d_4 as the enhancement gas is illustrated by the CD_4 enhanced NCI mass spectrum of desmetryne in Figure 1c. Under the experimental conditions we observe an apparent hydrogen/deuterium exchange attributable to the N–H hydrogens of the amino moiety. We have shown previously that hydrogen/deuterium exchange for the hydrogens on the alkylamino groups is unlikely (*20*). These data also suggest that alkyl substitution of the alkylthio group by CD_3, accompanied by exchange of the N–H hydrogen for deuterium, may be occurring. Hydrogen/deuterium exchange occurring during high-pressure NCI mass spectrometry using ND_3 as the enhancement gas has been reported previously (*23*). Our experiment confirms that an interaction between the hydrocarbon enhancement gas and the *s*-triazine substrate is taking place in the high-pressure chemical ionization source. Indeed, if methane is replaced by argon as the enhancement gas, the $[M + 13]^-$ and $[M + 25]^-$ adduct ions are no longer observed, as may be seen in Figure 1d for desmetryne.

Similar results are obtained for all the (alkylthio)-*s*-triazines examined. Figure 2a shows the methane-enhanced NCI mass spectrum of approximately 200 ng of prometryne introduced through the GC. There are abundant $[M + 13]^-$ and $[M + 25]^-$ adduct ions. These ions are not detected in the argon-enhanced NCI spectrum (Figure 2b) acquired under the same experimental conditions and recorded at the same retention time (RT) as the spectrum shown in Figure 2a. The methane-enhanced NCI mass spectrum of approximately 200 ng

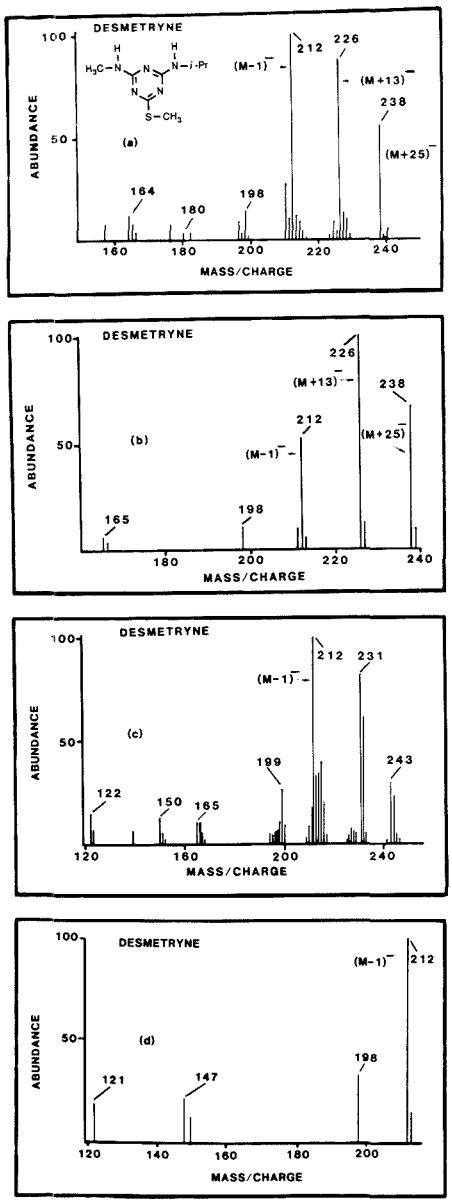

Figure 1. Negative chemical ionization mass spectra of desmetryne introduced through the GC at a source temperature of 300 °C using (a) $^{18}O_2/CH_4$, (b) CH_4, (c) CD_4, and (d) Ar as the enhancement gas.

of dipropetryne, introduced through the GC into the mass spectrometer source held at 300 °C, shows ions at m/z 240 and m/z 266, which correspond to $[M - 15]^-$ and $[M + 11]^-$, respectively (Figure 3a). If this dipropetryne spectrum is acquired by using argon as the enhancement gas, the spectrum shown in Figure 3b is recorded. The absence of both the [M − 15] and [M + 11] anions in Figure 3b shows that the methane gas is a crucial component in the reactions occurring in the high-pressure chemical ionization source with *s*-triazine

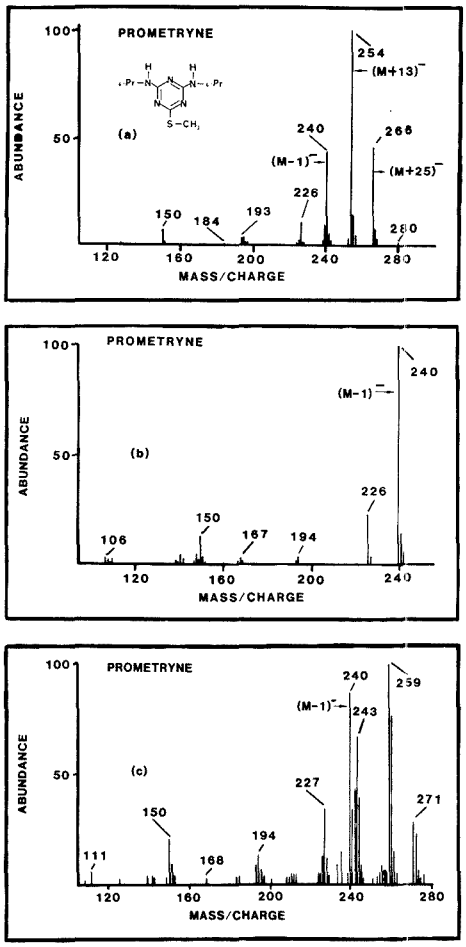

Figure 2. Negative chemical ionization mass spectra of prometryne introduced through the GC at a source temperature of 300 °C using (a) CH_4, (b) Ar, and (c) CD_4 as the enhancement gas.

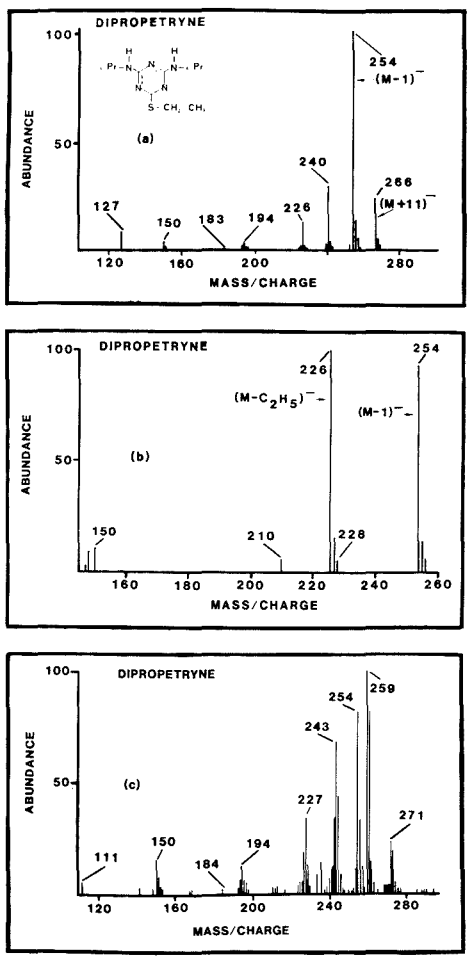

Figure 3. Negative chemical ionization mass spectra of dipropetryne introduced through the GC at a source temperature of 300 °C using (a) CH_4, (b) Ar, and (c) CD_4 as the enhancement gas.

substrates. This conclusion is confirmed by the NCI mass spectra for prometryne and dipropetryne in Figures 2c and 3c, respectively, acquired by using CD_4 as the enhancement gas.

Adducts are also observed for the 2-alkoxy-*s*-triazines. Figure 4a shows the methane-enhanced NCI mass spectrum of prometone with the $[M + 12]^{\cdot-}$ adduct at m/z 237. No adduct is observed in the NCI mass spectrum acquired under the same experimental conditions using argon as the NCI enhancement gas (Figure 4b). Similarly, the $[M + 12]^{\cdot-}$ adduct observed in the methane-enhanced NCI mass spectrum for the 2-ethoxy-*s*-triazine shown in Figure 5a is not observed when argon is used as the enhancement gas (Figure 5b).

For each compound included in this study the GC retention time is unique, reproducible, and independent of the source conditions such as ionization mode or enhancement gas. Under EI conditions library searchable spectra are obtained for the compounds. These observations together with the presence of adduct ions in the methane-enhanced NCI mass spectra and the absence of adduct ions in the argon-enhanced NCI mass spectra confirm that adduct ion formation must be a gas-phase phenomenon occurring within the high-pressure chemical ionization source when methane is used as the enhancement gas.

The experimental evidence obtained by using argon, oxygen-18, or methane-d_4 as the enhancement gas suggests clearly that the adducts are formed from the addition of carbon and hydrogen to the substrate. High-resolution accurate mass measurements were obtained to confirm the elemental formula of the adducts. Table III contains the predicted masses for the formula of the adducts based solely on the addition of carbon and/or hydrogen to the parent molecule. It also lists the experimentally observed masses for the adducts. The experimental values were obtained by introducing the *s*-triazine via the DIP into the source of a high-resolution magnetic sector Kratos MS50 operated in chemical ionization mode using methane as the enhancement gas. In addition to providing the accurate mass for the adduct ions, these experiments confirm that the observation of the adducts is not limited to the source of the HP 5988A quadrupole mass spectrometer.

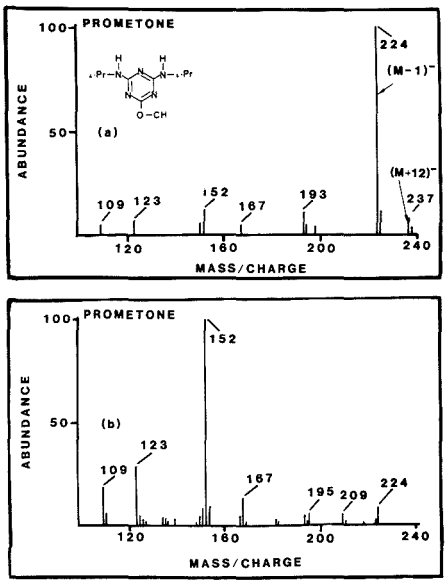

Figure 4. Negative chemical ionization mass spectra of prometone introduced through the GC at a source temperature of 200 °C using (a) CH_4 and (b) Ar as the enhancement gas.

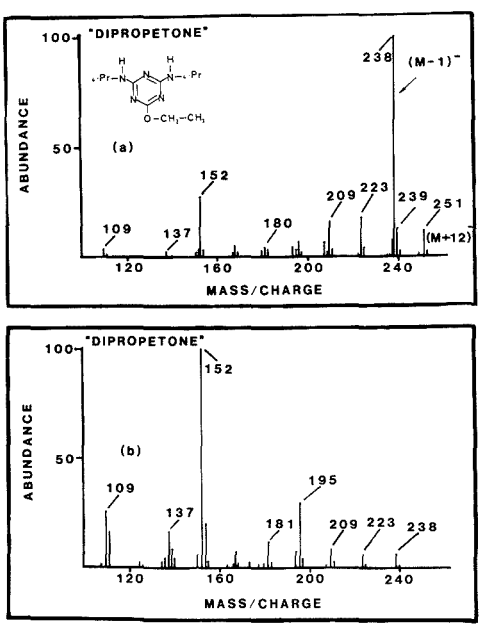

Figure 5. Negative chemical ionization mass spectra of "dipropetone" introduced through the GC at a source temperature of 200 °C using (a) CH_4 and (b) Ar as the enhancement gas.

Investigation of Structure and Formation of the Adducts. If the methane-enhanced NCI mass spectra of prometryne (a (methylthio)-*s*-triazine) and dipropetryne (an (ethylthio)-*s*-triazine) shown in Figures 2a and 3a, respectively, are compared, the striking similarity between the two spectra is apparent. This similarity suggests that an interconversion from one (alkylthio)-*s*-triazine to the other (alkylthio)-*s*-triazine may be occurring in the high-pressure chemical ionization source of the HP 5988A quadrupole mass spectrometer, resulting in indistinguishable NCI mass spectra for the two compounds. In order to determine if the structure of the m/z 254 ion as well as the structure of the m/z 266 ion is the same regardless of whether the ion is derived from prometryne or dipropetryne, the CAD daughter ion spectra of the parent ions m/z 254 and 266 were acquired on the Kratos MS50 magnetic sector mass spectrometer. These spectra are shown in Figures 6a–e. If the m/z 254 ion of dipropetryne is produced from either methane-enhanced electron capture NCI (Figure 6b) or argon-enhanced electron capture NCI (Figure 6c), the daughter ion CAD spectra are the same, indicating that the $[M - 1]^-$ ion of dipropetryne is largely intact in the Kratos MS50 source. If the m/z 254 ion is produced from the methane-enhanced NCI of prometryne (Figure 6a), however, a different CAD daughter ion spectrum is obtained. Since the spectrum in Figure 6b must represent the $[M - 1]^-$ ion of the intact dipropetryne molecule, the CAD spectra suggest that the m/z 254 ion (the $[M + 13]^-$ adduct) of prometryne does not have the identical structure as the m/z 254 ion from dipropetryne, at least under the experimental conditions employed. Similarly, the CAD daughter ion spectra of the m/z 266 ion are also different depending on whether the ion is derived from prometryne (Figure 6d) or dipropetryne (Figure 6e). A similar conclusion must be drawn that, under the experimental conditions employed, the structure of the m/z 266 adduct from prometryne differs from the structure of the m/z 266 adduct from dipropetryne.

The CAD daughter ion spectra were also acquired for the $[M + 12]^-$ adducts generated in the methane-enhanced NCI mass spectrometry of two 2-alkoxy-*s*-triazines, a methoxy-*s*-triazine (prometone), and the corresponding ethoxy-*s*-triazine. In this case the differences in the normal methane-enhanced NCI mass spectra of the two compounds obtained on the HP 5988A mass spectrometer (Figures 4a and 5a) do not suggest an interconversion between the 2-methoxy-*s*-triazine and the 2-ethoxy-*s*-triazine in the high-pressure mass spectrometer source.

While the CAD MS/MS spectra for the adduct ions obtained to date permit us to distinguish between isomers having the same elemental composition, none of the CAD spectra permits us to deduce unequivocally the structures of the adduct ions. For the 2-(alkylthio)- and 2-alkoxy-*s*-triazines, the weak S–alkyl bond (*24*, *25*) or the weak O–alkyl bond (*26*) as well as the labile amino N–H bond are potential reactive sites for interaction with the methane gas. Although we have concluded that the experimental evidence for several 2-chloro-*s*-triazine compounds supports the formation of [M +

Table III. Predicted and Observed Masses for Elemental Formula of (Alkylthio)- and Alkoxy-*s*-triazine Adduct Ions

	$C_{11}H_{20}N_5S^a$		$C_{12}H_{20}N_5S^b$	
compound	predicted	observed	predicted	observed
prometryne	254.1436	254.1439	266.1436	266.1440
dipropetryne	254.1436	254.1438	266.1436	266.1432
	$C_{11}H_{19}N_5O^c$		$C_{12}H_{21}N_5O^d$	
compound	predicted	observed	predicted	observed
prometone	237.1586	237.1590		
"dipropetone"			251.1746	251.1746

[a] This is the $[M + 13]^-$ ion for prometryne and the $[M - 1]^-$ ion for dipropetryne. [b] This is the $[M + 25]^-$ ion for prometryne and the $[M + 11]^-$ ion for dipropetryne. [c] This is the $[M + 12]^{\cdot-}$ ion for prometone. [d] This is the $[M + 12]^{\cdot-}$ ion for "dipropetone".

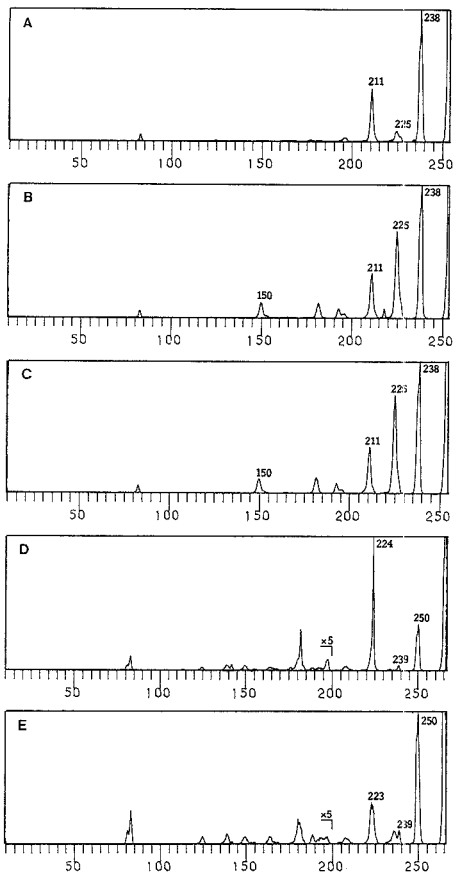

Figure 6. CAD MS/MS of m/z 254 from (a) prometryne and (b) dipropetryne using methane and (c) dipropetryne using Ar, and m/z 266 from (d) prometyne and (e) dipropetryne.

14]$^{\bullet-}$ and [M + 28]$^{\bullet-}$ adducts via the addition of CH_2 at the N–H bond of the amino groups (*27*), the formation of [M + 13]$^-$, [M + 25]$^-$, and [M + 11]$^-$ adducts observed in the methane-enhanced NCI mass spectra for the compounds listed in Table I supports the hypothesis that the S–alkyl bond is participating in the formation of the adducts of the 2-(alkylthio) compounds. Similarly, the formation of the [M + 12]$^{\bullet-}$ adducts observed in the methane-enhanced NCI mass spectra for the compounds listed in Table II supports the hypothesis that the O–alkyl bond is participating in the formation of the adducts of the 2-alkoxy compounds. It is apparent that the effective insertion of CH_2 into the amino N–H bond cannot account fully for the formation of the adducts of 2-(alkylthio)- and 2-alkoxy-*s*-triazines as it can for the adducts of 2-chloro-*s*-triazines. Further research using model compounds and isotopically labeled standards is planned in order to deduce the structures of the adducts. It is also of interest to obtain the CAD daughter ion spectra of the adduct ions using a triple stage quadrupole (TSQ) mass spectrometer. Source conditions in a TSQ (e.g., ion residence time) would reflect more closely the source conditions in the HP 5988A quadrupole.

Having established that the methane enhancement gas is the source of the reactive species for reaction with the *s*-triazine, it was of interest to investigate the mechanism through which the reaction occurs. The reactive species from the enhancement gas may be (1) a carbon-centered anion; (2) carbon-centered radicals, and H$^\bullet$ radicals, and (3) the CH_4 molecule. The reactive substrate may be (1) the neutral *s*-triazine or (2) the *s*-triazine anion. The mechanism for interaction between the substrate and the enhancement gas may involve (1) insertion of the reactive species from the enhancement gas into bonds of the substrate or (2) substitution of the original alkyl group at the 2 position of the *s*-triazine with an alkyl group derived from the hydrocarbon enhancement gas. We examined these different possibilities in some preliminary investigations.

Negative ions derived from the methane plasma are rarely detected under high-pressure chemical ionization conditions (*7*). In the HP 5988A quadrupole mass spectrometer used in our studies for high-pressure chemical ionization, anions at very low abundance were observed in the methane plasma at m/z values 25, 41, and 53. In light of our observations and those of other investigators, it seemed unlikely that anions derived from the enhancement gas could be resonsible for the formation of the adduct ions of the *s*-triazines.

In contrast to the lack of alkyl anions, alkyl radicals as well as the highly reactive methylidene (CH$^\bullet$) and methylene (CH_2) species are known to be present at significant concentration in the plasma formed with a hydrocarbon enhancement gas in the mass spectrometer source under high-pressure chemical ionization conditions (*2–7, 28*). Several studies have demonstrated that for adduct ion formation via a proposed radical/molecule pathway, the abundance of the adduct ion increases as the source temperature and sample pressure decrease. In the same studies the adduct ion abundance has been found to increase as emission current increases (*2, 7, 29*). On the contrary, for the 2-(alkylthio)-*s*-triazines which we examined, the ratio of the relative abundance of the adduct ions to the [M – 1] anion increases sharply as the source temperature increases. This is illustrated for prometryne in Figure 7a. The plot of the ratio of the adduct ion abundance to the [M – 1]$^-$ abundance for prometryne versus the sample pressure in Figure 7b shows an increase in the adduct ion abundance as the sample pressure increases. We observed no dependence of the adduct ion abundances of prometryne on the emission current as the emission current was varied from 100 to 500 μA.

Experiments were performed to determine if competition between the *s*-triazine and known radical traps for the radicals produced in the methane plasma could be demonstrated. Accordingly, a relatively large amount of a known radical trap, such a TCNE or TCNQ (*2, 3*), was introduced into the source via the DIP, simultaneously with the elution of the 2-(methylthio)-*s*-triazine from the GC. Under these conditions no changes in the abundance of the adducts for the *s*-triazine compounds were observed.

The above observations suggest either that (1) a radical mechanism is in effect for which the kinetics and the radicals are different from previously proposed radical reactions occurring in the high-pressure chemical ionization source or (2) that a nonradical mechanism is in effect. With regard to the first point Budzikiewicz has proposed that "alleged radical reactions prior to ionization" demand further investigation (*30*). From his data Budzikiewicz concludes that insertion of CH$^\bullet$ and CH_2 rather than substitution by alkyl radicals such as $CH_3^\bullet$ may be the pathway for formation of many adducts observed in methane-enhanced NCI mass spectrometry. Relative to the second point, a recent report in the literature describes the formation of an [M + H]$^-$ adduct for chlorprothixene and other aromatic sulfur compounds under methane-enhanced negative chemical ionization conditions

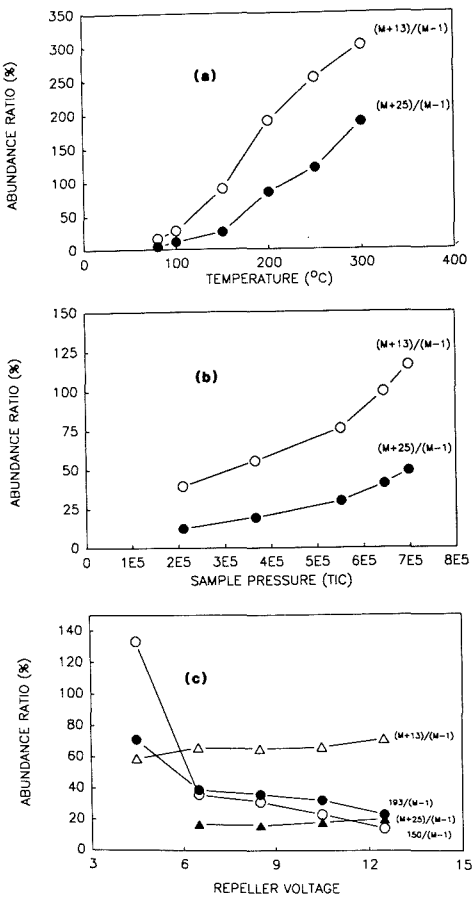

Figure 7. Variation of ionic abundance with (a) source temperature, (b) sample pressure, and (c) repeller voltage in the CH_4-enhanced negative chemical ionization mass spectra of prometryne.

(*31*). No variation of the abundance of the $[M + H]^-$ ion as the emission current was increased from less than 100 to 4000 μA was found. On the basis of their observations the authors proposed a pathway for the formation of $[M + H]^-$ in which $M^{\bullet-}$ reacts with neutral CH_4.

In order to check if an analogous reaction between $M^{\bullet-}$ and CH_4 accounts for adduct formation in *s*-triazines, the adduct ion abundance was measured as a function of the repeller voltage. As the repeller voltage is increased, the ion residence times in the quadrupole source are decreased (*32*). We would expect the adduct ion abundance to decrease as the repeller voltage increases if an anionic species is involved in adduct ion formation. Figure 7c shows the ratio of the abundance of $[M + 13]^-$ or $[M + 25]^-$ to the abundance of $[M - 1]^-$ as well as the ratio of the abundance of the fragment ions m/z 150 and 193 to the abundance of $[M - 1]^-$ for prometryne. The adduct ion abundance is independent of the repeller voltage, while the fragment ion abundance increases as the repeller voltage decreases. This suggests that neutral species only are responsible for adduct ion formation.

The apparently contradictory data from the above series of experiments indicate that further work is needed to deduce the mechanism of adduct ion formation in this series of *s*-triazine compounds. It may be that the criteria described above to identify radical/molecule reactions (*2*, *7*, *28*) are not valid for all such reactions.

Our experiments do not permit us to determine the relative amount of insertion versus substitution (*8*) pathways. The spectra in Figures 1c, 2c, and 3c suggest that in the HP 5988A quadrupole source a noticeable amount of substitution by $CD_3^{\bullet}$ is taking place at the S–alkyl bond. For the 2-(alkylthio)- and 2-alkoxy-*s*-triazine compounds at least two reactive sites are present in the molecule at which either or both insertion and substitution may occur. *s*-Triazine compound with ^{13}C labeled alkylthio or alkoxy groups would be useful in order to elucidate the competition between a substitution pathway and an insertion pathway at the S–alkyl or the O–alkyl bond.

CONCLUSIONS

We have demonstrated that the formation of adducts of 2-(alkylthio)- and 2-alkoxy-*s*-triazines competes very effectively with electron-capture ionization of these molecules during methane-enhanced negative chemical ionization mass spectrometry. Under certain experimental conditions the NCI mass spectra for two alkylthio compounds are indistinguishable. There are some significant analytical implications of these data. While the sensitivity of electron-capture NCI for the detection of many xenobiotic compounds is established, the use of methane as the enhancement gas in this technique can produce spectra for some compounds that may be easily misinterpreted. For such compounds a nonreactive chemical ionization enhancement gas such as argon is more appropriate. Although argon was proposed as the moderating gas for chemical ionization several years ago (*7*), this suggestion has gone unheeded. Recent experimental evidence (*33*) suggests that argon is useful for charge exchange PCI and our results suggest that it is essential for some classes of compounds in electron-capture NCI. The large abundance of the adducts and the variation of the adduct abundance with temperature and sample pressure, especially for the methane-enhanced NCI of the 2-(alkylthio)-*s*-triazines, can affect both the qualitative and quantitative analysis of these compounds.

ACKNOWLEDGMENT

We acknowledge a gift of triazines from the Ciba-Geigy Corporation. The technical assistance of Anthony Paiva and Anne Perron in the preparation of the paper is gratefully acknowledged.

LITERATURE CITED

(1) Harrison, A. G. *Chemical Ionization Mass Spectrometry*; CRC Press: Boca Raton, FL, 1983.
(2) McEwen, C. N. *Mass Spectrom. Rev.* **1986**, *5*, 521.
(3) McEwen, C. N.; Rudat, M. A. *J. Am. Chem. Soc.* **1979**, *101*, 6470.
(4) McEwen, C. N.; Rudat, M. A. *J. Am. Chem. Soc.* **1981**, *103*, 4343.
(5) Rudat, M. A.; McEwen, C. N. *J. Am. Chem. Soc.* **1981**, *103*, 4349.
(6) McEwen, C. N.; Rudat, M. A. *J. Am. Chem. Soc.* **1981**, *103*, 4355.
(7) Stockl, D.; Budzikiewicz, H. *Org. Mass Spectrom.* **1982**, *17*, 376.
(8) Dillow, G. W.; Gregor, I. K. *Org. Mass Spectrom.* **1986**, *21*, 386.
(9) Sears, L. J.; Campbell, J. A.; Grimsrud, E. P. *Biomed. Environ. Mass Spectrom.* **1987**, *14*, 401.
(10) Mattina, M. J. I.; Huang, L. Q. *Org. Mass Spectrom.* **1989**, *24*, 340.
(11) Lynn, B. C.; Marbury, G. D.; Tuschall, J. R. *Org. Mass Spectrom.* **1988**, *23*, 736.
(12) Maryanoff, C. A.; Caldwell, G. C.; Chang, S. Y. *Org. Mass Spectrom.* **1988**, *23*, 129.
(13) Buchanan, M. V.; Wise, M. B. *Fourier Transform Mass Spectrometry: Evolution, Innovation, and Applications*; Buchanan, M. V., Ed.; The American Chemical Society: Washington, DC, 1987; Chapter 11.
(14) Low, G.; Batley, G. E.; Ligard, R. O.; Duffield, A. M. *Biomed. Environ. Mass Spectrom.* **1986**, *13*, 95.
(15) Stemmler, E. A.; Buchanan, M. V. *Org. Mass Spectrom.* **1989**, *24*, 94.
(16) Kassel, D. B.; Kayganich, K. A.; Watson, J. T.; Allison, J. *Anal. Chem.* **1988**, *60*, 911.
(17) Lopes-Avila, V.; Hirata, P.; Kraska, S.; Flanagan, M.; Taylor, J. H. *Anal. Chem.* **1985**, *57*, 2797.
(18) Huang, L. Q. *J. Assoc. Off. Anal. Chem.* **1989**, *72*, 349.
(19) Leclercq, P. A.; Pacakova, V. *J. Chromatogr.* **1979**, *178*, 193.
(20) Huang, L. Q.; Mattina, M. J. I. *Biomed Environ. Mass Spectrom.* **1989**, *18*, 828.

(21) Nystrom, J. A.; Tondeur, Y.; Hass, J. R.; Bursey, M. M. Presented at the 28th ASMS Conference on Mass Spectrometry and Allied Topics, 1980, New York City, NY.
(22) Gross, M. L.; Chess, E. K.; Lyon, P. A.; Crow, F. w.; Evans, S.; Tudge, H. *Int. J. Mass Spectrom. Ion Phys.* **1982**, *42*, 243.
(23) Hunt, D. F.; Sethi, S. K.; Shabanowitz, J. *EHP, Environ. Health Perspect.* **1980**, *36*, 33.
(24) McMillin, D. F.; Golden, D. M. *Annu. Rev. Phys. Chem.* **1982**, *33*, 493.
(25) Sallans, L.; Lane, K. r.; Freiser, B. S. *J. Am. Chem. Soc.* **1989**, *11*, 865.
(26) Paul, S.; Back, M. H. *Can. J. Chem.* **1975**, *53*, 3330.
(27) Huang, L. Q.; Mattina, M. J. I.; Hayes, R. N. *Biomed. Environ. Mass Spectrom.*, in press.
(28) Dillow, G. W.; Gregor, I. K.; Guilhaus, M. *Org. Mass Spectrom.* **1986**, *21*, 151.
(29) Madhusudanan, K. P.; Seth, M.; Bhaduri, A. P. *Org. Mass Spectrom.* **1985**, *20*, 292.
(30) Budzikiewicz, H.; Drabner, G. *Org. Mass Spectrom.* **1989**, *24*, 535.
(31) Callery, P. S.; Garland, W. A.; Fukuda, E. K. *Org. Mass Spectrom.* **1989**, *24*, 385.
(32) Dillow, G. W.; Gregor, I. K.; Guilhaus, M. *J. Organomet. Chem.* **1985**, *294*, 131.
(33) Kuehl, D. W.; Butterworth, B. C.; Lundmark, E.; Marquis, P. J.; Larsen, M.; Holland, L. G. Presented at the 37th ASMS Conference on Mass Spectrometry and Allied Topics, 21–26 May 1989, Miami Beach, FL.

RECEIVED for review June 12, 1989. Revised manuscript received October 5, 1989. Accepted December 12, 1989. The Midwest Center for Mass Spectrometry (Lincoln, NE) is a National Science Foundation Regional Instrumentation Facility (Grant No. CHE 8620177).

Microchannel Plate for Surface-Induced Dissociation in Mass Spectrometry

William Aberth

University of California, Department of Pharmaceutical Chemistry, Mass Spectrometry Facility, San Francisco, California 94143-0446

A new method for surface-induced dissociation of molecular ions, applied to tandem mass spectrometry, is achieved by collisions at a grazing angle on the inside channel surfaces of a microchannel plate. This technique, termed microchannel SID, is demonstrated by using both positive and negative parent ions in the energy range of 500–2000 eV. Fragmentation spectra of the pentapeptide leucine-enkephalin (555 daltons) at 500 eV show good sequence information with a net fragmentation efficiency of 14%. High mass fragmentation is demonstrated on $(CsI)_{23}Cs^+$ (6113 daltons), with the resultant spectrum showing all cluster fragments from $n = 0$ to 23.

The technique of collision-induced dissociation (CID), as applied to tandem magnetic sector mass spectrometers, typically uses a gas target to collisionally fragment mass-selected molecular ions. The use of a gas for CID, however, has several drawbacks: large energy spreads can occur in the fragment ions resulting in reduced resolution and sensitivity; the efficiency of collision fragmentation decreases with increasing molecular size due in part to insufficient internal energy uptake and increased charge exchange losses (*1*, *2*); and the introduction of a collision gas raises the background pressure which results in poorer resolution and transmission of the high mass compounds.

Surface-induced dissociation (SID), was introduced to overcome some of the difficulties associated with gas targets (*3–7*). The use of a surface of collisionally fragment molecules does not degrade the instrument vacuum and offers the possibility of introducing larger amounts of internal energy conversion for effective high-mass fragmentation. The SID technique typically involves collisions of parent molecules with energies below 300 eV on a metallic surface at about a 45° angle of incidence (*3–6*), although an in-line type of geometry has recently been developed (*7*). Encouraging results have been achieved by this technique, using a variety of instrumental arrangements (*3–7*).

A new method for SID has been developed which utilizes a microchannel plate (MCP) for surface collision and is termed microchannel SID. In this arrangement parent molecular ions of 250–2000 eV translational kinetic energy undergo grazing collisions on the inner channel surface of a microchannel plate (see Figure 1). The in-line geometry and relative simplicity of the microchannel SID technique should facilitate its adaptation to different types of tandem mass spectrometers such as quadrupole, magnet sector and time of flight.

EXPERIMENTAL SECTION

A Wien mass spectrometer (WMS) (*8*, *9*) was operated in tandem with a second WMS to provide a WMS/WMS analyzer for the microchannel SID evaluation (see Figure 2). The instrument operates at 25 kV accelerating voltage and a resolution of 500 and 80, full width at half maximum, for MS-1 and MS-2, respectively. The ion source consists of an immersion lens type liquid secondary ion mass spectrometry (LSIMS) source operating with a 20-keV cesium primary beam (*10*). The mass-selected parent ion beam of MS-1 is decelerated to the desired collision energy by a set of 14 equally spaced aperture plates with exponentially set voltages and reaccelerated after collision by a similar set of plates. A portion of a MCP was clamped between two plates, each containing a $^1/_8$ in. diameter aperture. The structure was mounted on a rotatable axis and positioned in the collision cell. In addition, the MCP could be completely removed from the beam path as a means of determining its attenuation effect on the beam. The MCP used in this study is composed of channels which are 9.6 μm diameter by 432 μm long and have an open area ratio of 59% (Varian Palo Alto, CA, Model VUW-8946ES). The plane of the MCP can be rotated from outside the vacuum system relative to the beam center line. The procedure used to obtain microchannel SID spectra for most of the work reported here was first to optimize the parent ion beam signal in the MS-2 detector with the MCP removed from the beam path. Without the MCP intersecting the molecular beam, no fragmentation of significance was observed for any of the samples analyzed. The MCP was then inserted into the beam path and its angle adjusted to again maximize the parent beam in the MS-2 detector. With this procedure the axes of the MCP channels was positioned roughly parallel (within about 1°) with that of the parent beam center line. The convergence of the parent beam at the surface of the

0003-2700/90/0362-0609$02.50/0

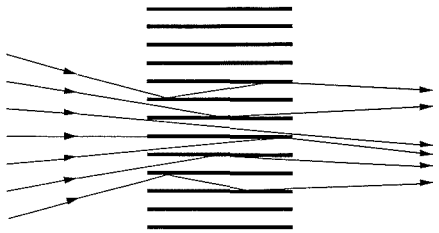

Figure 1. Schematic cross section of an MCP (not to scale) demonstrating the internal reflections of ions from a converging beam.

MCP is estimated to be about 2°. Since the solid angle subtended at the microchannel entrance by the channel exit area is only about 1°, most of the parent ions will undergo one or more grazing surface collisions inside the microchannels. Furthermore, the circular geometry of the microchannels coupled with the convergence of the parent beam will provide a continuous spread in the parent ion collision angle from 0 to 2° or 3°.

RESULTS AND DISCUSSION

The geometrical and physical nature of a MCP makes it an excellent means of producing in-line SID. Its high surface resistivity of about 10^{13} Ω reduces the neutralization effect on the colliding molecular ions, caused by mirror image charge concentration at the point of impact, while at the same time maintaining a good equipotential surface. Good ion optical characteristics are maintained for MS-2 since each ion of the beam entering the microchannel is confined to stay within the 9.6-μm inside diameter of the channel; the exiting beam cross section will remain relatively unchanged. In addition, the fragmentation region is confined to the short length of the MCP channels. Figure 3 shows the positive microchannel SID spectra of the pentapeptide leucine-enkephalin, (Tyr-Gly-Gly-Phe-Leu, 555 daltons) (Sigma Chemical Co. St. Louis, MO) obtained at parent ion translational energies of 500, 1000, and 2000 eV. The 500-eV spectrum shows good characteristic sequence structure of the peptide (*11*). Increasing the parent ion energy to 1000 eV shifts the fragmentation peaks to the lower mass region with a consequent loss in structural information. A further increase to 2000 eV results in almost a complete loss of sequence information. The fragmentation efficiency (integrated fragment spectrum/integrated total spectrum) of all three spectra was about 0.40. The total transmission of ions through the MCP (integrated total spectrum with MCP in beam path/total spectrum with MCP removed) was 0.35, 0.60, and 0.60 for the 500-, 1000-, and 2000-eV beams, respectively. This would indicate that for the 1000- and 2000-eV beams at least, little or no charge exchange neutralization was taking place during surface collision since the open area ratio of the MCP used was 0.59. Whether the lower 0.35 transmission of the 500-eV beam represents a surface neutralization effect or an ion optical effect would require further work to establish. The net fragmentation efficiency, as measured by the integrated fragmentation spectrum/integrated spectrum with MCP removed, is respectively 0.14, 0.24, and 0.24 for the 500-, 1000-, and 2000-eV beams. It thus appears that in spite of the 0.59 open area ratio of the MCP used in this experiment, sufficient fragmentation is produced for practical use.

Figure 4 shows a negative spectrum of leucine-enkephalin demonstrating the negative ion capability of the microchannel SID technique. An analysis of the leucine-enkephalin positive ion dimer (1111 daltons) at 1 keV is shown in Figure 5. This spectrum shows fragments from only the monomer, as one might expect assuming that the dimer binding energy is less than the typical bond energies. However, the excellent quality of the spectrum, compared with that shown in Figure 3a, and the marked increase in relative fragment intensity are surprising.

In order to demonstrate the effectiveness of microchannel SID on higher mass compounds and still maintain reasonable peak separation with the relatively low MS-2 resolution of 80, the analysis of alkali halides was undertaken. Figure 6 is a microchannel SID spectrum of $(CsF)_{22}Cs^+$ (3477 daltons) obtained at 1000 eV, which shows all the cluster fragments from $n = 0$ to 22. Similarly, the microchannel SID spectrum of $(CsI)_{23}Cs^+$ (6113 daltons see Figure 7), shows all of its cluster fragments and suggests that the technique may indeed be effective for high mass fragmentation.

CONCLUSIONS

The present results represent the first time an MCP was used to demonstrate fragmentation of molecular ions for mass analysis. Although the technique has yielded high fragmentation efficiency, several directions of further exploration can be suggested. The open area ratio of the MCP used in this work is 59%. Larger open area ratios of 0.75–0.80 have been fabricated on an experimental basis (*12*) and may prove more efficient than the MCP employed here. The length/diameter ratio of the microchannels in the MCP used is 45. Other ratios should be investigated as to their effect on the fragmentation process. For example, a larger length/diameter ratio might tend to produce more internal channel collisions and thereby affect the efficiency of fragmentation. MCPs with ratios of 100 and higher can be obtained commercially (Galileo Electro-Optics Corp., Sturbridge, Ma, Model MCP 18/5). Finally, a curved channel geometry may have some advantageous effects for microchannel SID applications. This type of ge-

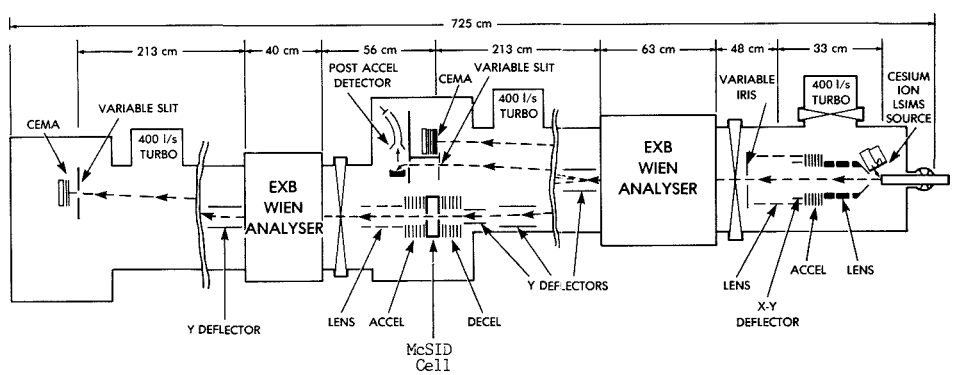

Figure 2. Schematic diagram of the tandem Wien mass spectrometer used to obtain the microchannel SID spectra of this study.

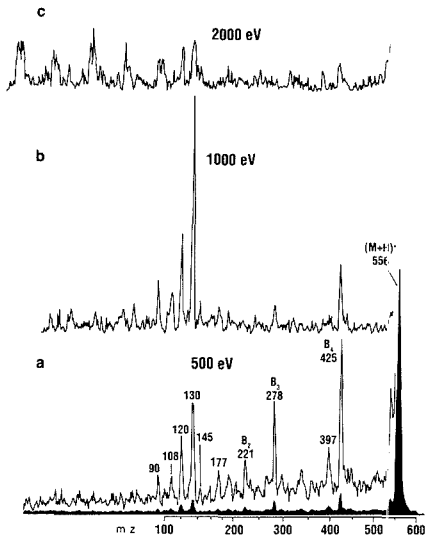

Figure 3. Positive ion microchannel SID spectrum of Leu-enkephalin obtained at 500-, 1000-, and 2000-eV parent beam energies.

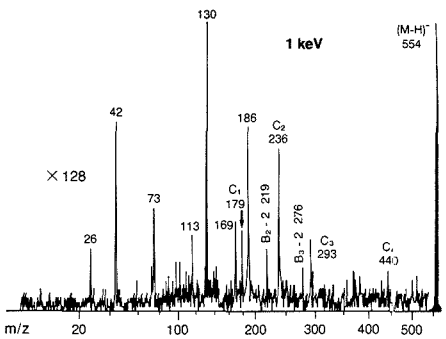

Figure 4. Negative ion microchannel SID spectrum of Leu-enkephalin obtained at 1000-eV parent beam energy.

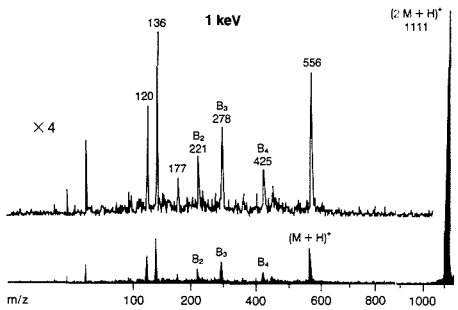

Figure 5. Positive ion microchannel SID spectrum of the dimer of Leu-enkephalin obtained at 1000-eV parent beam energy. Note the high level of fragmentation relative to the parent beam.

ometry has been experimented with (*12*) and is presently under development (*13*).

The in-line geometry and simplicity of application of the microchannel SID technique should make it readily adaptable to other types of MS/MS instruments including QMS and

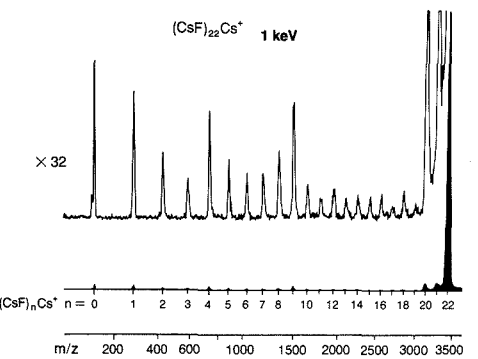

Figure 6. Positive ion microchannel SID spectrum of $(CsF)_{22}Cs^+$ obtained at 1000-eV parent beam energy.

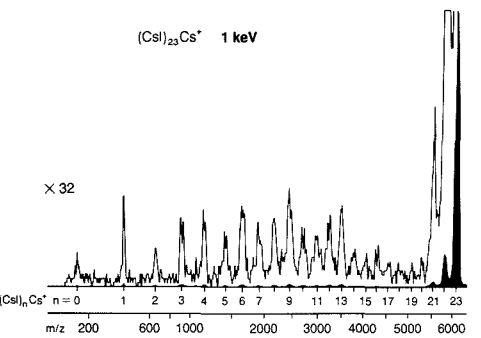

Figure 7. Positive microchannel SID spectrum of $(CsI)_{23}Cs^+$ obtained at 1000-eV parent beam energy.

time of flight (TOF). An important question to answer is whether microchannel SID can improve the fragmentation effectiveness for high mass biological type compounds (greater than 1500 daltons). We are now in the process of adapting the technique to a Kratos Analytical high-resolution MS/MS instrument and should answer this question shortly.

LITERATURE CITED

(1) Neumann, G. M.; Sheil, M. M.; Derrick, P. J. *Z. Naturforsch., A: Phys., Phys. Chem., Kosmosphys* **1984**, *39*, 584–592.
(2) Bricker, D. L.; Russell, D. H. *J. Am. Chem. Soc.* **1986**, *108*, 6174–6179.
(3) Mabud, M. A.; Dekrey, M. J.; Cooks, R. G. *Int. J. Mass Spectrom. Ion Processes* **1985**, *67*, 285–294.
(4) Dekrey, M. J.; Mabud, M. A.; Cooks, R. G.; Syka, J. E. P. *Int. J. Mass Spectom. Ion Processes* **1985**, *67*, 295–303.
(5) Bier, M. E.; Amy, J. W.; Cooks, R. G.; Syka, J. E. P.; Ceja, P.; Stafford, G. *Int. J. Mass Spectrom. Ion Processes* **1987**, *77*, 31–47.
(6) Shey, K.; Cooks, R. G.; Grix, R.; Wollnik, H. *Int. J. Mass Spectrom. Ion Processes* **1987**, *77*, 49–61.
(7) Cooks, R. G. *Proceedings of the 36th ASMS Conference on Mass Spectrometry and Allied Topics*, San Francisco, CA, June 5–10, 1988; pp 1299–1301.
(8) Aberth, W. *Biomed. Mass Spectrom.* **1980**, *7*, 367–371.
(9) Aberth, W. *Anal. Chem.* **1986**, *58*, 1221–1225.
(10) Aberth, W.; Burlingame, A. L. *Anal. Chem.* **1988**, *60*, 1426–1428.
(11) Katakuse, I.; Desiderio, D. M. *Int. J. Mass Spectrom. Ion Processes* **1983**, *54*, 1–15.
(12) Timothy, J. G. *Rev. Sci. Instrum.* **1981**, *52*, 1131–1142.
(13) Timothy, L. G., Stanford, California, personal communication, 1989.

RECEIVED for review August 22, 1989. Accepted December 1, 1989. This work was supported by the National Institutes of Health, Grants GM32315 and RR01614 (to A. L. Burlingame), and the National Science Foundation Grant DIR8700766 (to A. L. Burlingame).

Suspension Postcolumn Reaction Detection Method for Liquid Chromatography

Douglas T. Gjerde*

Sarasep, Inc., 1600 Wyatt Drive, Suite 10, Santa Clara, California 95054

James V. Benson

Benson Polymeric, Inc., 4255 Garlan Lane, Reno, Nevada 89509

A novel detection method for high-performance liquid chromatography utilizes the addition of a colloidal suspension of solid reagent postcolumn to the eluant stream. The average particle size of the insoluble solid reagent is small enough to keep it in suspension. The solid reagent may react with the sample to reduce the background signal or may react with the eluite making it detectable. Since the reagent is solid, it is "invisible" to detectors that repond only to the liquid phase, e.g. conductometric and potentiometric detectors. This paper examines the properties of sulfonated polystyrene-type solid reagents and describes their application in conductivity detection. Other potential uses of the solid phase reagents are discussed.

INTRODUCTION

The need for better detector selectivity and sensitivity has led to the development of postcolumn reaction (PCR) derivatization techniques. Reagents are added to the eluant stream to react with sample peaks and make them detectable (*1*). The simplest postcolumn reactions involve only the addition of energy e.g. heat, UV irradiation, or electrons. Similarly, reactants such as color-forming reagents can be added to the stream using a mixing chamber and a reagent pump. Often, the reagent itself causes a background signal. This can be a problem especially when highly concentrated reagent is used. Minute fluctuations in reagent flow can produce high background noise levels. Also, reagent addition to a stream may produce undesirable precipitation reactions.

Another PCR detection approach employs a packed bed column reactor containing a solid reagent. However, as the reagent is used, the column is depleted and must be replaced or regenerated. A third method uses a membrane. The membrane allows the continuous passage of selected reagents to and from the eluant stream. But, membranes have limited surface area and can be fragile, and only a few membrane types are available. Reactions that form precipitates may irreversibly damage the membrane.

The purpose of this paper is to introduce a new approach to PCR detection for liquid chromatography. A suspension of a particulate reagent is added postcolumn to the eluant stream. The reagent is insoluble, but the average particle size is small, and the reagent remains in suspension. The solid reagent can react with the eluant to reduce the background signal and/or with the sample to produce detectable peaks. A detector such as conductivity responds only to the species dissolved in the liquid phase. The solid phase reagent does not interfere with the detection process.

This paper shows the applications of suspended reagent PCR/conductivity detection for ion chromatography. A sulfonated polystyrene latex solid reagent is used to treat basic eluants used in the separation of anions. The suspension converts the eluant to low conducting weak acids while converting sample anions to highly conducting acids. Factors affecting the performance of the suspension detection method are discussed.

* Author to whom correspondence should be addressed.

EXPERIMENTAL SECTION

The LC instrument consisted of an Altex 110A eluant pump, Rheodyne 7125 injector equipped with a 20- or 100-μL injection loop, and Wescan 213A (3.3-cm^{-1} cell constant) conductivity detector. A LDC Perista peristaltic pump was used for pumping the suspension reagent through an Upchurch low void volume tee. After the reagent was introduced to the eluant, the mixture was directed to a serpentine mixer (*2*) and then directed to the conductivity cell. For most of this work, tubing size at the point of reagent addition and down stream was 0.030 in. i.d. In a few cases, smaller, 0.010 in. i.d. tubing, was used. The Sarasep AN1 column, 250 × 4.6 mm, is manufactured with PEEK tubing and ceramic frits.

The suspension reagent was taken from the "fines" leftover from the synthesis of a chromatographic grade cation exchange resin (Benson Polymeric OA850). This material is a fully sulfonated microporous polystyrene with 8% divinylbenzene cross linking. The <7-μm fraction of the resin was suspended in deionized (DI) water. The material that settled within an hour was discarded. The remaining material had an average particle size of about 2 μm (measured by SEM). This was converted to the H form by washing with 3 M sulfuric acid using a Millipore filter flask and a 0.2-μm filter. Then, all residual acid was washed away by washing several times with DI water. Finally, the material was suspended in DI water at about a 1% (w/v) concentration. In most cases, the flow of the suspension reagent into the PCR was 1.0–1.5 mL/min. Lower reagent flow rates were used with higher reagent concentrations.

In some experiments a Ag-form or Ba-form cation exchanger suspension was used. The same treatment procedure was used in these cases. In the conversion step, the appropriate salt was used in place of sulfuric acid.

RESULTS AND DISCUSSION

The detection concept was first demonstrated for anion chromatography and conductivity detection. High background conductance of the bicarbonate/carbonate eluant used in suppressor ion chromatography could prevent the use of conductivity detection unless some postcolumn eluant treatment is performed (*3*, *6*). Figure 1 shows the effect of adding an H-form suspension to an eluant mixture of 2.8 mM $NaHCO_3$ and 2.2 mM Na_2CO_3, flow rate 1 mL/min. The carbonate/bicarbonate eluant has a very high background conductance of 624 μS/cm. When the suspension was added to the eluant stream, the conductance was lowered to 18 μS/cm. Stopping the reagent addition resulted in a return to the original background conductance.

The suspension reagent converts the highly conducting alkaline eluant to weakly conducting carbonic acid by exchanging H^+ for Na^+. Since the suspension reagent itself is

0003-2700/90/0362-0612$02.50/0

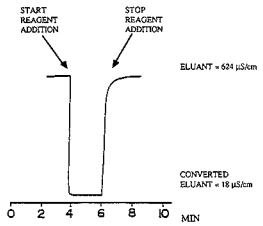

Figure 1. Effect of adding H-form suspension to a bicarbonate eluant: eluant, 2.8 mM $NaHCO_3$ and 2.2 mM Na_2CO_3 at 1.0 mL/min; suspension, 2.3 mequiv/g, sulfonated H-form polystyrene/8% DVB at 1.0 mL/min.

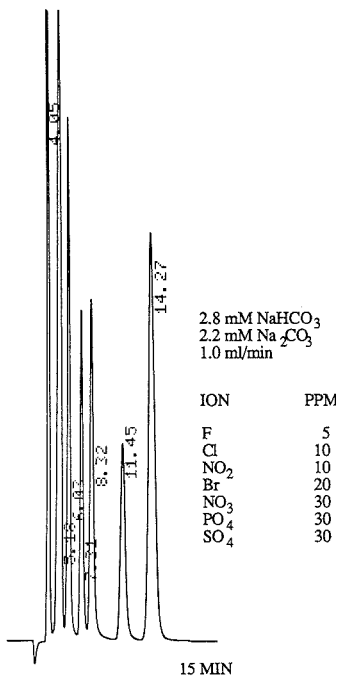

Figure 2. Separation and detection of fluoride, chloride, nitrite, bromide, nitrate, phosphate, and sulfate, respectively, on a Sarasep AN1 column, 250 × 4.1 mm, with 2.8 mM $NaHCO_3$ and 2.2 mM Na_2CO_3 eluant at 1 mL/min and H-form 2% suspension reagent at 1 mL/min.

weakly conducting, the overall conductance of the suspension/eluant mixture remains low. By the same mechanism, sample peaks in the stream such as NaCl or NaBr, are converted to highly conducting acids. A chromatogram using an carbonate/bicarbonate eluant and the suspension detection method is shown in Figure 2.

Properties of H-Form Suspension Reagent. Examination of the properties of the H-form suspension reagent was performed by titrating the polymer material with NaOH. Ten milliliters of a 1.00% suspension of the solid phase reagent was added to 50 mL of deionized water and titrated with 0.020 M NaOH. The progression of the titration was followed with pH and conductivity measurements. The results (Figure 3) show that the suspension converted about 2.3×10^{-4} mol of NaOH titrant. The pH end point occurs slightly before the conductivity end point indicating that the cation exchanger also contains some weaker acid ion exchange groups. Until the end point is also reached for the weaker acids, the large

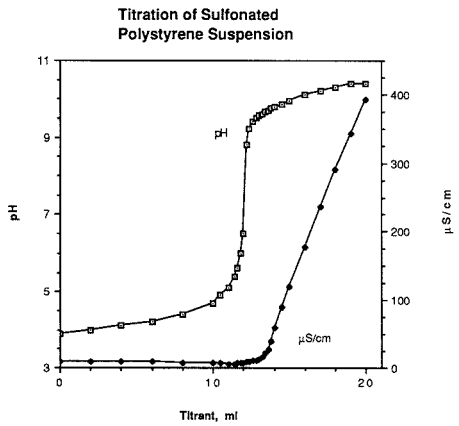

Figure 3. Conductivity and pH titration of H-form suspension (10 mg of solids) with 0.02 M NaOH.

change in pH corresponds to relatively small changes in ionic strength and therefore small changes in background conductance.

As titrant was added to the suspension, the conductance of the suspension remained low, but decreased even further until the end point was reached. These data show that this sulfonated solid phase reagent had a small background conductance, 8.2 µS/cm, that is reduced to 6.3 µS/cm as the reagent was converted to the Na form from the H form. The specific 5% suspension of the H-form reagent was measured to be 30 µS/cm. With a resin capacity of 2.3 mequiv/g, the concentration of acid groups in the suspension is 0.12 M. This indicates an equivalent conductance of 0.26 Ω^{-1} cm^2 $equiv^{-1}$ for the solid-phase reagent in suspension. A completely mobile acid group, i.e. benzenesulfonic acid, is 385 Ω^{-1} cm^2 $equiv^{-1}$. Thus, immobilizing the sulfonic acid functional group into a solid matrix reduces the equivalent conductance by a factor greater than 1500.

The above calculation of equivalent conductance is not entirely fair since conductance of solid-phase reagent is almost certainly due to the surface ion-exchange groups and counterions—not the interior ion pairs. Equivalent conductance is dependent on particle radii, ion-exchange capacity, density, and probably other parameters. Experiments are being performed to examine the relationships (*4*).

Concentration of Reagent. Because of the nature of the suspension reagent, concentrated reagent can be added to the eluant stream. This can be useful if the detection reaction must be driven to completion with excess reagent. Assuming a particle ion-exchange capacity of 2.3 mequiv/g, a particle density of 1.05 g/mL, and a 1% (w/v) concentration of the sulfonated suspension reagent, the average concentration of sulfonic acid groups in the suspension is 0.024 M. But the concentration of ion-exchange groups within the ion-exchange particle matrix is 2.4 M, while the concentration of acid group in the fluid between the particles is, in principle, zero.

The minimum concentration of sulfonated suspension reagent needed for the postcolumn reaction of sodium carbonate/bicarbonate eluant was measured. A 0.1% suspension amount of the sulfonated reagent was delivered to a mixing tee at a 1.0 mL/min flow rate. The eluant flow was increased until the capacity of the PCR reagent was exceeded and the background conductance increased. The results (Table I) show that for the typical sodium carbonate/bicarbonate eluant, and assuming a ion-exchange resin capacity of 2.3 mequiv/g, a suspension concentration of at least 0.5% is needed at a 1.0

Table I. Performance of 0.1%, 2.3 mequiv/g, 1 mL/min H-Form Suspension Reagent in Postcolumn Reaction of 0.75 mM $NaHCO_3$ and 2.2 mM Na_2CO_3

eluant flow, mL/min	conductance, μS/cm	eluant flow, mL/min	conductance, μS/cm
0.0	8.3	0.4	21.8
0.1	10.2	0.5	28.7
0.2	11.9	0.6	*a*
0.3	15.8		

[a] Off scale.

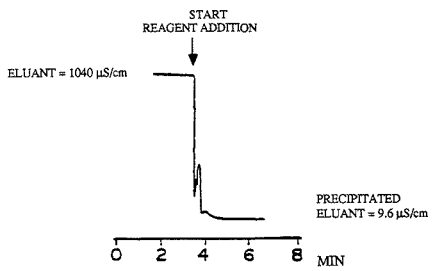

Figure 4. Effect of adding a stream of 2% Ag-form suspension at 1 mL/min to a 10 mM NaCl stream flowing at 1 mL/min.

mL/min flow. Higher suspension concentrations would make possible correspondingly lower flow rates. A 1% suspension would be required under most operating conditions. If the resin capacity is increased to 5 mequiv/g, a typical capacity for a classical cation exchanger, then the suspension concentration may be decreased by a factor of 2. The theoretical maximum exchange capacity, assuming two sulfonic acid groups per aromatic ring, is greater than 7.7 mequiv/g.

Along with the conversion of the eluant to carbonic acid, sample species are converted to highly conducting acids. The minimum suspension concentration needed to complete this reaction was determined by measuring sample peak height as a function of reagent flow. Sample peak heights increase with increasing suspension flow. Constant peak heights were achieved for 1 ppm F^-, Cl^-, and Br^- anion solutions with a 0.6 mL/min flow of 0.5%, 4.1 mequiv/g suspension. The linearity of the response for 4 orders of magnitude was comparable or better to that observed on conventional membrane postcolumn H^+-exchange systems utilizing carbonate eluants (*5*).

Unlike a packed bed suppressor (*6*), suspension conversion reactions operate under a single-stage equilibrium. The selectivity of K^+ over Na^+ for a sulfonated H-form cation exchanger is about 1.7. Because of the greater selectivity, it may be more favorable to use potassium salt eluants.

Ion Exchange Reaction Time. The residence time of the flow stream, from the mixing tee to the detector transducer, was less than 5 s. The conversion reaction obviously was complete within this time. No efforts were made to measure the minimum necessary reaction time.

Precipitation Reactions. Suspension reagents may also be used to perform postcolumn precipitation reactions prior to detection. The suspension contributes a reagent for precipitation of a component in the eluant and allows detection of the sample. A stream of 10 mM NaCl solution was reacted with a stream of 2% suspension of Ag-form sulfonated cation exchanger. The conductance of the NaCl stream is quite high, 1040 μS/cm. The results (Figure 4) show that there is a drop to 9.6 μS/cm conductance when the stream of reagent is added to the eluant. Factors that affect precipitate formation, i.e. temperature and suspension reactant concentrations, solvent polarity, etc. are the subject of a future publication.

Table II. Examples of Conversion Reactions on Ion Exchange Suspension PCR Reagents

chromatography	reactant	use	suspension reagent	reaction product
anion exchange	$NaHCO_3$/Na_2CO_3	eluant	catex-H[a]	H_2CO_3
anion exchange	KOH	eluant	catex-H	H_2O
anion exchange	KCl	sample	catex-H	HCl
anion exchange	$LiSO_4$	sample	catex-H	H_2SO_4
cation exchange	HNO_3	eluant	anex-OH	H_2O
cation exchange	NaCl	sample	anex-OH	NaOH
ion interaction anion exchange	$NH_4B_4O_7$	eluant	catex-H	H_3BO_3

[a] Catex denotes cation exchanger; Anex denotes anion exchanger. H and OH denote the ionic form of the suspension ion exchanger.

Table III. Examples of Precipitation Reactions on Ion Exchange Suspension PCR Reagents

chromatography	reactant	use	suspension reagent	reaction product
anion exchange	HCl	eluant	catex-Ag	AgCl ppt
anion exclusion	$NaCH_3CO_2$	sample	catex-Ag	$AgCH_3CO_2$
anion exclusion	HCl	eluant	catex-TBA	TBACl
anion exclusion	$NaCH_3CO_2$	sample	catex-TBA	$TBACH_3CO_2$

[a] Ag and TBA (tetrabutylammonium) denote the ionic form of the suspension ion exchanger.

The analogous precipitation of SO_4^{2-} from a H_2SO_4 stream via the precipitation of $BaSO_4$ with Ba-from resin could not be accomplished, even when performing static experiments. The selectivity of the Ba-form suspension reagent for H^+ was not great enough to displace Ba^{2+}. It is possible that the reaction may work with a –COOH type cation exchanger, which has a greater H^+/Ba^{2+} selectivity.

CONCLUSION

In addition to reactions described above, there are many other possible reactions that may be useful for suspension detection. An advantage of the new method is the ability to perform reactions on solutions with a wide variety of reactions with many types of reagents. Several eluants such hydroxide or borate or buffers used in ion interaction chromatography should react with the H-form suspension. Other suspension reagents, e.g. OH-form anion exchanger, offer interesting possibilities. Precipitation reactions are incompatible with membrane-based postcolumn reactors, but such reactions are possible with the new method. Chelating or absorbing solid phase reagents can be used to remove interfering substances from sample streams. Tables II and III list several possible reactions of eluants and samples.

All of the work reported here employed conductivity detection. Other detector transducers respond only to the liquid phase and should work with the suspension detection method. Examples include electrochemical detectors such as amperometric and potentiometric. Obviously, the detector cell and tubing must not contain any obstructions that would be plugged by the reagent. The suspension reagent may be filtered with a tangential flow-through filter or other type of filtering method such a spray evaporation. This may allow any type of detector to be used.

ACKNOWLEDGMENT

The authors acknowledge the helpful discussions and comments of Petr Jandik, James Fritz, David Burge, and Jeanne Li. Jandik and Li are also thanked for providing linearity and response data.

LITERATURE CITED

(1) *Reaction Detection in Liquid Chromatography*; Krull, I. S., Ed.; Chromatographic Science Series; Marcel Dekker: New York, 1986; Vol. 34.
(2) Curtis, M. A.; Shawan, G. J. *LC-GC*, **1988**, *6*, 158.
(3) Gjerde, D. T.; Fritz, J. S. *Ion Chromatography*, 2nd ed.; Huethig: Heidelberg and New York, 1987.
(4) Haddad, P., unpublished work, 1989.
(5) Jandik, P.; Li, J., unpublished work, 1989.
(6) Small, H.; Stevens, T. S.; Bauman, W. C. *Anal. Chem.* **1975**, *47*, 1801.

RECEIVED for review August 30, 1989. Accepted December 7, 1989.

Nile Red as a Solvatochromic Dye for Measuring Solvent Strength in Normal Liquids and Mixtures of Normal Liquids with Supercritical and Near Critical Fluids

Jerry F. Deye and T. A. Berger*

Hewlett-Packard, P.O. Box 900, Route 41 and Starr Road, Avondale, Pennsylvania 19311-0900

Albert G. Anderson

Central Research and Development Department, E. I. du Pont de Nemours and Co., Wilmington, Delaware 19880-0328

Nile Red was used as a solvatochromic probe to measure the solvent strength of 85 pure liquids and the results were compared to solvent strength scales from the better known Reichardt's $E_{t(26)}$ and $E_{t(30)}$ dyes. Nile Red is also soluble in some pure supercritical fluids and in polar mixtures of supercritical fluids and modifiers. The solvent strength of mixtures of organic modifiers in CO_2, Freon-13, and Freon-23 was measured as a function of modifier concentration with Nile Red and other solvatochromic dyes. Nile Red exhibits large shifts in the wavelength of its absorption maximum allowing subtle changes in solvent strength with fluid composition to be quantified, and it is stable in very strong acids. Relative scales of solvent strength comparing different modifiers added to CO_2 are presented and compared to a wide range of normal liquids.

INTRODUCTION

The polarity range of solutes that can be separated by supercritical fluid chromatography (SFC) can be greatly extended by the addition of polar modifiers to supercritical fluids. It has been widely reported (*1–4*) that the initial small additions (less than 1%) of polar modifiers (like methanol) to supercritical fluids (like carbon dioxide) significantly decrease the chromatographic retention of solutes on packed columns including those with a bonded stationary phase. Such large changes in retention caused by small changes in modifier concentration appear to be inconsistent with bonded phase chromatography (BPC). It is often assumed that bonded phases do not adequately cover silica surfaces and residual silanol groups produce long retention and very poor peak shapes. This can be viewed as a competition between a bonded phase retention mechanism and an adsorption retention mechanism which, in the absence of a modifier, favors the adsorption mechanism. Polar modifiers are assumed to decrease retention and improve peak shapes by covering the silanol sites (i.e. blocking the adsorption mechanism). It is uncertain whether, upon site deactivation, retention follows a bonded phase or adsorption mechanism.

Retention in BPC is normally a function of a mobile phase polarity parameter, P', which in turn is usually a linear function of composition according to the equation (*5*)

$$P' = \phi_a P_a + \phi_b P_b \quad (1)$$

where ϕ_a and ϕ_b are the volume fractions of mobile phase components a and b, and P_a and P_b are the solvent polarity parameters for the two pure components. These polarity parameters are based on experimental solubility data like those reported by Rohrschneider (*6*). Partition ratios (k') are not necessarily linearly related to P' but retention changes are generally limited to a 2.2-fold decrease in k' for a change in P' by 1.0 unit (*7*). If the P' values for carbon dioxide and methanol were 0 and 5.1, then the addition of 1% methanol to carbon dioxide should decrease retention by only a few percent compared to retention using pure carbon dioxide. Instead, much larger changes in retention are common. We recently observed that the addition of 1% methanol to carbon dioxide decreased the retention of chrysene on a SA column by 2.4 times ($k' = 17.9$ in pure CO_2 to 7.6 in 1% methanol). Such large retention changes suggest that eq 1 is inadequate for predicting retention in packed column SFC.

Adsorption chromatography is characterized by large changes in k' with small additions of polar modifiers and thus, at least superficially, appears to offer a better explanation of retention in packed column SFC than BPC. In the standard theoretical treatment (*8*), retention of solutes is related to the adsorption energy of the mobile phase solvent on the stationary phase through the equation

$$\log K^\circ = \log V_a + \alpha(S^\circ - A_s\epsilon^\circ)$$

where K° is the distribution coefficient for the adsorption of the solute, V_a is the adsorbent surface volume per weight, α is a measure of the activity of the adsorbent, S° the sample adsorption energy on the standard-activity adsorbent, A_s the surface area covered by a molecule of the mobile phase solvent, and ϵ° the adsorption energy of the mobile phase solvent per unit area of the standard adsorbent. In binary fluids, the mobile phase solvent strength, ϵ_{ab}, tends to be dominated by the more polar component, *b*

$$\epsilon_{ab} = \epsilon_a + \frac{\log (N_b\, 10^{\alpha n_b}\, (\epsilon_b - \epsilon_a) + 1 + N_b}{\alpha n_b}$$

where ϵ_{ab}, ϵ_a, and ϵ_b are the "solvent strengths" of the mixture

0003-2700/90/0362-0615$02.50/0

and pure components, respectively, N_b is the mole fraction of b in the mixture, and n_b is related to molecular size. A plot of ϵ_{ab} vs the mole fraction of b yields an adsorption isotherm for b. Retention is, thus, related to surface phenomena. Mobile phase interactions with the solute are generally ignored. Attempts to rationalize the solvent behavior of binary mixtures with chromatographic behavior (*9*, *10*) usually contain an implicit assumption that the mixtures behave as regular solutions.

It is also well-known that mobile phase interactions become more important as the difference in the polarity of the solvent components increases (*8*). We interpret this as increasing deviations from regular solution behavior. In the standard theory, there is no framework for measuring these deviations other than through the general equation for the net energy of adsorption (ΔE)

$$\Delta E = E_{xa} + mE_{sl} - E_{xl} - E_{sa}$$

where each term represents dimensionless partial molar free energies and the subscripts x and s refer to sample and solvent, and a and l refer to adsorbed and liquid phases, respectively. $E_{sl} - E_{xl}$ represents mobile phase interactions independent of the stationary phase.

Solvatochromic dye measurements offer the possibility of directly measuring some function related to P' or alternately to mobile phase free energies (i.e. $E_{sl} - E_{xl}$) independent of chromatographic retention. There is still considerable debate as to the value or general applicability of solvatochromic solvent strength scales (i.e., refs 11 and 12), but at the least they provide an approximate correlation to solvent polarity. They also point out some unexpected solution characteristics of mixtures of polar modifiers and supercritical fluids. Reichardt (*13*) developed a solvent strength scale, $E_{t(30)}$, using a pyridinium betaine dye, the adsorption maximum of which shifts depending on the polarity of the solvent in which it is dissolved. Note that in this context "solvent strength" is strictly related to solute (dye)–solvent interactions whereas in adsorption chromatography "solvent strength" is really an elution strength and normally has nothing to do with interactions in the mobile phase. We use the term "solvent strength" as a measure of the interaction between solutes and solvent in a fluid phase, independent of any stationary phase interactions.

Strong interactions in the mobile phase tend to produce deviations in retention in adsorption chromatography which cannot be explained by mobile phase adsorption (*8*). In spite of this, Reichardt's $E_{t(30)}$ scale has been compared to ϵ_{ab} values from adsorption chromatography (*6*) with "good" correlation, even though acidic and alcoholic solvents appear to produce a substantially different relationship between $E_{t(30)}$ and ϵ_{ab} than other solvents. Kamlett and Taft and co-workers (*14–16*) have developed separate scales, using a variety of carefully chosen dyes, to separately account for polarizability, ion–dipole interactions, acid–base, and hydrogen bonding. Unfortunately, the dyes employed often produce only minor wavelength shifts which make small changes in solvent strength difficult or impossible to observe. For example, the absorbance maximum of 2-nitroanisol, a widely used dye in measurements on Kamlet and Taft's π^* scale, shifts only 3.4 nm when the solvent is changed from tetrahydrofuran to methanol (*17*).

In the chemical engineering literature, clustering of polar modifier molecules around polar solute molecules (*18–28*) in a large excess of a supercritical fluid is widely accepted. Even in mixtures containing low bulk concentrations of modifier, solutes may be surrounded by a solvation sphere containing a high local concentration of the modifier. Such clustering becomes more pronounced as the difference in polarity between the supercritical fluid and the modifier is increased. This suggests that a substantial part of the nonlinear behavior of chromatographic systems using supercritical fluids mixed with polar modifiers may be due to mobile phase, not stationary phase, effects. If true, this has important implications on retention mechanisms in both packed column SFC and liquid chromatography.

Several solvatochromic studies have been performed (*17*, *29–31*) on pure supercritical fluids. Early unpublished reports established that pure carbon dioxide (CO_2) was in the same polarity range as hexane (*32*, *33*), and more detailed studies corroborate and expand on this finding. Yonker et al. (*17*, *31*) reported the solvent strength of NH_3, CO_2, and N_2O with changing pressure, using solvatochromic dyes. In addition, they measured the solvent strength of CO_2 containing several concentrations of methanol. They concluded that mobile phase solvent strength did not change dramatically with small additions of polar modifiers. Instead, they attributed dramatic shifts in retention accompanying small additions of modifier to a modification of packed column stationary phases through adsorption of the modifier (*15*) onto "active sites".

Carbon dioxide and methanol possess vastly different solvent strengths on all solvent strength scales and should produce extreme differences in retention in either BCP or adsorption chromatography. At the same time, the nonlinear solute–solvent interactions (clustering) in the mobile phase, which are generally accepted in chemical engineering, have been virtually ignored in discussions of retention in packed column SFC. This raises the possibility that retention may folow a BPC type mechanism but with a nonlinear relationship between solvent strength and composition. Alternately, solvent strength measurements obtained by using solvatochromic dyes may provide the means of correcting for deviations between retention and the adsorption isotherm for the solvent on the stationary phase, once adsorption measurements are made available. We believe that polar modifiers strongly interact with column packing materials, but we doubt such interactions represent a form of classic adsorption chromatography. The present work employs Nile Red to provide detailed measurements of the mobile phase solvent strength of mixtures of polar modifiers in CO_2, Freon-13, and Freon-23.

EXPERIMENTAL SECTION

Chemicals and Instrumentation. The adsorption maxima and the resulting calculated values of transition energies for Nile Red reported in Table I were collected by A. Anderson in 1983 with an IBM 9430 spectrophotometer. Extreme care was taken to exclude water from the solvents. The rest of the work reported here was recently done with a Hewlett-Packard (HP) Model 8450A photodiode array spectrophotometer. A high-pressure flow cell was made of 316 stainless steel. The flow path was 1.5 mm diameter with a 1 cm long path length. Fused silica windows were 6 mm thick and were transparent to UV to below 190 nm. The windows were sealed, leak tight, on the ends of the flow path with Kel-F washers compressed between the windows and the cell body. A Hewlett-Packard Model 1084 liquid chromatograph with an adaptor kit for SFC was used to pump pure supercritical fluids. A Brownlee Labs microsyringe pump was used to pump the pure modifiers. Flow from the two pumps was dynamically mixed inside the HP 1084.

Dyes were purchased commercially, except for Reichardt's $E_{t(26)}$, structure I, which was synthesized according to procedures in the literature (*13*). Nile Red, structure II, was purchased from Eastman Kodak, and the other dyes were purchased from Aldrich. For the most recent work involving modified supercritical fluids, solvents were of chromatographic grade or better; no special precautions were taken to exclude water. The effect of water was checked by adding water to the modifiers. Only very small concentrations of water could be added to ternary mixtures of water, modifier, and carbon dioxide. This added water (either purposely added or absorbed from room air) was most likely responsible for small differences between the 1983 and some of the 1988 data. SFC grade carbon dioxide in aluminum cylinders

Table I. Comparison of Nile Red Transition Energies to Reichardt's $E_{t(30)}$ and $E_{t(26)}$ in Normal Liquids[a]

	solvent	$E_{(NR)}$	wavelength, nm	$E_{t(30)}$	$E_{t(26)}$		solvent	$E_{(NR)}$	wavelength, nm	$E_{t(30)}$	$E_{t(26)}$
1	pentafluorophenol (40 °C)	44.85	637.5			44	*N,N*-dimethylformamide	52.83	541.2	43.8	39.4
2	formic acid	45.09	634.0			45	*N,N*-dimethylacetamide	52.87	540.8		
3	trifluoroacetic acid	45.47	628.8			46	1-methyl-2-pyrrolidinone	52.88	540.7		
4	pentafluoropropionic acid	45.47	628.8			47	2-propanol	53.02	539.2	48.6	40.4
5	heptafluorobutyric acid	45.50	628.4			48	carbon disulfide	53.14	538.0	32.6	
6	2,2,3,3,3-pentafluoropropanol	45.55	627.6			49	chloroform	53.18	537.6	39.1	36.1
7	pentadecafluorooctanoic acid	45.56	627.5			50	bromobenzene	53.26	536.8	37.5	
8	hexafluoro-2-propanol	46.93	609.2		57.2	51	2-methyl-2-propanol	53.29	536.5	43.9	37.4
9	*m*-cresol	47.49	602.0			52	1,2-dichloroethane	53.29	536.5	41.9	
10	phenol (45 °C)	47.65	600.0			53	*N,N*-dichloroethane	53.34	536.0		
11	water	48.21	593.2	63.1		54	chlorobenzene	53.34	536.0	37.5	35.0
12	hydrogen cyanide (15 °C)	48.46	590.0			55	methylene chloride	53.42	535.2	41.1	37.3
13	2,2,2-trichloroethanol	48.82	585.6		53.9	56	ethyl acetoacetate	53.42	535.2		
14	2,2,2-trifluoroethanol	48.86	585.2		57.2	57	phenylacetylene	53.58	533.6		
15	heptafluorobutanol	49.36	579.2			58	acetonitrile	53.78	531.6	46.0	41.4
16	water/methanol 1:1 (v/v)	49.43	578.4			59	anisol	53.78	531.6	37.2	
17	benzyl alcohol	50.26	568.8	50.8	46.5	60	fluorobenzene	53.89	530.5		
18	formamide	50.51	566.0	56.6		61	1,1,1-trifluoroacetone	53.90	530.4		
19	ethylene glycol	50.58	565.2	56.3	51.1	62	thiophene	53.90	530.4		
20	aniline	50.65	564.5	44.3	39.7	63	acetone	53.99	529.5	42.2	37.9
21	pentadecafluorooctanol	51.05	560.0			64	tetrahydrofuran	54.19	527.6	37.4	35.1
22	ethanol/water 80:20 (v/v)	51.16	558.8	53.6		65	benzene	54.42	525.4	34.5	33.2
23	acetic acid	51.31	557.2	51.9		66	ethylene glycol dimethyl ether	54.64	523.2	38.2	35.5
24	ethanolamine	51.35	556.8			67	toluene	54.81	521.6	33.9	33.0
25	ammonia (−34 °C)	51.51	555.0			68	ethyl acetate	54.94	520.4	38.1	35.4
26	*N*-methylformamide	51.98	550.0	54.1	48.8	69	isobutylamine	55.15	518.4		
27	methanol	52.02	549.6	55.5	50.8	70	furan	55.19	518.0		
28	dimethyl sulfoxide	52.06	549.2	45.0		71	perfluorobenzene	55.35	516.5		
29	quinoline	52.13	548.4	34.9		72	1,4-dioxane	55.36	516.4	36.0	34.2
30	ethanol	52.15	548.3	51.9	46.9	73	*tert*-butylamine	55.45	515.6		
31	1-butanol	52.21	547.6	50.2	45.0	74	CO_2/methanol 90:10 (v/v)	55.62	514.0		
32	nitrobenzene	52.25	547.2	42.0		75	tetramethylethylenediamine	55.93	511.2		
33	1-propanol	52.40	545.6	50.7	45.6	76	*N,N*-diethylamine	55.93	511.2		
34	sulfolane	52.44	545.2	44.0		77	*tert*-butyl methyl ether	56.24	508.4		
35	benzonitrile	52.44	545.2	42.0		78	*m*-xylene	56.41	506.8		
36	butyrolactone	52.51	544.5			79	diethyl ether	56.68	504.4	34.6	
37	1-octanol	52.56	544.0			80	CO_2/methanol 95:5 (v/v)	56.95	502.0		
38	iodobenzene	52.63	543.2			81	carbon tetrachloride	57.50	497.2	32.5	
39	acetophenone	52.63	543.2	41.3		82	triethylamine	57.87	494.0		
40	propionic acid	52.71	542.4			83	tributylamine	58.16	491.6		
41	1,3-dimethyl-2-imidazolidinone	52.71	542.4			84	cyclohexane	58.63	487.6		
42	nitromethane	52.75	542.0	46.3		85	*n*-hexane	59.02	484.4	30.9	
43	pyridine	52.79	541.6	40.2	37.3	86	pentane	59.12	483.6		
						87	CO_2, 24 °C, 1270 psig	59.54	480.2		

[a] Transition energy, E, of the solvatochromic band calculated by $E = 28\,591.44/(\text{nm})$ in kcal/mol.

was obtained from Scott Specialty Gases, Plumsteadville, PA. Freons were obtained from Du Pont through Melchior Armstrong, Edgemont, PA.

Choosing Dyes. We were primarily interested in measuring relatively subtle changes in solvent strength caused by small changes in solvent composition. Finding an appropriate dye or family of dyes became a bigger issue than expected. The dyes had to be reasonably soluble in a wide range of pure solvents and supercritical fluids. In addition, available instrumentation consisted of a spectrophotometer with limited wavelength resolution (1 nm spectral bandwidth between 200 and 400 nm, 2 nm spectral bandwidth between 400 and 800 nm). This required the use of dyes exhibiting large solvatochromic wavelength shifts.

Kamlet and Taft's π^* Scale. The systematic approach of Kamlet and Taft (*14–16*) appears to offer the best means of comparing the solvent strength of modifier-supercritical fluid mixtures to normal liquids and deconvoluting the contributions from dispersive forces, permanent dipoles, acid–base, and hydrogen bonding interactions. Unfortunately, our initial measurements with several of these dyes produced inadequate resolution of solvent strength differences and further work was dropped.

Reichardt's Dyes. Since the system of Kamlet and Taft could not provide the desired sensitivity, other alternatives were evaluated. Kosower's dye (*34*) was not soluble in a wide enough range of solvents. Reichardt's (*13, 35*) family of pyridinium betaine

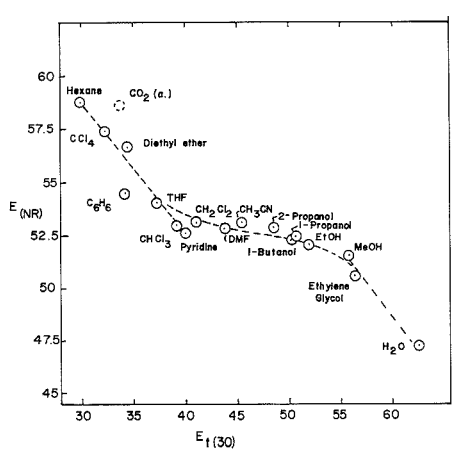

Figure 1. Comparison of transition energies calculated from the wavelengths of maximum absorption of Nile Red and $E_{t(30)}$ solvatochromic dyes in a number of common liquids. (a) is $E_{t(30)}$ value calculated in ref 27.

dyes including $E_{t(30)}$, structure III, has been the most popular

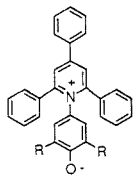

I, R = t Bu, Et(26)
III, R = Phenyl, Et(30)

solvatochromic dye due, in part, to the fact that it exhibits the largest known shifts in absorption maxima with changes in solvent polarity. Unfortunately, considerable concern has been expressed over this dye's susceptibility to solvent hydrogen bonding power (*16, 26, 36*) and it produces a hypsochromic shift with increasing solvent polarity in direct contrast to the family of dyes suggested by Kamlet and Taft (*14–16*). $E_{t(30)}$ is not very soluble in pure CO_2 and tends to precipitate from solution as modifier concentration becomes small. The penta(*t*-butyl) (*29, 35*) and $E_{t(26)}$ (*37*) derivatives were purported to be more soluble in CO_2 than $E_{t(30)}$, but we found little difference in the solubilities of $E_{t(26)}$ and $E_{t(30)}$ in carbon dioxide. However, we did observe a major decrease in the molar absorptivity of both $E_{t(26)}$ and $E_{t(30)}$ when CO_2 was added to many modifiers. Bubbling CO_2 through solutions of either of these dyes in polar solvents, such as methanol, resulted in the rapid loss of visible color. Subsequent purging of the solutions with either helium or nitrogen resulted in the rapid return of the color. The addition of acids also caused the color to disappear, while bases made color reappear. We concluded that these dyes are very susceptible to the presence of traces of water, solution acidity, and solvent polarity. This behavior led to uncertainty in interpreting the results. When water was excluded, significant concentrations of carbonic acid could not form or dissociate, and spectra with usable levels of absorption could be obtained.

Nile Red. Nile Red has found substantial use as a lipophylic dye for staining fatty tissues (*38*). However, although its solvatochromic behavior has been noted, it has not been examined extensively. The solvatochromism and fluorescence of oxazine dyes, especially those related to Nile Blue A (*39*), structure IV, have also been noted (*40–43*). Nile Red was previously used with

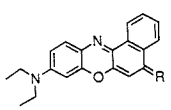

II, R = O, Nile Red
IV, R = NH, Nile Blue A

a limited number of solvents as a solvatochromic probe of solvent basicity in polar aprotic media (*42, 43*). Because of its photochemical stability and strong fluorescence peak (which is also solvatochromic), Nile Red has been suggested as a laser dye (*46*). Its low basicity ($pK_a = 1.00 \pm 0.05$) (*47*) permits observation of its solvatochromic peak in acidic media (*48*). Although not ideal, Nile Red provides the best available combination of characteristics for our requirements. Nile Red is soluble in solvents at the extremes of polarity of interest. This dye exhibits large shifts in the wavelength of maximum absorbance with solvent polarity (>160 nm shift between carbon dioxide and trifluoroacetic acid). Nile Red is uniquely stable in extremely acidic media and is not susceptible to a loss of molar absorptivity in the presence of acids like Reichardt's dye. The absorbance maximum of Nile Red does not appear to shift significantly when subjected to hydrogen bonding solvents. It also produces a bathochromic wavelength shift consistent with stabilization of the excited state in $p-\pi^*$ or $\pi-\pi^*$ electronic transitions and comparable with the π^* scale of Kamlet and Taft (*16*). This contrasts with the hypsochromioc shift of Reichardt's $E_{t(30)}$.

Nile Red is fluorescent in some solvents. In very acidic, polar solvents, absorption bands of the protonated form of Nile Red appear. Fluorescence emission band(s) overlap the solvatochromic absorption bands of the protonated form of Nile Red to create what appears to be a triplet in the absorption spectra. The solvatochromic absorption bands of the regular form of Nile Red are still present but are sometimes not very obvious. To avoid confusion and to deconvolute the overlapping bands, composition was varied while spectra were continuously monitored. Composition was varied by making mixtures of a low polarity solvent and the high polarity solvent of interest. At the beginning of the experiment, single spectral bands were observed. As the experiment progressed and increasing concentrations of the more polar solute was added, the band due to the normal form of the dye was observed to shift. New bands appeared but could be differentiated from the band of interest.

RESULTS AND DISCUSSION

Measurements in Normal Liquids. The wavelength of maximum absorption of Nile Red was measured in a number of common liquids used as solvents or modifiers in both LC and packed column SFC. Wavelength measurements were converted to transition energies in kilocalories per mole by dividing 28 592 by wavelength in nanometers (*34, 49*). Nile Red transition energies are designated $E_{(NR)}$. The Nile Red absorption maxima and transition energies in a large number of solvents are presented in Table I. Values for Reichardt's $E_{t(30)}$ and $E_{t(26)}$ are also presented for comparison. Neither of the latter dyes is stable in acidic media. From these data it appears that Nile Red, because it is more stable in acidic media, is somewhat more useful than $E_{t(30)}$ or $E_{t(26)}$ in measuring the solvent strength of acids and other very polar solvents. Solutions of Nile Red in neat, strong acids, such as trifluoroacetic acid, maintained nearly constant color for months. In solutions of bases, Nile Red tends to lose color over several days.

Some of the data in Table I are also presented graphically, in Figure 1, where values of $E_{(NR)}$ for Nile Red and Reichardt's $E_{t(30)}$ are plotted against each other. The figure shows that $E_{t(30)}$ is extremely sensitive to hydrogen bonding solvents, as previously observed by others (*36*), but, in contrast, that Nile Red is much less sensitive to hydrogen bonding and proton donor/acceptor solvents. Neither scale, by itself, provides a clear picture of the relative strengths of the solvents. Note that the data on the left and right extremes of Figure 1 allow parallel lines to be drawn with an offset occurring in the region where hydrogen bonding and donor/acceptor characteristics are important.

Results in Fluids Used in SFC. *Methanol Modifier in Carbon Dioxide and Freons.* Values of $E_{(NR)}$ vs $E_{t(30)}$ for mixtures of methanol in carbon dioxide, Freon-13, and Freon-23 are presented in Figure 2. The lower dashed line is the normal solvent $E_{(NR)}$ vs $E_{t(30)}$ curve from Figure 1. The numbers next to the curves are volume percents of methanol mixed into the various fluids.

The CO_2 data were obtained by using very dry methanol, but the intensity of absorption for $E_{t(30)}$ was low, making it somewhat difficult to be certain of the wavelength of maximum absorption. Two values of $E_{t(30)}$ for methanol are presented as half shaded circles in Figure 2. The less polar value was obtained by using methanol from a freshly opened bottle, and the more polar value was obtained from an older, used bottle of methanol. The two values represent the extremes observed over several months using methanol with no special preparation. Freshly opened bottles tended to produce slightly less polar readings than older bottles that had been opened many times. Freshly opened bottles gave the same results as scrupulously dried modifier. Small concentrations of water purposely added to the modifier gave small spectral shifts similar to those observed with "old" bottles of modifier.

Table II. Wavelengths of Absorption Maxima and Calculated Transition Energies for Mixtures of Common Modifiers with Carbon Dioxide (at 25 °C)

	$E_{(NR)}$							
	MeOH		CH_3CN		CH_2Cl_2		THF	
% modifier	nm	kcal/mol	nm	kcal/mol	nm	kcal/mol	nm	kcal/mol
1[a]	488	58.6						
2[a]	494	57.9						
3[a]	498	57.4						
4[a]	500	57.2						
5	504	56.7	496	57.6	492	58.1	490	58.3
10	512	55.8	504	56.7	496	57.6	494	57.9
20	522	54.8	512	55.8	504	56.7	498	57.4
40	532	53.7	522	54.8	516	55.4	508	56.3
60	540	52.9	526	54.4	524	54.6	518	55.2
80	548	52.2	532	53.7	530	53.9		54.5
100	554	51.6	538	53.1	538	53.1	528	54.1

[a] Collected at 29 °C.

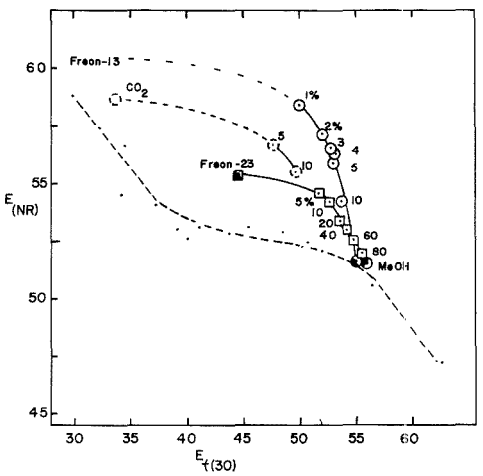

Figure 2. Comparison of energies, as in Figure 1, but for mixtures of methanol with three supercritical fluids. Lower dashed line is same as line in Fig. 1, for reference.

The results in Figure 2 are very informative. On either solvent strength scale ($E_{(NR)}$ or $E_{t(30)}$) the polarity of the pure fluids follows the order Freon-13 < CO_2 < Freon-23. Unpublished chromatographic results have demonstrated to us that these pure fluids follow the same order in their elution strength of many solutes from a wide range of stationary phases. The addition of methanol as modifier appears to shift the solvent strength of the mixtures dramatically. The larger the difference in solvent strength between the two pure fluids (supercritical fluid and modifier), the more dramatically the solvent strength of the mixture shifts. Thus, methanol–Freon-13 mixtures appear more polar than methanol–CO_2 mixtures of similar composition (on either solvent strength scale). This can be explained by using the concept of clustering (*17–28*). Polar molecules are only sparingly soluble in Freon-13 and tend to be rejected by it. At low concentrations they do not, however, form a second phase. Instead, polar molecules tend to cluster together forming a local environment that is much more polar than the bulk composition would suggest. The greater the difference in polarity between the components, the more intense the clustering and the more nonlinear the relationship between solvent strength and composition.

The solvent strength measurements summarized in Figure 2 do not precisely parallel the elution strengths of these mixtures in chromatography. Mixtures of methanol in Freon-13 are always less able to elute polar solutes than mixtures of methanol in carbon dioxide at the same concentration of modifier. We believe this is due to intense interactions between the modifier and the relatively polar stationary phases we usually use in packed column SFC (i.e. cyanopropyl or diol bonded phases on silica). If the supercritical fluid essentially rejects the modifier, causing clustering in the mobile phase, then it is probable that there will also be a strong association between the polar modifier and the polar stationary phase. Pooling of the modifier on the stationary phase causes a change in the polarity and/or volume of the stationary phase.

None of the dyes is soluble in pure Freon-13, so the position of the unmodified fluid is not shown in Figure 2. We could not produce mixtures of over 12% methanol in Freon-13 at temperatures between room temperature (25 °C) and 80 °C and over a wide range of pressures. With greater than 12% methanol added to Freon-13, the base-line noise increased dramatically, suggesting the fluid broke down into two phases.

2-Propanol in Hexane. Mixtures of 2-propanol in hexane were also evaluated with Nile Red to determine whether the behavior of methanol in nonpolar supercritical fluids is perceptibly different in comparison to mixtures of normal liquids. Hexane is very nonpolar while 2-propanol is moderately polar. Hexane and 2-propanol were chosen because they have one of the greatest differences in polarity possible among binary pairs of miscible, normal liquids. The results, shown in Figure 3, indicate similar but less dramatic behavior compared to the behavior observed for mixtures in supercritical fluids (see Figure 2). The similarity between the curves in Figures 2 and 3 gave some reassurance that the effects observed were realistic measurements of solvent strength. If plots like Figures 2 or 3 are linear, local composition and bulk composition are probably the same. The relatively more linear behavior of 2-propanol in hexane, compared to alcohols in carbon dioxide suggests that there is less clustering of the 2-propanol. The difference in behavior between the mixtures containing hexane and carbon dioxide can be attributed to the more limited compressibility of hexane compared to carbon dioxide (*18, 19*).

Other Modifiers in Carbon Dioxide. The Nile Red transition energies of mixtures of methanol, acetonitrile, methylene chloride, and tetrahydrofuran in carbon dioxide are listed in Table II and shown in Figure 4. In Figure 4, the vertical lines on the extreme left and right represent the solvent strengths of pure carbon dioxide and pure methanol, respectively. Horizontal lines connect these two extremes. The top three

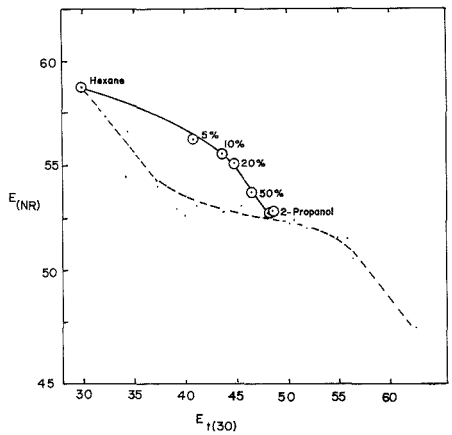

Figure 3. Comparison as in Figures 1 and 2 but for mixtures of two normal liquids, 2-propanol and hexane.

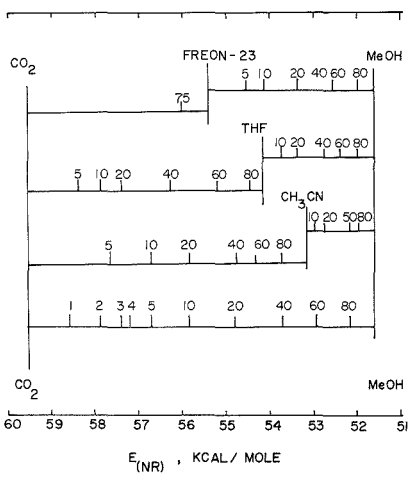

Figure 4. Transition energies obtained by using Nile Red for mixtures of carbon dioxide and common modifiers.

horizontal lines are broken by intermediate vertical lines representing the solvent strength of pure Freon-23, tetrahydrofuran (THF), and acetonitrile (ACN). The numbers above the tick marks on the horizontal lines are the concentration of the more polar modifier in the less polar solvent, in volume percent. Thus, on the bottom line the number 10 appears about half way between the vertical lines representing pure carbon dioxide and pure methanol. This means that 10% methanol in carbon dioxide has a solvent strength one might normally expect from 50% methanol in carbon dioxide (assuming ideal solutions). Apparently, the dye molecules are surrounded by a solvation sphere that has a higher concentration of modifier than is present in the bulk.

The data are presented in Figure 4 in a format similar to the format used to express elution strength (ϵ_{ab}) information in adsorption chromatography (*50*). However, in Figure 4, the nonlinearity is a mobile phase phenomenon involving the solute and the modifier whereas in adsorption chromatography the nonlinearity is due to a mobile phase–stationary phase interaction.

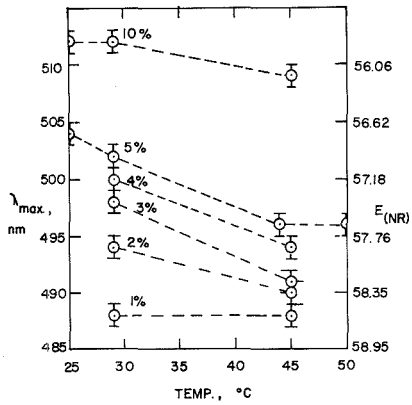

Figure 5. Effect of temperature on absorbance maxima of Nile Red in mixtures of carbon dioxide and methanol. The numbers next to the curves represent the volume percent of methanol in carbon dioxide.

Effects of Temperature and Pressure. One operating mode in SFC involves density programming where partition ratio's (k') can be changed by a factor of at least 10^3 times (i.e. 51). Such large variations in k', achievable with changes in density, have led many people to equate large changes in density with large changes in solvent strength. Such observations need to be put in perspective. Much larger changes in k' are achievable in LC by changing fluid composition. In adsorption chromatography, a change in solvent from hexane to methanol (through multistep substitutions) can result in a change in solute retention by as much as 10^9 or 10^{10} times. Thus, the apparently large changes in k' in SFC, achievable using only changes in the density of common supercritical fluids, are small compared to changes achievable in LC. They do not necessarily represent large changes in solvent strength and can only cover a small fraction of the full range of solvent strengths available with normal liquids. Experiments were undertaken to determine the range of solvent strengths achievable with density variations compared to composition changes using Nile Red transition energies.

Temperature. Several authors have shown (*52, 53*) that, for a pure fluid at constant density, there are no abrupt changes in chromatographic retention as temperature is increased from sub- to supercritical. Hyatt (*29*) reported similar mobile phase solvent strengths at sub- and supercritical temperatures of a number of Kamlet and Taft (*14–16*) dyes. We also observed only modest shifts in the wavelength of Nile Red absorption with changing temperature. These wavelength changes are similar in magnitude to shifts caused by small changes in fluid composition as shown in Figure 5. It is also interesting to observe that solvent strength decreases when the fluid temperature is changed from subcritical to supercritical.

The density vs temperature and pressure relationships of methanol–carbon dioxide mixtures were not known when these measurements were taken. However, subsequent measurements of density using a "U" tube densitometer shows that an increase in temperature from 24 to 50 °C (at 130 bar) decreases density from 0.87 to 0.69 g/cm^3. This result suggests that negative temperature programming of constant composition binary mixtures should produce increasing solvent strength which agrees with general experience in capillary SFC.

Pressure. Very little change in solvent strength was observed when pressure was increased from 76 bar (1100 psi) to 241 bar (3500 psi) at temperatures from 25 to 40 °C. The wavelength of maximum absorbance changes no more than

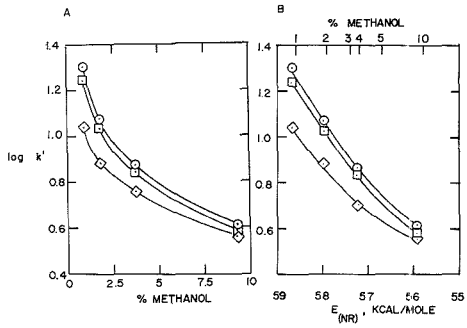

Figure 6. Preliminary correlation of retention with $E_{(NR)}$. Retention of the phenylthiohydantoin derivatives of proline (diamonds), isoleucine (squares), and α-aminobutyric acid (circles) on a cyanopropyl column as a function of (a) methanol modifier concentration and (b) solvent strength measured by using Nile Red.

2–4 nm, corresponding to a change in $E_{(NR)}$ of less than 0.5. The spectrophotometer resolution (2 nm) is on the same order of magnitude as the observed spectral shifts. Such findings are consistent with the observation that density changes produce much smaller changes in retention in SFC than composition changes produce in LC.

Results similar to those reported for pure carbon dioxide, were also observed with mixtures of modifiers in carbon dioxide. The wavelength of maximum absorbance was primarily determined by the amount of modifier added and was relatively insensitive to the pressure or density of the fluid, at least at high densities (>0.7 g/cm^3). This is consistent with previous observations (*18*) that the concentration of modifier inside clusters increases as the density decreases. The intensity of interaction between solutes and modifier in the clusters actually increases, but the number of clusters decreases substantially. This leads to a drop in solubility of polar solutes in the mixture (*27*). Clearly, solubility of such solutes is controlled by the identity and concentration of the modifier and the nature of the clustering phenomenon. The minimal effect of pressure on the apparent solvent strength of the mixtures suggests that chromatographic retention of polar solutes will likely be more a function of composition than density when polar modifiers are added to supercritical fluids.

Preliminary Correlation with Chromatography. The separation of phenylthiohydantoin (PTH) derivatives of amino acids have been extensively studied in our laboratory (*54*) as a function of methanol concentration in carbon dioxide. Plots of log k' vs percent methanol are nonlinear, as shown in Figure 6a for three PTH amino acids. Plots of the same retention data, but substituting $E_{(NR)}$ for methanol concentration, produce substantially improved linearity, as shown in Figure 6b. Residual nonlinearities in Figure 6b suggest that other important interactions, likely related to modifier–stationary phase interactions, are not being accounted for when log k' is plotted against $E_{(NR)}$.

CONCLUSIONS

The retention mechanism in many packed column SFC separations is still a matter of debate. The clustering of polar modifier molecules has been shown to produce local regions of high solvent strength. Such clustering produces very nonlinear solvent strength vs composition profiles and suggests a possible alternative to or an enhancement of previous models of retention. The possibility that solvent mixtures produce nonlinear changes in solute–solvent interactions vs composition has not been widely considered in chromatography even though discrepancies between retention and composition have been discussed (*49*). Binary mixtures of a supercritical fluid and a polar modifier appear to allow much wider variation in mixture solvent strength through composition adjustment than is possible by using binary pairs of normal liquids. Such wide variations allow nonlinearities between solvent strength and composition to be much more apparent. Solvatochromic shift measurements using Nile Red indicate a strong association between the dye and polar modifiers. Such "association", or "local composition", or "clustering" means that polar solutes are surrounded by a solvation sphere containing a substantially higher modifier concentration, and experience a subsequently higher polarity, than expected from bulk composition. Such mobile phase effects must have an impact on chromatographic retention, but the exact nature of such effects has not yet been determined. If packed column SFC follows a mechanism characteristic of BPC, the equation for solvent polarity, P', must be modified to account for the difference between bulk and local composition. If adsorption of the mobile phase solvent onto the stationary phase is important in retention, the equations for adsorption chromatography must be extended to quantify specific solute–solvent effects in the mobile phase. There is a reasonable likelihood that some aspects of both BPC and adsorption chromatography impact retention in normal phase, packed column SFC.

In supercritical fluids containing polar modifiers, the primary mobile phase interactions experienced by polar solutes should be with clusters of the modifier. System density primarily determines the nature of the modifier cluster and thus has only a secondary effect on retention adjustment (a limited range of solvent strength adjustment). Alternately, density programming is likely to produce very subtle changes in solvent strength and will likely be most useful in differentiating very similar molecules.

ACKNOWLEDGMENT

We thank Professor Keith Johnston of the Chemical Engineering Department of the University of Texas and Dr. Clement Yonker of Battelle Northwest Labs for helpful discussions. We also wish to thank the Du Pont Company for allowing us to publish the Nile Red measurements in Table I.

LITERATURE CITED

(1) Blilie, A. L.; Greibrokk, T. *Anal. Chem.* **1985**, *57*, 2239.
(2) Gere, D. R. Hewlett-Packard Application Note AN800-2, 1983.
(3) Taylor, L. T. Atlas of Chromatograms. *J. Chromatogr. Sci.* **1987**, *25*, 4–5.
(4) Yonker, C. R.; Smith, R. D. *J. Chromatogr.* **1986**, *361*, 25–32.
(5) Snyder, L. R. *J. Chromatogr.* **1974**, *92*, 223–230.
(6) Rohrschneider, L. *Anal. Chem.* **1973**, *45*, 1241.
(7) Snyder, L. R.; Kirkland, J. J. *Introduction to Modern Liquid Chromatography*, 2nd ed.; John Wiley and Sons: New York, 1979; Chapter 7.3.
(8) Snyder, L. R. *Principles of Adsorption Chromatography*; Marcel Dekker: New York, 1968; Chapter 8.
(9) Mourier, P.; Sassiat, P.; Caude, M.; Rosset, R. *J. Chromatogr.* **1986**, *353*, 61–75.
(10) Smith, P. L.; Cooper, W. T. *Chromatographia* **1988**, *25*(1), 55–60.
(11) Sjostrom, M.; Wold, S. *Acta Chem. Scand.* **1981**, *B35*, 537–554.
(12) Kamlet, M. J.; Taft, R. W. *Acta Chem. Scand.* **1985**, *B35*, 611–628.
(13) Dimroth, K.; Reichardt, C.; Siepmann, T.; Bohlmann, F. *Justus Liebigs Ann. Chem.* **1963**, *661*, 1.
(14) Kamlet, M. J.; Taft, R. W. *J. Am. Chem. Soc.* **1976**, *98*, 377–383.
(15) Taft, R. W.; Kamlet, M. J. *J. Am. Chem. Soc.* **1976**, *98*, 2886–2894.
(16) Kamlet, M. J.; Abboud, J. L.; Taft, R. W. *J. Am. Chem. Soc.* **1977**, *99*, 6027–6038.
(17) Frye, S. L.; Yonker, C. R.; Kalkwarf, D. R.; Smith, R. D. In *Supercritical Fluids: Chemical and Engineering Applications*; Squires, T. G., Paulaitis, M. E., Eds.; American Chemical Society: Washington, DC, 1987; Chapter 3.
(18) Kim, S.; Johnston, K. P. *AIChE J.* **1987**, *33*(10), 1603–1611.
(19) Johnston, K. P., private communication.
(20) Johnston, K. P.; Kim, S.; Wong, J. M. *Fluid Phase Equilib.* **1987**, *38* 39–62.
(21) Deiters, U. K. *Fluid Phase Equilib.* **1982**, *8*, 123–129; **1983**, *13*, 109–120.
(22) Whiting, W. B.; Prausnitz, J. M. *Fluid Phase Equilib.* **1982**, *9*, 119–147.
(23) Mathias, P. M.; Copeman, T. W. *Fluid Phase Equilib.* **1983**, *13* 91–108.
(24) Hu, Y.; Azevedo, E. G.; Prauznitz, J. M. *Fluid Phase Equilib.* **1983**, *13*, 351–360.
(25) Nitsche, K.-S.; Suppan, P. *Chimia* **1982**, *36*(9), 346–348.

(26) Figueras, J. J. Am. Chem. Soc. 1971, 93, 3255-3263.
(27) Dobbs, J. M.; Wong, J. M., Lahiere, R. J.; Johnston, K. P. Ind. Eng. Chem. Res. 1987, 26, 56-65.
(28) Walsh, J. M.; Ikonomou, G. D.; Donohue, M. D. Fluid Phase Equilib. 1987, 33, 295-314.
(29) Hyatt, J. A. J. Org. Chem. 1984, 49, 5097-5101.
(30) Sigman, M. E.; Lindley, S. M.; Leffler, J. E. J. Am. Chem. Soc. 1985, 107, 1471-1472.
(31) Yonker, C. R.; Frye, S. L.; Kalkwarf, D. R.; Smith, R. D. J. Phys. Chem. 1986, 90, 3022-3026.
(32) Bente, Paul; Weaver, Harry, Hewlett-Packard, private communication.
(33) Deye, J. F.; Anderson, A. G., Central Research and Development Department, E. I. du Pont de Nemours, unpublished work.
(34) Kosower, E. M. J. Am. Chem. Soc. 1958, 80, 3253, 3261, 3267.
(35) Reichardt, C.; Harbusch-Gornert, E. Justus Liebigs Ann. Chem. 1983, 721.
(36) Fowler, F. W.; Katritzky, A. R.; Rutherford, R. J. D. J. Chem. Soc. B 1971, 460.
(37) Andersen, A. G., unpublished work.
(38) H.J. Conn's Biological Stains, 9th ed.; Lillie, R. D., Ed.; The Williams and Wilkins Co.: Baltimore, MD, 1977; pp 372-430.
(39) Reissig, T. D.R.P. 45268, 1888.
(40) Mohlau, R.; Uhlmann, K. Justus Liebigs Ann. Chem. 1896, 289, 90.
(41) Kehrmann, F. Ber. Dtsch. Chem. Ges. 1904, 37, 3581.
(42) Thorpe, J. F. J. Chem. Soc. 1907, 91, 324.
(43) Kehrman, F.; Herzbaum, A. Ber. Dtsch. Chem. Ges. 1917, 50, 873.
(44) Kolling, O. W. Anal. Chem. 1976, 48, 884.
(45) Kolling, O. W. Anal. Chem. 1966, 38, 1424.
(46) Basting, D.; Ouw, D.; Schafer, F. P. Opt. Commun. 1976, 18, 260.
(47) Stuzka, V.; Simanek, V. Collect. Czech. Chem. Commun. 1973, 38, 194.
(48) Davis, M. M.; Hetzer, H. B. Anal. Chem. 1966, 38, 451.
(49) Dorsey, J. G. Chromatography 1987, 2(5), 34-41.
(50) Saunders, D. L. Anal. Chem. 1974, 46, 472.
(51) van Wassen, U.; Swaid, I.; Schneider, G. M. Angew. Chem., Int. Ed. Engl. 1980, 19, 575-587.
(52) Lauer, H. H.; Mcmanigill, D.; Board, R. D. Anal. Chem. 1983, 55, 1370.
(53) Doran, T. Gas Chromatography 1972; Applied Science Publishers: Essex, 1973; pp 133-143.
(54) Berger, T. A.; Deye, J. F.; Ashraf-Korassani, M.; Taylor, L. T. J. Chromatogr. Sci. 1989, 27, 105.

RECEIVED for review June 27, 1989. Accepted December 15, 1989. This document is contribution number 4980 from Du Pont's Central Research Department.

Extraction of Tervalent Lanthanides as Hydroxide Complexes with Tri-*n*-octylphosphine Oxide

Ted Cecconie and Henry Freiser*

Strategic Metals Recovery Research Facility, Department of Chemistry, University of Arizona, Tucson, Arizona 85721

The extraction behavior of lanthanum(III), praseodymium(III), europium(III), terbium(III), holmium(III), and ytterbium(III) from dilute chloride solutions into chloroform solutions containing tri-*n*-octylphosphine oxide (TOPO) was examined. The lanthanides were found to extract as hydroxide complexes of the form $Ln(OH)_3 \cdot n$TOPO. The extraction selectivity for this system increases with increasing TOPO concentration, rivaling those for common acidic organophosphorus extractants in the TOPO concentration range 0.025-0.100 M and surpassing them at higher concentrations. When TOPO concentrations of 0.25 M or greater are employed, the extraction system is, overall, the most selective for lanthanide separations to date. This is the first report of the lanthanides extracting as hydroxide complexes.

INTRODUCTION

The use of monodentate neutral phosphorus compounds in metal ion extraction is widely known (*1*). These compounds generally function as adductants, auxiliary complexing agents, which enhance the extractability of coordinatively unsaturated chelates by replacing water molecules remaining coordinated to the complexed metal ion. The report of extraction of lanthanides and actinides by sulfur ligands in the presence of tri-*n*-octylphosphine oxide (TOPO) (*2, 3*) led us to examine systems such as quinolin-8-thiol and dithizone in the presence of TOPO for selected Ln^{3+}. On observing the surprising extent of extraction in the absence of the S-containing ligand, we decided to examine this unusual phenomenon further. Our hypothesis of the formation and extraction of a lanthanide hydroxide complex was so unexpected that we took particular care to examine and reject alternate explanations.

EXPERIMENTAL SECTION

Apparatus. Infrared spectra were obtained with a Perkin-Elmer 1800 Fourier transform infrared spectrometer. ^{31}P NMR spectra were obtained at 250 MHz with a Bruker WM-250 spectrometer. Phosphorus and lanthanide concentrations were determined with a Perkin-Elmer 6500 ICP spectrometer.

Reagents. Stock solutions containing lanthanum(III), praseodymium(III), europium(III), terbium(III), holmium(III), and ytterbium(III) were prepared from chloride salts (Alfa Inorganics, 99.9%). Chloroform (AR grade) was washed 3 times with deionized water prior to use.

TOPO (courtesy of American Cyanamid, >99%) was purified to remove all traces of acidic impurities, such as di(*n*-octyl)phosphoric acid, which are found in commercial sources of TOPO. This purification involved equilibrating a concentrated (0.5 M) TOPO solution in chloroform 8 times with an equal volume of a 0.1 M acetate solution, pH $\approx$ 5, to remove the acidic impurities (*4*). The phosphorus level of all except the first of the eight washes was below the inductively coupled plasma limit of detection for P (5×10^{-6} M). The acetate-washed solution was equilibrated 12 times with an equal volume of deionized water to remove any acetic acid extracted by TOPO (*5, 6*). The final TOPO solution was placed in a Rotovap to remove the chloroform solvent, with the resulting oily material placed in a vacuum desiccator to crystallize overnight: mp, 50-52 °C; IR (KBr), $\nu_{(1145\ cm^{-1})}$ (P=O); ^{31}P NMR ($CDCl_3$), δ 48.7 ppm.

Distribution Studies. An unbuffered solution (μ = 0.1, HCl/NaCl) containing the lanthanides at $\sim 10^{-4}$ M was equilibrated with an equal volume of a TOPO solution in chloroform for at least 15 min, a time found adequate for equilibrium to be reached. The equilibrium pH of the aqueous phase was measured after phase separation. Metal distribution results were obtained by inductively coupled plasma atomic emission spectrometry (ICP-AES) analysis. The lanthanide concentration remaining in the aqueous phase was determined directly, employing manganese as an internal standard. The concentration of lanthanide extracted into the organic phase was determined by back extraction into

0003-2700/90/0362-0622$02.50/0

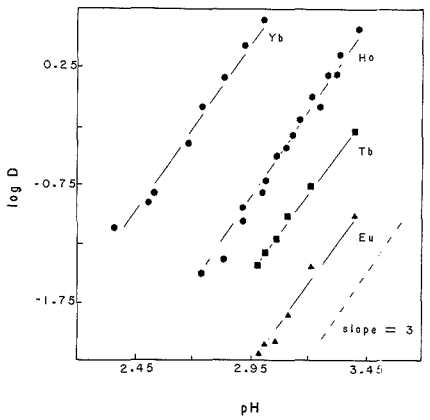

Figure 1. log D dependence on pH. [TOPO] = 0.0500 M in chloroform. Initial lanthanide concentrations were as follows: Yb(III), 12.5 ppm; Ho(III), 25.0 ppm; Tb(III), 25.0 ppm; Eu(III), 25.0 ppm.

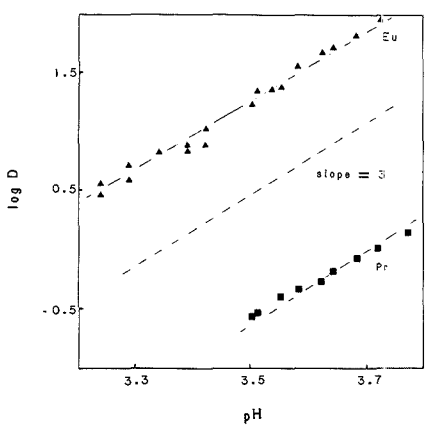

Figure 2. log D dependence on pH. [TOPO] = 0.500 M in chloroform; initial lanthanide concentrations were as follows: Eu(III), 12.5 ppm; Pr(III), 40.0 ppm.

0.1 M hydrochloric acid and determining the lanthanide concentration in the acid solution. The ICP-AES instrumental conditions are listed elsewhere (*7*). The concentration results were used to calculate the distribution ratio, D, defined as $D = C_{Ln_o}/C_{Ln}$.

RESULTS AND DISCUSSION

The extraction behavior of the lanthanides was evaluated from the relationships of log D on pH, log [TOPO], and log [Ln]. As shown in Figures 1 and 2 for Yb(III), Ho(III), Tb(III), and Eu(III) ([TOPO] = 0.0500 M in $CHCl_3$), log D was found to have a slope 3 dependence on pH under conditions of constant TOPO and initial lanthanide concentrations. The log D relationships on log [TOPO] and log [Ln] were subsequently viewed in terms of log D – 3 pH versus log [TOPO] and log [Ln] since, in the absence of a buffer, it was found difficult to control the equilibrium pH to a constant value while the TOPO or lanthanide concentration was varied. Plots of log D – 3 pH versus log [TOPO] (Figures 3 and 4), under conditions of constant initial lanthanide concentrations, indicated linear relationships with slopes intermediate between 2 and 3. Plots of log D – 3 pH versus –log [Ln] (Figure 5), under conditions of constant TOPO concentration, indicate *no* dependence on lanthanide concentration.

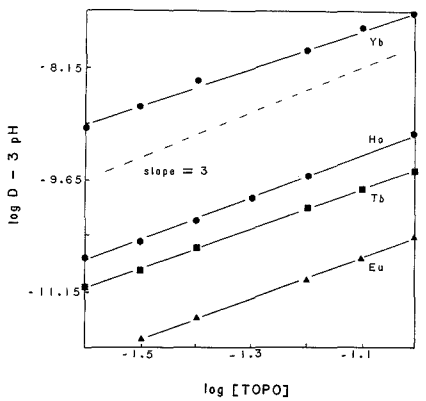

Figure 3. log D – 3 pH dependence on log [TOPO] in the range –1.60 to –1.00. Initial lanthanide concentrations were as follows: Yb(III), 12.5 ppm; Ho(III), 25.0 ppm; Tb(III), 25.0 ppm; Eu(III), 25.0 ppm.

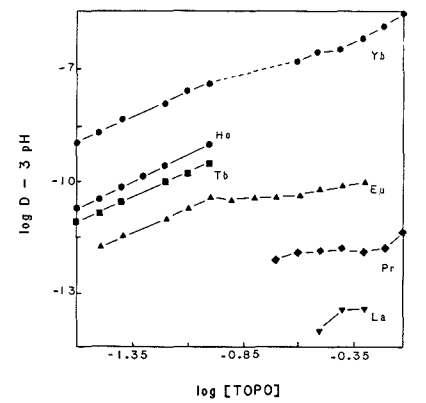

Figure 4. log D – 3 pH dependence on log [TOPO]. Initial lanthanide concentrations were as follows: Yb(III), 12.5 ppm; Ho(III), 25.0 ppm; Tb(III), 25.0 ppm; Eu(III), 12.5 ppm; Pr(III), 40.0 ppm; La(III), 25.0 ppm.

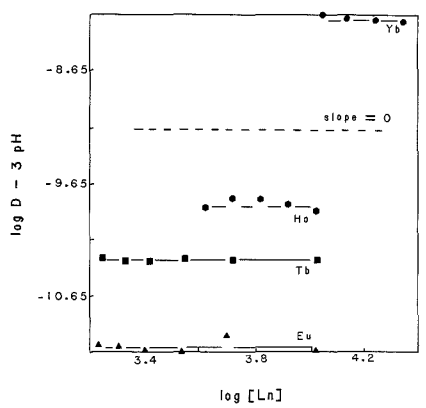

Figure 5. log D – 3 pH dependence on log [Ln]. [TOPO] = 0.0500 M in chloroform.

When TOPO concentrations of higher than 0.100 M are employed in extraction, although the least-squares slope re-

sults for log D – 3 pH versus log [TOPO] are between 2.5 and 2.8 in the TOPO concentration 0.025–0.100 M, the extracted complex is treated as though it contains three TOPO molecules.

On the basis of these results, the following extraction equilibrium holds:

$$Ln^{3+} + 3HA + n\overline{TOPO}_o \rightleftharpoons \overline{LnA_3 \cdot nTOPO}_o + 3H^+ \quad (1)$$

where n can be 2 or 3, HA represents a weak acid, $LnA_3 \cdot n$TOPO represents the extracted metal complex, and the subscript o refers to the organic phase.

Unlike the systems based on TBP, where the lanthanides extract as metallic salt complexes (*8–10*), the distribution results indicate the lanthanides extract as hydroxide complexes, since water should be the only weak acid present. Since this is both highly unexpected and unprecedented for the lanthanides, other possibilities for the weak acid, HA, were considered.

The presence of acidic impurities such as di(n-octyl)-phosphoric acid (DOPA) in commercial sources of TOPO makes them candidates for the weak acid. Chloroform solutions of TOPO were treated with 0.1 M acetate buffer washes, pH ≈ 5, prior to use for the removal of acidic impurities (*4*). The amount of phosphorus-containing species in each acetate wash was monitored by ICP-AES using the 213.618 p I Mission line. The phosphorus content was found to decrease with increasing wash number, typically from ≈ 170 mg/L in the first wash to no detectable amount in the eighth wash (<0.15 mg/L). Since it was observed that each successive acetate wash from the second to seventh had 40% the phosphorus content of the preceeding wash, one can estimate the amount of acidic impurity in purified TOPO to be <0.0001% by weight (as DOPA). At this low level, typical amounts of lanthanide extracted would be in 1000-fold excess of the impurity, indicating acidic impurities in TOPO cannot account for the extraction.

Another candidate for the weak acid is acetic acid extracted by TOPO during its purification (*5, 6*). Because acetic acid extraction occurs, the acetate-washed chloroform solutions of TOPO were equilibrated with deionized water. The pH of the deionized water washes was found to rise from 3.2 in wash 1 to 5.6 in washes 11 and 12. The pH of deionized water saturated with chloroform was also found to be 5.6. The steady rise in pH to a constant value corresponding to the value of chloroform-saturated deionized water indicated that essentially all the acetic acid ($<2.5 \times 10^{-6}$ M) had been removed from the chloroform solution of TOPO, eliminating acetic acid as the weak acid source.

The decomposition of TOPO to an organophosphorus acid could also be the source of weak acid. This is not expected, however, since phosphorus and carbon form a strong covalent bond that is not easily hydrolyzed. In any event, TOPO samples used in lanthanide extraction studies were isolated and examined for decomposition products. The Fourier transfer infrared (FT-IR) spectra of the used TOPO did not indicate the five-peak pattern characteristic of organophosphorus acids (*11*) and were the same as those for unused TOPO samples. The ^{31}P NMR spectra for used TOPO did not differ from those of unused TOPO. Furthermore, equilibration of a 0.0500 M used TOPO solution in chloroform with a 0.1 M acetate buffer solution, pH ≈ 5, did not lead to a detectable amount of phosphorus, which would be expected if decomposition to an organophosphorus acid had occurred. All these results eliminate decomposition products as the weak acid source.

Finally, to eliminate the possibility of chloride as part of the extracted complex, an extract containing ~100 ppm of Yb, obtained from an aqueous phase containing 0.1 M chloride was back extracted into Ultrex 0.1 M HNO_3, and gave no trace of Cl^- with $AgNO_3$ solution. Of course, had Cl been part of the complex, a different pH dependency of extraction would have been observed.

Table I. Extraction Constants for Ln^{3+} as $Ln(OH)_3 \cdot n$TOPO

Ln^{3+}	K_{ex} $n = 2$	K_{ex} $n = 3$
Yb	1.40×10^{-6}	2.64×10^{-5}
Ho	1.10×10^{-8}	7.51×10^{-7}
Tb	8.07×10^{-9}	2.18×10^{-7}
Eu	7.89×10^{-10}	2.91×10^{-8}

The elimination of organophosphorus acids, either as acidic impurities or decomposition products, and acetic acid as the weak acid source leave water as the only other possibility. Therefore, the relationships of log D on pH, log [TOPO], and log [Ln] in the TOPO concentration 0.025–0.100 M indicate the lanthanides are extracting by the hydrated metal ion, $Ln(H_2O)_x^{3+}$, coordinating with n, i.e., 2 or 3, TOPO molecules with the subsequent loss of three protons and water, as shown in the following process:

$$Ln(H_2O)_x^{3+} + n\overline{TOPO}_o \overset{K_{ex}}{\rightleftharpoons} \overline{Ln(OH)_3 \cdot nTOPO \cdot yH_2O}_o + 3H^+ \quad (2)$$

where $Ln(OH)_3 \cdot n$TOPO$\cdot yH_2O_o$ represents the extracted complex, and x and y are integers (y may be zero). The extraction constant, K_{ex}, can be represented by using the following equation:

$$K_{ex} = \frac{[\overline{Ln(OH)_3 \cdot 3TOPO \cdot yH_2O}]_o[H^+]^3}{[Ln(H_2O)_x^{3+}][TOPO]_o^3} = \frac{K_{DC}K_{AD}\beta_3}{K_{DR}^3} \quad (3)$$

where K_{DC} is the distribution constant for the metal complex between chloroform and water, K_{AD} is the overall adduct formation constant between $Ln(OH)_3 \cdot zH_2O$ and TOPO to form $Ln(OH)_3 \cdot 3$TOPO, β_3 is the overall formation constant of $Ln(OH)_3 \cdot zH_2O$, K_{DR} is the distribution constant of TOPO between chloroform and water, and z is an integer.

The extraction of hydroxide complexes of the lanthanides is unexpected, especially since the fractions of hydroxy species are small at pH values where extraction occurs. For example, significant amounts of Yb(III) are extracted into a 0.0500 M chloroform solution of TOPO at a pH of 3.4 (log $D \approx 2$), although the relative fractions of hydroxy species are low ($\alpha_{Yb^{3+}} = 0.9999$; $\alpha_{YbOH^{2+}} = 5.01 \times 10^{-5}$; $\alpha_{Yb(OH)_2^+} = 1.00 \times 10^{-9}$; $\alpha_{Yb(OH)_3} = 1.26 \times 10^{-14}$ (*12*). It appears, therefore, that the high concentrations of TOPO used in extraction (0.100 M = 4% (w/v) TOPO), along with possible high values of K_{DC} and/or K_{AD}, compensate for the low levels of aqueous hydroxy species. The extraction of hydroxide complexes, rather than metallic chloride complexes, occurs since the chloride concentration employed in the current study is significantly lower than those used in the TBP systems (*8*), and the lanthanides do not readily form chloride complexes (*13, 14*).

The TOPO extraction has analytical significance, since the extraction selectivity is either comparable or superior to those for organophosphorus acids. The selectivities of the different extractants can be compared by using separation factors (SF), as defined below

$$SF_{Ln_1/Ln_2} = \log K_{ex\,Ln_2} - \log K_{ex\,Ln_1} \quad (4)$$

Taking the logarithm of eq 3 yields the following result:

$$\log K_{ex} = \log D - 3\,pH - 3 \log [TOPO] \quad (5)$$

The values of log K_{ex} for Yb(III), Ho(III), Tb(III), and Eu(III) in the TOPO concentration range 0.025–0.100 M can be calculated by using eq 5 (Table I). As shown in Table II,

Table II. Separation Factors for Various Systems

	La/Pr	Pr/Eu	Eu/Ho	Ho/Yb	Eu/Yb	La/Yb
DEHPA (*13*)	0.76	1.19	1.67	1.43	3.10	5.05
BTMPPA (*14*)	1.78	1.50	1.46	1.24	2.70	5.98
DPPA (*13*)	1.38	2.01	1.48	1.34	2.82	6.21
TOPO (0.100 M)			1.36	1.65	3.01	
(0.500 M)	1.51	1.91	2.01	1.78	3.79	7.21

the extraction selectivity of TOPO systems rivals those for DEPHA in the TOPO concentration range 0.025–0.100 M and surpasses the DEHPA selectivity at TOPO concentrations of 0.2 M or higher.

LITERATURE CITED

(1) Morrison, G. H.; Freiser, H. *Solvent Extraction in Analytical Chemistry*; John Wiley and Sons: New York, 1957. Marcus, Y.; Kertes, A. S. *Ion Exchange and Solvent Extraction of Metal Complexes*; Wiley-Interscience: New York, 1969. Sekine, T.; Hasegawa, S. *Solvent Extraction Chemistry*; Dekker: New York, 1977.
(2) Smith, B. F.; Jarvinen, G. D.; Miller, G. G.; Ryan, R. R.; Peterson, E. J. *Solvent Extr. Ion Exch.*, **1987**, *5* (5), 895.
(3) Musikas, C. in *Proceedings of the International Symposium on Ac/Ln Separations*; Choppin, G. R., Navratil, J. D., Schultz, W. W., Eds.; Philadelphia, 1984; pp 19–30.
(4) Ke-an, L.; Muralidharan, S.; Freiser, H. *Solvent Extr. Ion Exch.* **1985**, *3*, 895.
(5) Wardell, J. M.; King, C. J. *J. Chem. Eng. Data* **1978**, *23*, 144.
(6) Watson, E. K.; Rickelton, W. A.; Robertson, A. J.; Brown, T. J. *Solvent Extr. Ion Exch.* **1988**, *6*, 207.
(7) Cecconie, T. Freiser, H. *Solvent Extr. Ion Exch.* **1989**, *7*(1), 15.
(8) Weaver, B. Solvent Extration in the Separation of Rare Earths and Trivalent Actinides. In *Ion Exchange and Solvent Extraction*; Marinsky, J. A., Marcus, Y., Eds.; Marcel Dekker: New York, 1974; Vol. 6, pp 189–277.
(9) Scargill, D.; Alcock, K.; Fletcher, J. M.; Hesford, E.; McKay, H. A. C. *J. Inorg. Nucl. Chem.* **1957**, *4*, 304.
(10) Hesford, E.; Jackson, E. E.; McKay, H. A. C. *J. Inorg. Nucl. Chem.* **1959**, *9*, 279.
(11) Thomas, L. C. *Interpretation of the Infrared Spectra of Organophosphorus Compounds*; Heyden: London, 1974; pp 39–45.
(12) Baes, C. F., Jr.; Mesmer, R. E. *The Hydrolysis of Cations*; John Wiley and Sons: New York, 1976; pp 129–146.
(13) Motomizu, S.; Freiser, H. *Solvent Extr. Ion Exch.* **1985**, *3*, 637.
(14) Komatsu, Y.; Freiser, H. *Anal. Chim. Acta*, in press.

RECEIVED for review August 2, 1989. Revised manuscript received December 11, 1989. Accepted December 11, 1989.

Reshaping of Staircase Voltammograms by Discrete Spherical Convolution

Sten O. Engblom* and Keith B. Oldham

Department of Chemistry, Trent University, Peterborough, Ontario K9J 7B8, Canada

Linear-scan staircase voltammetry and cyclic staircase voltammetry generate unsatisfactory current–voltage curves even for reversible electrode processes. A convolution method is described that converts such curves, obtained at spherical mercury electrodes, into the classical wave shape that is familiar from polarography. The plateaus of these waves are horizontal and their heights accurately match theoretical prediction.

The advantages of staircase voltammetry, namely the simplicity of the applied waveform and its high discrimination against capacitive current, have failed to bring this technique into the standard repertoire of the electroanalytical chemist. One reason for this is that the method's output, a sequence of instantaneous current values (i_1, i_2, ..., i_J, ...) measured at equally spaced potentials ($E_0 + \Delta E$, $E_0 + 2\Delta E$, ..., $E_0 + J\Delta E$, ...), is asymmetric and lacks easily delineated features that can be correlated with the concentration of the electroactive species, or its standard potential. Moreover, the shape of the i_J versus E_J curve depends in a complicated way on ΔE and on the times ($\phi\Delta t$, $\phi\Delta t + \Delta t$, $\phi\Delta t + 2\Delta t$, ..., $\phi\Delta t + (J-1)\Delta t$, ...) at which current measurements are made, where $t = 0$ corresponds to the start of the $J = 1$ step. There have been a number of attempts to overcome these problems. One approach (*1–4*) is to convert the staircase voltammogram into the more familiarly shaped linear scan voltammogram. A second approach (*5*) aims to reshape the staircase output into peaks reminiscent of differential pulse voltammograms or into waves resembling classical polarograms. The present article is an attempt to improve the performance of the latter transformation for cases of spherical diffusion, i.e., to convert staircase voltammograms into waves that have very flat, and therefore precisely quantifiable, plateaus.

*Permanent address: Laboratory of Analytical Chemistry, Åbo Akademi, Åbo, Finland.

THEORY

Earlier work (*5*) showed that the conversion of the reversible staircase voltammogram into the more tractable wave shape could be accomplished by discretely convolving the current data with a set of precalculated weights. This procedure, based on the theory of planar electrodes, was shown to yield a function known to follow the equation (*6*)

$$m = \frac{m_d}{2}\left[1 - \tanh\left\{\frac{nF}{2RT}(E - E_h)\right\}\right] \qquad (1)$$

where $m_d = nAFc_0^b D_O^{1/2}$ and $E_h = E^{o\prime} + (RT/2nF) \ln [D_R/D_O]$. All symbols have their usual meaning (see the Glossary). Notice that the function m depends on potential only; the influences of step height ΔE, step length Δt, and the time $\phi\Delta t$ of current sampling on a step, that make the interpretation of the original curve so difficult, are completely eliminated.

However, when the electrode is spherical, as is often the case in practice, it is observed that the procedure based on the theory for planar electrodes results in a wave with a rising plateau. A second difficulty is that the planar convolution of a *cyclic* staircase voltammogram produces a current–voltage curve that does not retrace itself, even for a fully reversible reaction. We intend to show how to take the sphericity of the electrode into account when discretely convolving the current to yield a self-retracing curve with a constant plateau value

0003-2700/90/0362-0625$02.50/0

of m_d, equal to that appearing in eq 1.

Let us consider the simple electrode reaction

$$O + ne \rightleftharpoons R \tag{2}$$

occurring reversibly at a spherical electrode in a system initially devoid of the reduced species R but with an initial bulk concentration c_O^b of the oxidized species O. Supporting electrolyte is present in excess so that migration of the species of interest is negligible. Electrolysis at the sphere will cause the electroactive substances to diffuse in accordance with Fick's second law

$$\frac{1}{D_i}\frac{\partial c_i}{\partial t} = \frac{\partial^2 c_i}{\partial x^2} + \frac{2}{x + r}\frac{\partial c_i}{\partial x}, \quad i = O \text{ or } R \tag{3}$$

where r is the radius of the sphere and x is the radial distance measured from and perpendicular to the surface of the sphere. If both O and R are soluble in the solution, the initial and boundary conditions of the system are

$$c_O = c_O^b,\ c_R = 0 \text{ for } t \le 0,\ x \ge 0 \tag{4a}$$

$$c_O = c_O^b,\ c_R = 0 \text{ for all } t,\ x \to \infty \tag{4b}$$

On the other hand, if R amalgamates, the conditions for O are as above while the new conditions for R are

$$c_R = 0 \text{ for } t \le 0,\ -r \le x \le 0 \tag{5a}$$

$$\partial c_R/\partial x = 0 \text{ for all } t,\ x = -r \tag{5b}$$

A final boundary condition is provided by the requirement that the fluxes of O and R are equal in magnitude at the electrode surface and proportional to the current. This condition is incorporated into the equations

$$\frac{i}{nAF} = D_O\left(\frac{\partial c_O}{\partial x}\right)_{x=0} = \mp D_R\left(\frac{\partial c_R}{\partial x}\right)_{x=0} \tag{6}$$

where the upper/lower sign applies when R dissolves in the solution/electrode, respectively.

Our problem is most conveniently solved in Laplace space. When the Laplace transform of eq 3 is combined with that of eq 6 and the other conditions, the result (7), when both species are solution soluble, is

$$\frac{\bar{i}}{nAF} = D_O^{1/2}\left(s^{1/2} + \frac{D_O^{1/2}}{r}\right)\left(\frac{c_O^b}{s} - \bar{c}_O^s\right) = D_R^{1/2}\left(s^{1/2} + \frac{D_R^{1/2}}{r}\right)\bar{c}_R^s \tag{7}$$

in Laplace space. When R forms an amalgam, the first equality in eq 7 is still valid while the second is replaced by (7)

$$\frac{\bar{i}}{nAF} = D_R^{1/2}\left(s^{1/2}\coth\{r(s/D_R)^{1/2}\} - \frac{D_R^{1/2}}{r}\right)\bar{c}_R^s \tag{8}$$

In many instances the time scale of the experiment and the size of the sphere are such that $\coth\{r(s/D_R)^{1/2}\}$ is closely approximated by unity, in which case

$$\frac{\bar{i}}{nAF} = D_R^{1/2}\left(s^{1/2} - \frac{D_R^{1/2}}{r}\right)\bar{c}_R^s \tag{9}$$

To be specific, this is effectively true as long as $D_R t \le 0.062r^2$ (7). From here onward we will assume that this inequality, and therefore eq 9, is valid in the amalgamation case.

We now define two quantities

$$\mu_O = nAFD_O^{1/2}(c_O^b - c_O^s) \tag{10a}$$

$$\mu_R = nAFD_R^{1/2}c_R^s \tag{10b}$$

which are linear functions of the surface concentrations. We can see that as the surface concentration of O approaches zero, μ_O approaches m_d. The semiintegral m, which occurs in planar voltammetry, is thus replaced in spherical voltammetry by two similar, but numerically slightly different, functions μ_O and μ_R. See the Appendix for a discussion of the relationship between these functions and their dependence on potential.

Equations 7 and 9 show that the Laplace transforms of these quantities are related to that of the current by

$$\bar{\mu}_O = \frac{\bar{i}}{s^{1/2} + D_O^{1/2}/r} \tag{11a}$$

$$\bar{\mu}_R = \frac{\bar{i}}{s^{1/2} \pm D_R^{1/2}/r} \tag{11b}$$

where, again, the upper/lower sign applies when R dissolves in the solution/electrode, respectively. Because these definitions are very similar, we shall henceforth not make a distinction between them but instead drop the subscripts and develop the theory without specifying a particular μ. In the end result it will then be a matter of a simple substitution to accommodate the theory to the appropriate μ.

Returning now to eqs 11 and dropping the subscripts, we see that the transform of the current can be expressed as

$$\bar{i} = s^{1/2}\bar{\mu} + \frac{D^{1/2}}{r}\bar{\mu} \tag{12}$$

or after inversion as

$$i = \frac{d^{1/2}\mu}{dt^{1/2}} + \frac{D^{1/2}}{r}\mu \tag{13}$$

Since the excitation signal in staircase voltammetry is a series of potential steps, it follows that the surface concentrations, and therefore the μ's, are discontinuously changed each time the potential is stepped. We can thus use the formula (8) for the semiderivative of a piecewise-defined function to express the semiderivative of μ at any time t during the Jth step as

$$\frac{d^{1/2}\mu_J(t)}{dt^{1/2}} = \frac{d^{1/2}\mu_{J-1}(t)}{dt^{1/2}} + \frac{d^{1/2}[\mu_J(t) - \mu_{J-1}(t)]}{[d\{t - (J-1)\Delta t\}]^{1/2}} \tag{14}$$

where $\mu_{J-1}(t)$ is what μ on the $(J-1)$th step would have continued to be during the time of the Jth step had the Jth step never occurred. Similar equations hold on the preceding steps and when all such equations are summed the result is

$$\frac{d^{1/2}\mu_J(t)}{dt^{1/2}} = \sum_{j=1}^{J}\frac{d^{1/2}[\mu_j(t) - \mu_{j-1}(t)]}{[d\{t - (j-1)\Delta t\}]^{1/2}} \tag{15}$$

Equation 15 assumes that E_0 has been chosen so that no reaction occurs initially, permitting us to set $i_0(t)$ and $\mu_0(t)$ to zero.

In dealing with the semiderivatives on the right-hand side in eq 15, we will now make the assumption that the surface concentrations, and therefore the μ's, are constant at constant potential during a reversible electrode reaction. This is true at planar electrodes (as is evident by taking the $r \to \infty$ limit of eq A.3 of the Appendix) and also at spherical electrodes if R is solution soluble and has a diffusion coefficient equal to D_O (as can also be proved from the exact equation A.3) (9, 10). However, the equality of μ_O and μ_R is not strictly true for spherical electrodes when R does not meet these two conditions, but it is nevertheless a valid approximation for the time scales of interest. The semiderivative of a constant is known (11) and thus eq 15 when combined with eq 13 becomes

$$i_J(t) - \frac{D^{1/2}}{r}\mu_J = \frac{d^{1/2}\mu_J}{dt^{1/2}} = \sum_{j=1}^{J}\frac{\mu_j - \mu_{j-1}}{[\pi\{t - (j-1)\Delta t\}]^{1/2}} \tag{16}$$

Current sampling usually occurs only once on each potential step, at time $t = (j - 1 + \phi)\Delta t$ where $0 < \phi < 1$. Substitution into eq 16 and rearrangement yields

$$i_J = \mu_J\left(\frac{D^{1/2}}{r} + (\pi\phi\Delta t)^{-1/2}\right) + (\pi\Delta t)^{-1/2}\sum_{j=1}^{J-1}\mu_j[(J + \phi - j)^{-1/2} - (J + \phi - j - 1)^{-1/2}] \quad (17)$$

Following a procedure that parallels the one adopted in the planar case (*5*), the equations for the current at all steps up to the Jth step can now be used to solve for μ_J, giving

$$\mu_J = (\pi\Delta t)^{1/2}(w_0 i_J + w_1 i_{J-1} + \ldots + w_{J-1} i_1) = (\pi\Delta t)^{1/2}\sum_{j=1}^{J-1} w_{J-j} i_j \quad (18)$$

where the weights are given by

$$w_0 = \left(\frac{(\pi D\Delta t)^{1/2}}{r} + \phi^{-1/2}\right)^{-1} \quad (19)$$

$$w_j = w_0\sum_{k=1}^{j} w_{j-k}([\phi + k - 1]^{-1/2} - [\phi + k]^{-1/2}) \quad (20)$$

Normally, the weights are precalculated by using eqs 19 and 20 and stored in a file on a suitable medium. The calculation of μ via eq 18 can then be performed on- or off-line depending on the available instrumentation. A plot of μ as a function of potential constitutes a wave, akin to the classical polarogram, with plateau height m_d.

Returning to the different definitions of μ, eqs 10 and 11, we can conclude this section by noting that μ_R is the result of the convolution if we replace $D^{1/2}$ in eq 19 with $D_R^{1/2}$ (R dissolves in the solution) or $-D_R^{1/2}$ (R dissolves in the electrode); μ_O is obtained by substituting $D_O^{1/2}$ for $D^{1/2}$.

EXPERIMENTAL SECTION

The solutions were made with reagent-grade chemicals and ion-exchanged and distilled water. A 0.993 mM ferrioxalate solution was made by dissolving crystals of potassium ferrioxalate in a solution of supporting electrolyte consisting of 1.0 M potassium oxalate and 0.05 M oxalic acid. The pH of the ferrioxalate solution was 5.1. Potassium ferrioxalate was freshly prepared before the experiments using ferrous ammonium sulfate as starting material (*12*). Because of the high photosensitivity of ferrioxalate (both crystals and solution), great care was taken to avoid light, both during the preparation of the chemical and during all experiments.

An EG&G PARC 303 static mercury drop electrode together with a PAR 273 potentiostat was used in the experiments and controlled by an HP-85 computer. The working electrode was a static mercury drop. Radii of 2.74×10^{-4} m (small drop), 3.53×10^{-4} m (medium drop), and 4.49×10^{-4} m (large drop) were used in the ferrioxalate work, but a different capillary used in the studies of amalgam-forming metals gave a "small drop" radius of 2.93×10^{-4} m. All drop radii were found by first collecting and weighing 100 drops. The volume of a drop was found by using the appropriate density of Hg (*13*) and its radius calculated, assuming the drop was a perfect sphere. Each drop radius given above is the average of three values found in this way. The area of the electrode (used in predicting the plateau heights) was calculated by again assuming that the electrode was a perfect sphere: $A = 4\pi r^2$. A platinum wire served as the counter electrode and the Ag/AgCl/saturated KCl reference electrode of the 303 SMDE was utilized. This reference electrode was calibrated before and after the experiments against an external Ag/AgCl/saturated KCl reference electrode. A saturated calomel electrode was used as the reference in some of the experiments. The temperature was measured during each experiment as was typically in the range 22.5–24.3 °C.

The convolutions were performed off-line on the HP-85 computer using files of precalculated weights. No background corrections were necessary and the current data were used as obtained.

Table I. Experimental Conditions for Curves Shown in Figures 1–5

	○	×	△	□	●
ΔE, mV	9	9	9	9	18
Δt, ms	80	80	80	40	80
ϕ	0.249	0.499	0.749	0.748	0.749
N	101	101	101	101	51

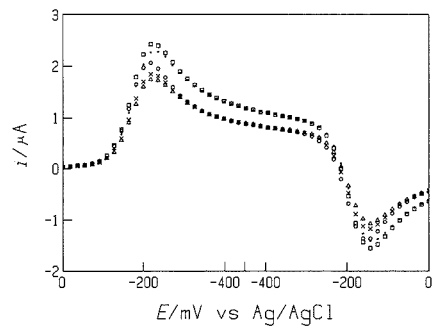

Figure 1. Five staircase voltammograms obtained at a small drop. See Table I for experimental details. Notice that in this and in the majority of the subsequent figures the potential axis has been unfolded for clarity. For curves ○, ×, △, and □ every second point is shown while for the ● curve every point is shown.

RESULTS AND DISCUSSION

We chose the reaction

$$Fe(C_2O_4)_3^{3-} + e^- \rightleftharpoons Fe(C_2O_4)_3^{4-} \quad (21)$$

in a supporting electrolyte of 1.0 M potassium oxalate and 0.050 M oxalic acid because it is known to be reversible, because both oxidation states are soluble in the solution, and because the two diffusion coefficients are equal within experimental precision. The literature values (*14*, *15*) of $D_R = D_O = 4.8 \times 10^{-10}$ m^2 s^{-1} were used in all our calculations, though other values have been reported (*2*, *16*). It is known (*9*) that under these circumstances the surface concentrations at a spherical electrode are constant at constant potential and the approximation in deriving eq 16 from eq 15 is thus avoided. In this way, the discrete spherical convolution procedure could be tested under the most rigorous conditions. It is evident from the results discussed below that the procedure meets the test almost perfectly in that experiment matches theory for different degrees of sphericity and for a variety of values of the experimental parameters ΔE, Δt, and ϕ.

Table I contains the experimental details of the curves shown in Figure 1 and at the same time identifies the symbols used in the figures. In the work with ferrioxalate, 12 experiments were performed (only five of which are shown in the figures, for the sake of clarity) at each of the three possible drop sizes (see the previous section for the radii), each experimental curve being the average of ten runs. Cyclic staircase voltammetry was used as the experimental technique so that the "retrace" feature could be tested as well as the flatness of the plateau. For the most part we present "unfolded" voltammograms for clarity but in Figure 2 the i versus E and μ versus E curves are shown in the usual "folded" way. This figure was specially drawn to demonstrate the retrace feature and, as can be seen in the figure, although the retracing is not perfect, it is satisfactory. Figure 3 shows μ_O versus E curves for the small and medium drop sizes, the symbols being the same as in Figure 1 and Table I. The qualitative shape of these curves is easily explained when it is realized that μ_O is directly proportional to the surface

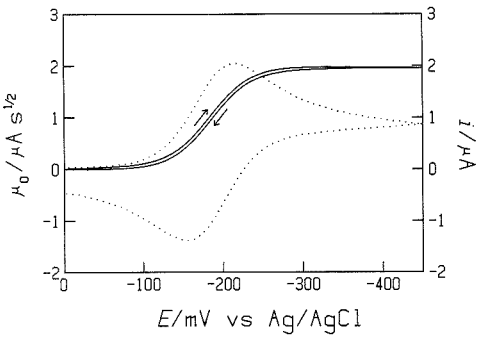

Figure 2. Current (dotted line) and convolved current (full line) shown in the usual "folded" way. The voltammogram used is the O curve from Figure 1. The curves were constructed by interpolating with straight-line segments between the data points.

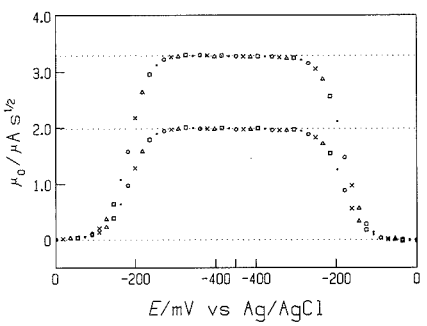

Figure 3. Results of discrete spherical convolution of curves obtained at a small (see Figure 1) and medium drop. The dotted lines represent the theoretical wave heights given by $nAFc_O^b D_O^{1/2}$, which equal 1.98 μA s$^{1/2}$ for the small and 3.28 μA s$^{1/2}$ for the medium drop. Every tenth point is shown for curves O, ×, △, and □, while every fifth point is shown for the ● curve.

concentration of the electroreactant. The potential at the beginning of the experiment is such that the surface concentration of the oxidized species is equal to its bulk value and μ_0 is therefore equal to zero. In the "escarpment region" (spanning $(4RT/nF)$ ln (7) in potential and centered at the half-wave potential) the surface concentration is reduced from its initial bulk value to zero causing the characteristic neopolarographic wave in the μ_0 versus E curve. Finally the plateau region is reached, the surface concentration is zero and is consequently not affected by further changes of potential in the negative direction. If the direction of the potential step is reversed, the surface concentration will respond accordingly, causing the μ_0 versus E curve to return to zero.

The performance of the spherical convolution as compared to the earlier planar variant (which can be arrived at by letting r in eq 19 become infinite) is demonstrated in Figure 4. It is evident that when the sphericity effect is strong (e.g. when using small drops), it cannot be ignored and the planar convolution is no longer adequate.

Notice in Figures 3–5 that not only are the plateaus almost perfectly horizontal but the plateau heights coincide with the theoretical m_d value calculated independently as $nAFc_O^b D_O^{1/2}$, and shown in the figures as dotted horizontal lines. Close inspection of Figures 3–5 shows a slight, but detectable, downward slope to the plateau. We do not understand the cause of this effect, which is too small to affect analytical applications of the discrete spherical convolution technique.

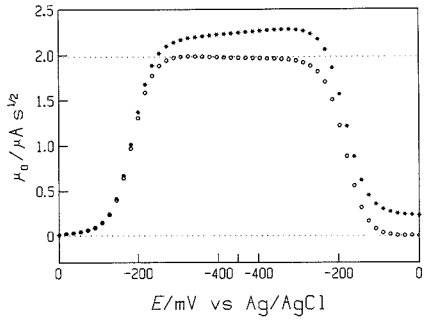

Figure 4. Comparison of the planar (•) and the spherical (O) convolution of the O curve from Figure 1. The dotted line corresponds to the theoretical plateau height 1.98 μA s$^{1/2}$.

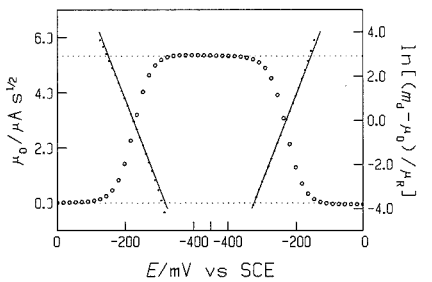

Figure 5. Result of a spherical convolution of a O curve at a large drop. The theoretical plateau value is 5.33 μA s$^{1/2}$ (dotted line). Also shown are the log plots for the forward and the reverse branches. The m_d value used in these calculations is the theoretical plateau value, 5.33 μA s$^{1/2}$. The straight lines are the least-squares regression lines obtained from the calculated points between −171.5 and −280.0 mV on the forward branch and between −179.8 and −288.8 mV on the reverse branch.

To assess whether the escarpment regions of the convolved voltammograms have the correct shape, we performed the so-called log-plot analysis (see the Appendix) shown in Figure 5. The experimental slopes 39.9 and 39.6 V^{-1} for the forward and the reverse branch, respectively, compare excellently with the theoretical value F/RT = 39.25 V^{-1} at 22.5 °C. The half-wave potentials are −224.0 and −226.7 mV vs SCE, respectively.

The strongest evidence that the convolution procedure is accurate comes from the near-perfect coincidence of the long-time μ_0 values with the base line. It should be recognized that μ_0 is a weighted average of *all* the data contained in a graph such as Figure 1 and that if the weights were even slightly in error, this would show up as a serious departure from zero of the long-time "tail" of graphs such as Figures 3 and 5. It should also be recognized that there have been no adjustable parameters in our analysis; all the quantities that enter our calculations have either been measured or, in the case of diffusion coefficients, taken from the literature.

As previously explained, an approximation enters our theory in the case of amalgam-forming electroreducible species. That this approximation has no serious effect on the efficiency of discrete spherical convolution, and that this technique can be applied to mixtures of analytes, is evident from Figure 6. Of course, with mixed analytes it is necessary to use a compromise value of the diffusion coefficient in calculating the weights. That the method is insensitive to small changes in D is clear from the miniscule difference between the full and dashed curves in this diagram.

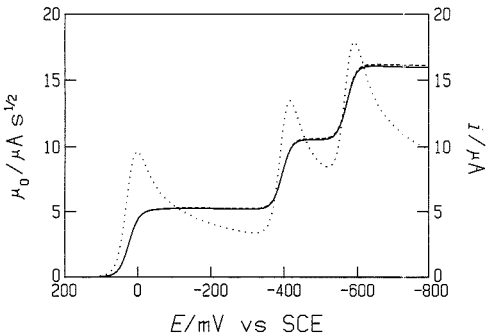

Figure 6. Current (dotted curve) and convolved current obtained at a small drop for a mixture of 1.0045 mM Cu(II), 1.0047 mM Pb(II), and 1.0043 mM Cd(II) in 1.00 M KNO_3 (acidified). The following diffusion coefficients (*17*) were used in the calculation of the weights: $D_{Pb(II)} = 8.02 \times 10^{-10}$ m^2 s^{-1} (solid line) and $D_{Cd(II)} = 6.81 \times 10^{-10}$ m^2 s^{-1} (broken line). The experimental parameters were as follows: $\Delta E = 5$ mV, $\Delta t = 15$ ms, and $\phi = 0.995$. The current is the average of ten runs, each run lasting 3.0 s, thus obeying the inequality $D_R t \leq 0.062r^2$ for all elements (using $D_R = 1.00 \times 10^{-9}$, 1.16×10^{-9}, and 1.53×10^{-9} m^2 s^{-1} for Cu, Pb, and Cd, respectively (*18*), and $r = 2.93 \times 10^{-4}$ m). The lines in the figure were constructed by interpolating with straight line segments between the data points.

APPENDIX

We have from eqs 7, 9, and 10 the following relation between $\bar{\mu}_O$ and $\bar{\mu}_R$

$$\bar{\mu}_O\left(s^{1/2} + \frac{D_O^{1/2}}{r}\right) = \bar{\mu}_R\left(s^{1/2} \pm \frac{D_R^{1/2}}{r}\right) \quad \text{(A.1)}$$

where, as earlier, the upper sign applies when R is soluble in solution while the lower sign is relevant when R dissolves in the electrode. Equation A.1 can be rearranged to yield

$$\bar{\mu}_R = \bar{\mu}_O\left(1 + \frac{D_O^{1/2} \mp D_R^{1/2}}{rs^{1/2} \pm D_R^{1/2}}\right) \quad \text{(A.2)}$$

An inverse Laplace transformation gives the equivalent time domain relation

$$\mu_R = \mu_O + \frac{D_O^{1/2} \mp D_R^{1/2}}{r}\int_0^t \mu_O(t-\tau) \times \left[(\pi t)^{-1/2} \mp \frac{D_R^{1/2}}{r}\exp\{D_R\tau/r^2\}\,\mathrm{erfc}\,\{\pm(D_R\tau)^{1/2}/r\}\right] d\tau \quad \text{(A.3)}$$

which is the general equation relating μ_O and μ_R. For the purpose of simplifying later expressions, let us denote the convolution integral term on the right-hand side in eq A.3 by ci.

Since we are considering reversible reactions, we can make use of the Nernst equation

$$E = E_h + \frac{RT}{nF}\ln\frac{D_O^{1/2}c_O^s}{D_R^{1/2}c_R^s} \quad \text{(A.4)}$$

which when combined with eqs 10 can be written as

$$\mu_O + \mu_R \exp\left\{\frac{nF}{RT}(E - E_h)\right\} = m_d \quad \text{(A.5)}$$

Further rearrangement of eq A.5 gives a form suitable for a logarithmic analysis (*19*)

$$E = E_h + \frac{RT}{nF}\ln\frac{m_d - \mu_O}{\mu_R} \quad \text{(A.6)}$$

It is evident that both μ_O and μ_R are required for this analysis. We recommend the use of eq A.6 if a good estimate of E_h is essential. The reason for this is that the potential $E = E_h$ does not exactly correspond to the $m_d/2$ point on, for example, the μ_O vs E curve. Substituting eq A.3 for μ_R into eq A.5 or A.6 gives the value $\mu_O = (m_d - ci)/2$ for $E = E_h$. Conversely, one finds that the value $\mu_O = m_d/2$ corresponds to the potential $E = E_h + (RT/nF)\ln\{m_d/(m_d + 2ci)\}$.

GLOSSARY

A	electrode surface area (m^2)
c_O	concentration of O (mol m^{-3})
c_O^b	bulk concentration of O (mol m^{-3})
c_O^s	surface concentration of O (mol m^{-3})
c_R	concentration of R (mol m^{-3})
c_R^s	surface concentration of R (mol m^{-3})
D	diffusion coefficient (m^2 s^{-1})
D_O	diffusion coefficient of O (m^2 s^{-1})
D_R	diffusion coefficient of R (m^2 s^{-1})
E	electrode potential (V vs some reference)
ΔE	step height (V)
$E^{o\prime}$	formal potential (V vs reference)
E_h	half-wave potential (V vs reference)
E_J	constant potential, equal to $E_0 + J\Delta E$ (V vs reference), during the Jth step
E_0	initial potential (V vs reference)
e	electron
F	Faraday constant (96485 C mol^{-1})
i	faradaic current (A)
i_J	faradaic current measured at time $(J - 1 + \phi)\Delta t$ (A)
$i_J(t)$	faradaic current at time t, where $(J-1)\Delta t < t < J\Delta t$ (A)
J	serial number of step in staircase
j	summation index
k	summation index
m	semiintegral of faradaic current flowing at a planar electrode during a reversible reaction (A s$^{1/2}$)
m_d	$nAFc_O^bD_O^{1/2}$
N	number of points recorded in an experiment
n	moles of electrons to reduce 1 mol of O
O	oxidized species
R	reduced species
R	gas constant (8.31441 J mol^{-1} K^{-1})
r	radius of the spherical electrode (m)
s	dummy variable of Laplace transformation (s^{-1})
T	thermodynamic temperature (K)
t	time measured from start of experiment (s)
Δt	step length (s)
w_j	weighting factor for i_{J-j}
x	distance measured outward from and normal to the electrode surface
ϕ	ratio of measurement delay time to step length
μ	spherically convolved current (A s$^{1/2}$)
μ_J	spherically convolved current during the Jth step at constant surface concentration (A s$^{1/2}$)
$\mu_J(t)$	spherically convolved current during the Jth step (A s$^{1/2}$)
μ_O	$nAFD_O^{1/2}(c_O^b - c_O^s)$
μ_R	$nAFD_R^{1/2}c_R^s$

ACKNOWLEDGMENT

We wish to thank Jan C. Myland for skilled technical assistance and helpful discussions.

LITERATURE CITED

(1) Seralathan, M.; Osteryoung, R. A.; Osteryoung, J. G. *J. Electroanal. Chem.* **1986**, *214*, 141.
(2) Bilewicz, R.; Osteryoung, R. A.; Osteryoung, J. G. *Anal. Chem.* **1986**, *58*, 2761.
(3) Seralathan, M.; Osteryoung, R. A.; Osteryoung, J. G. *J. Electroanal. Chem.* **1987**, *222*, 69.
(4) Bilewicz, R.; Wikiel, K.; Osteryoung, R.; Osteryoung, J. *Anal. Chem.* **1989**, *61*, 965.

(5) Myland, J. C.; Oldham, K. B. *Anal. Chem.* **1988**, *60*, 62.
(6) Goto, M.; Oldham, K. B. *Anal. Chem.* **1973**, *45*, 2043.
(7) Myland, J. C.; Oldham, K. B.; Zoski, C. G. *J. Electroanal. Chem.* **1985**, *193*, 3.
(8) Oldham, K. B.; Spanier, J. *The Fractional Calculus*; Academic Press: New York, 1974; p 107.
(9) Myland, J. C.; Oldham, K. B.; Zoski, C. G. *J. Electroanal. Chem.* **1987**, *218*, 29.
(10) Anderson, J. E.; Myland, J. C.; Oldham, K. B. *J. Electroanal. Chem.* **1987**, *218*, 41.
(11) Oldham, K. B.; Spanier, J. *The Fractional Calculus*; Academic Press: New York, 1974; p 63.
(12) Palmer, W. G. *Experimental Inorganic Chemistry*; Cambridge University Press: Cambridge, 1962; pp 519–522.
(13) *CRC Handbook of Chemistry and Physics*, 69th ed.; Weast, R. C., Ed.; CRC Press: Boca Raton, FL, 1988; p F-6.
(14) Rohko, T.; Kogoma, M.; Aoyagui, S. *J. Electroanal. Chem.* **1972**, *38*, 45.
(15) van der Pol, F.; Sluyters-Rehbach, M.; Sluyters, J. H. *J. Electroanal. Chem.* **1973**, *45*, 377.
(16) Struijs, J.; Sluyters-Rehbach, M.; Sluyters, J. H. *J. Electroanal. Chem.* **1983**, *146*, 263.
(17) Heyrovský, J.; Kůta, J. *Principles of Polarography*; Academic Press: New York, 1966; p 106.
(18) Galus, Z. *Pure Appl. Chem.* **1984**, *56*, 635.
(19) Bard, A. J.; Faulkner, L. R. *Electrochemical Methods*; John Wiley & Sons: New York, 1980; p 160.

RECEIVED for review July 6, 1989. Accepted December 6, 1989. A personal grant from the Research Institute of the Åbo Akademi Foundation to one of us and an operating grant from the Natural Sciences and Engineering Research Council of Canada to the other are gratefully acknowledged.

Continuous Generation System for Low-Concentration Gaseous Nitrous Acid

Masafumi Taira and Yukio Kanda*

National Laboratory for High Energy Physics, Oho, Tsukuba, Ibaraki-ken, 305 Japan

A flow type generation system based on the reaction of sodium nitrite solution with sulfuric acid has been developed for parts per billion levels of nitrous acid. The reagent solutions are continuously pumped into a reaction vessel and drawn off to waste. A carrier gas is passed through a mixture of the reagent solutions in the vessel and continuously purges nitrous acid vapor from the mixture. Nitrous acid output of the generator is characterized by using a Na_2CO_3-impregnated filter and a chemiluminescent NO_x monitor. A stable generation of nitrous acid of known concentration can readily be achieved by adjusting the concentration of sodium nitrite solution.

INTRODUCTION

Gaseous nitrous acid in the atmosphere has been observed to be built up during the night and to decay rapidly after sunrise (*1*, *2*). These findings suggested that nitrous acid plays an important role in photochemical oxidant formation as a major source of chain reaction-initiating OH radicals through its photodissociation, especially in the early morning when other photochemical activity is low. Increasing interest has been directed toward the measurement of atmospheric nitrous acid (*3*, *4*) as well as the laboratory studies of nitrous acid formation and decay reactions.

Developing and testing of analytical methods for measurement of the ambient nitrous acid inevitably require a well-characterized, stable, and reproducible low concentration source of nitrous acid. Calibrated permeation and diffusion tube devices provide an excellent low concentration source for some gaseous compounds and are widely used for the instrument calibration. However, the tubes for nitrous acid are not available due to its chemical instability. Recently, Braman and de la Cantera (*5*) have developed an interesting generation method for nitrous acid based on the sublimation of oxalic acid onto solid sodium nitrite. This method can produce low vapor concentration of nitrous acid containing only small amounts of NO, NO_2, and HNO_3 at relative humidities in the 30–60% range.

In this study, the generation of nitrous acid is based on the reaction of sodium nitrite solution with sulfuric acid

$$NaNO_2 + H_2SO_4 \rightarrow HNO_2 + NaHSO_4$$

Cox and Derment (*6*) have produced gaseous nitrous acid for the measurement of its ultraviolet absorption spectrum by passing nitrogen over the mixture of sodium nitrite and sulfuric acid solutions agitated with a magnetic stirrer. This resulted in the production of much NO and NO_2. We have successfully developed a method for continuous generation of high-purity nitrous acid by adopting a flow reactor system instead of batch system. The reaction takes place in a glass vessel with a glass ground frit at its base (Figure 1b). The dilute solutions of sodium nitrite and sulfuric acid are continuously pumped into a reaction vessel and are drawn off to waste. A carrier gas is introduced into the reagent mixture through the frit and continuously purges nitrous acid vapor from the mixture. Distinct advantages of the proposed generation system are a good output stability and a capability of producing pure nitrous acid of an acculately known concentration by simple procedure.

EXPERIMENTAL SECTION

Reagents. All reagents used were of analytical reagent grade. High-purity water was produced by a Millipore Milli-Q purification system and used to prepare reagent solutions.

NO_x Monitor. Measurements of NO, NO_2, and HNO_2 were made by a Dylec DY-8400 chemiluminescent NO_x monitor (Dylec Corp., Tokyo) based on the reaction of NO with O_3. This is a dual channel monitor that provides simultaneous measurement of both NO and NO_x (NO + NO_2). A carbon converter operating at ca. 290 °C is employed in the NO_x channel to reduce NO_2 to NO for measurement. The converter also reduces HNO_2 to NO. The monitor was calibrated against the NO gas mixture provided by diluting a standard cylinder gas mixture (3.02 ppm NO in N_2, Nihon Sanso) with high-purity N_2 by means of a gas blending system (Kofloc GB-2B, Kojima Seisakusho).

Generation System. A schematic diagram of the generation system is shown in Figure 1a. A typical configuration of glass reaction vessel is shown in Figure 1b. The reaction vessel was similar to that used for the measurement of atmospheric SO_2 by Marshall and Midgley (*7*). Temperature of the vessel was con-

0003-2700/90/0362-0630$02.50/0

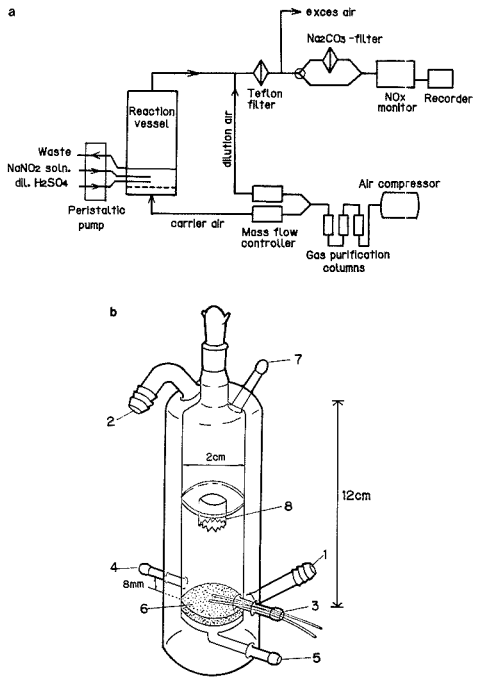

Figure 1. Apparatus arrangement for nitrous acid generation (a) and reaction vessel (b).

trolled by circulating water at constant temperature through a water jacket via entry port 1 and exit port 2 by means of a Haake D1-G thermocirculator (Haake, West Germany). The water jacket could be replaced by submerging the vessel directly in a water bath.

Sodium nitrite and H_2SO_4 solutions are separately pumped into the vessel at port 3 at the same flow rate Rr, and drawn together with entrained carrier gas from port 4 at a rate Rw, by a three-channel Masterflex PA-21A peristaltic pump (Cole-Parmer, Chicago, IL). To prevent flooding of the vessel with the reagent solutions, the pump rates were chosen so that Rw > 2Rr. This arrangement ensured that the level of solution in the vessel was virtually constant at the height of exit port 4. The volume of solution in the vessel was approximately 0.4 mL. A carrier gas enters at port 5 and passes through frit 6 of porosity 2 into the reagent mixture. Nitrous acid vapor is swept into the carrier gas stream and leaves at port 7 through the bubble breaker 8 constructed of jagged glass tube and is then mixed with a dilution gas. After the removal of mist through a Teflon filter, the HNO_2 gas mixture is introduced to a NO_x monitor.

A carrier gas and dilution gas were air from a compressor, which was purified by passing through silica gel, molecular sieve 4A, and activated charcoal columns successively. The flow rates were controlled by mass flow controllers (SEC-410, Stec Co.).

Chemiluminescent Method for HNO_2 Measurement. The method involves the measurement of the difference between the total NO_x ($NO + NO_2 + HNO_2$) measured by bypassing a Na_2CO_3-impregnated filter and the NO_x ($NO + NO_2$) measured by passage through the filter. To test the removal of HNO_2 by Na_2CO_3 filter, the generator effluent was sampled with two Na_2CO_3 filters connected in series at a flow rate of 3.0 L/min. The amount of HNO_2 collected on the filters was determined as nitrite ion by analyzing the filter extracts with an ion chromatograph as is described below. The results showed that the HNO_2 collection efficiency was about 100% in a single filter. No detectable amount of nitrite was present on the backup filter. The collection capacity was approximately 100 μg as nitrite ion. Chromatogram of the filter extract showed the presence of HNO_3 in the HNO_2 output, but its amount was found to be less than 1% of that of HNO_2 under the conditions examined in this work. Consequently, the HNO_3 produces no interference in the HNO_2 measurement, though the NO_x monitor makes a response to HNO_3 as well. No adsorption of NO and NO_2 on the filter was verified through the experiments by monitoring the respective gas mixtures of 0.604 ppm NO from a standard gas cylinder and 1.03 ppm NO_2 from a permeation tube device downstream of the filter with a NO_x monitor.

Table I. Nitrous Acid Measurements with Chemiluminescent Method and Na_2CO_3 Filter Collection Method[a]

chemiluminescent method, ppb	Na_2CO_3 filter collection method, ppb	chemiluminescent method, ppb	Na_2CO_3 filter collection method, ppb
104	101	510	526
212	222	717	703
315	306	813	794
417	425	1015	984

[a] Slope, 0.964; intercept, 13.214; correlation coefficient, 0.999.

Table I shows the results on the determination of the HNO_2 outputs by two methods: the chemiluminescent method and the method based on the Na_2CO_3-filter collection followed by ion chromatographic analysis. Excellent agreement between the methods is apparent from a linear regression analysis of the data. These results demonstrate that the chemiluminescent method can be used for the HNO_2 measurement.

Na_2CO_3 Filter Preparation, Extraction, and Analysis. Cellulose filter circles (Toyo No.5A, 50 mm diameter) were prewashed with high-purity water and air-dried. They were immersed in 0.5% (w/v) Na_2CO_3 aqueous solution and dried under an infrared lamp after excess solution was drained off. Nitrous acid collected on the filter was ultrasonically extracted into 5 mL of 1 mM $NaHCO_3$/1.5 mM Na_2CO_3 solution. A Dionex Model 4010i ion chromatograph (Dionex, Sunnyvale, CA) equipped with AS5A anion separation column, membrane suppressor, and conductivity detector was used to determine NO_2^- in the filter extracts. The gradient elution with 4.9 and 97.5 mM NaOH eluants resulted in a complete separation of NO_2^- peak from a strong Cl^- peak of the Na_2CO_3-filter blank.

RESULTS AND DISCUSSION

Parameter Optimization. Effects of several parameters on the HNO_2 output and the output composition were investigated. These parameters include concentration of H_2SO_4, reaction temperature, carrier gas flow rate, and pumping rate of the reagent solutions. To determine precisely the output composition, experiments were carried out under the conditions where the HNO_2 was generated in relatively higher concentrations than those of interest, because NO and NO_2 were present only at small percentages in the HNO_2 output.

The effect of H_2SO_4 concentration on the HNO_2 output and the composition was examined by varying its concentration from 2.5×10^{-3} to 2.5×10^{-2} M while holding all of other parameters constant. In Figure 2 the HNO_2 output and the concentration ratios of NO to HNO_2 and NO_2 to HNO_2 are plotted against the H_2SO_4 concentration. As shown in Figure 2, the HNO_2 output is increased with the increase in H_2SO_4 concentration and almost constant output was obtained at the H_2SO_4 concentration above 5×10^{-3} M. The NO/HNO_2 ratio showed a slight rising trend and the NO_2/HNO_2 ratio remained nearly constant in the range of H_2SO_4 concentration examined. The amounts of NO and NO_2 were very small compared to that of HNO_2 (from 2.4% to 4.5%, and about 3%, respectively). The subsequent experiments were carried out with 1×10^{-2} M H_2SO_4 solution.

Figure 3 shows the effect of reaction temperature on the HNO_2 output and the composition. The results indicate that

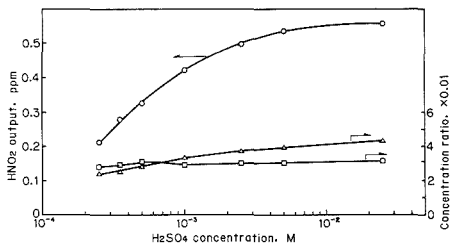

Figure 2. Effect of sulfuric acid concentration on nitrous acid output and composition: $NaNO_2$, 5.0 × 10^{-4} M; reaction vessel temperature, 25 °C; carrier gas flow rate, 1.0 L/min; dilution gas flow rate, 2.0 L/min; pumping rate of reagents, 0.25 mL/min; (O) HNO_2, (△) NO/HNO_2, (□) NO_2/HNO_2.

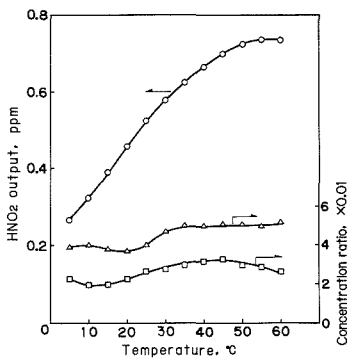

Figure 3. Effect of reaction vessel temperature on nitrous acid output and composition: $NaNO_2$, 5.0 × 10^{-4} M; H_2SO_4, 1 × 10^{-2} M; carrier gas flow rate, 1.0 L/min; dilution gas flow rate, 2.0 L/min; pumping rate of reagents, 0.25 mL/min; (O) HNO_2, (△) NO/HNO_2, (□) NO_2/HNO_2.

working at high temperatures is advantageous for the efficient generation of HNO_2. But at these temperatures the evaporation of water from the reagent solutions is greater, leading to condensation of water vapor onto the inner wall of transport tube. In addition, Figure 3 shows that in point of source purity, a temperature below 30 °C is desirable. A temperature of 25 °C was then chosen as a compromise.

The HNO_2 output was measured for the carrier gas flow rates in the range from 0.2 to 2.0 L/min, keeping a total flow rate of carrier gas and dilution gas at 3.0 L/min. As can be seen from Figure 4, the carrier gas flow rate significantly affected the output composition as well as the HNO_2 output. With increasing carrier gas flow rate, the HNO_2 output increased while the NO/HNO_2 and NO_2/HNO_2 ratios decreased. It is obvious that the carrier gas flow rate is a key parameter in the proposed generation system. The results show clearly that working at high flow rates of carrier gas is advantageous for efficient generation of high-purity HNO_2. At these high flow rates, however, the rupture of bubbles in the vessel is more violent, leading to entrainment of spray into the HNO_2 gas mixture stream and to lowering in output stability. Accordingly, a flow rate of 1.0 L/min was chosen as a compromise.

Experiments were also performed by varying the rate of pumping the reagent solution into the reaction vessel from 0.25 to 3.8 mL/min. The increase in the HNO_2 output was found to be relatively small at increasing pumping rates, which indicates that most of the reagents are pumped out to waste before they react. The HNO_2 output obtained at 3.8 mL/min was only 1.5 times higher than that at 0.25 mL/min. On the other hand, the NO/HNO_2 and NO_2/HNO_2 ratios remained almost constant in the range examined. Then a pumping rate of 0.25 mL/min was chosen because of effective utilization of the reagents.

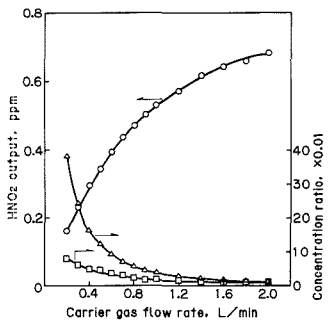

Figure 4. Effect of carrier gas flow rate on nitrous acid output and composition: $NaNO_2$, 5.0 × 10^{-4} M; H_2SO_4, 1 × 10^{-2} M; reaction vessel temperature, 25 °C; total gas flow rate, 3.0 L/min; pumping rate of reagents, 0.25 mL/min; (O) HNO_2, (△) NO/HNO_2, (□) NO_2/HNO_2.

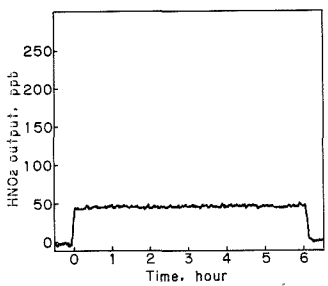

Figure 5. Recorded nitrous acid output with time: $NaNO_2$, 5.0 × 10^{-5} M; H_2SO_4, 1 × 10^{-2} M; reaction vessel temperature, 25 °C; carrier gas flow rate, 1.0 L/min; dilution gas flow rate, 2.0 mL/min; pumping rate of reagents, 0.25 mL/min.

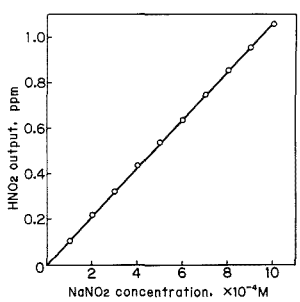

Figure 6. Correlation between nitrous acid output and $NaNO_2$ concentration: H_2SO_4, 1 × 10^{-2} M; reaction vessel temperature, 25 °C; carrier gas flow rate, 1.0 L/min; dilution gas flow rate, 2.0 L/min; pumping rate of reagents, 0.25 mL/min.

The compromised values for experimental parameters were summarized as follows: H_2SO_4 concentration, 1 × 10^{-2} M; reaction vessel temperature, 25 °C; carrier gas flow rate, 1.0 L/min; and pumping rate of reagents, 0.25 mL/min.

Performance Characteristics. For experimental testing and developing of analysis techniques and for studying air chemistry, output stability is an important feature of the generator. Variations in HNO_2 output may be due to a combination of several factors including variations in reaction

vessel temperature, gas flow rates, and drift of NO_x monitor. Figure 5 is a recorder chart showing the HNO_2 output of the generator with time, which was obtained with 5.0×10^{-5} M $NaNO_2$ solution under the compromised conditions described in the preceding section. The figure shows a satisfactory output stability. At a HNO_2 level of 45 ppb, the stability was ±4% over a 6-h period.

To examine a capability of generating HNO_2 of desired concentration, the HNO_2 generation was carried out for the $NaNO_2$ solutions at concentrations ranging from 1×10^{-4} to 1×10^{-3} M under compromised conditions. Figure 6 shows clearly that there is an extremely good linearity between the HNO_2 output and the $NaNO_2$ concentration. The correlation coefficient was 1.000. It is evident that the HNO_2 output of an accurately known concentration can readily be obtained by adjusting the concentration of $NaNO_2$ solution.

The generator has provided a great aid to the development of analytical method for determination of ambient HNO_2, which is now under study in our laboratory.

LITERATURE CITED

(1) Platt, U.; Perner, D.; Harris, G. W.; Winer, A. M.; Pitts, J. N., Jr. *Nature* **1980**, *285*, 312-314.
(2) Harris, G. W.; Carter, W. P. L.; Winer, A. M.; Pitts, J. N., Jr.; Platt, U.; Perner, D. *Environ. Sci. Technol.* **1982**, *16*, 414-419.
(3) Sjödin, A.; Ferm, M. *Atmos. Environ.* **1985**, *19*, 985-992.
(4) Braman, R. S.; de la Cantera, M. T.; Han, Q. X. *Anal. Chem.* **1986**, *58*, 1537-1541.
(5) Braman, R. S.; de la Cantera, M. T. *Anal. Chem.* **1986**, *58*, 1533-1537.
(6) Cox, R. A.; Derment, R. G. *J. Photochem.* **1976/1977**, *6*, 23-33.
(7) Marshall, G.; Midgley, D. *Anal. Chem.* **1982**, *54*, 1490-1494.

RECEIVED for review October 10, 1989. Accepted December 18, 1989.

Enhanced Signal-to-Noise Ratios in the Nuclear Magnetic Resonance Analysis of Solids, Using Large-Sample Magic-Angle Spinners

Ming Zhang and Gary E. Maciel*

Department of Chemistry, Colorado State University, Fort Collins, Colorado 80523

A previously reported 2.5-cm³ magic-angle spinning (MAS) device is shown to provide major enhancements in signal to noise ratios (S/N) for single-pulse (SP) and cross-polarization (CP) MAS analyses with ^{13}C, ^{15}N, and ^{29}Si at 4.7 T. The increased S/N makes it possible to obtain useful ^{15}N CP-MAS spectra of synthetic polymers and proteins in natural abundance. A newly developed 6.0-cm³ MAS device dramatically improves the efficiency of ^{29}Si SP-MAS analyses of a variety of silicon-containing samples (e.g., ceramics, zeolites, silica), often making it possible to obtain analytically useful spectra with a single scan.

INTRODUCTION

Magic-angle spinning (MAS) techniques (*1-5*) have thrust high-resolution NMR strategies into the arena of solid-state science. Although solid-state MAS experiments have been carried out on a wide range of nuclides, by far the most popular case has been ^{13}C, especially when MAS is used in combination with cross polarization (CP) and high-power ^1H decoupling. ^{13}C MAS and ^{13}C CP-MAS NMR have found application in subject areas as diverse as natural and synthetic organic polymers, fossil fuels, plant materials, adsorbed species, and catalysis. Most of the solid-state ^{13}C NMR literature has been based on studies with ^{13}C present in its natural abundance of 1.1%.

After ^{13}C, ^{29}Si is the nuclide that has been next in popularity in solid-state MAS and CP-MAS applications (*6-10*). Although the natural abundance of ^{29}Si (4.7%) is not miniscule, for some important types of samples, a scarcity of protons may render it impossible to obtain a CP enhancement and large T_1 values may preclude the efficient use of multiple repetitions to enhance the signal-to-noise ratio (S/N). Examples include various zeolites and silicon-based ceramics (e.g., silicon nitrides, silicon carbides).

Because of the important roles of nitrogen in the structures of a wide variety of important solids, e.g., synthetic polymers and proteins, the availability of a routine solid-state nitrogen NMR technique would be immensely important. There have been a few promising indications that the highly abundant ^{14}N nuclide may ultimately be useful as the basis for natural-abundance solid-state NMR techniques, especially based on an overtone strategy (*11*). ^{15}N MAS NMR signals can be observed in natural abundance (0.37%) in highly favorable cases and there have been some reports of ^{15}N-based solid-state NMR investigations. However, such studies have invariably been based either on ^{15}N-enriched samples (*12-14*) or on samples that are unusually favorable for natural-abundance experiments (extremely simple, homogeneous structures) (*15, 16*) or have suffered from very poor S/N characteristics (*17*). There are many examples of natural or synthetic polymer systems in which it is impractical or virtually impossible to employ ^{15}N-enriched samples, and for such cases a practicable natural-abundance ^{15}N NMR approach would be extremely attractive. The problem, of course, is sensitivity, or the achievable signal-to-noise ratio.

The development of large-volume MAS systems (*5*), which are capable of placing roughly an order of magnitude more sample in the NMR coil than is customarily the case with standard MAS systems, has pointed to one avenue for achieving improved S/N in MAS experiments in which sensitivity is a problem, e.g., natural abundance ^{15}N in general and ^{29}Si in cases with very large spin-lattice relaxation times. For many cases in categories like commercial polymers (e.g., polyurethanes, nylons, or polyimides), certain zeolites, and various ceramics (e.g., silicon nitrides) samples of virtually unlimited size are available. The present note explores this

* To whom correspondence should be addressed.

0003-2700/90/0362-0633$02.50/0

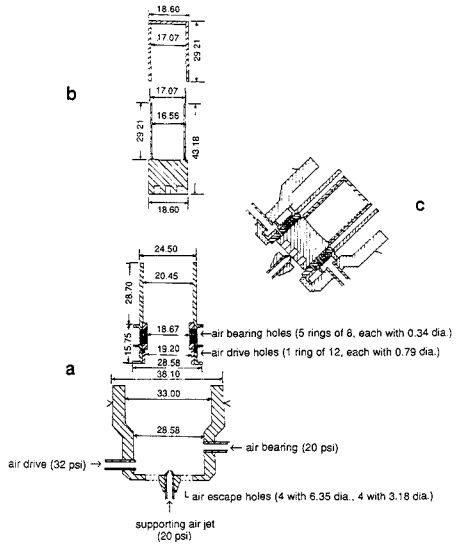

Figure 1. Diagram of the 6-cm^3 MAS system. All dimensions are shown in millimeters. (a) Details of stator in a partially exploded view: lower, Delrin or Kel-F piece, with threaded Delrin or Kel-F air-bearing and air-drive tubing (5.33 mm o.d.; 3.18 mm i.d.) and glass air jet tubing (5 mm o.d., 2 mm i.d., with 0.34 mm i.d. outlet); upper, brass inner piece inserted into Delrin or Kel-F outer piece. (b) Details of rotor shown in exploded view: upper, zirconia sleeve; lower, single-piece Delrin or Kel-F chamber. (c) Overall assembled system.

possibility in a few representative ^{15}N and ^{29}Si cases.

EXPERIMENTAL SECTION

NMR Experiments. The NMR measurements were made on severely modified NT-200 and NT-360 spectrometers, using home-built solid-sample probes. The probe used at 4.7 T is a double-tuned unit based on the 2.5 cm^3 MAS system reported previously (*5*), using a spinner constructed from a combination of zirconia and Delrin (up to 4.5 kHz spinning speed). The probe used at 8.5 T is a single-tuned unit based on extrapolation of the 2.5-cm^3 MAS design to 6.0 cm^3. The zirconia–Delrin version spins at speeds up to 2.5 kHz, while the zirconia–Kel-F version spins up to 1.5 kHz. The design of the 6.0 cm^3 MAS system is shown in Figure 1. Although these MAS systems have not been tested scrupulously for air-sensitive samples, they share with other sleeve-type systems an apparently good performance in this regard, especially if an inert grease is used as a sealant for the zirconia sleeve and if dry N_2 is used as the drive gas. Furthermore, we see no incompatibility with the requirements of variable-temperature operation (assuming there is sufficient space in the probe to permit adequate insulation).

Samples. Glycine (99% ^{15}N enriched) and ammonium chloride (95% ^{15}N enriched) were obtained from MSD Isotopes. The collagen (bovine), bovine serum albumin, and calf thymus DNA were obtained from Sigma. Adamantane, hexamethylbenzene, and α-silicon nitride were obtained from Aldrich. Silica gel (S-679) and silicon carbide (Carborundum) were obtained from Fisher. The Na-A and Na-X zeolites were obtained from Davison Chemical Co. The HPZ silicon nitride fibers were obtained from Dow Corning. Torlon (Amoco) and Vespel (Du Pont) were obtained from the manufacturers. The nylon (Polymer Corp.) and polyurethane (Anderson Development) were obtained from Cadillac Plastics.

Tetrakis(trimethylsilyl)methane (*18*) and $(CH_3)_3Si$-derivatized silica gel (*19*) were synthesized by known procedures. The isocyanurate-rich resin was synthesized from

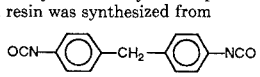

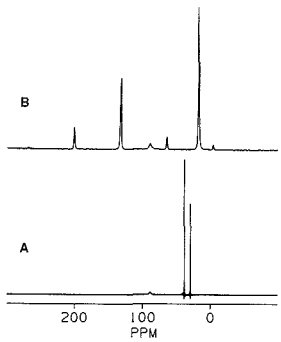

Figure 2. 50.3-MHz ^{13}C CP-MAS spectra of (A) adamantane (56 scans, 5 s repetition delay, 4 ms contact time) and (B) hexamethylbenzene (8 scans, 3 s repetition delay, 5 ms contact time) obtained by using 2 5-cm^3 spinners.

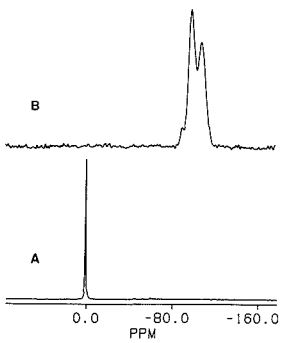

Figure 3. 39.8-MHz ^{29}Si CP-MAS spectra of (A) tetrakis(trimethylsilyl)methane (TTMSM, 8 scans, 15 s repetition delay, 20 ms contact time) and (B) silica gel (80 scans, 5 s repetition delay and 10 ms contact time) obtained by using 2.5-cm^3 spinners.

(Eastman Kodak), using stannous octoate (Sigma) as the catalyst (*20*).

RESULTS AND DISCUSSION

The high-speed (up to 4.5 kHz) 2.5 cm^3 MAS system employed successfully in single-pulse (SP) and cross-polarization ^{13}C experiments at 22.6 MHz (2.1 T) was examined at 4.5 T for ^{13}C, ^{15}N, and ^{29}Si in a home-built multinuclear probe, using a severely modified Nicolet NT-200 spectrometer. Parts A and B of Figure 2 show the 50.3-MHz ^{13}C CP-MAS spectra of adamantane and hexamethylbenzene, respectively. The line widths in these two spectra are 5.3 and 42 Hz, respectively, showing good B_0 homogeneity characteristics for these large samples. The spinning side band pattern evident in the hexamethylbenzene spectrum shows a MAS speed of about 3500 Hz, using zirconia/Delrin spinner. The peak at 88.8 ppm in each of these spectra is due to the Delrin $-OCH_2O-$ moieties. The S/N value of 630 obtained for the methyl carbon peak in the eight-scan spectrum of hexamethylbenzene in Figure 2B is 3–4 times what we typically obtain on the same spectrometer using a probe with a MAS system that contains one-fifth the volume.

The performance of the 2.5 cm^3 MAS system for ^{29}Si at 39.8 MHz in CP-MAS experiments is shown in parts A and B of Figure 3, representing tetrakis(trimethylsilyl)methane (TTMSM) and silica gel, respectively. The line width of the TTMSM spectrum is 5.0 Hz and its S/N value after eight scans is 1000; the latter value is about 4 to 5 times larger than

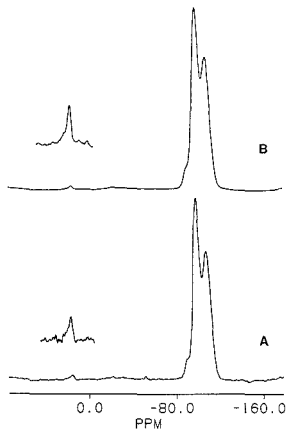

Figure 4. 39.8-MHz ^{29}Si CP-MAS spectra of silica gel derivatized with $(CH_3)_3SiCl$, obtained by using a 2.5-cm^3 spinner: 5 s repetition delay and 4 ms contact time; A, 920 scans; B, 16 000 scans.

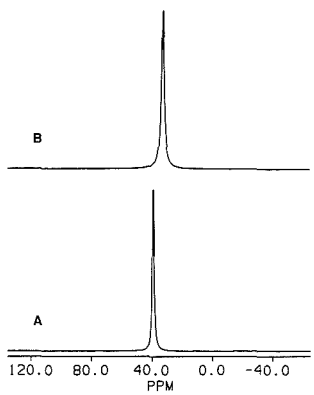

Figure 5. 20.3-MHz ^{15}N CP-MAS spectra of (A) 147 mg of 95% isotopically enriched ammonium chloride mixed with MgO (8 scans, 5 s repetition delay and 20 ms contact time) and (B) 261 mg of 99% isotopically enriched glycine mixed with MgO (8 scans, 3 s repetition delay and 2 ms contact time), obtained in 2.5-cm^3 spinners.

what is correspondingly obtained on the same spectrometer with a MAS system of more conventional volume (about 0.50 cm^3). The 80 scan CP-MAS ^{29}Si spectrum of silica gel in Figure 3B has a S/N value of 110 for the largest peak, which belongs to $(\gt Si–O–)_3\mathbf{SiOH}$ moieties at the surface; this is roughly 5 times the S/N obtained with a comparable number of scans on the same spectrometer, but employing a 0.45-cm^3 spinner.

Figure 4 shows 39.8-MHz ^{29}Si CP-MAS spectra obtained with the 2.5-cm^3 MAS system on a silica gel sample that has been lightly derivatized with surface $(CH_3)_3Si–$ groups via treatment with $(CH_3)_3SiCl$. Both spectra, which represent different numbers of scans, show the peak with its maximum at 16 ppm due to the $(CH_3)_3Si–$ groups (*19*). The excellent S/N characteristics of this peak in these spectra permit a clear confirmation of a low-shielding shoulder that is suggested less conclusively by analogous results obtained on conventional MAS hardware (*21*).

Figures 5–9 represent the characteristics of the 2.5-cm^3 Delrin/Zirconia MAS system for 20.3-MHz CP-MAS ^{15}N NMR performance. The efficiency of the large-volume probe

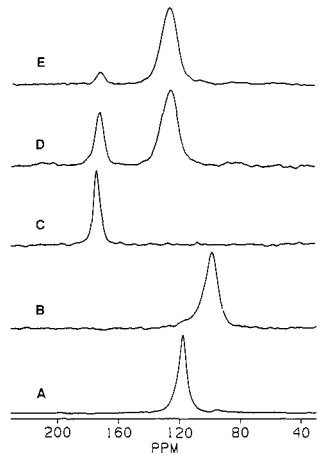

Figure 6. 20.3-MHz ^{15}N CP-MAS spectra of synthetic polymers in 2.5-cm^3 spinners: (A) nylon (2000 scans, 4 s repetition delay, and 1 ms contact time); (B) polyurethane (10 000 scans, 2 s repetition delay, 1 ms contact time); (C) Vespel (12 000 scans, 3 s repetition delay, 5 ms contact time); (D) Torlon (10 000 scans, 3 s repetition delay, 5 ms contact time); and (E) Torlon (10 000 scans, 3 s repetition delay, 1 ms contact time).

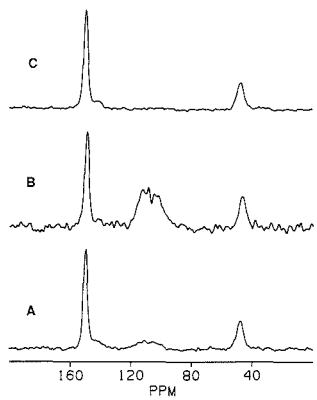

Figure 7. 20.3-MHz ^{15}N CP-MAS speectra of polyisocyanurate-rich resin prepared from MDI, obtained in 2.5-cm^3 spinners: (A) 18 000 scans, 3 s repetition delay, and 6 ms contact time; (B) 30 000 scans, 2 s repetition delay and 0.6 ms contact time; (C) 18 000 scans, 3 s repetition delay, 6 ms contact time, and 70 μs dephasing period.

was examined by comparing the S/N for the *same* amount of ^{15}N-enriched ammonium chloride or glycine with a standard-volume MAS system (0.50 cm^3) on the same spectrometer; the S/N obtained with the 2.5 cm^3 configuration was 70% better than that obtained with a 0.50-cm^3 system. Figure 5 shows the eight-scan ^{15}N CP-MAS spectra of 147 mg of ^{15}N-enriched ammonium chloride (95 atom % ^{15}N) mixed with MgO and 261 mg of glycine (99 atom % ^{15}N) mixed with MgO. In both cases sharp lines and excellent S/N characteristics were obtained, the former having a line width of 5 Hz. The fact that the S/N enhancement for this multinuclear probe was better for ^{15}N than for ^{13}C or ^{29}Si is not surprising, because the radio frequency coil was optimized for ^{15}N.

Figures 6 and 7 show the natural-abundance 20.3-MHz ^{15}N CP-MAS spectra of various synthetic polymers. The nylon spectrum in Figure 6A shows a dominant peak centered at 117 ppm, due to the amide nitrogens in structures of the type

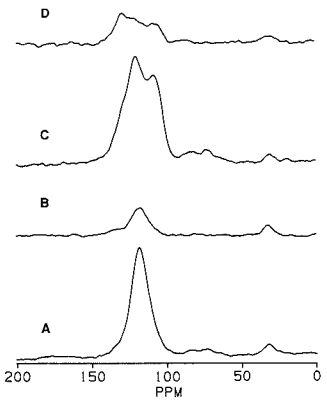

Figure 8. 20.3-MHz ^{15}N CP-MAS spectra of proteins, obtained by using 2.5-cm^3 spinners: (A) bovine serum albumin (16 000 scans, 1 s repetition delay, 8 ms contact time); (B) bovine serum albumin (30 000 scans, 1 s repetition delay, 0.8 ms contact period, 70 μs dephasing period); (C) collagen (40 000 scans, 1 s repetition delay, 0.8 ms contact time); and (D) collagen (40 000 scans, 1 s repetition delay, 0.8 ms contact time, 70 μs dephasing period).

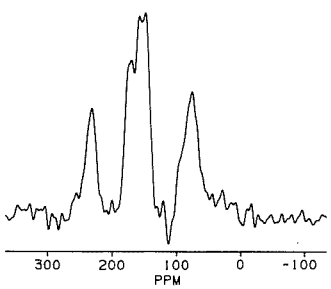

Figure 9. 20.3-MHz ^{15}N CP-MAS spectrum of calf thymus DNA in 2.5-cm^3 spinner (90 000 scans, 1 s repetition delay, 0.8 ms contact time).

$[-(CH_2)_6NHCO(CH_2)_4CONH-]_n$ and a much smaller peak at about 97 ppm, which is due to another type of nitrogen-based linkage, e.g., possibly a urethane linkage ($RNHCO_2R'$). The polyurethane spectrum in Figure 6B shows a dominant urethane resonance at 98 ppm, with a small, low-shielding shoulder that may reflect the presence of some amide-type moieties, possibly including substituted ureas.

The Vespel spectrum in Figure 6C shows only the imide

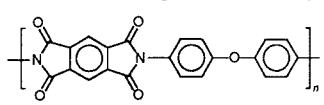

Vespel

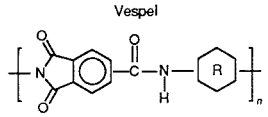

(R is proprietary)
Torlon

resonance at 175 ppm, due to structures of the type RN(COR′)$_2$ in this polyimide resin. A major peak in the same general region, 172 ppm, is seen in the spectra of Torlon (Figure 6D,E), which also show an amide resonance (RCONHR′) at about 127 ppm. Comparison of the spectra in Figure 6D,E shows the strong effect of the CP contact time on the relative intensities (*22*). The longer contact time (5 ms, Figure 6D) yields a much larger intensity of the 175 ppm imide peak, relative to the RCONHR′ peak at 127 ppm, than does the shorter contact time (1 ms, Figure 6E). This simply reflects the presence or absence of a directly bonded hydrogen on the nitrogen atom in determining the CP efficiency and clearly indicates the need for variable contact-time measurements if one wishes to use CP-MAS for quantitative purposes (*23*).

Figure 7 shows natural-abundance ^{15}N CP-MAS results obtained on an isocyanurate-rich resin prepared from the diisocyanate monomer

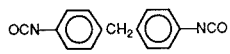

(MDI). Figure 7A shows the spectrum obtained with a 6-ms contact time, a period long enough to permit strong polarization of nitrogens without directly attached hydrogen atoms. Accordingly, the strongest peak in the spectrum is the peak at 150 ppm, which can be identified with the isocyanurate moiety, I. There is a slight, higher-shielding shoulder on that

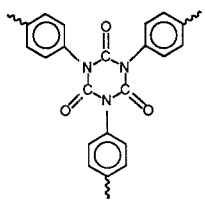

I

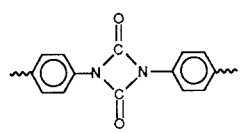

II

dominant peak, at about 144 ppm; this shoulder has been identified with a uretidione structure, II, in which the nitrogen atoms have no directly attached hydrogens. The distinct peak at 46 ppm corresponds to (unreacted) isocyanate groups (-N=C=O). The intensity represented by the broad pattern between 100 and 120 ppm corresponds to urea and amide linkages, in which the nitrogen atoms bear directly bonded hydrogens. The spectrum in Figure 7B was obtained at a much shorter CP contact time, 0.6 ms; these conditions strongly favor nitrogen atoms with directly attached hydrogens. Hence, in Figure 7B the broad amide/urea pattern in the 100-120 ppm range is strongly favored. Figure 7C shows the spectrum obtained with a 6-ms contact time and a 70-μs interrupt time between the end of cross polarization and the beginning of data acquisition, a dipolar dephasing period (*23*, *24*). It is seen that the amide/urea region between 100 and 120 ppm is completely surpressed by this dephasing period, because of the directly attached hydrogens.

One of the most exciting capabilities provided by the large MAS systems is natural-abundance ^{15}N CP-MAS for protein samples; this capability is represented by Figure 8. Previously published natural-abundance solid-state ^{15}N spectra that are most relevant have been based on homopolypeptides (*16*). Previous solid-state ^{15}N NMR studies of proteins have been limited to ^{15}N-enriched samples (*15*). The bovine serum albumin spectrum in Figure 8A is dominated by a broad peak with a maximum at about 120 ppm, which can be assigned to nitrogens in peptide linkage (*25*, *26*). These nitrogens, each of which bears a directly bonded hydrogen, suffers a major attenuation in the corresponding dipolar dephasing spectrum, given in Figure 8B. A small, broad peak with a distinct maximum at 32 ppm is tentatively identified mainly with $-NH_3^+$ moiety of lysine segments, which constitute 10% of the amino acid units in this protein. The fact that this peak is accentuated in relative intensity in the dipolar dephasing

spectrum (Figure 8B) implies that these $-NH_3^+$ groups rotate rapidly in the protein, thereby markedly attenuating the $^{15}N-^1H$ dipolar effects.

The broad, weak intensity pattern in the 65–85 ppm range in Figure 8A is likely due to non-peptide NH_2 nitrogens of the pendant $H_2^+N{=}C(NH_2)NH$ groups in the 6 mol % arginine units in this protein. The NH nitrogens in these groups probably contribute intensity to the high-shielding peak centered at 32 ppm. The relative intensity associated with these hydrogen-bearing nitrogens should be strongly attenuated in the dipolar dephasing spectrum (Figure 8B).

Figure 8C shows the ^{15}N CP-MAS spectrum of the protein, collagen. This spectrum is dominated by strong peptide nitrogen peaks at 108 and 122 ppm, with substantial intensity in a shoulder ranging past 130 ppm. The peak at 108 ppm can probably be attributed to peptide linkages of glycine moieties (*25*), which constitute 25 mol % of the amino acid units in collagen. The spread of peptide nitrogen intensity past 130 ppm in Figure 8C can be attributed to proline moieties (*26*); proline constitutes 14 mol % of the amino acid units in this protein. The fact that the 130 ppm intensity is accentuated in the dipolar dephasing spectrum reflects the fact that the proline nitrogen atom does not bear a hydrogen atom in a peptide linkage (III). The 65–85 ppm intensity in

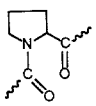

III

Figure 8C, which is largely eliminated by the dipolar dephasing period (Figure 8D), is again attributed to NH_2 nitrogens of the pendant $H_2^+N{=}C(NH_2)NH-$ groups. The NH nitrogens of this pendant group are the main contributors to the peak at about 30 ppm.

Clearly, the primary features of these protein spectra are readily accounted for in terms of the main amino acid constituents. Of course, there are many other types of amino acid units that contribute to these proteins and, taken together, may contribute substantially to the ^{15}N CP-MAS spectra. More extensive work in this general direction seems warranted.

Figure 9 shows the ^{15}N CP-MAS spectrum of calf thymus DNA. This spectrum consists of three main broad peaks centered at about 230, 150, and 80 ppm. This DNA sample contains 21–29% of each of the four base units: adenine (IV), guanine (V), cytosine (VI) and thymine (VII). Although

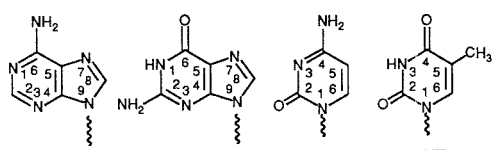

IV V VI VII

definitive chemical shift assignments cannot be made at this time, because of a paucity of relevant background data, one can make tentative assignments based on ^{15}N chemical shifts of nucleosides in the literature (*27*, *28*). One should note that no relaxation experiments, even qualitative, were carried out on this sample, so the relative intensities should be interpreted only qualitatively. The broad peak with a maximum at about 80 ppm can be identified with the $-NH_2$ nitrogens of adenine, guanine, and cytosine units. The broad peak centered at about 150 ppm can be attributed to positions 9 in adenine and guanine units and positions 3 of the latter and thymine units, along with positions 1 of guanine, cytosine, and thymine units. Positions 1 and 7 of adenine units, and 7 of guanine units contribute to the peak centered at 230 ppm. One must recognize that, for the ^{15}N resonances of all of the basic nitrogens, the chemical shift can be effected substantially by hydrogen bonding. Although the general quality of this natural-abundance spectrum is not high, one should note that no attempt was made to optimize the experimental conditions in order to maximize the S/N characterisitics.

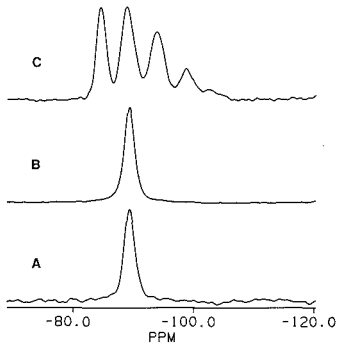

Figure 10. 71.5-MHz ^{29}Si SP-MAS spectra obtained with the 6-cm^3 spinner: (A) Na-A zeolite (1 scan); (B) Na-A zeolite (24 scans, 60 s repetition delay); and (C) Na-X zeolite (200 scans, 60 s repetition delay).

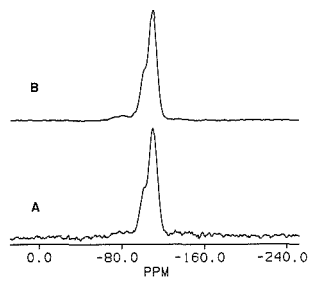

Figure 11. 71.5-MHz ^{29}Si SP-MAS spectra of silica gel obtained by using a 6.0-cm^3 spinner: (A) 1 scan; (B) 24 scans, 240 s repetition delay.

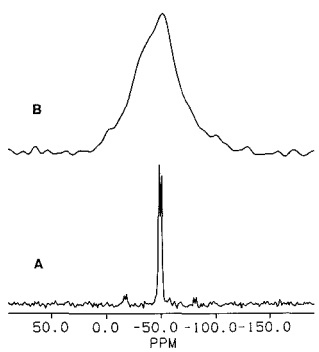

Figure 12. 71.5-MHz ^{29}Si SP-MAS spectra of (A) α-Si_3N_4 (1 scan) and (B) HPZ ceramic fibers (4 scans, 60 s repetition delay), obtained by using 6-cm^3 spinners.

The general design of the double-tuned 2.5-cm^3 MAS system employed at 2.1 and 4.7 T was extrapolated to the single-tuned 6.0 cm^3 MAS system shown in Figure 1. In contrast to the 3.5–4.5-kHz MAS speeds typically employed with the 2.5 cm^3 MAS system, the 6.0-cm^3 spinner operates typically at 1.5–2.5 kHz. Figures 10–13 show the preliminary results of utilizing this MAS system in 71.5-MHz ^{29}Si single pulse (SP)-MAS

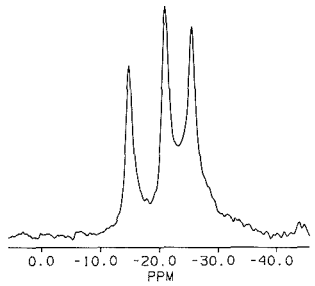

Figure 13. 71.5-MHz ^{29}Si SP-MAS spectrum of silicon carbide/carborundum (1 scan), obtained by using a 6.0-cm^3 spinner.

experiments on a variety of silicon compounds.

Figure 10 shows the ^{29}Si SP-MAS spectra obtained in one scan (A) or 24 scans (B) on a Na–A zeolite sample. The S/N figures of 72 and 360, respectively, are nearly in the theoretical ratio of $24^{1/2}$ expected for time averaging and represent a S/N improvement of more than eight compared to what can be obtained in a conventional spinner that contains about one-tenth the sample amount, using the same spectrometer. This nearly optimal time averaging and the nearly equivalent line widths (about 130 Hz) in the spectra of Figure 10A,B indicate good stability in probe performance. Figure 10C shows the SP-MAS ^{29}Si spectrum of Na-X zeolite; this spectrum displays the presence of structures of the types, $Si(OAl\equiv)_4$, $\equiv SiOSi(OAl\equiv)_3$, $(\equiv SiO)_2Si(OAl\equiv)_2$, $(\equiv SiO)_3SiOAl\equiv$, and $(\equiv SiO)_4Si$ (*8*).

Figure 11 shows analogous results for silica gel obtained with the 6.0-cm^3 MAS system. In contrast to the CP-MAS results shown in Figure 3B obtained with the 2.5-cm^3 MAS system, these spectra are dominated by the 110 ppm peak that represents $Si(OSi\equiv)_4$ silicons, largely in the interior of the particles. Parts A and B of Figure 11 show ^{29}Si SP-MAS silica gel spectra of 1 scan and 24 scans, respectively.

Parts A and B of Figure 12 show the ^{29}Si SP-MAS spectra obtained on α-silicon nitride fibers and HPZ (hydridopolysilazane) ceramic fibers, in one and four scans, respectively. These spectra are similar to those that have previously been reported (*9*, *10*), with the two types of tetrahedral site symmetries clearly displayed in the α-Si_3N_4 case and the largely amorphous nature of the HPZ sample displayed in the broad pattern. The spectra in Figure 12 were obtained in small fractions of the experiment times reported previously. The importance of being able to obtain useful spectra with just a small number of scans derives from the very long spin–lattice relaxation times (e.g., minutes) often found for these systems.

Figure 13 shows the one-pulse ^{29}Si SP-MAS spectrum of carborundum (silicon carbide). The chemical shift and intensity patterns indicate that this sample largely consists of the 6H polytype, with the three peaks corresponding to the three nonequivalent sites in the unit cell (*29*).

SUMMARY AND CONCLUSIONS

The results presented here clearly demonstrate the S/N advantages of large-sample MAS systems for CP and/or SP experiments on samples for which large quantities are available. Such advantages are clearly present for natural-abundance ^{15}N CP-MAS experiments on synthetic polymers and proteins and possibly for nucleic acids. Clear advantages can be expected for both SP-MAS and CP-MAS ^{29}Si experiments on silicas and aluminosilicates, including zeolites with long ^{29}Si T_1 values. Applications for ^{29}Si and other nuclides in a variety of ceramics can be expected. One can anticipate that even better results can be obtained when the relevant relaxation parameters are determined on representative samples, so that experimental conditions can be correspondingly optimized.

ACKNOWLEDGMENT

The authors gratefully acknowledge Dr. J. Lipowitz of Dow Corning Corporation for providing the HPZ fiber sample and are grateful to D. Duff, D. Kinney, and H. V. Pan for preparing the isocyanurate-rich resin, the derivatized silica gel, and the TTMSM samples, respectively.

LITERATURE CITED

(1) Andrew, E. R. *Prog. NMR Spectrosc.* **1971**, *8*, 1.
(2) Kessemeier, H.; Norberg, R. E. *Phys. Rev.* **1967**, *155*, 321.
(3) Lowe, I. J. *Phys. Rev. Lett.* **1959**, *2*, 285.
(4) Dec, S. F.; Wind, R. A.; Maciel, G. E.; Anthonio, F. E. *J. Magn. Reson.* **1986**, *70*, 355.
(5) Zhang, M.; Maciel, G. E. *J. Magn. Reson.* **1989**, *85*, 156.
(6) Sindorf, D. W.; Maciel, G. E. *J. Phys. Chem.* **1983**, *87*, 5516.
(7) Sindorf, D. W.; Maciel, G. E. *J. Am. Chem. Soc.* **1983**, *105*, 3767.
(8) Klinowski, J. *Prog. NMR Spectrosc.* **1984**, *16*, 237.
(9) Carduner, K. R.; Carter, R. O., III; Milberg, M. E.; Crosbie, G. M. *Anal. Chem.* **1987**, *59*, 2794.
(10) Lipowitz, J.; Turner, G. L. *Polym. Prepr.* **1988**, *29*, 74.
(11) Tycko, R.; Opella, S. J. *J. Am. Chem. Soc.* **1986**, *108*, 3531.
(12) Stewart, P. L.; Valentine, K. G.; Opella, S. J. *J. Magn. Reson.* **1987**, *71*, 45.
(13) Sardashti, M.; Maciel, G. E. *J. Phys. Chem.* **1988**, *92*, 4620.
(14) Hatfield, G. R.; Maciel, G. E. *Macromolecules* **1987**, *20*, 608.
(15) Schaefer, J.; Stejskal, E. O.; Jacob, G. S.; McKay, R. A. *Appl. Spectrosc.* **1982**, *36*, 179.
(16) Skoji, A.; Ozaki, T.; Fujito, T.; Deguchi, K.; Ando, I. *Macromolecules* **1987**, *20*, 2441.
(17) Mathias, L. J.; Powell, D. G.; Sikes, A. M. *Polym. Commun.* **1988**, *29*, 192.
(18) Merkes, R. L.; Scott, M. J. *J. Organomet. Chem.* **1965**, *4*, 98.
(19) Sindorf, D. W.; Maciel, G. E. *J. Phys. Chem.* **1982**, *86*, 5208.
(20) Sandler, S. R. *J. Appl. Polym. Sci.* **1967**, *11*, 811.
(21) Zeigler, R. C. Ph.D. Thesis, Colorado State University, 1989.
(22) Mehring, M. *Principles of High Resolution NMR in Solids*; Springer-Verlag: New York, 1983; pp 152–154.
(23) Opella, S. J.; Frey, M. H. *J. Am. Chem. Soc.* **1979**, *101*, 5854.
(24) Alemany, L. B.; Grant, D. M.; Alger, T. G.; Pugmire, R. J. *J. Am. Chem. Soc.* **1983**, *105*, 6697.
(25) Posner, T. B.; Markowski, V.; Loftus, P.; Roberts, J. D. *J. Chem. Soc., Chem. Commun.* **1975**, 769–770.
(26) Kricheldorf, H. R.; Hull, W. E. *Makromol. Chem.* **1979**, *180*, 161.
(27) Markowski, V.; Sullivan, G. R.; Roberts, J. D. *J. Am. Chem. Soc.* **1977**, *99*, 714.
(28) Hawkes, G. E.; Randall, E. W.; Hull, W. E. *J. Chem. Soc., Perkin Trans.* **1977**, *2*, 1268.
(29) Hartman, J. S.; Richardson, M. F.; Sherriff, B. L.; Winsborrow, B. G. *J. Am. Chem. Soc.* **1987**, *109*, 6059.

RECEIVED for review August 22, 1989. Accepted December 11, 1989. The authors gratefully acknowledge partial support of this research by National Science Foundation Grant Nos. CHE-8610151 and DMR-854818846 and use of the Colorado State University Regional NMR Center, funded by National Science Foundation Grant No. CHE-861643.

Jet-Enhanced Sputtering Cell as an Ion Source for Mass Spectrometry

Hyo J. Kim and Edward H. Piepmeier*

Department of Chemistry, Oregon State University, Corvallis, Oregon 97331

Gary L. Beck, Gary G. Brumbaugh, and O. Thomas Farmer, III

Analytical Laboratory, Teledyne Wah Chang Albany, Albany, Oregon 97321

A jet-enhanced sputtering cell, the Atomsource from Analyte Corp., is interfaced to a VG PlasmaQuad inductively coupled plasma mass spectrometer replacing the inductively coupled plasma. The sputtering cell allows for the direct analysis of flat metal samples by clamping them over a round opening, surrounded by an O-ring, in one side of the cell. Six streams of argon, accelerated to high speed by passage through small nozzles and ionized by the current, strike the sample in a hexagonal pattern, sputtering out atoms and rapidly eroding the sample surface. Ions produced by the electrical discharge enter the mass spectrometer through a modified sampling "cone" or flange. The influences of pressure, current, anode-to-sampling flange voltage, sampling distance, and sampling flange orifice diameter are optimized to obtain improved performance for analytical applications. Because air and water are not present during sample atomization (except as surface contaminants), there are reduced interferences from ArO, ArC, and ArN relative to inductively coupled plasma mass spectrometry (ICP-MS). Detection limits are generally comparable to those obtained with the ICP-MS. Differences in interferences improve the detection limits in some cases, such as B and some transition elements in Zircaloy.

In recent years, glow discharge mass spectrometer applications in the analytical laboratory have increased substantially. The possibilities of the gas glow discharge as an ion source were discovered by Goldstein (*1*) as early as 1886. Among the pioneering developments, Aston (*1*) used the glow discharge as an ion source for the determination of isotope ratios, and Bainbridge (2) used a glow discharge tube in which Zn was sputtered from the cathode for a similar application.

A spark discharge source (*3*, *4*) is suitable for both the vaporization and the ionization of inorganic samples. Although this source has excellent sensitivity, offers good ionization efficiency, and allows use of a variety of sample types, its use poses several problems, including ion beam fluctuations resulting in poor analytical precision and a large ion energy spread requiring the use of an expensive double focusing mass spectrometer.

The development of the secondary ion mass spectrometer (SIMS) (*5*) helped to improved the mass spectrometer analysis of inorganic samples. Secondary ions from the sample surface are released when the surface is struck by the energetic primary ions, following which the secondary ions are extracted and analyzed. This technique is good for both bulk analysis and depth profile determinations. Its disadvantages are similar to those of the spark source, including poor analytical precision and expensive instrumentation.

Recently, glow discharge sources have been developed for a number of optical spectroscopy and analytical applications because of their stability, precision, and sensitivity. Coburn et al. (*6*) used glow discharges as ion sources for the analysis of thin film and bulk samples. Oechsner and Gerhard (*7*) reported direct solid analysis with the use of a high-frequency plasma source interfaced to a mass spectrometer for sputtering and ionization of samples. In 1978, Harrison et al. (*8*) first applied a direct current (dc) glow discharge ion source in combination with a quadrupole mass filter. They obtained successful analytical results. Since then they have extensively investigated the uses of glow discharges for elemental determinations (*9–11*). A commercial glow discharge mass spectrometer, the VG 9000 (VG Isotopes, Ltd., Cheshire, Great Britain), uses a reverse Nier-Johnson geometry double-focusing mass spectrometer to obtain high resolution. A 27-cm-radius magnetic sector is coupled to a 38-cm-radius electrostatic analyzer, achieving up to 6000–8000 resolving power. This device has been used in a variety of direct analysis applications, including electrically conducting and semiconducting solid materials, nonconducting materials mixed with electrical conducting materials, and liquid samples absorbed on a suitable support matrix (*12*, *13*). However, this commercial system has not gained widespread use, probably due to its high cost.

Several attempts have been made to reduce costs by the use of quadrupole mass filters (*14–16*). In particular, Jakubowski, Stuewer, and Toelg (*17*, *18*) constructed two new glow discharge ion sources with improved designs for use with quadrupole mass spectrometers. Use of these types of sources has made it possible to improve performance for analytical applications.

For the current study, the newly developed jet-enhanced sputtering source, the Atomsource (Analyte Corp., Grants Pass, OR), was tested to determine its possible applications (*19*). A flat sample can be conveniently mounted on the outside of the cell. The jet-enhanced sputtering cell is a flow discharge similar to the Grimm discharge, but has six strategically located gas jets that improve the analytical performance. The six argon jets strike the sample surface causing the atoms to be removed from the sample at a much faster rate than ordinary glow discharges. The surface is quickly removed and the main bulk of the sample reached in a matter of seconds. The jets also quickly sweep the sample ions toward the observation region, into the mass spectrometer, thereby increasing the ion current. For this study, the jet-enhanced sputtering source was interfaced with the mass spectrometer of a VG PlasmaQuad ICP-MS (VG Elemental, Great Britain), without major changes. Upon computer command, the ICP moves out of the way, leaving room to mount the sputtering cell.

EXPERIMENTAL SECTION

Ion Source. Figure 1 shows a schematic of the gas-jet-enhanced sputtering ion source and its interface with the mass spectrometer. More detailed descriptions of the gas-jet-enhanced sputtering system are found in refs 19 and 20. Asterisks indicate added or modified parts. No changes were made in the skimmer

0003-2700/90/0362-0639$02.50/0

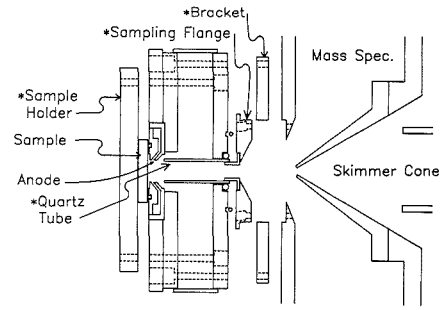

Figure 1. Schematic (exploded cross section) of the gas-jet-enhanced sputtering ion source and its interface with the mass spectrometer of an ICP-MS. Added or modified components are indicated with an asterisk. Dashed lines indicate bolt holes.

cone (0.7-mm-diameter orifice) of the mass spectrometer. After studies to be discussed shortly, the sampling cone of the mass spectrometer was replaced with a flat sampling "cone" or flange that allows inserts with different diameter holes. The sampling flange used the same mounting bolts as the original sampling cone, and the bracket holds the body of the gas-jet-enhanced sputtering cell tightly against the sampling flange. A quartz tube (12-mm i.d.) is used to guide the ions from the region near the anode to the orifice of the sampling flange. A mechanical pump that is ordinarily used to maintain a low pressure inside the ion source was not used for this study because the plasma was unstable due to competition between the ion source and mass spectrometer vacuum pumps. The pumping speed and vacuum in the expansion stage of the mass spectrometer are sufficient to maintain the required gas flow and low pressure in the sputtering cell. The operating pressure of the ion source is maintained by controlling the Ar gas flow rate into the source with a mass flow controller (Sierra Instrument, Carmel Valley, CA). The pressure is measured by a variable reluctance transducer (Validyne AP10, Northridge, CA) with a carrier demodulator (Validyne CD15) pressure gauge attached to a "T" connector at the gas entrance to the sputtering cell.

The sampling flange is connected to ground potential. In order to bias the anode positively against the sampling flange, an additional variable 60-V power supply (Model EUW-17, Heath Instruments, Benton Harbor, MI) is used. A series of up to three variable 400-V, 100-mA Heath power supplies (Model EUW-15, Heath Instruments, Benton Harbor, MI) is used as an external power supply for the sputtering current (for reasons which will be discussed later).

Typical operating conditions are 28 mA sputtering current, 900 V sputtering cell voltage, 2.5 Torr in the sputtering cell, 0.3 Torr at the pressure measuring port in the first expansion stage of the mass spectrometer, and an argon flow rate of 0.2 L/min.

Sample Preparation. One zirconium standard (X-866), one Zircaloy standard (X-868), and one Zircaloy sample are used for this study. Samples were analyzed directly without major preparation. The samples were polished and then surface cleaned by rinses in ethanol, dilute HNO_3, and deionized-distilled water.

RESULTS AND DISCUSSION

Power Supply. After a mount and an interface were constructed between the six-jet sputtering cell and the mass spectrometer, a spectrum of a zirconium standard (X-866) showed unexpectedly strong $^{58}Ni^+$ and $^{60}Ni^+$ peaks. These peaks were attributed to sputtering of the original Ni sampling cone ordinarily used with the ICP. Various types of sampling cones and interfaces were constructed in an attempt to avoid etching of the sampling cone. However, geometric modification failed to completely solve this problem because both the sample and the sampling cone were connected to ground potential and the Ar ions attacked both. This problem was solved by using a different power supply configuration in which the anode was connected to ground potential and the cathode (sample) was connected to a negative potential. In the original sputtering cell power supply, the anode is at a positive potential and the cathode is connected to ground potential. The resulting mass spectra showed an increase in Zr peaks by a factor of 10000 and no Ni peaks, indicating that this problem was solved. Further improvements in ion signal were obtained with an additional adjustable power supply that kept the anode 40–50 V positive with respect to the grounded sampling cone.

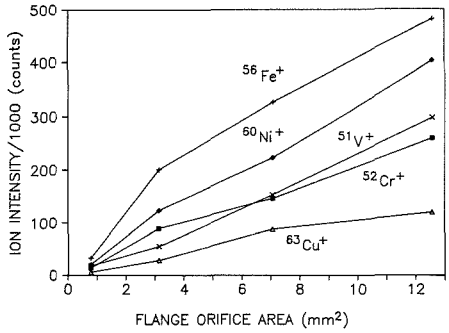

Figure 2. Ion intensities for zirconium standard (X-866) vs sampling flange orifice area.

Sampling Zone Distance and Sampling Flange Orifice Area. The sampling distance between the cathode surface and the sampling cone exit aperture is an important variable. Jakubowski et al. (*17*) investigated the dependence of ion intensities on the sampling distance for a glow discharge. The intensities of the molecular ions show a rapid decrease with decreasing sampling distance, whereas the intensities of the analyte ions show an exponential increase. They also noted that further decreases in the sampling distance appear to be advantageous but subsequently lead to depression of the extracted ion current as deposition of the sputtered material begins to clog the exit aperture.

Sampling cones that protruded different distances into the main body of the sputtering cell were designed but were found to quickly clog. Therefore, to generate strong ion signals, but also reduce the possibility of clogging, it was necessary to choose a compromise value for the sampling distance and orifice diameter. Finally a flat sampling flange with a maximum 5-mm-diameter orifice (Figure 1) was designed to replace the original sampling cone. This reduced the sampling distance as for as possible for this relatively large orifice without redesigning the main housing of the sputtering cell.

The sampling flange orifice affects the pressure gradient between the sputtering cell and the inside of the mass spectrometer, and thereby probably affects the efficiency of extraction of the analyte ions into the mass spectrometer. Figure 2 shows the influence of sampling flange orifice area on ion intensities. The ion intensities increase with increases in orifice area, but progressive increases of the area of this orifice lead to deposition of the sputtered material on the skimmer cone and eventually to clogging the skimmer cone orifice. Therefore a 3-mm-diameter sampling flange orifice, 1.0 cm long was finally chosen.

Optimization of Operating Conditions. During preliminary adjustments, the behavior of signals for all singly charged analyte ions studied showed maxima similar to that exhibited by $^{56}Fe^+$. Since $^{56}Fe^+$ had convenient signal strength and was in an interesting m/z range, the behavior of its signal was studied in detail as operating variables were adjusted.

Gas Pressure is a critical parameter in glow discharge sputtering processes. It is known that a decrease in pressure increases the sputtering rate due to an increase in the voltage

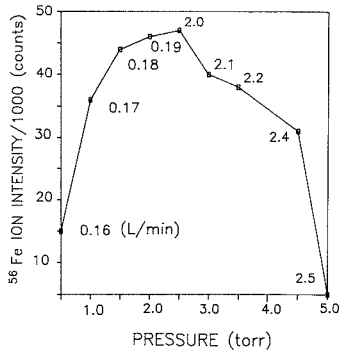

Figure 3. Pressure influence on $^{56}Fe^+$ ion intensity (Zr standard X-866).

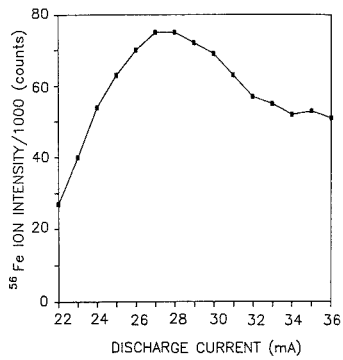

Figure 4. Discharge current influence on $^{56}Fe^+$ ion intensity (Zr standard X-866).

required to maintain the same current and due to an increase in the mean free path of the argon ions, which then gain more energy before striking the surface. Lower pressure can also reduce redeposition near the cathode surface because the sputtered atoms escape into the vacuum more freely.

However, Figure 3 shows that the ion intensity for $^{56}Fe^+$ initially increases with increases in pressure. This is likely the result of several effects. The increase in ion intensity with increased pressure may result from the greater pressure differential between the source and the inside of the mass spectrometer, which increases the rate at which ions enter the mass spectrometer. An increase in pressure is accomplished by an increase in jet gas flow rate, which may increase the efficiency with which atoms are swept away from the surface before they can diffuse back and redeposit. It is also possible that Penning ionization efficiency may be increased due to increases in argon metastable density at the higher pressure (*15*). Analyte ions must be generated in the gaseous part of the discharge, because ions sputtered off of the sample surface are forced back to the surface by the electric field. Eventually the ion intensity decreases with further increases in pressure, because the sputtering rate decreases as ordinarily expected with increasing pressure. This curve shows a rather broad and flat maximum, a region which offers good signal stability during pressure variations.

The dependence of $^{56}Fe^+$ ion intensity on the discharge current is shown in Figure 4. Ion intensity initially increases with increasing discharge current, up to 27 mA. As the current increases, the number of bombarding ions increases, leading to an increase in sputtering. Above 28 mA, there is an unexpected decrease in ion signal. It may be that the increase

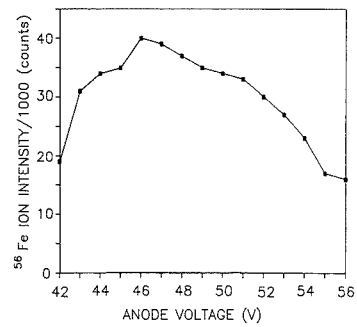

Figure 5. Anode voltage influence on $^{56}Fe^+$ ion intensity (Zr standard X-866).

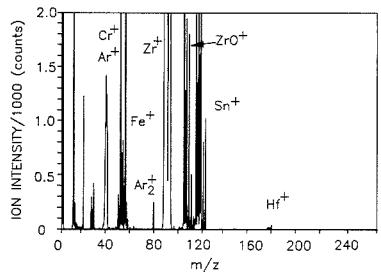

Figure 6. Spectrum after optimization (standard X-868).

in electrical power increases the gas temperature and thereby shifts the position of what may be a slightly radially asymmetric flowing stream so that a different part of the plasma is sampled by the skimmer cone orifice. A nonuniform distribution of ions in the cross section of the flowing plasma could then produce such a change in ion signal. Another explanation is that the higher anode-to-cathode voltages associated with the higher currents attract more ions back toward the cathode. If this were the case, then it would mean that analyte ions were formed near the cathode fall region since this region is where most of the voltage drop occurs.

Figure 5 shows the influence of anode voltage (with respect to the grounded sampling flange) on ion intensity at a current of 27 mA and a pressure of 2 Torr (the anode-to-cathode voltage remains constant). There is an optimum anode voltage for maximum ion intensity.

All of the maxima in the operating variables help to improve signal stability. Although there is some interaction among the variables, a global maximum is readily obtained by adjusting each variable in turn to reach a maximum and going through this cycle only a few times.

Auxiliary Discharge. A high-voltage secondary glow discharge, as proposed by Harrison and Bentz (*16*) was used to increase ion intensity. Two W electrodes for the secondary discharge were introduced radially through holes in the quartz tube which were located two-thirds the distance from the anode to the sampling flange. It made little difference whether the ends of the electrodes were flush with the quartz wall or were pulled back 2 mm. All of the ion intensities increased approximately 30% when the secondary discharge was used. However, unwanted W ion and W oxide molecule signals, resulting from sputtering of the secondary electrodes, were also obtained. After lengthy periods of operation, instability was another problem connected with the secondary discharge. The reason may be that sputtered sample material was deposited on the W electrodes, causing a change in their electrical

Table I. Concentrations in the Zirconium Standards and Sample

elements	concentration, μg/g		
	X-866	X-868	sample
Al	310	122	32.3
B	6.9	3.2	
Nb	612	570	
Co	42	42	<5
Cr	255	580	1130
Cu	240	83	3.8
Fe	1620	2790	2180
Hf	198	178	47.6
Mn	42	56	<5
Mo	123	128	<5
Ni	129	134	8.6
Pb	33	101	1.4
Si	215	179	106
Sn	37	1.23%	1.54%
Ta	709	716	5.8
Ti	191	122	7
V	71	93	<5
W	140	95	1.2
U	0.97	0.79	0.3

characteristics. Because of these problems and the relatively small increase in signal, further studies were not made with the auxiliary electrodes.

Multielement Determination. Figure 6 shows the Zr alloy spectrum resulting when the optimum values for the operating parameters are used. This spectrum was obtained with a 700-V, 28-mA discharge at 2-Torr pressure. The Zr alloy (X-868) contained 20 elements with certified values listed in Table I. Identified are isotopic peaks for Cr, Fe, and Sn, at concentrations of 500 ppm, 2700 ppm, and 1.23%, respectively. To prevent detector saturation resulting from ion counts that are too high, mass ranges of 16–20 (O^+), 32–42 (Ar^+), and 89–97 (Zr^+) were skipped during the scan.

Select Group Determination. In order to obtain more accurate information for isotopes of particular interest, the scan range was reduced to the region near these isotopes. A 1024-channel data acquisition was set around each isotope region. The dwell time at each channel was 200 μs and 1000 sweeps were accumulated. The isotopes of interest for a Zr alloy analysis may be all of the elements that the Zr sample contains. However, one of the objectives of this project is to determine how the gas-jet-enhanced sputtering ion source and the ICP ion source might complement each other. Thus, elements of a select group were chosen which might pose problems for ICP-MS determinations due to spectral interference and/or contamination during the sample preparation. These elements include boron, some of the transition elements, and some of the rare-earth elements. Boron is regarded as one of the more difficult elements to determine in Zircaloy with the ICP-MS because of contamination from borosilicate glass in the ICP spray chamber and torch when dilute HF solutions are used.

The spectrum for a Zircaloy standard (X-868) containing 3 μg/g boron is shown in Figure 7. This spectrum, covering the range m/z 9 to m/z 16, was taken in 3 min. The observed boron isotope abundance ratio of ^{10}B to ^{11}B is 0.24, compared to the natural abundance ratio of 0.247, well within the uncertainty caused by counting statistics. Mass discrimination was accounted for by multiplying the peak area of the lighter isotope by $1 + 1/Z$, where Z is the atomic number (*21*).

The integrated peak channel count for $^{11}B^+$ was 910. The background channels between m/z 9 and m/z 10 had an accumulated count of 30. The detection limit, determined by dividing 3 times the standard deviation of the background count by the slope of a two-point standard curve (the first point being the background average, designated as zero concentration) for B in Zircaloy is estimated to be 0.2 μg/g for ^{10}B and 0.06 μg/g for ^{11}B, optimistically assuming that an integration range can be found where the tail of the $^{12}C^+$ peak does not contribute significantly to the background. Because of this tail, the actual detection limit is between 0.06 and 0.2 μg/g. For this ICP-MS the detection limit of boron (above its background interference mentioned earlier) is 10 ng/mL, or 10 μg/g in a solid dissolved in a 0.1% solution. The use of an HF resistant torch and spray chamber would improve the ICP-MS detection limit (*22*).

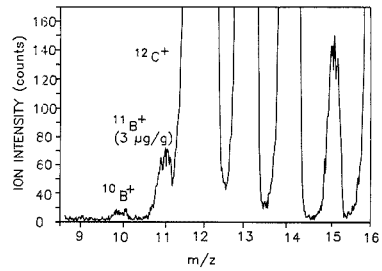

Figure 7. Boron spectrum obtained in 3.4 min for X-868 (1024 channels, 200-μs dwell time, 1000 sweeps).

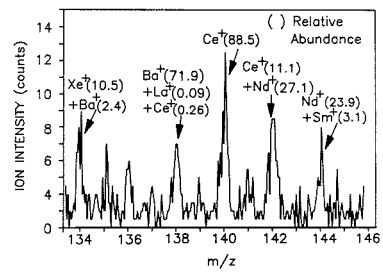

Figure 8. Rare-earth spectrum obtained in 3.4 min for X-868 (1024 channels, 200-μs dwell time, 1000 sweeps).

Although rare-earth elements are routinely determined in zirconium alloys by ICP-MS (*20*) there are occasional difficulties. Sources of interference found in earlier ICP-MS instruments are rare-earth oxide and hydroxide ions (*23*). Proper selection of isotopes can reduce these interferences. At higher concentrations of rare earths or other elements whose fluorides precipitate, precipitation or coprecipitation during acid digestion of the sample may cause problems.

Figure 8 shows the spectrum obtained with the same settings used for boron, but covering the range m/z 133–146. The spectrum is noisy but the rate-earth peaks are obvious and well resolved (except for isotopes with essentially the same m/z). In the ICP-MS no peaks in this mass range are observed with the same sample dissolved in a 0.1% solution (1000 dilution factor with respect to the solid). The peak channel count for the $^{140}Ce^+$ ion is 13. The lowest channels between the $^{140}Ce^+$ ion and the $^{141}Pr^+$ ion have an accumulated count of 0 or 1. Although several peak superpositions occur, every element has at least one isotope free from such interference.

The zirconium alloy contains several transition elements, including Ti, V, Cr, Mn, Fe, Co, Ni, Cu, and Zn. However, Ti and Fe pose a number of problems to the ICP-MS method because of spectral interferences. Some of the Ti isotopes of 46 (8.0% natural abundance), 47 (7.5%), and 48 (73.7%), are interfered with by the doubly charged zirconium isotopes, 90 (51.4%), 91 (11.2%), 92 (17.1%)8 94 (17.5%), and 96 (2.8%). The Fe isotopes are 54 (5.8%), 56 (91%), 57 (2.14%), and 58 (0.31%) and the major $^{56}Fe^+$ peak is interfered with by

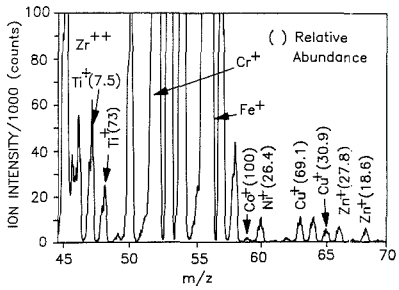

Figure 9. Transition element spectrum obtained in 3.4 min for X-868 (1024 channels, 200-μs dwell time, 1000 sweeps).

$^{56}(ArO)^+$, and the next most abundant ^{54}Fe isotope is interfered with by $^{54}(ArN)^+$, both of which are derived from water and plasma gas. In ICP-MS, the assigned species for m/z 56 and 58 were confirmed by substitution of natural water with $H_2{}^{18}O$ (*24*). Only $^{57}Fe^+$ reflects a good choice, free from spectral interference, but its 2% natural abundance makes it difficult to determine the lowest Fe concentrations.

Figure 9 shows the spectrum obtained with the same experimental settings as for boron, covering a range between m/z 45 and m/z 70, and showing excellent resolution between masses. The lack of base-line resolution between m/z 45 and 46 is most likely due to $^{91}Zr^{2+}$. Natural abundance isotope ratio calculations indicate that there is little if any spectral interference from $^{56}ArO^+$ and $^{54}ArN^+$ on $^{56}Fe^+$ and $^{54}Fe^+$ using the gas-jet-enhanced sputtering ion source. For example, the Fe isotope abundance ratio of ^{56}Fe to ^{57}Fe (an isotope with no interference) is 0.024 (corrected for mass discrimination (*21*)), which differs by only 3% from the natural abundance ratio of 0.0234.

CONCLUSION

This investigation has shown that a commercially available jet-enhanced sputtering cell can be interchanged with the ICP on an ICP-MS to complement its analytical capabilities, especially for the direct analysis of metal alloys. The sample is conveniently mounted on an O-ring sealed hole outside the ion source. High and low concentrations can be observed with the gas-jet-enhanced ion source mass spectrometer without the necessity of dissolving the alloy. Although a quadrupole mass spectrometer does not have the mass resolution of a commercial GD-MS, the relatively low cost of adding a jet-enhanced sputtering cell to the mass spectrometer of an ICP-MS makes this an attractive alternative when an ICP-MS is already available in the laboratory. Analytical performance and further comparisons to the ICP-MS will be discussed in more detail in a subsequent section of this study.

ACKNOWLEDGMENT

We gratefully acknowledge a grant from Teledyne Wah Chang Albany and the loan of the Atmosource by Analyte Corp.

LITERATURE CITED

(1) Aston, F. W. *Mass Spectra and Isotopes*; Edward Arnold & Co.: London, England, 1933.
(2) Bainbridge, K. T. *Phys. Rev.* **1932**, *39*, 847.
(3) Beske, H. E.; Hurrle, A.; Jochum, K. P. *Z. Anal. Chem.* **1981**, *309*, 257.
(4) Bacon, J. R.; Ure, A. M. *Analyst* **1984**, *109*, 1229.
(5) McHugh, J. A. In *Methods for Surface Analysis*; Wolsky, S. P., Czanderna, A. W., Eds.; Elsevier: Amsterdam, 1975.
(6) Coburn, J. W. *Rev. Sci. Instrum.* **1970**, *41*, 1219.
(7) Oechsner, H.; Gerhard, W. *Phys. Lett.* **1972**, *40A*, 211.
(8) Bentz, B. L.; Bruhn, C. G.; Harrison, W. W. *Int. J. Mass Spectrom. Ion Phys.* **1976**, *28*, 409.
(9) Mattson, W. A.; Bentz, B. L.; Harrison, W. W. *Anal. Chem.* **1976**, *48*, 489.
(10) Harrison, W. W.; Hess, K. R.; Marcus, R. K.; King, F. L. *Anal. Chem.* **1986**, *58*, 341A.
(11) Bruhn, C. G.; Bentz, B. L.; Harrison, W. W. *Anal. Chem.* **1979**, *51*, 673.
(12) Cantle, J. E.; Hall, E. F.; Shaw, C. J.; Turner, P. J. *Int. J. Mass Spectrom. Ion Phys.* **1983**, *46*, 11.
(13) Robinson, P. K.; Hall, E. F. *Am. Lab.* **1987**, August, 74–85.
(14) Colby, B. N.; Evans, C. A., Jr. *Anal. Chem.* **1974**, *46*, 1236.
(15) Loving, T. J.; Harrison, W. W. *Anal. Chem.* **1983**, *55*, 1526.
(16) Harrison, W. W.; Bentz, B. L. *Anal. Chem.* **1979**, *51*, 1853.
(17) Jakubowski, N.; Stuewer, D.; Toelg, G. *Int. J. Mass Spectrom. Ion Processes* **1986**, *71*, 183.
(18) Jakubowski, N.; Stuewer, D.; Toelg, G. *Anal. Chem.* **1987**, *59*, 1825–1830.
(19) Kim, H. J.; Piepmeier, E. H. *Anal. Chem.* **1988**, *60*, 2040–2046.
(20) Bernhard, A. E. *Spectroscopy (Eugene, Oreg.)* **1987**, *2*, 24–27.
(21) Brumbaugh, G. G. Real World Isotope Abudances by ICP-MS; Paper F12, Abstracts, 1988 Winter Conference on Plasma Spectrochemistry, San Diego, CA, Jan 3–9, 1988.
(22) Gregoire, D. C. *Anal. Chem.* **1987**, *59*, 2479–2484.
(23) Beck, G. L.; Farmer, O. T., III *J. Anal. At. Spectrom.*, **1988**, *3*, 771–773.
(24) Longerich, H. P.; Fryer, B. T.; Strong D. F.; Kantipuly, C. *J. Spectrochim. Acta* **1987**, *42B*, 75–92.

RECEIVED for review May 17, 1989. Revised manuscript received October 31, 1989. Accepted December 21, 1989.

Bicontinuous Microemulsions as Media for Electrochemical Studies

Maurice O. Iwunze,[1] Artur Sucheta, and James F. Rusling*

Department of Chemistry (U-60), University of Connecticut, Storrs, Connecticut 06269-3060

Bicontinuous microemulsions of didodecyldimethylammonium bromide (DDAB)/dodecane/water were explored as media for voltammetric reductions and oxidations of ruthenium(III) hexaammine, ferrocyanide, ferrocene, cob(II)alamin, and several polycyclic aromatic hydrocarbons (PAHs). These clear microemulsions are conductive and are believed to contain a dynamic extended network of interconnected water tubules. Agreement of simulated and experimental voltammetric data shows that electrochemical theory for homogeneous media is followed to a good approximation in DDAB microemulsions. Diffusion of electroactive solutes did not reflect the high bulk viscosities of the microemulsions. Nonpolar molecules and ions diffuse as if they were in neat oil or aqueous media, respectively, and voltammograms with good signal to noise ratio are obtained. Reductions of PAHs in the microemulsions occurred by an ECE-type pathway, with nearly reversible one-electron reductions achieved at high scan rates.

Water and hydrocarbon oils do not mix at normal ambient temperature and pressure. Addition of surfactant to water and oil can lead to a clear, thermodynamically stable, macroscopic phase which has come to be known as a microemulsion (*1–3*). In some cases, salt and cosurfactants such as alcohols are used in such systems. Microemulsions, though homogeneous to the eye, are microscopically heterogeneous. The continuous liquid "phase" in the system may be water, with surfactant solubilizing most of the oil in globular aggregates resembling swollen micelles. These are oil-in-water (o/w) microemulsions. Conversely, the oil phase may be continuous, with the surfactant forming inverted aggregates having water in their centers. These are water-in-oil (w/o) microemulsions. Bicontinuous microemulsions are a third type of system, in which both oil and water are continuous throughout with surfactant residing at extended oil–water interfaces. Microemulsions are used widely in domestic and industrial applications ranging from detergency to cosmetics and pharmaceuticals to tertiary oil recovery (*1–3*).

Among the important properties of microemulsions is their ability to dissolve significant amounts of solutes of different types. Thus, a microemulsion can be used as a medium to bring together ionic and nonpolar reactants. Control of the structural aspects of microemulsions offers the possibility of selecting reactant microenvironments to control chemical kinetics and reactivity for specific applications (*1–4*). A case in point for electrochemistry is electrocatalysis, which can be used to amplify analytical sensitivity. In this technique, electrons are transferred between an electrode and a substrate whose electrode reaction is slow via a chemical mediator (catalyst). We recently reported catalytic reduction of oil-soluble vicinal dihalides mediated by water-soluble vitamin B_{12} in a w/o microemulsion. Because of the high resistivity of the isooctane-based w/o microemulsion, ultramicroelectrodes were needed for voltammetry in this system (*5*).

In contrast to w/o microemulsions, o/w and bicontinuous microemulsions conduct electricity. In principle, they should be usable in electrochemical studies with electrodes of any size. Bicontinuous microemulsions might offer unique properties for electroanalytical studies in addition to those discussed above, including the chance to study reductions and oxidations of nonpolar compounds in a continuous oil phase of nearly pure hydrocarbon with conventional-sized electrodes. Several reports have appeared in which steady-state voltammetric methods were used to study diffusion of probe molecules in o/w microemulsions (*6–11*). In a few of these, measurements were extended to bicontinuous microemulsions (*9–11*). However, fundamental studies of electrochemical reactions in such systems are lacking. Thus, we began a systematic investigation of the electrochemistry of a series of ionic and nonionic redox couples in a model bicontinuous microemulsion of didodecyldimethylammonium bromide (DDAB)/dodecane/water.

Phase diagrams and physical properties of three-component bicontinuous microemulsions of DDAB, water, and oils have been thoroughly investigated by Evans, Ninham, and coworkers (*12–18*) with the aim of determining factors controlling microstructure. DDAB is insoluble in water and oil and resides almost entirely at the interface between the two. Its microemulsions can be prepared by titrating DDAB/oil suspensions with water. Conducting bicontinuous microemulsions can be prepared with as little as 7% water if hexane is the oil or 2% water if cyclohexane is used. Bulk viscositites of these microemulsions are usually considerably larger than that of the neat oil. Addition of more water eventually results in a transition to a nonconducting, less viscous w/o microemulsion. This transition becomes less sharp as chain length of the oil is increased. On the basis of physical properties and NMR self-diffusion studies, microstructure of conducting, bicontinuous microemulsions of DDAB is believed to feature a dynamic, interconnecting network of water tubules surrounded by surfactant with head groups facing the water (*16*).

In this paper, we report the cyclic voltammetry (CV) of water-soluble ferrocyanide, ruthenium(III) hexaammine, and vitamin B_{12} and oil-soluble ferrocene, pyrene, perylene, and 9-phenylanthracene in bicontinuous microemulsions of DDAB/water/dodecane. Glassy carbon was chosen as the working electrode because of its wide potential window. Comparisons of experimental data with computer-simulated CVs showed that to a good approximation, the electroreductions and oxidations behaved as if the solutes were diffusing in a homogeneous medium. The polycyclic aromatic hydrocarbons (PAHs) were reduced by ECE-type mechanisms.

EXPERIMENTAL SECTION

Chemicals and Solutions. Ferrocene, perylene, pyrene, 9-phenylanthracene, and 4,4′-dichlorobiphenyl were obtained from Aldrich Chemical Co. in >98% purities. Potassium ferrocyanide and *n*-dodecane were ACS certified grade from Fisher Scientific. Didodecyldimethylammonium bromide (DDAB, 99+%) was from Eastman Kodak. Vitamin B_{12} was hydroxocob(III)alamin hy-

[1] Present address: Department of Chemistry, Trinity College, Hartford, CT.

0003-2700/90/0362-0644$02.50/0

Table I. Composition and Properties of DDAB/Dodecane/Water Systems

wt %				
surfactant	water	oil	viscosity, cP	$10^6\kappa$, Ω^{-1} cm^{-1}
		100	1.35	
13[a]	28	59	19	0.11
21[a]	39	40	38	1.05
24[b]	14	62	27	1.79

[a] Microemulsion. [b] Emulsion.

drochloride (99%) from Sigma Chemical Co. Ruthenium(III) hexaammine was from Strem Chemicals. Distilled water was purified with a Sybron-Barnstead Nanopure system to a specific resistance >15 MΩ cm. All other chemicals were reagent grade.

Microemulsions were prepared by titrating a mixture of DDAB and dodecane with pure water until a clear solution with a suitably high conductance was obtained. The initial mixture of DDAB and oil was made such that the titration would bring the composition into the microemulsion region of the three-component phase diagram (*15*). Microemulsions prepared in this way were optically clear and stable at room temperature for several months. The one emulsion used was prepared in the same way. Its final composition was slightly out of the microemulsion region of the phase diagram, toward the surfactant corner. This emulsion appeared opaque immediately after vigorous shaking, but two phases separated within an hour. Emulsions were brought to the opaque condition immediately before each experiment.

Apparatus and Procedures. Cyclic voltammetry was done with a Bioanalytical Systems BAS-100 electrochemistry system and a three-electrode cell containing a glassy carbon disk (A = 0.071 cm^2) working electrode, a saturated calomel reference electrode (SCE), and a platinum wire counter electrode. The SCE was connected to the cell by a salt bridge containing microemulsion. Glassy carbon was prepared and polished on a metallographic wheel with successively smaller particles of SiC, diamond paste, and alumina (smallest 0.05 μm), and subsequent ultrasonication in pure water, as described previously (*19*). Before each scan, the electrode was polished for 2 min with 0.3-μm alumina, ultrasonicated for 2 min in purified water, polished with 0.05 μm alumina, and finally ultrasonicated again in pure water. Ohmic drop of the cell was fully compensated in all CV experiments. All electrochemical experiments were thermostated at 25.0 ± 0.1 °C.

Conductance was measured with a YSI Model 3400 conductivity cell calibrated with 0.1 M KCl and a YSI Model 31 conductivity bridge. Bulk viscosities were measured at 25.00 ± 0.01 °C with an Ostwald viscometer calibrated with pure water.

Analysis of Data. Apparent diffusion coefficients (D') were obtained from the cyclic voltammetric (CV) peak currents by using the Randles–Ševčik equation. For quasireversible redox couples, peak currents at scan rates (v) below 1 V s^{-1} were regressed vs $v^{1/2}$ and the slope of this line extrapolated to 0 V s^{-1} was used to estimate D'. This provides an approximate correction for nonlinearity caused by quasireversible charge transfer (*20*). Formal potentials ($E^{\circ\prime}$) were taken as the midpoint between the cathodic and anodic peak potentials of the same CVs. Apparent standard heterogeneous rate constants (k°) were estimated from anodic–cathodic peak potential differences (*21*, *22*) of CVs over a range of scan rates where these differences exceeded about 65 mV, assuming equal diffusion coefficients of reduced and oxidized forms of the redox couple and electrochemical transfer coefficients of 0.5.

Simulations of cyclic voltammograms were done by a previously described (*23*) expanding space grid explicit digital simulation program compiled in Turbo Basic on a PC-AT type microcomputer. Simulations assumed equal diffusion coefficients of both halves of the redox couples and electrochemical transfer coefficients of 0.5.

RESULTS

Physical Properties. Two microemulsion compositions and an emulsion showed good conductivities (Table I) for electrochemical studies. Their bulk viscosities were much higher than either the oil or water from which they were made. Values of conductivity and viscosity for the microemulsions are in agreement with previously reported measurements (*13*).

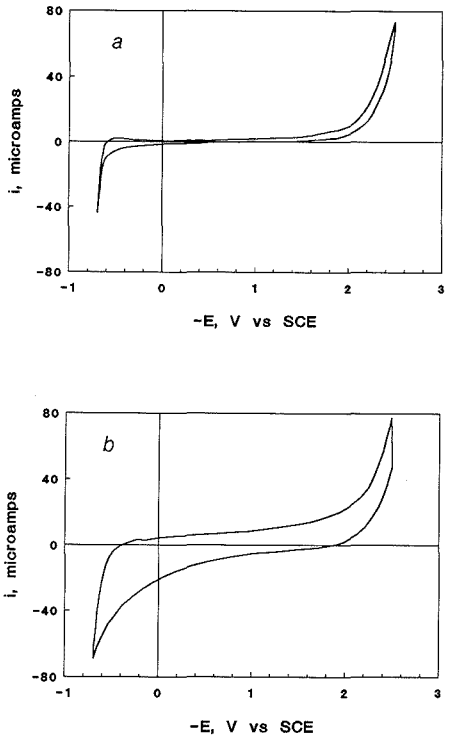

Figure 1. Cyclic voltammograms of DDAB/dodecane/water (21/40/39) at glassy carbon electrode: (a) 0.10 V s^{-1}; (b) 2.0 V s^{-1}.

Reversible and Quasireversible Redox Couples. Cyclic voltammetry of DDAB microemulsions not containing solute revealed a region between about +0.7 and −2.2 V in which the background current is flat at glassy carbon electrodes (Figure 1). Charging current increased as scan rate (v) was increased. Redox reactions of solutes reduced or oxidized within this potential window were easily observed. Well-defined cyclic voltammograms of both water-soluble and oil-soluble redox couples were obtained in this medium (Figure 2). At concentrations above about 0.7 mM, ionic solutes caused turbidity in the medium. However, solubility of nonpolar organic compounds in the microemulsion was good. For example, more than 32 mmol of 4,4′-dibromobiphenyl was solubilized in a liter of the 21% DDAB microemulsion (cf. Table I) at 25 °C compared to equilibrium solubilities at 30 °C of 0.3 mM in aqueous micelles of 0.10 M cetyltrimethylammonium bromide (CTAB)/0.1 M KBr, and about 10^{-4} mM in pure water.

Peak currents in the DDAB microemulsions were linearly dependent on concentration of solute up to about 0.7 mM for ionic solutes and about 2 mM for the nonpolar molecules. In contrast to behavior in some aqueous micellar media (*24*), D' values estimated by CV were independent of solute concentration for all solutes. To test the data against voltammetric theory, values of D', k°, and $E^{\circ\prime}$ (Table II) obtained from CV in the 21% DDAB microemulsion for ferrocyanide, ferrocene, and ruthenium(III) hexaammine were used in computer simulations of a series of CVs. Simulated and experimental CVs were similar in appearance. Comparisons of simulated and

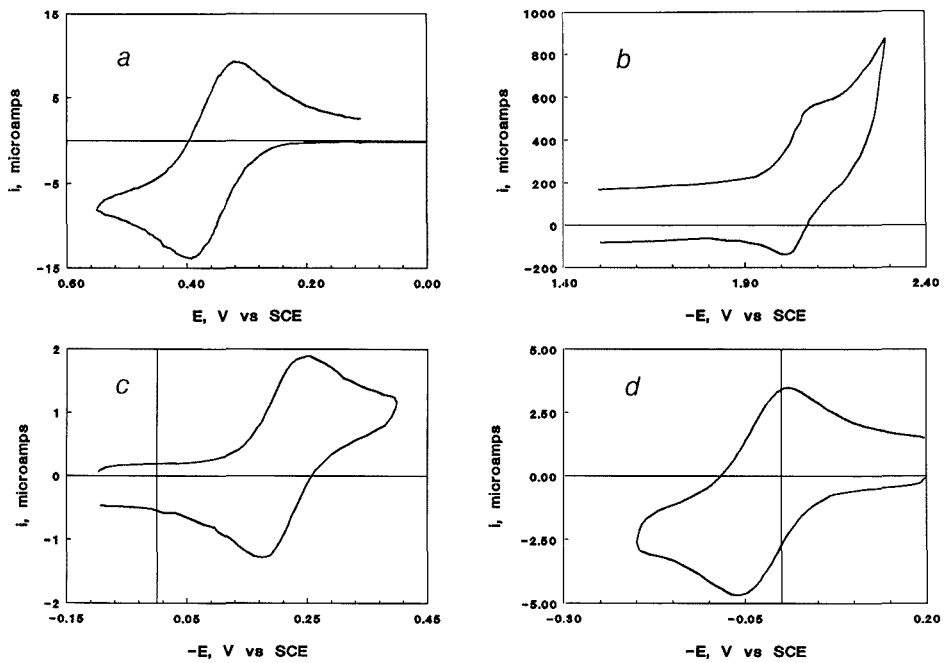

Figure 2. Cyclic voltammograms at glassy carbon electrodes in 21% DDAB microemulsion for (a) 1 mM ferrocene at 0.1 V s^{-1}, (b) 1 mM pyrene at 51 V s^{-1}, (c) 0.5 mM ruthenium(III) hexaammine at 0.050 V s^{-1}, and (d) 0.58 mM ferrocyanide at 0.20 V s^{-1}.

Table II. Apparent Electrochemical Parameters at Glassy Carbon Electrodes in DDAB/Dodecane/Water Systems

species	% DDAB[a]	$10^6D'$, cm^2 s^{-1}	$k°$, cm s^{-1}	$E°'$, V vs SCE
ferrocyanide	21	1.0	0.027	0.027
	13	0.79	0.017	0.022
	24	1.0	0.019	0.030
$Ru^{III}(NH_3)_6$	21	0.68	0.016	−0.213
cob(II)alamin	21	0.3	0.0002	−0.87
ferrocene	21	6.3	0.010	0.34
	13	5.6	0.004	0.38
	24	3.1	0.009	0.41
perylene	21	5	0.2	−1.64
pyrene	21	6	0.1	−2.06
9-PA	21	8	0.2	−1.95

[a] Compositions of microemulsions (13% and 21% DDAB) and emulsion (24% DDAB) as in Table I.

experimental peak currents, peak potentials, and anodic–cathodic peak separations (Figures 3–5) showed that theory developed for diffusion-kinetic controlled voltammetry in homogeneous solutions is obeyed quite well for these three quasireversible redox couples in bicontinuous DDAB microemulsions. Scatter in the data is attributed mainly to normal variance in electrode polishing (*19*).

CVs of similar quality were obtained for ferrocene and ferrocyanide in a microemulsion with 13% DDAB, as well as an emulsion (Table II). Only small differences were observed in D', $E°'$, and $k°$ values from those found in the 21% DDAB microemulsion.

Polycyclic Aromatic Hydrocarbons. PAHs such as perylene, pyrene, and 9-phenylanthracene yield anion radicals as products of their one-electron reductions. Water can rapidly donate a proton to these aromatic anion radicals (*25–28*). The resulting free radical is more easily reduced than its parent hydrocarbon. It is usually reduced as soon as it is formed at the electrode. Thus, transfer of two electrons to PAHs may be achieved by the well-known ECE (electron transfer–chemical step–electron transfer) mechanism. If the anion radical is used up by protonation and reduction, it will not be detected on the reverse CV scan. For perylene, CVs in the 21% DDAB microemulsion showed an anodic peak current a significant fraction of the cathodic peak height at scan rates as low as 1.0 V s^{-1}, with nearly equal heights at 41 V s^{-1} (Figure 6). This suggests stability of the anion radical greater than that in aqueous CTAB micelles, in which a partial anodic peak is found at Hg electrodes only at $v > 40$ V s^{-1} (*29*). For pyrene, an anodic peak about 50% of the height of the cathodic peak was found at 10 V s^{-1}. For 9-PA, at $v > 41$ V s^{-1} an anodic peak only a small fraction of the cathodic peak height was observed.

Cathodic peak currents (i_p) of perylene, pyrene, and 9-PA in the DDAB microemulsion expressed as the peak current function $i_p/v^{1/2}$ increased with decreasing scan rate. For perylene the current function at $v < 0.5$ V s^{-1} was about twice its value at $v > 1$ V s^{-1} (Figure 7). 9-PA and pyrene did not show full 2-fold changes in current function over the v-range studied, but similar trends were found. At $v < 0.5$ V s^{-1}, the cathodic peak for perylene shifted to more positive potentials as scan rate decreased. These results are consistent with occurrence of a two-electron ECE-type electrode reaction at lower scan rates as found for reduction of PAHs in organic solvents in the presence of proton donors (*27–30*). At higher scan rates, the chemical step, presumably protonation, does not have time to occur and the reaction becomes a nearly reversible one-electron process. Electrochemical parameters were estimated under the latter conditions from CV data (Table II).

DISCUSSION

Electrochemical Parameters of Redox Couples. Figures 3–5 show that voltammetric behavior in the DDAB microemulsion is similar to that in homogeneous solutions. Formal

Table III. Electrochemical Parameters of Redox Couples in Homogeneous Media

species	medium (elec)[a]	10^6D, cm^2 s^{-1}	$k°$, cm s^{-1}	$E°'$, V vs SCE	ref
ferrocyanide	0.5 M KNO_3, pH 6.3 (GC)	7.0	0.098	0.204	19
$Ru^{III}(NH_3)_6$	pH 6.2 phosphate (GC)	3.4	0.03	−0.261	tw[a]
cob(II)alamin	aq pH 4–7 (GC)	1.8	0.0002	−0.85[b]	31
ferrocene	MeCN (GC, CMD)	24	>0.8	0.311	19, 34
perylene	DMF (Hg)	5.7	5	−1.62	32
9-PA	DMF (Hg)	8	>0.8	−1.855	33
pyrene	DMF (Hg)			−2.09	25

[a] Abbreviations: GC, glassy carbon; CMD, carbon microdisk; tw, this work. [b] Reduction of base-on cob(II)alamin to base-off cob(I)alamin.

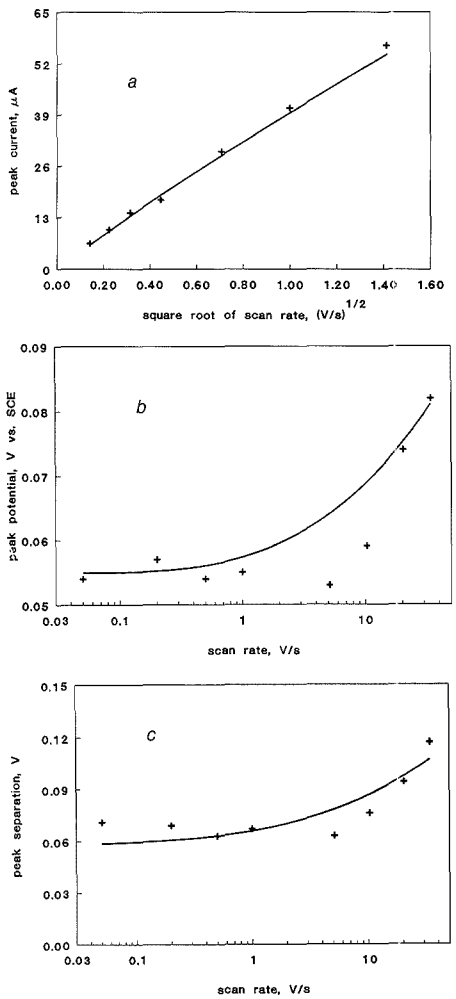

Figure 3. Comparison of simulated (—) and experimental (+) results for cyclic voltammetry of 0.58 mM ferrocyanide ion in 21% DDAB microemulsion for the influence of scan rate on (a) anodic peak current, (b) anodic peak potential, and (c) separation between anodic and cathodic peaks. Simulation parameters $D = 1 \times 10^{-6}$ cm^2 s^{-1}, $k° = 0.027$ cm s^{-1}, and $E°' = 0.027$ V.

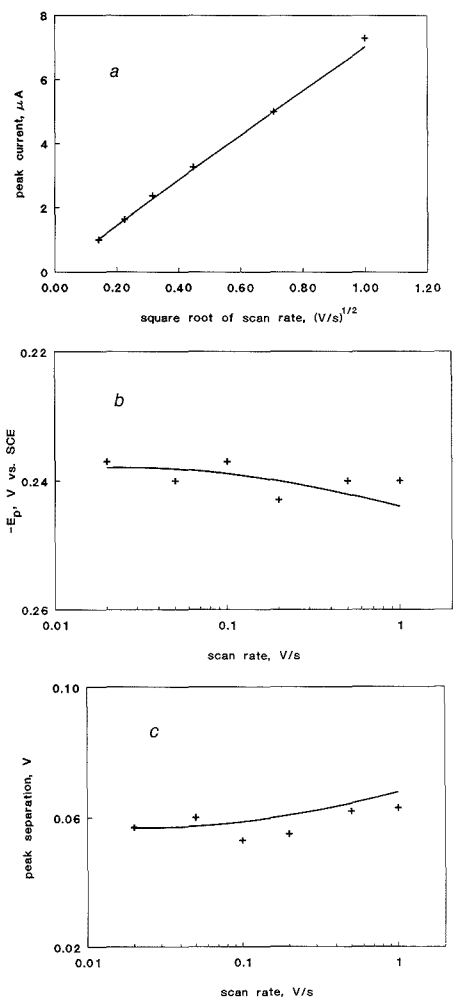

Figure 4. Comparison of simulated (—) and experimental (+) results of cyclic voltammetry of 0.5 mM ruthenium(III) hexaammine in 21% DDAB microemulsion for the influence of scan rate on (a) cathodic peak current, (b) cathodic peak potential, and (c) separation between anodic and cathodic peaks. Simulation parameters $D = 0.68 \times 10^{-6}$ cm^2 s^{-1}, $k° = 0.016$ cm s^{-1}, and $E°' = -0.213$ V.

potentials and $k°$'s of ruthenium(III) hexaamine were similar in water and the microemulsion (cf. Tables II and III). The same is true for cob(II)alamin (the Co(II) form of vitamin B_{12}), assuming that electrochemical reduction in the microemulsion corresponds to electron transfer from the five-coordinate base-on cob(II)alamin to yield base-off, four-coordinate cob(I)alamin as in pH 4–7 homogeneous aqueous solutions (*31*). For ferrocyanide, the formal potentials in microemulsions and

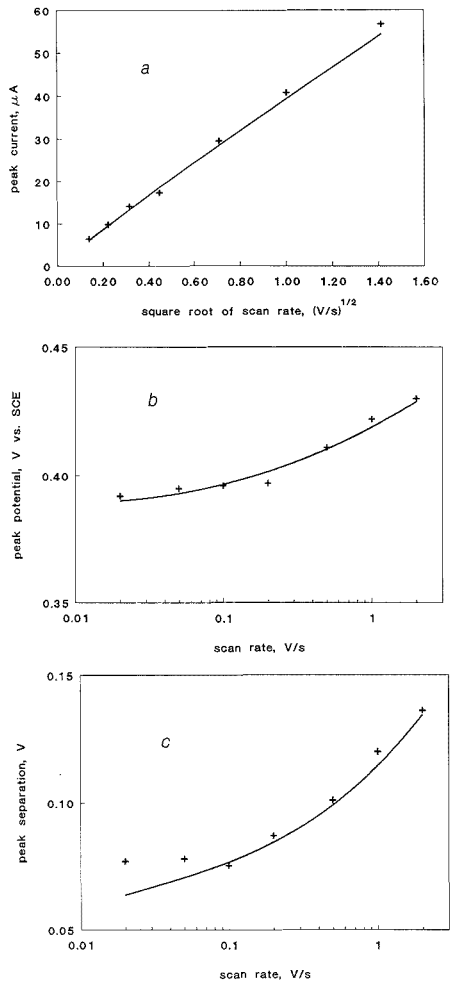

Figure 5. Comparison of simulated (—) and experimental (+) results for cyclic voltammetry of 1.0 mM ferrocene in 21% DDAB microemulsion for the influence of scan rate on (a) anodic peak current, (b) anodic peak potential, and (c) separation between anodic and cathodic peaks. Simulation parameters $D = 6.3 \times 10^{-6}$ cm^2 s^{-1}, $k^\circ = 0.01$ cm s^{-1}, and $E^{\circ\prime} = 0.336$ V.

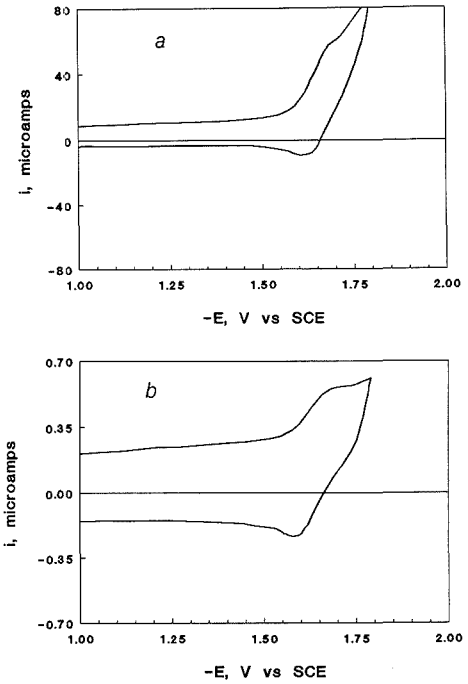

Figure 6. Cyclic voltammograms at glassy carbon electrodes in 21% DDAB microemulsion for 1.0 mM perylene at (a) 1.0 V s^{-1} and (b) 41 V s^{-1}.

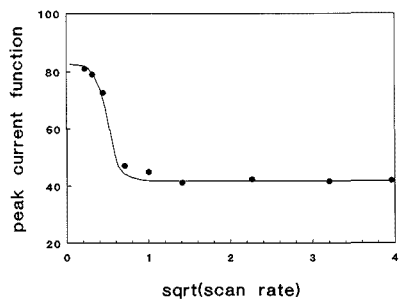

Figure 7. Influence of scan rate on cathodic peak current function ($i_p/v^{1/2}$) for cyclic voltammograms of 1.0 mM perylene at glassy carbon electrodes in 21% DDAB microemulsion.

the emulsion are about 175 mV more negative than in water. Negative shifts of about 100 mV were also found in formal potentials of ferrocyanide at Pt and pyrolytic graphite electrodes in micellar solutions of 0.1 M hexadecyltrimethylammonium bromide (CTAB) (*35*). Such shifts could possibly reflect interaction of ferrocyanide(−4) anion with the positively charged head groups of the surfactants. Indeed, at concentrations below 0.01 M, CTAB formed an insoluble precipitate with potassium ferrocyanide (*35*), also suggesting interactions between ferrocyanide and cationic head groups. Ferrocyanide k°'s were similar in microemulsions of different composition and in the emulsion and were slightly smaller than that in pH 6.3 aqueous potassium nitrate solution. Such small differences in k° may be caused by variable surface preparations of the glassy carbon, by a higher pH (*36*) at the electrode surface in the unbuffered microemulsion, or by inhibition of heterogeneous electron transfer by microemulsion components adsorbed on the electrode.

Diffusion coefficients of ferrocyanide, ruthenium(III) hexaammine, and cob(II)alamin in the 21% DDAB microemulsion were 5–7 times smaller than in water (cf. Tables II and III). This is in line with a self-diffusion coefficient of water in conductive DDAB microemulsions that is 5-fold smaller than in bulk water (*15*). These results are consistent with residence of these ions almost entirely in the water phase.

The D' value of ferrocene in the microemulsions is about one-fourth that of its value in acetonitrile. Assuming that ferrocene resides entirely in the oil phase, this diffusivity ratio follows from the 4-fold greater viscosity of dodecane (Table I) over acetonitrile (*37*), as is consistent with the inverse Stokes–Einstein proportionality between D and viscosity. The D' values found are similar to the average of 6×10^{-6} cm^2 s^{-1}

Scheme I

$$A + e^- = A^{\bullet -} \qquad E^\circ_1 \tag{1}$$

$$A^{\bullet -} + H_2O \underset{k_{-1}}{\overset{k_1}{=}} HA^\bullet + OH^- \tag{2}$$

$$HA^\bullet + e = HA^- \qquad E^\circ_2 \tag{3}$$

$$HA^\bullet + A^{\bullet -} = HA^- + A \tag{4}$$

$$HA^- + H_2O = H_2A + OH^- \tag{5}$$

found for self-diffusion of dodecane in its microemulsions with DDAB and water (*15*). Ferrocene's electrochemical parameters (Table II) do not change much at different compositions of the microemulsion. Its k° was smaller in the microemulsions than in acetonitrile.

Values of k° for PAHs in DDAB microemulsions were somewhat smaller than at Hg electrodes in dry organic solvents, but still reflected rather fast charge transfer at the electrode. E°'s were similar to those in organic solvents. These compounds, soluble mainly in the oil phase, also had D' values similar to that of dodecane in the DDAB microemulsions.

Electroreduction of PAHs. Data for perylene, pyrene, and 9-PA in DDAB microemulsions are consistent with their reduction in an ECE-type pathway at low scan rates. Such a mechanism resulting in hydrogenation of PAHs (A = PAH) can be formulated (*28*) as shown in Scheme I. Equations 1–3 are the classical ECE pathway. If $E^\circ_2 \gg E^\circ_1$, $HA^\bullet$ will be reduced as soon as it is formed. Provided the rate of formation of $HA^\bullet$ is fast with respect to the experimental time scale controlled by scan rate in CV, a two-electron cathodic peak will be observed. Increasing the scan rate may lead to "tuning out" of the chemical step in eq 2 such that only a one-electron reversible CV characteristic of eq 1 is observed. This happens for perylene, and to a partial extent for pyrene and 9-PA as well. However, where electrode reactions of PAHs in the presence of proton donors have been studied in sufficient detail, notably for anthracene and naphthalene (*27*, *28*), the alternative DISP1 pathway has been demonstrated. DISP1 (eqs 1, 2, and 4) is an ECE variant featuring eq 2 as the chemical step following initial charge transfer but substituting homogeneous (eq 4) for heterogeneous charge transfer (eq 3) as the source of the second electron.

Analysis of CV current function or anodic/cathodic peak ratio vs scan rate data leads to slightly different values of the rate parameter $k = k_1[H_2O] + k_{-1}$ for the ECE and DISP1 pathways (*38*). Thus, precise estimates of k by comparing the data to published working curves relating current function to log (k/v) requires a knowledege of the exact electrode reaction mechanism, the analysis of which is beyond the scope of the present work. However, consideration of both mechanisms leads, after neglect of k_{-1}, to a range of lifetimes for the PAH anion radicals in the 21% DDAB microemulsion. Half-lives of 15-40 ms for perylene, 2-4 ms for pyrene, and <1 ms for 9-PA were estimated from the CV data. These lifetimes are smaller than those obtained in dry *N*,*N*-dimethylformamide in which reversible one-electron CVs found (*39*) at scan rates as low as 50 mV s^{-1} suggest half-lives on the order of a second or more for these anion radicals.

CONCLUSIONS

Conductive bicontinuous microemulsions are microheterogeneous fluids with interesting properties for electrochemical studies. Decreases of similar magnitude in diffusion coefficients of electroactive ions and water (self-diffusion) suggest that ions dissolved in the water phase diffuse with D values characteristic of that phase. Molecules dissolved in the oil phase have diffusion coefficients characteristic of the oil phase. Even though DDAB/dodecane/water microemulsions have viscositites 20–40 times that of bulk water (Table I), diffusion of electroactive species is not greatly influenced by bulk viscosity and voltammetric signals with good signal to noise ratio are obtained. Charge transfer reactions controlled by mass transport and kinetics in DDAB microemulsions behave as if they occurred in homogeneous solutions.

Results for the PAHs suggest that water is accessible to ions formed by reduction of oil-soluble molecules. Stability of the anion radicals in the 21% DDAB microemulsion is less than in dry organic solvents, but greater than expected in the presence of large amounts of water.

LITERATURE CITED

(1) Fendler, J. H. *Membrane Mimetic Chemistry*; Wiley: New York, 1982.
(2) Evans, D. F.; Mitchell, D. J.; Ninham, B. W. *J. Phys. Chem.* **1986**, *90*, 2817–2825.
(3) Shinoda, K.; Lindman, B. *Langmuir* **1987**, *3*, 135–149.
(4) O'Connor, C. J.; Lomas, T. D.; Ramage, R. E. *Adv. Colloid Interface Sci.* *1984*, *20*, 21–97.
(5) Owlia, A.; Wang, Z.; Rusling, J. F. *J. Am. Chem. Soc.* **1989**, *111*, 5091–5098.
(6) Mackay, R. A. In *Microemulsions*; Robb, I. D., Ed.; Plenum Press: New York, 1982; pp 207–219.
(7) Mackay, R. A.; Dixit, N. S.; Agarwal, R. *ACS Symp. Ser.* **1982**, *No. 177*, 179–194.
(8) Mackay, R. A.; Dixit, N.; Agarwal, R.; Seiders, P. *J. Dispersion Sci. Technol.* **1983**, *4*, 397–407.
(9) Mackay, R. A.; Brajter-Toth, A. Paper presented at Congress on Applications of New Trends in Colloid and Surfactant Science, Torino, Italy, June 1989.
(10) Georges, J.; Chen, J. W. *Colloid Polym. Sci.* **1986**, *264*, 896–902.
(11) Georges, J.; Chen, J. W.; Arnaud, N. *Colloid Polym. Sci.* **1987**, *265*, 45–51.
(12) Angel, L. A.; Evans, D. F.; Ninham, B. W. *J. Phys. Chem.* **1983**, *87*, 538–540.
(13) Chen, S. J.; Evans, D. F.; Ninham, B. W. *J. Phys. Chem.* **1984**, *88*, 1631–1634.
(14) Ninham, B. W.; Chen, S. J.; Evans, D. F. *J. Phys. Chem.* **1984**, *88*, 5855–5857.
(15) Blum, F. D.; Pickup, S.; Ninham, B. W.; Chen, S. J.; Evans, D. F. *J. Phys. Chem.* **1985**, *89*, 711–713.
(16) Chen, S. J.; Evans, D. F.; Ninham, B. W.; Mitchell, D. J.; Blum, F. D.; Pickup, S. *J. Phys. Chem.* **1986**, *90*, 842–847.
(17) Fontel, K.; Ceglie, A.; Lindman, B.; Ninham, B. W. *Acta Chem. Scand.* **1986**, *A40*, 247–256.
(18) Allen, M.; Evans, D. F.; Mitchell, D. J.; Ninham, B. W. *J. Phys. Chem.* **1987**, *91*, 2320–2324.
(19) Kamau, G. N.; Willis, W. S.; Rusling, J. F. *Anal. Chem.* **1985**, *57*, 545–551.
(20) Kamau, G. N.; Leipert, T.; Shukla, S. S.; Rusling, J. F. *J. Electroanal. Chem. Interfacial. Electrochem.* **1987**, *233*, 173–187.
(21) Nicholson, R. *Anal. Chem.* **1965**, *37*, 1351–1355.
(22) Amatore, C.; Saveant, J. M. Tessier, D. *J. Electroanal. Chem. Interfacial. Electrochem.* **1983**, *146*, 37–45.
(23) Arena, J. V.; Rusling, J. F. *Anal. Chem.* **1986**, *58*, 1481–1488.
(24) Rusling, J. F.; Shi, C.-N.; Kumosinski, T. F. *Anal. Chem.* **1988**, *60*, 1260–1267.
(25) Perichon, J. In *Encyclopedia of Electrochemistry of the Elements*; Bard, A. J., Lund, H., Eds.; Marcel Dekker: New York, 1978; Vol. XI, pp 71–161.
(26) Dietz, R. In *Organic Electrochemistry*, 2nd Ed.; Baizer, M. M., Lund, H., Eds.; Marcel Dekker: New York, 1983; pp 237–258.
(27) Amatore, C.; Saveant, J. M. *J. Electroanal. Chem. Interfacial. Electrochem.* **1980**, *107*, 353–364.
(28) Amatore, C.; Gariel, M.; Saveant, J. M. *J. Electroanal. Chem. Interfacial Electrochem.* **1983**, *147*, 1–38.
(29) Rusling, J. F.; Couture, E. C. *Langmuir*, in press.
(30) Nicholson, R. S.; Shain, I. *Anal. Chem.* **1965**, *37*, 178–188.
(31) Lexa, D.; Saveant, J. M. *Acc. Chem. Res.* **1983**, *16*, 235–243.
(32) Kojima, H.; Bard, A. J. *J. Am. Chem. Soc.* **1975**, *97*, 6317–6324.
(33) Connors, T. F. M.S. Thesis, University of Connecticut, 1983.
(34) Owlia, A.; Rusling, J. F. *Electroanalysis* **1989**, *1*, 141–149.
(35) Zhang, H.; Rusling, J. F., unpublished results, 1989, University of Connecticut.
(36) Deakin, M. R.; Stutts, K. J.; Wightman, R. M. *J. Electroanal. Chem. Interfacial Electrochem.* **1985**, *182*, 113–122.
(37) Mato, F.; Hernandez, J. L. *An. Quim.* **1969**, *65*, 9–18.
(38) Nadjo, L.; Saveant, J. M. *J. Electroanal. Chem. Interfacial Electrochem.* **1971**, *33*, 419–451.
(39) Connors, T. F.; Rusling, J. F.; Owlia, A. *Anal. Chem.* **1985**, *57*, 170–174.

RECEIVED for review September 12, 1989. Accepted December 21, 1989. This work was supported financially by U.S. PHS Grant ES03154 awarded by the National Institute of Environmental Health Sciences.

CORRESPONDENCE

Ion-Exchange Electrokinetic Chromatography with Polymer Ions for the Separation of Isomeric Ions Having Identical Electrophoretic Mobilities

Sir: High-performance capillary electrophoresis (HPCE) is a rapidly growing separation method (*1*, *2*). The separation principle of HPCE is based on differences in electrophoretic mobilities, and therefore, analytes have to have different electrophoretic mobilities to be separated from each other. The electrophoretic mobility depends on the charge of the analyte, molecular size and shape, number of solvation molecules, etc. In order to increase the selectivity, we have to select conditions where the differences in electrophoretic mobilities become maximum.

The pH of the separation solution is the most important factor for the separation of ionic compounds, except for completely ionized ions. The pH dependence of the ionization of some proteins has been theoretically calculated by Mosher et al. (*3*). The optimum pH value for the separation of analytes having very similar pK_a values has been calculated to be close to the pK_a values (*4*). The second choice to alter the selectivity is the use of organic modifiers such as methanol and acetonitrile (*5*). Another choice is to add complexing ligands and metals (*6*). Constituents of the buffer solution and temperature may also alter the relative magnitudes of electrophoretic mobilities.

It is possible that some compounds will have very similar electrophoretic mobilities over a wide pH range, in particular, this will be the case with isomers of strong acids and bases. The electrophoretic separation of this mixture of analytes is almost impossible. However, we can modify their electrophoretic mobilities by introducing a chemical equilibrium, in which the ionic analyte participates to form a dynamic complex with an additive. In other words, even if analytes have identical electrophoretic mobilities, they should have apparently different electrophoretic mobilities, provided their complex formation constants are different.

Although the technique may be termed a modification of electrophoretic mobilities through complex formation, we think that this should be classified as electrokinetic chromatography (EKC), which combines the experimental technique and high efficiency of HPCE with the separation principles of chromatography (*7*). Micellar EKC, or MEKC, is presently a well-known technique that belongs to EKC and has been developed for the separation of electrically neutral analytes by HPCE (*8*, *9*). The ionic micelle added to the separation solution can modify the electrophoretic mobility of the neutral substance, which is actually zero, through micellar solubilization. We have also described cyclodextrin EKC, which uses a cyclodextrin derivative having an ionic group, instead of the ionic micelle in micellar EKC, and which allows a separation based on inclusion–complex formation (*7*, *10*).

In this paper, we describe ion-exchange EKC with polymer ions, which is developed for the separation of ionic analytes having very similar electrophoretic mobilities. In this method, a polymer ion having an opposite charge to the analyte ions is added to the separation solution as a modifier. A brief consideration of the principles and a successful application of this technique are presented.

THEORY

Figure 1 shows schematically the separation principle of ion-exchange EKC. In this figure, a polymer cation and analyte anions, and their electrophoretic migrations are illustrated, but other ions, such as buffer constituents and counterions of both analyte anions and the polymer cation, are intentionally omitted. The electroosmotic flow also is not shown. The analyte anion that combines with the polymer cation, through ion-pair formation, will migrate with the same velocity as other polymer cations. That is because only a partial neutralization of the positive charge occurs on the polymer, and a small increase in molecular size will not significantly alter the electrophoretic velocity of the polymer cation. The free analytes and the bound analytes migrate in the opposite directions, as shown in Figure 1. Accordingly, the apparent velocity of the analyte anion depends on what extent the analyte forms the ion pair with the polymer ion.

The velocity of the analyte solute, v_s, is described as

$$v_s = v_{eo} + Rv_{ep}(\text{free}) + (1 - R)v_{ep}(\text{pi}) \quad (1)$$

where v_{eo}, v_{ep}(free), and v_{ep}(pi) are electroosmotic velocity, electrophoretic velocity of the free analyte ion, and the electrophoretic velocity of the polymer ion, respectively. The electrophoretic velocity of the bound analyte is supposed to be equal to that of the polymer ion, as mentioned above. The quantity R is the fraction of the analyte ion free from the polymer ion.

Since the technique is mainly applicable to the separation of ions having very similar electrophoretic mobilities, it is reasonable to assume that ionic solutes 1 and 2 have identical electrophoretic mobilities. Therefore, the difference in migration velocities between the two solutes 1 and 2, Δv_s, is given as

$$\Delta v_s = v_{s1} - v_{s2} = (R_1 - R_2)\{v_{ep}(\text{free}) - v_{ep}(\text{pi})\} \quad (2)$$

where R_1 and R_2 are the R values of the solutes 1 and 2.

The equilibrium reaction between the solute, S^-, and the polymer ion, P^+, is supposed to be

$$S^- + P^+ \rightleftharpoons S^-{\cdot}P^+ \quad (3)$$

$$K_{ip} = [S^-{\cdot}P^+]/[S^-][P^+] \quad (4)$$

where K_{ip} is the ion-pair formation constant. Here, S^- and P^+ do not always mean singly charged species. The R value is related to K_{ip} through

$$R = [S^-]/([S^-] + [S^-{\cdot}P^+]) = 1/(1 + K_{ip}[P^+]) \quad (5)$$

The concentration of free polymer ion, $[P^+]$, is considered to be substantially equal to the total concentration of the polymer ion, $[P^+]_0$, provided that the concentration of the analyte ion is low compared with $[P^+]_0$. Combination of eq 5 with eq 2 gives

$$\Delta v = \frac{(K_{ip2} - K_{ip1})[P^+]_0\{v_{ep}(\text{free}) - v_{ep}(\text{pi})\}}{(1 + K_{ip1}[P^+]_0)\,(1 + K_{ip2}[P^+]_0)} \quad (6)$$

where K_{ip1} and K_{ip2} are the ion-pair formation constants of

0003-2700/90/0362-0650$02.50/0

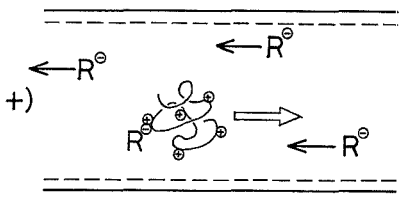

Figure 1. Schematic diagram of the principle of ion-exchange electrokinetic chromatography: a polymer cation is shown; R^-, analyte anion; arrows show the electrophoretic migrations.

the solutes 1 and 2, respectively. Equation 6 predicts that Δv is proportional to the difference between the two formation constants, $(K_{ip2} - K_{ip1})$, and also to the difference between the two electrophoretic velocities, $\{v_{ep}(\text{free}) - v_{ep}(\text{pi})\}$. It should be noted that $v_{ep}(\text{free})$ and $v_{ep}(\text{pi})$ have different signs, because they have opposite charges. Equation 6 suggests that the relationship between Δv and the concentration of the polymer ion $[P^+]_0$ will be complicated, depending on the sizes of the values $K_{ip}[P^+]_0$ relative to unity. However, we will not discuss the dependence of Δv on $[P^+]_0$ further in this paper.

EXPERIMENTAL SECTION

Apparatus and Procedure. An apparatus similar to that described (*3, 8*) was employed. Fused silica capillaries of 50 μm i.d. from two different sources (Scientific Glass Engineering, Ringwood, Victoria, Australia, and Polymicro Technologies, Phoenix, AZ) were used. Sample solutions were introduced manually into the capillary by the hydrostatic method or siphoning. The solute band migrating in the capillary was detected on-column by UV absorption at 210 nm with a Jasco Uvidec-100-V (Tokyo, Japan). Electropherograms or electrokinetic chromatograms were recorded with a Shimadzu C-R6A Chromatopac (Kyoto, Japan). All experiments were carried out at ambient temperature (ca. 25 °C).

Materials. Poly(diallyldimethylammonium chloride) (PDDAC) was purchased from Polysciences, Inc. (Warrington, PA), as 15% solids in water and (diethylamino)ethyldextran (DEAE-dextran) was obtained from Pharmacia (Uppsala, Sweden). Hydroxypropylcellulose (HPC) was purchased from Tokyo Kasei Kogyo (Tokyo, Japan). Sodium 1- and 2-naphthalenesulfonates and disodium 1,5-, 2,6-, and 2,7-naphthalenedisulfonates were purchased from Wako Pure Chemical Industries (Osaka, Japan) and disodium 1,6- and 1,7-naphthalenedisulfonates were gifts from Sumitomo Chemical Co. (Osaka, Japan). Water and purified with a Milli-Q system (Nihon Millipore, Tokyo, Japan). All other reagents were of analytical-reagent grade, and all materials were used without further purification.

RESULTS AND DISCUSSION

Figure 2 shows an electropherogram of a mixture of two isomers of naphthalenesulfonates and five isomers of naphthalenedisulfonates, which was obtained with a 50 mM phosphate buffer solution (pH 7.0) containing 0.1% HPC. Since electroosmosis was almost completely suppressed in the presence of HPC, all the analyte anions migrated toward the positive electrode. Group separation by the number of the sulfonate groups was easily brought about, as expected from the difference in charge, but isomer separation was not successful.

Although 1- and 2-naphthalenesulfonic acids may have different pK_a values, they are considered to be fully ionized at pH 7.0. The electrophoretic mobilities of the two naphthalenesulfonate ions must be very similar, judging from the result shown in Figure 2.

The five disodium naphthalenedisulfonates employed in this study were also considered to be completely ionized at pH 7.0, because these isomeric ions were not resolved, but migrated much faster than the monosulfonate ions toward the positive electrode. This result suggests that the isomeric

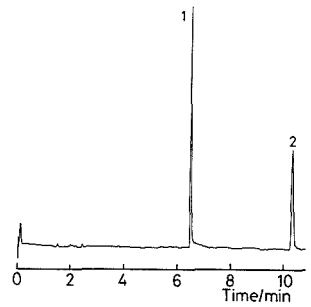

Figure 2. Electropherogram of 1- and 2-naphthalenesulfonates and 1,5-, 1,6-, 1,7-, 2,6-, and 2,7-naphthalenedisulfonates: (1) five naphthalenedisulfonates, (2) two naphthalenesulfonates; capillary, 71 cm in total length, 46 cm to the detection point; applied voltage, 20 kV; current, 35 μA.

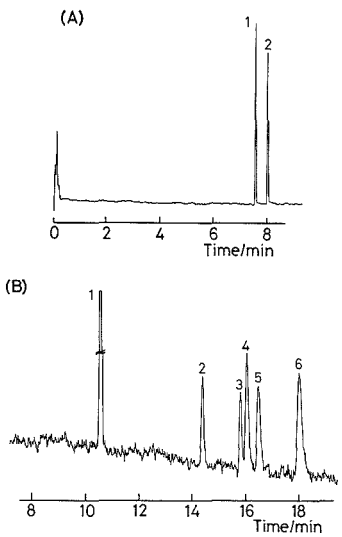

Figure 3. Ion-exchange electrokinetic chromatograms of the analytes shown in Figure 2: (A) 1, 2-; 2, 1-naphthalenesulfonate; (B) 1, 1- and 2-naphthalenesulfonates; 2, 2,6-; 3, 2,7-; 4, 1,6-; 5, 1,5-; 6, 1,7-naphthalenedisulfonates. Separation solution, (A) 0.3% DDAC in 50 mM phosphate buffer (pH 7.0), (B) 2% DEAE-dextran in the same buffer as in (A); capillary, 75 cm in total length, 50 cm to the detection point; applied voltage, 20 kV; current, (A) 48 μA, (B) 58 μA.

dianions seem to have very similar electrophoretic mobilities, and hence, it is very difficult to separate these isomers under fully ionized conditions. It may be possible to resolve these isomeric disulfonic acids by HPCE under acidic conditions, under which the pH should be close to the second pK_a values of the disulfonic acids (*4*). However, we adopted another technique to resolve them, as described below.

Figure 3 shows ion-exchange electrokinetic chromatograms of the same analytes employed in Figure 2. In Figure 3A, 0.3% PDDAC was added to the same 50 mM phosphate buffer solution (pH 7.0) as employed in the above HPCE experiments, and in Figure 3B, 2% DEAE–dextran was added. Although analyte ions migrated toward the positive electrode, the monosulfonates migrated faster than the disulfonates, as shown in Figure 3B, in contrast to the result shown in Figure 2. The electroosmotic flow was very weak, but toward the positive electrode in the presence of the polymer ions.

Although the two monosulfonates were not resolved with the 2% DEAE-dextran solution, as shown in Figure 3B, they were easily separated with the 0.3% PDDAC solution, as shown in Figure 3A. Use of the 0.3% PDDAC solution also permitted the separation of the five naphthalenedisulfonates shown in Figure 3B, but migration times were too long compared with those obtained with DEAE-dextran solutions.

The reversed migration order of the monosulfonates and disulfonates between Figures 2 and 3B indicates that the disulfonates interact with the polymer cation more strongly than the monosulfonates. It is reasonable that dianions tend to form more stable ion pairs with polymer cations than monoanions, from the viewpoint of electrostatic interaction, but it seems difficult to reasonably explain the relative stability of ion pairs between the isomeric ions and with the polymer ions. The relative migration orders shown in Figure 3 suggests that the sulfonate group at the 1 position of the naphthalene structure binds to the polymer cation more strongly than that at the 2 position, because the stronger ion-pair formation causes a slower migration velocity.

In conclusion, in order to increase selectivity in HPCE, electrophoretic mobilities can be manipulated through the ion-pair formation reaction of analyte ions with polymer ions. We have tried to modify mobilities in a similar manner with ionic micelles, such as dodecyltrimethylammonium chloride, instead of polymer ions, but this was not very successful. A long chain configuration of the polymer ion is probably more effective to discriminate isomers than the spherical and dynamic structure of the micelle. It may be possible to extend this technique to the separation of polymer anions, such as oligonucleotides.

ACKNOWLEDGMENT

We thank Professor S. Hjertén for his suggestion of using DEAE-dextran for the technique described.

LITERATURE CITED

(1) Gordon, M. J.; Huang, X.; Pentoney, S. L., Jr.; Zare, R. N. *Science* **1988**, *242*, 224–228.
(2) Wallingford, R. A.; Ewing, A. G. *Adv. Chromatogr.* **1989**, *30*, 1–76.
(3) Mosher, R. A.; Dewey, D.; Thormann, W.; Saville, D. A.; Bier, M. *Anal. Chem.* **1989**, *61*, 362–366.
(4) Terabe, S.; Yashima, T.; Tanaka, N.; Araki, M. *Anal. Chem.* **1988**, *60*, 1673–1677.
(5) Fujiwara, S.; Honda, S. *Anal. Chem.* **1987**, *59*, 487–490.
(6) Gassmann, E.; Kuo, J. E.; Zare, R. N. *Science* **1985**, *230*, 813–814.
(7) Terabe, S. *TrAC, Trends Anal. Chem.* **1989**, *8*, 129–134.
(8) Terabe, S.; Otsuka, K.; Ichikawa, K.; Tsuchiya, A.; Ando, T. *Anal. Chem.* **1984**, *56*, 111–113.
(9) Terabe, S.; Otsuka, K.; Ando, T. *Anal. Chem.* **1985**, *57*, 834–841.
(10) Terabe, S.; Ozaki, H.; Otsuka, K.; Ando, T. *J. Chromatogr.* **1985**, *332*, 211–217.

Shigeru Terabe*
Tsuguhide Isemura
Department of Industrial Chemistry
Faculty of Engineering
Kyoto University
Sakyo-ku, Kyoto 606, Japan

RECEIVED for review November 3, 1989. Accepted December 21, 1989. This work is partially supported by grants from Yokogawa Electric Corp. and Shimadzu Corp.

TECHNICAL NOTES

Preparative Method for Fabricating a Microelectrode Ensemble: Electrochemical Response of Microporous Aluminum Anodic Oxide Film Modified Gold Electrode

Kohei Uosaki,* Kentaro Okazaki, and Hideaki Kita

Department of Chemistry, Faculty of Science, Hokkaido University, Sapporo 060, Japan

Hideaki Takahashi

Analytical Chemistry Laboratory, Faculty of Engineering, Hokkaido University, Sapporo 060, Japan

INTRODUCTION

Recently, much attention has been paid to microelectrode arrays (ensembles) because of their various advantages in many applications, including high signal to noise (S/N) ratio compared to conventional electrodes with the same electrode area (*1*).

Various approaches have been taken to prepare microelectrode arrays. Hepel and Osteryoung constructed microelectrode arrays that are composed of disks of 0.375-μm radius, employing electron beam lithography (2). Martin and colleagues used microporous polycarbonate membranes (Nuclepore) as hosts and Pt (r = 0.1–0.5 μm) or carbon (r = 8 or 12 μm) as an electrode material (*3*, *4*). Morita and Shimizu prepared a microelectrode array employing platinized carbon fiber (5–7 μm) as an electrode and epoxy resin as a substrate (*5*). The smallest radius of an individual electrode reported is 0.1 μm. It is known that the smaller the active electrode area, the higher the S/N ratio (*6*).

In this paper, we propose a novel method for the preparation of a microelectrode ensemble with smallest electrode size reported by using micropores of aluminum anodic film as templates. Such oxide films, formed on Al in acidic media, are known to possess micropores of 10–200 nm diameter normal to the surface with a barrier layer between the anodic oxide film and Al substrate (*7*, *8*). Recently, Majda and his colleagues reported the electrochemical behavior of electroactive species confined within the micropores of the aluminum anodic oxide film (*9–14*). Tierney and Martin deposited "transparent" Au microcylinders within the micropores of the anodic oxide film (*15*). We have thought that these pores can be used as templates for microelectrode disks. Thus, after the anodic oxide film was removed from the Al substrate, gold was vacuum evaporated into the micropores of the oxide film, and the barrier layer was gradually removed. At a certain level of barrier layer removal, voltammograms of sigmoidal shape having a current independent of scan rate were observed, confirming the formation of an ensemble of microe-

0003-2700/90/0362-0652$02.50/0

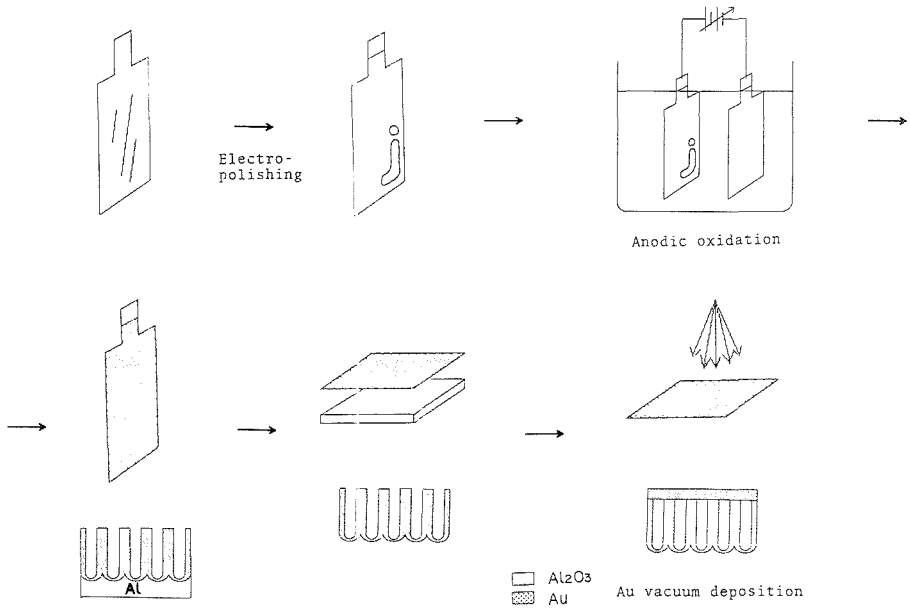

Figure 1. Schematic diagram of the preparation of an aluminum anodic oxide film modified Au electrode.

lectrode disks. The effects of pore size, level of barrier layer removal, and gold deposition method on electrochemical properties are also discussed.

EXPERIMENTAL SECTION

Materials. Al foil (0.3 mm thick, 99.99%) was obtained from Nippon Chemical Condenser Co., Ltd. Au wire (0.5 mm diameter, 99.99%) used for vacuum deposition was obtained from Tanaka Noble Metals Co., Ltd. All chemicals were reagent grade (Wako Pure Chemicals Ind., Ltd.) and were used as received.

Preparation of Microporous Aluminum Anodic Oxide Film (*7–14*). Figure 1 shows the procedure for the preparation of the microporous aluminum anodic oxide thin film modified gold electrode. An aluminum plate (4 cm × 1.5 cm) was electropolished in a mixed acid (780 mL of acetic acid and 220 mL of 60% perchloric acid) after being degreased with methanol. The electropolishing was carried out with a two-electrode configuration with aluminum as a counter electrode. The bias voltage was 30 V, and the temperature of the solution, which was continuously stirred, was kept at 10 °C. The electropolished aluminum plate was dried and stored in a desiccator after being washed by water. Anodic oxidation of the electropolished aluminum was carried out in 4% H_3PO_4 solution at 65 V and 20 °C or in 10% H_2SO_4 solution at 15 V and 5 °C by also employing a two-electrode configuration with aluminum as a counter electrode. The anodic oxidation time was 45 min, and the thickness of the anodic oxide films was 4 μm in both cases. For electropolishing and anodic oxidation of Al, a regulated dc power supply (Takasago, Ltd., GP0110-3) and an electrometer (Takeda Riken Ltd., TR-8651) were used to control the bias voltage and monitor the current passed, respectively. The anodic oxide film was separated from the aluminum substrate by immersing the anodized Al in a saturated $HgCl_2$ aqueous solution. The anodic oxide films thus obtained were washed with water and dried in air. The pore size of the oxide film was determined by SEM (Hitachi Ltd., S-2100A) and TEM (Hitachi Ltd., H-700H).

Vacuum Deposition of Au. To form an electrode, Au was vacuum deposited onto the open pore side of the film (see Figure 1). The deposition was carried out by using a vacuum evaporation apparatus (Shimadzu Ltd., EA-400S) at a pressure of 5×10^{-5} mmHg with two deposition angles, 30° and 90°, against the surface. Usually the thickness of the Au was ca. 100 nm.

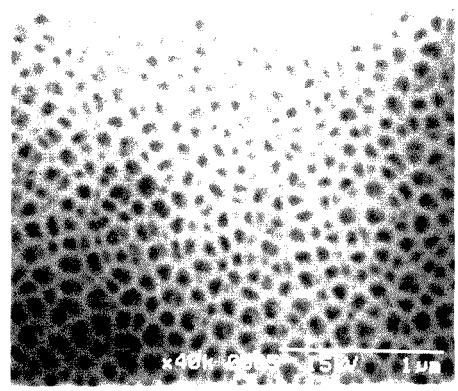

Figure 2. SEM image of a microporous anodic oxide film of Al, obtained in 4% H_3PO_4 solution at 65 V and 20 °C.

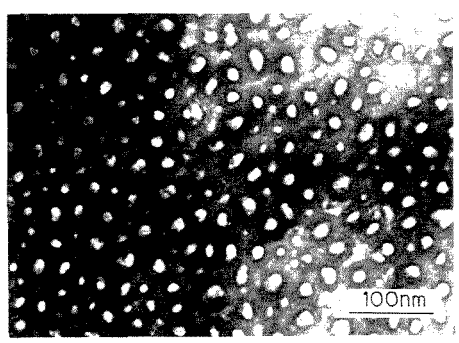

Figure 3. TEM image of a microporous anodic oxide film of Al, obtained in 10% H_2SO_4 solution at 15 V and 5 °C.

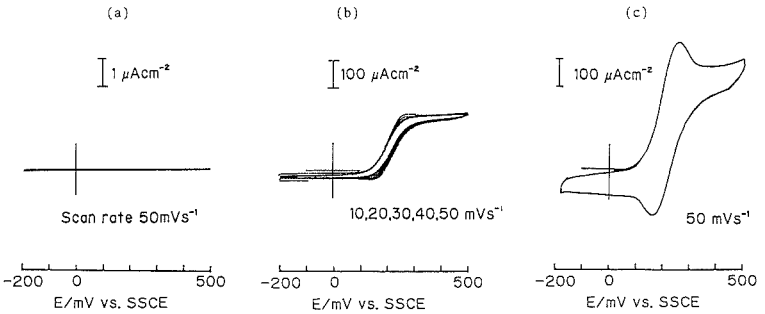

Figure 4. Cyclic voltammograms of an aluminum anodic oxide film (pore diameter, 15 nm) modified Au electrode, which was prepared by Au deposition with a deposition angle of 90°, in 50 mM $Fe(CN)_6^{4-}$ aqueous solution at different degrees of dissolution of the barrier layer: (a) before dissolution, (b) after 2 min, and (c) after 10 min immersion in 10 mM NaOH.

Electrochemical Procedure. The gold-evaporated oxide film was placed on a glassy carbon (GC) disk, which was used as a current collector, with the gold facing the GC. A copper wire was attached to the other side of the GC and the microporous oxide film/Au/GC/Cu assembly was placed in a Teflon electrode holder.

A potentiostat (Hokuto Denko Co., Ltd., HA-301) was used to control the potential of the working electrode with respect to a sodium-saturated calomel electrode (SSCE) in electrochemical measurements. A Pt foil was used as a counter electrode. External potential was provided by a function generator (Hokuto Denko Co., Ltd., HB-105). A three-electrode, three-compartment cell was employed for electrochemical measurements. Current–potential relations were recorded on an X–Y–t recorder (Rika Denki Co., Ltd., RW-11T).

RESULTS

The oxide film obtained in 4% H_3PO_4 solution at 65 V and 20 °C has pores of 100 nm diameter; that obtained in 10% H_2SO_4 solution at 15 V and 5 °C has pores of 15 nm diameter, as shown in Figure 2 and Figure 3, respectively. These pore sizes are in good agreement with the values that one of us reported before (*7*, *8*).

Figure 4 shows the cyclic voltammograms (CV) of a microporous oxide film (pore diameter, 15 nm) modified Au electrode, which was prepared by Au deposition with a deposition angle of 90°, in 50 mM $Fe(CN)_6^{4-}$ aqueous solution after different degrees of dissolution of the barrier layer. Before the dissolution of the barrier layer, the electrode showed no response to $Fe(CN)_6^{4-}$ as shown in Figure 4a. The electrochemical response appeared after the electrode was immersed in 10 mM NaOH solution for 2 min as shown in Figure 4b. In this case, the shape of the CV is sigmoidal and does not depend on the sweep rate. This response is similar to that observed at a microelectrode (*16*, *17*). The limiting current is, however, very large compared with the value at a typical microelectrode (approximately nanoamperes). The sigmoidal shape gradually changed to peak-shaped CVs as the dissolution of the barrier layer proceeded, as shown in Figure 4c.

The microporous oxide film modified Au electrode with pore diameter of 100 nm showed a CV very similar to that of Figure 4c, at an even very early stage of barrier layer dissolution, as shown in Figure 5. Thus, the sigmoidal curve was obtained only at a low sweep rate and peak-shaped curves were observed at higher sweep rates.

Figure 6 shows the CV of the microporous oxide film modified Au electrode with a pore diameter of 100 nm, which was prepared with a deposition angle of 30°, measured in 50 mM $Fe(CN)_6^{4-}$ solution. Figure 6a shows that the electrode did not respond to $Fe(CN)_6^{4-}$ before the barrier layer was dissolved, as was the case shown in Figure 4a. Figure 6b is the CV observed in the same solution of Figure 6a after the

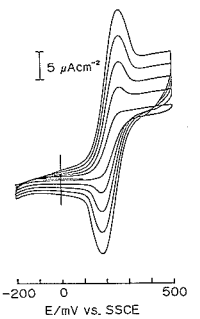

Figure 5. Cyclic voltammograms of an aluminum anodic oxide film (pore diameter, 100 nm) modified Au electrode, which was prepared by Au deposition with a deposition angle of 90°, measured in 50 mM $Fe(CN)_6^{4-}$ aqueous solution at various sweep rates. CVs were recorded after 1 min immersion in 10 mM NaOH.

electrode was immersed in 10 mM NaOH solution for 1 min. Symmetric waves with a peak separation of 30 mV, showing exhaustive redox behavior, were observed. Figure 7a shows the scan rate dependence of the peak current at the electrode whose CV is shown in Figure 6b. The peak current is proportional to scan rate and it is confirmed that the electrochemical response of this electrode is like that of a thin layer cell (*18*). Figure 6c shows the CV of the electrode after 4-min immersion in a 10 mM NaOH solution, measured in 50 mM $Fe(CN)_6^{4-}$ solution. The shape of the CV is now very close to that expected of the electrode for a linear diffusion-controlled situation. Figure 7b shows the scan rate dependence of the peak current at the electrode whose CV is presented in Figure 6c. The peak current is proportional to the square root of the scan rate.

DISCUSSION

The electrochemical behavior during the barrier layer removal of the electrode on which Au is deposited at an angle of 90° can be explained by a model schematically shown in Figure 8. In this case, Au is expected to enter deep into the pores and is deposited on their inner walls, forming columns of Au. At the early stage of dissolution when the sigmoidal curve is obtained, only a part of Au in the pores seems exposed to the solution. It is also likely that only a small fraction of the pores becomes open; otherwise, the separation between the individual pores is too small to give the sigmoidal curve. Since the exposed area of each Au column is very small, microelectrode behavior is expected, but because the number of the microelectrodes is large, the current observed is quite significant. It must be emphasized here that although various

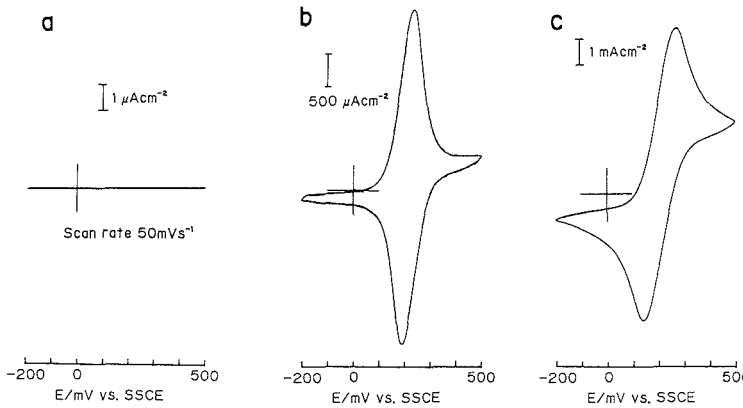

Figure 6. Cyclic voltammograms of aluminum anodic oxide film (pore diameter, 100 nm) modified Au electrode, which was prepared by Au deposition with deposition angle of 30°, in 50 mM $Fe(CN)_6^{4-}$ aqueous solution at different degrees of dissolution of the barrier layer: (a) before dissolution, (b) after 1 min, and (c) after 4 min immersion in 10 mM NaOH.

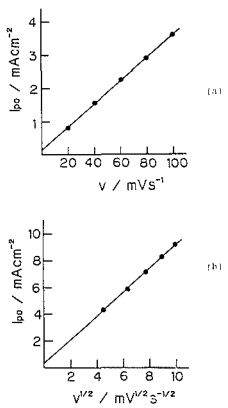

Figure 7. (a) Scan rate dependence of the peak current of Figure 6b. (b) Scan rate dependence of the peak current of Figure 6c.

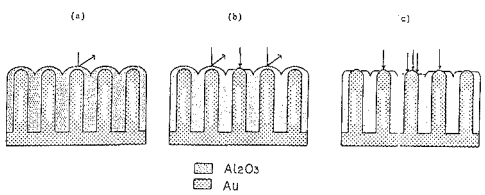

Figure 8. Barrier layer removal process at the oxide film (pore diameter, 15 nm) modified Au electrode, which was prepared by Au deposition with a deposition angle of 90°: (a) before dissolution, (b) at an early stage of dissolution at which a sigmoidal CV is observed, and (c) at a much later stage.

attempts have been made to obtain microelectrode arrays (ensembles), the perfect sigmoidal curves demonstrated in this paper have not been reported. One reason for such a perfect response in this case may be the very small active area of each Au electrode disk. Since the separation between micropores is relatively small compared to the diameter of the micropores, radial diffusion is not expected if the barrier layer is totally removed. Thus, the sigmoidal CVs can be observed only at early stages of dissolution of the barrier layer and should change to peak-shaped CVs when dissolution proceeds, as experimentally observed. The results in Figure 4c show the

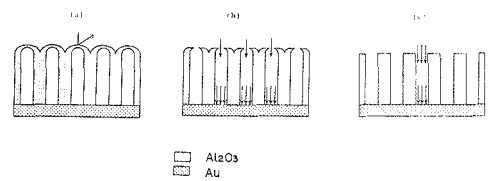

Figure 9. Barrier layer removal process at the oxide film (pore diameter, 100 nm) modified Au electrode, which was prepared by Au deposition with a deposition angle of 30°: (a) before dissolution, (b) at an early stage at which thin-layer-cell behavior is observed, and (c) at a much later stage.

transition from radial diffusion to linear diffusion. At the electrodes with larger pore diameters, it seems to be much more difficult to observe the perfect sigmoidal CV due to a much higher electrode-to-insulator ratio (Figure 3).

The process of the barrier layer removal from the oxide film on which Au is deposited with a deposition angle of 30° is schematically shown in Figure 9. Before the dissolution of the barrier layer, the electrode cannot respond to $Fe(CN)_6^{4-}$ because the $Fe(CN)_6^{4-}$ is blocked by the barrier layer (Figure 9a). If the small pore is opened by the barrier layer dissolution, $Fe(CN)_6^{4-}$ can enter into the micropores, reach the electrode surface, and give an electrochemical response. Since the transport of $Fe(CN)_6^{4-}$ into the miocropore is still limited by the barrier layer at this stage, $Fe(CN)_6^{4-}$ in the micropore is exhaustively consumed in the oxidation process. Thus, the electrode shows the thin layer cell behavior (Figure 9b). When the barrier layer is totally dissolved, the limitation for transport of $Fe(CN)_6^{4-}$ is also removed and the response becomes the typical response of a Au macroelectrode, i.e., linear-diffusion-controlled, reversible behavior (Figure 9c).

A more quantitative analysis of the electrochemical responses of these electrodes with different degrees of barrier layer dissolution is under way.

CONCLUSION

A novel method for the preparation of an ultramicroelectrode ensemble is demonstrated. At the initial stage of barrier layer removal following the vacuum evaporation of Au into micropores of aluminum anodic oxide films, sigmoidal CVs, which are expected for the microdisk electrode, were observed. When Au was deposited with a deposition angle of 30°, to avoid filling the micropores with Au, the CV of a thin layer cell showing exhaustive redox behavior with a peak separation

of 30 mV and symmetric waves, was observed.

ACKNOWLEDGMENT

Thanks are due to Mr. Ueda for the TEM measurement and to Professor A. B. Ellis for the critical reading of the manuscript.

LITERATURE CITED

(1) Weber, S. G. *Anal. Chem.* **1989**, *61*, 295, and references therein.
(2) Hepel, T.; Osteryoung, J. *J. Electrochem. Soc.* **1986**, *133*, 752.
(3) Penner, M. R.; Martin, C. R. *Anal. Chem.* **1987**, *59*, 2625.
(4) Cheng, I. F.; Martin, C. R. *Anal. Chem.* **1988**, *60*, 2163.
(5) Morita, K.; Shimizu, Y. *Anal. Chem.* **1989**, *61*, 159.
(6) Cassidy, J.; Sarfaraz, F.; Smith, J. J.; Pons, S. *Electrochim. Acta* **1986**, *31*, 629.
(7) Ebihara, K.; Takahashi, H.; Nagayama, M. *Kinzoku Hyomen Gizyutsu* **1982**, *33*, 156.
(8) Ebihara, K.; Takahashi, H.; Nagayama, M. *Kinzoku Hyomen Gizyutsu* **1983**, *34*, 548.
(9) Miller, C. J.; Majda, M. *J. Am. Chem. Soc.* **1985**, *107*, 1419.
(10) Miller, C. J.; Majda, M. *J. Electroanal. Chem.* **1986**, *207*, 49.
(11) Miller, C. J.; Majda, M. *J. Am. Chem. Soc.* **1986**, *108*, 3118.
(12) Miller, C. J.; Widrig, C. A.; Charych, D. H.; Majda, M. *J. Phys. Chem.* **1988**, *92*, 1928.
(13) Gass, C. A.; Miller, C. J.; Majda, M. *J. Phys. Chem.* **1988**, *92*, 1937.
(14) Miller, C. J.; Majda, M. *Anal. Chem.* **1988**, *60*, 1168.
(15) Tierney, M. J.; Martin, C. R. *J. Phys. Chem.* **1989**, *93*, 2878.
(16) Wightman, R. M. *Anal. Chem.* **1981**, *53*, 1125A.
(17) Pons, S.; Fleischmann, M. *Anal. Chem.* **1987**, *59*, 1391A.
(18) Bard, A. J.; Faulkner, L. R. Electrochemical Methods; John Wiley & Sons Inc.: New York, 1980.

RECEIVED for review June 5, 1989. Accepted December 6, 1989. This work was partially supported by the Grant-in-Aid on Priority-Area Research on "Energy Conversion and Utilization with High Efficiency", Ministry of Education, Science and Culture, Japan (No. 63603502, 01603502).

CORRECTION

Manual Headspace Method To Analyze for the Volatile Aromatics of Gasoline in Groundwater and Soil Samples

Valerie D. Roe, Michael J. Lacy, James D. Stuart, and Gary A. Robbins (*Anal. Chem.* **1989**, *61*, 2584–2585).

Equation 2 should read

$$H = \frac{1 - (A_1/A_2)}{(A_1/A_2)(V_v/V_w)_1 - (V_v/V_w)_2}$$

Are you tired of . . .

. . . journals so narrowly focused that they don't provide insight into other areas of importance to all chemists?

. . . having to be an expert in every field before you can understand the material presented?

. . . scanning dozens of periodicals to find new insights you can apply to your work?

Join your most successful colleagues and discover the CHEMTECH difference.

Each month, **CHEMTECH** provides you with imagination-stirring applications that stretch across all chemical disciplines. Written by recognized experts, **CHEMTECH** covers everything from people management and new chemical technologies, to the latest engineering methods and uses of computers and robotics. **CHEMTECH**'s unique features and fresh approach make it essential reading for all those involved in the chemical professions.

See for yourself the difference CHEMTECH can make.

Subscribe today!

1990 Subscription Prices		U.S.	Canada & Mexico	Europe**	All Other Countries**
Members*	One Year	$39	$48	$52	$55
	Two Years	$66	$84	$92	$98
Nonmembers (Personal)	One Year	$69	$78	$82	$85
	Two Years	$117	$135	$143	$149
Nonmembers (Institutional)	One Year	$299	$308	$312	$315
	Two Years	$508	$526	$534	$540

* Subscriptions at ACS member rates are for personal use only.
**Air Service Included.

CHEMTECH subscriptions may start any month of the year and expire one year later. Please indicate desired starting month. Allow 45 days for your first copy to be mailed. Foreign payment must be made in U.S. dollars by international money order, UNESCO coupons, or U.S. bank draft. Orders accepted through your subscription agency. For nonmember rates in Japan, contact Maruzen Co., Ltd.

To subscribe, write:
American Chemical Society,
Marketing Communications Dept.,
1155 Sixteenth Street, NW, Washington, DC 20036

In a hurry? Call TOLL FREE (800)227-5558 (U.S. only) or (202)452-4363 (in D.C. and outside the U.S.) and charge your order! Fax (202)872-4615 Telex 440159 ACS UI or 89 2582 ACSPUBS

ACS Guarantee–If you are not satisfied with CHEMTECH we will promptly refund the entire unused portion of your subscription price. No questions asked.

Finally, a real GC/MS for under $50,000!

HP 5890 Series II GC sets new industry standards with high temperature operation, cool-on-column injection and pressure programming.

MS ChemStation (DOS series) is 386-based to provide speed and multitasking for highest lab productivity.

Sensitive, universal and specific, the HP 5971A MSD produces true EI spectra even from dirty, complex matrices.

$49,770

Complete quadrupole GC/MS system actually fits on a five-foot lab bench.

Mouse interface simplifies operation.

Now any lab can afford a GC/MS with an HP mass selective detector (MSD). Our new PC-controlled system costs only $49,770,* yet gives you high performance.

There's multitasking for acquiring and analyzing data simultaneously. There's true, classical EI spectra that stand up to challenge. There's Microsoft® Windows software for ease of use. Plus access to PC word processing, spreadsheets and desktop publishing. And for total automation, you can add an optional autosampler and bar-code reader.

Put the system to work in *any* size laboratory. Even network it to other vendors' data systems. Then enjoy the highest uptime in the industry because HP is consistently rated number 1 for reliability, service and support. For more, call **1 800 556-1234, Ext. 10218.** In CA, **1 800 441-2345, Ext. 10218.**

*U.S. list price.
Microsoft® is a U.S. registered trademark of Microsoft Corporation.

HEWLETT PACKARD